Thermal Evolution of the Mid-Crust From the Himalayan Orogen

Thesis

UNRESTRICTED

Thermal evolution of the mid-crust from the Himalayan orogen

A thesis presented for the degree of Doctor of Philosophy

Jennifer Ann Chambers

MGeol. (Leeds) 2004

Department of Earth and Environmental Sciences

The Open University, UK

Submission date: 17 July 2008

Date of award: 22 December 2008

ProQuest LLC.
789 East Eisenhower Parkway
P.O. Box 1346
Ann Arbor, MI 48106 – 1346

Thermal evolution of the mid-crust from the Himalayan orogen

The Haimanta Group, at the top of the exhumed mid-crust in the western Himalaya (Sutlej valley), underwent prograde metamorphism to depths of 25 to 30 km at c. 30 Ma. Initial exhumation of the Haimanta Group was accompanied by further heating, from 610–620 °C up to 660 °C at c. 23 Ma; further exhumation (at c. 1.3 mm/yr) to a depth of c. 7 km during the Early Miocene resulted in cooling to 300–350 °C. Meanwhile, the underlying Greater Himalayan Sequence (GHS) was rapidly exhumed due to coeval extension on the South Tibetan Detachment above and compression on the Main Central Thrust below. The Jutogh Group, with Palaeoproterozoic (c. 1810 Ma) leucogranites characteristic of the Lesser Himalayan Sequence, was buried and metamorphosed beneath the overthrust GHS, and involved the partial recrystallisation of uraninite in leucogranite at 11 Ma.

The Chekha Formation (Radi klippe) in the eastern Himalaya (Bhutan), in a similar structural position to the Haimanta Group, also reveals a history of Oligocene prograde metamorphism, to c. 7 kbars and 550–620°C at c. 22 Ma, synchronous with prograde metamorphism in the underlying GHS (peak metamorphism, c. 24 Ma). Comparable metamorphism and deformation in the Haimanta Group and Chekha Formation, distinct from that in the underlying GHS, is the result of a common tectono-thermal process in the early evolution of the orogen. Pressure–temperature–time data from the metamorphic core are generally consistent with the channel flow model, but may be equally compatible with contesting models.

Uranium(–thorium)–lead isotope analysis of monazite (which formed above 580 °C after, or during the final stages of garnet growth, and probably via the breakdown of allanite and apatite) provided a robust method for dating prograde–peak metamorphism. Samarium–neodymium garnet geochronology was hampered by Ca-bearing Nd-rich garnet inclusions (e.g. allanite).

Acknowledgements

First and foremost I thank both Tom and Nigel for their support, encouragement and general enthusiasm about all aspects of my research – it truly has been a pleasure to have known and worked with you. The same goes for Randy and Matt (geochronology superstars) at NIGL, and Mark Caddick (pseudosection master) at ETH Zurich. I also acknowledge NERC, for without their funding this project would not have been possible.

I thank the various members of other OU earth science staff for their help as I've passed through their labs (Parky, Bruce, Nick, Sam, Andy, Michelle and Kay), as well as the secretaries (Janet and Anita) and Science-IT chaps for dealing with admin and computer-related problems respectively. Life in MK outside of academia has been enjoyed with the likes of Monkey (Chris), Sam, Wes, Josh, Bryony, Mags, Amy, Jess, Susan, Saskia, and all the rest of the postgrads, past and present, who have always been up for a pint in the cellar/pavilion bar. Special mention to my non-earth science fellow postgraduates, Tom and Adèle (to whom I had to rationalise my work in the Himalaya, while they worked on topics related to the semantic web, and genetics and bioethics in Africa), and of course my housemates in Stony, including the Pastafarian (Ziggy), Jen, Russ, Marie and Marc…I have fond, fond memories of life at 10 Market Square. Thanks too to BBC Radio 4 for its countless hours of company during sleepless nights in the last few months of writing up (namely, the World Service and Today programmes), and to my trusty mini-personal radio.

And finally, this thesis is dedicated to Bob, my true 'rock'.

Contents

Appendices

List of Figures

List of Tables

Commonly used abbreviations

LHS	Lesser Himalayan Sequence
LHCS	Lesser Himalayan Crystalline Sequence
GHS	Greater Himalayan Sequence
TSS	Tethyan Sedimentary Series
MCT	Main Central Thrust
STD(S)	South Tibetan Detachment (system)

Cenozoic geologic time scale

From *A geologic time scale 2004*

(edited by Felix M. Gradstein, James G. Ogg,

and Alan G. Smith).

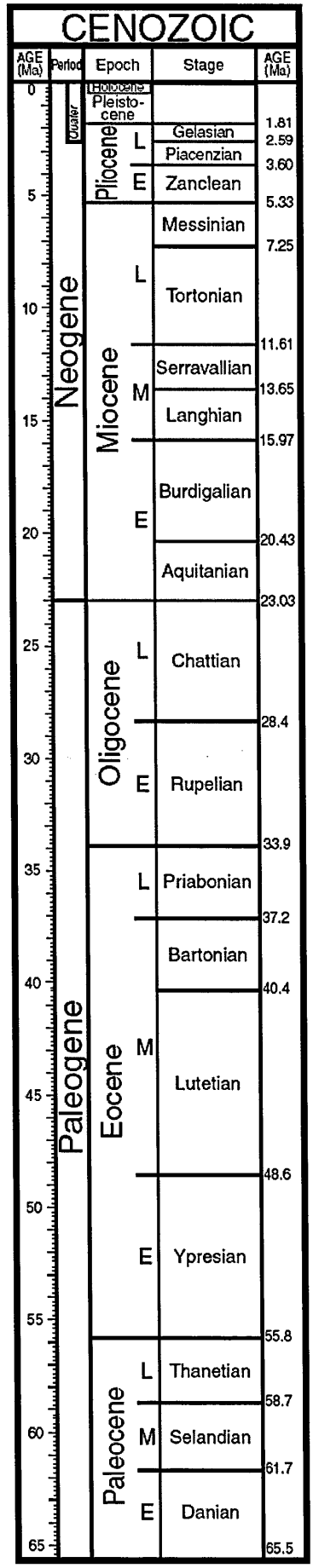

Chapter 1

Introduction

1.1 Project aims

The nature of tectonic processes involved in continental collision can be inferred from the thermal evolution of the crust deformed within this zone. This study aims to contribute to our understanding of the processes involved in the formation of the Himalaya (an active zone of continental collision) through an examination of the tectono-thermal history of the exhumed mid-crust of the orogen. A combination of metamorphic petrology and novel geochronological techniques permit the construction of pressure–temperature–time (*P–T–t*) paths, from which rates and mechanisms of burial and exhumation may be determined. Synthesis of these data with published data from other sources allows a re-examination of the thermal evolution of the exhumed mid-crust of the Himalaya in light of recent models.

1.2 Why study the Himalaya?

The Himalaya, a 2400 km long chain of mountains along the northern margin of India, are the result of deformation during continental collision at the Indian–Eurasian plate boundary. Since collision, at least 34 Myr ago (Aitchison et al., 2007; Hodges, 2000), the orogen has accommodated over 500 km, and in some regions over 900 km of crustal shortening (Searle et al., 2008 and references therein; Yin, 2006). During this time sedimentary rocks initially deposited on the northern continental margin of India have been buried, metamorphosed, exhumed and partially eroded, and crustal deformation continues today (e.g. Bettinelli et al., 2006). Thus the Himalaya present snapshots of the geological phenomena of modern orogenesis: for instance, the crystalline core represents the palaeo-mid-crust, whereas sub-surface structure and seismic activity reflect neo-tectonic processes. Hence we are presented with an ideal natural laboratory in which to test models pertaining to the tectonics of orogenesis. Furthermore, there are several outstanding debates concerning large-scale Himalayan tectonics, including the mode of extrusion of the crystalline core (Section 1.2.2), which demand investigation.

1.2.1 Overview of Himalayan Geology

Detailed descriptions of the geology of each field area studied are presented in the relevant chapters, but the major litho-tectonic units, from north to south (Fig. 1.1) are briefly discussed here. The reader is also directed to Hodges (2000) and Yin (2006) for comprehensive reviews of the geology of the Himalaya.

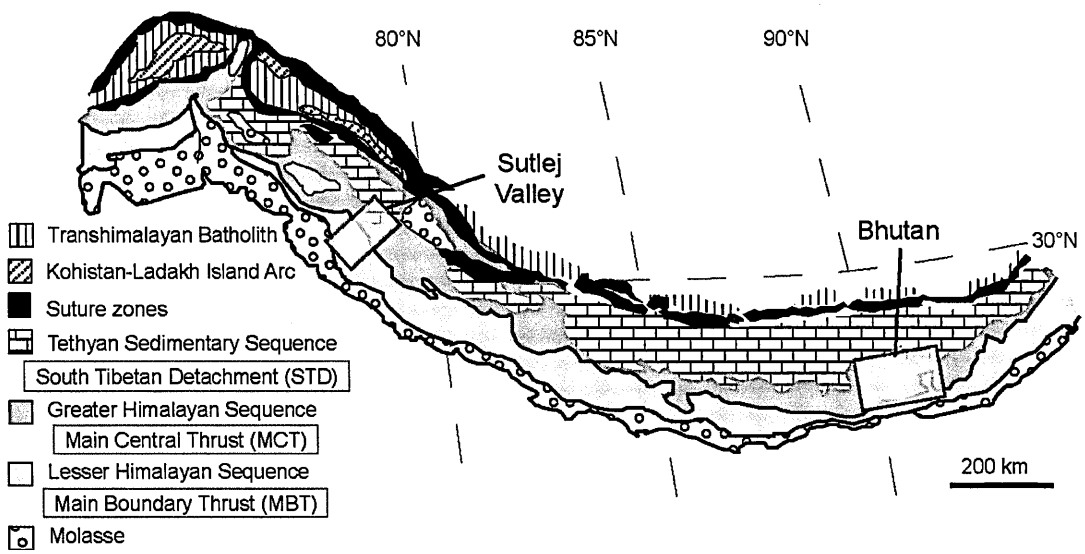

Fig. 1.1 Simplified geological map of the Himalaya. Field areas highlighted.

Trans-Himalayan Batholith and the Kohistan–Ladakh Island Arc

These units form what is known as the Trans-Himalayan Zone, and represent the southern margin of Eurasia prior to collision with the Indian continent. Northward subduction of the Neotethys oceanic crust beneath the Eurasian plate led to Andean-style plutonism, resulting in the numerous granitic to granodiorite intrusions now aligned along the southern margin of the Asian plate, in southern Tibet (north of the Himalayan mountain peaks). The Kohistan–Ladakh island arc (cropping out in the western Himalaya) was accreted to the southern margin of the Eurasian plate before closure of the Tethyan Ocean, and a near-complete section through the island arc is exposed, from layered ultra-mafic cumulate rocks to marine sediments (Hodges, 2000 and references therein). Subduction-related calc-alkaline magmatism dates from c. 100 Ma (mid-Cretaceous) to at least 37 Ma (latest Eocene), and provides a maximum constraint on the age of collision, assuming

that shortly after collision the presence of continental lithosphere (as opposed to oceanic) in the subduction zone effectively 'shut-off' calc-alkaline melt generation (Aitchison et al., 2007).

Indus–Tsangpo Suture Zone

This zone of metabasites and metasedimentary rocks intercalated with ophiolitic rocks marks the point of collision between the Indian and Eurasian plates. Blueschist-facies metamorphism (high-pressure, low-temperature conditions) provides evidence of subduction in the mid-Cretaceous (80 and 100 Ma), followed by rapid exhumation (Guillot et al., 2008 and references therein).

Tethyan Sedimentary Series (TSS)

This thick (10–15 km) succession of Cambrian to Eocene sediments represents the upper deposits on the northern passive margin of the Indian continent (Aitchison et al., 2007; Gaetani and Garzanti, 1991). The Tethyan sediments were originally considered conformable on the crystalline orogenic core (e.g. Gansser, 1964), but since then a series of north-dipping low angle detachments (ductile and brittle), known collectively as the South Tibetan Detachment System (STDS), have been recognised at the base of the unit (Burchfiel et al., 1992; Burg et al., 1984). The sediments are typically unmetamorphosed, save for the basal TSS in some regions where rocks reach amphibolite-grade (e.g. the Haimanta Group in the western Himalaya, Chapter 2).

A series of gneiss domes crop out in the TSS within the North Himalayan antiform (NHA) (Fig. 1.2; also see Figure 1 in Guo et al., 2008). Some 'North Himalayan gneiss domes' (NHGD) are cored by Cambrian granitoid plutons (variably deformed and metamorphosed during Himalayan orogenesis) and most domes studied to date incorporate syn- to post-tectonic Miocene leucogranite intrusions (Table 1 in Quigley et al., 2008). It has been proposed that the NHGD represent hinterland doming that has exposed mid-crustal rocks (e.g. Murphy, 2007; Quigley et al., 2008 and references therein).

Greater Himalayan Sequence (GHS)

Also known as the High Himalayan Crystalline Sequence, this high-grade, highly deformed metasedimentary unit forms the metamorphic core to the Himalayan orogen. Provenance studies of

the GHS (e.g. DeCelles et al., 2000; Parrish and Hodges, 1996; Richards et al., 2005) suggest Neoproterozoic to early Palaeozoic (c. 800–500 Ma) deposition of the sedimentary protolith.

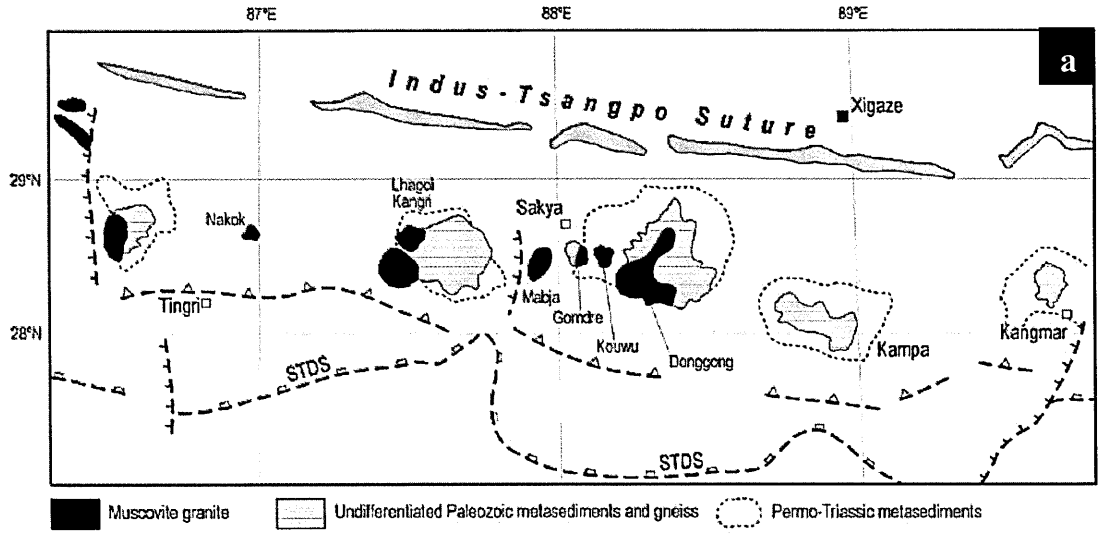

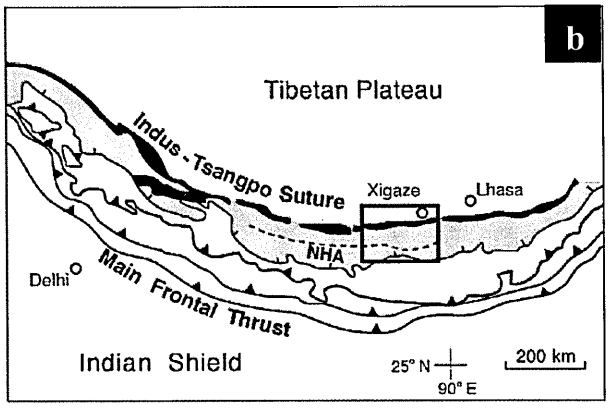

Fig. 1.2 a) Geological map of the North Himalayan gneiss domes in the central Himalaya, b) their location within the orogen in the core of the North Himalayan antiform (NHA). Both Figures from Watts and Harris (2005).

Deformed Cambrian granites intrude the GHS (Miller et al., 2001) and constrain the minimum age of the GHS. The uppermost GHS typically contains abundant leucogranite intrusions (dykes, sills and plutons termed the High Himalayan leucogranites) (Harrison et al., 1999, and references therein), the product of early Miocene crustal anatexis (Harris and Massey, 1994). The base of the GHS is bounded by a major shear zone, the Main Central Thrust (MCT) (Heim and Gansser, 1939). The MCT has been the subject of some controversy in the literature, and a summary is presented below (Section 1.2.2) in order to provide some clarification. Extrusion of the GHS occurred during the early Miocene, via coeval movement on the MCT and the STD. Further details on extrusion mechanisms are presented in Section 1.2.2.

Lesser Himalayan Sequence (LHS)

This represents the Palaeoproterozoic to Mesoproterozoic (c. 2500–1000 Ma) sedimentary cover to the Indian basement, metamorphosed typically up to greenschist-grade, but in some transects, up to amphibolite-grade where it may be termed the Lesser Himalayan Crystalline Sequence (LHCS, Vannay et al., 1999) (e.g. Jutogh Group in the Sutlej valley, Chapter 2). The LHS also features Proterozoic acidic and basic intrusions (Miller et al., 2000). These rocks form the foothills of the Himalaya, the base of which is bounded by the Main Boundary Thrust.

Sub-Himalaya

This unit encompasses early Miocene to modern day molasse deposits (Siwalik Group) derived from the exhumed crystalline units to the north (LHS, GHS). These deposits provide a record of the unroofing of the crystalline core though the early Miocene (White et al., 2002), invaluable to exhumation models (presented below). The Sub-Himalaya is actively being internally deformed and thrust southwards onto the Indian craton along the Main Frontal Thrust.

1.2.2 Fieldwork

There is great lateral consistency along the strike of the Himalaya with respect to the major lithotectonic units (Fig. 1.1). However, there are geological distinctions to be made from one transect to another, and these provide important clues as to the tectonic processes responsible for the architecture of the orogen. The Sutlej valley, NW India (western Himalaya) and Bhutan (eastern Himalaya) (Fig. 1.1) are two contrasting regions; for example, the width of the GHS in the Sutlej valley is one of the narrowest, whereas Bhutan has the widest outcrop of GHS, including klippen of the TSS (see Chapters 2, 4 and 6 for more detail). Regional-scale tectonic models should account for the localised lateral variation observed, in order to provide a robust tectonic reconstruction of Himalayan evolution.

Fieldwork was conducted in the Sutlej valley and in Bhutan during the Springs of 2005 and 2006 respectively. Study in the western Himalaya complements previous work undertaken at the Open University by former PhD students (e.g. H. Williams, C. Prince , G. Foster and A. Richards), one of which (Richards) completed an isotopic study characterizing different Himalayan units in

both the Sutlej valley and in Bhutan. This paved the way for further geological expeditions, vital to the study in Bhutan whose geology remains relatively under-explored. Another aspect of this comparative study between eastern and western Himalayan regions is the variation in present (and probably past) climate between the two (precipitation rates generally increase eastwards along the Himalaya) (Harris, 2007), providing an opportunity to compare possible climate–tectonic feedback mechanisms (see below).

1.2.3 Models of extrusion of the crystalline core

With increasing depth, the temperature of the continental crust also increases. Thus, the greater the depth to which a crustal rock is buried in response to continental collision, the higher its temperature of equilibration (given sufficient time for heat to conduct into the buried rock). The mid-crustal rocks now exposed across the Main Central Thrust (MCT) shear zone (from garnet-grade schists of the upper LHS into the gneissose GHS above) exhibit an *inverted* metamorphic field gradient (i.e. higher grade at shallower depths). This does not however, necessarily represent an inverted geotherm at any one time; for example post-peak folding of isograds may cause apparent inversion, or preserved assemblages may have formed diachronously. Nonetheless, the geological phenomenon of apparent inverted metamorphism observed in a number of Himalayan transects must be indicative of a major tectono-thermal process, and has spawned a generation of models of mid-crustal extrusion to account for it. At the same time these models seek to offer explanations for other first-order observations e.g. the North Himalayan gneiss domes, and normal shear along the STDS. Below I summarise these models, from which the popular channel flow model (Beaumont et al., 2001) has developed (an assessment of which was the original intention of this PhD project). It is useful to remember that *exhumation* is the exposure by denudation of overlying material (after burial), *denudation* is the all-encompassing name for the processes involved in exposure of rock (including, for example, erosion and weathering), and *extrusion* is the process of pushing or thrusting.

Identification of the STDS (Burg et al., 1984; Burchfiel et al., 1992) led to the concept of the extrusion of a wedge of mid-crustal (GHS) material, facilitated by simultaneous movement on the extensional fault system and the MCT during the Miocene (refer to Figure 4 in Godin et al., 2006b)

(Fig. 1.3). It was considered the expression of gravitational collapse of the topographic front, triggered by a major reduction in crustal strength in the wedge as a result of melting, effectively decoupling the upper crust (Burchfiel et al., 1992). This decoupling of crustal layers is required as the Himalaya represent a zone of regional compression, ongoing in the mid to lower crust. In fact, Vanderhaeghe and Teyssier (2001), in their review of the thermo-mechanical evolution of four orogenic belts of various ages, suggest that the Tibet–Himalayan system is representative of a large orogen *before* gravitational collapse. Hodges et al. (1993) present the thermal consequences of wedge extrusion between the STD and MCT: rocks in the middle of the GHS experienced isothermal decompression, whereas closer to the MCT at the base of the GHS section, more significant cooling during decompression took place, in response to underthrusting of cooler (LHS) rocks. Ultimately, an inverted temperature gradient was generated.

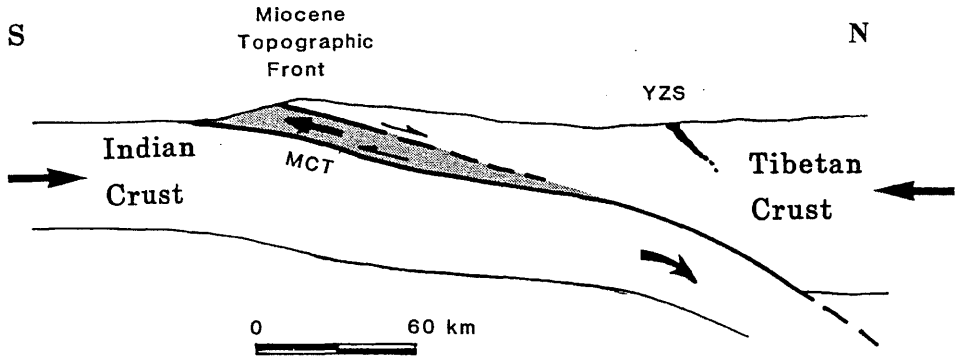

Fig. 1.3 Schematic cross-section of the Himalayas in Miocene time, featuring gravitational collapse of the topographic front and extrusion of a mid-crustal wedge (Burchfiel et al., 1992). YZS = Yarlang–Zangbo suture.

The formation of the inverted metamorphic sequence documented in the Himalaya has also been attributed to the tectonic modification of an originally right-way-up (normally-zoned) metamorphic sequence through 1) ductile folding of pre-existing isograds (Searle and Rex, 1989), 2) imbricate thrusting (Arita, 1983), and 3) ductile shearing (Hubbard, 1996; Jain and Manickavasagam, 1993). Combined with the concept of an extruding wedge (i.e. coeval movement on the MCT and STD), models now encompassed penetrative ductile shearing of the entire GHS wedge in which pre-existing (right-way-up) metamorphic isograds were folded or translated to create an inverted metamorphic sequence (Fig. 1.4a) (Davidson et al., 1997; Grasemann et al.,

1999; Grujic et al., 1996; Vannay and Grasemann, 2001). Grujic et al. (1996) related this extrusive flow to channel flow models used to describe subduction zone processes (e.g. England and Holland, 1979; Mancktelow, 1995; Shreve and Cloos, 1986), and accounted for the extrusion of the GHS wedge not by gravitational collapse, but rather by the flow of low viscosity mid-crustal material driven by a lateral pressure gradient. High-temperature decompression, strain heating and/or crustal melting are all considered viable mechanisms that would reduce the viscosity of the GHS sufficiently to allow channel flow (Grujic et al., 1996 and references within); indeed, strain (or shear) heating has previously been proposed as a cause of inverted metamorphism in the Himalaya (Molnar and England, 1990).

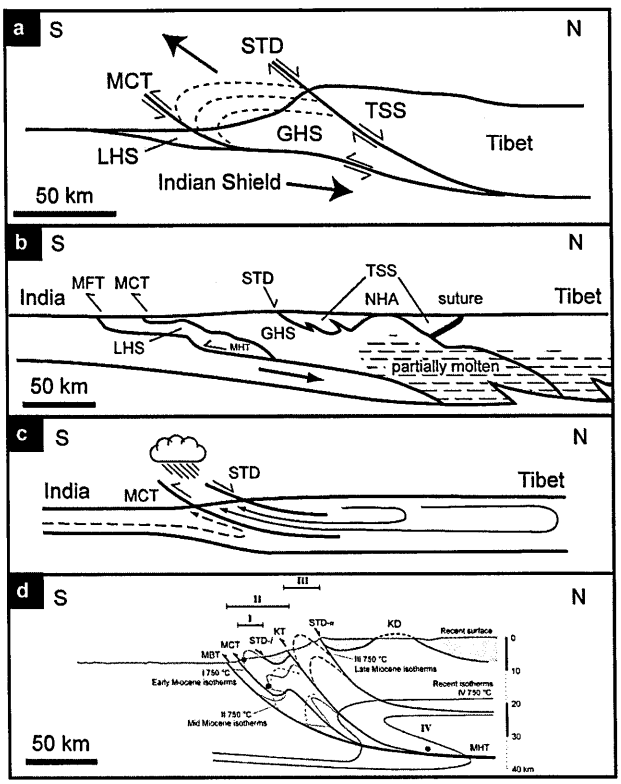

Fig. 1.4 Schematic cross-sections to illustrate exhumation models for the Himalaya: a) depicts the wedge-shaped geometry of the GHS, and its southward extrusion facilitated by coeval movement on the MCT and STD (after Hodges et al., 1993), while pervasive ductile deformation during extrusion of the wedge folds isograds (dashed lines) to form an inverted metamorphic sequence at lower structural levels (e.g. Grujic et al., 1996); b) interpretation of the sub-surface geology based on the INDEPTH profile (Nelson et al., 1996); c) the channel flow model, where arrows represent particle paths illustrating the 'entrainment' of material above and below the weakened extruding mid-crustal channel (Beaumont et al., 2001; Jamieson et al., 2004). d) pulsed channel flow model proposed for Bhutan (Hollister and Grujic, 2006). Greater Himalayan Sequence (GHS), Lesser Himalayan Sequence (LHS), Tethyan Sedimentary Series (TSS), Main Central Thrust (MCT), South Tibetan Detachment (STD), Main Himalayan Thrust (MHT), North Himalayan antiform (NHA).

Imaging of the crustal structure beneath the Himalaya revealed that the MCT and STD shear zones may not converge at depth (Hauck et al., 1998; Makovsky et al., 1999; Nelson et al., 1996). Furthermore, results from the International Deep Profiling of Tibet and the Himalaya (INDEPTH) project, imply that a partially molten mid-crustal layer (low viscosity zone) exists under southern

Tibet (Fig. 1.4b) (Alsdorf et al., 1998; Hauck et al., 1998; Nelson et al., 1996). The channel flow model (Beaumont et al., 2001) encompasses both of these observations: a channel of low-viscosity material in the mid-crust (equivalent to the exhumed GHS) beneath southern Tibet extrudes out towards the topographic front as a result of 'melt-weakening' (by radioactive self-heating) in the tectonically-thickened crust (Fig. 1.4c). The channel flow model is sensitive not only to lateral pressure gradients and viscosity, but also to focussed surface denudation (precipitation and/or river incision) at the topographic front. This concept of feedback between erosion and tectonics in the Himalaya was established at the syntaxes of the orogen, where focussed erosion along major rivers is associated with rapid exhumation rates (Zeitler et al., 2001). Variations in the surface denudation rate and upper crustal rheology may lead to hinterland doming and exhumation of the channel (analogous to the North Himalayan gneiss domes) (Jamieson et al., 2006), and eastward lower crustal flow from beneath the Tibetan plateau (Clark and Royden, 2000) is considered an expression of channel flow in the absence of denudation (Beaumont et al., 2001; Jamieson et al., 2004). The channel flow model is also compatible with the observed inverted metamorphic sequence, and Jamieson et al. (2004) predict a systematic trend in model *P–T–t* path styles across the putative channel. Recent developments of the channel flow model include the pulsed channel flow model wherein three pulses of extrusion of the mid-crust are identified (Hollister and Grujic, 2006) (Fig. 1.4d; also see Chapter 6). A comprehensive critical review of channel flow in the Himalayan–Tibetan orogen is presented by Harris (2007), and other orogens have been interpreted through similar models, e.g. the Appalachians (Hatcher and Merschat, 2006) and the Canadian cordillera (Brown and Gibson, 2006), demonstrating that channel flow may represent a fundamental process during orogenesis.

An objective of this project is to enlighten the debate on channel flow, and provide additional constraints for future tectonic models of orogenesis. Since the metamorphic core of the Himalaya suffered the effects of high-temperature re-setting (e.g. garnet profiles are homogenised with respect to major elements), thus eradicating much of the prograde history of the rock, the bounding edges of the putative channel (GHS), characterised by lower-grade metasediments, were targeted areas for sampling. It is hoped that quantified tectono-thermal histories of the units

bounding the GHS will permit a more complete assessment of the thermal evolution of the exhumed mid-crust of the Himalayan orogen.

Two other models have recently been applied to Himalayan orogenesis, and are summarised below. Although they may share some of the fundamental kinematics with the channel flow model, e.g. southward extrusion of the GHS over the LHS on the MCT during the Early Miocene, they differ in terms of their dynamics, e.g. a strong climate–tectonic feedback is not required for rapid exhumation of the GHS as established in the channel flow model. Unfortunately, neither model offers thermal predictions specific to the upper GHS/lower TSS (i.e. across the STD). This limits the discussion of *P–T–t* results from this thesis (namely Chapters 3 and 6) to the channel flow model (Chapter 7).

Critical taper model

The basic principle of this model is that the orogenic wedge is rheologically and therefore mechanically homogeneous, and everywhere is at the point of critical failure (and hence may also go by the name of a 'Coulomb wedge') (e.g. Dahlen 1990). The analogy, of a bulldozer scraping up a wedge of sand, is shown in Figure 1.5. Accretion/underplating of new material at the toe/base of the wedge, and erosion, increase and decrease the taper of the wedge respectively. In order to maintain the critical taper of the wedge (and a dynamic steady-state), the wedge deforms internally. In detail, an orogenic wedge that is thick enough to induce metamorphism is unlikely to conform to models that exclusively prescribe brittle or ductile deformation mechanisms (Platt, 1986). At depth ductile deformation will dominate, as opposed to brittle deformation near the surface and toe of the wedge (Fig. 1.6). Brittle (discrete) deformation however, is not currently a feature of the tectonic models discussed here (including the channel flow model that is based on continuum mechanics), which consider a larger crustal section and are therefore dominated by ductile processes.

The critical taper model of Kohn (2008) (based on Henry et al., 1997 and Bollinger et al., 2006) of Himalayan orogenesis (Fig. 1.7) assumes that the MCT is the Early Miocene equivalent of the present ductile decollement, the Main Himalayan Thrust, to which all Himalayan faults are believed to sole into (Fig. 1.4b). Thrust sheets are successively abandoned as deformation (thrusting) propagates towards the foreland in response to frontal accretion and/or underplating of

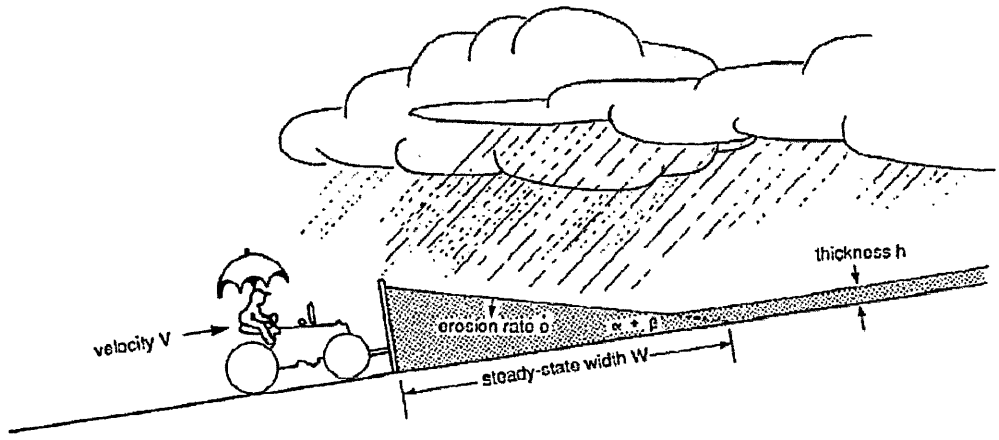

Fig. 1.5 A bulldozer wedge: the cartoon analogy to an accretionary prism or fold–and–thrust belt. The eroding wedge shown attains a dynamic steady-state width (Dahlen, 1990).

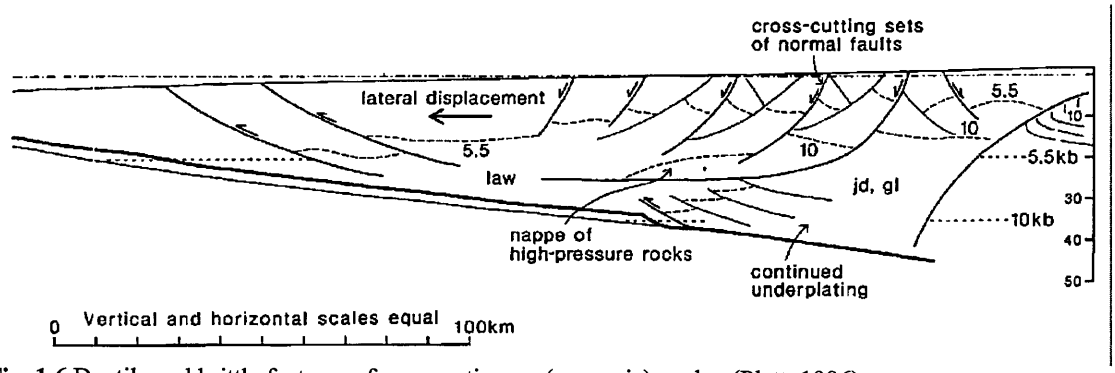

Fig. 1.6 Ductile and brittle features of an accretionary (orogenic) wedge (Platt, 1986).

material from the underthust Indian lithosphere. In contrast to the channel flow model, normal faulting in the hinterland (comparable to the STD) is not a primary feature. The main distinction between critical taper and channel flow, is that in the latter the large-scale flow of the weak mid-crust dominates the thermo-mechanic evolution of the orogen. Critical taper models do not preclude weak portions of the crust, but any flow is restricted and has a minor influence on the thermal structure. These differences in the scale of flow are reflected in contrasting model *P–T–t* data (see Table 2, Kohn, 2008). Empirical data from Nepal favour critical taper as the dominant orogenic process, whereas other regions of the Himalaya currently lack the data resolution (and often precision) to confidently assign the governing mechanism. Note that no *P–T–t* predictions specific to the upper GHS/lower TSS (i.e. across the STD shear zone) are made in the critical taper model.

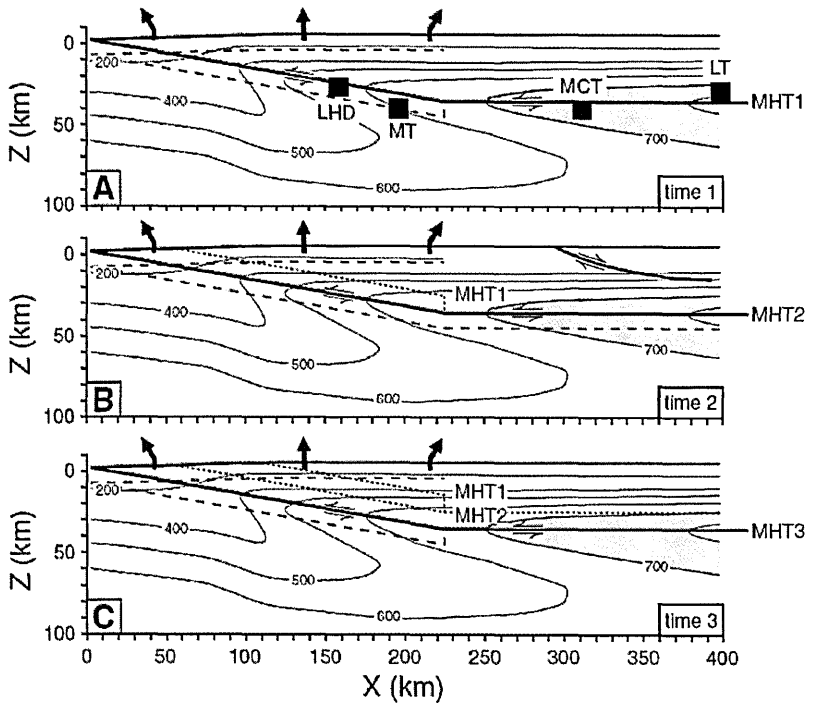

Fig. 1.7 Schematic steady-state, critical taper model for the Himalaya (Kohn, 2008). Erosion (black arrows) is distributed uniformly across the frontal part of the orogen; migmatite zone shown by grey shading; future position of wedge shown by dashed lines; past traces of Main Himalayan Thrust (MHT) shown by dotted lines

Tectonic–wedging model

In NW India, the Main Central Thrust–South Tibetan detachment branch line, i.e. the tip of the GHS, has been identified (Webb et al., 2007). This is inconsistent with the channel flow model, which requires that the MCT and STD to be surface-breaching faults. Furthermore, the evidence for alternating top-to-the-north and top-to-the-south shear fabrics in the STD shear zone in this region is deemed incompatible with channel flow, which simply prescribes top-to-the-north sense of shear on the STD. However, it is plausible that these are small-scale/near-surface features not resolved in the large(crustal)-scale channel flow models. Thus a new kinematic model is presented, compatible with the observed geometry and kinematics (Fig. 1.8). This 'tectonic-wedging' model will be more valuable to petrologists once it is presented as an integrated thermal and mechanical model.

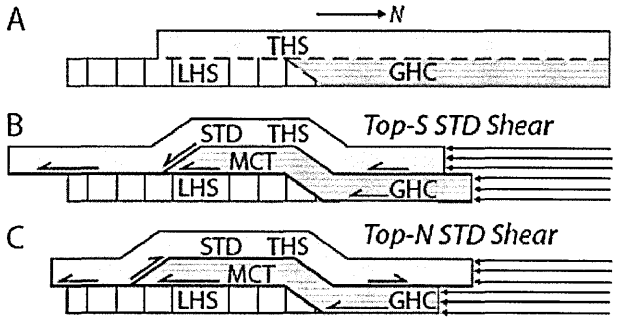

Fig. 1.8 Tectonic wedge model for emplacement of the GHS (Webb et al., 2007). A: pre-deformation geometry. B and C: GHC emplacement during top-to-the-S (B), and top-to-the-N (C), faulting along South Tibet detachment.

The Main Central Thrust (MCT)

During the course of this project, it became apparent that the definition of the lower boundary, the MCT (Harris, 2007; Searle et al., 2008), is still contentious (Kohn, 2008; Searle et al, 2008). The following overview of the usage of the term 'the MCT' may serve as a useful guide to anyone new to Himalayan geology, and aims to clarify what is a complicated, and to some degree purely semantic issue.

Heim and Gansser (1939) and Gansser (1964) are responsible for much of the Himalayan geological terminology still in use today, such as the Higher Himalayan (crystalline) series (HHCS or GHS), Lesser Himalayan series (LHS), and the MCT which lies at the contact between the two units. The Main Central Thrust *mass* was described as "an enormous deep-rooted body of injected crystalline rocks", where thrusting took place at depth, not along a discrete plane but rather over a ductile zone (Heim and Gansser, 1939). This is equivalent to the Main Central Thrust Zone (MCTZ) of distributed shear over a section up to 10 km thick (e.g. Grujic et al., 2002). Gansser (1964) identified the MCT as a discrete fault at the bottom of this crystalline mass, but cautioned that "rarely [is] a clear cut thrust line is visible in the field" (p.95). In the Kumaon Himalayas (also known as the Garwhal Himalaya), where Gansser spent much of his geological investigations, the MCT was identified as the (lithological) contact between quartzite and gneiss, yet the exact location was difficult to define due to intercalations of crystalline (hanging wall) rocks with (footwall) quartzites. The contrast in lithology between the LHS and GHS is still used to infer the trace of the MCT in some places (e.g. in Bhutan, Daniel et al., 2003).

Other indirect criteria have been used to identify and define the MCT, including Nd isotopes and U–Pb zircon ages to characterise the provenance of the LHS and GHS metasediments. (Imayama and Arita, 2008 and references therein). This 'stratigraphic' MCT represents either a pre-Himalayan unconformity between two laterally continuous basinal deposits, or a proto-MCT (i.e. pre-Himalayan fault zone), variably tectonized during Himalayan orogenesis (Goscombe et al., 2006).

Strictly-speaking, the MCT, a major shear zone, should be identified using structural mapping and strain indicators alone, and defined by a clear localisation of strain, i.e. the maxima within a shear gradient (Searle et al., 2008). However, there are difficulties in strain analysis owing to the differing rheological response of various lithologies, and pre-existing structures (tectonic and stratigraphic), which both present planes of relative weakness along which shear strain will be more readily accommodated.

In reality, the whole GHS, the Main Central zone mass (Heim and Gansser, 1939) is penetratively deformed by top-to-the-south shear. Within this mass, a higher-strain zone (<2 km thick) towards the base is often recognisable, within which there are likely to be multiple planes of maximum strain (mylonites), undoubtedly exploiting zones of relative weakness. One (or two, e.g. Arita, 1983) of these may stand out from the rest and be identified as *the* MCT. Alternatively, Searle et al. (2008) suggest that the *brittle* fault at the base of this zone be identified as the MCT fault. However, this idealised picture is obscured by the fact that the main locus of thrusting on the MCT may have migrated over time to deeper structural levels. The location of a major thrust here relies on the determination (and discrimination) of the tectono-thermal histories for the hanging wall and footwall rocks via *P–T–t* analysis (e.g. in the Sutlej valley, Caddick et al., 2007).

1.3 Dissertation structure

Chapters 2 and 3 of this thesis present results from the exhumed mid-crust in the Sutlej valley (western Himalaya). The first of these presents new data characterising the crystalline LHS (Jutogh Group), including Palaeoproterozoic intrusions which recrystallized during the Miocene. These data firmly establish this unit as a tectonic block distinct from the overthrust GHS. This chapter has been published verbatim in the Journal of the Geological Society of London, and also

features contributions from T. Argles (field and structural geology), N. Harris (igneous geochemistry), M. Horstwood and R. Parrish (U–Pb geochronology) and Talat Ahmad (field work). Chapter 3 complements the first, as it constrains earlier tectonic processes in the same transect, in upper levels of the metamorphic core (Haimanta Group) in the hanging wall to the STD. This work has been presented at the American Geophysical Union (AGU) Fall meeting (2007) and has been submitted as a manuscript to Tectonophysics, as a contribution to a thematic volume based upon the AGU session topic. Contributions from M. Caddick (pseudosection construction), T. Argles (field and structural geology, petrology), M. Horstwood and R. Parrish (U–Pb geochronology), S. Sherlock (Ar/Ar geochronology), N. Harris (petrology) and Talat Ahmad (field work) are acknowledged.

The fourth chapter chronicles development of Sm–Nd garnet geochronology, using metapelitic samples from the Sutlej valley. The objective was to obtain garnet ages (i.e. constrain the age of prograde metamorphism) from samples across the crystalline core (from structurally low to high levels), and to assess variations in the timing and extent of metamorphism. The results of garnet leaching experiments (to exclude problematic Nd-rich garnet inclusions e.g. monazite and allanite) are important to the future development of Sm–Nd isotopic garnet analysis.

Chapter 5 is a short chapter summarising the data from the Sutlej valley and proposes possible further work.

Chapter 6 presents field, chronological and metamorphic data from Bhutan (eastern Himalaya), specifically from the east of the country at the base of the Radi klippe. Samples from either side of the 'lower' STD here (Chekha Formation in the hanging wall, GHS in the footwall) yield data that allow an investigation into the proposed 'pulsed' channel flow model (Hollister and Grujic, 2006), as well as a comparative study with the western Himalaya (Chapter 3) which forms the meat of the penultimate chapter (Discussion).

The final chapter is a brief review of the most pertinent conclusions of this thesis. Enjoy.

Chapter 2

Tectonic implications of Palaeoproterozoic anatexis and Late Miocene metamorphism in the Lesser Himalayan Sequence, Sutlej Valley, NW India

Abstract: Unravelling the kinematic evolution of orogenic belts requires that the defining tectono-stratigraphic units, and structural elements that bound them, are properly identified and characterized. In the Sutlej Valley (western Himalaya), the Munsiari and Vaikrita thrusts have both been correlated with the Main Central Thrust. The sequence of amphibolite-grade rocks (the Jutogh Group) bounded by these faults has been variously assigned to the Lesser Himalayan Sequence (based on provenance ages) and to the Greater Himalayan Sequence (from their metamorphic grade). Trace-element and geochronological data from leucogranites in the Jutogh Group (i) indicate crustal melting at *c.* 1810 Ma, before the deposition of the Greater Himalayan Sequence, thus correlating the Jutogh Group with the Lesser Himalayan Sequence, and (ii) record Proterozoic metamorphism overprinted at 10.5 ± 1.1 Ma (established from U–Pb analysis of uraninite) during the Himalayan orogeny. Pressure–temperature–time data affirm that the Jutogh Group and Greater Himalayan Sequence represent distinct tectonic units of the metamorphic core that were decoupled during their extrusion. This precludes extrusion along a single, widening channel, and requires a southward shift of the locus of movement during the Late Miocene, coincident with present-day precipitation patterns.

2.1 Introduction

Key litho-tectonic units in the Himalaya e.g. the Greater Himalayan Sequence, and the major faults that bound them e.g. the Main Central Thrust, can be traced continuously along the 2400 km strike of the orogen (Fig. 1.1). Understanding the metamorphic evolution of such units together with the recognition of the nature, location and timing of the principle structural elements of an orogenic belt is fundamental both to defining the tectonic architecture of that belt and to understanding the mechanical behaviour of continental crust during its deformation.

The Greater and Lesser Himalayan Sequences are two key litho-tectonic units in the Himalaya. Using provenance studies based on detrital zircon ages (DeCelles et al., 2000; Richards et al., 2005) and Nd isotopic compositions (Parrish and Hodges, 1996; Ahmad et al., 2000; Robinson et al., 2001; Richards et al., 2005) the sequences are stratigraphically defined; the deposition age of the Lesser Himalayan Sequence is Palaeoproterozoic to Mesoproterozoic (*c.* 2500 to 1000 Ma), in contrast with the younger Greater Himalayan Sequence (synonymous with the High Himalayan Crystalline Series), deposited in Neoproterozoic to Cambrian times (*c.* 800 to 500 Ma). The sequences represent two laterally continuous basinal sequences deposited on the Indian passive margin (Le Fort, 1975), and prior to continental collision may have been separated by either a 'proto-Main Central Thrust' lineament or the Himalayan Unconformity (Goscombe et al., 2006).

In general, the crystalline core of the Himalayas (the Greater Himalayan Sequence) was thrust southward over the lower grade Lesser Himalayan Sequence on the Main Central Thrust. This shear zone is a key component in all tectonic reconstructions of the orogen (e.g. Yin, 2006 and references therein) yet its characteristics, significance and specific location have challenged Himalayan geologists for many decades (Gansser, 1964; Le Fort, 1975; Hodges, 2000).

One reason for this uncertainty is that the crustal architecture of the orogen is complicated in some areas by at least two major thrusts, one or both of which have been referred to as the Main Central Thrust using various criteria (reviewed in Yin, 2006), hindering correlation of the adjacent tectonic units. Such is the case for the Sutlej Valley of NW India (Fig. 2.1). Although lithologies

assigned to the Lesser Himalayan Sequence are typically unmetamorphosed, or at most are metamorphosed to chlorite or biotite metamorphic grade, the Sutlej Valley exposes a more complex transect within which a crystalline zone, the Jutogh Group, is assigned by some authors to the Lesser Himalayan Sequence, and termed the Lesser Himalayan Crystalline Sequence (Vannay et al., 1999; Thiede et al., 2004). This is supported by a marked contrast in isotope geochemistry, pressure–temperature–time paths, garnet morphologies and monazite ages between these rocks and the Greater Himalayan Sequence (Catlos et al., 2001; Kohn et al., 2004; Richards et al., 2005; Caddick et al., 2006). Other authors, using metamorphic grade as the primary criterion for recognising Lesser Himalayan Sequence lithologies and thus the Main Central Thrust (e.g. Sharma, 1977; Singh et al., 2006), assign the crystalline rocks to the Greater Himalayan Sequence.

This study clarifies tectono-stratigraphic relationships in the Sutlej Valley through analysis of leucogranite emplaced into the enigmatic Jutogh Group. We use trace-element data to establish the mode of melting for the leucogranites, and U–Pb dating of accessory phases to a) constrain the ages of both melting and protolith formation, and b) identify a later recrystallization event. In comparing the results with those for the well-documented High Himalayan leucogranites, which intruded high-grade rocks unambiguously assigned to the Greater Himalayan Sequence, we establish the true affinity of the Jutogh Group. Finally, we consider the tectonic evolution of the metamorphic core of the Sutlej Valley with regards to recent thermo-mechanical orogenic modelling.

2.2 Field relations and petrology

In the Sutlej Valley, a zone of metasediments and orthogneiss separates the high-grade metasediments of the Vaikrita Group (Valdiya, 1988) of undisputed Greater Himalayan Sequence affinity from the greenschist-grade sediments of the Rampur window of clear Lesser Himalayan Sequence affinity (Fig. 2.1, 2.2). This enigmatic zone is often viewed as part of the Greater Himalayan Sequence (e.g. Singh and Jain, 1993) but has also been mapped as the Lesser Himalayan Crystalline Sequence (e.g. Vannay et al., 1999). These crystalline rocks, termed the Jutogh Group, include the Wangtu Gneiss Complex and the amphibolite-grade Jutogh (or Jeori) metasediments (Singh and Jain, 1993; Vannay et al., 2004; Richards et al., 2005) (Fig. 2.2).

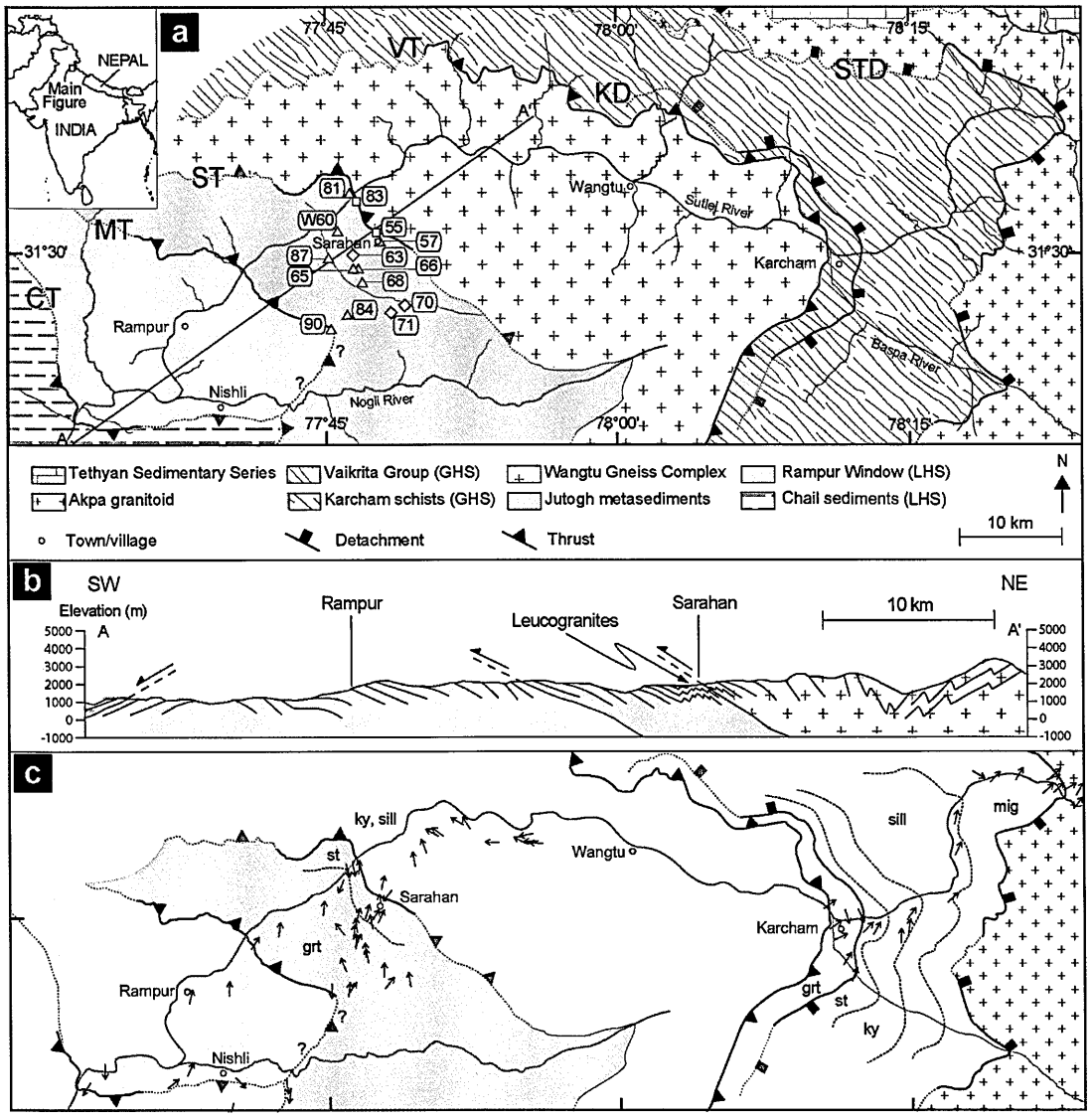

Fig. 2.1 (**a**) Geological sketch map of a section of the Sutlej Valley after Caddick et al. (2007), based on Vannay et al. (1999), with modifications from own field observations. Jutogh Group localities (sample set 'JC I05') marked by diamonds (leucogranites), triangles (metasediments) and squares (sheared amphibolite); 'W60' from Richards et al. (2005). Line A–A' marks the location of the cross-section in (b). Abbreviations: GHS = Greater Himalayan Sequence; LHS = Lesser Himalayan Sequence; STD = South Tibetan Detachment; VT = Vaikrita Thrust; KD = Karcham Detachment; ST = Sarahan Thrust; MT = Munsiari Thrust; CT = Chail Thrust. (**b**) Cross-section with detailed foliation trajectories projected onto the line of section (A–A' in (a)) from field measurements. (**c**) Simplified geological sketch map showing stretching lineations and metamorphic isograds (where the zone, as opposed to the 'mineral-in' line, is labelled). Abbreviations: grt = garnet; st = staurolite; ky = kyanite; sill = sillimanite; mig = migmatite.

There is a gradual transition down-section from the main 1.87 Ga Wangtu orthogneiss (Richards et al., 2005), through intercalated orthogneiss, paragneiss and calc-silicate rocks, into the metasedimentary gneisses and mica schists. If the relationship between the gneiss and the metasediments was originally intrusive it is now obscured by subsequent deformation and tectonism, including a 50 to 80 m wide thrust zone which strikes broadly NW–SE between the town of Sarahan and the Sutlej River, here termed the Sarahan Thrust (Figs. 2.1, 2.2), and probably equivalent to the Chaura Thrust (Jain et al., 2000). This thrust zone is marked by a tectonic mélange (locality 55) of sub-rounded clasts (several centimetres to tens of metres across) of fine-grained, mafic amphibolite in a friable, sheared biotite–chlorite matrix with top-to-the-SE kinematic indicators (Figs. 2.2, 2.3). A strongly sheared mafic amphibolite exposed on the banks of the Sutlej River near Jeori (Fig. 2.1a, locality 83, and Fig. 2 in Singh and Jain, 1993), featuring micro-fine laminae and euhedral garnet porphyroblasts, is interpreted to be the SW continuation of the Sarahan Thrust where the scarcity of pelitic material has inhibited the formation of a mélange as described above.

In the immediate hanging wall of the Sarahan Thrust, kink and chevron-type folds in the Jutogh metasediments verge consistently to the south implying that they are related to the top-to-the-south motion on the Sarahan Thrust. Within the Wangtu Gneiss stretching lineations change orientation progressively from west-plunging in the core of the complex (probably representing a pre-existing lineation orientation) to north- or NNE-plunging in both the hanging wall and footwall of the Sarahan Thrust (Fig. 2.1c), suggesting a genetic relationship with the south-directed thrusting.

Jain et al. (2000) show that the Sarahan (Chaura) Thrust marks a sharp discontinuity in apatite and zircon fission track data, indicating faster exhumation of the Wangtu Gneiss Complex (hanging wall) compared to the Jutogh metasediments (footwall) during the Plio-Pleistocene. However, this contrast in exhumation rates is *not* clear from other fission track studies based in the Sutlej Valley, nor does it appear to be reflected in muscovite cooling age profiles (Thiede et al., 2005, Fig. 1b). Consequently, this suggests that the Sarahan Thrust has *not* caused significant differential exhumation of its footwall and hanging wall; i.e. the Jutogh metasediments and the

Wangtu Gneiss Complex were not decoupled during their exhumation, and we consider the Jutogh Group as a complete litho-tectonic package exhumed by simultaneous thrusting on the Munsiari Thrust and extension on the Karcham detachment (Jain et al., 2000; Janda et al., 2001; Vannay et al., 2004).

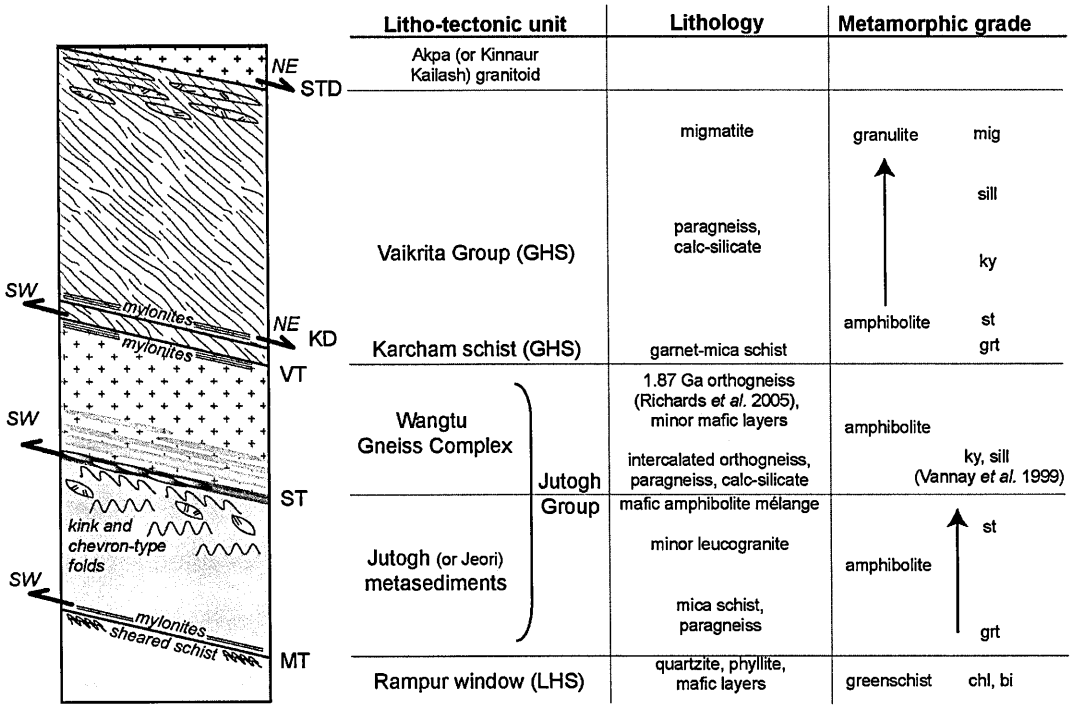

Fig. 2.2 Tectono-stratigraphic column across the metamorphic core exposed in the Sutlej Valley. Not to scale. Abbreviations as for Fig. 2.1, plus chl = chlorite, bi = biotite.

Metamorphic grade increases up-section through the Jutogh metasediments from garnet to staurolite (Fig. 2.2). The lowest metamorphic grade of the Jutogh Group may be as low as upper-greenschist, represented by a quartz-rich kyanite–chlorite–muscovite schist (locality 90, Fig. 2.1, Table 2.1) wherein kyanite has almost certainly formed via the dehydration reaction of pyrophyllite, restricted to high-Al pelites, relative to alkalis (Miyashiro, 1994). Pant et al. (2006) map a kyanite schist zone, located immediately in the hanging wall to the Munsiari Thrust, i.e. above the Rampur Window. However, they provide no localities, and we did not observe kyanite schist along the Sutlej Valley anywhere in the Jutogh metasediments. In light of this and a lack of structural control around locality 90 due to poor exposure we cannot be confident in the structural

position of the kyanite schist. At the top of the inverted metamorphic sequence, Vannay et al. (1999, Fig. 1) identified both sillimanite and kyanite in what we here recognize as the hanging wall of the Sarahan Thrust, i.e. in the Wangtu Gneiss Complex. Oxygen isotope studies through this inverted metamorphic field gradient (garnet to sillimanite) suggest a modest increase in recorded temperature, but a *decrease* in recorded pressure up-section. The inverted metamorphic field gradient may reflect diachronous mineral growth rather than an inverted geotherm at any one time (Vannay et al., 1999). However, simple thermal modelling suggests conduction from the overriding thrust sheet could have generated a transient inverted thermal gradient that was partially preserved by rapid exhumation (Caddick et al., 2007).

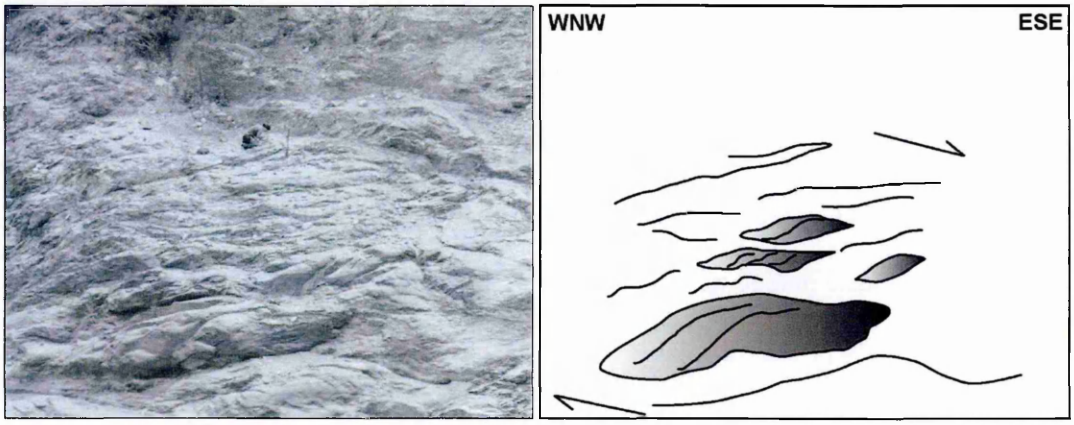

Fig. 2.3 Tectonic mélange of the Sarahan Thrust (locality 55, Figs. 2.1, 2.2). Sigmoidal clasts of mafic amphibolite within a friable, sheared biotite–chlorite matrix indicate a top to the SSE sense of shear (see bold arrows) determined from S–C fabrics, σ porphyroclasts, rotated fractured clasts and slickenlines; stretching lineations plunge gently to the NW. JC for scale, top centre.

Hitherto unrecognised leucogranites in the Jutogh metasediments south of Sarahan have been observed at three localities (63, 70 and 71, Figs. 2.1, 2.2). At localities 63 and 70 the leucogranite bodies form medium to coarse-grained boudins, 1 to 2 m in length, and are aligned with the country rock foliation (Fig. 2.4), whereas at locality 71 deformed, concordant cm-scale fine- to medium-grained leucocratic veins are common. Importantly, there is no evidence for post-tectonic granites intruding the Jutogh Group. The mineralogy of the leucogranites is quartz, alkali feldspar, plagioclase, muscovite; accessory phases include tourmaline, zircon, uraninite and titanite.

Tourmaline forms abundant prisms up to 2 cm in diameter at localities 70 and 71. In thin section tourmaline is characterised by a network of colour changes associated with numerous annealed microcracks suggesting alteration by fluid infiltration. High fluid pressure during deformation is indicated by quartz-filled fractures in feldspars whilst deformation lamellae in quartz support a relatively low temperature (c. 300 to 400 °C) deformation regime (Passchier and Trouw, 1998). Leucogranite margins are undulose but sharp, and interpreted as originally intrusive (rather than formed in situ) due to the lack of significant biotite-rich selvages. However, the small size of the Jutogh leucogranites suggests they did not travel far from their source, which is therefore probably the Jutogh metasediments. No evidence for contact metamorphism was observed in the country rocks so either the thermal contrast between intrusion and country rock was low, or contact metamorphic textures have been overprinted by subsequent mineral growth. The paragneiss that encloses the leucogranite lenses contains quartz, alkali feldspar, biotite, muscovite ± plagioclase, with pre-tectonic garnets (1 to 2 mm) at localities 63 and 71.

Since leucogranites of Early Miocene age are prevalent throughout much of the Greater Himalayan Sequence, determining the age of these leucogranites is critical to the interpretation of host unit affinity (whether with the Lesser or Greater Himalayan Sequence).

Fig. 2.4 Leucogranite boudin (dashed outline) in Jutogh paragneiss (locality 70, Fig. 2.1): positions of samples i and ii are shown, and lie at the edge of the leucogranite body. Foliation dips moderately to the NE; stretching lineations plunge gently to the north.

Table 2.1. Major and trace element data for leucogranites and pelites from the Jutogh Group

	Jutogh Group leucogranites				Miocene HH	Jutogh Group pelites														
Sample	63i	63i *	70i	70ii	leucogranite †	57	63ii	65 ‡	66i	68i	68ii	68iii	68iv	70iiix ‡	70iiiy	71i	71ii	81	84 §	87	90
wt. %																					
SiO_2	75.93	76.33	74.47	76.40		66.35	68.98	61.17	64.81	67.30	70.94	58.42	66.20	65.17	67.29	64.91	67.84	70.70	66.29	59.13	73.65
TiO_2	0.048	0.050	0.058	0.045		0.574	0.611	0.734	0.768	0.835	0.757	1.065	0.877	0.772	0.705	0.859	0.718	0.494	0.640	0.993	0.895
Al_2O_3	14.93	14.94	15.54	14.29		17.41	15.91	16.63	18.20	15.58	13.41	20.35	16.39	15.88	15.10	15.24	15.39	14.47	16.93	19.19	15.98
$Fe_2O_3^T$	0.93	0.91	0.99	1.06		6.15	4.86	6.72	5.19	6.69	6.23	8.06	6.81	6.10	5.66	6.68	5.47	4.74	6.23	7.51	3.30
MnO	0.023	0.021	0.013	0.014		0.052	0.042	0.044	0.055	0.099	0.036	0.054	0.101	0.087	0.081	0.068	0.077	0.254	0.07	0.053	0.005
MgO	0.26	0.27	0.47	0.43		2.51	1.51	6.41	1.99	2.07	1.73	2.52	1.81	3.00	1.29	2.42	1.52	1.32	1.69	2.93	0.25
CaO	1.02	1.02	0.92	0.68		0.24	1.95	0.29	1.89	1.58	0.39	0.61	1.12	0.31	2.21	1.55	2.62	2.92	0.79	0.40	0.33
Na_2O	2.76	2.73	4.54	3.80		0.69	1.85	0.31	0.64	0.57	0.35	0.45	0.43	0.45	2.70	1.74	3.12	2.74	1.10	1.38	0.70
K_2O	2.98	2.92	1.75	1.98		4.50	3.73	4.02	4.75	3.98	3.99	5.73	4.29	5.76	3.41	4.29	2.54	2.24	4.34	6.37	3.51
P_2O_5	0.161	0.152	0.189	0.199		0.192	0.153	0.196	0.222	0.182	0.162	0.187	0.179	0.179	0.171	0.154	0.167	0.106	0.20	0.199	0.243
LOI	1.43	1.43	1.16	1.26		1.89	1.41	3.05	1.90	2.03	2.23	2.77	1.93	2.24	1.31	1.46	0.96	0.82	2.62	2.26	2.09
Total	100.48	100.77	100.09	100.14		100.55	101.00	99.58	100.42	100.92	100.22	100.22	100.13	99.96	99.92	99.37	100.42	100.81	100.89	100.41	100.96
ppm																					
Rb	110	111	84	77	314	258	163	190	252	240	193	281	223	324	248	223	131	152	250	265	203
Sr	96	97	121	71	75	35	158	20	66	35	33	41	32	13	146	111	185	78	55	31	196
Y	16.5	15.3	26.1	25.3	14.4	30.2	30.6	26.0	30.8	44.1	32.1	47.8	43.6	30.7	39.7	37.0	36.1	31.6	36.4	39.3	41.4
Zr	27	25	34	25	50	166	176	209	213	239	217	303	250	232	217	227	213	149	214	291	260
Nb	12.1	12.7	10.0	5.4	6.9	14.7	12.9	16.0	16.4	14.8	14.3	19.8	16.2	23.1	16.4	17.2	14.9	10.8	16.3	18.4	15.0
Ba	172	177	130	144	217	613	727	367	844	746	676	1004	866	462	534	783	748	322	611	813	678
Pb	36	35	29	22		7	18	7	23	13	22	25	12	7	25	18	30	85	12	14	39
Th	2	4	5	2	7.9	19	18	25	27	25	22	33	25	24	23	23	24	19	26	32	24
U	4	4	9	12		5	7	6	5	7	4	9	5	8	7	4	4	4	6	7	5
Rb/Sr	1.14	1.15	0.70	1.09	4.19	7.42	1.03	9.66	3.81	6.89	5.94	6.82	7.09	24.15	1.70	2.00	0.71	1.93	4.56	8.47	1.04

* duplicate analysis; † average Miocene High Himalayan (HH) leucogranite from Dietrich and Gansser (1981), Le Fort *et al.* (1987), Scaillet *et al.* (1990), Inger and Harris (1993), Ayres and Harris (1997) and Prince et al. (2001); ‡ plagioclase-free; § sample not in situ; LOI, loss on ignition

2.3 Sampling and Methodology

Samples of leucogranite and paragneiss were collected from localities 63 and 70 (Fig. 2.4) for geochemical and petrological analysis. Locality 71 was sampled for petrological analysis only, as the small volume of leucocratic material available precluded a robust geochemical analysis.

Whole-rock major and trace element analyses were obtained on an ARL Fisons wavelength-dispersive XRF spectrometer at the Open University, from glass disks and pressed powder pellets, respectively.

Bulk-rock paragneiss samples from localities 57 and 66 were prepared for isotopic analysis following standard techniques as described in Cohen et al. (1988) and analysed for Nd isotope data at the Open University using a Triton thermal ionization mass spectrometer (TIMS). Repeat analyses of the La Jolla standard (n=17) gave $^{143}Nd/^{144}Nd$ ratios of 0.511849 ± 0.000004 (2σ) over the analysis period. Total procedural blanks were negligible compared to associated analytical errors.

For chronometric studies, zircon ($ZrSiO_4$) and uraninite (UO_2) grains were mounted into a 1 inch diameter epoxy resin stub following conventional separation techniques (including diodomethane heavy liquid separation). Most zircons are euhedral (magmatic) and markedly metamict (grey and semi-opaque), between 100 μm and 300 μm in length (Fig. 2.5a). Back-scatter electron (BSE) imaging of zircons showed no evidence of internal zoning, but did reveal two types of uraninite inclusions, one finely disseminated and the other coarser, <25 μm in diameter (Fig. 2.5c). This characteristic of uraninite in zircon may be the product of exsolution but they are referred to here as inclusions. A small number of zircons separated from sample 70ii were notably different in size (much smaller with an average length of 120 μm), shape (rounded to sub-rounded, characteristic of detrital grains) and degree of metamictization (none) (Fig. 2.5a), and BSE imaging revealed no evidence of internal zoning within them, as well as no inclusions (Fig. 2.5d). Discrete uraninite grains 250 μm in diameter, also exclusive to sample 70ii, were affixed directly onto a resin block and not polished. One was notably euhedral and lustrous, in comparison to the remainder of uraninite grains which were anhedral and appeared corroded (Fig. 2.5b). Presumably

because of a low modal abundance (e.g. Thorpe et al., 1995), no uraninite grains were located in any thin sections precluding further textural analysis.

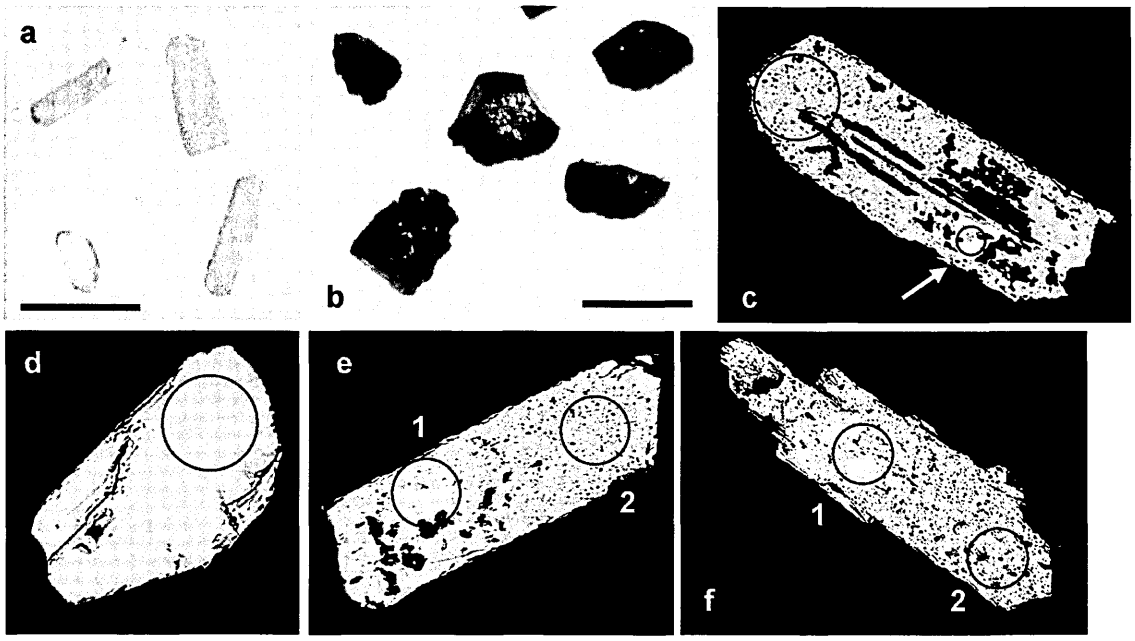

Fig. 2.5 Accessory phases separated from Jutogh leucogranite samples: incident-light images of (**a**) the two different zircon populations, i.e. magmatic (three grey, semi-opaque, euhedral grains) and detrital (one clear, sub-rounded grain, bottom left), and (**b**) of uraninite grains. BSE images of (**c**) a high-U magmatic zircon crystal (analysis 70ii 7.1, Table 2.3), peppered with bright uraninite inclusions and one relatively coarse-grained euhedral uraninite inclusion (shown by the white arrow, analysis 70ii 7.2, Table 2.3), (**d**) a detrital (clear, sub-rounded) zircon (analysis 70ii 8.1, Table 2.3), (**e**) and (**f**) high-U magmatic zircons, 70i 2 and 4 respectively (Table 2.3), with analyses in both richly 'peppered' and more pristine zones of the zircon crystal. Scale bar in (a) and (b) is 250 μm. Black circles outline the ablation pits in (c) to (f), where the spot size was 35 μm in all cases except for the smaller one in (c) which was 10 μm.

Laser ablation multi-collector inductively coupled plasma mass spectrometry (LA–MC–ICP–MS) was used in the analysis of the three phases identified above, which are 1) zircon (both magmatic and detrital grains), 2) coarse uraninite inclusions in magmatic zircon, and 3) discrete uraninite grains. A UP193SS New Wave Research laser ablation system was utilised in conjunction with an Axiom MC–ICP–MS instrument. A 35 μm spot was used statically to ablate samples of zircon using laser fluences of 1 to 2 J/cm^2, compared to the static ablation of uraninite (both discrete and included crystals) using a 10 μm spot and laser fluences of 2 to 3 J/cm^2.

The analysis of zircon followed methods similar to those of Horstwood et al., (2003) and used the 554 Ma Manangotry monazite standard for Pb/U calibration, coupled with a static ablation pattern. The overall reproducibility of the standard for $^{206}Pb/^{238}U$ during the course of these analyses was 4 to 6% (2σ), which has been propagated into the uncertainties for each individual spot analysis. The use of a non-matrix-matched standard for the zircon analyses, coupled to a static ablation protocol, could be expected to introduce a matrix effect and hence Pb/U inaccuracy, on the order of a few percent. However, in this instance, concordant zircon data after normalization to monazite suggest that this effect is either absent or negligible. Also, for the majority of sample zircons analysed here, where small uraninite inclusions are 'peppered' throughout, a matrix effect might well be expected even if zircon was used as a standard due to the severe metamictization of the zircon structure. Due to the resulting severely discordant nature of these zircons, any inaccuracy due to non-matrix matched standardisation in this instance is minor and has no significant effect on the interpretation.

Analyses of uraninite, both discrete grains and coarse inclusions in zircon, were normalized to uraninite crystals separated from a leucogranite near the Rongbuk monastery, South Tibet, and dated by isotope dilution-TIMS, thereby providing an additional calibration control relevant to matrix matching. Data from this 'standard uraninite' are available online at http://www.geolsoc.org.uk/SUP18307 (reproduced in Appendix D2). Reproducibility of the 'standard uraninite' (18% 2σ) was more heterogeneous than that typically expected for zircon and monazite (2 to 3% 2σ) and indeed for the sample uraninite grains, reflecting a clear difference between the ablation characteristics of both sample and 'standard' uraninites. However, significant (*c.* 19%) difference could be seen in the relative Pb/U normalization values between monazite and uraninite, so despite its poor reproducibility the TIMS-determined uraninite remained the most appropriate standard. As there is no other 'uraninite standard' suitable, propagated measurement uncertainties are therefore larger for dated uraninite, approximately 8% 1σ for individual spot analyses.

One euhedral uraninite crystal proved concordant at *c.* 11 Ma with no common-Pb; whereas four other anhedral grains had much older components with in part large common-Pb corrections.

Precise analysis of uraninite inclusions in zircons proved impossible owing to the small size of the included uraninites leading to uraninite-zircon mixture on a 10 to 20 μm scale. This, coupled with the extreme pulse-to-pulse variations in the Pb and U signals and the need for a large common-Pb correction in many of these grains, resulted in complex results that proved equivocal in their interpretation. Even with time-resolved analysis and a fast washout laser ablation cell, some data were discarded as the results were insufficiently robust.

2.4 Results

2.4.1 Granite geochemistry

Major and trace element XRF data for leucogranite samples 63i, 70i and 70ii (Table 2.1) were compared with two well-characterized generations of leucogranites intruding the Greater Himalayan Sequence; the Miocene High Himalayan leucogranite sheets and plutons (emplaced between 24 and 17 Ma) that have been sampled from across the Himalayan orogen (Inger and Harris, 1993; Hodges, 2000 and references therein; Singh and Jain, 2003), and a less commonly recognized, but probably widespread, suite of deformed leucogranite lenses (*c.* 1 m thick) of Eocene (39 ± 3 Ma) age, studied in the Saraswati Valley of the Garhwal Himalaya, 150 km SE of the Sutlej Valley section (Prince et al., 2001). Both leucogranite suites provide distinctive trace-element patterns indicative of their differing conditions of formation.

Major-element compositions define all three leucogranite suites as peraluminous; the Jutogh leucogranites display silica compositions (74 to 76%) intermediate between those of the Miocene (73 to 75%) and Eocene (75 to 77%) leucogranites. The Jutogh leucogranites show depletions in Rb, Ba, Th and Zr relative to an average Miocene High Himalayan leucogranite composition (Fig. 2.6, Table 2.1). In contrast the Eocene leucogranites show strong enrichments in Ba and major depletions in all analysed high-field-strength elements (Th, Nb, Zr, Y) (Fig. 2.6). Rb/Sr ratios are significantly lower for the Jutogh leucogranites compared to the Miocene leucogranites (Fig. 2.7, Table 2.1).

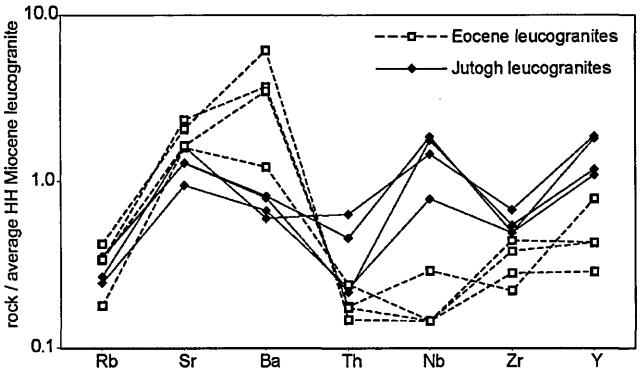

Fig. 2.6 Element-variation diagram for trace-element compositions of the Jutogh leucogranites, and for Eocene leucogranites in the Greater Himalayan Sequence (Prince et al., 2001), normalized against an average composition for High Himalayan (HH) Miocene leucogranites (Table 2.1).

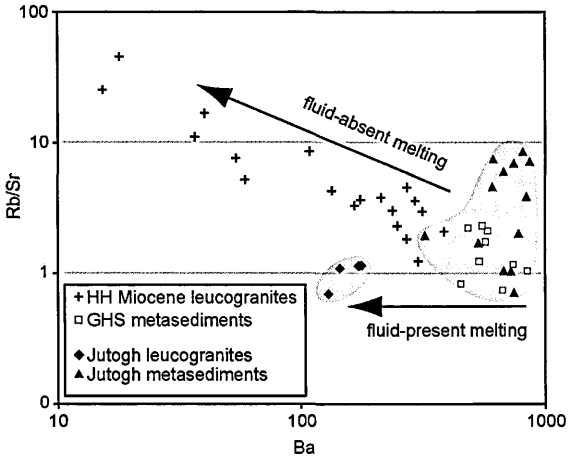

Fig. 2.7 Rb/Sr vs. Ba for High Himalayan (HH) Miocene leucogranites and for the Jutogh leucogranites. Plagioclase-bearing metasediments from the Greater Himalayan Sequence (GHS) and the Jutogh Group are also shown and represent possible melt-sources. Fluid-present and fluid-absent melting trends are indicated (Inger and Harris, 1993). Data from Table 2.1, Debon et al., (1986), Inger and Harris (1993) and references therein.

2.4.2 Bulk-rock Nd isotopic data

Pelitic Jutogh Group samples in the region around the intruding leucogranites (localities 57, 66 and W60, Fig. 2.1a) provide ε_{Nd} (500) values in the range of -16.6 to -20.8 and model Nd ages from 2.52 to 2.82 Ga (Table 2.2). These data are consistent with an 'Inner' Lesser Himalaya (i.e. Late Archaean) provenance signature (Martin et al., 2005; Richards et al., 2005).

Table 2.2. Nd bulk-rock data for selected Jutogh metasediments

Sample	57	66	W59*	W60*
$^{147}Sm/^{144}Nd$	0.1189	0.1129	0.1173	0.1328
$^{143}Nd/^{144}Nd$	0.51143	0.51130	0.51147	0.51158
Error (2σ)	0.000002	0.000002	0.000008	0.000008
ε_{Nd} (500)	-18.7	-20.8	-17.7	-16.6
T_{DM} (Ga)	2.65	2.69	2.52	2.82

* from Richards *et al.* (2005), sample W59 from same exposure as sample 57

2.4.3 U–Pb zircon and uraninite data

U–Pb analyses of anhedral uraninite grains from sample 70ii define a discordia with an upper intercept at 1810.8 ± 10 Ma (95% confidence, MSWD = 2.3), when regressed on a chord anchored to the 10.5 ± 1.1 Ma (95% confidence, MSWD of concordance = 1.2) concordia age of the three concordant data points from the euhedral uraninite crystal (Fig. 2.8a). The anhedral uraninite grains evidently suffered modest Pb loss. Analyses of magmatic zircon from the same sample, variably peppered with uraninite inclusions (reflected in the high U content of these zircons), scatter slightly about this chord and probably record multiple periods of Pb loss in some zones, although an inappropriate common-Pb (over)correction may be partly responsible for scatter. Combined with a textural analysis, the more richly 'peppered' zones in these zircons suffered the most Pb loss, in contrast to more pristine looking zones that have older ages (Figs. 2.5e and f, Table 2.3). This suggests that high-U zones of the zircon crystals experienced significant metamictization while zones less riddled with uraninite did not. Two clear, inclusion-free, relatively low-U (*c.* 200 ppm) xenocrystic detrital zircon crystals from sample 70ii (Fig. 2.5a and d) gave concordant data at *c.* 1920 Ma (Fig. 2.8b).

All analyses from sample 63i, including both zircons variably peppered with uraninite and coarse uraninite inclusions in zircon, are collinear on discordia, reflecting two-component mixing. The lower intercept lies close to 11 Ma as defined by young uraninite from sample 70ii. When tied to this value, a regression of the data yields an upper intercept of 1797 ± 20 Ma (95% confidence, MSDW = 6.5) (Fig. 2.8c), which is within error of the upper intercept calculated for sample 70ii.

A third sample, 70i showed a similar range of high-U zircon data points; however the data are not collinear and do not define the end members described above.

Despite complicated U–Pb systematics, three leucogranite samples from two localities present low-U detrital *c.* 1920 Ma zircons, *c.* 1810 Ma magmatic high-U zircons and uraninites, and *c.* 11 Ma uraninite (as both coarse inclusions in high-U zircons and as discrete euhedral grains). Pb-loss from the high-U zircons was both multi-episodic (data points scattered above chord between 1.8 Ga and 11 Ma) and discrete, as is evident from a fan of all data points terminating at a

young (*c.* 11 Ma) age (Fig. 2.8d). Importantly, the data reflects the formation of high-U zircon and uraninite during igneous crystallization at 1.8 Ga; therefore the Jutogh leucogranites were emplaced during the Palaeoproterozoic.

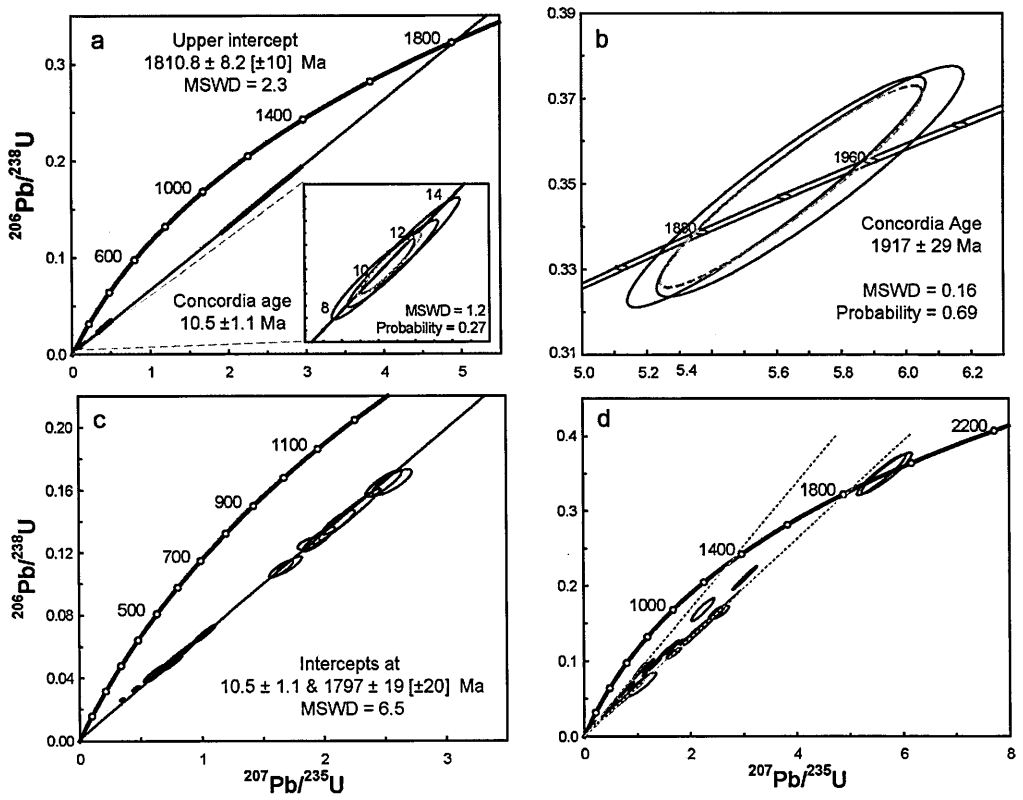

Fig. 2.8 U–Pb data from analyses of (**a**) discrete uraninites (from sample 70 ii); (**b**) detrital zircons (from sample 70 ii); (**c**) zircons and uraninites in zircons (from sample 63i); (**d**) zircons and uraninites from all three samples (63i, 70i, 70ii). Concordia ages in (a) and (b) marked by bold dashed grey ellipses. Data point error ellipses are 2σ.

2.5 Discussion

Like the Greater Himalayan Sequence throughout the Himalaya, the Jutogh metasediments of the Sutlej Valley display amphibolite-grade metamorphism and are intruded by tourmaline-bearing leucogranites. However, there is persuasive evidence that these intrusives are distinct from the leucogranites that intrude the Greater Himalayan Sequence.

Table 2.3. U–Pb isotopic data of uraninite and zircon grains separated from Jutogh leucogranites

Analysis	Comment/position	^{206*}Pb (mV)	^{207*}Pb (mV)	^{238}U (mV)	^{206}Pb$_c$ (%)	U (ppm)*	^{207}Pb/^{206}Pb	1σ (%)	^{206}Pb/^{238}U	1σ (%)	^{207}Pb/^{235}U	1σ (%)	Rho	^{207}Pb/^{206}Pb age (Ma)	2σ abs	^{206}Pb/^{238}U age (Ma)	^{207}Pb/^{235}U age (Ma)
Sample 63i																	
magmatic zircon																	
1.1	tip	103	10	587	0.6	5186	0.1007	0.6	0.0820	1.0	1.14	1.2	0.86	1638	22	508	772
1.2	core	45	4.9	191	0.3	4009	0.111	1.2	0.112	2.2	1.72	2.5	0.87	1823	44	683	1014
2.1	relatively inclusion-free	162	18	601	bd	5306	0.108	1.6	0.126	1.2	1.88	2.0	0.61	1771	57	764	1073
2.2	relatively inclusion-free	75	8.3	229	0.1	4806	0.110	1.2	0.139	2.3	2.12	2.6	0.88	1805	44	841	1156
2.3	inclusion-rich	40	4.4	250	0.1	5258	0.110	1.0	0.0683	3.4	1.02	3.6	0.96	1793	35	426	720
3.1 a ‡		36	3.4	550	12	4857	0.0966	1.6	0.0263	1.2	0.351	2.0	0.60	1559	60	168	305
3.1 b ‡		44	4.5	550	bd	4857	0.103	1.7	0.0428	5.0	0.607	5.3	0.95	1676	62	270	482
3.2		18	1.8	270	0.2	5657	0.100	1.3	0.0333	2.1	0.461	2.4	0.86	1632	47	211	385
4.1		276	30	2269	0.5	20035	0.1075	0.4	0.0574	5.3	0.851	5.3	1.00	1757	14	360	625
4.2	rim/edge	71	7.8	208	0.1	4362	0.110	1.2	0.164	2.1	2.49	2.4	0.87	1803	44	979	1270
5.1	tip, relatively inclusion-free	91	10	266	0.1	2345	0.113	1.6	0.165	2.0	2.56	2.6	0.79	1844	56	984	1290
5.2 a ‡	edge, relatively inclusion-free	83	9.3	808	bd	16953	0.111	1.2	0.0498	3.8	0.763	4.0	0.95	1819	44	313	576
5.2 b ‡	"	48	5.4	174	0.3	3656	0.111	1.1	0.143	5.1	2.19	5.2	0.98	1814	39	863	1178
6.1	fragment	38	4.1	179	0.3	3748	0.109	1.2	0.110	2.1	1.65	2.4	0.86	1789	45	670	990
7.1	fragment	45	5.0	185	bd	3883	0.111	1.2	0.129	2.5	1.96	2.8	0.90	1808	44	780	1102
uraninite in magmatic zircon																	
2.4		22	2.5	173	bd	44976	0.108	1.5	0.0504	10.5	0.748	10.6	0.99	1761	54	317	567
4.3		370	40	1891	bd	492747	0.1089	0.3	0.0525	9.1	0.788	9.1	1.00	1781	9	330	590
Sample 70i																	
magmatic zircon																	
1.1		87	8.7	214	9.3	4504	0.0963	1.4	0.168	3.6	2.24	3.9	0.93	1554	54	1003	1192
2.1 §	core	57	5.9	215	0.1	4533	0.103	1.0	0.118	3.2	1.65	3.3	0.96	1681	36	718	999
2.2 §	near tip	32	3.0	232	0.3	4889	0.0962	1.0	0.0670	3.2	0.861	3.5	0.91	1551	37	416	643
3.1		43	4.1	455	1.1	9582	0.105	1.0	0.0444	3.3	0.588	3.4	0.94	1712	37	285	511
4.1 §	tip	53	4.7	300	0.7	6329	0.0933	1.0	0.0847	3.9	1.03	4.0	0.96	1494	39	528	752
4.2 §	core	48	4.7	258	0.8	5443	0.103	1.0	0.0911	3.2	1.21	3.3	0.95	1672	37	568	847
5.1	near tip	84	7.8	885	10	18645	0.149	5.7	0.0422	3.4	0.530	3.8	0.90	2336	195	287	671
uraninite in magmatic zircon																	
5.3		3.4	0.4	10	0.6	2573	0.114	4.1	0.0692	9.3	1.08	10.2	0.91	1859	150	431	746
Sample 70ii																	
magmatic zircon																	
1.1	fragment	17	1.5	192	0.6	4039	0.0923	1.1	0.0401	3.2	0.510	3.4	0.95	1474	41	253	418
2.1	near tip	26	2.5	253	0.3	5330	0.0953	1.0	0.0419	3.4	0.551	3.5	0.96	1535	38	265	446
3.1		45	4.0	490	1.2	10324	0.0895	1.2	0.0453	3.9	0.558	4.1	0.96	1414	45	285	451
3.2	core	44	4.1	373	1.3	7857	0.0919	1.1	0.0571	3.4	0.723	3.6	0.95	1465	41	358	553
4.1	near tip	61	5.4	338	1.7	7120	0.0874	1.1	0.0903	3.5	1.09	3.6	0.95	1369	42	558	748
5.1	near tip	155	15	708	0.4	14914	0.0983	0.5	0.111	3.1	1.50	3.1	0.99	1593	17	676	930
5.2	core	151	16	356	0.1	7502	0.1043	0.5	0.210	3.1	3.02	3.1	0.99	1702	17	1231	1414
6.1		94	9.5	503	1.2	10607	0.1005	0.7	0.0961	3.4	1.33	3.5	0.98	1633	25	592	860
6.2	core	51	4.8	275	0.7	5800	0.0930	1.0	0.0947	3.4	1.21	3.5	0.96	1488	37	583	807
7.1 §	tip	41	3.9	540	0.3	11374	0.0954	1.2	0.0420	4.3	0.552	4.5	0.96	1535	46	265	446
uraninite in magmatic zircon																	
4.2		8	0.7	82	1.7	21350	0.1036	3.0	0.034	10.2	0.49	10.6	0.96	1689	110	218	405
4.3 a ‡		5	0.5	40	bd	10538	0.0966	3.7	0.0370	9.1	0.492	9.8	0.93	1559	138	234	406
4.3 b ‡		11	0.9	199	0.2	51850	0.0785	2.5	0.0167	9.0	0.180	9.3	0.96	1158	100	106	168
7.2 §	largest uraninite inclusion	32	2.3	2274	0.3	592802	0.0740	1.4	0.00418	9.1	0.0426	9.2	0.99	1040	57	27	42
uraninite																	
U1_1	euhedral grain	18	0.9	3077	bd	801927	0.0495	2.5	0.00178	9.0	0.0122	9.3	0.96	171	116	11.5	12.3
U1_2	on same grain as U1_1	15	0.7	2772	bd	722568	0.0475	2.7	0.00165	8.9	0.0108	9.3	0.96	74	130	10.6	10.9
U1_3	on same grain as U1_1	13	0.6	2496	0.2	650596	0.0464	3.2	0.00152	9.0	0.00971	9.5	0.94	18	155	9.8	9.8
U1_4	on same grain as U1_1	18	0.8	2785	0.2	725950	0.0474	2.6	0.00180	9.0	0.0117	9.3	0.96	69	123	11.6	11.8
U2	anhedral grain	287	30	2528	13	658823	0.1043	1.2	0.0289	8.7	0.416	8.7	0.99	1702	44	184	353
U3	anhedral grain	1429	159	2850	bd	742694	0.1104	0.1	0.160	8.6	2.43	8.6	1.00	1806	4	955	1252
U4	anhedral grain	147	15	2467	11	642929	0.1029	0.8	0.0151	8.7	0.214	8.8	1.00	1676	29	97	197
U5	anhedral grain	73	7.0	2241	5.1	584201	0.0962	0.9	0.0102	8.7	0.136	8.7	0.99	1552	35	66	129
detrital zircon																	
8.1 §		7.9	0.9	12	0.3	251	0.117	1.1	0.348	3.2	5.60	3.4	0.94	1906	40	1925	1916
10.1		5.0	0.6	8.1	0.6	170	0.118	1.3	0.351	3.1	5.70	3.4	0.93	1926	46	1938	1932

^{206}Pbc (%) indicates the common-Pb portion in total ^{206}Pb; ^{206}*Pb and ^{207}*Pb refers to the radiogenic ^{206}Pb and ^{207}Pb. bd, below detection. * The concentration uncertainty is estimated at ± 25%. † split analysis. ‡ see Figure 2.5c-f

2.5.1 Geochemistry

The trace-element geochemistry of the Jutogh leucogranites is quite distinct from that of the widespread Miocene leucogranites of the Greater Himalayan Sequence (Table 2.1, Figs. 2.6 and 2.7). Assuming melt saturation of high field strength (HFS) elements during anatexis, lower values of the HFS elements, particularly Zr, are indicative of cooler melt conditions for the Jutogh leucogranites. Applying the data from Table 2.1 to the equations of Watson and Harrison (1983) for zircon saturation thermometry and assuming the quantity of inherited zircon was negligible, we

derive a maximum crystallization temperature of 670 to 690 °C for the Jutogh leucogranites, compared with maximum values of 700 to 750 °C (using the same equations) for the Miocene melts (Ayres et al., 1997). Rb, Sr, Ba systematics shed further light on their contrasting petrogeneses. For the Miocene leucogranites, Rb/Sr increases with decreasing Ba, and Rb/Sr ratios are distinctly higher compared with the source pelites (Fig. 2.7). As discussed by Harris and Inger (1992), these trends indicate melting under fluid-absent conditions where low melt fractions and peritectic alkali feldspar contribute to a significant feldspar component in the restite. For the Jutogh leucogranites, Rb/Sr ratios remain constant with varying Ba and are similar to those of coexisting pelites in the Jutogh metasediments, which indicates high H_2O activity during melting. Fluid-present melting for Eocene leucogranites from the Greater Himalayan Sequence of Garhwal was proposed on the basis of increased silica compositions and low HFS-element abundances; Zr thermometry (Watson and Harrison, 1983) indicates values of 610 to 670 °C (Prince et al., 2001), even lower than for the granites in this study. The extreme enrichment of Ba seen in the Eocene leucogranites (but not in the Jutogh leucogranites, Fig. 2.6) may be indicative of elemental transfer during Eocene melting, Ba being a particularly mobile element at magmatic temperatures (Harris et al., 2003). Taken together, the geochemical evidence from the Jutogh leucogranites suggests melting of pelitic compositions under conditions of elevated water activity, but possibly not sufficient for H_2O saturation as in the Eocene crustal melting event. In any case, conditions during melting of the Jutogh metasediments were quite distinct from the widespread fluid-absent melting conditions during the Early to Middle Miocene inferred from the High Himalayan leucogranites.

2.5.2 Chronometry

U–Pb ages of crystallization of the Jutogh leucogranites (upper intercept, Fig. 2.8a) provide robust evidence for Palaeoproterozoic partial melting (*c.* 1810 Ma) followed by crystallization of high-U zircon and uraninite. As crystallization progressed and the residual melt became increasingly saturated in uranium (Guilbert and Park, 1986), zircon crystallizing out from the melt became increasingly U-rich. This is now evident in zircons that have a relatively inclusion-free or more pristine 'core' but are peppered with bright uraninite inclusions outside the core (also reflected in the degree of metamictization, indicated by the black spots in Fig. 2.5e and f). These

melts inherited a few low-U zircons, *c.* 1920 Ma, unaffected by metamictization, Pb loss, or uraninite crystallization. The Jutogh leucogranites thus pre-date the Neoproterozoic to Cambrian (800 to 500 Ma) age of deposition for the Greater Himalayan Sequence in the western and central Himalaya established from detrital zircon ages and the ages of intruded granites (Parrish and Hodges, 1996; Ahmad et al., 2000; Godin et al., 2001). Moreover, granitic gneisses in the Lesser Himalayan Sequence (including the Jutogh Group) are invariably Palaeoproterozoic (1.8 to 1.9 Ga), as determined by accessory-phase dating (e.g. Miller et al., 2000; DeCelles et al., 2001; Richards et al., 2005) and supported by a marked peak in detrital zircons of the same age from the Lesser Himalayan Sequence sediments (DeCelles et al., 2000; Richards et al., 2005; Richards et al., 2006). The Wangtu orthogneiss (1866 ± 6 Ma, Richards et al., 2005), coeval with orthogneiss intrusions into the Lesser Himalayan Sequence across the Himalaya (e.g. Munsiari granite, Nepal, 1865 ± 60 Ma, Trivedi et al., 1984; the Iskere gneiss, Pakistan, *c.* 1850 Ma, Zeitler et al., 1989) represents a Palaeoproterozoic period of granite intrusion with which the Jutogh leucogranites in this study (1808 ± 10 Ma) may be associated. However, whereas the Jutogh leucogranites unambiguously intruded Jutogh metasediments, this cannot be confidently said about the Wangtu Gneiss Complex, which is bounded at its base by the Sarahan Thrust (this study). Thus, without further evidence it would be unwise to directly correlate the two intrusive events.

In summary, a Palaeoproterozoic metamorphic event resulted in crustal melting of the Jutogh Group sediments at temperatures of less than 700 °C, under conditions of high water activity, as determined from the trace-element geochemistry. Thus, despite previous correlations of the Jutogh Group with the Greater Himalayan Sequence (Singh and Jain, 1993; Singh et al., 2006) we conclude that the Jutogh Group in the Sutlej Valley is distinct from the Greater Himalayan Sequence, confirming earlier studies that also recognised a major discontinuity between the two units (Vannay et al., 2004; Richards et al., 2005).

We interpret the 10.5 ± 1.1 Ma concordia age to reflect uraninite recrystallization in response to increased fluid activity related to Miocene prograde metamorphism of the Jutogh metasediments, where localized U was mobilized from sites in the metamict crystal lattices of Proterozoic zircon, uraninite and possibly titanite (Webb and Brown, 1984). Whether Miocene uraninite nucleated on

pre-existing grains or self-nucleated, the analyses of both old and young uraninite from one mineral separate is clear evidence of localized fluid-assisted U dissolution–reprecipitation, as are relatively coarse and euhedral Miocene uraninite inclusions in heavily metamict Proterozoic zircon crystals (e.g. Fig. 2.5c, Table 2.3). The absence of a positive Ba anomaly (Fig. 2.6), in contrast to that seen in the fluid-flushed melts in the Greater Himalayan Sequence (Prince et al., 2001), provides further evidence that element mobility has been minimal, or localized, even for the most mobile of elements (Nabelek and Labotka, 1993), an inference supported by the localization of tourmaline alteration in the vicinity of microcracks.

Although uraninite provides a powerful chronometer, the scarcity of published information on its formation and behaviour during metamorphism hinders the assignment of either a pressure (P) or temperature (T) to the proposed mid-Miocene prograde dehydration metamorphic event. However, metamorphic monazite (included and matrix crystals) from a pelitic Jutogh Group sample located within 7 km of the uraninite-bearing leucogranite (Caddick et al., 2007), and from Jutogh Group samples in an unpublished study (cited in Vannay et al., 2004) yield crystallization ages of 10.6 ± 0.9 Ma and 9.9 ± 0.2 to 6.4 ± 0.5 Ma respectively; that is, within error of the uraninite concordia age presented in this study. Despite the potential uncertainty concerning the interpretation of some monazite age data (Martin et al., 2007), Caddick et al. (2007) appropriately justify their monazite dates as primary crystallization ages using systematic textural and trace element analysis. Assuming therefore that the ages of uraninite recrystallization and monazite crystallization are products of the same metamorphic event, the peak P–T conditions experienced by the Jutogh leucogranites and surrounding Jutogh metasediments in the Miocene were 7 to 8 kbars and 600 to 700 °C (Vannay et al., 1999; Caddick et al., 2007).

Miocene metamorphism (*c.* 11 Ma, amphibolite grade) related to the Himalayan orogeny overprints Proterozoic metamorphism (*c.* 1.8 Ga, at least upper-amphibolite grade resulting in crustal anatexis). The Jutogh leucogranites are relicts of this Proterozoic metamorphism, as is marked gneissic banding (quartz/feldspar and mica-rich layers segregated on a cm scale) displayed in many Jutogh metasedimentary rocks, which belies their now relatively moderate metamorphic grade. To date, no monazite ages from the Jutogh Group reflect a pre-Miocene metamorphic event,

indicating that they have not been sampled and analysed, and/or pre-existing grains were reset during Miocene metamorphism.

Polymetamorphism is widely recognised in the lithologies of the Himalayan core, e.g. garnets, monazites and zircons from the Greater Himalayan Sequence preserve evidence of a *c.* 500 Ma metamorphic event, now overprinted by Tertiary metamorphism (Argles et al., 1999; Godin et al., 2001; Martin et al., 2007). The Lesser Himalayan Sequence also records pre-Tertiary (early Palaeozoic or Precambrian) metamorphism, later overprinted in the Himalayan orogeny, e.g. at Nanga Parbat (western syntaxis of the orogen) and in Nepal (Wheeler et al., 1995; Paudel and Arita, 2000). Such evidence for polymetamorphism cautions strongly against assuming all metamorphic features (mineralogy, textures) in the metamorphic core of the Himalaya reflect the most recent orogenic phase (Gehrels et al., 2003). Without chronology it may be impossible to distinguish between pre-Tertiary and Tertiary metamorphism, even for fabric-forming index minerals. Inherited metamorphism has obvious implications for thermo-barometry (e.g. Argles et al., 1999) and as a result, for tectonic models (e.g. Gehrels et al., 2003). Relicts of earlier deformation (e.g. lineations in the core of the Wangtu gneiss) may further obfuscate tectonic interpretations.

2.5.3 Tectonic evolution of the metamorphic core of the Sutlej Valley

This combined field and geochronological study confirms that the crystalline Jutogh Group is part of the Lesser Himalayan Sequence. Together, the Jutogh Group and the Vaikrita Group (Greater Himalayan Sequence) form the metamorphic core in the Sutlej Valley, juxtaposed by the Vaikrita Thrust which therefore coincides with the Himalayan Unconformity (Goscombe et al., 2006) in this transect. The Jutogh and Vaikrita Groups represent discrete litho-tectonic units (summarised in Table 2.4), with distinct geochemical affinities (Richards et al., 2005) and tectonic styles, evident from contrasting *P–T–t* paths (Caddick et al., 2006; Harris, 2007) and distinct patterns and timing of cooling and exhumation (Vannay et al., 2004; Thiede et al., 2005). Rapid exhumation of the Vaikrita Group following peak metamorphism at *c.* 23 Ma was facilitated by coeval movement on the Vaikrita Thrust below and the South Tibetan Detachment above, until *c.* 16 Ma when motion ceased on the bounding faults (Vannay et al., 2004 and references therein). In

contrast, the Jutogh Group was (and continues to be) exhumed from *c.* 11 Ma, shortly following peak metamorphism, via concurrent thrust motion on the Munsiari Thrust and extensional movement on the Karcham detachment, where semi-brittle top-to-the-east structures are now superimposed on ductile Vaikrita Thrust fabrics (Vannay et al., 2004). The modelled cooling history profile across the metamorphic core of the Sutlej Valley published by Vannay et al. (2004) reflects comparatively rapid tectonic extrusion of the Jutogh Group compared to the Vaikrita Group, requiring that extrusion of the two crystalline units has been decoupled since the Late Miocene. The combination of cooling age data and other observations suggests that, since *c.* 11 Ma, exhumation of the Jutogh Group has been dominated by tectonic extrusion, whereas much slower exhumation of the overlying Vaikrita and Haimanta Groups has been mainly due to erosion.

Table 2.4. Characteristics of the metamorphic core of the Sutlej Valley

	Vaikrita Group	Jutogh Group
Geochemical affinity *	Greater Himalayan Sequence	Lesser Himalayan Sequence
Age of peak metamorphism (t) † ‡	*c.* 23 Ma	*c.* 11 Ma
Pressure (P), bottom to top of unit §	*c.* 8 kbar	*c.* 9 to 7 kbar
Temperature (T), bottom to top of unit §	*c.* 570 to 750 °C	*c.* 610 to 700 °C
P-T-t path geometry †	clockwise; isothermal decompression after peak P-T before cooling (broad path)	clockwise; peak P coincided with peak T; uplift with immediate cooling (tight path)
Period of exhumation via tectonic extrusion ‡	*c.* 23 to 16 Ma	*c.* 11 Ma to present
- thrust motion on	Vaikrita Thrust	Munsiari (Jutogh) Thrust
- extensional motion on	South Tibetan Detachment	Karcham Detachment
Average exhumation rate (Late Miocene to present) ‡	*c.* 0.7 mm/yr	*c.* 2.3 mm/yr

* Richards et al. (2005); † Caddick et al. (2006), see also Harris (2007); ‡ Vannay et al. (2004); § Vannay et al. (1999)

This finding is consistent with tectonic models that incorporate foreland thrust propagation (e.g. Dahlen, 1990; Bollinger et al., 2006). Moreover, the pattern of exhumation has implications for thermo-mechanical orogenic models incorporating the extrusion of the metamorphic core as a ductile channel or wedge (Beaumont et al., 2004). In one formulation of this process (Jamieson et al., 2004) the extruding channel is predicted to widen with time by drawing in material from the footwall. *P–T* paths and ages of peak metamorphism from the NW Himalaya (Caddick et al., 2007) are consistent with predictions from this model, wherein the upper Lesser Himalayan Sequence (Jutogh Group) was exhumed following accretion to the base of the over-thrust, extruding Greater Himalayan Sequence (Vaikrita Group). However, the predicted concomitant exhumation of the two units is not consistent with the published Ar isotope data from the Sutlej Valley (Thiede et al.,

2005, and references therein), which suggest they have been decoupled at least during their exhumation. If ductile flow is the mechanism responsible for the exhumation history of these lithologies then the location of focused surface denudation (which partly drives channel flow) has clearly migrated southwards, with early movement along the base of the channel on the Vaikrita Thrust being transferred towards the foreland onto the Munsiari Thrust from *c.* 11 Ma. In support of this implication, we note that current precipitation (surface denudation) is focused on the exposed slopes of the Jutogh Group where the most rapid recent exhumation rates are also recorded (Thiede et al., 2004, Fig. 4a). We suggest that exposures of these lithologies represent the site of ongoing climate–tectonic feedbacks allowing southern extrusion of metamorphic assemblages from the Indian plate.

2.6 Conclusions

This study has established that uraninite, a common accessory mineral in anatectic granites (Bea, 1996) and pegmatites (Guilbert and Park, 1986), may provide a valuable geochronometer as employed by earlier studies (Fraser et al., 2001; Santosh et al., 2003). It is of particular value in defining Neogene events where the high U content of uraninite will produce appreciable amounts of radiogenic Pb within a few million years.

The Palaeoproterozoic melting of the Jutogh Group of the Sutlej Valley that has been established by this work confirms that this previously enigmatic unit is part of the Lesser Himalayan Sequence and can not be correlated with the Greater Himalayan Sequence whose deposition post-dates the emplacement of anatectic granites into the Jutogh metasediments. These metasediments exhibit evidence of subsequent Himalayan metamorphism, extending the known range of polymetamorphism preserved in the Himalaya.

Thus, the metamorphic core exposed in the Sutlej Valley comprises both Lesser and Greater Himalayan Sequence rocks (Jutogh Group and Vaikrita Group respectively) that are both geochemically and tectonically distinct. The discrete exhumation paths of the Jutogh Group and the Vaikrita Group specifically contradict their exhumation as a single unit, as implied by models that require the Himalayan core to be the product of a single, widening ductile channel. Such models thus require modification, and incorporating migrating focused surface denudation may result in

more realistic predictions. Further integrated metamorphic and structural studies are required to test and refine tectono-thermal models of India–Asia collision in the Sutlej Valley, to which the effects of climate, including palaeo-climate, can be assessed.

Chapter 3

Empirical constraints on extrusion mechanisms from the upper margin of an exhumed high-grade orogenic core, Sutlej Valley, NW India

Abstract: The Early–Middle Miocene exhumation of the crystalline core of the Himalaya is a relatively well-understood process compared to the preceding phase of burial and prograde metamorphism in the Eocene–Oligocene. Highly deformed rocks of the Greater Himalayan Sequence (GHS) dominate the crystalline core, and feature a strong metamorphic and structural overprint related to the younger exhumation. The Tethyan Sedimentary Series was tectonically separated from the underlying GHS during the Miocene (by the South Tibetan Detachment), and records a protracted and complex history of Cenozoic deformation. Unfortunately these typically low-grade or unmetamorphosed rocks generally yield little quantitative pressure–temperature–time information to accompany this deformation history. In parts of the western Himalaya, however, the basal unit of the Tethyan Sedimentary Series (the Haimanta Group) includes pelites metamorphosed to amphibolite-grade, thus presenting a unique opportunity to explore the tectono-thermal evolution of the rocks overlying the GHS, and the early history of the orogen.

Pressure–temperature–time–deformation (*P-T-t-d*) paths modelled for two high-grade Haimanta Group pelitic rocks reveal three distinct stages of metamorphism: (1) prograde Barrovian metamorphism to 610–620 °C at c. 7–8 kbars, with garnet growing over an early tectonic fabric (S_1); (2) initial decompression during heating to peak temperatures of 640–660 °C at c. 6–7 kbars, with development of a pervasive crenulation cleavage (S_2) and staurolite and kyanite porphyroblast growth; (3) further exhumation during cooling, with minor retrograde metamorphism and modification of the pervasive S_2 fabric. Monazite U–Pb crystallization ages constrain the timing of initial garnet growth (>34 Ma), the start of D_2 and maximum burial (c. 30 Ma), and the termination of garnet growth (c. 28 Ma). Muscovite Ar/Ar ages indicate that the Haimanta Group cooled through c. 310 °C at around 13 Ma, from which we derive an initial exhumation rate of c. 1.3 mm yr^{-1}. During this time the GHS (footwall to the South Tibetan Detachment) was being exhumed at a rate of 2–4 $mmyr^{-1}$. Thus Early Miocene motion on the detachment resulted in demonstrably

differential exhumation rates of its hanging wall and footwall rocks. At c. 13 Ma both units experienced a significant decrease in their rates of exhumation, to c. 0.6 mm yr^{-1}, implying a re-coupling of the Haimanta Group to the GHS as the units passed through the brittle–ductile transition, and their exhumation as a relatively coherent tectonic block since this time.

3.1 Introduction

As an active zone of Cenozoic crustal deformation (e.g. Aitchison et al., 2007; Hodges, 2000), the Himalayan orogen is the focus of numerous studies examining the mechanical response to this process (Harris, 2007 and references therein). Critical to this challenge are tectonic reconstructions and models revealing how, when, and on what scale rocks were deformed, metamorphosed and transported within the evolving orogen. Pressure–temperature–time–deformation (*P–T–t–d*) data are essential to such modelling, because the particle paths experienced by any rock record the integrated effects of the thermal and mechanical processes that it experienced. Furthermore, identification of distinct tectono-stratigraphic units (e.g. the Greater Himalayan Sequence, (GHS)) and their bounding faults (e.g. shear zones such as the Main Central Thrust, (MCT)) provides an invaluable framework for tectonic reconstructions. Here we present new *P–T–t–d* data from the uppermost tectono-stratigraphic unit of the crystalline core.

Gneisses and migmatites of the GHS (Le Fort, 1975; Yin, 2006) dominate the crystalline core of the Himalaya (Fig. 1.1). *P–T–t–d* data from the GHS have provided key constraints for mechanical models of the evolving Himalayan orogen (e.g. for the channel flow model, Beaumont et al. (2001) and Jamieson et al. (2004)). These data suggest that the GHS was overthrust, buried and metamorphosed during the Eocene–Oligocene (also referred to as the 'M1' or 'Eohimalayan' phase), and then exhumed as the highly-deformed GHS during the Early–Middle Miocene (the 'M2' or 'Neohimalayan' phase) (Hodges, 2000; Vance and Harris, 1999; Vannay et al., 2004). Exhumation was facilitated by simultaneous thrusting on the Main Central Thrust and extension on the South Tibetan Detachment (STD) (Godin et al., 2006b; Yin, 2006), with coeval isothermal phase of decompression (Harris and Massey, 1994). In many cases, the younger 'Neohimalayan' phase has strongly overprinted metamorphic and structural products of the preceding 'Eohimalayan' phase. A notable exception appears to be in the uppermost GHS of central Nepal

(Coleman and Hodges, 1998; Gleeson and Godin, 2006; Godin et al., 2001; Vannay and Hodges, 1996) but generally the early tectono-thermal evolution of the crystalline core is much less well-constrained than its Miocene exhumation overprint (Godin et al., 2001; Hodges, 2000).

Studies on the major tectono-stratigraphic unit above the GHS, the Tethyan Sedimentary Series (TSS, Fig. 1.1) (Thakur, 1992) reveal a long and complex history of Tertiary deformation invaluable for understanding early orogenic processes (Godin, 2003; Ratschbacher et al., 1994; Wiesmayr and Grasemann, 2002). However, as the TSS is typically unmetamorphosed or low-grade, detailed structural studies may not always be coupled to *P–T* data and absolute ages (due to the general absence of well-developed U–Pb or Sm–Nd bearing metamorphic phases). Yet in parts of the western Himalaya, the base to the Phanerozoic TSS, the Haimanta Group, is metamorphosed up to amphibolite-grade. This unit has been correlated to the Phe Formation in Zanskar (Thakur, 1992), the North Col Formation in eastern Nepal (Lombardo et al., 1993), the Upper Bhimphedi Group in the Kathmandu Nappe (Yin, 2006), and also to the Harsil Formation in Garhwal, (Metcalfe, 1990; Prince, 1999). Due to the location of the Haimanta Group in the hanging wall of the STD, this unit is likely to retain valuable information regarding the early evolution of the Himalaya, owing to its tectonic separation from the underlying GHS during 'Neohimalayan' high-grade deformation.

This study uses petrographic, geochemical and geochronological (Ar/Ar mica and U–Pb monazite) data to record, date and model the high-grade metamorphism of the Haimanta Group in the Sutlej valley, NW India. We present the first comprehensive account of the *P–T–t–d* evolution of this unit, which constitutes the structurally highest crystalline rocks in the Himalayan core. These data help to constrain the Eocene to Oligocene development of the young Himalayan orogen, and contribute further to our understanding of the thermo-tectonic evolution of the crystalline core into and since the Miocene.

3.2 Geology of the upper Sutlej valley

Metasediments of the Haimanta Group (Fig. 3.1) (Hayden, 1904) consist of interlayered psammitic and pelitic schists with minor calcareous layers. The main foliation is a regular crenulation cleavage (Fig. 3.2a) with a broadly ENE-directed associated stretching lineation (Fig.

3.1c). The crenulation cleavage decreases in intensity up-section towards a low-grade spaced solution-cleavage (locality 18, Fig. 3.1a). Competent psammitic and calcareous beds define meso-scale folds (Fig. 3.2b), to which the main foliation is axial planar. On the macro-scale, a broad synform strikes ~NW–SE across the upper Sutlej valley (fold axis inclined to the SW) (Fig. 3.1b and c), folding the dominant foliation.

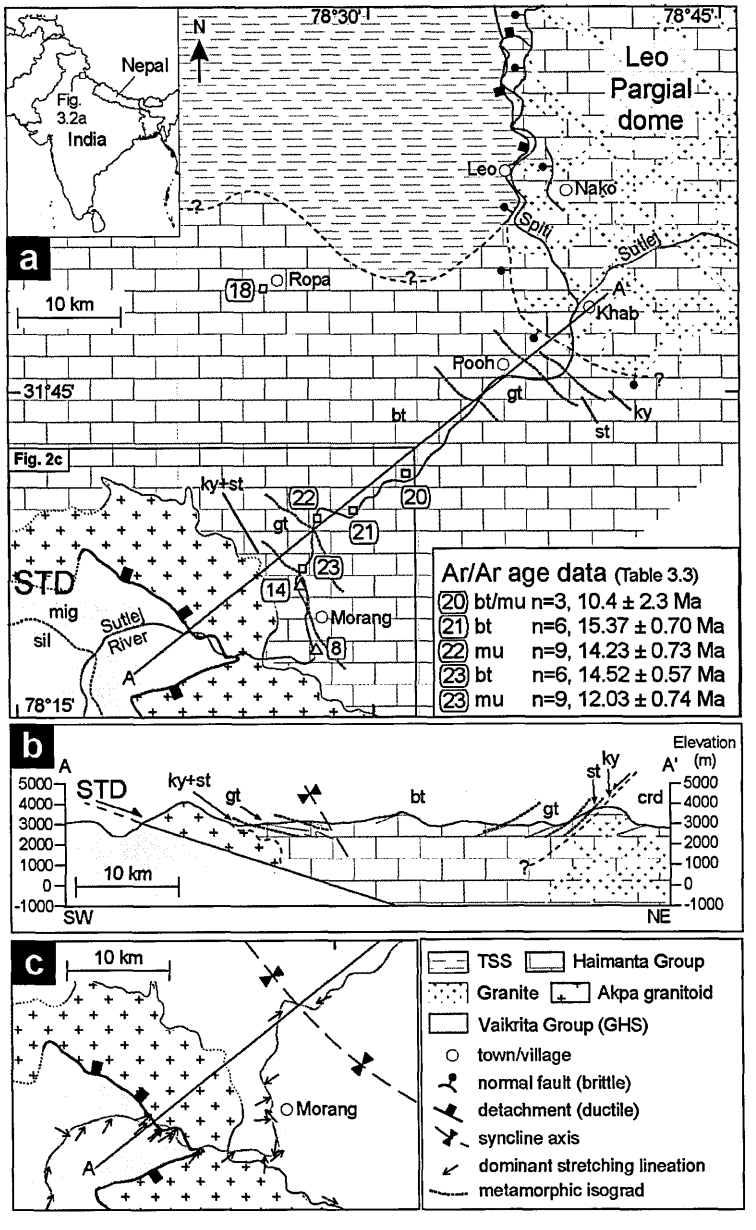

Fig. 3.1 (**a**) Geological sketch map of the upper Sutlej Valley, after Marquer et al. (2000; 2002), Wiesmayr and Grasemann (2002), Thiede et al. (2006) with modifications from the authors' field observations. Includes metamorphic isograds: bt, biotite; gt, garnet; st, staurolite; ky, kyanite; crd, cordierite (where the zone, as opposed to the 'mineral-in' line, is labelled). Ar/Ar ages are shown for samples from localities marked by open squares (bt, biotite; mu, muscovite). Grey triangles mark localities sampled for *P–T–t–d* analysis. Line A–A' marks the location of the cross-section in (b). (**b**) Cross-section with detailed foliation trajectories from field measurements, and metamorphic isograds, projected onto the line of section A–A' shown in (a). (**c**) Simplified and cropped geological sketch map showing stretching lineations from field measurements. STD, South Tibetan detachment; GHS, Greater Himalayan Sequence; TSS, Tethyan Sedimentary Sequence.

The Lower Haimanta Group was intruded by the Ordovician (c. 488 Ma) Akpa (also termed 'Kinnaur Kailas') granite (Marquer et al., 2000; Miller et al., 2001). Pelites in close proximity to the granite show highly variable structures (Fig. 3.1c), probably reflecting strain heterogeneities in the 'shadow' of the granite during Himalayan deformation. In places, the margin of the granite itself has been deformed and has developed synkinematic kyanite, presumably during Tertiary orogenesis. The interior of the granite is relatively undeformed. Xenoliths of the Haimanta Group have been found within the granite (Marquer et al., 2000; Vannay and Grasemann, 1998). The sharp contact between the base of the Akpa granite (locally deformed to augengneiss) and migmatitic gneisses of the Vaikrita Group (Greater Himalayan Sequence) represents a ductile–brittle strand of the South Tibetan detachment (STD), locally termed the 'Sangla detachment'. Mylonites in this shear zone preserve evidence of both early SW-directed and later E-directed ductile shearing, as a result of the extensional reactivation of a foreland-propagating thrust (Vannay et al., 2004). These ductile fabrics have been overprinted by a broad zone of steep brittle faults accommodating further E-directed extension (Vannay and Grasemann, 1998 and own authors' observations).

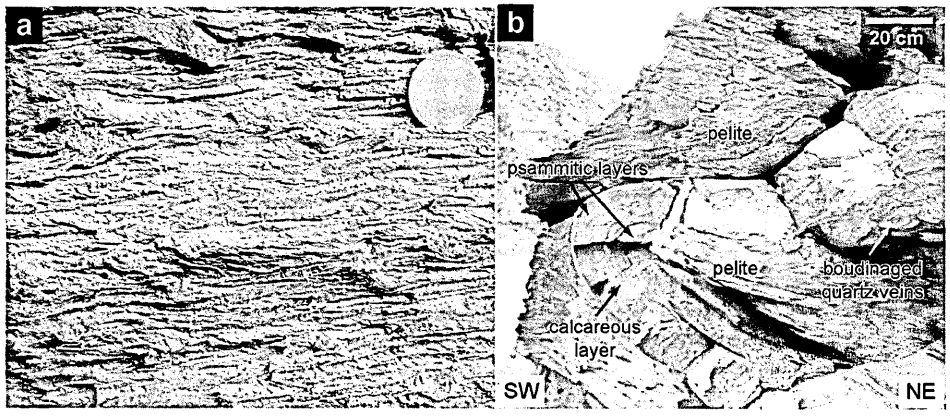

Fig. 3.2 Outcrop photographs at locality 8 (Fig. 2a) of (**a**) the dominant fabric in the Haimanta Group pelites, a crenulation cleavage (S_2). Garnet porphyroblasts have been wrapped by this foliation (see bulge top centre, and indentation where garnet has fallen out, bottom right). Coin 2.5 cm; (**b**) Near flat-lying meso-scale fold (hinge line dips 3° towards SSE) depicted by competent psammitic and calcareous layers. Pelites show axial planar cleavage.

Metamorphic grade in the Haimanta Group decreases rapidly up-section; kyanite-staurolite-garnet mica schists are exposed at the structurally lowest level (adjacent to the Akpa granite) and are successively overlain by lower grade rocks up to greenschist grade within a structural distance of approximately 6 km (Fig. 3.1a, b). Kyanite porphyroblasts near Morang (Fig. 3.1a) occur as large (average 4 cm long) blades restricted to certain compositional layers. A detailed metamorphic description of these high-grade rocks is presented in the following section. The uppermost (biotite) zone, midway between the Akpa granite and the Leo Pargil dome, preserves original sedimentary features including ripples and clay drapes.

Metamorphic grade increases systematically further northeast, reaching kyanite grade near the Leo Pargil dome (which is comparable to the North Himalayan gneiss domes observed further east (Watts and Harris, 2005)). The metasediments exposed within the Leo Pargil dome (Fig. 3.1) are indistinguishable in appearance from the Haimanta Group seen south of the Sutlej–Spiti confluence, with the exception of chaotically-orientated, mainly discordant leucogranite veins which increase in proportion towards the centre of the dome, where granite constitutes more than 50% of the exposures at Nako (Fig. 3.1a). The western edge of the dome is flanked by both ductile and brittle detachments, and although no detachment has yet been traced south across the Sutlej valley in the field, a continuation of the brittle detachment is inferred from satellite imagery (Thiede et al., 2006). Unmetamorphosed Tethyan sediments lie in the hanging wall of the detachment that exhumed the Leo Pargil dome (Thiede et al., 2006), and in sections to the west these clearly overlie the Haimanta Group on an unconformity (Wiesmayr and Grasemann, 2002).

3.3 Pressure-temperature-deformation (*P–T–d*) analysis

Petrographic examination of c. 100 thin sections from over 30 samples revealed two pelitic samples, 8i and 14i (see Fig. 3.1a for respective localities), that are representative of proposed *P-T-d* trends and are described in some detail below. Textural and chemical analyses were undertaken to relate growth and/or resorption of mineral phases to microstructures, and quantify major-phase compositions and zoning trends (Appendix C2.1). Combined with whole-rock major element analyses (Table 3.1), these data allow us to model *P–T–d* evolution using the pseudosection approach (Powell et al., 1998).

Table 3.1. Whole-rock major element data (in weight %) for two high-grade Haimanta Group pelites

	SiO_2	TiO_2	Al_2O_3	Fe_2O_3	MnO	MgO	CaO	Na_2O	K_2O	P_2O_5	LOI	Total
8i	56.79	0.89	21.07	8.40	0.10	3.82	0.42	1.28	5.43	0.21	1.60	100.01
14i	53.25	0.83	19.10	9.54	0.11	6.13	1.59	4.44	3.67	0.18	0.44	99.29
"typical" pelite*	59.80		16.57	5.81	0.10	2.62	1.09	1.73	3.53			91.25

* from Mahar et al. (1997)
LOI, loss on ignition

3.3.1 Textural analysis

Sample 8i

An early tectonic fabric (S_1) consists of aligned plagioclase feldspar (euhedral to subhedral and with distinct zoning), biotite and minor white mica. This was deformed by D_2, and developed a crenulation cleavage (S_2) that is the dominant fabric of the Haimanta Group (Figs. 3.2a and 3.3). S_2 is defined by mats of fine-grained white mica aligned in parallel bands along the limbs of the crenulated S_1 fabric (Fig. 3.3a, c). S_1 biotite and white mica feature sweeping extinction and/or polygonal recrystallization as a result of deformation and/or recrystallization in crenulation hinges, whereas S_1 plagioclase (stronger than quartz and micas) is either fractured or internally altered (Fig. 3.3a). Quartz inclusion trails in subhedral garnet porphyroblasts (0.5–2 mm), and oblique to the external foliation (Fig. 3.3b, d), also represent S_1. Trails are either straight, or weakly sigmoidal suggesting synkinematic garnet growth over a weakly deformed S_1 fabric during the early stages of D_2. In places biotite grew mimetically upon plagioclase and garnet, from which we infer that biotite growth outlasted the growth of these other phases.

Porphyroblasts of staurolite (0.5–3 cm) and kyanite (1–3 mm) grew during a later stage of D_2, overprinting S_2 and occluding garnet (Fig. 3.3b–d). The final stage of deformation (D_3) tightened the S_2 crenulation cleavage about these porphyroblasts (including garnet where not occluded), modifying (but not completely transposing) S_2 to form 'S_2m' (Fig. 3.3c, d). Asymmetric pressure shadows around porphyroblasts suggest a component of simple shear (Fig. 3.3c). However, determining an unequivocal shear sense for this late deformation phase was not possible, because the geometry of the pressure shadows appears to have been modified by minor rotation of the porphyroblasts.

Staurolite continued to grow during D_3, overprinting a progressively modified S_2 fabric (the orientation of inclusion trails in staurolite changes continuously towards the tip, finally merging with S_2m, Fig. 3.3b). However, D_3 outlasted staurolite growth, as shown by deformed white mica crystals wrapping around the end of staurolite porphyroblasts and featuring a sweeping extinction. Meanwhile, kyanite suffered internal deformation, and the crystal lattice is now either kinked (Fig. 3.3d), and/or degraded along crystal edges parallel to D_3 microfolds.

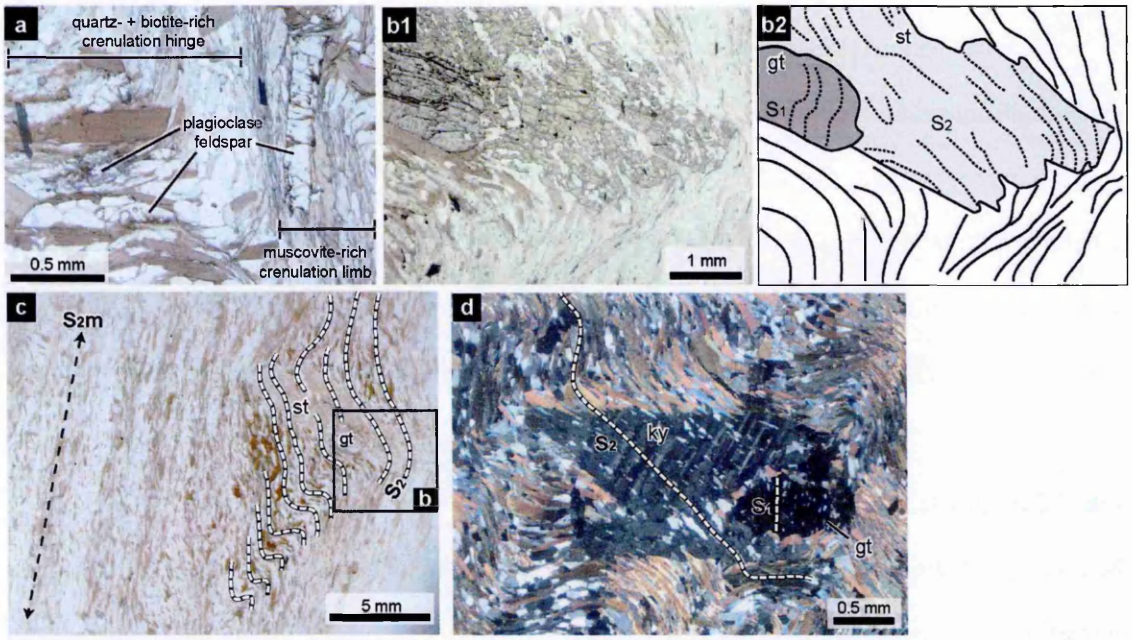

Fig. 3.3 Microphotographs of pelites from locality 8: (**a**) Sample 8i. S_1 plagioclase feldspar in S_2 crenulation cleavage is both fractured and altered (fractures rimmed by red-orange alteration product and/or dusty-looking internal alteration). Quartz is clear with low relief; laths of biotite and muscovite are dark and light grey respectively; (**b**) Sample 8i (b2 is a line-drawing of b1). Syn-tectonic garnet porphyroblast with faintly sinusoidal inclusion trails (S_1 weakly deformed by D_2) occluded by a large staurolite porphyroblast. Staurolite overprints S_2 (inclusion trails oblique to S_1 in garnet), and towards its tip overprints a modified (by D_3) S_2 fabric (also see (c)). D_3 out-lasts staurolite growth and fine laths of S_2 muscovite are wrapped around the tip of staurolite; (**c**) to show context of (b). S_2 (inclusion trails in staurolite) have been subsequently modified (S_2m) by D_3, tightening the S_2 crenulation cleavage and wrapping large porphyroblasts. Asymmetric pressure shadows suggests a component of simple shear and/or rotation of staurolite during D_3; (**d**) Sample 8ii. Cross polarised light. A garnet porphyroblast with S_1 inclusion trails is occluded by a kinked kyanite porphyroblast, with S_2 inclusion trails oblique to S_1. Post-kyanite growth, S_2 has been micro-folded against the porphyroblast during D_3.

Sample 14i

Sample 14i shares a number of features with sample 8i: garnet porphyroblasts overgrew S_1 and grew up to early-D_2 (Fig. 3.4); staurolite porphyroblasts post-dated garnet growth (in places

occluding garnet) and overprinted the main crenulation cleavage (S_2); D_3 modified S_2 into a tighter crenulation cleavage, forming pressure shadows around porphyroblasts which are asymmetric but lack an unambiguous sense of shear.

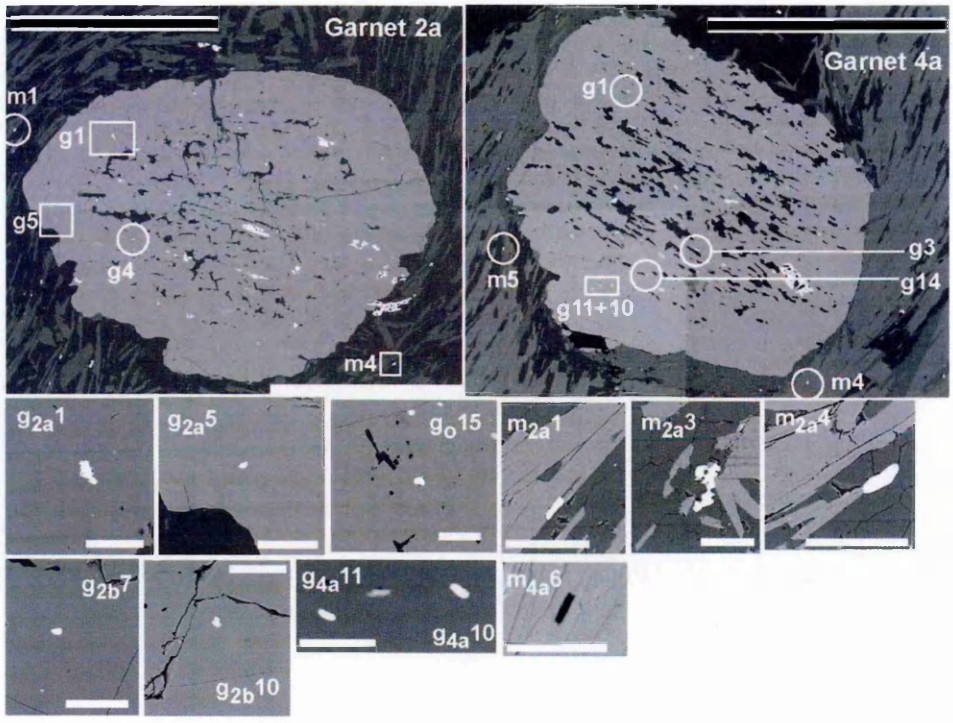

Fig. 3.4 Back-scatter electron images of two garnet porphyroblasts from sample 14i, plus a selection of the monazite grains analysed (including one Mg-element map, of monazite "m4a6"). Garnets overprint a pre-existing S1 fabric, as well as an S1–S2 fabric at the rim consistent with late stage garnet growth syn-tectonic with early D2. S2, defined by the biotite/plagioclase matrix (light and dark grey matrix phases respectively), is oblique to S1 and wraps garnet porphyroblasts. Chlorite (mid-grey between biotite and plagioclase) is present in the pressure shadows to garnet 4a (top and bottom of the image). Monazites are labelled with a prefix 'g' (garnet) or 'm' (matrix) which refers to the host phase, a subscript which refers to the section name (e.g. '2') and the occluding or adjacent garnet (e.g. 'a'), and a suffix which indicates the analysis number (Table 3.2). Where elongate, monazite grains are aligned with the tectonic fabric (e.g. "m2a1", "m4a6"). Some other grains are distinctly anhedral (e.g. "g2a1" and "m2a3"). Black scale bar (garnet images) 2 mm; white scale bar (monazite grain images), 100 μm.

Garnet (2–5 mm) is the most abundant porphyroblast, with euhedral crystals preserved alongside more anhedral grains, including some which were evidently fractured. This sample contains no white mica and S_2 is defined by biotite laths (<0.5 mm) in a polygonally recrystallized plagioclase-rich matrix (anhedral grains with an average size of 50 μm). S_2 strongly wraps garnet porphyroblasts (Fig. 3.4). Staurolite porphyroblasts are relatively small (1–3 mm). Tightly folded and boudinaged mm-scale quartz veins preserve evidence of the S_2 crenulated cleavage, that has

been eradicated and/or underdeveloped elsewhere. These quartz veins are also kinked about porphyroblasts, as a result of D_3 shearing/porphyroblast rotation.

Retrograde metamorphism

Minimal retrograde metamorphism is found in samples 8i and 14i, although minor chlorite alteration of garnet and staurolite rims (more pronounced in D_3-related pressure shadows) is seen. The edges of some staurolite porphyroblasts in sample 14i are retrogressed to biotite and quartz, and more rarely, completely replaced by chlorite. All retrograde phases are randomly aligned, indicating post-tectonic crystallization.

Several samples from nearby localities preserve evidence of more extensive retrograde metamorphism, characterized by a partial to complete replacement of garnet by chlorite, and often restricted to particular lithological layers. Thus retrograde metamorphism was probably controlled mainly by the localized presence of fluids, resulting in a variably-retrogressed Haimanta Group.

3.3.2 Chemical zoning

Garnet porphyroblasts in the Haimanta Group feature prograde zoning (i.e. 'bell-shaped' $X_{garnet}^{spessartine}$ and $[Fe/Fe+Mg]_{garnet}$ profiles from crystal core to rim; Fig. 3.5 and Appendix C2.1). These trends are reversed in the outer 50–100 μm of the analysed crystals, recording late-stage diffusional re-equilibration with the matrix.

Complex zoning trends are observed across profiles of plagioclase feldspar in sample 8i (Fig. 3.5 and Appendix C2.1): anorthite content sharply decreases at the rim of the high-anorthite core, and either continues to decrease (although less significantly) or increases towards the edge of the crystal. Plagioclase in 14i is characterised by a more simple zoning profile, with low-anorthite cores increasing smoothly to anorthite-rich rims (Appendix C2.1).

3.3.3 Modelled P–T–d evolution

The textural and chemical data above help to constrain detailed *P–T–d* paths through pseudosection diagrams, calculated for the bulk rock compositions of samples 8i and 14i (Table 3.1) with the mineral end-member data of Holland and Powell (1998). Free energy minimisations

utilised the Perplex program of Connolly (1990), following the gridding scheme discussed by Connolly (2005). High compositional resolution was achieved following the adaptive

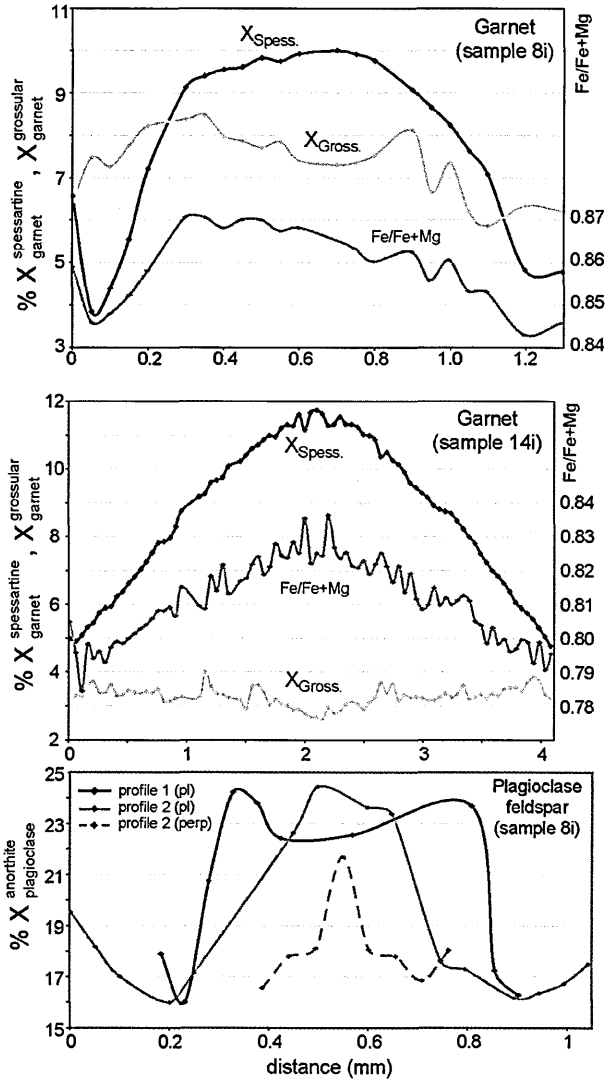

Fig. 3.5 Major element profiles across zoned porphyroblasts (data provided in Appendix C2.1). Plagioclase profiles are plotted so that their cores are aligned; 'pl' and 'perp' refer to parallel and perpendicular (respectively) to the length of the crystal.

pseudocompound generation method implemented in Perplex07 and outlined by Caddick and Thompson (2008). Solution models for complex phases were taken from White et al. (2000), Powell and Holland (2001), Coggon and Holland (2002), Mahar et al. (1997), Holland et al. (1998), and Furhman and Lindsley (1988), as detailed in Appendix I of Caddick and Thompson (2008). Here we discuss the *P-T-d* histories implied by comparing the pseudosection predictions with the presence, absence and modal abundance of phases observed in samples 8i and 14i, and the measured chemical compositions of these phases

Sample 8i

An early stage of prograde metamorphism at between 450 and 500 °C and at 6 to 7 kbars is associated with an appreciable increase in the volume proportion of biotite (Fig. 3.6b) and muscovite. Low-anorthite plagioclase is also stable at these *P–T* conditions (for the observed volume proportion of c. 5 % plagioclase), consistent with the analyzed plagioclase rims. Plagioclase cores however, with high- anorthite contents, are predicted to have formed under high-*T* (> 550 °C), low-*P* (1–4 kbars) conditions; distinct from the moderate pressure history modelled (Fig. 3.6a). Therefore we suggest that the plagioclase cores are relicts of a pre-Himalayan (contact?) metamorphic event (e.g. Gehrels et al., 2003; Marquer et al., 2000). Between c. 500 and 600 °C on the best-fit path, neither plagioclase nor rutile are predicted as stable phases, and *P* and *T* increase are associated with consumption of pre-existing rutile by ilmenite forming reactions.

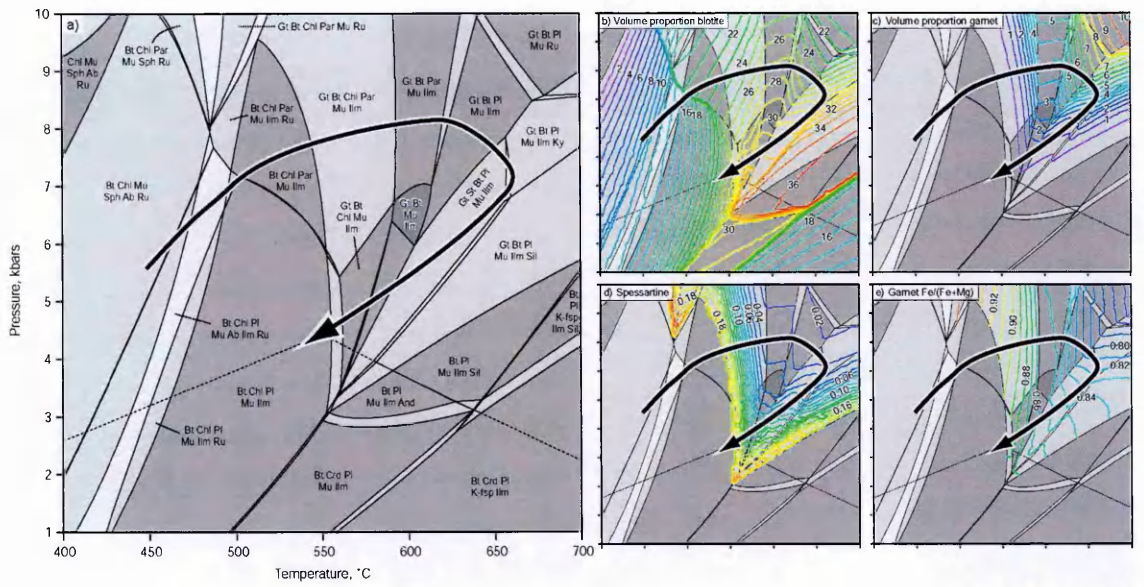

Fig. 3.6 (**a**) Pseudosection diagram for sample 8i, quartz and water also stable in every field. Abbreviated phases are garnet (Gt), staurolite (St), biotite (Bt), chlorite (Chl), muscovite (Mu), paragonite (Par), ilmenite (Ilm), rutile (Ru), plagioclase (Pl), titanite (Sph), albite (Ab), kyanite (Ky), sillimanite (Sil), andalusite (And), cordierite (Crd) and K-feldpsar (K-fsp). Al_2SiO_5 phase transitions are shown with solid lines in Al_2SiO_5-bearing fields and are extended into Al_2SiO_5-absent fields with dashed lines. Small assemblage fields unlabelled for clarity. Melt was not considered. Subplots (**b**) and (**c**) show calculated abundance of biotite and garnet, respectively. Subplots (**d**) and (**e**) show calculated garnet composition, $X_{garnet}^{spessartine}$ and Fe/Fe+Mg ratio, respectively.

Garnet is predicted to be stable above 550 °C (Fig. 3.6c), but contours representing the $X_{garnet}^{spessartine}$ and $[Fe/Fe+Mg]_{garnet}$ ratios in garnet cores (Figs. 3.6d and 3.6e, see also Fig. 3.5) suggest that garnet growth began nearer 575 °C. Thus garnet appears to overstep the predicted garnet-in reaction line by c. 25 °C, as previously observed by Waters and Lovegrove (2002). Compositional contours for garnet rims suggest that garnet growth ended at c. 625 °C, at an approximate garnet volume proportion of 4 % (agreeing well with observed proportions). Pressure is less well-constrained than temperature for this part of the prograde path but textural evidence confirms the growth of garnet *then* staurolite, with this being most easily achieved at pressures above c. 6 kbars (Fig. 3.6a).

Peak *T*, 660 °C at c. 7 kbars, is constrained by the growth of kyanite (for a volume proportion of <1% as observed) (Fig. 3.6a), and the best-fit path experiences decompression and heating, from a point of maximum burial towards this peak *T* (thus the prograde path approaching peak *P* must be above c. 7 kbars). Garnet modal isopleths in this region imply minor growth followed by weak resorption during this stage (Fig. 3.6c); details that are probably lost in the thin, diffusionally-modified rims. The path through staurolite stability fields around peak *T* suggest staurolite grew before and beyond that of kyanite, consistent with petrographic observations. Although plagioclase is also predicted as a stable phase throughout the high-temperature part of the modelled *P–T* path (Fig. 3.6a) no plagioclase with anorthite compositions predicted for this region were identified. This may reflect the sequestration of some Ca and Al into pre-existing high-anorthite plagioclase cores. As the start of D_2 is marked by the end of garnet growth, this deformation event was active during this initial phase of exhumation accompanied by heating. The start of D_3 is inferred to coincide with or closely follow peak *T* as both staurolite and kyanite overprint S_2 yet only staurolite overprints S_2m.

The early part of the modelled retrograde path (decreasing *P* and *T*) is constrained to pressures above the sillimanite stability field as no sillimanite was observed in sample 8i, and staurolite is considered to have continued to grow after peak *T* (between 660 and 640 °C). Abundant suitable nucleation substrates for sillimanite (e.g. biotite and white mica) in addition to matrix (D_3) deformation during this retrogressive phase suggests that the absence of observed

sillimanite is a record of protracted stability above the kyanite–sillimanite transition, rather than inhibited sillimanite growth due to sluggish reaction rates.

Sample 14i

Sample 14i yields a similar best-fit *P–T–d* path (Fig. 3.7) to sample 8i, described above, despite the two samples' strongly contrasting bulk-rock compositions (Table 3.1). In particular, 14i contains significantly more Fe, Mg, Ca and Na, and less Si and Al than 8i. Plagioclase feldspar constrains the early part of the *P–T* history to pressures above 6 kbars, as lower pressure at the plagioclase-in reaction yields significantly higher $X_{\text{plagioclase}}^{\text{anorthite}}$ than any analysed grains. With increasing temperature the modelled volume proportion of plagioclase and biotite increase towards 50 % and 40 % of the whole rock, respectively, consistent with petrographic observations.

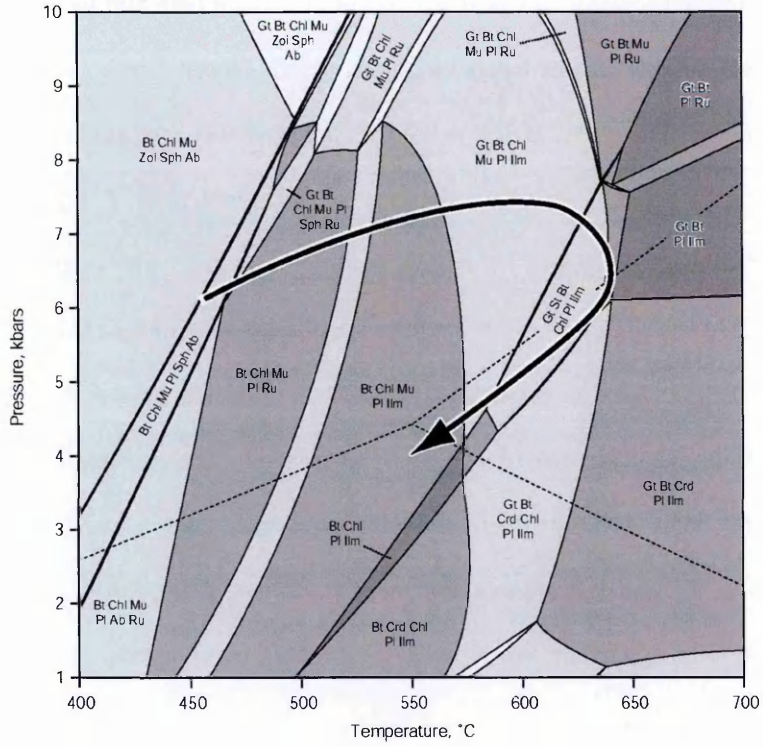

Fig. 3.7 Pseudosection diagram for sample 14i, quartz and water also stable in every field. Abbreviated phases as in Figure 7 plus zoisite (Zoi). Al_2SiO_5 phase transitions are shown with solid lines in Al_2SiO_5-bearing fields and are extended into Al_2SiO_5-absent fields with dashed lines. Small assemblage fields unlabelled for clarity. Melt was not considered.

$X_{\text{garnet}}^{\text{spessartine}}$ and $[\text{Fe/Fe+Mg}]_{\text{garnet}}$ contours for values representative of analysed crystal cores and rims constrain garnet growth to between 585 and 620 °C . As for sample 8i, an overstep of the garnet-in reaction line of c. 25 °C is implied before initiation of garnet growth. Pressure is less well-constrained, but the grossular content of analysed garnet crystals would be exceeded at pressures above c. 8 kbars. Peak *P* of the best-fit path (c. 7.5 kbars) coincides with a garnet volume

proportion of 4 %, corresponding well with petrographic evidence. Furthermore, the absence of rutile indicates a maximum pressure of c. 7.5 kbars when peak T (c. 640 °C) is eventually reached.

A period of decompression accompanied by an increase in T to 640 °C is inferred as coeval with D_2. As peak T is approached staurolite growth is predicted (as observed petrographically) and the modal proportions of both white mica and chlorite decrease to 0 % (again consistent with the absence of these prograde phases in this sample). These observations coupled to the pseudosection tightly constrain a peak T of c. 640 °C at c. 6–7 kbars (Fig. 3.7).

The absence of stable cordierite precludes isothermal decompression from peak T and the retrograde path is constrained to pressures above the cordierite-in reactions (Fig. 3.7). As D_3 post-dated staurolite formation in this sample, this deformation phase is restricted to the retrograde path.

Summarised P-T-d modelling results

The geometry of the two independently modelled *P–T–d* paths is strikingly similar, and is characterized by a distinctive three-phase evolution: (1) a moderate dP/dT prograde path to between 610 and 620 °C, 7–8 kbar; (2) an initial phase of c. 1 kbar decompression associated with continued T increase to between 640 and 660 °C; (3) a retrograde path constrained by the lack of high-T, low-P minerals such as sillimanite or cordierite.

3.4 Geochronology

3.4.1 Monazite sampling and U–Pb methodology

Monazite ((Ce, La, Th) PO_4) grains are common throughout sample 14i, as is the case in other medium to high grade Himalayan metasediments (Martin et al., 2007). The grains are located in the matrix (typically as isolated inclusions in biotite) and in garnet porphyroblasts. If monazite grew throughout the period of garnet growth, along the prograde metamorphic path, then age data from included and matrix monazites would bracket the age of garnet growth. In turn, this can, tightly constrain a segment of the *P–T–t* history.

Monazite grains from a number of thin sections of sample 14i were texturally characterized and chemically mapped (for Y and Th) using a Cameca SX100 electron microprobe. Both matrix monazites and monazite inclusions in garnet exhibit a similar shape (typically elongate and sub-

rounded, but occasionally more rounded or anhedral), size (average 30 x 10 μm), and Y and Th contents (Y barely detectable and no hint of zoning; patchy Th zoning but consistently high-Th cores relative to rims, i.e. normally zoned). Given that it was not possible to distinguish matrix monazite from included grains on morphological or chemical grounds, they were analysed *in-situ* (in thin section) using a laser ablation (LA) source to retain the textural context essential to our methodology. Monazite grains from three of the studied thin sections (including inclusions in six garnet porphyroblasts) were analysed. Grains exceeding 10 by 20 μm in size were considered analytically viable.

A UP193SS New Wave Research LA system was used in conjunction with a Nu multi-collector inductively coupled plasma mass spectrometer (MC–ICP–MS) instrument to ablate single spots (10 μm diameter) in monazite grains using laser fluences of 4–5 J cm^{-2}. Analysis followed methods similar to those described in Cottle et al. (2007a) using the instrumental set-up modified from Simonetti et al. (2005). The 554 Ma Manangotry monazite was used as the reference for the Pb/U calibration, coupled with a static ablation pattern. The overall reproducibility of the Manangotry standard for $^{206}Pb/^{238}U$ during the course of these analyses was 2 % (2σ), which has been propagated into the uncertainties for each spot analysis.

Considering that the sample grain sizes were barely larger than the LA spot size, it is expected that some analyses will have also sampled the surrounding phase; that is, garnet or biotite, and in one case, plagioclase feldspar. The U and ^{206}Pb concentrations of garnet were negligible; however those of biotite and feldspar could affect the data and thus great care was taken to avoid sampling these phases. Data points with an obvious common-Pb contribution have been rejected from the interpretation. Inferred ages of monazite growth are based on U–Pb measurements, using Tera–Wasserburg concordia plots with projections through sample measurements onto the concordia from either a common-Pb composition or using linear arrays.

3.4.2 U–Pb monazite results (LA–MC–ICPMS)

The data have been carefully scrutinized and, despite very small grain sizes, young ages, and the consequent small signals for Pb isotopes (Table 3.2), are valid. All analyses of monazites occluded in garnet have Tera–Wasserburg age intercepts between c. 34 and 30 Ma, which may

Table 3.2. U-Pb isotopic data of monazite grains in a garnet-mica schist (Haimanta Group sample 14i)

Analysis	^{204}Pb	^{206}Pb	^{207}Pb	^{238}U	Pb	U	Uncorrected isotopic ratios							Uncorrected ages (Ma)					
	(cps)	(mV)	(mV)	(mV)	(ppm) †	(ppm) †	$^{207}Pb/^{206}Pb$	1σ (%)	$^{238}U/^{206}Pb$	1σ (%)	$^{207}Pb/^{235}U$	1σ (%)	Rho	$^{207}Pb/^{206}Pb$	2σ abs	$^{206}Pb/^{238}U$	2σ abs	$^{207}Pb/^{235}U$	2σ abs
Monazite in garnet																			
O.13	33	0.2	0.01	62	16	1319	0.0613	6.7	214	1.59	0.0396	6.9	0.23	651	287	30.1	1.0	39	5
O.15*	3	0.3	0.02	82	57	1752	0.0621	4.6	196	0.97	0.0437	4.7	0.20	676	198	32.9	0.6	43	4
O.16	120	0.3	0.02	81	46	1730	0.0642	4.5	193	0.97	0.0459	4.6	0.21	748	189	33.3	0.6	46	4
O.17	116	0.5	0.02	140	27	3003	0.0511	3.6	204	0.96	0.0346	3.7	0.26	247	165	31.5	0.6	35	3
2a.1*	-51	0.4	0.02	125	42	2675	0.0533	3.9	204	0.91	0.0360	4.0	0.23	344	178	31.5	0.6	36	3
2a.2	-69	0.3	0.02	92	84	1974	0.0596	4.3	192	1.35	0.0427	4.5	0.30	587	187	33.4	0.9	42	4
2a.4*	67	0.2	0.01	67	94	1424	0.0583	6.3	201	0.90	0.0399	6.3	0.14	539	274	32.0	0.6	40	5
2a.5*	104	0.3	0.02	90	56	1931	0.0579	4.7	202	0.94	0.0395	4.8	0.20	527	206	31.8	0.6	39	4
2a.6	-20	0.3	0.02	91	99	1944	0.0620	4.2	188	0.95	0.0456	4.3	0.22	676	178	34.2	0.6	45	4
2b.7*	54	0.3	0.01	83	33	1777	0.0568	5.1	199	0.96	0.0393	5.2	0.18	482	227	32.3	0.6	39	4
2b.10*	-26	0.5	0.02	139	20	2979	0.0511	3.7	207	1.09	0.0341	3.8	0.28	243	170	31.1	0.7	34	3
4a.1*	-32	0.2	0.01	63	21	1515	0.0540	6.3	187	1.08	0.0397	6.4	0.17	371	282	34.3	0.6	40	5
4a.3*	-152	0.3	0.01	75	20	1788	0.0526	5.5	187	1.22	0.0388	5.6	0.22	310	251	34.4	0.7	39	4
4a.10*	-162	0.4	0.02	101	114	2244	0.0546	4.3	187	1.02	0.0402	4.4	0.23	395	191	34.3	0.5	40	3
4a.11*	31	0.3	0.01	78	72	1735	0.0556	5.7	210	1.07	0.0366	5.8	0.18	437	255	30.7	0.5	36	4
4a.14*	-97	0.4	0.02	94	64	2074	0.0529	4.7	186	1.02	0.0391	4.8	0.21	324	211	34.5	0.5	39	4
4b.17	-13	0.2	0.01	66	54	1461	0.0540	6.7	200	1.03	0.0372	6.8	0.15	372	302	32.1	0.5	37	5
4c.19	20	0.4	0.02	103	157	2283	0.0516	4.5	196	1.05	0.0363	4.6	0.23	267	206	32.8	0.5	36	3
4c.21	3	0.3	0.01	92	23	2031	0.0505	5.7	215	1.24	0.0323	5.8	0.21	217	264	29.9	0.6	32	4
Matrix monazite																			
2a.1*	67	0.3	0.02	120	93	2562	0.0694	3.8	249	0.91	0.0384	3.9	0.23	911	158	25.8	0.5	38	3
2a.3*	-8	0.4	0.04	101	28	2150	0.1062	3.0	187	1.00	0.0783	3.2	0.31	1736	111	34.4	0.7	77	5
2a.4*	160	0.4	0.02	115	110	2454	0.0568	3.9	201	1.02	0.0389	4.0	0.25	482	171	31.9	0.6	39	3
2b.9	102	0.2	0.02	65	50	1393	0.0932	4.1	198	0.99	0.0650	4.2	0.24	1491	154	32.5	0.6	64	5
2b.11	32	0.3	0.02	89	57	1900	0.0806	7.5	209	1.64	0.0532	7.6	0.21	1211	294	30.8	1.0	53	8
2b.12	251	0.5	0.03	122	24	2599	0.0805	4.9	192	1.02	0.0579	5.0	0.21	1209	192	33.5	0.7	57	6
4a.4*	-304	0.3	0.02	84	119	2012	0.0560	4.7	182	1.03	0.0425	4.8	0.22	454	207	35.3	0.6	42	4
4a.5*	-41	0.3	0.02	79	40	1895	0.0811	4.0	196	1.03	0.0569	4.1	0.25	1223	157	32.8	0.5	56	4
4a.6*	-62	0.2	0.02	65	188	1447	0.0945	4.2	190	1.06	0.0687	4.3	0.25	1518	157	33.9	0.7	67	6
4a.7	200	0.3	0.02	75	193	1672	0.0841	4.5	211	1.14	0.0551	4.6	0.25	1295	174	30.5	0.7	54	5
4a.8	70	0.3	0.02	92	89	2050	0.0673	4.5	219	1.12	0.0423	4.6	0.24	847	187	29.3	0.5	42	4

* See Figure 3.4, † c. 20 % uncertainty on concentration

represent two crystallisation events: one at c. 34 Ma, represented by the data for four monazite grains from one garnet; the other event recorded by the majority of monazite inclusion analyses which define a colinear array of points yielding a lower intercept age of 29.61 ± 0.91 Ma and an upper intercept suggesting a Stacey and Kramers (1975) common-Pb composition equivalent to an age of c. 2588 Ma (Fig. 3.8a). The analysis that plots above and right of this linear array was not included in the regression as it is associated with relatively large errors which we infer to be the result of the impure nature of this particular grain (inclusions were identified and may not have been successfully avoided). Two analyses both with minor common-Pb and Tera–Wasserburg age intercepts between 32 and 33 Ma are inferred to have crystallized at c. 34 Ma and since suffered Pb-loss. Alternatively, these monazite grains plus others included in garnets from the same thin section (all with minor common-Pb) indicate a spread of $^{206}Pb/^{238}U$ ages from c. 34 to 30 Ma (Table 3.2, Fig. 3.8).

Two matrix grains also grew at c. 34–30 Ma (analyses plot in the dense cluster of data in Fig. 3.8b); one probably aged c. 34 Ma and the other c. 30 Ma, where each analysis includes a small component of common-Pb. However, the co-linearity of the majority of matrix monazite data suggests that a younger group of matrix grains formed at 27 ± 3 Ma. One discordant data point, plotting with a $^{206}Pb/^{238}U$ age of c. 26 Ma and with equivalent amounts of common-Pb to the other matrix grains, is interpreted simply to reflect the effect of Pb-loss from one of these monazites, the probable result of not being wholly occluded by its biotite host ("$m_{2a}1$", Fig. 3.4).

As with all monazite U–Pb data, excess ^{206}Pb tends to be a common occurrence. Unfortunately, the imprecision of ^{207}Pb–^{235}U ages (due to very low ^{207}Pb signals and lack of resolvable and correctable common-^{204}Pb) does not allow the extent of excess ^{206}Pb to be resolved, in contrast to the large ablation volume and high signal intensity data described by Horstwood et al. (2003) and Cottle et al. (2007a). A compilation of the amount of excess of ^{206}Pb commonly present in monazite by Parrish (1990), suggests that the excess age attributable to excess ^{206}Pb in our samples is likely to lie in the range of 0.5–2.0 Myr. Thus, the ages ranges quoted above represent maximum ages of growth, possibly overestimating by 0–2 Myr. Taking this into account we

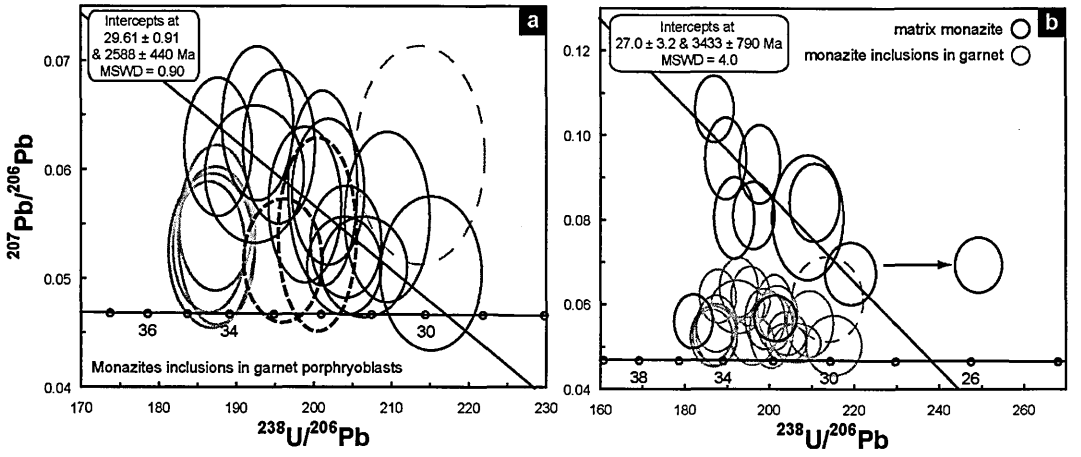

Fig. 3.8 U–Pb monazite data from sample 14i. (**a**) Monazite inclusions in garnet porphyroblasts: black ellipses used in regression to a c. 30 Ma U–Pb age; bold grey ellipses (of inclusions in the same garnet crystal) indicate a U–Pb age of c. 34 Ma; dashed black ellipses are inferred to represent c. 34 Ma monazites with a component of Pb loss; dashed grey ellipse omitted from regression owing to relatively large errors. (**b**) All data: grey ellipses represent all analyses shown in a); the regression is through all analyses of matrix monazite grains bar 3. See text for more details. Data point error ellipses are 2σ.

interpret that early monazite growth (predominantly grains occluded by garnet) and later (matrix) monazite growth took place in the periods 34–28 Ma and 30–22 Ma, respectively.

3.4.3 Ar/Ar mica sampling and methodology

Six samples of micaceous, greenschist to amphibolite facies metasediments were chosen for *in situ* Ar/Ar dating from a 25 km transect through the Haimanta Group. Sample selection aimed to provide a suite of unaltered schists ranging from close to the base of the Haimanta up to near the Cambro–Ordovician unconformity NW of Ropa village, representing a structural distance of approximately 6 km.

Micas in most samples crystallized during formation of the main (S_2) foliation, a crenulation cleavage, with the exception of those in sample 18. Bent, clear muscovite laths in this sample appear detrital, but the two muscovite analyses were performed on matrix domains of finely recrystallized white mica. Biotite in this sample was fine-grained and poorly developed, evidently at the lower limit of its metamorphic stability.

To determine the age of the samples, laser spots of approximately 50 μm in diameter were positioned in mica-rich domains using a focused CW Nd–Yag infrared laser with an external shutter. The samples were prepared by cutting 300 μm thick sections, polished on one side and

ultrasonically cleaned alternately in methanol and de-ionised water. Pieces of thick section, approximately 5mm x 5mm in size, were wrapped in aluminium foil and irradiated at the McMaster Reactor (Canada) for 50 hours. The GA1550 biotite standard, with an age of 98.79 ± 0.96 Ma (Renne et al., 1998), was used to monitor the fast-neutron flux; the calculated J value is 0.01001 ± 0.0000501. The extracted argon isotopes ^{36}Ar to ^{40}Ar were measured in a MAP 215-50 noble gas mass spectrometer. Analyses were corrected for blanks measured either side of two consecutive samples analyses, ^{37}Ar decay and neutron-induced interference reactions using the correction factors: $(^{39}Ar/^{37}Ar)_{Ca} = 0.00065$, $(^{36}Ar/^{37}Ar)_{Ca} = 0.000264$ and $(^{40}Ar/^{39}Ar)_{K} = 0.0085$, and the mass discrimination value used was 283.

3.4.4 Ar/Ar mica results

Ar/Ar ages (Table 3.3, Fig. 3.1a) are based on weighted averages of between 3 and 9 separate analyses as calculated using Isoplot 3 (Ludwig, 2003). Inverse isochron correlation diagrams have not been constructed due to the insufficient levels of ^{36}Ar in each measurement. The young age obtained from sample 20 (10.4 ± 2.3 Ma) most likely reflects the significantly finer grain size of the micas analyzed compared to other samples, as older ages would otherwise be expected from samples structurally higher in the section. Closure temperatures are lower for such fine-grained micas, which hence yield younger ages.

We note that although all Ar/Ar ages presented here are younger than those previously documented for both the Haimanta Group and underlying GHS (19 to 17 Ma, and 17 to 15 Ma, respectively (Vannay et al., 2004)), it is likely (especially for GHS samples) that the separated muscovite grains analyzed by those authors were coarser grained, and thus the older ages define an earlier point on the cooling path. The *in situ* muscovite ages and closure temperatures presented here correspond more closely to the zircon fission track data presented by Vannay et al. (2004).

We exclude biotite data from further calculations in the discussion because of the likely presence of excess ^{40}Ar. This common problem in metamorphic rocks (e.g. Sherlock and Kelley, 2002) is evident in our samples: for example, biotite and muscovite Ar/Ar ages for sample 23 are 14.5 Ma and 12.0 Ma, respectively, but closure temperature theory predicts that this relationship should be reversed (i.e. younger biotite than muscovite).

Table 3.3. Infrared laserprobe Ar/Ar age data. All measurements are in volts, the calculated ages include the error on J and are 2σ

Sample-Mineral	^{40}Ar	±	^{39}Ar	±	^{38}Ar	±	^{37}Ar	±	^{36}Ar	±	$^{40}Ar^*/^{39}Ar$	±	Age (Ma)	+/-
20-Wm	1.1618	0.0110	0.9917	0.0047	0.0125	0.0004	1.3427	0.0074	0.0021	0.0004	0.5577	0.1053	10.0	1.9
20-Wm	2.1705	0.0024	0.4868	0.0010	0.0082	0.0001	0.3855	0.0001	0.0064	0.0001	0.5859	0.0860	10.6	1.5
20-Wm	0.2096	0.0005	0.2173	0.0004	0.0024	0.0001	0.1177	0.0000	0.0003	0.0002	0.6108	0.2859	11.0	5.1
21-Bt	0.3481	0.0014	0.3488	0.0019	0.0043	0.0001	0.0029	0.0001	0.0002	0.0001	0.7948	0.0849	14.3	1.5
21-Bt	0.1623	0.0005	0.1404	0.0007	0.0017	0.0000	0.0005	0.0000	0.0001	0.0000	0.9138	0.0120	16.4	0.2
21-Bt	0.1843	0.0005	0.1605	0.0006	0.0021	0.0000	0.0010	0.0000	0.0002	0.0000	0.8075	0.0102	14.5	0.2
21-Bt	0.3641	0.0010	0.3868	0.0025	0.0032	0.0002	0.0147	0.0007	0.0002	0.0001	0.8076	0.0431	14.5	0.8
21-Bt	0.4121	0.0013	0.3555	0.0013	0.0039	0.0002	0.0083	0.0007	0.0006	0.0001	0.6314	0.0467	11.4	0.8
21-Bt	0.1643	0.0003	0.1354	0.0003	0.0015	0.0000	0.0062	0.0003	0.0002	0.0000	0.8867	0.0691	15.9	1.2
22-Wm	0.3344	0.0003	0.3478	0.0015	0.0040	0.0000	0.0005	0.0000	0.0003	0.0001	0.7150	0.0602	12.9	1.1
22a-Wm	0.2531	0.0004	0.2343	0.0010	0.0029	0.0001	0.0010	0.0000	0.0002	0.0000	0.8407	0.0183	15.1	0.3
22a-Wm	0.2137	0.0007	0.2031	0.0006	0.0023	0.0000	0.0005	0.0000	0.0002	0.0000	0.7464	0.0210	13.4	0.4
22a-Wm	0.3242	0.0006	0.3426	0.0002	0.0033	0.0001	0.0014	0.0001	0.0002	0.0000	0.7522	0.0216	13.5	0.4
22a-Wm	0.2218	0.0009	0.2102	0.0010	0.0025	0.0001	0.0012	0.0001	0.0002	0.0000	0.7921	0.0619	14.2	1.1
22a-Wm	0.2104	0.0008	0.2239	0.0015	0.0027	0.0000	0.0009	0.0001	0.0001	0.0000	0.7588	0.0582	13.6	1.0
22a-Wm	0.4092	0.0033	0.3922	0.0010	0.0046	0.0001	0.0010	0.0001	0.0002	0.0001	0.8797	0.0403	15.8	0.7
22a-Wm	0.1978	0.0003	0.1863	0.0002	0.0021	0.0000	0.0005	0.0001	0.0002	0.0000	0.8238	0.0502	14.8	0.9
22a-Wm	0.2615	0.0003	0.2602	0.0012	0.0033	0.0001	0.0004	0.0000	0.0001	0.0001	0.8745	0.0973	15.7	1.7
23-Bt	2.8174	0.0054	1.1911	0.0033	0.0157	0.0002	0.0020	0.0001	0.0063	0.0000	0.8098	0.0117	14.6	0.2
23-Bt	0.3705	0.0006	0.1527	0.0006	0.0021	0.0000	0.0001	0.0001	0.0008	0.0000	0.8588	0.0614	15.4	1.1
23-Bt	0.2776	0.0017	0.1655	0.0009	0.0020	0.0001	-0.0001	0.0004	0.0005	0.0000	0.8118	0.0340	14.6	0.6
23-Bt	0.7917	0.0010	0.3438	0.0015	0.0042	0.0000	0.0002	0.0001	0.0018	0.0000	0.7928	0.0369	14.2	0.7
23-Bt	1.0926	0.0013	0.4885	0.0016	0.0043	0.0002	0.0006	0.0001	0.0023	0.0000	0.8592	0.0288	15.4	0.5
23-Bt	1.0469	0.0013	0.5364	0.0014	0.0065	0.0000	0.0008	0.0001	0.0022	0.0000	0.7524	0.0261	13.5	0.5
23-Wm	0.7105	0.0015	0.4702	0.0022	0.0059	0.0001	0.0008	0.0001	0.0014	0.0000	0.6186	0.0203	11.1	0.4
23-Wm	0.2957	0.0006	0.2478	0.0015	0.0026	0.0001	0.0024	0.0003	0.0005	0.0000	0.6446	0.0380	11.6	0.7
23-Wm	0.2336	0.0011	0.1719	0.0013	0.0012	0.0001	0.0034	0.0007	0.0004	0.0000	0.7487	0.0364	13.5	0.7
23-Wm	0.4360	0.0009	0.3878	0.0027	0.0047	0.0002	0.0007	0.0001	0.0007	0.0000	0.6059	0.0246	10.9	0.4
23-Wm	0.8057	0.0014	0.4508	0.0003	0.0055	0.0001	0.0006	0.0001	0.0016	0.0000	0.7186	0.0239	12.9	0.4
23-Wm	0.5825	0.0007	0.4759	0.0003	0.0058	0.0001	0.0014	0.0001	0.0010	0.0000	0.6340	0.0224	11.4	0.4
23-Wm	0.6531	0.0015	0.4474	0.0010	0.0057	0.0000	0.0011	0.0001	0.0011	0.0000	0.7332	0.0212	13.2	0.4
23-Wm	0.2334	0.0005	0.2535	0.0010	0.0023	0.0001	0.0014	0.0003	0.0001	0.0001	0.7983	0.0998	14.4	1.8
23-Wm	0.2726	0.0004	0.2470	0.0010	0.0031	0.0001	0.0027	0.0001	0.0004	0.0000	0.6670	0.0324	12.0	0.6
23-Wm	0.3008	0.0007	0.2801	0.0011	0.0034	0.0001	0.0071	0.0005	0.0004	0.0000	0.6941	0.0336	12.5	0.6
Average blank	0.0096	0.0016	0.0005	0.0001	0.0005	0.0002	0.0003	0.0007	0.0012	0.0006				

3.5 Discussion

Figure 3.9 provides a summary of the relative timing (and where possible, absolute ages) of metamorphism and deformation recorded in the Haimanta Group.

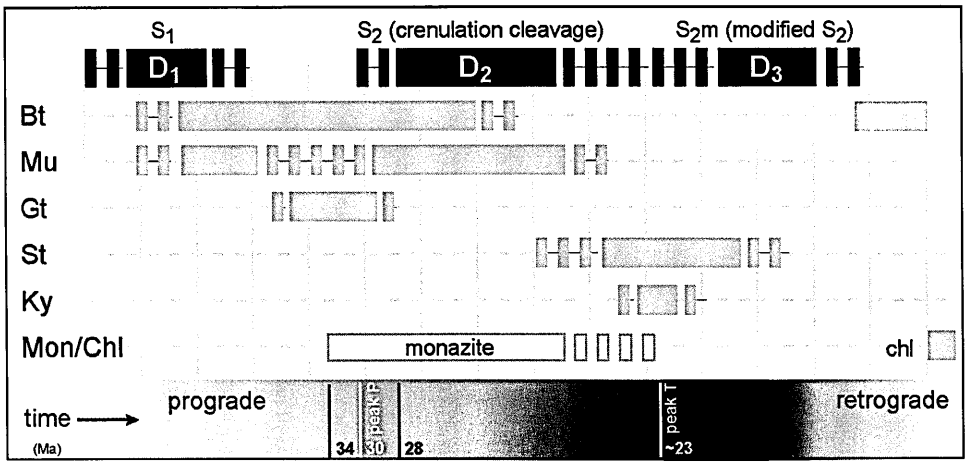

Fig. 3.9 Summary of the relative timing of metamorphism and deformation recorded in the Haimanta Group. Abbreviated mineral phases as in Figure 3.6.

3.5.1 Timing of the modelled P–T–d path

The timing of monazite crystallization, derived from U–Pb monazite data (sample 14i), is assigned to the modelled prograde *P–T* path based on several lines of evidence: (1) simple Thorium zoning in monazite is consistent with fractionation during growth upon heating (Kohn and Malloy, 2004); (2) we found no textural evidence for the formation of retrograde monazite (e.g. after allanite; Bollinger and Janots, 2006); (3) zoning profiles in garnet do not support the hypothesis that occluded monazite grains grew post-garnet growth along now annealed cracks; (4) retrograde metamorphism for this sample is minimal. Given that the garnet porphyroblasts preserve included phases from core to rim, and that monazite is restricted to the outer-core to rim regions (Fig. 3.4), monazite growth (beginning at c. 34 Ma) is interpreted to have post-dated the initiation of garnet growth. This explains the low Y content of the monazite grains, Y having been sequestered by earlier garnet growth (Foster et al., 2002a; Pyle and Spear, 1999) as indicated by decreasing Y concentration from core to rim of garnet crystals. If monazite grew as the result of a single reaction (implied by the simple Th zoning in the analyzed grains (Kohn and Malloy, 2004)), we infer that the garnet-in reaction involving the breakdown of muscovite and chlorite released the necessary P and LREE to form monazite (Kohn and Malloy, 2004). The observed monazite-free garnet cores,

however, suggest a delay between the first growth of garnet and the earliest recorded monazite grains. These observations imply monazite formation at ≥ 600 °C (given the implied overstep of the garnet-in reaction, Figs. 3.6 and 3.7) rather than at lower *T* as a product of allanite breakdown (c. 350-400 °C, e.g. Wing et al., 2003). Furthermore, the monazite forming reaction may have been promoted by recrystallization and grain size coarsening if LREE and Th are concentrated along grain boundaries, as the surface area onto which grain boundary LREE can adsorb is reduced (Corrie and Kohn, 2008). Monazite growth in the Haimanta Group sample contrasts with that in the GHS of Garhwal, where monazite grew both before and after garnet growth (Foster et al., 2000).

The ages of the youngest monazite grains occluded by garnet (c. 28 Ma) and of the analysed matrix grains (c. 27 Ma) bracket the end of garnet growth to c. 28 Ma. As the rims of garnet crystals grew syntectonically with early D_2, we infer that this phase of deformation began c. 30 Ma. Hence most matrix monazite grains, aged 27 ± 3 Ma, crystallized during D_2 with continued heating. Two older matrix grains (c. 34 and c. 30 Ma, Fig. 3.8b) are located in garnet pressure shadows (Fig. 3.4), and we infer that these were protected from D_2 recrystallization. All other matrix monazite grains may have initially grown between 34 and 30 Ma and been subsequently recrystallized during D_2. Alternatively, matrix grains may merely preserve their various crystallisation ages (c. 34, 30 and 27 Ma), as the peak temperature for this sample (640 °C, Fig. 3.7) is significantly below the closure temperature for monazite (820 ± 30 °C, Parrish, 1990; Spear and Parrish, 1996).

Garnet growth in the latest Eocene to Early Oligocene is consistent with data from elsewhere in the north-west Himalaya, notably in the Harsil Formation, Garhwal (c. 36–30 Ma, Foster et al., 2000), but also in the underlying GHS of Garhwal (c. 36–30 Ma, Foster et al., 2000) and Zanskar (c. 33–28 Ma, Vance and Harris, 1999). Monazite crystallization during peak metamorphism following 'Eohimalayan' Barrovian metamorphism in the upper GHS in the Everest region of Nepal, also has an Early Oligocene age of 32.2 ± 0.4 Ma (Simpson et al., 2000). A 35 ± 3 Ma kyanite-bearing leucosome in the uppermost GHS in central Nepal (comparable to leucosomes found in the uppermost GHS of the Sutlej section) provides further evidence of high-grade Early Oligocene metamorphism (Godin et al., 1999).

The Oligocene high-grade metamorphism experienced by the Haimanta Group questions the suggestion that a pre-Tertiary event was responsible for the main deformation fabrics and metamorphic minerals (Marquer et al., 2000). Other than early plagioclase cores (that we can only tentatively assign to a pre-Himalayan metamorphic event) we found no evidence for pre-Himalayan deformation and metamorphism (including a striking lack of pre-Tertiary monazite; see Martin et al., 2007). This clearly does not preclude a pre-Tertiary metamorphic history for these samples, although it does imply a pervasive Oligocene overprint. Synkinematic kyanite observed in sheared Akpa granite at its upper contact with the Haimanta Group probably formed during Tertiary metamorphism, and it is possible that deformation fabrics in xenoliths of the Haimanta Group also record Tertiary strain, especially where they are close to the granite margin.

3.5.2 Exhumation of the Haimanta Group

Maximum depth of burial (c. 26–30 km for a lithostatic gradient of 3.7 km $kbar^{-1}$) occurred at c. 30 Ma, during the final stage of garnet growth (Figs. 3.6 and 3.7). An exhumation rate can be estimated for the interval between this point of maximum burial and the assumed depth at which an effective Ar diffusion closure temperature was reached for muscovite. Closure temperatures were calculated at 306 to 347 °C using the Dodson equation (Dodson, 1973) and the diffusion parameters of Hames and Bowring (1994) for cooling rates of 10 to 60 °C Myr^{-1} (corresponding to the range of cooling rates calculated for the GHS and Haimanta Group by Vannay et al. (2004)). Extrapolation of the modelled retrograde path at constant dP/dT equates to a closure pressure of c. 2 kbars, equivalent to a depth of c. 7.4 km. Thus the Haimanta Group was exhumed by c. 23 km during the interval from c. 30 Ma to c. 13 Ma (the average age of the weighted mean muscovite ages for samples 22 and 23, where sample 20 was excluded on the basis that its younger age with relatively high errors was probably a consequence of the very fine grain size and/or the small number of analyses). This is equivalent to a moderate exhumation rate of c. 1.3 mm yr^{-1}.

Exhumation and cooling of both the GHS and TSS (including the Haimanta Group) was controlled by thrusting along the MCT between c. 23 Ma and c. 16 Ma (Vannay et al., 2004). However, estimated rates of exhumation for the GHS in this period are 2–4 mm yr^{-1} (Searle et al., 2006), far higher than our estimation for the basal Haimanta Group (c. 1.3 mm yr^{-1}). This implies

more efficient extrusion of the GHS between the MCT and the STD (Sangla detachment) than the rocks overlying the STD. In fact, c. 1 mm yr^{-1} is consistent with modern erosional rates for the southern edge of the Tibetan Plateau (Vance et al., 2003), and may represent a 'steady state' where exhumation is balanced by erosion, implying that by 23 Ma the Haimanta Group was essentially decoupled from the tectonically-extruding GHS beneath.

Calculations as described above yield lower average Haimanta Group exhumation rates (c. 0.6 mm yr^{-1}) from c. 13 Ma to the present. A decrease in exhumation rate is also recorded by GHS rocks at about this time (Vannay et al., 2004; Vance et al., 2003), suggesting that as the locus of thrusting propagated southwards into the Lesser Himalaya (Caddick et al., 2007; Chambers et al., 2008; Vannay et al., 2004), both units were exhumed less rapidly (and at similar rates of c. 0.6 mm yr^{-1}). From this we infer that following the cessation of GHS extrusion between the MCT and STD, both the Haimanta Group and the underlying GHS behaved as a more coherent block. Given that this re-coupling occurred at approximately the closure temperature of argon in muscovite (c. 300 °C), the rocks were passing through the brittle–ductile transition for quartz–feldspar aggregates (Passchier and Trouw, 1998), inhibiting ductile motion on the Sangla detachment between them. Brittle structures are poorly developed along this segment of the STD, consistent with a lack of differential exhumation of the two units at high levels in the crust as suggested by these data.

The pervasive, gently-dipping crenulation cleavage in the Haimanta Group, as well as randomly-oriented kyanite crystals in the schists near sample 8, suggests oblate (flattening) strain was dominant during initial exhumation. The preserved metamorphic field gradient between samples 8 and 18 (a kyanite–staurolite–garnet–mica schist and a phyllite containing patchily developed biotite, respectively; Fig. 3.1a) is c. 43 °C km^{-1} (Table 3.4). Comparison with an estimated gradient of c. 20 °C km^{-1} between the same samples at their peak temperatures implies flattening after peak metamorphism occurred in this section. The preserved field gradients calculated here cannot be equated with instantaneous geotherms, but the difference between these estimates is sufficient to demand explanation. Although the implied ductile flattening is not as extreme as examples reported from some other orogens (e.g. Argles et al., 1999), it provides important insights into the tectonic evolution of the STD hanging wall. We propose that the

Haimanta Group experienced ductile, dominantly coaxial flattening during initial exhumation and S_2 fabric formation from c. 30 Ma until c. 23 Ma. Further exhumation of the underlying GHS between c. 23 Ma and c. 16 Ma was accomplished by ductile extrusion beneath the extensional Sangla detachment. This phase is represented in the hanging wall (Haimanta Group) by the development of non-coaxial ductile structures that modify S_2 (i.e. the D_3 stage), which may also have contributed to flattening of the section. It is important to note that we did not observe any major brittle structures between samples 8 and 18 that could have excised substantial parts of the section, as was demonstrated in the Betic Cordillera by Argles et al. (1999). From this structural evolution we infer the age of peak *T* on the modelled *P–T–t–d* paths (Figs. 3.6 and 3.7), which is marked by the transition from D_2 to D_3 preserved in sample 8i, at c. 23 Ma (Fig. 3.9).

Table 3.4. Calculations of metamorphic field gradients in the Haimanta Group

Sample/ section	Peak *T* (° C)	Peak *P* (kbar)[1]	Peak depth (km)[2]	Present distance (km)	Peak gradient (° C km^{-1})[3]	Present gradient (° C km^{-1})[3]	Vertical shortening factor
18	400	3.54	13	-	31	-	-
8	660	7	26	-	25	-	-
18 to 8	260	3.5	13	~6[5]	20	43	~2

[1] *P* at peak *T* conditions

[2] Calculated assuming lithostatic gradient of 3.7 km/kbar

[3] Metamorphic field gradient, not necessarily instantaneous geothermal gradient

[4] Estimated for biotite isograd (Ferry, 1984)

[5] Structural distance between samples 18 and 8 (Fig. 3.1a)

3.5.3 Tectonic implications of the Haimanta Group

Despite a relatively minor difference in metamorphic grade between the basal Haimanta Group and the uppermost GHS seen in the Sutlej valley, there are several crucial reasons for separating them into two distinct tectonic units: (1) they are separated by a mylonite zone with both top-to-the-SW (thrust) and overprinting top-to-the-NE (normal) shear sense indicators that clearly define a major tectonic boundary; (2) they display different structural styles: a consistent crenulation cleavage in the Haimanta Group, but a highly disrupted and deformed migmatitic foliation in the GHS gneisses; (3) the Haimanta Group lacks any evidence of *in situ* melt, which is abundant in the underlying rocks, both as deformed kyanite-bearing leucosomes and later segregations associated with sillimanite-grade metamorphism; (4) decoupled exhumation between

c. 23 and 16 Ma resulted in distinct retrograde *P–T* paths, which for the GHS are characterised by decompression through muscovite-out reactions (Caddick, 2004; Harris et al., 2004; Vance and Harris, 1999).

As the consistent, regular set of structures in the Haimanta Group is incompatible with extreme ductile flow, this precludes the assignment of this unit to a low-viscosity crustal channel (e.g. Beaumont et al., 2001). The notable absence of *in situ* melt in the Haimanta Group supports this deduction, with *in situ* melting as identified in parts of the GHS providing a means of weakening leading to flow beneath southern Tibet (Zhang et al., 2004). Thus, the Haimanta Group may represent a passive 'lid' to a 'GHS channel' below. Having been buried to greater depths than the Haimanta Group, and consequently attained higher temperatures, a sufficiently melt-weakened GHS in the Sutlej valley may have formed a south-directed plastic flow during the Late Oligocene–early Miocene, as proposed for mid-crustal rocks in central Nepal (Godin et al., 2007). The rheological contrast between the middle and upper crust (effectively the GHS and the Akpa granite/Haimanta Group, respectively) became such that they were decoupled during this phase of exhumation. Decompression before significant cooling in the GHS resulted in the 'Neohimalayan' phase of metamorphism, i.e. the high-*T* (sillimanite-grade) 'event' associated with melt generation, while the Haimanta Group was exhumed at more moderate rates associated with steady cooling. The lower peak temperatures attained in the Haimanta Group helped to preserve evidence of its 'Eohimalayan' burial history.

Ductile flattening of the Haimanta Group during initial exhumation is consistent with predictions of the critical orogenic wedge model (Platt, 1986) for rocks near the rear of the wedge. However, this model assumes a uniform rheology for the wedge material (on a large scale), which is contrary to the weak mid-crustal layer (represented by the GHS) prescribed in the channel flow model of Beaumont et al. (2001; 2004). Vertical compression of the channel lid (i.e. the STD hanging wall) is not explicitly predicted by most channel flow model results, although simulations involving a weakened upper crust produce localised thinning, and doming of the underlying high-grade material (Beaumont et al., 2004). The thinned Haimanta section could be an expression of such crustal thinning above the nearby Leo Pargil dome, as is recognised in some crustal sections

surrounding the North Himalayan Gneiss Domes further east (Quigley et al., 2008). The Leo Pargil dome may thus represent the closest channel doming to the STD currently recorded.

The Haimanta Group represents a distinct tectonic unit of the crystalline core of the Himalaya. We recognise that it shares a strikingly similar tectonic evolution to that of the uppermost GHS in central Nepal (Coleman and Hodges, 1998; Gleeson and Godin, 2006; Godin et al., 2001; Vannay and Hodges, 1996), where the ductile Chame and brittle Phu detachments are likely equivalent structures to the Sangla detachment and the detachment bounding the northern and western flanks of the Leo Pargil dome (see Figure 1 in Thiede et al., 2006), respectively. Gleeson and Godin (2006) propose that the uppermost GHS in central Nepal may be equivalent to units up to 300 km further east along-strike, including the Everest Series. As in the Haimanta Group, this unit is devoid of leucogranites, and as in the uppermost GHS in central Nepal, this unit is bounded by two low-angle normal faults (the Lhotse detachment below and the Qomolangma detachment above) (Simpson et al., 2000). Indeed, if the Haimanta Group can be correlated with these units then it is of greater regional significance than has been previously recognised.

3.6 Conclusions

Amphibolite-grade metasediments of the Haimanta Group, seen in the western Himalaya at the base of the Tethyan sediments and structurally above the GHS, record a history of burial and heating to a maximum depth of <8 kbars at c. 600 °C. The ensuing phase of decompression during further heating began at c. 30 Ma, and was accompanied by (D_2) deformation resulting in the formation of a pervasive crenulation cleavage (S_2), and the growth of staurolite and kyanite porphyroblasts. Continued cooling from a peak T of <660 °C (for the examined samples) accompanied further decompression, and a temperature of 300–350 °C was reached at approximately 2 kbars, by c. 13 Ma. The initial average exhumation rate of c. 1.3 mm yr^{-1} during the interval c. 30 and 13 Ma was followed by a reduced average rate of c. 0.6 mm yr^{-1} from 13 Ma to the present. During the first part of this exhumation history the underlying GHS was more rapidly exhumed than the Haimanta Group, with the two units remaining decoupled until c. 16 Ma. After c. 13 Ma, both units were exhumed at equal rates (c. 0.6 mm yr^{-1}), implying exhumation as a single tectonic unit. The Haimanta Group is recognized as a distinct tectono-thermal unit from the

underlying GHS and, with along-strike correlatives, is important to reconcile with current models of Himalayan orogenesis.

Chapter 4

Sm–Nd garnet geochronology

4.1 Introduction

It has been demonstrated that the *in-situ* (in thin section) dating of accessory phases such as monazite can be a successful means of bracketing garnet-growth, and thus determining the age of prograde metamorphism in garnet-bearing pelites (Chapter 3). However, a number of possible reactions and hence a relatively wide range of pressure-temperature conditions under which accessory phases may form (Corrie and Kohn, 2008 and references therein) presents a challenge to this technique, which relies on the accessory phase(s) being in isotopic equilibrium with garnet. A thorough textural and chemical analysis of not only the accessory phases to be dated, but of the other phases in the sample assemblage, is necessary if the most likely mode of accessory mineral formation is to be ascertained. This is a time-consuming and potentially complex process. The geochronometric study of metamorphic garnet solves this predicament, as chemical zonation provides information regarding the pressure and temperature during growth, and the typically elevated Sm/Nd ratio found in pelitic garnets (Table 4.1) represents a useful chronologic tool when combined with the analysis of the relatively low Sm/Nd whole rock. Textural details such as the orientation of inclusion fabrics relative to the exterior matrix fabric can add constraints on the timing of deformation relative to the growth of minerals during regional metamorphism. A combination of these data from garnet has the potential to yield a detailed and accurate pressure-temperature-time-deformation history, from which the rates of heating, burial and deformation can be investigated (Caddick et al., 2007; Stowell and Goldberg, 1997; Vance and Holland, 1993).

This chapter will first review the basic principle of radioactive decay, then the application of this to the Sm–Nd isotope system. The inherent problems for Sm–Nd garnet geochronology will be discussed before a summary of the methods (with detailed protocols in Appendix B1), after which the results will be presented. An in-situ trace element study of garnets from the samples studied provides further data to inform discussions of Sm–Nd garnet chronometry.

Table 4.1 Nd and Sm concentrations of common rock-forming minerals

Mineral	Formula	Nd (ppm)	Sm (ppm)	$^{147}Sm/^{144}Nd$
Amphibole	$(Mg,Fe,Ca,Na)_{2-3}(Mg,Fe,Al)_5(Si,Al,Ti)_8O_{22}(OH,F)_2$	6.84 – 40.5	2.01 – 11.5	0.22 – 0.32
Biotite	$K(Mg,Fe)_3AlSi_3O_{10}(F,OH)_2$	0.11 – 20.5	0.04 – 4.34	0.21 – 0.36
Clinopyroxene	$(Ca,Mg,Fe,Al)_2(Si,Al)_20_6$	0.84 – 4.64	0.33 – 1.16	0.25 – 0.39
Cordierite	$Mg_2Al_3(AlSi_5)O_{18}$	0.12 – 0.89	0.03 – 0.15	0.16 – 0.28
Garnet	$(Fe, Mg, Mn, Ca)_3(Al, Fe)_2Si_3O_{12}$	**0.02 – 7.67**	**0.02 – 13.2**	**0.5 – 17.8**
K-feldspar	$KAlSi_3O_8$	0.07 – 6.57	0.02 – 0.59	0.07 – 0.29
Muscovite	$KAl_3Si_3O_{10}(F,OH)_2$	0.08	0.03	0.38
Plagioclase	$NaAlSi_3O_8$ - $CaAl_2Si_2O_8$	0.5 – 38.4	0.07 – 4.43	0.08 – 0.28
Accessory phases				
Allanite	$(Ca,Ce,Y,La,Th)_2(Al,Fe)_3Si_3O_{12}(OH)$	**300-50,600**	**800-14,000**	**0.06 – 0.21**
Apatite	$Ca_5(PO_4)_3(OH,F,Cl)$	**25 – 7885**	**2 – 7983**	**0.03 – 0.43**
Epidote	$Ca_2(Fe,Al)Al_2(SiO_4)(Si_2O_7)O(OH)$	2.75 – 20.0	0.53 – 3.74	0.13 – 0.34
Monazite	$(Ce,La,Th,Nd,Y)PO_4$	**43,000-370,000**	**5500-55,700**	**0.05 -0.36**
Titanite (sphene)	$CaTiSiO_5$	831 – 7773	120 – 2475	0.13 – 0.36
Tourmaline	$Na(Al,Fe,Li,Mg,Mn)_3Al_6(Si_6O_{18})(BO_3)_3(OH,F)_4$	0.06 – 6	0.001 – 1.6	0.15 – 0.44
Xenotime	YPO_4	615-5300	300-10,300	0.42 – 2.9
Zircon	$ZrSiO_4$	3.34 – 100	1.43 – 30	0.16 – 1.207

All data is LA–ICPMS or electron microprobe with the exception of biotite. Data from Amelin (2004), Bea (1996), Bea and Montero (1999), Bingen et al. (1996), Broska et al. (2000), Corrie and Kohn (2008), (Finger and Krenn (2007), Finger et al. (1998), Forster and Harlov (1999), Foster and Vance (2006), Giere and Sorensen (2004), Grauch (1989), Krenn and Finger (2007), Li (1994), McFarlane and McCulloch (2007), Pan (1997), Prince et al. (2000) Romer and Xiao (2005) and Scherer et al. (2000). Text in bold highlights minerals of particular interest to this study.

4.2 The basic principle of radioactive decay and the Sm–Nd isotope system

The probability of decay of a radiogenic parent atom (P) is proportional to the time interval over which decay occurs (dt) multiplied by the decay constant for that radionuclide (λ).

$$(-dP/P) = \lambda dt \qquad (1)$$

With integration over time equation (1) becomes:

$$\ln P/P_o = -\lambda t \qquad (2)$$

$$P_o = Pe^{\lambda t} \qquad (3)$$

Where P is the number of parent atoms remaining or at present, and P_o is the number of parent atoms originally or initially.

If the radiogenic daughter isotope (D) is stable, then D equals the number of parent atoms consumed, i.e. $P_o - P$. Equation (3) substituted into this yields the following equation:

$$D = P(e^{\lambda t} - 1) \qquad (4)$$

Leading to the age equation:

$$t = \ln [D/P + 1] / \lambda \quad (5)$$

However, the fact that atoms of the daughter isotope pre-exist in the system means that this equation alone cannot be used, and we must find an alternative which takes into account pre-existing isotopes.

If the number of radiogenic daughters at t=0 is D_o, then

$$D = D_{total} - D_o \quad (6)$$

Combining equations (4) and (6) the following is derived

$$D_{total} = D_o + P (e^{\lambda t} - 1) \quad (7)$$

Samarium (Sm) has 7 naturally occurring isotopes, 3 of which are radioactive (Dickin, 2005). The half lives of ^{148}Sm and ^{149}Sm are so long (c. 10^{16} yr) that no measurable variations in the respective daughter isotopes (^{144}Nd and ^{145}Nd) are produced. The radioactive alpha decay of ^{147}Sm to ^{143}Nd however, with a half life of 106 Ga, is useful for geochronological purposes. The following equation is used, where t and the initial ^{143}Nd are unknown:

$$^{143}Nd/^{144}Nd = (^{143}Nd_{initial}/^{144}Nd) + [(^{147}Sm/^{144}Nd) e^{\lambda t} - 1)] \quad (8)$$

This equation is equivalent to equation (7) above, normalised to ^{144}Nd, the second most abundant Nd isotope. Isotopic ratios are analysed, rather than individual isotope intensities, as there is greater analytical precision in measuring ratios on a mass spectrometer. The most abundant Nd isotope, ^{142}Nd, is avoided as a normalising isotope as it may not be constant owing to the relatively rapid decay of its radioactive parent (^{146}Sm) and the subsequent possible early earth Sm–Nd fractionation (e.g. Caro et al., 2006.; Harper and Jacobsen, 1992).

4.3 Problems for Sm–Nd garnet geochronology

4.3.1 Inclusions

Despite the potential for Sm–Nd garnet geochronology to be a powerful tool for the study of tectonic processes in regionally metamorphosed terranes, there are two obvious problems: (1) garnets have low Nd concentrations (typically less than 1 ppm) making *precise* analysis of garnet

samples technically difficult, (2) if present, Nd-rich inclusions (see accessory phases in Table 4.1) can dominate both the Nd budgets of impure garnet analyses (i.e. a mixture of pure garnet and Nd-rich inclusions) and of whole rock analyses (including garnet and its inclusions). The equivalent of even a 20 μm diameter grain of monazite or allanite in a 100 mg garnet separate will reduce the $^{147}Sm/^{144}Nd$ ratio of the pure garnet by over 50%! Figure 4.1 illustrates the effect of increasing proportions of an Nd-rich inclusion, for an inclusion mass ranging from 1 - 13 μg (equivalent to a 40 - 93 μm diameter grain) in increments of 1 μg, in a 100 mg garnet separate. This effect is more pronounced with monazite than with allanite (cf. Figs. 4.1f and g with the same model inputs including volume proportion of inclusion, except for the inclusion phase) as monazite has a greater concentration of Nd (Table 4.1). Crucially, therefore, even minor contamination will cause a significant reduction in the *precision* of age determinations and the loss or complete eradication of age resolution, i.e. data points may be isochronous but the Sm/Nd range between end-members (i.e. whole rock and garnet) is too small to resolve an meaningful age (e.g. Bowtell et al., 1994; Vance and O'Nions, 1990).

With regards to Nd-rich inclusions in the whole rock analysis, there will be a negligible effect on the whole rock–garnet isochron (and measured age of the garnet) if a pure enough garnet separate is analyzed and the inclusions were in isotopic equilibrium with the whole rock at the time of garnet growth, because i) REE-rich inclusions dominate the whole rock Nd and Sm budget, and ii) Sm/Nd ratios of most accessory phases are similar to whole rock values (DeWolf et al., 1996). However, there is a more serious consequence if a pure garnet analysis cannot be guaranteed, and Nd-rich inclusions are *not* the same age as the garnet (and are isotopically isolated from the whole rock for times longer than the age of the garnet). The significant isotopic disequilibrium between the inclusion and the rest of the rock at the time of garnet growth will result in a totally inaccurate (yet precise (!) if the Sm/Nd of the impure garnet separate is not too low) analysis. Where the inclusion is older than the occluding garnet, the effect on geochronology has been modelled by Prince et al. (2000) (monazite effect for Sm–Nd), Scherer et al. (2000) (zircon effect for Lu–Hf), and here in Figure 4.1 (c and d) and is discussed in Section 4.6.

Table 4.2 Data used in inclusion modelling

phase	[Nd][1]	[Sm][1]	proportion of whole rock
allanite	25000	4800	0.00136
monazite	110000	17500	not applicable
garnet	[2]	[2]	0.04 [3]

[1]average based on LA-ICPMS data from pelitic rocks Finger and Krenn (2007), Krenn and Finger (2007) and Bea and Montero (1999). [2]garnet and analysed whole rock data as in Table 4.7 (samples 14i and 78ii). [3]estimated modal abundance from sample 14i

Recently it has been shown that young monazite (relative to garnet) may form via a retrograde reaction in the presence of a fluid (Bollinger and Janots, 2006 and references therein). This may be in a closed system, with pore fluid and allanite as the source of REE, or in an open system where REE are externally-sourced, e.g. from hydrothermal fluids. Only closed systems are suitable for geochronology. Cracks in garnet porphyroblasts may act as possible fluid pathways, and these pathways may go undetected, or at least be under-estimated in terms of their abundance, because cracks may intersect inclusion grains out of the plane of the thin section used for textural analysis. Under the right conditions for retrograde monazite crystallization, it would be reasonable to assume that all matrix monazite would belong to this retrograde generation, whereas 'inclusions' in garnet may be any mixture of three monazite generations, these being (1) retrograde (younger than the 'occluding' garnet); (2) peak to prograde (approximately the same age as the occluding garnet); (3) pre-existing (older than the occluding garnet).

In light of some non-isochronous Sm–Nd data (Section 4.6), some modelling was performed in an attempt to gain insights into the effects of different Nd-rich inclusions in garnet, especially for scenario (1) above, which has not been modelled before. The method and assumptions are briefly explained here. Isotopic compositions of garnet, inclusion, whole rock and 'effective bulk composition' (EBC) evolve through time according to the decay equation. The EBC was defined as the whole rock minus the earliest-grown phase (either inclusion or garnet), which in effect extracted a certain proportion of Nd and Sm from the whole rock at time T_0, at which point, the whole rock, EBC and earliest phase were all assumed to be in isotopic equilibrium. Hence, when the later phase (garnet or inclusion respectively) grew at time T_1, it was assumed to have

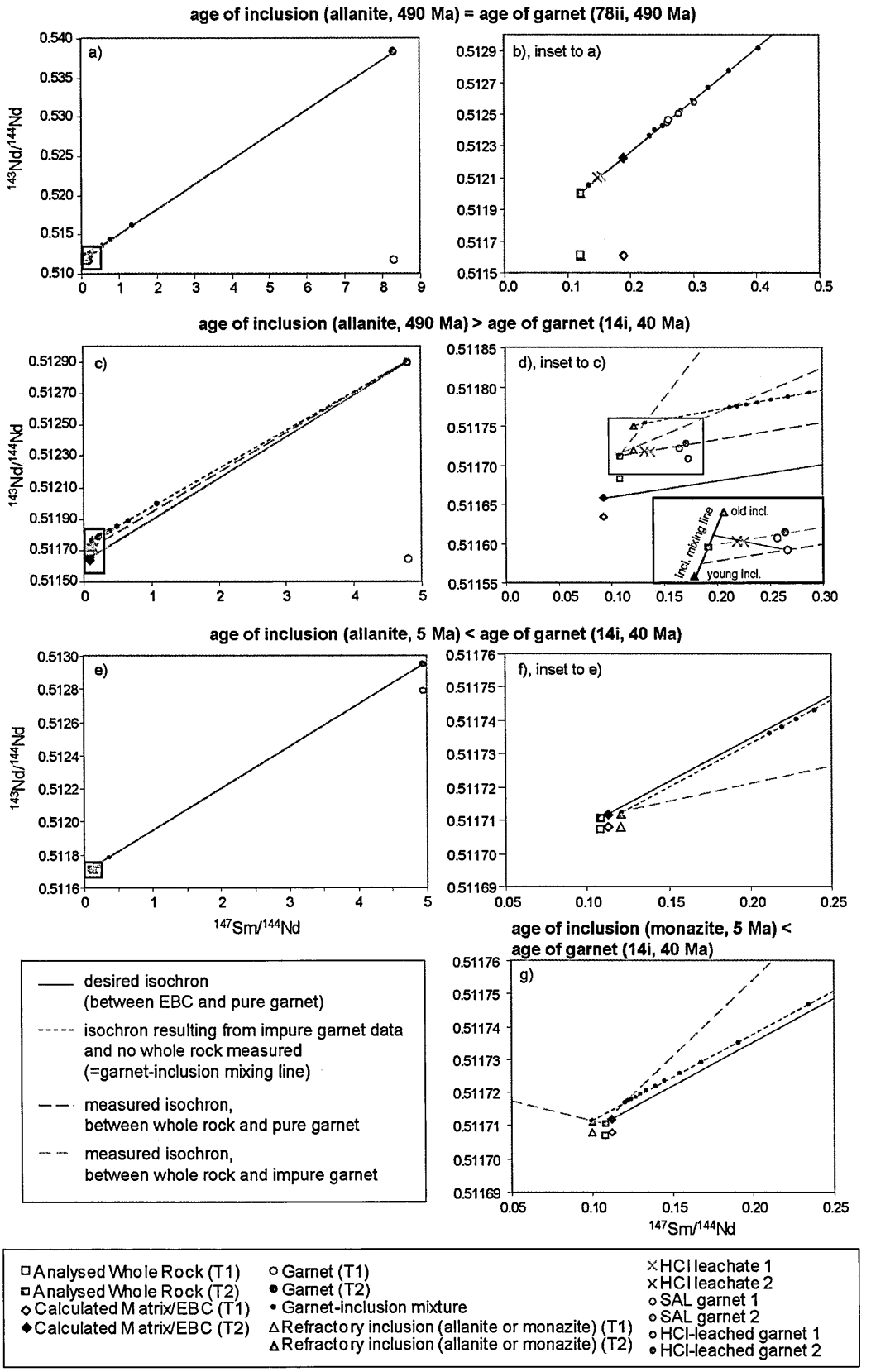

Fig. 4.1 Model Sm–Nd results based on real LA–ICPMS garnet data (see section 4.7) and assumptions made in Table 4.2. See text for discussion.

equilibrated not with the whole rock, but with the EBC (due to the localized, heterogeneous distribution of REE in metamorphic rocks, this assumption may not be true in nature, but it is necessary for the modelling). The Nd isotopic compositions of all phases were then evolved through to the present day (T_2). This required the following inputs (Tables 4.2 and 4.7):

- [Nd], [Sm] and $^{147}Sm/^{144}Nd$ of whole rock, garnet and inclusions;
- Relative proportions of garnet, inclusions and EBC in whole rock;
- $^{143}Nd/^{144}Nd$ of whole rock at present day
- Times of inclusion and garnet growth

Results of the above modelling were combined with modelled isotopic compositions of garnet-inclusion mixtures using the compositional data in Table 4.2, in addition to $^{147}Sm/^{144}Nd$ values for 'pure' garnet derived from Sm/Nd ratios obtained by LA–ICMPS.

Two simplified models of young 'inclusions' in an older host garnet are presented, using a Tertiary-aged garnet and 5 Ma Nd-rich inclusions (Fig. 4.1e to g). These ages reflect existing geochronological data from the Himalaya (e.g. Catlos et al., 2002). In one model allanite is the inclusion (Fig. 4.1f), to compare with models also with allanite inclusions but with different ages relative to the garnet (Figs. 4.1a to d). This model also broadly represents the effect of any inclusion with a higher $^{147}Sm/^{144}Nd$ than the whole rock (as for zircon or xenotime inclusions, Table 4.1). In the second of the models monazite (with a lower $^{147}Sm/^{144}Nd$ than the whole rock) is the problematic Nd-rich inclusion (Fig. 4.1g), and as outlined above, is a geologically possible young 'inclusion'. The first observation is that with a pure garnet analysis there is negligible effect on the isochron and the age determined (Fig. 4.1e, modelled using allanite but identical to the model with monazite, not shown). If impure garnet is analyzed, then alongside the reduction in the accuracy of the age, depending on the $^{147}Sm/^{144}Nd$ of the inclusion, apparent isochrons may be younger (high $^{147}Sm/^{144}Nd$ relative to the whole rock, Fig. 4.1f) or older (low $^{147}Sm/^{144}Nd$ relative to the whole rock, Fig. 4.1g).

Hand-picking garnet material from sieved crushate fractions allows a degree of optical screening of inclusions, but this approach will not avoid incorporating sub-microscopic (<30 μm)

inclusions in a garnet separate (Anczkiewicz and Thirlwall, 2003). The safest method to obtain robust ages, whether Nd-rich inclusions are known to be present or not, is to perform duplicate analyses for each sample on different aliquots of the garnet separate. Any contamination will be evident from variable Sm/Nd ratios, and a reproducible age can be regarded as robust. It is highly unlikely (if inclusions are *not* the same age as garnet) that analysis of impure garnet separates, with a spread of Sm/Nd ratios due to variable amounts of garnet-inclusion mixing, would yield isochronous relationships. For non-reproducible ages, the isochron age of the garnet analysis with the highest Sm/Nd ratio (and thus closest to the isotopic composition of the pure garnet) may be taken as the best minimum or maximum age depending on the $^{147}Sm/^{144}Nd$ of the inclusion and its age (Table 4.3), and it is encouraging to note that if Sm/Nd ratios of the measured impure garnet separates are 50 to 100 % of the true garnet value, the deviation of the apparent age from the true age will be less than, or similar to, typical analytical uncertainties (0 to 10 %) (Prince et al., 2000). However, the sobering news is that, given the Sm–Nd concentrations of Himalayan pelitic garnets, only an order of one part-per-million of the garnet separate need be monazite to reduce the Sm/Nd ratio by 50 % (Prince et al., 2000). Finally, the story may become even more complex if there is more than one type of Nd-rich inclusion present, each potentially with its own crystallization age. The resulting data would be complicated to unravel and interpret, and equally challenging to forward model, especially given the broad ranges of Sm and Nd concentrations in such contaminating phases (Table 4.1).

Table 4.3 Effect of Nd-rich inclusions on the apparent age of garnet

$^{147}Sm/^{144}Nd$ of inclusion relative to whole rock	high	low	high	low
age of inclusion relative to the garnet	old	old	young	young
apparent age relative to true age (between whole rock and pure garnet)	younger	older	older	younger
refer to	Prince et al., 2000	Fig. 4.1c and d	Fig. 4.1g	Fig. 4. e and f

4.3.2 Sampling bias

Metamorphic garnets typically grow over a protracted period of time of ~ 5 to 10 Myr (Christensen et al., 1989; Vance and Harris, 1999; Vance and O'Nions, 1992), so given that the achievable precision of Sm–Nd chronometry can be as good as ~1 Ma (2σ) (e.g. Vance and Harris,

1999) and routinely 2 to 3 Ma (2σ), it may be that duplicate analyses will not be isochronous, simply because neither aliquot is sampling exactly the same portion of the studied garnet. A sampling bias may arise as a result of trying to ensure the desired optical purity of the garnet separate where there is distinct zonation e.g. with respect to inclusions, and separates that are analysed must be well-characterized from a prior petrologic textural study (e.g. Argles et al., 1999; Vance et al., 1998b). Alternatively an estimate of the sampling bias should be made which may explain a degree of intra-sample age variation (and not exclusively contamination from Nd-rich inclusions). The aliquots of garnet separates analyzed here though were identical fractions of the same original separate, because there was either weak or no evidence for distinct phases of garnet growth.

4.3.3 Sm–Nd compared to other chronometric methods

As there is an obvious difficulty in dating garnets by Sm–Nd, complementary U–Th–Pb dating of accessory phases was performed (Chapter 3.4). The reasons why other isotopic systems were not considered for garnet geochronology are briefly discussed below.

Rb–Sr: Very low concentration of the parent isotope (^{87}Rb); high mobility of both elements in response to post-crystallisation events (Vance and O'Nions, 1990; 1992).

U–Pb: Very low concentration of the parent isotope (U); dominated by U-rich inclusions (DeWolf et al., 1996; Vance et al., 1998b).

Lu–Hf: As garnet strongly fractionates Lu and Hf (leading to very high $^{176}Lu/^{177}Hf$ ratios) and both elements have slow diffusion rates, this would be a suitable geochronological technique were it not for the inclusion of zircon which contains a significant amount of Hf and is extremely resistant to leaching (Connelly, 2006; Scherer et al., 2000). Apatite inclusions with higher $^{176}Lu/^{177}Hf$ than garnet may also be problematic, and it is uncertain whether sulphuric acid leaching (SAL) is effective in removing these inclusions from garnet separates. Anczkiewicz et al. (2004) suggest that two leached samples were effectively leached of apatite, although apatite was not identified as a garnet inclusion in either of the samples. In any case, Scherer et al. (2000) suggest that apatite has little or no effect on the Lu–Hf garnet-whole rock system. While the Lu–Hf method appears to be successful for dating garnets separated from mafic rocks (e.g. Anczkiewicz et al., 2004), no equally

successful cases of Lu–Hf dating of pelitic garnets have been published, to the author's knowledge. In any case, the lack of the Lu–Hf capability at the Open University at the start of this project precluded the application of this technique (which would have been interesting to test on garnet-bearing amphibolite samples I05/83 and B06/73, Appendix A).

4.4 Selected samples

Five samples were selected from the Sutlej valley (Table 4.4) for Sm–Nd garnet dating, having met the following criteria:

a) from key localities

Samples from four different units (including the Shimla klippe as a separate unit) were studied, in order to obtain information on discrete metamorphic events affecting individual tectonic units. One sample was from the same locality where an age of garnet growth had been constrained from *in situ* monazite analysis (Caddick et al., 2007). Successful analysis of this sample would provide a test of the reproducibility between the two methods of dating garnet growth.

b) major element garnet profiles show prograde zoning patterns

The diffusion rates of rare earth elements (REE) including Sm and Nd are equal or slower than divalent cation (e.g. Mn, Fe, Mg) diffusion rates (Cohen et al., 1988; Kohn, 2003 and references therein). Therefore, if major element profiles (from electron microprobe analysis) preserve prograde zoning profiles (e.g. Mn bell-shaped profiles indicative of Raleigh fractionation) it can be inferred that the Sm–Nd system has also not been perturbed since garnet growth. In such samples, the age of the pure garnet separate will be equivalent to the period of prograde metamorphism during which garnet grew.

In light of the preservation of major (and therefore REE) element prograde zonation, the closure temperature of the Sm–Nd isotopic system (strongly dependent upon cooling rate, grain size and peak temperature, e.g. Ganguly et al., 1998) was of little concern in this study. In any case, garnet typically has a Sm–Nd closure temperature > 600 °C (Jung et al., 2007 and references therein). Temperatures above 600 °C may not have been attained by the samples studied here long enough to allow even partial diffusion of Sm and Nd (cf. peak temperatures of ~ 650 °C recorded

in samples from the Sutlej valley from the Lesser Himalayan Sequence (sample 52, which also broadly corresponds to sample 66i) in Caddick et al. (2007), and the Haimanta Group (sample 14i) in Chapter 3).

c) relatively abundant and large garnet grains (<1mm)

This minimised the amount of time spent sieving crushate and hand-picking, and maximised the amount of garnet material to provide as many aliquots for duplicate analyses and/or further leaching experiments as possible.

d) minimal REE-enriched inclusions

To minimise problems inherent with contamination from Nd-rich inclusions, a thorough study utilising back-scatter electron (BSE) imaging and the energy dispersive system (EDS) on the electron microprobe was undertaken to identify inclusions in garnet. The drawbacks to this technique are that i) very small inclusions (<1 μm) are below the resolution of the EDS and cannot be identified, and ii) only the two-dimensional exposed sample surface can be screened, meaning that problematic inclusions may be present elsewhere in the sample.

e) other metamorphic minerals/low variance assemblage (e.g. staurolite, kyanite)

Since the final goal is to combine Sm–Nd garnet age data with well-constrained pressure-temperature paths, additional prograde phases will allow more precise thermobarometry (especially if they are texturally significant).

Table 4.4 Summary of details of samples from the Sutlej valley selected for Sm-Nd garnet analysis

Sample (I05)	Lithology	Index minerals	Unit	LREE-enriched accessory phases		Weight (mg) of garnet material before / after leaching with...			% weight loss from SAL garnet after HCl-leach	
				In garnet	In the matrix	H_2SO_4*	HCl (2 hr)	HCl (4hr)	2hr	4hr
14i	Mica-schist	gt st	Haimanta Group	mon ap (zr)	mon ap	- / 125	87 / 82	82 / 77	6	7
32ii	Paragneiss	gt ky st	Vaikrita/ Karcham	all? ap (zr)	mon ap (zr)	- / 108	66 / 59	61 / 53	11	14
57	Mica-schist	st gt	Jutogh Group	ap > mon	mon ap (zr)	- / 69	-	-	-	-
66i	Mica-schist	gt	Jutogh Group	ap (zr)	all ap (zr)	- / 120	91 / 78	92 / 80	14	13
78ii	Psammitic-schist	gt st	Jutogh Group (Shimla klippe)	mon ap (zr)	mon ap	- / 111, - / 113	87 / 81	88 / 82	7	7

Mineral abbreviations: garnet (gt), staurolite (st), kyanite (ky), monazite (mon), apatite (ap), allanite (all), zircon (zr). * no weight of the garnet separate prior to leaching with H_2SO_4. Note that material is inevitably lost during cleaning however, and not just from the leaching process.

4.5 Method

A summary of the method is provided here and outlined in Figure 4.2. Further details are provided in the protocols presented in Appendix B1.

Garnets were **handpicked** from sieved fractions of whole rock crushate in a rather 'indiscriminate' fashion (that is with respect to inclusions) to a) test the sulphuric leaching method of Anczkiewicz and Thirlwall (2003), and b) separate enough garnet material for multiple analyses. Garnet separates were then coarsely crushed and passed through **heavy liquid** to further separate garnet from other phases. LST Fastfloat (density = 2.9 gcm^{-3}) was successful at removing the vast majority of rock-forming minerals (which floated) from garnet material (which sank; density = 3.5 to 4.2 gcm^{-3}). However, some phases also have densities greater than LST Fastfloat, and may have contaminated the separates. These include: apatite (3.2 gcm^{-3}); titanite (3.5 gcm^{-3}); staurolite (3.7 gcm^{-3}); allanite (3.8 gcm^{-3}); rutile (4.3 gcm^{-3}); zircon (4.7 gcm^{-3}); ilmenite (4.8 gcm^{-3}); and monazite (5.1 gcm^{-3}). Visual inspection of the separates suggested that contamination by these phases was minimal, and not all of them would drastically affect the Sm–Nd characteristics of the separate anyway (e.g. rutile, ilmenite). Some passes of crushed garnet separate through the heavy liquid were rapid, and light mineral phases such as micas were carried down with the heavy (garnetiferous) fraction and prevented from floating back up. Therefore a **crude mica separation** was performed on some samples (especially mica-rich ones) following heavy liquid separation. This involved paper and/or a large acetate sheet and/or plastic vials, and relied on the static nature of micas to adhere to these surfaces, concentrating garnet in the non-static fraction. All samples were subjected to **magnetic (Frantz) separation** which effectively removed residual matrix minerals e.g. quartz from the garnet separate. The optical purity of the garnet separates before finely crushing in preparation for leaching was estimated $\geq$ 95%. As Nd-rich phases included in garnet could not be totally eliminated by the physical separation methods outlined above, the garnet separates were subjected to leaching (described below), which was aimed at removing some of these troublesome phases from the Thermal Ionisation Mass Spectrometer (TIMS) analyses. Chemical leaching does not appear to fractionate REE (Anczkiewicz and Thirlwall, 2003; Jung et al 2007 and references therein; Thoni, 2002).

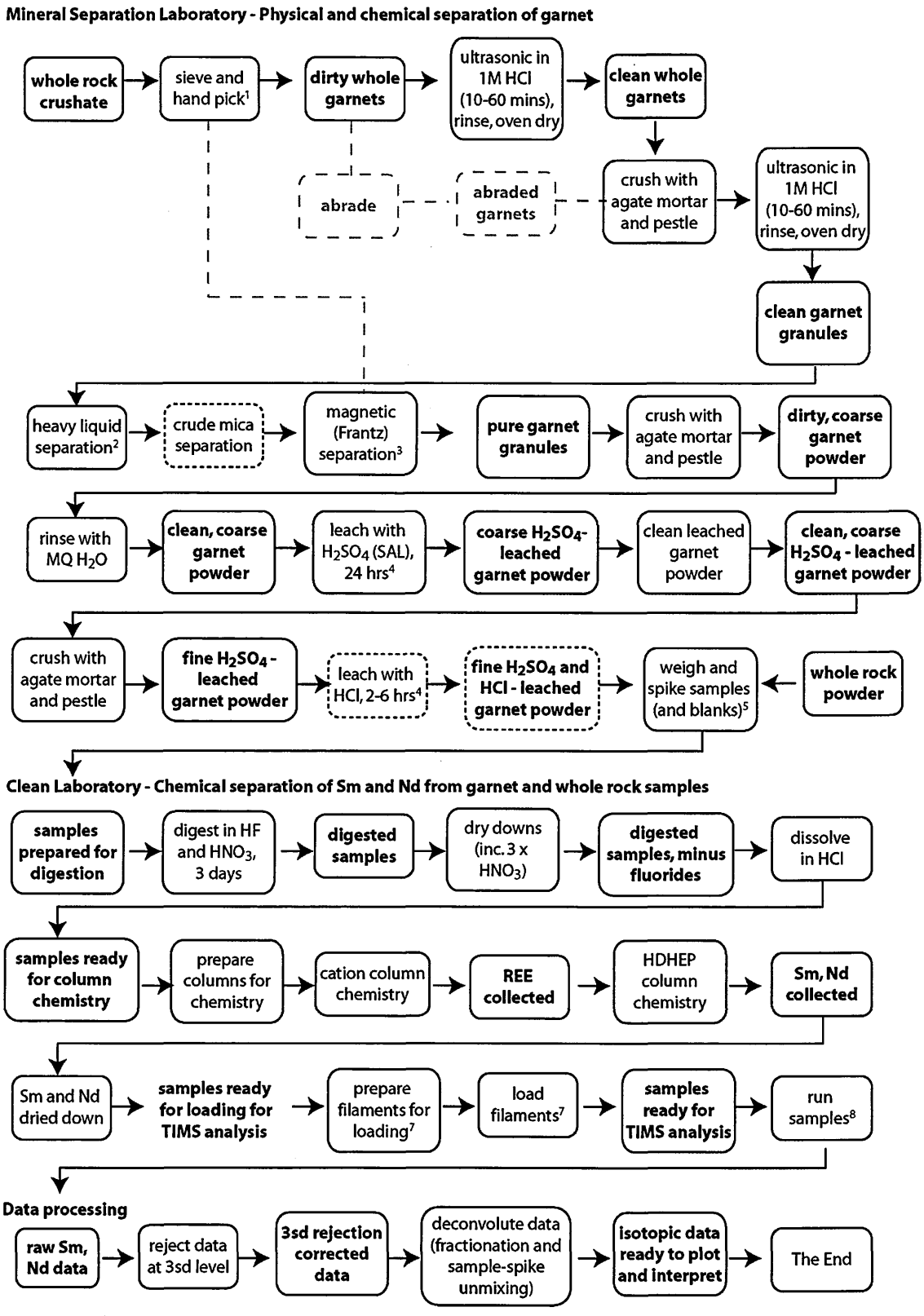

Fig. 4.2 Flowchart detailing the method for whole-rock and garnet geochronology. Steps 1 to 8 refer to protocols in Appendix B1. Stages in boxes that are short-dashed were optional. Stages/routes greyed out and in boxes that are long-dashed represent methods not taken here but were considered.

Following the physical separation of garnet from the whole rock, aliquots of finely-crushed (<50 μm) garnet powder from each of the five selected samples were initially **leached** with H_2SO_4 (Sulphuric Acid leaching, SAL) at 180°C for 24 hours (Anczkiewicz and Thirlwall, 2003). This method effectively removes Nd-rich phosphates such as apatite and monazite (one or both of which were identified as inclusions in the selected samples, see Table 4.4) and does not dissolve garnet (cf. HF and HCl leaching where up to 50 % by weight of the garnet separate can be 'lost' during the process; Anczkiewicz and Thirlwall, 2003 and references therein). TIMS analysis of all these SAL garnet separates yielded low [Sm]/[Nd] values, and three out of the five samples had [Nd] > 10 ppm (Table 4.7), indicating that the separates were still partially contaminated. Assuming that this was not merely a result of not having ground the garnet separate fine enough to expose inclusions to H_2SO_4, this strongly suggested that not all Nd-rich inclusions had been successfully leached. As SAL targets phosphate inclusions, silicate inclusions such as allanite and zircon were suspected culprits, especially given that the two SAL garnet samples with [Nd] in excess of 20 ppm (Table 4.7) were from allanite-bearing rocks, and all samples contained zircon, with four out of the five samples having zircon as an inclusion in garnet (Table 4.4). Although only one sample (32ii) was identified as possibly having allanite as an inclusion in garnet (Table 4.4), it is feasible that this phase was overlooked in other samples, as it is not easy to discriminate between allanite and ilmenite in BSE images, and the two phases can also be morphologically very similar (cf. Chapter 6.2.2). Zircon typically has low [Nd] (and [Sm]) (Amelin, 2004; Grauch, 1989; Li, 1994), and would have little effect on garnet-whole rock Sm–Nd systematics. Yet if zircon is abundant or Nd-rich enough, and/or garnet has very low [Nd], there will be a considerable effect on the Sm–Nd garnet age (DeWolf et al., 1996; Jung et al., 2007; Thoni, 2002). Zircon is highly refractory and unless a high mass of garnet material is to be sacrificed during leaching it may never be completely removed from the garnet separate (although fortuitously, it may not, for the same reason, be subsequently digested and contaminate the garnet TIMS analysis either).

Prior to the advent of SAL, hydrochloric acid (HCl)-leaching was used to target and leach both phosphate (monazite) and silicate (zircon) inclusions (DeWolf et al., 1996; Zhou and Hensen, 1995). This method was only partially successful in leaching monazite, and the effect on zircon

was difficult to quantify as this phase may have too low a [Nd] (Table 4.1) to have any considerable effect whether it was leached out or not. To test the ability of HCl-leaching to a) further improve (raise) the $^{147}Sm/^{144}Nd$ of garnet separates with possible residual monazite inclusions (following SAL), and b) leach allanite (i.e. a silicate with an influential [Nd], Table 4.1) from garnet separates likely to have allanite in them (samples 32ii and 66i), the remaining SAL garnet powders (except sample 57 from which there was no remaining material) were split into two more aliquots and subjected to HCl-leaching (DeWolf et al., 1996), for either 2 ('HCl-L garnet 1') or 4 ('HCl-L garnet 2') hours, in a heated (69 °C) ultrasonic bath (Anczkiewicz and Thirlwall, 2003). Note that by this stage garnet powders had been pre-crushed to as fine a grain size as possible in an agate mortar.

A more aggressive leaching technique using HF on garnet separates has been successful in raising the $^{147}Sm/^{144}Nd$ ratio of impure garnet separates (Amato et al., 1999; Baxter et al., 2002), but this has not been tested on garnets with allanite inclusions. Therefore, bearing in mind the obvious safety concern associated with using HF, and the fact that HF-leaching can dissolve a substantial amount (<50%) of the garnet separate being leached (severely limiting the number of duplicate analyses possible), this route was not taken.

Samples (whole rocks, leached garnets and leachates) and total procedural blanks were then **weighed** and **spiked** with a mixed ^{149}Sm and ^{150}Nd spike solution (a correctly spiked mixture should have a $^{150}Nd/^{144}Nd$ value between 0.4 and 10, i.e. half-way between the natural and spike compositions). The required spike weight was roughly calculated in order to optimise both isotopic and concentration measurements. In all cases the error associated with the spike correction was less than internal analytical errors associated with the isotopic determinations. The addition of a spike allows the precise determination of Sm and Nd concentrations by the isotope dilution (ID) method. Spiking samples prior to digestion ensures complete equilibration of the spike with the sample before chemical separation and analysis (Cohen et al., 1988). A potential source of error in isotope dilution measurements is the incomplete homogenisation of sample-spike solution, which is more likely to occur with later spiking of samples, e.g. just prior to mass spectrometric analysis.

Samples were then **digested** in sealed PFA screw-top vials using a HF-HNO_3 mixture for 3 days at 180 °C on a hot plate, followed by repeated dry-downs and additions of HNO_3 (to convert fluorides to nitrides) and finally dissolved and dried-down in 6M HCl (to convert nitrides to chlorides). Methods for both digestion and column chemistry (below) are modified from the standard techniques described in Cohen *et al.* (1988).

Garnet is inherently refractory and hence difficult to dissolve and gel-like milky white residues initially remained in all of the garnet samples following this digestion protocol. These gels (probably Al-complexes) may sequester REE, so it is vital that they be dissolved for a valid Sm–Nd analysis. Thus the samples were centrifuged to separate the gels from the solution, the supernatant liquid extracted, and the gels retained to be redissolved and redigested (the entire digestion protocol using HF and HNO_3 through to the final addition of HCl, was required). These 'aliquots' were recombined with their sample solutions from which they were separated, following separate passes through the cation columns, but preceding Sm–Nd column chemistry separation.

The amount of undesirable gel was minimal in samples with the least amount of garnet material (e.g. 57), i.e. where the ratio of acid to garnet was largest. The size of the garnet particles (undoubtedly somewhat variable between garnet separates) will have also played a part, with finer grained separates being more efficiently digested (greater surface area exposed to the acid). However, $^{147}Sm/^{144}Nd$ values from the analysis of a suite of micro-drilled garnet separates (ultrafine powder) were significantly lower than expected for typical garnets (Pollington and Baxter, 2007), suggesting that too fine a grain size may also lead to problematic garnet digestion (in detail, the paper presented preliminary evidence for the formation of a, as yet unidentified, secondary precipitate). The ratio of HF to HNO_3 in the digestion (i.e. more HNO_3 'dilutes' the effect of the HF, which is primarily to break Al-Si bonds) may have been too low, but for health and safety reasons the minimum amount of HF necessary was used. The composition of garnet also affects its solubility, with grossular–andradite being more soluble than pyrope–almandine (DeWolf et al., 1996). The amount of garnet material 'lost' (dissolved) during HCl leaching (Table 4.2) is consistent with this (i.e. relatively Ca-rich garnets in samples 32ii and 66i are more rapidly dissolved than relatively Fe and Mg-rich garnets in samples 14i and 78ii, Table 4.5, Fig. 4.3), and

although not quantified, is also broadly consistent with the degree of digestion observed between the same samples. Graphite in samples 14i and 32ii also resisted digestion.

Table 4.5 Average garnet end-member compositions (%) from electron microprobe analysis (Fig. 4.3 and Appendix C2)

Sample	Almandine	Spessartine	Pyrope	Grossular
14i	72	9	16	3
32ii	63	7	11	18
57	76	8	12	5
66	67	7	7	18
78	77	9	11	3

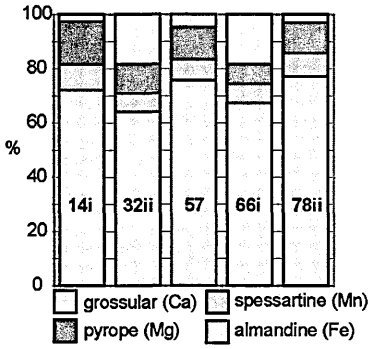

Fig. 4.3 Average garnet end-member compositions from electron microprobe analysis (Table 4.5).

The use of bombs or microwave digestion techniques (e.g. Richards, 2004) may be more successful and efficient at removing unwanted refractory phases. However, bombs were avoided partly due to safety concerns (acid leakage has occurred in the past), and partly due to limited suitable oven facilities. The use of perchloric acid ($HClO_4$) to aid digestion was also considered, but rejected owing to the lack of suitable fume cupboards at the Open University. In any case, any of these more aggressive digestion methods may have led to zircon dissolution, which having survived leaching, would be best kept separate from the digested garnet as not to contaminate the garnet analysis (see above).

Clear and homogeneous sample solutions (dried down and taken up in 1M HCl) were passed through pre-cleaned **cation columns** to separate rare earth elements (REE) from other cations. Subsequently, samples were dried down and redissolved in 50µl 0.33M HCl to be passed through **HDEDP columns** for REE separation. Neodymium and Sm cuts were then dried down, loaded onto double Re filaments, and analysed at the Open University using a Triton thermal ionization mass spectrometer (Table 4.6). During Nd analysis ^{147}Sm was monitored to check the effectiveness

of the column chemistry. Despite the inefficiency of the column chemistry protocol in removing Ce from the Nd cut, Ce monitoring was not necessary since ^{142}Nd was not required for data processing and so the overlap of a long Ce 'tail' on ^{142}Nd was not a significant problem. However, the cup configuration was modified to ensure that the main Ce peak (at mass 140) was deflected away from the nearest Faraday cup, so that detector damage from large Ce beams was avoided.

Table 4.6 Summary of protocol details for Sm-Nd TIMS analysis

		Nd	Sm
Filaments		Double, Rhenium	Single, Tantalum
Loading		2.5M HCl + 0.01M H_3PO_4	0.01M H_3PO_4
TIMS analysis	Evaporation filament T	~1750 °C	~1450 °C
	Measured beam	3–7 V on ^{144}Nd	2–6 V on ^{152}Sm
	Run length	270 ratios	90 ratios
	Standards	La Jolla	SmE

Volatilisation and ionisation of sample on the source filament requires the breaking of bonds. This is a mass-dependent process: light isotopes have a higher vibrational frequency than heavier isotopes; hence their bonds are more readily broken and preferentially released from the hot filament during analysis. The effect is less pronounced at higher temperatures. With continuing fractionation the reservoir of lighter isotopes is depleted and the isotopic composition becomes increasingly heavy (the 'reservoir effect'). This mass fractionation effect follows the Rayleigh fractionation law. Fractionated isotopic ratios of elements with two or more non-radiogenic isotopes can be corrected for the effect using an internal normalisation, e.g. $^{145}Nd/^{144}Nd$ is normalised using $^{146}Nd/^{144}Nd$ (natural value 0.7219). Fractionation correction using a linear or power law assumes that the fractionation is proportional to the mass difference only and is independent of the absolute masses of the fractionating species. For 'light' elements such as Ca there is a significant deviation from these laws, and an exponential law correction provides a better fit to Ca isotope data (Dickin, 2005). Although this fractionation effect is less pronounced in the isotope analysis of relatively 'heavy' Sm and Nd, the exponential law correction is applied to the analyses in this study.

In processing data, measured $^{143}Nd/^{144}Nd$ ratios further than 3 standard deviations from the run mean (typically one ratio per analysis but occasionally up to four) were rejected before offline data deconvolution (fractionation correction and sample-spike unmixing).

4.6 Results

4.6.1 Leaching

The leaching of Nd-rich phases was most successful in samples 14i, 57 and 78ii, where [Nd] and [Sm] abundances in the leached garnet separates were significantly lower than in the respective whole rock and leachates (Table 4.7, Fig. 4.4). Garnet separates from samples 32ii and 66i were clearly not successfully leached of Nd-rich inclusions as [Nd] and [Sm] remain as high (66i) if not higher (!) (32ii) than their respective whole rocks. Considering these first-order observations and the accessory phases identified in these samples (Table 4.4), it is apparent that the garnet separates from samples 14i, 57 and 78ii, with no allanite and low CaO (relative to MnO and MgO, Fig. 4.7), were leached of some of their Nd-rich inclusion(s), that is, monazite and/or apatite (both phosphates). In contrast, analyses of garnet separates from samples 32ii and 66i were evidently dominated by Nd-inclusions not removed by SAL or HCl-leaching methods (e.g. apatite and/or allanite; as mentioned above, allanite may have been overlooked, and is not unlikely in garnets with relatively high-CaO, Fig. 4.7). Furthermore, the variation in 147Sm/144Nd with respect to degree of leaching (Fig. 4.5) reveals that problematic inclusions in garnet separates from 32ii and 66i were not preferentially leached, as the 147Sm/144Nd ratio remains relatively constant at about ~0.2. The small reduction in [Sm] and [Nd] between SAL garnet and the successive HCl-leached garnets is therefore merely the result of having leached proportional amounts of inclusion(s) and garnet (also documented by Anczkiewicz and Thirlwall, 2003). With progressive leaching of Nd-rich inclusions from a garnet separate, a trend more akin to that shown by 78ii is expected. Sample 14i also shows this trend, apart from 'HCl-leached garnet 2', which is evidently anomalous.

Table 4.7 Sm-Nd TIMS data (in ppm) from a selection of Sutlej valley pelites

Sample (I05)		[Nd]	[Sm]	[Sm]/[Nd]	$^{147}Sm/^{144}Nd$	2σ	$^{143}Nd/^{144}Nd$[1]	2σ
14i	whole rock	46.389	8.333	0.180	0.1086	0.0000	0.511711	0.000002
	SAL garnet	9.953	2.723	0.274	0.1654	0.0000	0.511721	0.000003
	HCl leachate 1	25.663	5.827	0.227	0.1372	0.0000	0.511715	0.000003
	HCl-L garnet 1	8.420	2.421	0.288	0.1738	0.0000	0.511707	0.000002
	HCl leachate 2	30.768	6.695	0.218	0.1315	0.0000	0.511717	0.000003
	HCl-L garnet 2	2.405	0.171	0.071	0.1714	0.0000	0.511727	0.000003
32ii	whole rock	26.339	4.960	0.188	0.1138	0.0000	0.511691	0.000003
	SAL garnet[3]	27.862	5.899	0.212	0.1280	0.0000	0.511727	0.000002
	HCl leachate 1	9.448	2.362	0.250	0.1511	0.0000	0.511718	0.000004
	HCl-L garnet 1	na	5.592	-	-	-	-	-
	HCl leachate 2	9.415	na	-	-	-	0.511591	0.000006
	HCl-L garnet 2	25.803	5.458	0.212	0.1279	0.0000	0.511714	0.000003
57	whole rock	38.451	7.565	0.197	0.1189	0.0000	0.511425	0.000002
	SAL garnet	11.086	3.270	0.295	0.1783	0.0000	0.511398	0.000002
66i	whole rock	50.358	9.414	0.187	0.1130	0.0000	0.511296	0.000002
	SAL garnet	43.906	8.031	0.183	0.1106	0.0000	0.511275	0.000002
	HCl leachate 1	22.718	4.260	0.188	0.1133	0.0000	0.511303	0.000002
	HCl-L garnet 1	44.441	8.110	0.182	0.1103	0.0000	0.511273	0.000004
	HCl leachate 2	20.352	3.835	0.188	0.1139	0.0000	0.511298	0.000002
	HCl-L garnet 2	42.097	7.698	0.183	0.1105	0.0000	0.511276	0.000003
78ii	whole rock	36.392	7.256	0.199	0.1205	0.0000	0.511997	0.000004
	SAL garnet 1	3.599	1.549	0.430	0.2602	0.0000	0.512448	0.000002
	SAL garnet 2	5.298	2.286	0.432	0.2609	0.0000	0.512451	0.000002
	HCl leachate 1	17.204	4.396	0.256	0.1545	0.0000	0.512108	0.000005
	HCl-L garnet 1	4.494	2.060	0.458	0.2772	0.0000	0.512499	0.000002
	HCl leachate 2[3]	21.451	5.244	0.244	0.1478	0.0000	0.512102	0.000003
	HCl-L garnet 2	4.002	1.997	0.499	0.3016	0.0000	0.512572	0.000002

SAL, sulphuric acid-leached (98% H_2SO_4, 24hrs, hot plate at 180 °C); HCl-L, hydrochloric acid-leached *after* SAL (6M HCl, 2 or 4 hrs (garnet 1 and 2 respectively), ultrasonic bath at 69 °C; na, not analyzed; [1]corrected data to 3 standard deviations; [2] t, 500 Ma; [3]An unknown quantity of sample material was lost during the digestion/dry-down stages. Although the sample was already spiked, it was presumably homogenously mixed by this stage. Repeat analyses of the La Jolla standard (n=17) gave $^{143}Nd/^{144}Nd$ ratios of 0.511849 ± 0.000004 (2σ) over the analysis period (Appendix C3). No blank correction was required as the $^{143}Nd/^{144}Nd$ contribution from total procedural blanks (between 11 and 286 pg, greatest for procedures involving more reagents, and/or total number of stages involved) was less than the external error.

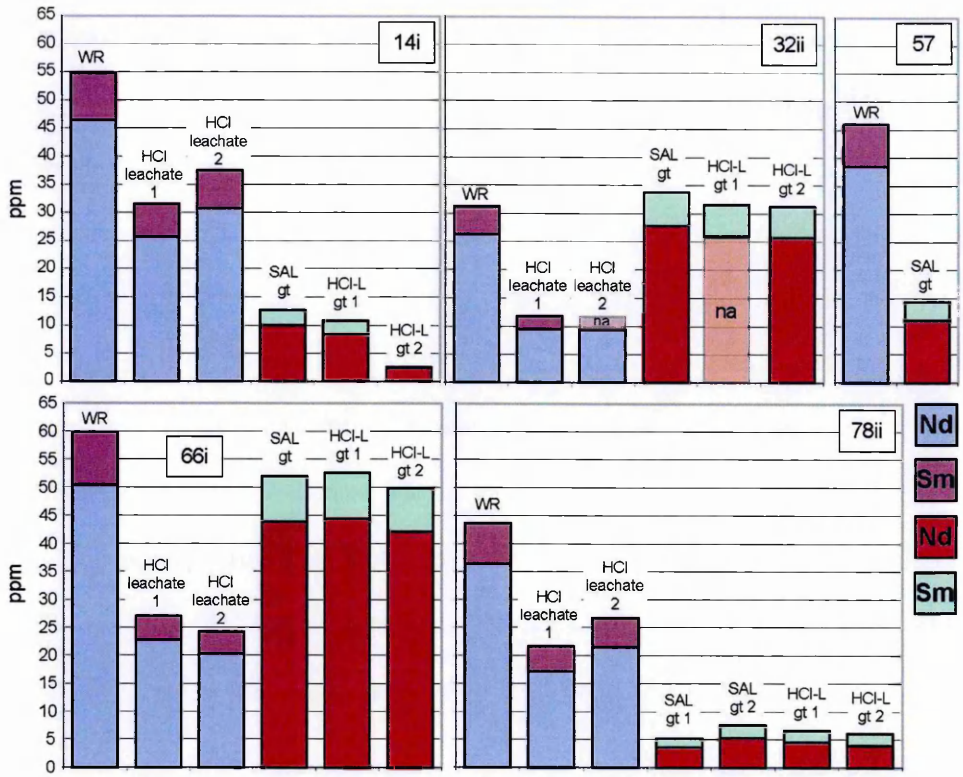

Fig. 4.4 Concentrations of Sm and Nd from TIMS analysis of whole rocks (WR), leached garnets and their respective leachates (see Table 4.7). Where analyses of Sm and Nd are missing for sample 32ii (na, not analyzed), concentrations are estimated from similar analyses (e.g. [Nd] of HCl-leached garnet 1 is assumed approximately equivalent to [Nd] of HCl-leached garnet 2, seeing as [Sm] are near identical).

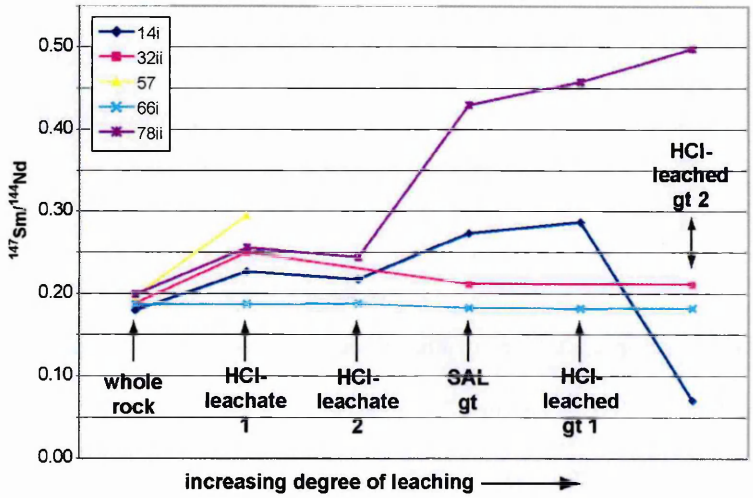

Fig. 4.5 $^{147}Sm/^{144}Nd$ variation with progressive leaching (Table 4.7).

In summary, the leaching of phosphate inclusions with H_2SO_4 appears to be a relatively successful method (although note that all garnet separates had [Nd] > 1 ppm, more than is typical for garnet, suggesting that perhaps the grain size of the garnet separate was not fine enough to expose all the inclusions), whereas HCl-leaching aimed at removing remaining (non-phosphate, i.e. silicate) inclusions such as allanite, is of limited success. This is not in agreement with the findings of previous studies that used either dilute or concentrated HCl to dissolve allanite (e.g. Harlavan and Erel, 2002), which suggest that allanite is susceptible to HCl leaching. An alternative hypothesis is that apatite (an inclusion in garnet from all the samples) survived the leaching methods used in this study, but then this would require apatite to have significantly greater [Nd] and [Sm] in samples 32ii and 66i than the other samples (which may be possible). This would also be the case for zircon. Finally, another LREE-enriched inclusion phase may have been completely overlooked, but this can only be speculation.

4.6.2 Samples

Although all analyses yielded very low $^{147}Sm/^{144}Nd$ as a result of contamination from Nd-rich inclusions, if inclusions are the same age as their host garnet it is still possible to derive an age estimate (notwithstanding higher errors associated with the restricted range of $^{147}Sm/^{144}Nd$ values). This case is only reflected in data from sample 78ii, with the remaining samples presenting more complicated results to interpret. Each sample is discussed in turn with reference to Figure 4.6 (based on Table 4.7), and aided by some simple modelling of a few possible scenarios regarding the relative age of inclusions to their host garnet (Fig. 4.1, Table 4.2).

14i

A three-point isochron between isotopic analyses of the whole rock, HCl-leachate 2 and the garnet separate from which it was leached (HCl-L garnet 2, Fig. 4.6a) yields an age of 39.9 ± 8.8 (MSWD 0.027). Despite the relatively large error (as a result of the small spread of $^{147}Sm/^{144}Nd$ values) this age is within error of the age of garnet growth determined from in-situ monazite U–Pb dating, of 34 to 30 Ma (Chapter 3, Fig. 3.8), and may therefore be a near-accurate, although imprecise, isochron.

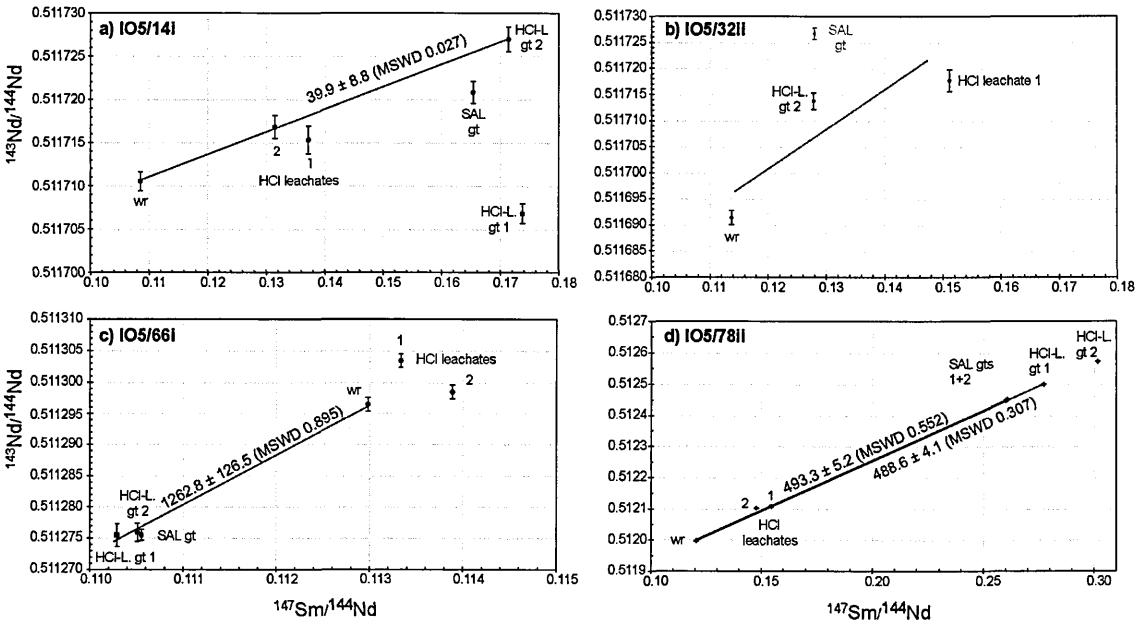

Fig. 4.6 Sm–Nd TIMS data from analyses of whole rocks (wr), sulphuric acid-leached (SAL) garnets, hydrochloric acid-leached (HCl-L) garnets and their leachates (HCl-leachates) (Table 4.7). Error bars are plotted at 1σ.

The spurious-looking data point from the analysis of HCl-L garnet 1 is more difficult to interpret. When paired with its leachate (HCl-leachate 1), the slope of the line between them is negative, therefore suggesting that whichever phase is being leached lies above the whole rock and left of the leachate (i.e. the top of the plot in Fig. 4.6a). Modelling reveals that this may be an older inclusion phase (Fig. 4.1d), which has evolved to a higher $^{143}Nd/^{144}Nd$ than the measured whole rock. However, there must be another inclusion phase dominating the isotopic analysis of this garnet separate, with a *lower* $^{143}Nd/^{144}Nd$ than the whole rock, in order that the impure garnet data point lies on a line that can be drawn up to the pure garnet data point. A younger 'inclusion' (i.e. recrystallized along cracks through garnet) with a *lower* $^{147}Sm/^{144}Nd$ than the whole rock (inset to Fig. 4.1d) would cause this effect. The remaining data, which lie in roughly the same trajectory towards pure garnet, are interpreted as a mixture between the two inclusions, approximately equivalent to the isotopic composition of the measured whole rock.

32ii

Unfortunately no three-point isochrons can be constructed owing to a lack of data, as a result of one frazzled filament (in the process of loading a sample), no detectable beam from another filament, and data corresponding to the SAL garnet separate not being considered robust as some

material was lost during the digestion/dry-down stages (greyed out data point, Fig. 4.6b). Therefore, interpretation can only be speculative. An errorchron (Dickin, 2005) (dashed line, Fig. 4.6b) based on all robust data yields an age of 116.0 ± 19.8 (MSWD 42.6). Such a poor correlation, with HCl-leached garnet 2 and HCl-leachate 1 evidently lying on different trajectories from the whole rock, suggests that there are at least two types of Nd-rich inclusion (different phases and/or ages). Furthermore, the lack of any notable regional geologic event at ~116 Ma, or at either of the ages defined by the two possible two-point 'isochrons' (of 107 and 243 Ma), leads me to conclude that these data are not reliable as an indication of the age of garnet growth.

Rutile is present as an inclusion in this sample, and although Anczkiewicz and Thirlwall (2003) suggest that it will have no significance on the Sm–Nd systematics, perhaps the data shown here imply otherwise (also proposed by Vance and O'Nions, 1990). Presently lacking REE data for rutile would be required to test this hypothesis.

57

Despite the intention to split this sample into two aliquots to investigate the possible effect of staurolite contamination (easily hand-picked along with garnet, and not separated thereafter by either heavy liquid or magnetic methods), garnet analyses were limited to just the one SAL garnet as a result of the small amount of garnet material separated. This analysis yielded the most significant improvement (increase) in $^{147}Sm/^{144}Nd$ on leaching out of all the samples (Fig. 4.5), yet has a lower $^{143}Nd/^{144}Nd$ than the whole rock (Table 4.7). This is similar to the analysis of HCl-L garnet 1 from 14i (Fig. 4.6a), and as postulated for sample 14i, if the analysis is valid it may represent a mixture between two types of inclusions. Strictly speaking, without data corresponding to the leachate, no firm conclusions can be drawn. No comparison to the age of garnet from the same locality, derived from U–Pb monazite data (~10 Ma, Caddick et al., 2007), is therefore possible either.

66i

All garnet separates plot at lower $^{147}Sm/^{144}Nd$ and $^{143}Nd/^{144}Nd$ values than the whole rock (as does the garnet analysis in Figure 14 in Jahn et al., 2005) and form a tight cluster of points (Fig.

4.6c, note the scale of the axes). Considering the lack of any preferential leaching (and as a result, the constant $^{147}Sm/^{144}Nd$, Fig. 4.5), the only interpretation is that all garnet analyses were dominated by Nd-rich inclusion(s). Allanite and/or apatite may be responsible for such an effect in this sample. Allanite can be considerably Nd-rich (Table 4.1), and although it was identified in the matrix and not in garnet, it may have been overlooked as an inclusion phase. Zircon, another inclusion in this sample, may also have affected the Sm–Nd system, but a) it may not have been digested and made its way into the analysis of the garnet separates, b) with relatively low [Nd] it would have to have been present in abundance, and c) zircon can have a relatively high $^{147}Sm/^{144}Nd$ (Table 4.1) and might not be so likely to plot at values lower than the whole rock as in Figure 4.6c. Hence allanite is considered the more likely culprit.

A four-point isochron between this cluster of 'garnet' analyses and the whole rock analysis yields an age of 1262.8 ± 126.5, and with an MSWD of 0.895 may be considered robust (Fig. 4.6c), i.e. all components crystallized in a single event (equilibrated together), at ~ 1250 Ma. This probably dates the age of the inclusions, as opposed to the garnet (not represented by these 'garnet' analyses), and is consistent with crystallization during a Proterozoic event (GHS and LHS rocks contain detrital zircons of about this age). However, without knowing the relative [Nd] of garnet and inclusions, this again, is speculation. The small spread of $^{147}Sm/^{144}Nd$ values that defines this isochron results in an imprecise age, and also weakens the interpretation that the HCl-leachates, which lie on two different trajectories from the whole rock (Fig. 4.6c), may indicate more than one garnet age component (possibly reflected by the stepped MnO garnet profile in Figure 4.7).

78ii

This sample shows the most successful leaching of Nd-rich inclusions of all the samples with the highest $^{147}Sm/^{144}Nd$ garnet separate result (Fig. 4.5). In addition to successful multiple analyses (including a duplicate SAL garnet analysis, simply because there was more original garnet material to begin with), a tightly constrained garnet age can be calculated (Fig. 4.6d). An isochron between the whole rock, "HCl leachate 1" and the corresponding garnet separate ("HCl-L garnet 1") yields an age of 488.6 ± 4.1 (MSWD 0.307), and is within error of another isochron, between the whole rock and the two SAL garnet separates, which yields an age of 493.3 ± 5.2 (MSWD 0.552).

Relatively low $^{147}Sm/^{144}Nd$ values and high [Nd] for the garnet analyses implies that some inclusions remained to contaminate the garnet separates, but the duplicated ages indicate that these inclusions most likely grew at the same time as (and were in isotopic equilibrium with) the garnet. Thus, the age of garnet growth and hence prograde metamorphism in this sample is ~ 490 Ma. This scenario has been modelled in Figure 4.1a.

Considering that the inclusions are also pre-Tertiary in age, and the relatively effective SAL (i.e. raising the $^{147}Sm/^{144}Nd$) and (although to a lesser extent) HCl-leaching with respect to the other samples with similar inclusions (14i and 57), I suggest that these inclusions were more susceptible to leaching in general due to metamictization. Susceptibility to leaching related to the degree of metamictization has been suggested previously for allanite (Blichert-Toft and Frei, 2001).

Of all the samples analyzed here, only sample 78ii may have provided a source of sample bias, with apparent pale orange garnet cores with pink garnet rims, and small pink garnets potentially indicative of two different garnet growth stages. Duplicate ages do not support a two-stage garnet growth history, at least not one that can be resolved (there may have been episodic garnet growth within the uncertainties of the isochron, a maximum of ~10 Ma). However, the uninterrupted major element zonation in garnet in this sample does not support this and I suggest that the different colours of garnet simply reflect the chemical zonation and/or the density of inclusions (i.e. more dense in the core).

4.7 LA–ICPMS

4.7.1 Introduction

Despite the treatment of garnet separates to leach out Nd-rich inclusions it is evident that this process was not wholly successful: TIMS-derived Sm/Nd values for garnet separates (Table 4.7, Fig. 4.4) are too low to represent pure garnet (cf. Table 4.1; Prince et al., 2000) and non-isochronous relationships between whole rock, garnet leachate and garnet separate analyses imply contamination from Nd-rich phases that are either significantly older or younger than garnet (Fig. 4.6a to c). Analysing garnets from each sample using *in-situ* laser-ablation inductively-coupled mass spectrometry (LA–ICPMS) provides a means of determining their true Sm/Nd values and hence allows an assessment of the leaching methods used above. The LA–ICPMS technique

combines high-precision trace element measurement with a high spatial resolution, allowing the user to position points for analysis avoiding inclusions and cracks. Where unavoidably analyzed, Nd-rich phases such as allanite (silicate) or monazite (phosphate) and their respective Nd and Sm concentrations are of value to assess further modifications of the leaching methodology used in the preceding TIMS study (section 4.6) and for future modelling of TIMS Sm–Nd garnet data. Moreover, LA–ICMPS data from profiles through garnets may reveal zonation patterns that can inform studies on REE diffusivity which has implications for coupled Sm–Nd, Lu–Hf studies (e.g. Anczkiewicz et al., 2007).

4.7.2 Method

Polished sections (100 μm thick) exposing a cross-section through at least one large garnet (and also staurolite if present, as it may have been incorporated into some garnet separates) in each sample were made and then subjected to major element analysis of profiles across the selected phases using the electron microprobe (Fig. 4.7, Appendix C2.2). Concentrations of Ca or Si (if the Ca concentration was too low) were used for LA–ICPMS calibration. Back-scattered electron images of the same phases were taken to help locate clean areas to ablate (i.e. free of cracks or inclusions), mark on laser ablation spots, and determine the corresponding Ca content (variable across the profile) if used for calibration.

Analyses were made at the Open University on a New Wave laser system (213 nm) linked to a quadrupole ICP–MS (Agilent 7500). The output energy was set to 80% for a 60 μm spot size (diameter) and a repetition rate of 10 Hz. The sample was ablated in a pure He atmosphere, and mixed with Ar via a "Y" connector, prior to ionisation in the plasma. Integration time per point was either 0.01 or 0.03 s (less time for heavier elements) and the total measurement time for each analysis was 238 s, of which the first 100 s is for the gas blank measurement and laser (blocked by the shutter) warm-up. The resulting penetration depth was ~50 microns. The wash-out time was 150 s. Note that phosphorous (an aid in the discrimination of different inclusions, e.g. phosphates from silicates) was only added to the method file for the analysis of garnet in samples 66i and 78ii. On-line data reduction was carried out using version 3.4 (2000) of the GLITTER software (Van

Achterbergh et al., 1999). Concentrations were considered meaningful when they were greater than the minimum detection limit (99% confidence).

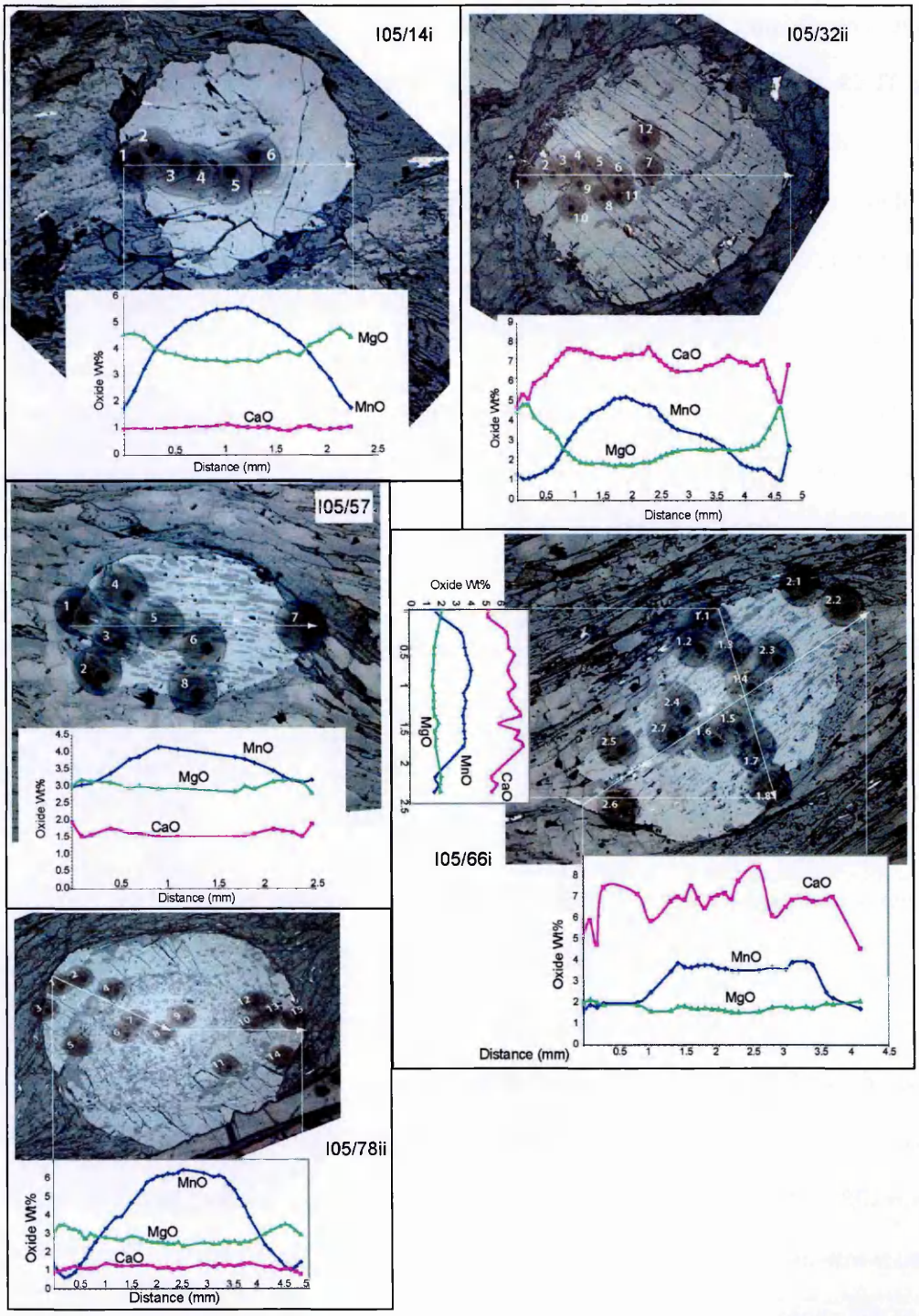

Fig. 4.7 Back scatter electron images of garnets analyzed using LA–ICPMS. Electron microprobe major element (oxide) profiles also presented (Appendix C2.2).

A glass standard (NIST 612 50 ppm, Pearce et al., 1997) was used for external calibration (analysed twice at the start of each run, and after every 6 to 8 sample analyses) with CaO (or SiO_2 if Ca content too low) determined from electron microprobe analysis for internal normalisation. However, a glass standard may not provide the best standard for the calibration of garnet analyses, for at least two reasons: i) the range in abundances of the trace elements in garnet (over several orders-of-magnitude) is far greater than the glass standard, thus some elements may be less well-calibrated; and ii) the 'matrix effect' (glass and garnet have different matrices). To address this concern a garnet standard was sought but no published garnet standard was found. Instead, an unpublished garnet 'standard' (K23) was acquired and analysed. The details of this sub-study are presented in Appendix D1.

Time-resolved analyses clearly reveal if an inclusion is encountered during analysis of garnet, e.g. a marked increase in the proportion of LREE is indicative of the analysis of a LREE-enriched inclusion such as allanite or monazite (cf. Figure 2 in Prince et al., 2000). In this study, ablation of pure garnet throughout the analysis was rare, and often multiple phases were encountered. However, time intervals can be manually selected (through 'Review' in the GLITTER software) in order to screen out these inclusions. Screening was refined to produce an element profile as close to true garnet values as possible (e.g. for Mn concentration, an element not influenced by the analysis of an inclusion or not, and typically with a distinctive bell-shaped profile, Fig. 4.7), and eliminate inclusions with elevated [Nd] and [Sm] (and usually, most of the other light REE). In order to retain a reasonable amount of the garnet analysis, inclusions enriched in heavy REE (HREE) (e.g. zircon, with relatively low [Nd] and [Sm]) were not screened out. So although a representative [Nd] and [Sm] for the garnet analysis was obtained, the same cannot not be said for the HREE (implying that the data cannot be used reliably for garnet zonation and/or reaction studies). Screened garnet measurements are referred to as 'garnet' analyses, despite the fact they actually represent analyses of garnet–HREE inclusion mixtures. Each time-resolved analysis was also screened to obtain the *most* contaminated measurement during the ablation, to assist in identification of inclusions. In the results below these measurements are referred to as 'inclusion' analyses despite the fact they actually represent analyses of inclusion– garnet mixtures.

4.7.3 Results

The [Nd] and [Sm] of all garnets (excepting K23) is less than 1 and 0.1 ppm respectively, and both were at times, and for several different analyses, below detection (Table 4.8 and Appendix C4). For all samples the garnet [Sm]/[Nd] is greater than 1, in contrast to all bar one of the inclusion analyses (78ii), plus staurolite in sample 14i, that yield [Sm]/[Nd] values of less than 1. In detail, samples 32ii and 66i (and K23) have a much lower [Sm]/[Nd] than the other three samples. The [Nd] and [Sm] of the inclusion-contaminated garnet analyses are a factor of 10 to 10,000 times that of their respective garnet analyses.

Table 4.8 LA-ICPMS garnet data (ppm)

sample (section)	phase	normalised to (wt %)	[Sm]	[Nd]	[Sm]/[Nd]	inclusion-contaminated			cf. TIMS garnet data			garnet
						[Sm]	[Nd]	[Sm]/[Nd]	[Sm]	[Nd]	[Sm]/[Nd]	CaO wt %
I05/14i (7)	gt	SiO_2 37.75	0.50	0.065	**7.65**	3.54	6.53	**0.54**	2.42	8.42	0.29	1.0
I05/14i (7)	st	SiO_2 28.07	0.0032*	0.013	0.24	2.18	5.11	0.43	na	na	na	
I05/32ii (a)	gt (1)	variable CaO	0.19	0.090	**2.07**	67.65	356.93	**0.19**	5.46	25.80	0.21	6.8
I05/57 (T)	gt	SiO_2 37.81	0.53	0.04*	**13.23**	21.97	119.14	**0.18**	3.27	11.09	0.29	1.6
I05/66i	gt (1b)	variable CaO	0.0033*	0.003	**1.14**	1.97	8.98	**0.22**	7.70	42.10	0.18	6.6
I05/78ii (T)	gt (1)	SiO_2 37.32	0.59	0.045	**13.10**	30.38	18.89	**1.61**	2.00	4.00	0.50	1.1
K23	gt	CaO 5.3	1.36	1.180	1.15	na	na	na	na	na	na	5.3
K23	gt	CaO 5.3	1.29	1.110	1.16	na	na	na	na	na	na	

For garnet (gt), values quoted are analyses with the lowest [Sm], [Nd] (representative of the purest garnet); for "inclusion-contaminated" garnet, values quoted are analyses with the highest [Sm], [Nd] (representative of the most contaminated garnet); TIMS garnet data represent only the most-leached garnet separates (i.e. the purest garnet analyses, typically HCl-leached garnet 2, Table 4.7); K23 data are mean values. Reference material was NIST 612 50ppm (Pearce et al, 1997). * below detection, hence detection limit is used to approximate [Sm]/[Nd]). na, not analysed. Staurolite (st).

The trace element patterns for all 'garnet' and most 'inclusion' analyses are presented in Figure 4.8. The complete dataset in Appendix C4 includes all 'inclusion' analyses, although in reality some of these, where analyses did not encounter an inclusion, are broadly equivalent to the 'garnet' analysis. In these cases the 'inclusion' analyses are not plotted as they do not provide information useful to the identification of inclusions. For most of the samples a "good" 'inclusion' analysis could be screened from each time-resolved analysis. However, only two out of seven ablations in sample 57 garnet, and half the ablations of garnet from sample 78ii yielded "good" 'inclusion' analyses, from which it may be inferred that these samples have a smaller abundance

and/or less densely distributed suite of inclusions. Nevertheless, as demonstrated above (Section 4.3.1), even a small number of Nd-rich inclusions can seriously compromise garnet TIMS analyses if not leached from the garnet separate.

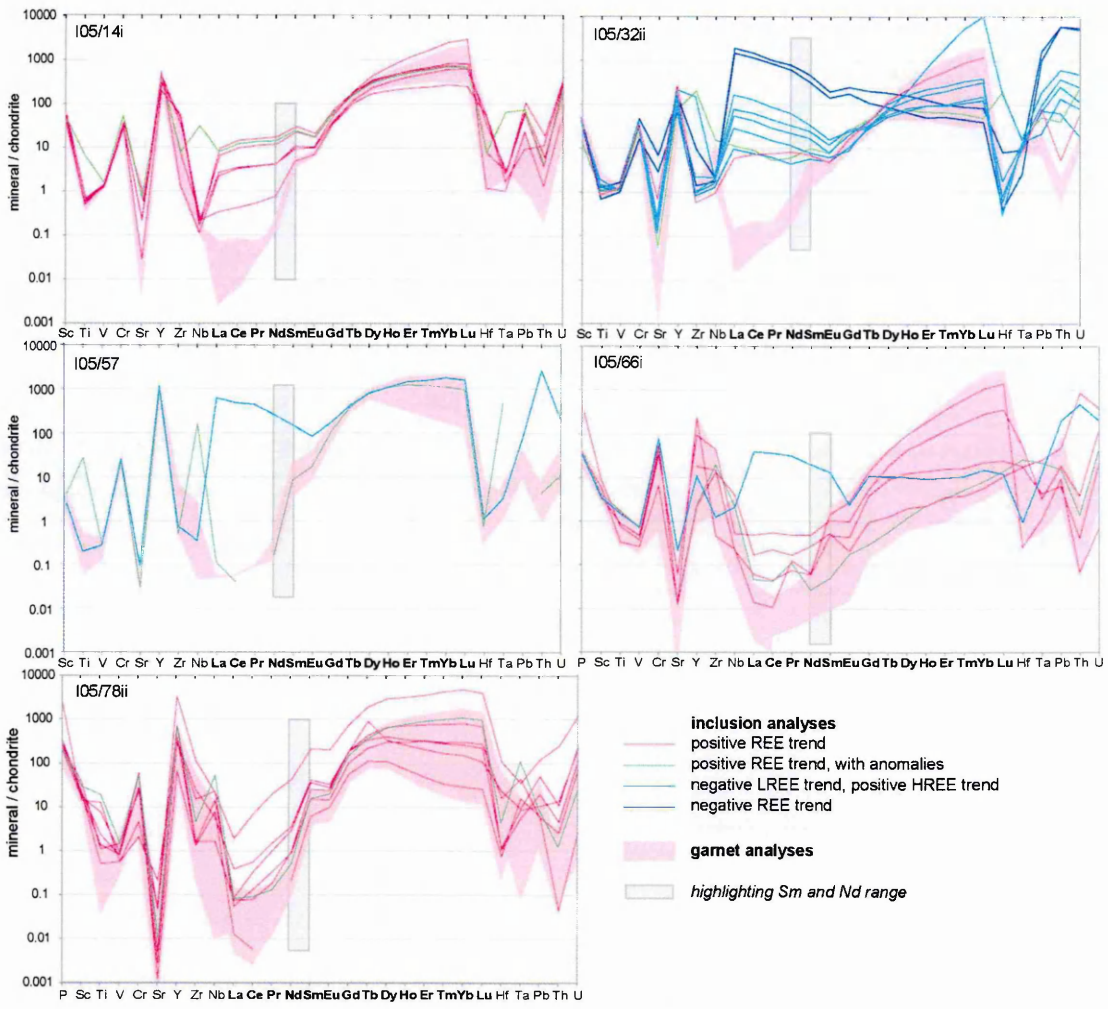

Fig. 4.8 Trace element spider diagrams for samples from the Sutlej Valley, showing LA–ICPMS data screened with respect to concentration of Sm and Nd for both the *purest* garnet measurements ('garnet analyses') and those evidently contaminated by inclusions ('inclusion analyses'). REE labelled in bold. Note that only samples 66i and 78ii include data for phosphorus. See Appendix C4 for complete data set.

In general, the REE (La to Lu) patterns for 'garnet' analyses (pink block area, Fig. 4.8) feature a smooth positive (i.e. 'uphill') trend, through the LREE into the HREE. The HREE are enriched relative to typical garnet as a result of the screening method used wherein HREE inclusions (namely zircon (see Fig. 4.9) which has been identified as an inclusion in the garnets sampled) contaminate the 'garnet' analyses. The REE patterns for 'inclusion' analyses (i.e. LREE-

enriched inclusions) can be divided into three groups: type 1 those with a positive trend; type 2 those with a negative ('downhill') LREE trend, followed by a positive HREE trend; and type 3 those with a negative REE trend. With reference to Figure 4.9, type 1 analyses are inferred to represent analyses contaminated by LREE from apatite whilst retaining the garnet and/or zircon HREE signature. Allanite, with a characteristic negative REE trend is responsible for the negative REE trends in analyses belonging to types 2 and 3. The 'sinusoidal' type 2 REE pattern, the result of analyses where allanite dominates the LREE spectra while the HREE remain characteristic of garnet, has been previously documented by Blichert-Toft and Frei (2001).

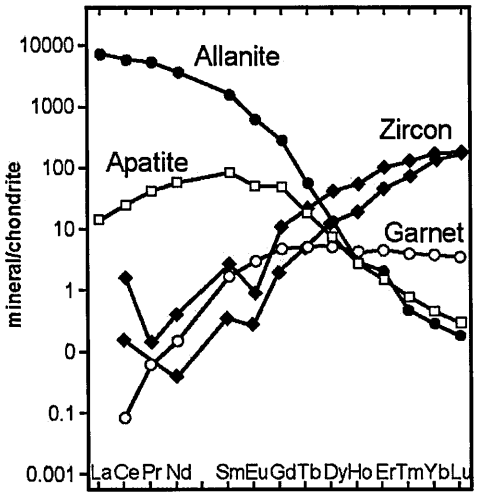

Fig. 4.9 REE spider diagram, showing LA–ICPMS data from various minerals in garnet-bearing eclogite (reproduced from Giere and Sorensen (2004) based on data from Hermann (2002).

Samples 14i and 78ii yield exclusively type 1 'inclusion' analyses, therefore reflecting the ablation and subsequent analysis of apatite inclusions. Monazite reportedly has a REE spectrum similar to allanite (Blichert-Toft and Frei, 2001). However, as there are no type 2 or 3 analyses in these two samples, and monazite is the only other REE-enriched inclusion identified in them (excepting zircon), this suggests that this is not strictly the case (unless no monazite grains were encountered and analysed). One analysis, with a relatively high Th value and generally elevated REE trend (in 78ii) is thought to reflect at least some of the REE spectrum of monazite, since trace element characteristics are consistent with monazite (a Th and REE-rich phase).

Samples 14i, 78ii and 57 have a type 1 inclusion with anomalously high Nb and Ta. These are commonly associated with Ti-bearing phases such as rutile, ilmenite and titanite, of which only ilmenite was identified in the samples. It of little consequence to [Sm] and [Nd] in samples 57 and

78ii where the traces of these 'inclusion' analyses (green in Fig. 4.8) have very low, to below detection levels, of LREE. The green trace in 14i has relatively high LREE, but it is quite possible that the REE spectrum of this 'inclusion' analysis reflects the analysis of more than one type of inclusion e.g. ilmenite (contributing Nb and Ta) and apatite (contributing LREE).

Type 2 and 3 'inclusion' analyses in samples 32ii, 57 and 66i suggest contamination from allanite, with significantly elevated [Sm] and [Nd] relative to the 'garnet' analyses. These traces are often associated with a Th peak, which is consistent with allanite as a Th-bearing phase (to the extent that is may be used in U–Th–Pb geochronology e.g. Gregory et al., 2007). The fact that only sample 32ii shows examples of type 3 'inclusion' analyses, suggests that more allanite was sampled during the analyses. Type 1 'inclusion' analyses in 32ii and 66i suggest the presence of apatite inclusions, consistent with petrographic observations (Table 4.4). The anomalous Hf and Zr peaks for a couple of type 1 'inclusion' analyses (green traces, Fig. 4.9) for the same two samples are inferred to be contributions from zircon inclusions.

In summary, inclusions of allanite, apatite and (more rarely but more significantly) monazite in the garnets sampled here have a considerable effect on concentrations of Sm and Nd. Zircon probably also contaminates a number of analyses, but at most only affects concentrations of HREE (the evidence of which is presented in Appendix C4.1, e.g. sample 66, garnet analysis #6, where the abundance of Zr and Hf indicate that an inclusion of zircon has contaminated the analysis, yet [Nd] and [Sm] are as low if not lower than in other analyses of the same garnet). Inclusions with anomalously high Nb and Ta probably relate to inclusions of ilmenite common in these garnet samples.

4.8 Discussion

Direct comparison of TIMS and LA–ICPMS data requires analysis of the same material. However, conventional isotopic analysis is a destructive process, and the material mounted for laser ablation cannot be satisfactorily removed and cleaned of the mounting medium. Therefore the approach taken assumes that there are no large variations between garnets in any one hand specimen (e.g. two distinct garnet populations). The initial petrographic study involved in this work

suggested that this is not a cause for concern as chemical zonation across garnet porphyroblasts, the inclusion assemblages, and the morphology of garnet crystals were consistent within samples.

Comparing the results of garnet analyses made by TIMS and LA–ICPMS it is evident that all the TIMS analyses were to some degree contaminated by LREE-enriched inclusions, as concentrations of Sm and Nd exceed respective LA–ICPMS analyses representing pure garnet (at least for LREE) (Table 4.8). In fact, the [Sm]/[Nd] obtained from TIMS isotope dilution analyses is more like the [Sm]/[Nd] for LA–ICPMS analyses most contaminated by inclusions, typically less than a value of 1. A plot of [Sm]/[Nd] against log([Nd]) clearly illustrates the contamination of Nd-rich inclusions on the TIMS garnet data (Fig. 4.10). Therefore, the leaching methods used here do not remove all problematic inclusions.

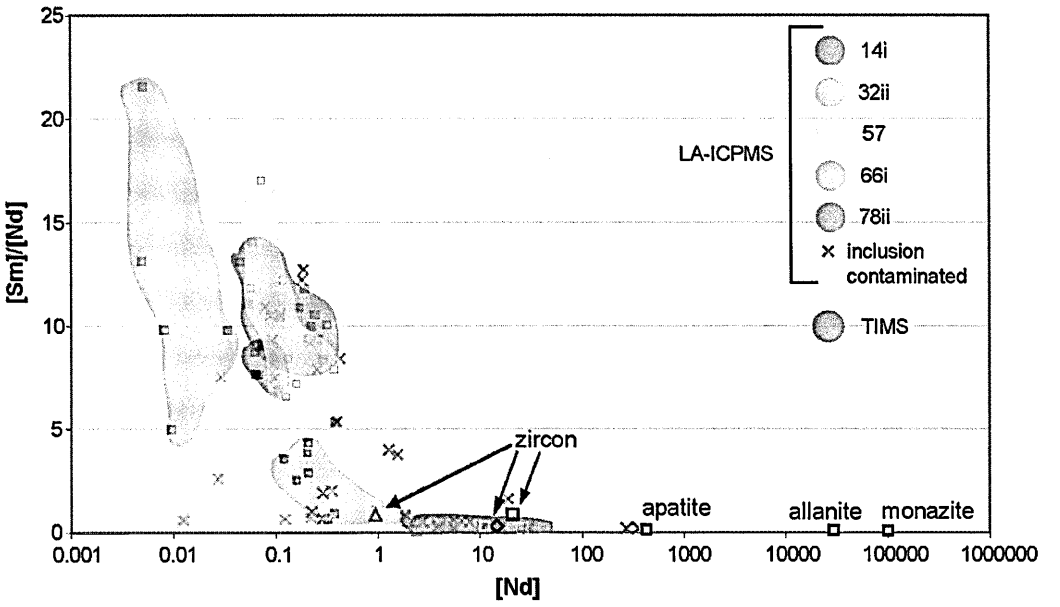

Fig. 4.10 All garnet data analysed by TIMS and LA–ICPMS (Tables 4.7, 4.8 and Appendix C4.4), plus possible LREE-rich inclusions (from Amelin (2004), Finger and Krenn (2007), Finger and Krenn (2007) and Li et al (1994)).

For samples 14i and 78ii the problematic inclusion is monazite, and to a lesser extent, possibly apatite. Monazite was preferentially leached by sulphuric acid (in agreement with Anczkiewicz and Thirlwall, 2003), although the relatively low Sm/Nd for the garnet separates from these samples suggest that not all monazite was removed. This may be a consequence of not having ground the garnet separate fine enough to expose all the inclusions to sulphuric acid (Anczkiewicz

et al., 2007; Anczkiewicz and Thirlwall, 2003). Alternatively, apatite, the other phosphate inclusion in these samples, is the guilty suspect, despite the rationale that this phosphate should also be leached by sulphuric acid similarly to monazite. This suggestion is strengthened in light of the fact that SAL had negligible effect on garnet separates from samples 32ii and 66i, which also have apatite inclusions. Despite the incomplete removal of monazite, at least some preferential leaching can start to make a significant improvement on (i.e. increase) the Sm/Nd ratio of the garnet separate. With a sufficient range in Sm/Nd a precise (even if not accurate) isochron may be constructed.

Silicate inclusions such as allanite, in samples 32ii and 66i, were evidently not leached by SAL or HCl, and thus the [Nd] and [Sm] of the garnet separates from these samples were severely compromised. A more aggressive leaching technique e.g. using HF and $HClO_4$ (Baxter et al., 2002) is probably required (as suggested by DeWolf et al., 1996) to separate allanite inclusions from garnet. As this necessitates a larger fraction of garnet sample to begin with (garnet dissolution will also be enhanced), this is likely to be the limiting factor when considering Sm–Nd garnet dating where silicate inclusions are present.

The most CaO-rich whole-rock samples out of the group of five analysed, 32ii and 66i (Appendix C1.1) also feature (as expected) the most grossular-rich garnets (Tables 4.5 and 4.8, Figs. 4.3 and 4.7) and Ca-accessory phases e.g. allanite and apatite. Apatite may be a problematic inclusion for Sm–Nd garnet geochronology, and allanite certainly appears to be (see above). Future Sm–Nd garnet dating may heed this information, and preclude rocks with relatively high amounts of calcium if there are more Fe- and Mg-rich alternatives. Otherwise, there is a risk that stubborn Ca-silicate inclusions will compromise the accuracy of the analysis. Perhaps a more aggressive leaching technique would do the trick, but if the chosen acid(s) are intended to target the silicate allanite (as it should, over apatite which has a much lower [Nd]), then expect the garnet separate to dissolve too. Alas, since grossular-rich garnet is the most soluble garnet end-member (DeWolf et al, 1996), the number of duplicate analyses possible (crucial in the construction of an isochron) is also compromised. And that's not all: the data presented here reveal that relatively grossular-rich garnets have a consistently lower Sm/Nd than more Fe- and Mg-rich garnets (Table 4.8), which

will automatically compromise the precision of any data. This has also been documented for andradite-rich garnet, whose crystallographic structure results in the diminished fractionation between Sm and Nd (DeWolf et al., 1996).

Although it was hoped that the LA–ICMPS data would reveal REE zonation in garnets, the fact that 'garnet' analyses were screened so that Sm and Nd were as close to the true values in garnet, means that only the LREE concentration data are available for identifying zonation. However, even ignoring the fact that some 'garnet' analyses may still be contaminated by one or more inclusions (Appendix C4.1), the concentration of LREE in garnet are so low that no conclusions can be drawn. With respect to Sm and Nd zonation, and the subsequent potential bias towards dating early or late garnet growth (depending on whether the core or rim be REE-enriched) via TIMS analysis, there is little for concern considering the age uncertainties involved. This could only be a significant effect where high-precision dates (± a few Ma) were possible to achieve. For TIMS garnet analysis, a more serious effect would result from the presence of one or more garnet growth zones with very different ages.

4.9 Conclusions

The mineral garnet is an invaluable source of information in the reconstruction of pressure–temperature–time–deformation histories, providing the data can be extracted. Despite its powerful potential, Sm–Nd whole-rock–garnet geochronology is not without its problems. Below I highlight the main conclusions from a study of five pelitic samples subjected to the technique.

- The treatment of garnet separates with H_2SO_4 and (although to a lesser extent) HCl preferentially leaches the phosphate monazite, confirming earlier work of Anczkiewicz and Thirlwall (2003). Although inclusions are not completely removed from the garnet separate, the resultant Sm/Nd of the (impure) garnet analysis may be sufficiently high, so that in the case where inclusions were in isotopic equilibrium with garnet (i.e. are the same age), an accurate isochron can be constructed, and with duplicate analyses (especially if they yield a range of Sm/Nd), also precise. Grinding a garnet separate to a finer grain size prior to leaching may be

all that is required for more effective leaching (although too fine a sample may also incur problems later with secondary precipitates during digestion).

- If inclusions were not in isotopic equilibrium with the host garnet at the time of growth, erroneous (although potentially reasonably precise if the Sm/Nd of the impure garnet analysis is high enough) isochrons can result (unless several duplicate analyses are performed). In simple models where there is only one type of inclusion phase, this effect is more pronounced if the inclusions are older than the host garnet and have sequestered LREE prior to garnet growth, as opposed to younger 'inclusions' (i.e. a phase that crystallised in garnet fractures, via late-stage, retrograde fluids). Impure garnet analyses with lower $^{143}Nd/^{144}Nd$ and higher $^{147}Sm/^{144}Nd$ values than the whole rock suggest contamination from an inclusion phase with lower $^{143}Nd/^{144}Nd$ and $^{147}Sm/^{144}Nd$ values than the whole rock, and perhaps one or more different inclusion phases too. Considering the large range of [Nd] and [Sm] in accessory phases, and the possibility of more than one type of inclusion, there are an endless number of effects in reality. However, duplicate analyses (including leachates), and whether these are isochronous or not, will always provide the best indication of the presence of Nd-rich inclusions.

- If a LREE-rich inclusion (e.g. allanite, apatite) is incorporated into an *in-situ* analysis of garnet, it is invariably evident, as they dominate the LREE spectra (including Nd and Sm). In contrast, ilmenite and zircon (with characteristic Nb and Ta, and Hf and Zr peaks respectively) have no discernible effect on Sm and Nd budget in the samples analysed here.

- There are inherent problems for the Sm–Nd isotopic analysis of Ca-rich rocks: Ca-accessory phases (apatite and allanite) require a more aggressive leaching method (e.g. with HF), leading to more significant loss (dissolution) of the garnet material. In light of the greater solubility of grossular-rich garnet than pyrope and almandine end-members, and its typically lower Sm/Nd values, much more garnet material is required initially.

Chapter 5

Summary of results from the Sutlej valley and further work

5.1 Summary

Although in general the GHS is equivalent to the crystalline core of the Himalayan orogen, in the Sutlej valley the crystalline core consists of not only the GHS (Vaikrita Group), but also the amphibolite-facies rocks above and below: the Jutogh Group (the Lesser Himalayan Crystalline Sequence) in the MCT (Vaikrita Thrust) footwall (Chapter 2), and the Haimanta Group in the STD (Sangla detachment) hanging wall (Chapter 3). The Jutogh Group, the Vaikrita Group and the Haimanta Group each have their own distinct *P–T–t* path, and present a complex tectono-thermal evolution of the mid-crust in NW India, summarised below and in Table 5.1.

Table 5.1 *P-T-t* summary of the metamorphic core of the Sutlej valley (including average exhumation rates)

Epoch	Haimanta Group (TSS)	Vaikrita Group (GHS)	Jutogh Group (LHCS)
Eocene - Early Oligocene > 30 Ma	burial, prograde metamorphism	burial, prograde metamorphism	
Late Oligocene 30 to 23 Ma ('STD' thrust?)	decompression during heating	burial, prograde meta. *or* isobaric heating	
Early Miocene 23 to 16 Ma (MCT, STD active)	decompression and cooling, 1.3 mm yr^{-1}	~isothermal decompression, 2 - 4 mm yr^{-1}	burial (MCT overthrust), prograde metamorphism
Middle Miocene 16 to 11 Ma	decompression and cooling, exhumation rate decreases	decompression and cooling, exhumation rate decreases	~isobaric heating
Late Miocene - present < 11 Ma (MT, KD active)	decompression and cooling, ~0.6 mm yr^{-1}	decompression and cooling, ~0.6 mm yr^{-1}	decompression and cooling, ~2.3 mm yr^{-1}

Tethyan Sedimentary Series (TSS), Greater Himalayan Sequence (GHS), Lesser Himalayan Sequence (LHS), Main Central Thrust (MCT), South Tibetan Detachment (STD), Munsiari Thrust (MT), Karcham Detachment (KD)

The early tectono-thermal evolution of the Sutlej valley is characterised by the prograde metamorphism of the GHS and Haimanta Group during the Eocene–Early Oligocene. In the Late Oligocene, the Haimanta Group records a period of decompression during continued heating, accompanied by ductile flattening interpreted as the result of crustal thinning above the Leo Pargil dome. It is proposed here that the underlying GHS may have undergone further burial if the STD represented a S-directed thrust during this time, uplifting the Haimanta Group. Either way,

thermobarometry suggests that the GHS underwent a period of isobaric heating prior to decompression (Figure 5c in Vannay and Grasemann, 2001).

Coeval movement on the MCT and STD (now an extensional fault) facilitated rapid exhumation (and isothermal decompression) of the GHS in the Early Miocene, compared to the Haimanta Group, which had now begun to cool. The Jutogh Group was overthrust by the GHS along the MCT, buried and metamorphosed.

During the mid-Miocene the Haimanta Group and GHS were re-coupled at, or near, the brittle–ductile transition and exhumed as one coherent tectonic block, coeval with cessation of movement on the MCT and STD. Rates of exhumation for the GHS and Haimanta Group slowed as a result of the transition from tectonic to erosion-related exhumation. The Jutogh Group, meanwhile, experienced isobaric heating indicative of thermal relaxation post- (MCT) thrusting.

From the Late Miocene, thrusting propagated towards the foreland of the orogen, and the Jutogh Group was rapidly exhumed between the Munsiari Thrust (below) and the Karcham Detachment (above). Decoupled exhumation of the GHS and Jutogh Group at this time is not consistent with current channel flow models (Jamieson et al., 2004), but may be reconciled with a southward (foreland-directed) migration of the locus of focused surface denudation (which partly drives channel flow) during the mid-Miocene.

5.2 Further work

5.2.1 Leo Pargil dome

Despite the similarity in the lithology of metasediments in the Leo Pargil dome to the Haimanta Group (also see p. 42, Chapter 3), their affinity, with either the Haimanta Group or the Vaikrita Group (GHS), has not yet been firmly established. Thiede et al. (2006) map the Leo Pargil dome as a structurally lower section of the Haimanta Group, whereas others consider the Leo Pargil dome to be the westernmost gneiss dome in the North Himalayan antiform (Chapter 1) owing to the similarity in structural setting (i.e. north of the STD, in the TSS) and the presence of Miocene granite intrusions (e.g. Hassett and Leech, 2007). Thus, the Leo Pargil rocks have been interpreted as the expression of hinterland doming of a mid-crustal GHS-channel (Leech, 2007). However,

whole-rock Sr and Nd isotopic analysis of the Leo Pargil rocks would determine whether they have GHS- or LHS-type isotopic signatures. Both GHS- and LHS-type rock units are exposed in the Gurla Mandhata gneiss dome (the next recognised gneiss dome to the east, 300–350 km away), implying a different crustal architecture than that envisaged within the channel flow model (Murphy, 2007). Further geochemical and geochronologic analysis of the various granite bodies in the Leo Pargil dome is required to determine the source, mechanism and timing of intrusion, which may also prove diagnostic of the LHS or GHS (see analysis of Jutogh leucogranites, Chapter 2). At least two types of granite were recognised in the course of this study; an older two-mica grey granite, and a younger tourmaline-bearing leucogranite (key granite–metasedimentary relationships, including stoped blocks and ductile and/or brittle deformation can be found at localities I05/20 and I05/21, Fig. A1.1).

Having proposed that the Haimanta Group may correlate with the uppermost GHS in central Nepal (Nar valley, Gleeson and Godin, 2006), the Leo Pargil dome may be analogous to the Chako dome. In contrast to the hinterland-doming mechanism introduced above, the Chako dome is considered to be the result of large-amplitude buckling of the GHS that folded the STD and overlying TSS (Godin et al., 2006a). A detailed structural analysis in and around the Leo Pargil dome could enlighten this discussion, as should further petrographic details to amplify the following observations made in this study.

At what is considered the periphery of the Leo Pargil dome, mineral assemblages indicate equilibration at high *T*, low *P* conditions: at locality I05/28 (Fig. A1.1), well-preserved large (~1 cm) cordierite poikiloblasts, envelop large staurolite poikiloblasts and anthophyllite/gedrite (?) porphyroblasts (sample I05/28ii, Fig. 5.1); kyanite and abundant sillimanite (fibrolite) are well-developed at locality I05/22 (Fig. A1.1). In sample I05/28ii staurolite is embayed and surrounded by cordierite, from which it may be inferred that cordierite has partially replaced staurolite (Fig. 5.1b). However, as staurolite constitutes a relatively large proportion of the rock and also features some straight crystal edges (i.e. unaltered nor embayed, Fig. 5.1a) this suggests that staurolite coexisted in equilibrium with cordierite (which simply grew after staurolite, therefore enveloping it). Also note that cordierite does not look entirely post-tectonic, and graphite is abundant (Fig.

5.1a). Major element XRF data suggest that this rock is not a typical pelite (cf. Table 3.1), with ~44–45 weight % SiO_2 and 11– 12 weight % MgO (Appendix C1.1). Indeed, cordierite–staurolite assemblages are associated with metamorphosed ultramafic rocks (Spear, 1993). Cordierite formation is restricted to depths of less than ~20 km (~6 kbars), and the presence of coexisting staurolite forms a small stability field between 600 and 675 °C and 4 and 6 kbars (Spear, 1993). Thus, if staurolite and cordierite *do* form an equilibrium assemblage, then the *P–T* conditions at this time can be very well constrained.

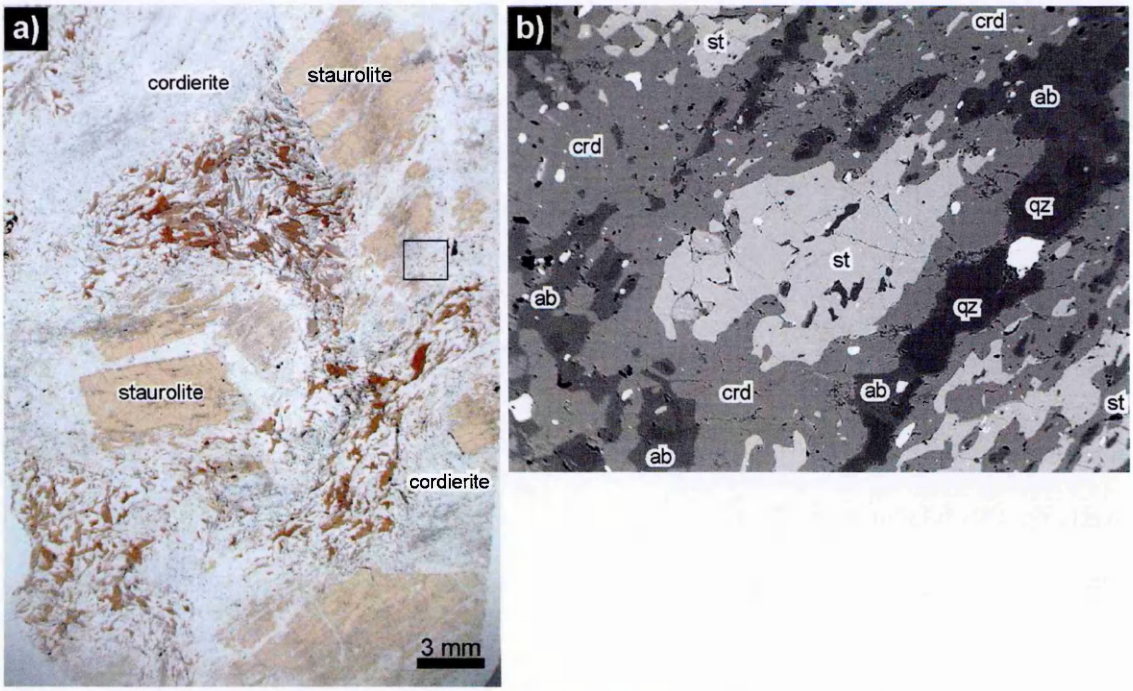

Fig. 5.1 a) Plane polarised light image of staurolite and cordierite porphyroblasts in the Leo Pargil dome (sample I05/28ii). b) Back scatter electron image of area boxed in a) to illustrate textural detail. Quartz (a darker shade of grey compared to albite) is isolated from cordierite by anhedral albite. Staurolite (st), cordierite (crd), quartz (qz,), albite (ab). field of view (width) 2.5 mm.

Accessory rutile, both as older (?) rounded grains and younger (?) clear prisms suggests once higher pressure conditions, and the evidence for brittle deformation such as fractured staurolite (Fig. 5.1a) and kinked kyanite are consistent with decompression into the upper crust (brittle regime) whilst still at relatively high temperatures. However, the heat source is unconstrained, and could have been advected with the rocks during rapid exhumation from depth, or heat advected into the upper crust by granite emplacement. One argument against the latter is that, on the periphery of the dome, leucogranite density is much lower than in the centre. There might be a larger body of

leucogranite just below the surface, but the small granite dikes observed would not create a significant metamorphic aureole. It could, of course, be a combination of both. Rapid exhumation would almost certainly cause some of the fertile pelitic rocks in the section to partially melt, so generating granites, and would be consistent with the inference that a major detachment lies west and south of these localities.

Cordierite-bearing assemblages have been found in correlative units (see Chapter 7), in the Harsil Formation (Garhwal Himalaya; Prince, 1999) and in the Everest Series (Jessup et al., 2004; Searle et al., 1997; Searle et al., 2003). A more detailed petrographic analysis of the Leo Pargil dome metasediments will be useful to ascertain if a similar mechanism was responsible for cordierite formation in all of these rocks.

5.2.2 Shimla klippe

Garnet-grade metasediments (predominantly schists) crop out in a klippe in the lower Sutlej valley near Shimla, surrounded by low grade metasediments, e.g. Shimla slates of the LHS (Fig. A1.2). The metamorphism and deformation of the Shimla klippe rocks were first documented by Pilgrim and West (1928) and then later by Naha and Ray (1970). Mukhopadhyay et al. (1997) compare the Shimla klippe metasediments to those surrounding the Chor granite (~40 km to the SE) which are similar with respect to lithology and metamorphic grade, and also bound by a thrust at their base. Preliminary petrographic results from this study are in agreement with the conclusion made by Mukhopadhyay et al. (1997), that an early phase of high-grade metamorphism producing garnet, staurolite, kyanite and sillimanite (although only garnet and staurolite were found in our reconnaissance of the Shimla klippe, which was not extensive) was pre-kinematic with respect to ductile shearing, which was accompanied by a much lower grade of metamorphism (chlorite, and at most, biotite grade).

This is interesting given that the (*low*-grade) ductile thrust that soles the Shimla klippe is commonly correlated with the MCT (e.g. Figure 4b in Thiede et al., 2004; Figure 2 in Vannay et al., 2004), yet syn-tectonic garnet porphyroblasts (from Jutogh Cantonment, just NW of Shimla, Fig. A1.2) with major element bell-shaped profiles (Fig. 4.7) are consistent with shearing during (relatively high-grade) prograde metamorphism. Add to this the fact that these garnets are ~ 490

Ma (Sm–Nd, sample I05/78ii, Chapter 4), and it provides compelling evidence for high-grade metamorphism and deformation in the early Palaeozoic, and thus the Shimla klippe can be correlated to the Kathmandu and Dadeldhura thrust sheets in Nepal (Gehrels et al., 2003; Gehrels et al., 2006a; Gehrels et al., 2006b).

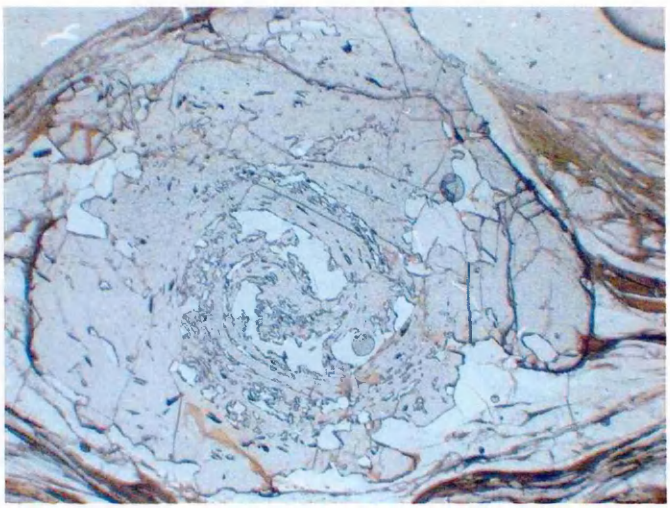

Fig. 5.2 Plane polarised light image of garnet porphyroblast (in sample I05/78i) from the Shimla klippe with a spiral inclusion trail indicative of syn-tectonic growth (rotation > 360°). Garnet diameter 4.5mm. [Note uncanny likeness to garnet from 'Paro window' in Bhutan (sample B06/102iii), Fig. 6.19]

If the MCT is the basal thrust to the Shimla klippe then the metasediments should be analogous to the GHS. Indeed, the Nd bulk-rock isotopic data (see Chapter 2.3 for method) are consistent with a Greater Himalayan affinity: ε_{Nd} (500) equals -7.6 and the model Nd age is 1.72 Ga (sample I05/78ii), and the rocks may be grouped with what are known as the 'Outer Lesser Himalaya' (Richards et al., 2005). Note that these isotope data cannot distinguish between the GHS and Haimanta Group. This result could be corroborated with similar data from the only other sample I collected from the Shimla klippe (I05/75, Appendix A1). In contrast to the GHS, there is no sign of partial melting within the Shimla klippe, although this is compatible with observations in the Haimanta Group (Chapter 3). However, the variety of lithologies exposed in the section studied in the Shimla klippe (of only 10s of metres), including mafic amphibolites (some with chlorite), pelites (including garnet–mica schist), quartzitic schists, banded calc-silicates, and granular, intermediate meta-igneous rocks, has not been recognised in either the GHS or the Haimanta Group on such a small scale.

Nonetheless, the Shimla klippe metasediments have been established as *distinct* from the Lesser Himalayan Crystalline Series (LHCS) as originally mapped in Figure A1.2 and in Richards

et al. (2005). Thus the type locality for the Jutogh metasediments (in the Shimla klippe) does not share the same sedimentary provenance or age of metamorphism as the Jutogh metasediments/LHCS exposed in the immediate footwall of the Vaikrita Thrust to the north-east. It would be wise to be wary of the possible confusion regarding the definition of the Jutogh Group *sensu stricto*. The name should perhaps refer to the Shimla klippe-Jutogh Group, as this is where the metasediments were originally characterised (Pilgrim and West, 1928). However, since the LHCS-Jutogh Group terminology has been used in more recent publications (Chambers et al., 2008; Jain et al., 2000; Pant et al., 2006; Richards et al., 2005; Singh and Jain, 1993), it perhaps warrants the continued application of this name to these rocks. It would be satisfactorily unambiguous to call the Shimla klippe-Jutogh Group the "Shimla klippe metasediments".

The timing and mechanism(s) for thrusting of the 'Outer Lesser Himalaya' units (including the Shimla klippe) obviously requires further investigation. The Shimla klippe metasediments record intense shearing during the Palaeozoic in garnet inclusion trails, as well as shearing at lower grades (chlorite to biotite) in the matrix, presumably during the Himalayan orogeny. For Himalayan tectonic reconstructions, it is essential to understand the early Palaeozoic tectonic history and the resultant tectonic architecture. Overestimates on the degree of metamorphism and deformation are otherwise highly probable, which in turn will yield erroneous models of orogenesis.

Chapter 6

Bhutan

6.1 Introduction

The Kingdom of Bhutan, located in the eastern Himalaya (Fig. 1.1), remained an isolated country until the 1950's, and not until an expedition headed by A. Gansser in 1963 was any significant geological information made public (Gansser, 1964; Gansser, 1983). Since then, visa restrictions and the cost of travel (especially in relation to neighbouring Himalayan countries) means that Bhutan has remained relatively undiscovered. This chapter begins with an overview of the geology of Bhutan, highlighting areas that have been the focus of recent studies (Bhargava, 1995; Daniel et al., 2003; Davidson et al., 1997; Gansser, 1964; Gansser, 1983; Grujic et al., 1996; Grujic et al., 2002; Hollister and Grujic, 2006; Richards, 2004; Stüwe and Foster, 2001; Swapp and Hollister, 1991). Following this is a tectono-metamorphic study focused on the Radi klippe in the east of Bhutan, which presents the first pressure–temperature data on the klippen schists, and addresses the possibility that pulsed channel flow operated in Bhutan (Hollister and Grujic, 2006). The chapter closes with a look at areas for further work in Bhutan.

6.1.1 Regional geology

It is apparent that between the Sutlej valley in the western Himalaya (Chapters 2 and 3) and Bhutan there exists a remarkable along-strike continuity of the major Himalayan units and structures (Fig. 1.1). However, it is important to note several geological features unique to Bhutan (Fig. 6.1) with respect to the Sutlej valley: 1) klippen of the Tethyan Sedimentary Series (TSS) overlying the Greater Himalayan Sequence (GHS); 2) a thicker GHS package owing to the presence of the Kakhtang thrust (KT), which duplicates GHS strata; 3) a steeper mountain front and a narrower N–S width of outcrop of the Siwalik Group in the frontal zone.

Details of these are presented in the descriptions below of the major tectono-stratigraphic units and their respective bounding structures (starting at the top of the structural section, and working down) (see also Yin, (2006), Tables 3 and 7). It is worth noting that that rock exposure in Bhutan is poorer than in some other Himalayan regions (e.g. upper Sutlej valley, Chapter 3), owing

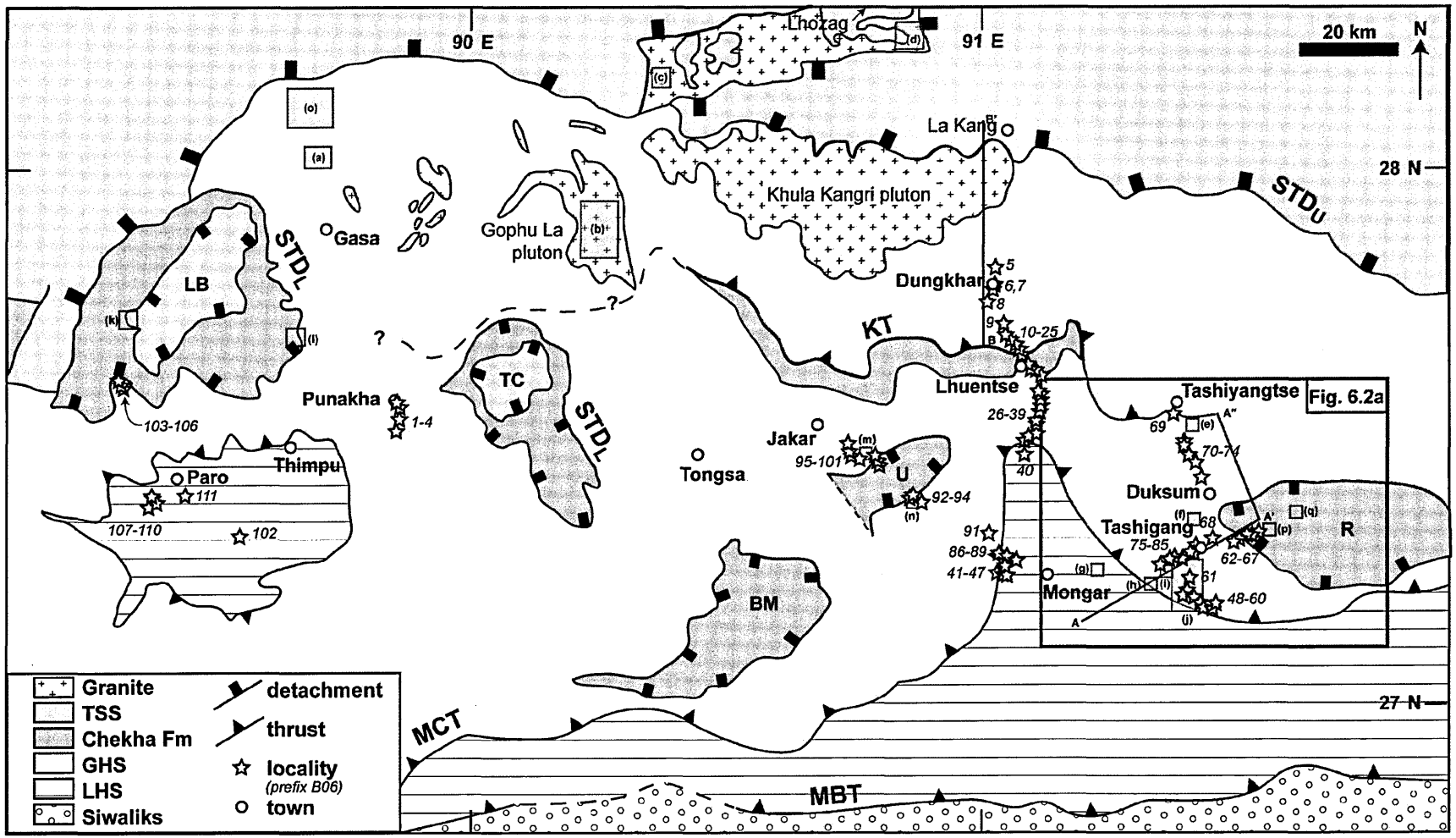

Fig. 6.1 Simplified geological map of Bhutan after Hollister and Grujic (2006). MBT, Main Boundary Thrust; MCT, Main Central Thrust; STD_L and STD_U, South Tibetan Detachment, lower and upper respectively; KT, Kakhtang Thrust; TSS, Tethyan Sedimentary Series; GHS, Greater Himalayan Sequence; LHS, Lesser Himalayan Sequence; LB, Lingshi Basin; TC, Tang Chu klippe; BM, Black Mountain klippe; U, Ura klippe; R, Radi klippe. Lines A-A'-A" and B-B' refer to cross sections (Figure 6.18). Letters (a) to (q) refer to key Cenozoic geochronologic data (Table 6.5).

to Bhutan's relatively high precipitation rates and therefore lush vegetation. This presents a challenge to field mapping. Furthermore, rock exposed at high elevations and thus persistently in wet and misty conditions, weathers at an increased rate. As a result, sampling also suffers.

Tethyan Sedimentary Series (TSS)

The four known klippen of TSS are structurally isolated outliers that form open, upright synclines (with variable axial orientation) in the GHS outcrop, as a result of a folded South Tibetan detachment (STD, see below) (Edwards et al., 1996; Grujic et al., 2002). They are, from west to east, the Tang Chu, Black Mountain, Ura and Radi (also known as Sakteng) klippen (Fig. 6.1). Other klippen may still be discovered and the extents of the known klippen are still only approximate. Schistose rocks of the Chekha Formation (see review in Bhargava, 1995) at the base of the klippen (and of the Lingshi basin, Gansser (1983)) contrast with gneisses and migmatites of the underlying GHS. Metamorphic grade rapidly decreases up section from garnet ± staurolite mica schists and hornblende schists, through phyllites and quartzite, into unmetamorphosed sediments comprising limestone and quartz conglomerate. In contrast with the basal Chekha Formation, which preserves a pervasive tectonic fabric, the dominant planar fabric in upper structural levels is sedimentary bedding (Grujic et al., 2002). The Chekha Formation is assumed to be Late Proterozoic in age (Bhargava, 1995; Gansser, 1983) as it is unconformably overlain by Early Cambrian sediments (Tangri and Pande, 1995). These characteristics have led to correlations to similar tectono-stratigraphic units along the length of the Himalaya, including the Haimanta Group in Chapter 4 (see Table 7 in Yin, 2006).

The TSS exposed in northern Bhutan/southern Tibet is less extensively studied than the TSS which forms the (more accessible) klippen. Observations based on the Lhozhag–La Kang region (Burchfiel et al., 1992) (Fig. 6.1) also record a rapid decrease in metamorphic grade, structurally upward, through garnet and chlorite zones. The structurally lowest rocks superficially resemble the amphibolite-grade GHS, but are inferred to be the metamorphic equivalents of the rocks of the TSS into which the metamorphic section grades.

South Tibetan Detachment (STD)

At the base of the TSS klippen, at the contact between the Chekha Formation and the GHS, well-developed kinematic indicators including deformed leucogranite intrusions (Grujic et al., 2002), asymmetric pressure shadows on garnet porphyroblasts and asymmetric foliation boudinage (basal Radi klippe and underlying GHS respectively, see Section 6.2.1), and asymmetric shear bands (SW basal Ura klippe, localities B06/93 and B06/94, Appendix A2; as documented by Daniel et al. (2003)), indicate a consistent NE to NW normal displacement of the hanging wall (TSS) under ductile conditions. These shear zones have been referred to as part of the 'lower' or 'southern' STD (Hollister and Grujic, 2006). No brittle (i.e. discrete) detachment has been observed at the lower STD, and so the high-strain contact between the GHS and TSS (base of the klippen) is always continuous, concordant and gradational. This is reminiscent of the STD in the Dzakaa Chu valley, Tibet (45 km NE of the Everest region), represented by a ~1 km thick zone of distributed ductile shear from amphibolite facies gneiss of the GHS at the base, grading up into unmetamorphosed Palaeozoic sediments of the TSS at the top (Cottle et al., 2007a). The shear zone exposed here is interpreted as a relatively deeper and older section of the STD, consistent with the nature of the STD observed in other parts of the Himalaya, where relatively early ductile fabrics are overprinted by later brittle deformation (Burchfiel et al., 1992). Ductile-only extensional zones have been observed in a minority of core complexes and extended regions elsewhere in the world; amongst the earliest discovered were in British Columbia (e.g. Valkyr shear zone on the western flank of the Valhalla complex, Parrish et al., 1988).

Elsewhere, the nature of the GHS–TSS contact invariably features late-stage steep brittle faults that cut mylonitic fabrics associated with previous ductile motion along the STD shear zone (Wu et al., 1998 and references therein). This includes the 'upper' or 'northern' STD in Bhutan/southern Tibet (Burchfiel et al., 1992; Edwards et al., 1996). The crystallization ages of deformed granites in the immediate footwall to the upper STD (Edwards and Harrison, 1997; Wu et al., 1998), and muscovite cooling ages from one of these granites (the Khula Kangri pluton, Maluski et al., 1988), constrain ductile motion on the upper STD to between 12 and 10 Ma.

Grujic et al. (2002) use the crystallization age of a deformed leucogranite (17–22 Ma) from the Radi (Sakteng) klippe to constrain the maximum age of north-directed shear across the lower STD. However, the geochronologic data were never actually published in the cited paper (that is, Daniel et al, 2003). The only (unpublished) data from that area were from two granitic samples from entirely within the klippe: one from a pegmatite (RP 87, Fig. 6.4) and the other, from a larger granite pluton (RP 106, note sample not *in situ*, Fig. 6.4) (R. Parrish, pers. comm., 2008). The pegmatite, which features some brittle deformation, yields a monazite U–Pb age of 18.5 ± 1 Ma. Monazite U–Pb ages for the undeformed granite pluton are <23 Ma, plus an inherited component (R. Parrish, unpublished). Both the pegmatite and granite bodies are discordant to the main foliation in the metasedimentary country rock, suggestive of post-tectonic intrusion. Brittle deformation in the pegmatite could result from the late-stage folding of the Radi klippe and basal detachment, and not necessarily be related to extension on the lower (notably ductile) STD. Therefore, neither sample represents a firm age constraint on the age of the lower STD shear zone (R. Parrish, pers. comm. 2008). If anything, as the samples are undeformed or at most feature brittle deformation, their ages constrain a *minimum* age for ductile deformation across the 'lower' STD. However, these samples may have simply not been in close enough proximity to the shear zone to constrain the age of ductile movement on it. Furthermore, it is recognised that a more brittle mode of intrusion, resulting from an increase in the pore fluid pressure associated with the intrusion of melts, would misrepresent the true (deeper) depth of intrusion.

Greater Himalayan Sequence (GHS)

The GHS covers most of Bhutan and comprises amphibolite-grade schist, gneiss, migmatite and leucogranite. The entire unit is penetratively deformed with top-to-the-south shear fabrics formed by motion along the MCT (lower boundary to the GHS, see below) and the Kakhtang thrust, and overprinted in the highest structural levels by top-to-the-north shear fabrics, related to movement on the STD. Several localised zones of deformation exist within the GHS showing that the south-directed deformation was heterogeneous in space and time (Grujic et al., 2002).

Kakhtang Thrust (KT) and the upper GHS

This major south-directed thrust fault, predicted by Swapp and Hollister (1991), has been recognised as an important structure that almost doubles the thickness of the GHS, cross-cutting penetrative south-directed shearing related to the MCT and metamorphic isograds (Davidson et al., 1997; Grujic et al., 1996; Grujic et al., 2002). Where the previously mapped KT was crossed between Lhuentse and Dungkhar during field work (Fig. 6.1), no discrete shear zone was recognised, but the trace could be approximately inferred from a) the marked absence of migmatites in the footwall to the thrust compared to the hanging wall, b) the presence of brittle faults (with or without associated mineralization, thin fault gouges and calcareous flowstone) (Fig. 6.2). The latter suggests that the KT has been an active upper crustal fault. The KT hanging wall ('upper' GHS) is dominated by gneiss and migmatitic rocks (Fig. 6.3) bearing massive sillimanite ± K-feldspar ± cordierite (Davidson et al., 1997; Gansser, 1964; Gansser, 1983; Stüwe and Foster, 2001). The largest leucogranite bodies in Bhutan e.g. Khula Kangri and Gophu La (Fig.6.1) are spatially restricted to the uppermost KT hanging wall. Coupled pressure–temperature data and petrographic observations show that the upper GHS experienced high-temperature decompression, and that peak temperatures here were laterally heterogeneous as a result of localized heat advection from leucogranite intrusions (Davidson et al., 1997; Swapp and Hollister, 1991). Moreover, eclogite-facies rocks (indicative of exhumation from depths of at least 30 km) have only been found in the upper GHS of Bhutan. These rocks have been strongly overprinted during high-temperature (granulite facies) metamorphism, but metamorphic zircon, dated at 14–15 Ma, is considered 'eclogitic' according to zircon rare earth element chemistry (Warren et al., 2008), making these Bhutanese eclogites remarkably young compared to other Himalayan eclogites (46 Ma, Kaghan, e.g. Parrish et al., 2006; 53 Ma, Tso Morari, e.g. Leech et al., 2005, both of which are found in the western Himalaya).

The upper GHS (NW Bhutan) has been deformed by top-to-the-north normal shear zones, allegedly active between 21 and 17 Ma (Carosi et al., 2006). South-directed motion on the KT has deformed (boudinaged) leucogranite dykes and kyanite-bearing pegmatites. Monazite and xenotime from one such pegmatite (immediate KT footwall in eastern Bhutan) yield crystallization ages from

15.0 to 14.2 Ma (Daniel et al., 2003) and constrain the maximum age of ductile deformation on the KT (as well as dating kyanite metamorphism in the lower GHS).

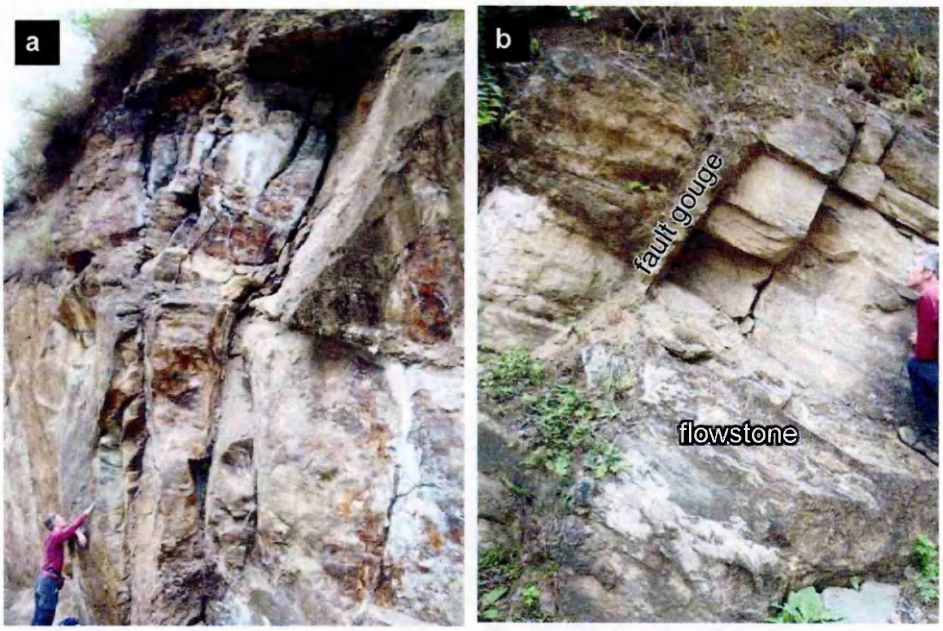

Fig. 6.2 Geological features across the approximate trace of the Kakhtang thrust between Lhuentse and Dungkhar (see Figure. 6.1): a) steeply-dipping brittle faults in GHS psammites; b) steeply dipping brittle fault, lined with fault gouge (in which no unambiguous sense-of-shear indicators were observed) and calcareous flowstone along a foliation plane. T. Argles for scale in both photographs.

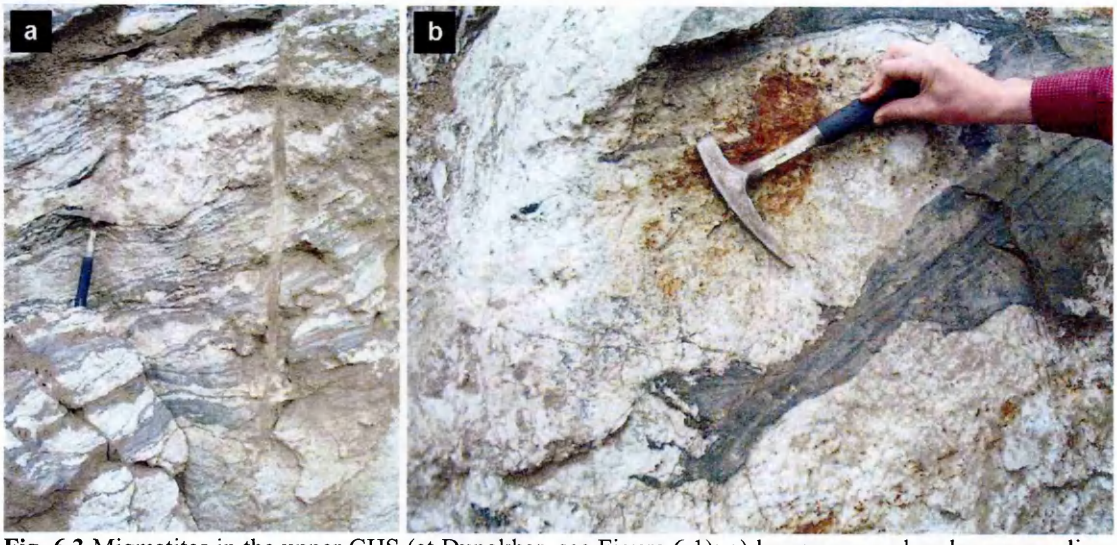

Fig. 6.3 Migmatites in the upper GHS (at Dungkhar, see Figure 6.1): a) leucosome and melanosome aligned with the foliation in the gneiss 'protolith' from injection of melts along the foliation and/or *in-situ* melting; b) Evidence for in-situ melting where melanosome intermingles with leucosome. Hammer for scale in both photographs.

Main Central Thrust (MCT) and the lower GHS

The south-directed MCT is easily recognised in eastern Bhutan around the Mongar half-window, where LHS quartzites and phyllites are juxtaposed against GHS schists and gneisses across a relatively narrow (<1 km), high-strain (mylonitic) zone (Fig. 6.1) (Daniel et al., 2003 and author's own observations). Thus, at this location the MCT not only marks a relatively discrete shear zone with the highest recognisable finite deformation, but is also coincident with a lithological, metamorphic and isotopic boundary (Richards et al., 2006). South-directed shearing associated with the MCT is distributed across a much wider zone than the thrust shown in Figure 6.1, extending from ~2 km below the MCT upwards throughout the whole GHS (Grujic et al., 2002).

The lower GHS is characterised by garnet–staurolite mica schists and gneisses (in places, with kyanite and/or fibrolitic sillimanite) and subordinate migmatite (Daniel et al., 2003; Davidson et al., 1997; Gansser, 1983; Swapp and Hollister, 1991). Peak temperatures were lower than those attained in the upper GHS, and together the upper and lower units of the GHS form an inverted metamorphic field gradient (Davidson et al., 1997). The lower GHS is interpreted to have been overthrust by the upper GHS along the KT (Davidson et al., 1997; Swapp and Hollister, 1991).

Lesser Himalayan Sequence (LHS)

Quartzites dominate the greatest exposure of the LHS in Bhutan (Mongar half-window, Fig. 6.1). In detail, immediately below the MCT is the Jaishidanda Formation, characterised by garnet–mica schists interlayered with quartzites and phyllites (Dasgupta, 1995). This unit varies in thickness from 30–600 m, and extends continuously across Bhutan, save for some sections in the east where it is faulted out (see Figure 1 in Hollister and Grujic, 2006). Near Khaling village in eastern Bhutan, the MCT zone also contains the enigmatic Barsong Formation, which consists of pure quartzites and layers of shale superficially similar lithologically to the underlying rocks, but isotopically distinct (Richards, 2004). Below the Jaishidanda Formation (and Barsong Formation) is the Shumar Formation (Dasgupta, 1995) or Daling–Shumar Group (Gansser, 1983), consisting of interlayered quartzites and chlorite phyllites, with some mafic bodies, tectonically interleaved with lenses of Palaeoproterozoic granite (Daniel et al., 2003) and carbonates of the Baxa Formation.

6.1.2 Aims of this study

Hollister and Grujic (2006) have suggested that the GHS in Bhutan was exhumed via channel flow that operated during three discrete pulses. Pulse 1 was active between 22 and 16 Ma, facilitated by coeval movement on the MCT and lower STD. Pulse 2 was more cryptic: it required movement on the Main Boundary Thrust to the south and extension somewhere around the present location of the KT, and lasted until ~13 Ma. Pulse 3 occurred between 12 and 10 Ma, was bounded by the KT and upper STD shear zones, and exhumed deeper GHS (mid-crustal) material. Fundamental to this model is that normal sense motion on the lower STD bounding the southerly klippen ceased before motion began on the upper STD. Although the timing of movement on the upper STD shear zone is relatively tightly constrained (~12–10 Ma), equivalently robust data to constrain movement on the lower STD shear zone do not yet exist (see above). One of the aims of this study therefore was to investigate the nature and timing of motion on the lower STD.

The area around the western Radi klippe (eastern Bhutan) has been the subject of a number of studies (Daniel et al., 2003; Davidson et al., 1997; Stüwe and Foster, 2001), none of which directly address the tectono-metamorphic history of the Chekha Formation in the klippe, or the timing of motion on the lower STD. However, geological data (including estimates of peak and retrograde metamorphic conditions) from the uppermost LHS and lower GHS (KT footwall) in this area provide a tectonic framework in which to incorporate new pressure–temperature–time (*P–T–t*) data from the Chekha Formation. In the following section I present new *P–T–t* data pertaining to samples within 2 km of each other structurally, but on either side of the lower STD at the base of the Radi klippe.

6.2 Tectono-metamorphic insights into the Radi klippe/ lower South Tibetan Detachment

6.2.1 Field relations and petrology

The Radi (also known as Sakteng) klippe is the most easterly outlier of TSS exposed in the GHS in Bhutan (Figs. 6.1 and 6.4). The base of the klippe is characterised by amphibolite-grade metasediments of the Chekha Formation, e.g. garnet–staurolite schist at locality B06/62 (Fig. 6.4). Garnet in this sample appears to be an early-grown metamorphic phase, overprinting a micro-

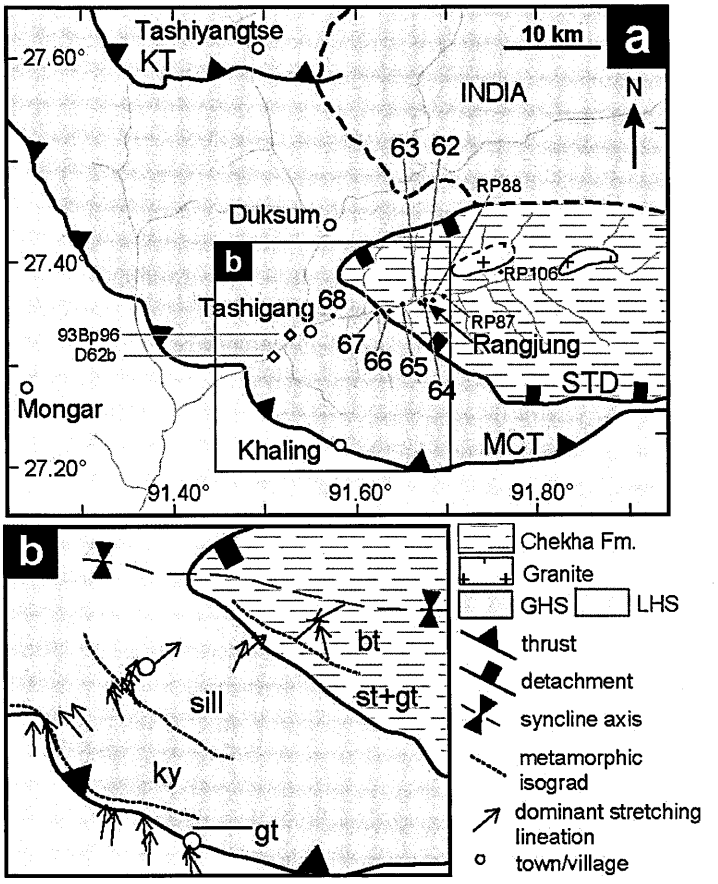

Fig. 6.4 (a) Geological map of the Radi klippe, east Bhutan (see Fig. 6.1) after Bhargava (1995) and Hollister and Grujic (2006), with modifications from the author's field observations. All sample localities from JC's set (B06) apart from samples RP87 and RP106 (RP, R. Parrish), 93Bp96 (Davidson et al., 1997) and D62b (Daniel et al., 2003), of which the latter two are only approximate locations. (b) Simplified and cropped geological sketch map showing stretching lineations from field measurements and metamorphic isograds: bt, biotite; gt, garnet; st, staurolite; ky, kyanite; sill, sillimanite (where the zone, as opposed to the 'mineral-in' line, is labelled). Abbreviations as in Fig. 6.1.

folded fabric (S1) (Figs. 6.5a–c, and Fig. 6.14). Staurolite appears to post-date garnet, and curved inclusion trails (S2–S3) aligned with the matrix foliation (S3) at the ends of staurolite crystals suggest this mineral grew during deformation (Figs. 6.5a–c). The main fabric in these schists is a crenulation foliation. Metamorphic grade decreases rapidly up section from this locality, to fine-grained greenschist-grade biotite schist over a structural distance of less than 1 km. Although observations were not made further east into the klippe (i.e. further up the structural section), metamorphic grade presumably decreases further still into unmetamorphosed, possibly fossiliferous, TSS sediments *sensu stricto*, as recognised in other TSS klippen (Grujic et al., 2002). The Chekha Formation and TSS are folded about an east–west trending axis, forming a syncline.

In addition to the granite plutons mapped (Bhargava, 1995) and shown in Figure 6.4a, a number of relatively small (metre-scale) leucogranite and pegmatite bodies intrude the Chekha Formation (e.g. Figs. 6.5d and e). These intrusions typically cross-cut the main foliation at an oblique angle, and preserve signs of both ductile and brittle deformation, e.g. boudinage (evident

where the host rock is pelitic) and angular intrusive contacts (evident in more psammitic lithologies, e.g. Fig. 6.5e). These observations suggest that the intrusions were syn- to late-tectonic and occurred at about the brittle–ductile transition, although it is noted that an elevated pore fluid pressure (as a result of intrusions driving dehydration reactions in the host metasediments), and the resultant tendency towards a more brittle mode of intrusion, may lead to an underestimate of the true depth of intrusion.

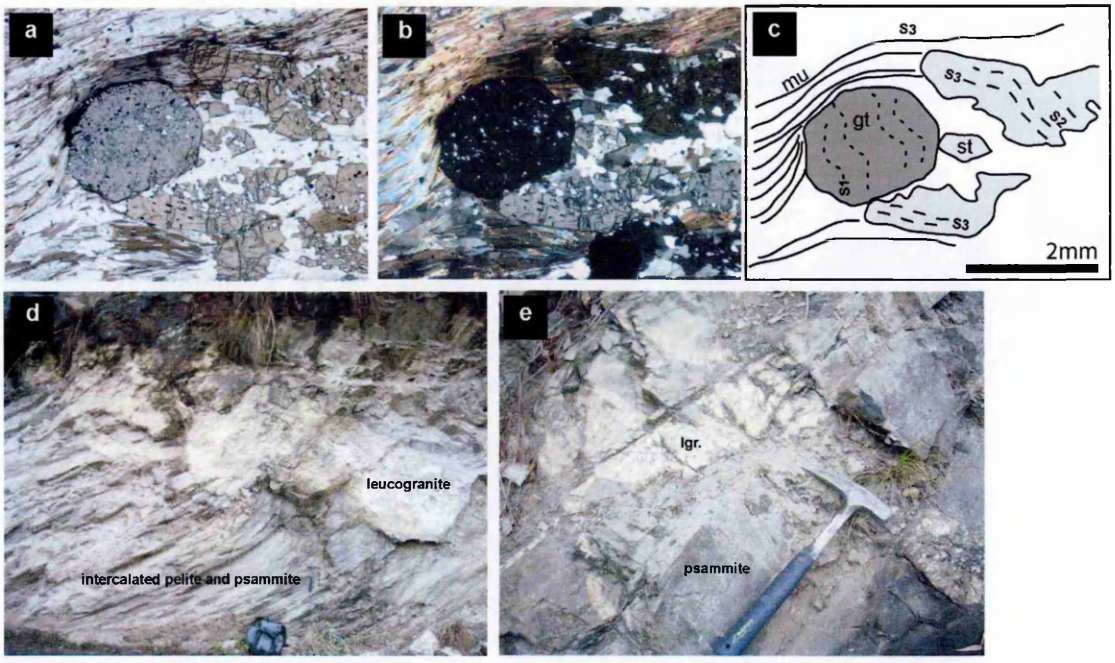

Fig. 6.5 Photographs of the Chekha Formation sample and locality B06/62: a) plane polarised microphotograph of a garnet-staurolite mica schist; b) cross polarised view of a); c) line-drawing of a). Garnet (gt), with a weak but discernible early micro-folded inclusion fabric (S1), is loosely wrapped on one side by staurolite (st), which features a syn-tectonic inclusion fabric, evolving from S2 to S3, that represents the main foliation. S3 is defined largely by the matrix phase muscovite (mu), which strongly wraps garnet (sweeping extinction, top of field of view in b). Biotite, plagioclase and quartz are the other visible matrix phases. d) cross-cutting tourmaline-muscovite leucogranite intrusion into intercalated pelites and psammites (rucksack for scale); e) as in d) highlighting brittle intrusion, i.e. angular contacts with psammitic host rock, perhaps reflecting high pore fluid pressure (hammer for scale).

Coarse-grained sillimanite gneiss of the GHS (e.g. B06/67), in the footwall to the lower STD, contrasts strongly with the crenulated schists of the Chekha Formation. Sillimanite is abundant, as fibrolite in the matrix (Figs. 6.6a–e) and as mats of more prismatic crystals lining shear surfaces (Figs. 6.6f, h). As no kyanite was observed (not even as a relict included phase), the most likely sillimanite (fibrolite)-forming reaction involves muscovite breakdown. K-feldspar is a

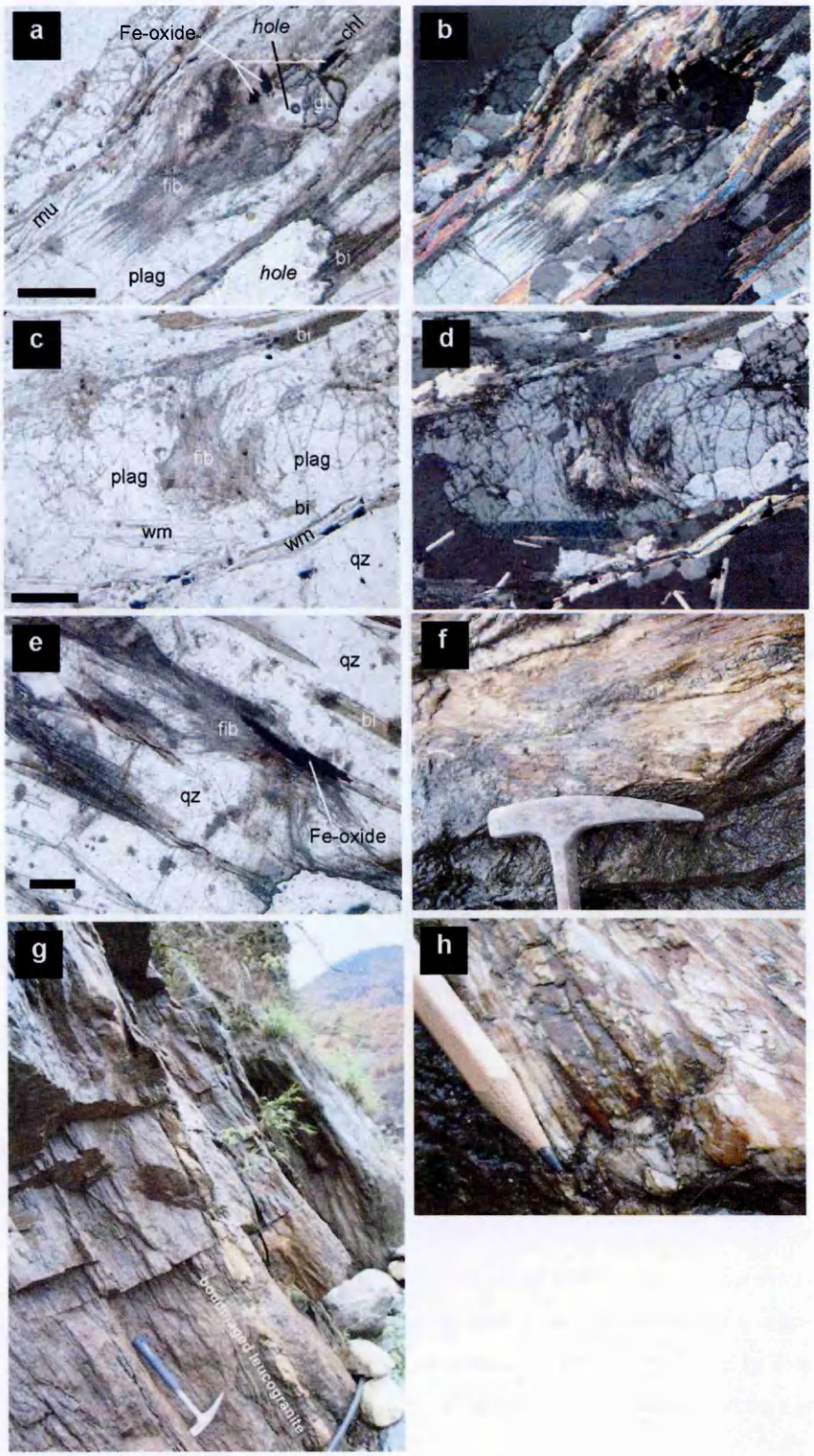

Fig. 6.6 Photographs of 'lower' GHS sample and locality B06/67: a)-e) plane and cross polarised microphotographs of fibrolite (fib) at grain boundaries between quartz (qz), biotite (bi), muscovite (mu), plagioclase (plag). Abbreviations: garnet (gt); chlorite (chl). Cracks perpendicular to the main foliation (bottom left to top right) across the sheath of fibrolite and plagioclase suggest continued deformation (stretching) in the same orientation, i.e. post-sillimanite growth. Scale bar 0.5 mm. f) Matted pearly-white prismatic sillimanite on surface of leucosome (close up in h). g) Looking ~W along strike of sillimanite–gneiss outcrop. Leucogranite is aligned with foliation and boudinaged. Hammer or pencil for scale in f)-h).

product of this reaction, and in its absence from the mineral assemblage suggests a subsequent back reaction with melt to form new muscovite, plagioclase and quartz. Some coarse-grained, and non-sericitic but apparently secondary muscovite (laths), support this hypothesis. Pale pink, small (< 1 mm) garnets are locally abundant. The garnet crystals are fractured, and cracks as well as garnet rims are lined by a red–brown Fe-rich alteration product (Fig. 6.6a). Tourmaline ± white mica ± garnet leucosome pods and boudinaged veins are also common. Asymmetric foliation boudinage and minor shear zones at this locality (B06/67) record NE-directed sense of shear (normal motion), in contrast to lower levels in the GHS (towards the MCT) that display a pervasive south-directed sense of shear (thrust motion). Asymmetric pressure shadows on garnet porphyroblasts in the basal Chekha Formation exhibit both (relatively weak) NE-directed (locality B06/64) and SW-directed (locality B06/62) shear sense. Therefore, the width of the lower STD shear zone at the base of the Radi klippe is estimated at less than 2 km wide. The record of SW-directed shearing at the base of the Chekha Formation suggests that the lower STD may be a reactivated (south-directed) thrust, as has been inferred for the upper STD in southern Tibet, north of Bhutan (Burchfiel et al., 1992), and for the STD elsewhere in the Himalaya (e.g. Vannay and Hodges, 1996; Wyss et al., 1999).

6.2.2 Samples

Garnet-bearing samples of the Chekha formation (B06/62 and B06/64) and the GHS (B06/67) were collected from localities as close to the trace of the lower STD as possible (Fig. 6.4). Thin sections of these samples allowed a thorough petrographic study detailing textures and mineralogy. Major element analyses of the key minerals, including profiles through garnet porphyroblasts, were made using an electron microprobe at the Open University (see below for details). Accessory phases suitable for U–Th–Pb geochronology (e.g. monazite, allanite, zircon) were identified using the energy dispersive system (EDS) and element mapping (Appendix B2.1, Figs. 6.7 and 6.8) on the electron microprobe. Considering the amphibolite grade of these metasediments, zircon was disregarded as a phase to date because U–Pb ages would be likely to yield inherited ages of crystallization (i.e. igneous rather than metamorphic growth). The textural context of each accessory mineral grain was recorded and mapped for trace elements (Th, P, Y and Ce); information valuable to the interpretation of the mode of formation, including relative timing

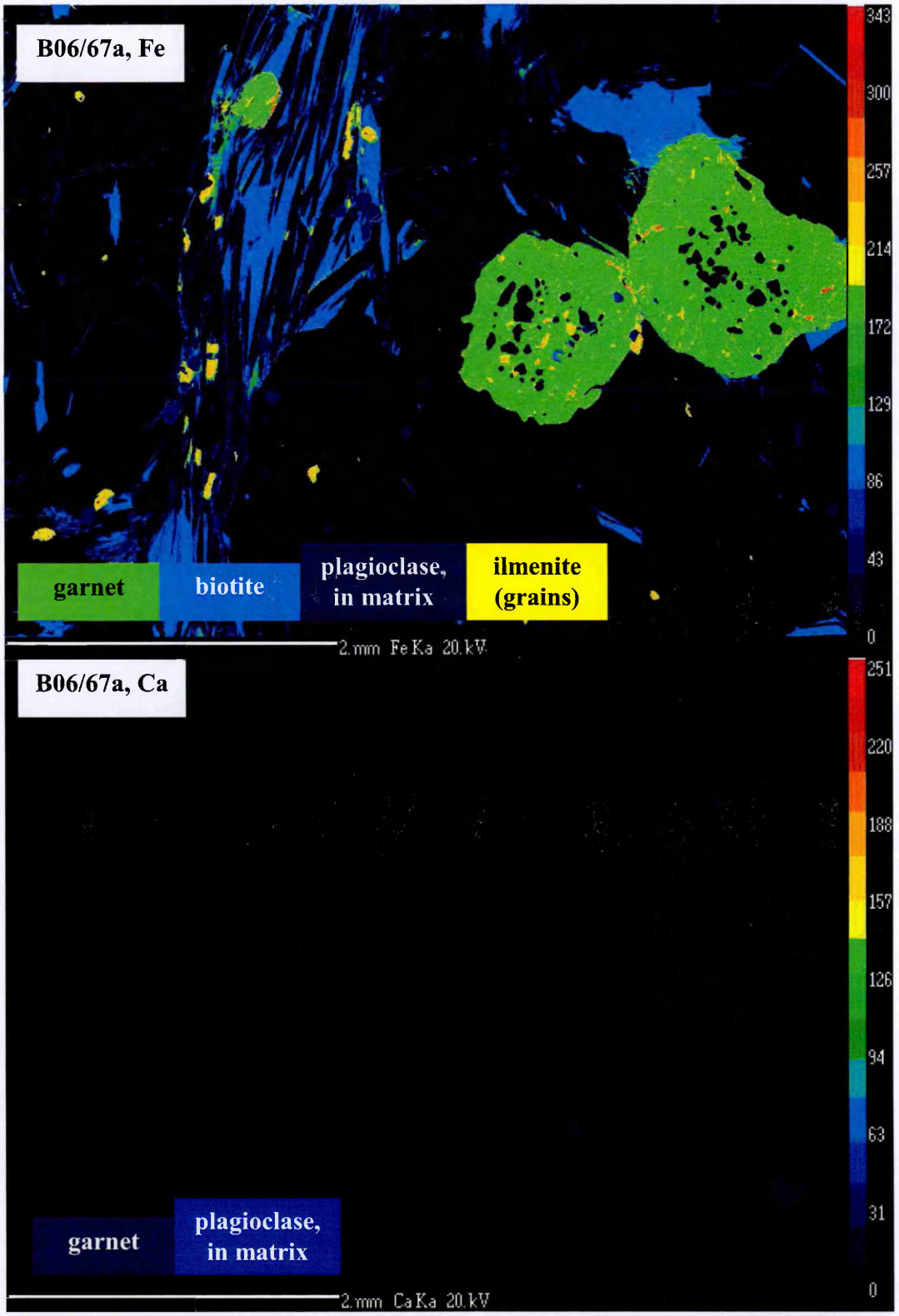

Fig. 6.7 Element maps (Fe, Ca, La and P) of two areas in the GHS sample, B06/67 (one in each of two sections cut). Page 1 of 4.

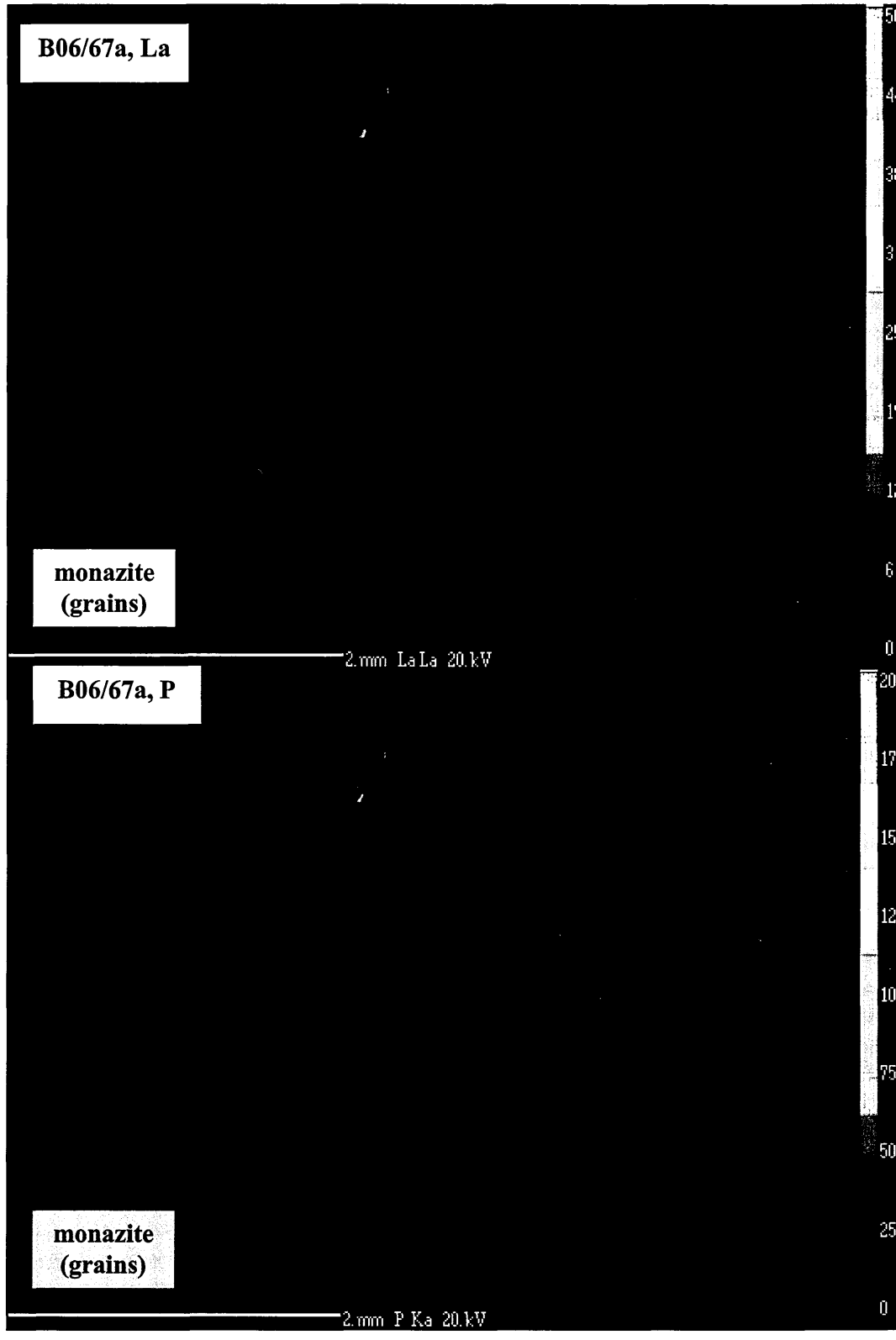

Fig. 6.7 Element maps (Fe, Ca, La and P) of two areas in the GHS sample, B06/67 (one in each of two sections cut). Page 2 of 4.

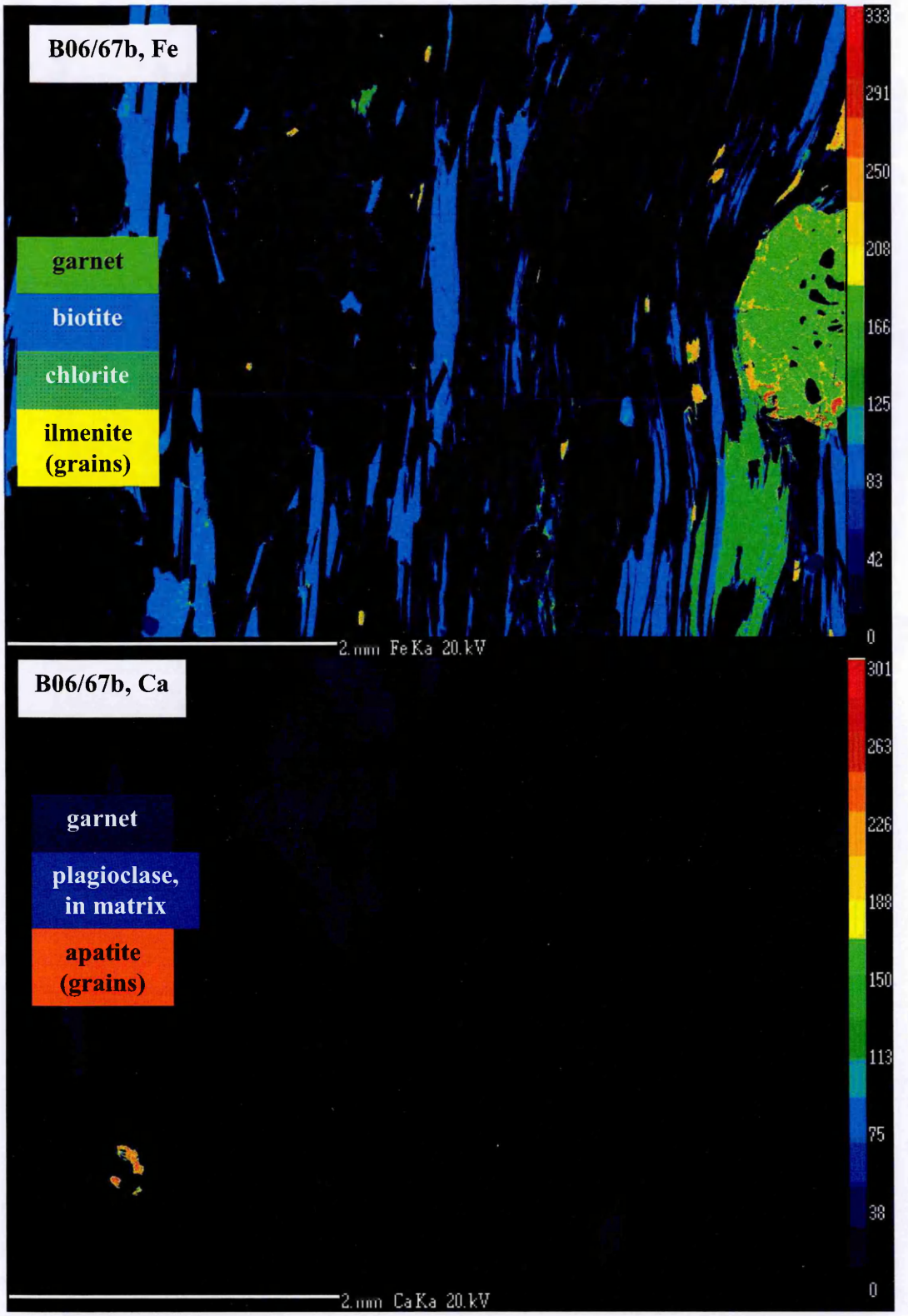

Fig. 6.7 Element maps (Fe, Ca, La and P) of two areas in the GHS sample, B06/67 (one in each of two sections cut). Page 3 of 4.

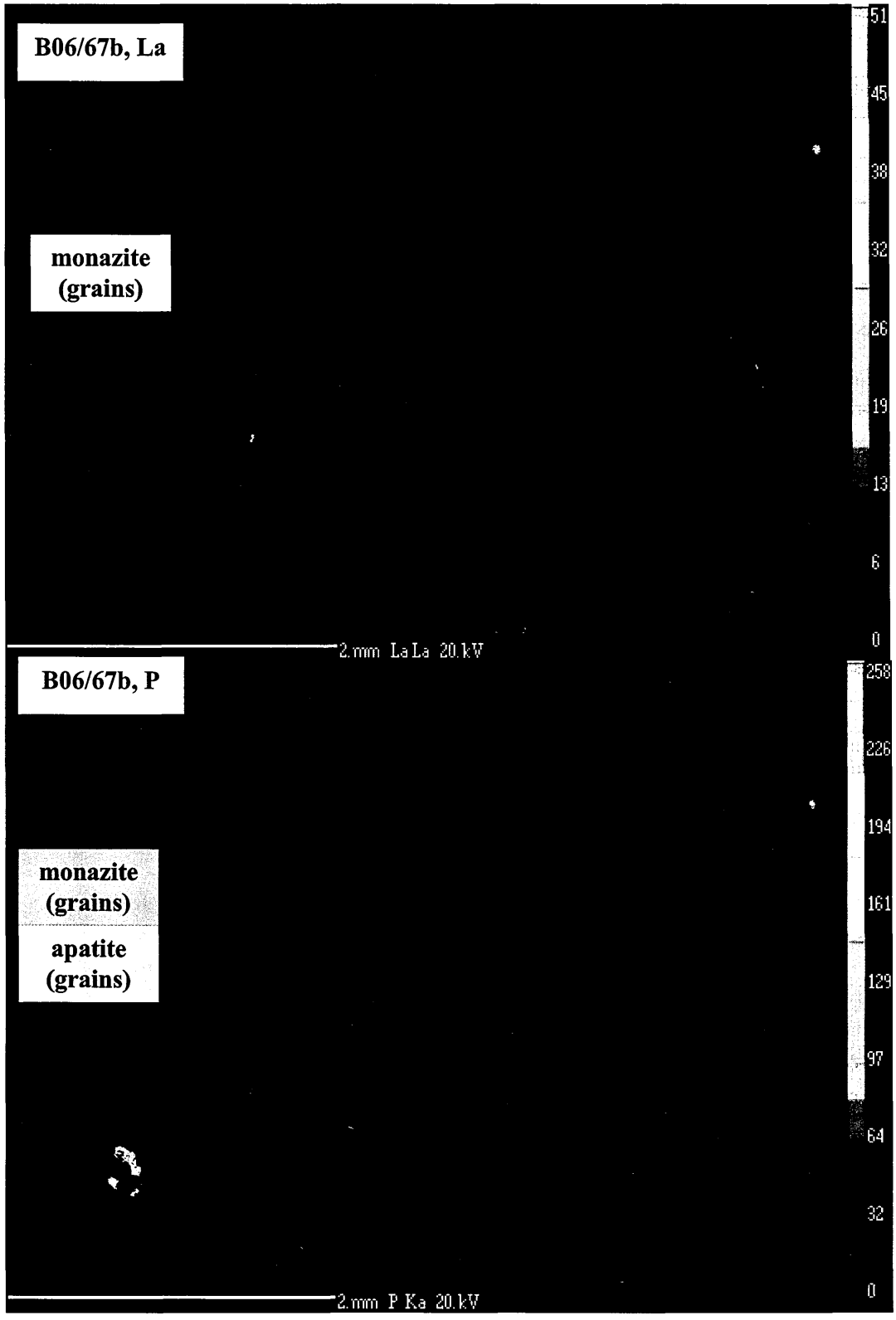

Fig. 6.7 Element maps (Fe, Ca, La and P) of two areas in the GHS sample, B06/67 (one in each of two sections cut). Page 4 of 4.

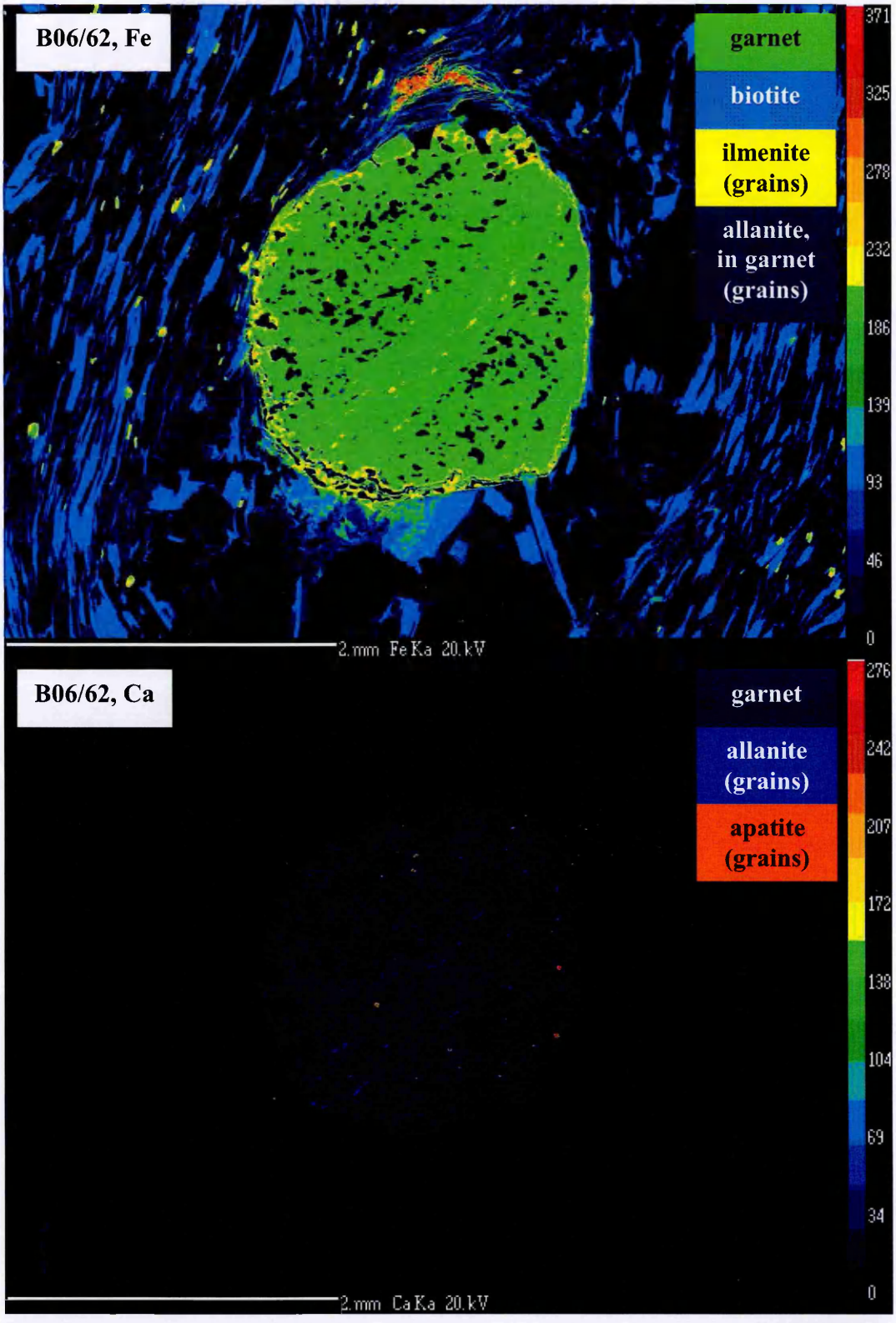

Fig. 6.8 Element maps (Fe, Ca, La and P) of three areas from both Chekha Formation samples, B06/62 and B06/64 (one from sample B06/62, the other two from two sections cut from B06/64). Page 1 of 6.

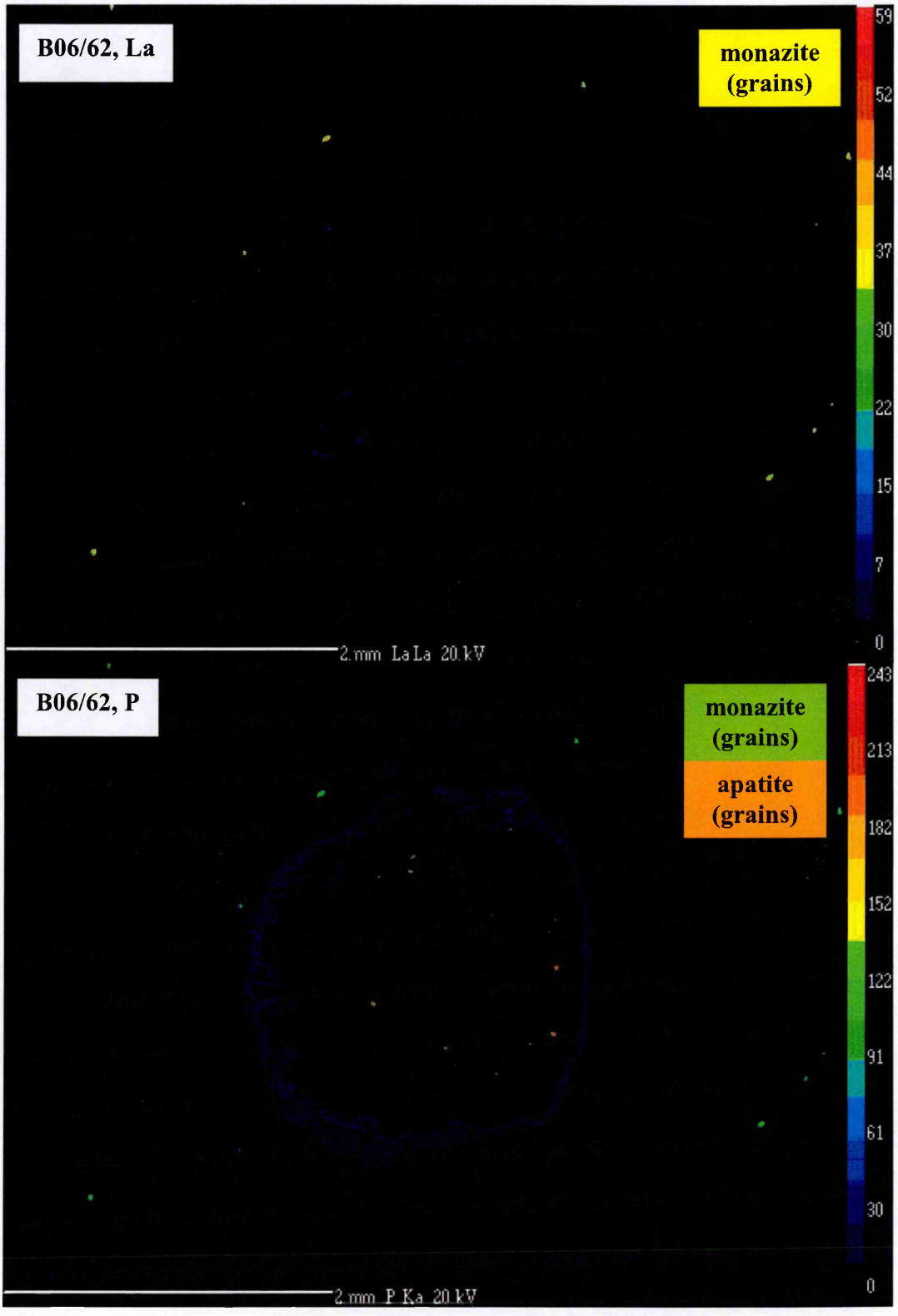

Fig. 6.8 Element maps (Fe, Ca, La and P) of three areas from both Chekha Formation samples, B06/62 and B06/64 (one from sample B06/62, the other two from two sections cut from B06/64). Page 2 of 6.

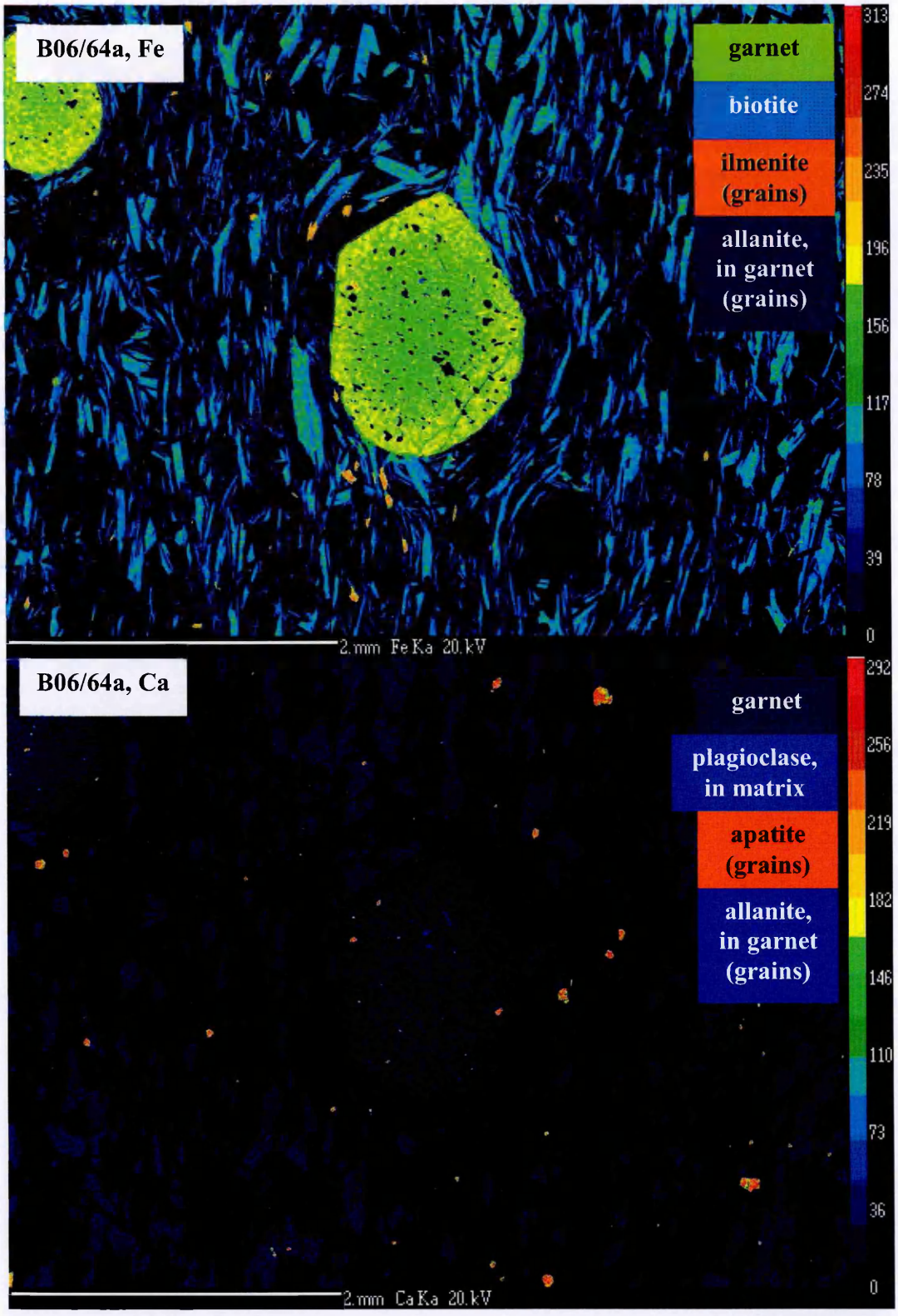

Fig. 6.8 Element maps (Fe, Ca, La and P) of three areas from both Chekha Formation samples, B06/62 and B06/64 (one from sample B06/62, the other two from two sections cut from B06/64). Page 3 of 6.

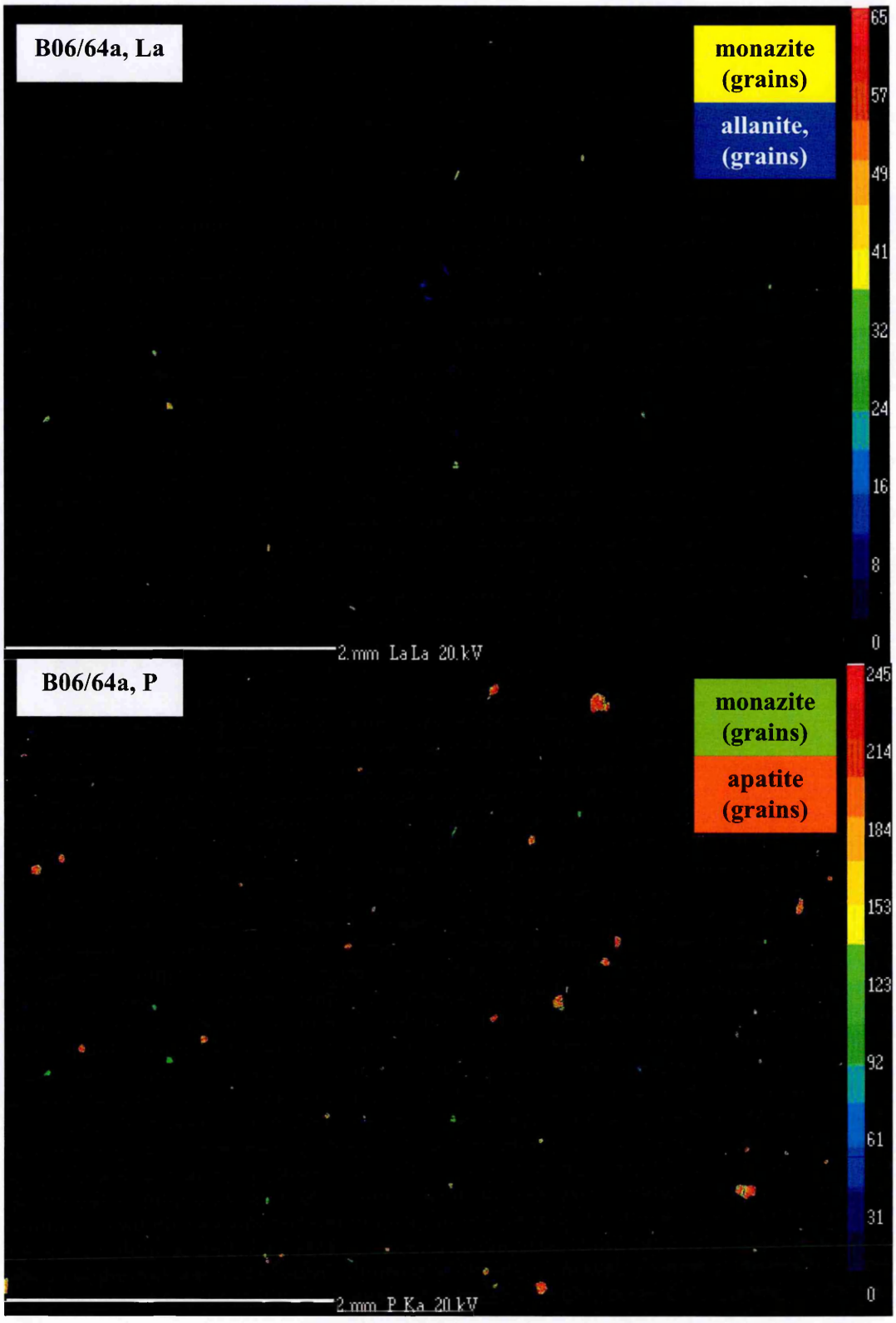

Fig. 6.8 Element maps (Fe, Ca, La and P) of three areas from both Chekha Formation samples, B06/62 and B06/64 (one from sample B06/62, the other two from two sections cut from B06/64). Page 4 of 6.

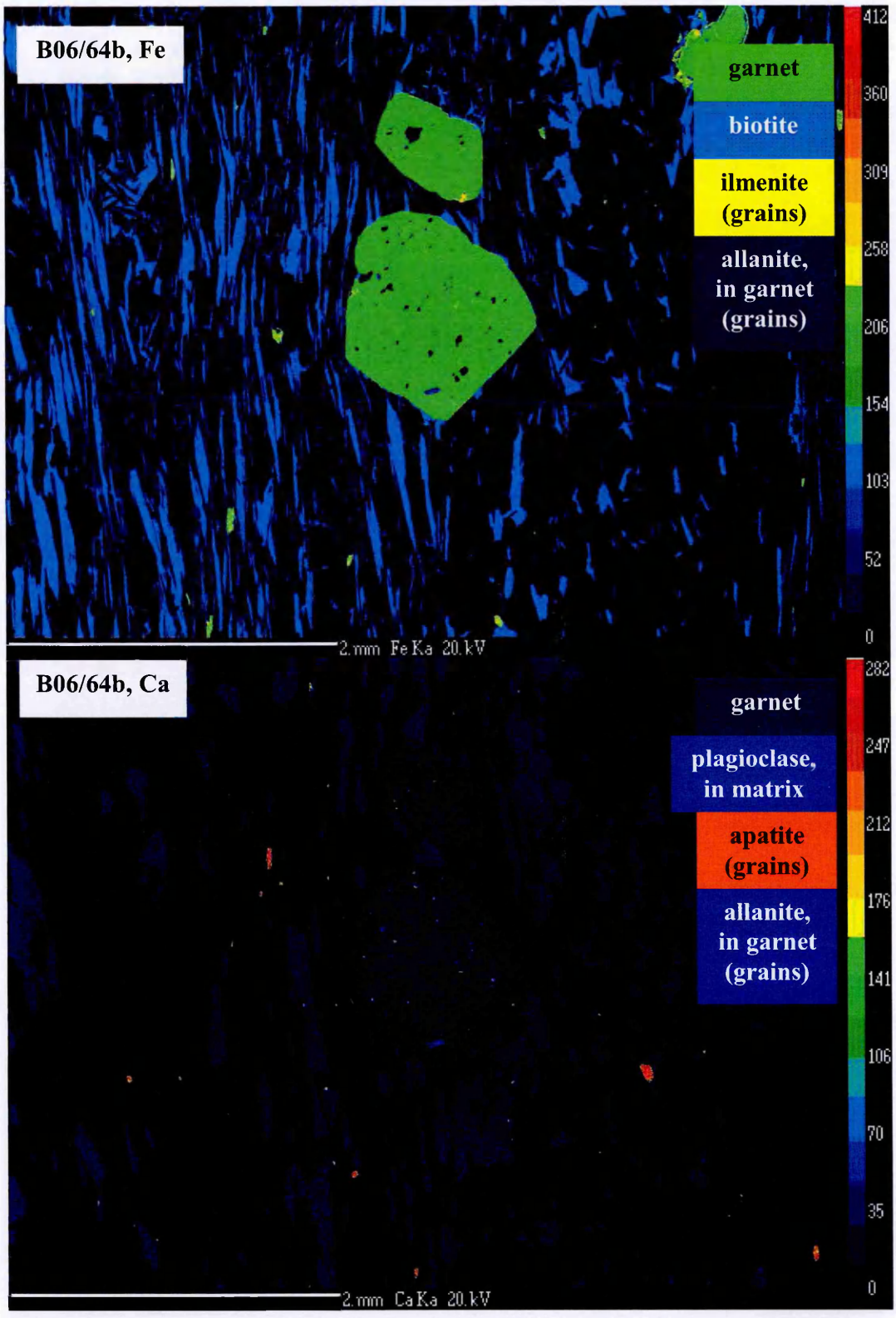

Fig. 6.8 Element maps (Fe, Ca, La and P) of three areas from both Chekha Formation samples, B06/62 and B06/64 (one from sample B06/62, the other two from two sections cut from B06/64). Page 5 of 6.

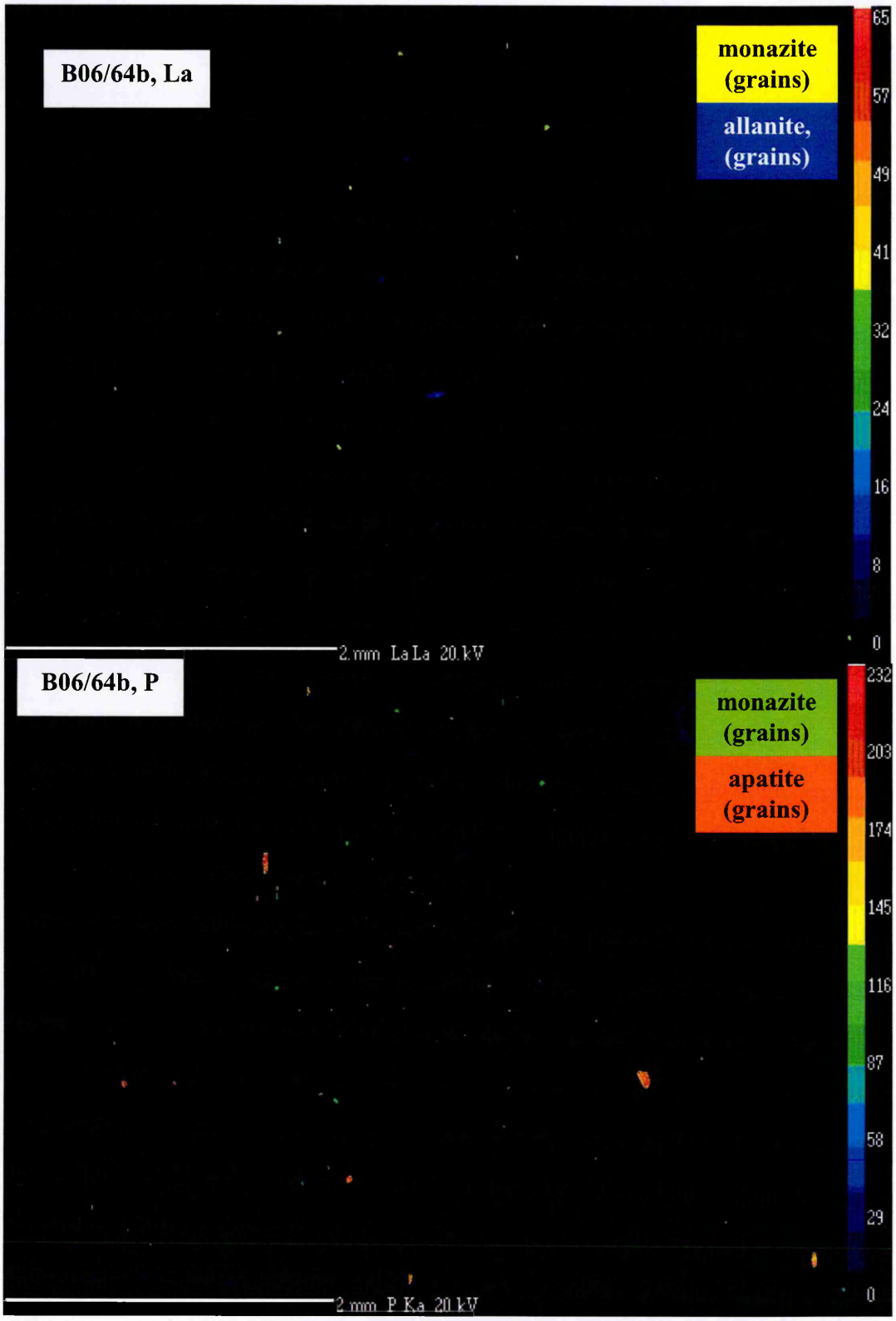

Fig. 6.8 Element maps (Fe, Ca, La and P) of three areas from both Chekha Formation samples, B06/62 and B06/64 (one from sample B06/62, the other two from two sections cut from B06/64). Page 6 of 6.

with respect to the growth of other mineral phases (Kohn et al., 2005 and references therein). Details regarding the accessory phases found in the selected samples from the Chekha Formation and GHS are presented separately below. Note that where chemical zonation is described, Ce consistently reflected the opposite pattern to Th, whereas in La and Y the pattern was less pronounced and often homogenous across the grain.

GHS (B06/67)

In general, REE-enriched accessory phases in this sample are relatively rare, with monazite and apatite in the matrix (Fig. 6.7). Monazite grains are commonly elongate (~50 x 100 μm) and subhedral (Figs. 6.9 and 6.10). The grains are rarely occluded by a single phase and typically lie adjacent to or within (and aligned with) laths of mica (biotite and muscovite). Less often, monazite is found adjacent to plagioclase, or near or even intergrown with ilmenite (monazites 5 and 7, Fig. 6.9; monazites 2 and 4, Fig. 6.10). Apatite is larger than monazite and anhedral (Fig. 6.7).

With respect to inclusions in garnet, only one monazite and one allanite were found in over 20 garnet porphyroblasts (two thin sections). These grains may not be truly occluded as the host garnet is heavily fractured (monazite 1 and allanite, Fig. 6.10). In contrast to monazite grains in the matrix, the 'occluded' monazite is euhedral and smaller (25 x 15 μm), and exhibits more regular Th and Y zonation, with relatively high concentrations of both these elements in the core of the grain with respect to its rim (B06/67 monazite 1 in Figs. 6.10 and 6.13). The allanite grain is also small (20 x 20 μm) but anhedral. Unfortunately due to time constraints these two 'inclusions' were not analysed for their U–Th–Pb ages.

Chemical zonation in all the monazite grains is variable. However, some grains reveal a relatively high-Th patchy 'core' surrounded by a low-Th outer zone (e.g. monazites 2 and 5, Fig. 6.10). This zonation is far from regular, and other monazite grains mapped in this sample exhibit more irregular patterns. Similar zonation for monazite grains in other (non-Himalayan) sillimanite-grade rocks has been recorded (Tomkins and Pattison, 2007).

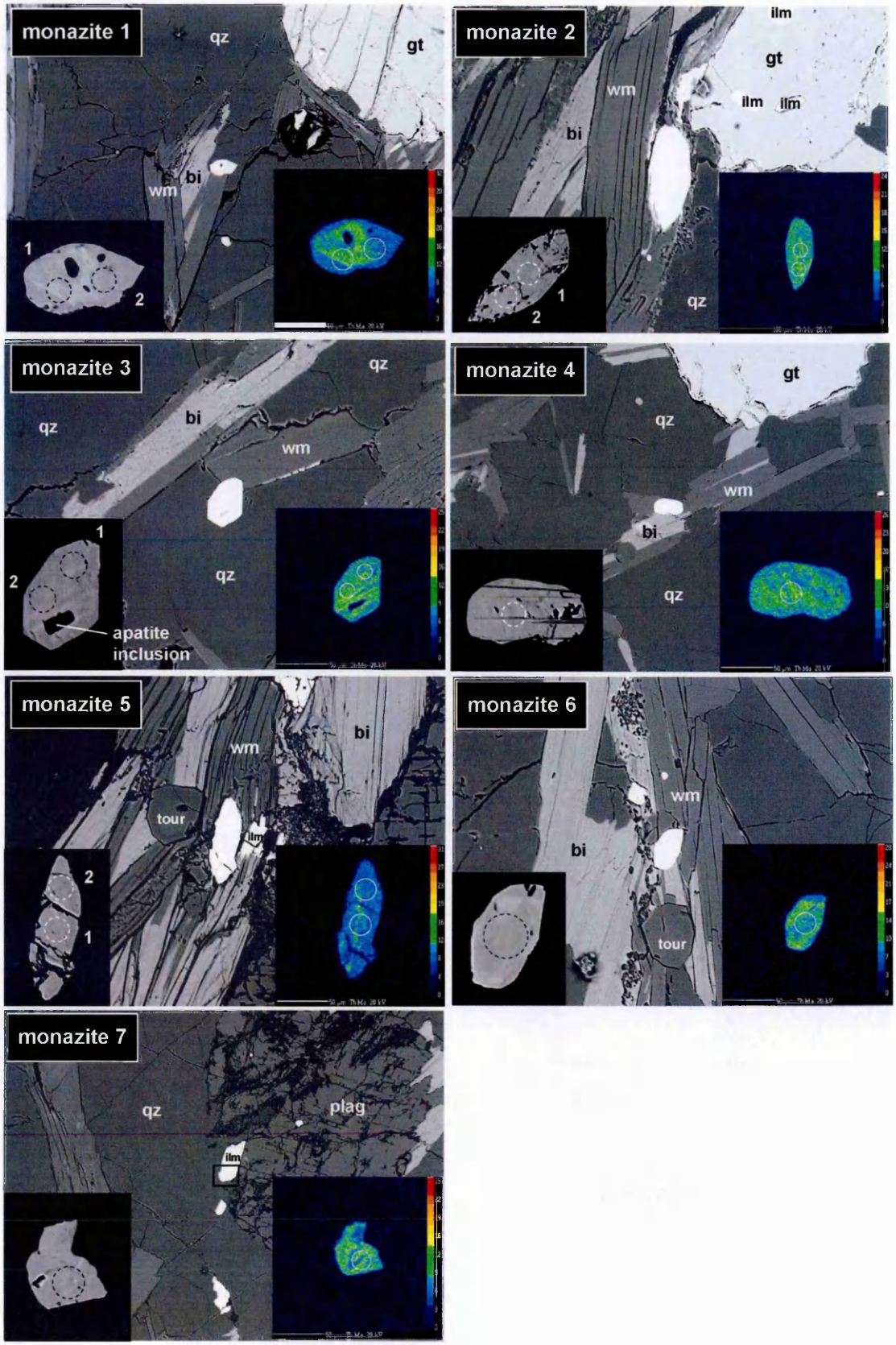

Fig. 6.9 Back scatter electron (BSE) images of monazite (centre of image), sample B06/67a. Insets are: enlarged high-contrast BSE image (bottom left); Th map (bottom right), including scale bar. Areas analysed outlined by circles (spot size 15 μm). Mineral abbreviations are bi, biotite; wm, white mica; gt, garnet; qz, quartz; plag, plagioclase; ilm, ilmenite; tour, tourmaline.

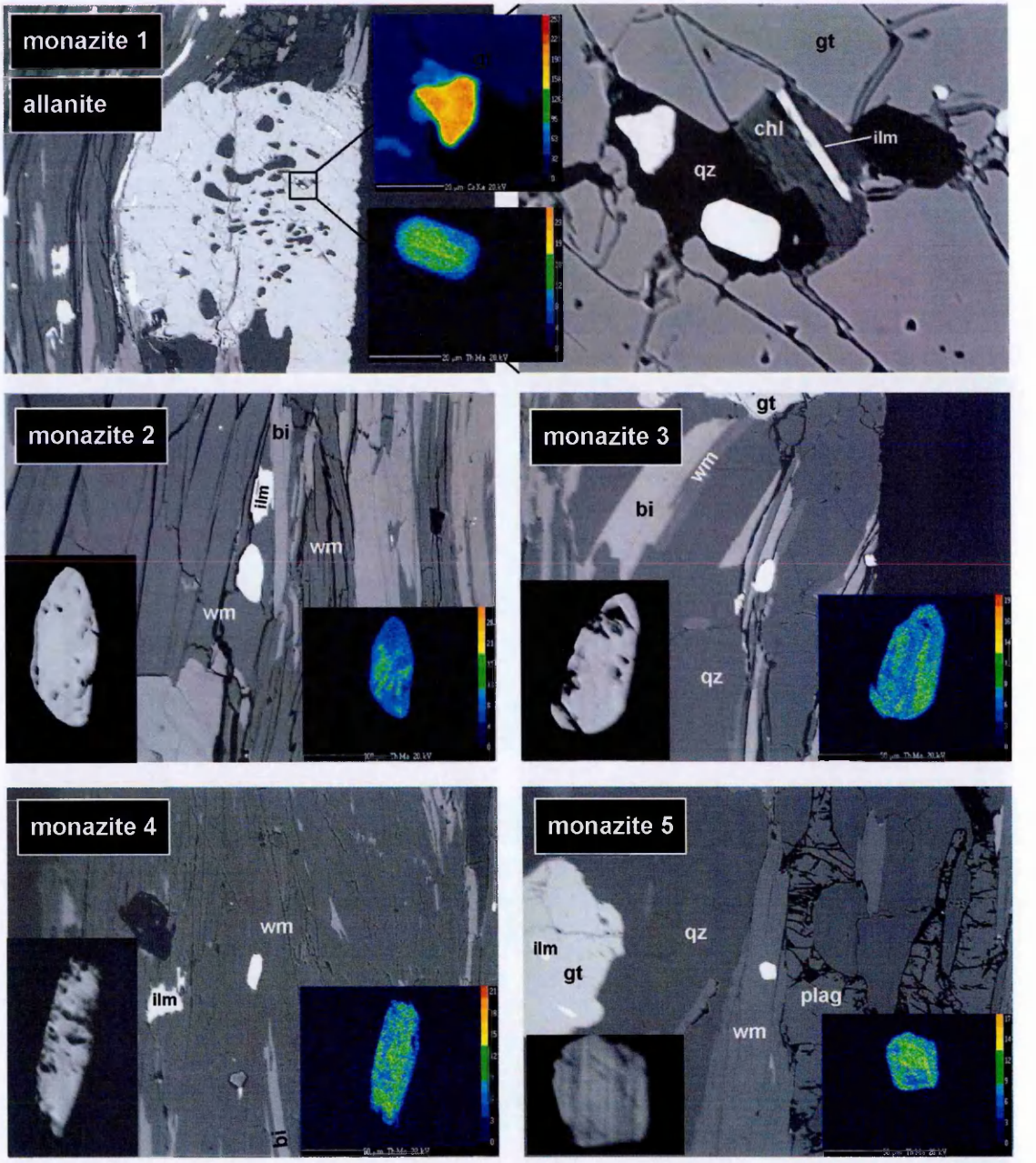

Fig. 6.10 Back scatter electron (BSE) images of monazite and one allanite (centre of image), sample B06/67b. Insets and mineral abbreviations are as in Figure 6.9, apart from element map for allanite is Ca (not Th), and chl, chlorite.

Chekha Formation (B06/62 and B06/64)

These samples also feature monazite, and again, this phase is exclusive to the matrix (Fig. 6.8). In general the monazite grains are similar to those in the GHS sample described above, that is rarely occluded by a matrix phase and closely associated with white mica, plagioclase or ilmenite (Fig. 6.11). In detail the grains appear slightly smaller, more euhedral, and feature fewer (often no) inclusions or alteration. Some grains are clearly associated with cracks, along which monazite (or

some other REE-enriched phase, bright in the back scatter electron image) has crystallised (monazites 3 and 4, Fig. 6.11). All the monazite grains show three distinct Th-zones: 1) a high-Th 'core' (not always central to the grain); 2) a relatively lower-Th 'mid-zone'; and 3) a high-Th rim, relative to the 'mid-zone', but always lower in Th than the 'core' (Fig. 6.11). The zones are rarely concentric or of even width. A few of the monazite grains exhibit subtle Y zonation, from Y-poor cores to relatively Y-rich rims (or 'overgrowths') (Fig. 6.13). These high-Y overgrowths correspond to zone 3 in Th zonation.

Also present in these samples is allanite. It is absent from the matrix and occurs *only* in garnet as an inclusion (Fig. 6.8). The average grain size is 30 x 20 μm, and euhedral to subhedral. Some allanite grains are larger (50 x 100 μm) and more anhedral, one example of which is located at the end of a fracture in its host garnet (allanite 3, Fig. 6.12). All allanite grains have inclusions. Chemical zonation in allanite is either patchy and diffuse (in part a reflection of the inclusions, e.g. allanite 3, Fig. 6.12), or reveals a relatively low-Th 'core' with a relatively high-Th 'rim'. As in the monazite grains, the zonation is not concentric. The 'rim' in allanite grains is often asymmetric (e.g. allanites 2, 5 and 6, Fig. 6.12).

In sample B06/62 apatite is only present as inclusions in garnet, whereas in sample B06/64 apatite is ubiquitous throughout the sections cut (i.e. present in both the matrix and in garnet) with significantly larger matrix apatite than apatite inclusions in garnet (Fig. 6.8). Where there is no apatite in the matrix (sample B06/62), there is a conspicuous phosphorus-rich rim to garnet porphyroblasts. The GHS sample (B06/67) also exhibits this phosphorus garnet 'rimming' (apatite is present in the matrix, but only in small abundance), and not only *around* the garnet porphyroblasts but also along garnet fractures (at the bisection of which there are P 'hotspots') (Fig. 6.7). The texture (i.e. interstitial) and chemistry (Fe-rich, amongst Al and Si) suggests that this is a late-stage alteration product.

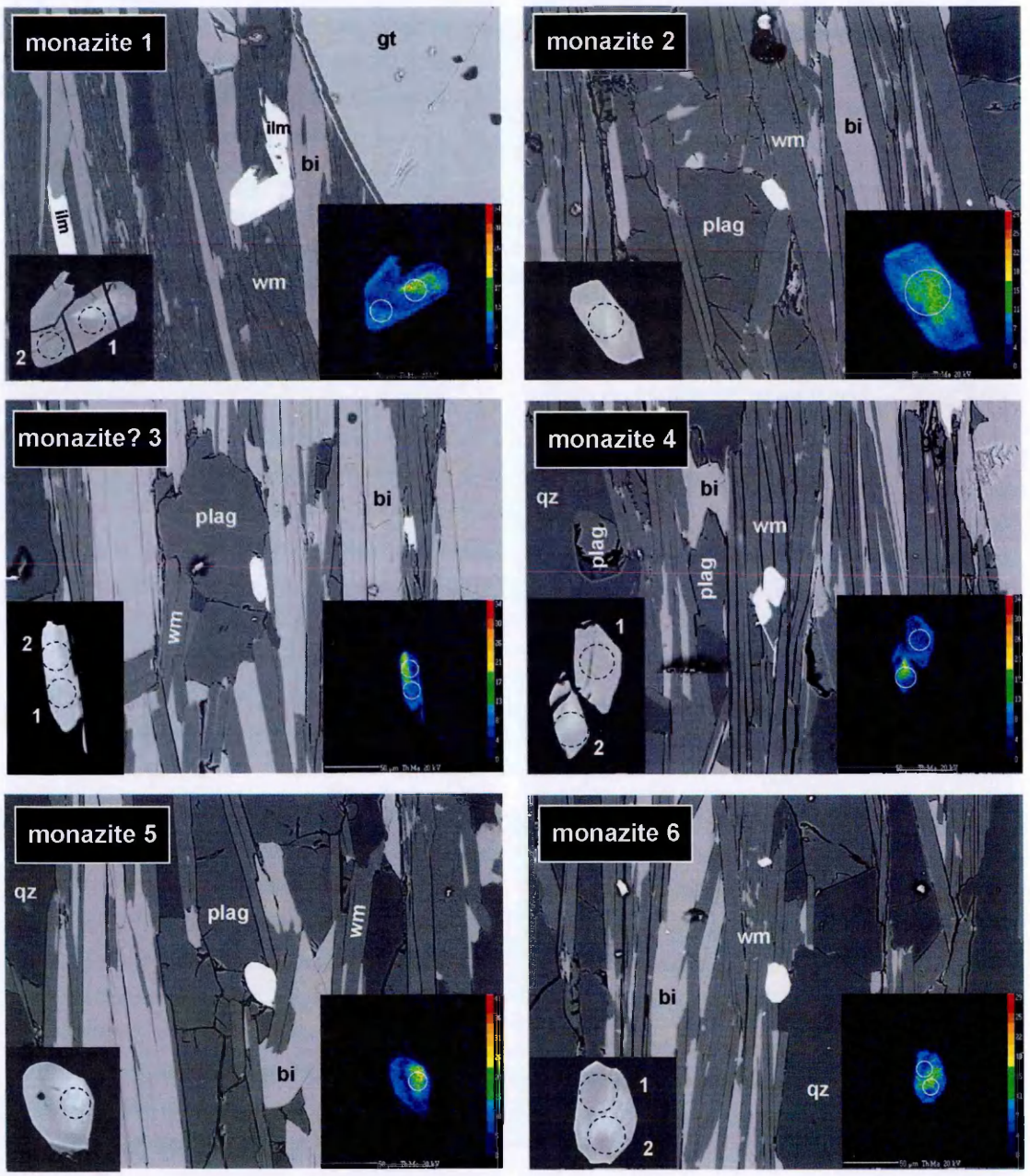

Fig. 6.11 Back scatter electron (BSE) images of monazite (centre of image), sample B06/64ii (b). Insets and mineral abbreviations are as in Figure 6.9.

6.2.3 Methods

i) *P–T* analysis

Analysis of major minerals from samples B06/62 (Chekha formation) and B06/67 (GHS) were made using a Cameca SX100 electron microprobe, with an accelerating potential of 20 kV, a 20 nA current, and beam sizes of 10 μm for micas and plagioclase and 5 μm for garnet and staurolite. Profiles through garnet porphyroblasts were analysed (taken parallel and perpendicular

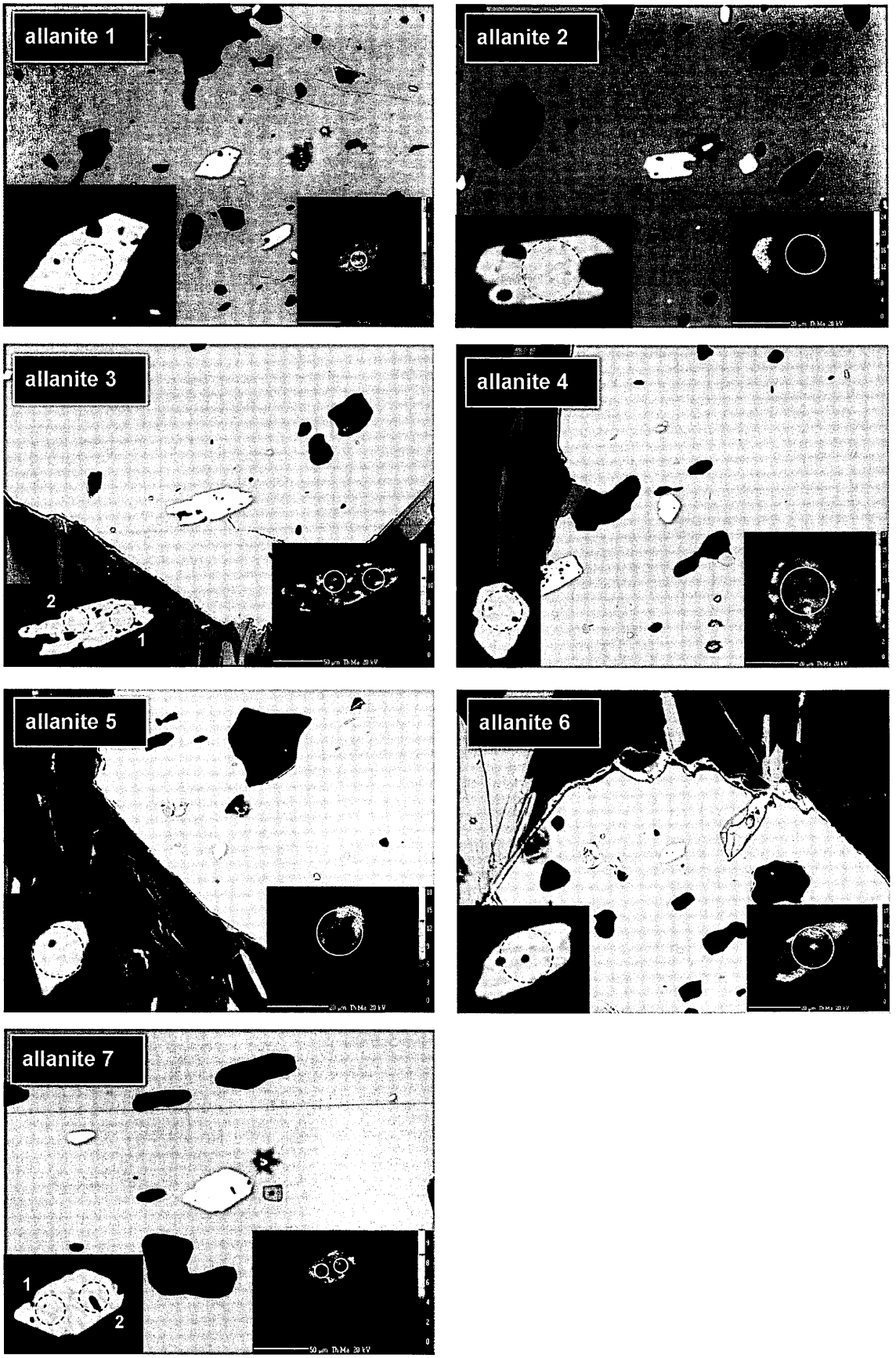

Fig. 6.12 Back scatter electron (BSE) images of allanite (inclusions in garnet, centre of image), sample B06/64ii (b). Insets and mineral abbreviations are as in Figure 6.9.

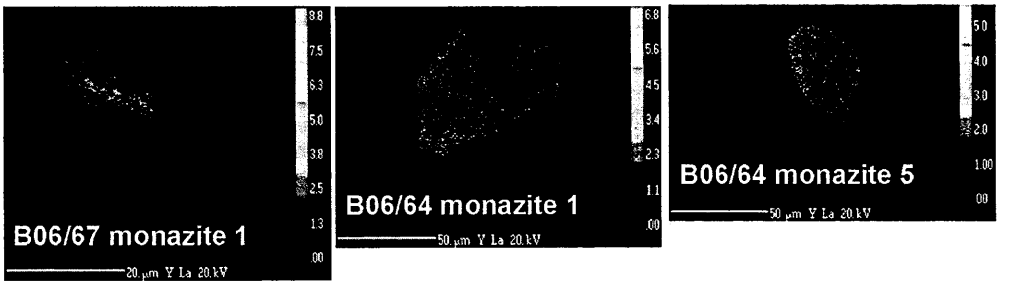

Fig. 6.13 Subtle but distinct Y zonation in monazites. Monazites in the GHS sample (B06/67) show no zonation apart from the 'included' monazite (shown here, see text) which has a high-Y core, and decreases towards the rim. Y zonation in the Chekha sample (B06/64) monazites is either homogeneous or hints at relatively high-Y rims. Shape and size of zones match those reflected in Th (Figs. 6.9–6.11).

to the matrix foliation), whereas the other phases analysed were generally too small to obtain profile or rim and core analyses and thus a mean (core) analysis was taken (Appendix C2.3).

Using the 'average *P–T* mode' in the THERMOCALC program (v. 3.26, 2007) (Powell and Holland, 2001), estimates of the average *P–T* conditions, as defined by a set of independent reactions among end-members of each sample's mineral assemblage, were obtained (with the internally consistent thermodynamic dataset of Holland and Powell, 1998). Initially, raw microprobe data (weight % oxides) were input to the AX program (Holland, 2007) which calculates activities for end-members of minerals for a specified temperature and pressure. Values for typical peak upper-amphibolite metamorphism were initially chosen (600 °C, 7.0 kbars). An iterative process was developed depending on the THERMOCALC result, in which additional AX calculations were made using the approximate THERMOCALC temperature and pressure output values, forming the basis for another set of THERMOCALC calculations. 'Core' and 'rim' mineral assemblages were calculated for, substituting for either the core or rim (or inner rim where re-equilibration with the matrix was evident) garnet analyses respectively. Although the core of garnet is less likely than its rim to have equilibrated with the matrix phases now observed, it is possible, that having analysed the centre of the matrix phases and given sluggish diffusion (more likely in plagioclase than in biotite), that they do represent an equilibrium assemblage.

As the results from THERMOCALC were somewhat unsatisfactory (see results in Section 6.2.3), the following calibrations were also applied (having been recast using the Holland and

Powell (1998) thermodynamic dataset for consistency with THERMOCALC estimates): (Fe–Mg) garnet–biotite (GB) (Bhattacharya et al., 1992; Thompson, 1976) and garnet–staurolite (GS) thermometers (Koch-Müller, 1997); Fe and Mg garnet–plagioclase–muscovite–biotite (GPMB) barometers (Hoisch, 1990). Only 'rim' assemblage analyses were used in these calculations.

ii) Geochronology

Dating garnet directly would be the most rigorous test of when the Chekha Formation (Radi klippe) and underlying GHS underwent prograde metamorphism, and if this was synchronous or diachronous (essential data in the elucidation of the thermal evolution of the mid-crust during orogenesis). However, the isotopic method of dating garnet has problems inherent with the analysis of inclusion-rich garnets (see Chapter 4). So, allanite and monazite grains (characterised above) were analysed using laser ablation multi-collector inductively coupled plasma mass spectrometry (LA–MC–ICP–MS) *in-situ* (in thin section). This provided the necessary textural control for this type of study, where it is important for example to identify i) whether the analysis may have incorporated any of its host phase (and which mineral this was), ii) whether the grain was associated with any cracks or alteration products, and iii) which part of the grain was sampled (e.g. Th-rich core).

As allanite is clearly an early phase in the Chekha Formation (forming inclusions in garnet), and monazite a later phase (restricted to the matrix), age data from these accessory phases would bracket the age of garnet growth. Furthermore, considering that monazite may form as a result of allanite breakdown during prograde metamorphism (Janots et al., 2008 and references therein), it is likely that both allanite and monazite crystallised during the same metamorphic event, and would therefore tightly constrain the age of prograde metamorphism in the Chekha Formation. This information is currently sorely lacking and limits tectonic modelling of Bhutan. Although no allanite was present (in garnet or otherwise) in the GHS sample (bar the one aforementioned, and not analysed), the age(s) of matrix monazite would be interesting to compare with the age(s) of matrix monazite in the Chekha Formation sample.

A UP193SS New Wave Research LA system was used in conjunction with a Nu MC–ICP–MS instrument to ablate single spots (15 μm diameter) in monazite and allanite grains using laser

fluences of 2–3 J cm^{-2} (i.e. 50 % power, 5 Hz). Also see Appendix B2.2 for a guide to locating small grains for LA–ICPMS analysis. Analysis of monazite followed methods similar to those described in Cottle et al. (2007a) using the instrumental set-up modified from Simonetti et al. (2005). The 554 Ma Manangotry monazite standard and a 54.5 Ma monazite standard, FC–1 were used for Pb/U and Pb/Th normalization respectively, coupled with a static ablation pattern. The FC–1 standard cannot be directly used for U–Pb calibration as it contains variable excess ^{206}Pb. Continual aspiration with a Tl, U-bearing acid throughout the analysis period acts as a constant internal standard, allowing an initial mass bias correction to be made, monitoring of inter-element behaviour and of the plasma, and a source to which the instrument can be tuned. However, background counts of Pb isotopes were unusually high, indicating a possible problem with the acid aspiration (e.g. plasma too damp). Given that the sample sizes being analysed were so small (the success of which depends on minimal background Pb isotope counts), we chose to aspirate with air. This method was applied to both samples and standards. The overall reproducibility of both standards during the course of these analyses was 2 to 8 % (2σ), which has been propagated into the uncertainties for each spot analysis.

Dating of young metamorphic allanite is technically challenging given that i) it may contain 20–90 % common-Pb, ii) the common-Pb correction is crucial, iii) U is often no higher than 200 ppm meaning that there might only be 1 ppm radiogenic ^{206}Pb or less, iv) there is the problem of excess ^{206}Pb from ^{230}Th, and v) there are no widely available standards (Gregory et al., 2007). Single-spot analysis is more appropriate than raster analysis given the chemical and textural complexity of allanite (Gregory et al., 2007). Analyses of an allanite 'standard' (LU–1, courtesy of R. Parrish) bracketed allanite sample analyses. This 'standard' remains uncharacterized to date (including no TIMS-derived age) and so the analyses of the Manangotry and FC–1 standards, which also bracket the allanite sample analyses, were relied upon to normalise the data. The analysis of syn-genetic plagioclase would have been appropriate for a common-Pb correction; however, no plagioclase inclusions in garnet were found, and given that allanite (in garnet) and plagioclase (in the matrix) may have crystallised at different times, this correction was not applied.

Instrumental protocols meant that U–Pb and Th–Pb could not be measured simultaneously and were therefore measured sequentially, returning to the exact location to run the remaining analysis sequence. In an attempt to try and detect any age difference in zoning (where preserved), multiple spot analyses were made for a given grain. However, only one to two analyses per grain were possible to ensure sputter cross-contamination was avoided (Figs. 6.9, 6.11 and 6.12). Despite the fact that the size of laser beam required to ablate an adequate amount of sample for analysis disallowed isolating chemically-distinct zones in monazite, and as a result most analyses were 'mixed', i.e. analyses of different zones, the analyses are still considered to cover the range of zones identified. Of course, this is only the zonation as seen in two-dimensions, and the zonation at depth (also analysed) was unknown.

The analysis of allanite grains occluded by garnet was not affected by garnet ablation as garnet has a negligible contribution to U, Th and Pb. However, analysis of monazite in the matrix may sample the surrounding phase (perhaps at depth); in the case of the samples here, this includes biotite, muscovite, plagioclase, or ilmenite, of which the U and ^{206}Pb concentrations could affect the data.

6.2.4 Results

i) Garnet morphology and chemistry

Garnets in sample B06/67 (GHS) are subhedral and fractured, and wrapped by the matrix. The largest garnets in the sample have inclusion-rich cores. The inclusion trails in some garnet cores are sinusoidal, and therefore suggest early garnet growth was syn-tectonic or overprinted a micro-folded fabric (top left image in Fig. 6.10). Garnet morphology in the Chekha Formation samples is more variable. Some porphyroblasts are perfectly euhedral (Fig. 6.14a) which can sometimes be indicative of post-tectonic formation. However, although foliation warping is not pronounced round the garnet (in support of post-tectonic formation), there is some wrapping. As these euhedral garnets also have no discernible oriented inclusions and therefore don't appear to have overprinted the fabric, it is inferred that these garnets are early grown phases (with respect to the main foliation forming event), despite the temptingly post-tectonic crystal shape. Also, some weakly wrapped garnets have evidently just grown in crenulation arcs (quartz-rich zones). The

characteristics of other garnets in the Chekha Formation are consistent with this theory, with inclusion trails representing a pre-existing fabric (Figs. 6.14b and c). As in the GHS sample, this included fabric appears crenulated, and occasionally hints at an s–c fabric (Fig. 6.14c). One inclusion pattern in garnet is more curious (Fig. 6.14b), from which it is inferred that this garnet overgrew a crenulation which is now ~45° to the external matrix fabric, but the origin of the ilmenite-rich garnet band down the middle is obscure (see below).

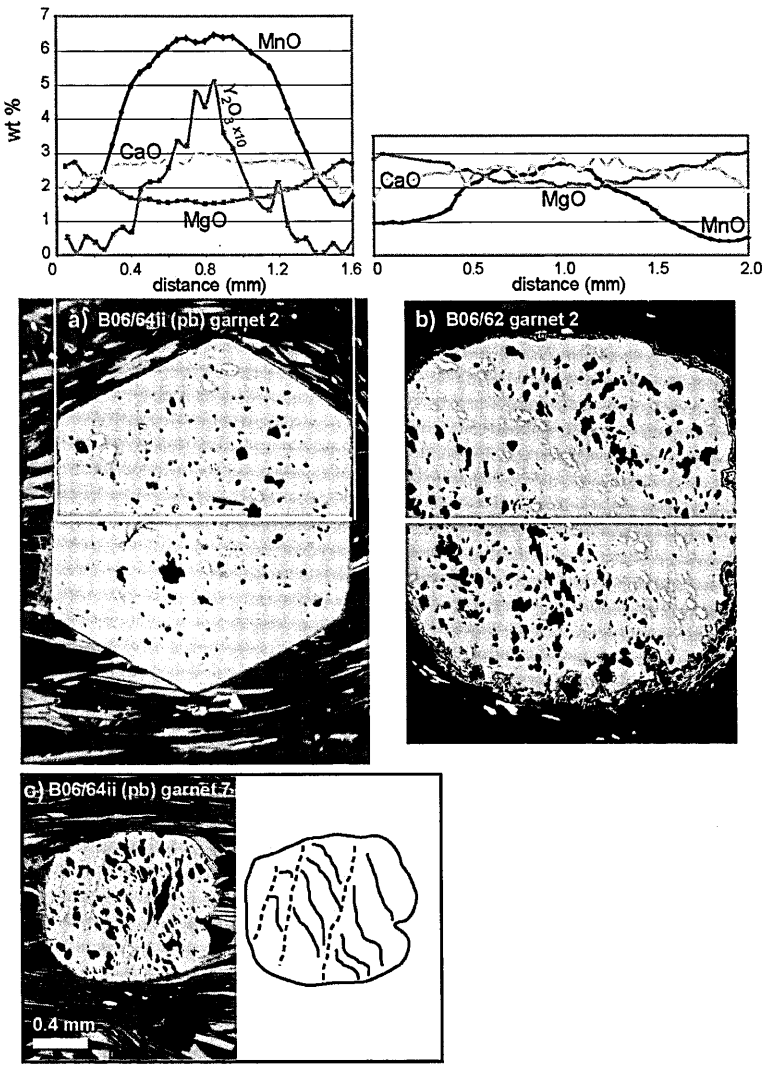

Fig. 6.14 Garnet morphologies (BSE images) and respective major element (oxide) profiles (electron microprobe data, Appendix C2.3) for samples from the Chekha Formation a) euhedral garnet, b) and c) subhedral garnets with crenulated inclusion trails. Garnet in b) same as in Fig. 6.8 (B06/62).

The largest garnet porphyroblasts in sample B06/67 (GHS) preserve bell-shaped major element (e.g. Mn) zonation (e.g. Fig. 6.15) (and as this corresponds to prograde growth, one of these garnets was selected for *P–T* analysis). Other (smaller) garnets in this sample are more homogenous with respect to the distribution of major elements. These observations suggest that the GHS underlying the Radi klippe reached high enough temperatures for sufficiently long enough to

allow partial to complete major element homogenisation in garnet (depending on its size). All garnet porphyroblasts analysed from the Chekha Formation (samples B06/62 and B06/64) consistently reveal well-developed bell-shaped major element zonation (Figs. 6.14 and 6.15), with no discernible difference between morphologically-different garnets (such as euhedral with no alignment of inclusions, and subhedral with inclusions preserving a crenulated fabric Fig. 6.14). The bell-shaped MnO profile (albeit weakly asymmetric) for the garnet porphyroblast with the bizarre inclusion texture (Fig. 6.14b) suggests that garnet grew quickly over a crenulation with a central, linear, ilmenite-rich zone. The alternative, that the garnet crystal had cracked down the middle and then resealed, overgrowing aligned ilmenites, would have shown up as a perturbed zonation profile.

Garnet rims typically show reversed zonation (< 100 μm width) indicative of re-equilibration with the surrounding matrix. This is more marked in garnets from the sampled Chekha Formation than in the largest garnets analysed in the underlying GHS (Figs. 6.14 and 6.15).

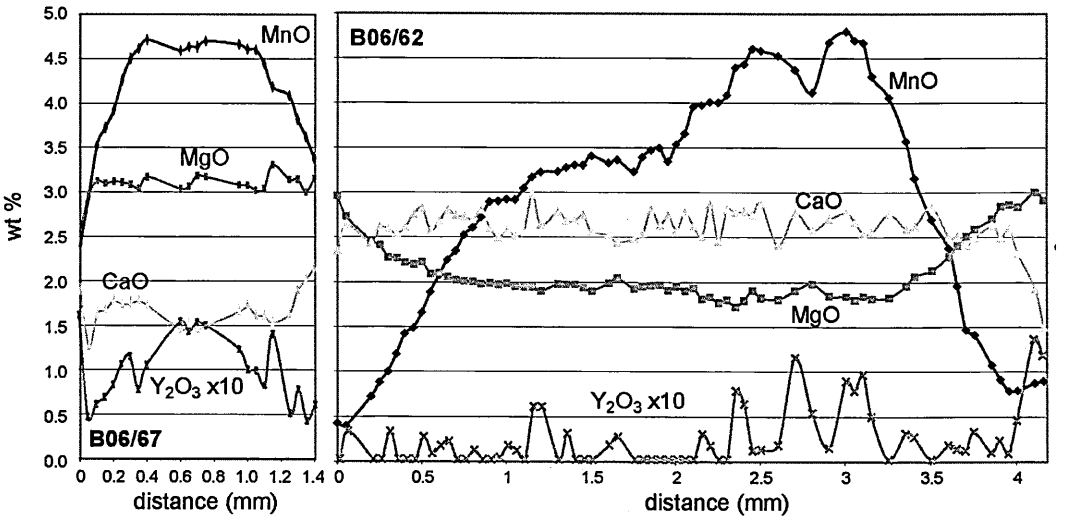

Fig. 6.15 Garnet major element (oxide) profiles (electron microprobe data, Appendix C2.3) for samples from the GHS (B06/67) and Chekha Formation (B06/62) representing the most strongly zoned porphyroblasts analysed. Core and rim (or inner rim in the case of the GHS sample) analyses used in pressure–temperature calculations.

ii) *P–T* analysis

All 'assemblages' modelled in THERMOCALC (bar the 'core' assemblage of B06/67) relied upon the exclusion of the pyrope end-member (in addition to those phases THERMOCALC

automatically excludes) to yield a statistically acceptable fit (σfit, equivalent to the √MSWD) based on six or seven independent reactions (Table 6.1), owing to the consistently large errors associated with this end-member. Better fits to the data were achieved for models with a H_2O activity of less than one (i.e. CO_2 is present in the fluid phase).

Table 6.1 THERMOCALC results

Sample	input to AX		free	XH_2O	XCO_2	phases excluded (by	output					
	T (°C)	P (kb)	fluid?			THERMOCALC)	No. independent rxns	T (°C)	±	P (kb)	±	fit (significant fit)
Chekha Fm.												
B06/62 core	600	7.0	yes	0.77	0.23	py (spess, ilm, CO_2)	7	706	24	9.4	0.9	1.35 (1.49)
B06/62 inner rim	600	7.0	yes	0.98	0.02	py (ilm, CO_2)	7	733	19	9.8	0.7	0.80 (1.49)
"	"	"	"	1	0	gr, mst (ilm, CO_2)	6	655	29	6.3	1.4	1.35 (1.54)
GHS												
B06/67core	650	7.0	yes	1	0	(spess, ilm, CO_2)	7	704	21	6.9	0.8	1.09 (1.49)
"	"	"	"	0.5	0.5	(spess, ilm, CO_2)	7	654	18	6.6	0.7	0.86 (1.49)
"	600	6.5	no	0.8	0.2	(spess, ilm, CO_2)	7	666	18	6.7	0.7	0.94 (1.49)
B06/67 rim	650	6.0	yes	0.85	0.15	py (spess, ilm, CO_2)	6	735	22	8.8	0.9	0.31 (1.54)

py (pyrope), spess (spessartine), gr (grossular), ilm (ilmenite), mst (Mg-staurolite)

Both 'rim' and 'core' assemblages in sample B06/62 (Chekha Formation) yielded unexpectedly high *P–T* values (for a garnet–staurolite schist) of 700–750 °C and 9–10 kbars, that is, unless grossular and Mg-staurolite end-members (with minimal activities and "hat", aka relative weight or importance) were excluded from the model, which resulted in more typical values of ~650 °C at ~6.5 kbars (with pyrope included). Although one of the independent reactions is lost and the fit consequently poorer this result is still statistically acceptable (i.e. 95 % confident). The reduction in the calculated pressure of more than 3 kbars (which inevitably controls the decrease in temperature too) suggests that the analyses of end-members involved in the barometric calculations (e.g. anorthite plagioclase and grossular) do not form part of an equilibrated system.

The 'core' assemblage for sample B06/67 (GHS) yielded an acceptable fit without the exclusion of any other phases than those THERMOCALC automatically excludes. A mixed H_2O–CO_2 fluid phase led to even better results, although the smallest fit value was achieved with a rather low H_2O activity (<0.5) for a free fluid phase in a typical pelite (possible, however, in a graphitic or carbonate-rich rock). Modelling with no free fluid phase (plausible given that there may have been an active melt phase in this sample) and a more reasonable H_2O activity of 0.8 yielded equilibrium

conditions of 666 ± 18 °C and 6.9 ± 0.7 kbars. The temperature and pressure calculated for the 'rim' assemblage in B06/67 were higher, at 735 ± 22 °C and 8.8 ± 0.9 kbars, for which pyrope again had to be excluded to allow a statistically significant result.

The requirement to exclude end-members such as pyrope from three out of the four assemblages modelled, and as a consequence variable results with THERMOCALC, are not reassuring, hence the resort to independent geothermobarometric calibrations, the results of which are distinct from those from THERMOCALC modelling (Table 6.2). Most notably, the calculated temperatures from two garnet–biotite thermometers are much lower (550–600 °C, cf. >650 °C in THERMOCALC). The temperature estimated using the garnet–staurolite thermometer (728 °C) is comparable to values calculated by THERMOCALC; however this thermometer is known to overestimate the temperature and is not considered robust by some studies (Koch-Müller, 1998). As the same thermodynamic database was used in both, it is thought that the THERMOCALC *P–T* estimates were elevated by erroneous *P* estimates resulting from an unequilibrated grossular–anorthite system.

Table 6.2 Geothermobarometric results

Sample	T (°C)			mean P[4] (kb)
	Fe-Mg garnet-biotite[1]	Fe-Mg garnet-biotite[2]	Fe-Mg garnet-staurolite[3]	
B06/62 inner rim	581 ± 33	583 ± 33	728 ± 33	7.31 ± 1.4
B06/67 rim	550 ± 33	551 ± 33	-	6.06 ± 1.4

[1]Bhattacharya et al. (1992), [2]Thompson (1976), [3]Koch–Müller (1998), [4]Hoisch (1990). Errors quoted are based on the uncertainty on the calibration of the thermobarometer, the analytical uncertainty on the mineral analyses, and the uncertainty in activity–composition relationships.

Pressures calculated for 'rim' assemblages were ~7.3 kbars for the schistose Chekha Formation (B06/62), and notably lower for the underlying sillimanite-bearing GHS (B06/67), at ~6 kbars. This may indicate retrograde re-equilibration of the assemblage, and/or decompression at relatively high *T*, i.e. the *P* recorded by the mineral phases relates to a *P* at maximum *T*, which occurred at a lower *P* than in the Chekha Formation due to a different shape of *P–T* path at high *T*. The major element variation across the GHS garnet porphyroblast (the data from which was used for *P–T* analysis) does not suggest that re-equilibration strongly affected this crystal (e.g. MnO decreases to the rim, with no inflection, cf. MnO of garnet profiles in the Chekha Formation with a

marked inflection towards the edge of the crystal, Figs. 6.14, 6.15). As such, the theory that the *P* estimate for the GHS sample ('rim' assemblage) reflects *P* at T_{max}, seems realistic. However, *T* estimates for the GHS sample (Table 6.2) are also unexpectedly low for a sillimanite-bearing rock, and this then suggests that at least some analyses used in the *P–T* calculations were of minerals that re-equilibrated post-peak conditions. Having considered garnet's major element zonation, biotite is the likely culprit, exchanging Fe cations more readily than garnet during the retrograde metamorphic path (e.g. Spear, 1991; Fitzsimons and Harley, 1994).

Although a more detailed *P–T* analysis is really required of these samples (e.g. to include electron microprobe analysis of profiles across plagioclase and biotite grains, and/or pseudosection analysis), for the purpose of further discussion, the results from the independent geothermobarometers on the 'rim' assemblages are carried forward for the following reasons: 1) the two garnet–biotite thermometers yield the same temperature (within error); 2) *P–T* estimates for the Chekha Formation (sample B06/62), which are an important contribution to understanding the early thermal evolution of the mid-crust in Bhutan, and currently lacking, are more reasonable than those determined via THERMOCALC.

iii) U–Pb accessory phase data

The allanite data (Appendix C5) are somewhat imprecise, as expected, with large common-Pb contributions (1000–3000 counts per second, ^{204}Pb) and low U contents (<150 ppm). When U–Pb data are plotted on a Tera–Wasserburg plot, projections through a broadly linear array of allanite sample measurements onto the Concordia yield an imprecise age of 47 ± 14 Ma. This age is likely to be inaccurate too, due to the lack of knowledge of the degree to which this Th-rich allanite has excess ^{206}Pb, and that the data lack an appropriately ID–TIMS-dated allanite for a calibration standard. Therefore the age of allanite is not tightly constrained, which thwarts attempts to date prograde metamorphism in the Chekha Formation via dating of accessory phases that bracket garnet growth. However, this preliminary dataset is consistent with an early to mid Tertiary age for allanite growth even though it cannot be more precisely defined.

Inferred ages of monazite growth are based on U–Pb and Th–Pb measurements (Table 6.3). The data from monazite 3 in the Chekha Formation are excluded, as the amounts of Th and U

detected were particularly low compared to the other grains analysed, and it was concluded that this grain was not monazite but another REE accessory phase (other than xenotime, as the Y content was too low for this phase). All remaining analyses (bar the second analysis of monazite 1 in the Chekha sample (B06/64) as it had an obvious common-Pb contribution) were plotted on a (U–Pb) Tera–Wasserburg plot. For each sample, a distinct group of monazite data defines a linear array, apart from two data points from the GHS sample (B06/67) that lie in between the two groups of data (Fig. 6.16). These data points represent analyses of monazite in close proximity to ilmenite (analyses 5.2 and 7, Fig. 6.9) and may therefore be contaminated analyses (with possible Pb loss). They are thus rejected from the age determination.

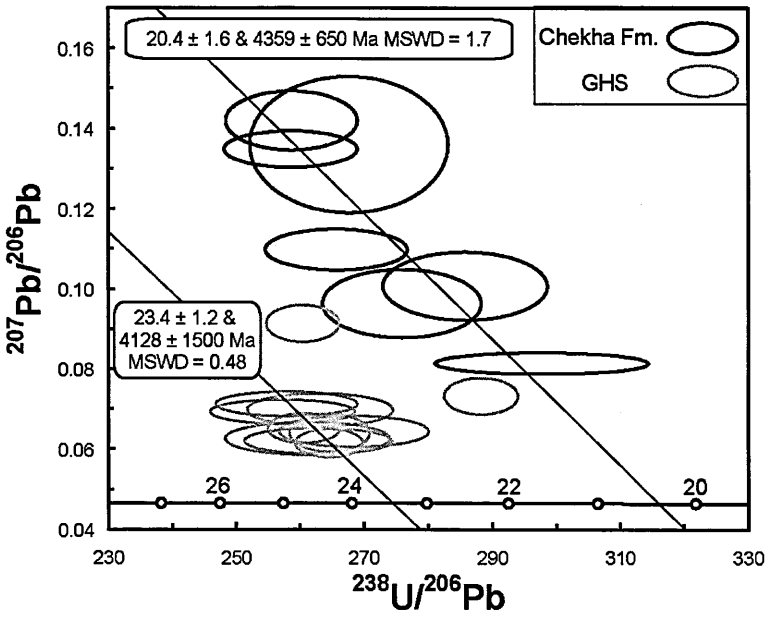

Fig. 6.16 Tera-Wasserburg (U–Pb) plot showing monazite data from the Chekha Formation (B06/64ii) and underlying GHS (B06/67) (Table 6.3). Error ellipses are 2σ.

Each array of data on the Tera–Wasserburg plot arises from analyses with different proportions of radiogenic and common-Pb, and the intercept with Concordia reveals the age. Projections through the two linear arrays of sample data yield monazite ages of 23.4 ± 1.2 (MSWD = 0.48) in the GHS (B06/67) and 20.4 ± 1.6 (MSWD = 1.7) in the Chekha Formation (Radi klippe, B06/64). Well-constrained linear arrays of data for each sample suggest that the complete crystallisation history of the monazite grains analysed occurred over a relatively short period of

time, and there are no discernible patterns between the different monazite zones analysed (e.g. core or rim) and the resultant ages.

Monazite ^{208}Pb–^{232}Th common-Pb corrected ages were also calculated. As ^{204}Pb is hard to measure with the LA–ICP–MC–MS method on such very small amounts of sample, a common-Pb correction for ^{208}Pb was made using the following method: 1) the measured final isotope ratios (which include common-Pb) are used to determine the isotope compositions for each analysis; 2) the amounts of ^{206}Pb and ^{207}Pb common-Pb components are then calculated by assuming that the intercept (for each sample) with Concordia on the Tera–Wasserburg plot is the correct age, and calculating the composition of the concordant component (i.e. free of common-Pb); 3) the ^{208}Pb is then calculated by taking the amounts of common-Pb (^{206}Pb and ^{207}Pb) in each analysis and assuming a Stacey and Kramers (1975) model Pb isotope composition for ~20 Ma; 4) the ^{208}Pb common-Pb is subtracted from the total ^{208}Pb (as measured) to yield the radiogenic ^{208}Pb; 5) finally, the radiogenic ^{208}Pb–^{232}Th age is recalculated. Steps 4 and 5 obviously have two possible answers, depending on whether ^{206}Pb or ^{207}Pb is used to calculate ^{208}Pb in step 3. The resultant common-Pb corrected monazite Pb–Th ages (corrected using ^{206}Pb) are presented in Figure 6.17, and all U–Th–Pb ages are presented in Table 6.4. Thorium–Pb monazite ages are slightly older but consistent with the Tera–Wasserburg-derived U–Pb ages.

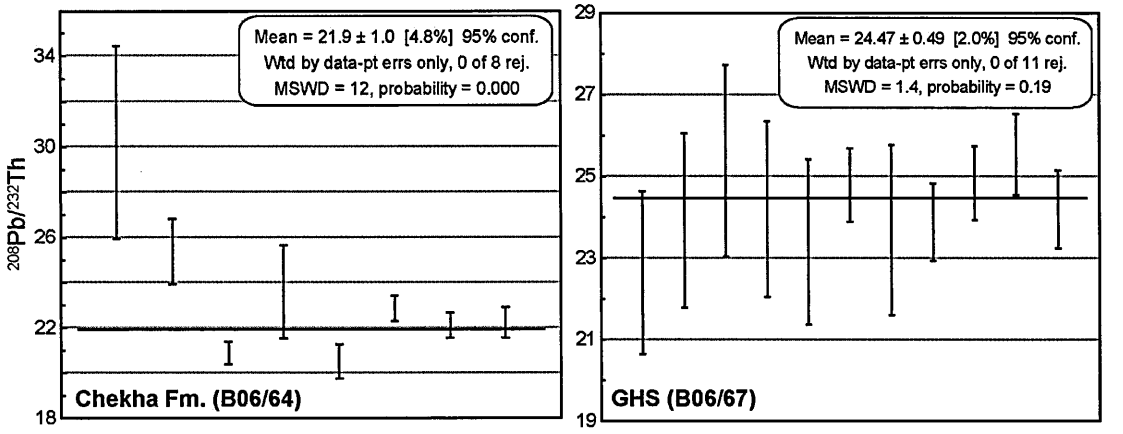

Fig. 6.17 Mean $^{208}Pb/^{232}Th$ corrected (using ^{206}Pb) monazite ages in a) Chekha Formation (B06/64ii) and b) GHS (B06/67) (Table 6.3). Data point error symbols are 2σ.

Table 6.3 U-Th-Pb isotopic data of monazite grains in pelitic samples from the GHS and Chekha Formation

Sample	^{206}Pb (mV)	^{207}Pb (mV)	^{208}Pb (mV)	^{232}Th (V)	^{238}U (mV)	Pb (ppm) †	Th (ppm) †	U (ppm) †	Th/U	Uncorrected isotopic ratios $^{207}Pb/^{206}Pb$	1σ (%)	$^{238}U/^{206}Pb$	1σ (%)	$^{207}Pb/^{235}U$	1σ (%)	$^{208}Pb/^{232}Th$	1σ (%)	Rho
Chekha*																		
1.1	0.42	0.13	1.1	0.50	169	187	22467	2263	9.9	0.0814	1.34	297.78	2.28	0.038	2.65	0.0016	7.05	0.86
1.2	0.20	0.12	0.5	0.10	28	102	4294	377	11.4	0.6313	1.29	85.66	5.28	1.016	5.44	0.0033	2.88	0.0001
2	0.49	0.07	1.3	0.71	154	190	31587	2067	15.3	0.1359	5.10	267.64	2.36	0.070	5.62	0.0012	1.17	0.42
4.1	0.39	0.07	1.0	0.53	144	189	24636	2006	12.3	0.1348	1.37	258.57	1.64	0.072	2.14	0.0014	4.38	0.77
4.2	0.46	0.06	1.5	0.94	153	202	43954	2131	20.6	0.1419	2.11	258.68	1.63	0.076	2.67	0.0011	1.85	0.61
5	0.47	0.05	2.3	1.39	168	215	65078	2340	27.8	0.1098	1.90	265.67	1.71	0.057	2.55	0.0012	1.22	0.67
6.1	0.22	0.02	1.3	0.79	87	106	37261	1213	30.7	0.1007	3.45	285.78	1.84	0.049	3.91	0.0011	1.25	0.47
6.2	0.22	0.02	1.1	0.65	86	106	30570	1204	25.4	0.0963	3.62	275.90	1.83	0.048	4.06	0.0012	1.49	0.45
GHS **																		
1.1	0.57	0.03	1.8	0.87	205	239	47069	2613	18.0	0.0645	2.46	268.32	1.78	0.033	3.03	0.0011	4.39	0.59
1.2	0.53	0.04	1.5	0.66	198	235	35822	2518	14.2	0.0698	2.38	263.07	1.77	0.037	2.97	0.0012	4.46	0.60
2.1	0.58	0.05	1.8	0.76	161	196	41233	2053	20.1	0.0693	1.77	257.21	1.79	0.037	2.52	0.0013	4.62	0.71
2.2	0.58	0.04	1.6	0.69	225	268	37505	2858	13.1	0.0621	2.13	262.77	1.79	0.033	2.78	0.0012	4.45	0.64
3.1	0.57	0.03	1.2	0.56	197	230	30176	2509	12.0	0.0627	2.65	261.10	2.01	0.033	3.33	0.0012	4.33	0.61
3.2	0.45	0.03	1.4	0.68	163	72	36980	2119	17.4	0.0641	2.97	264.55	0.97	0.033	3.12	0.0013	1.82	0.31
4	0.77	0.05	1.9	0.85	275	331	45796	3498	13.1	0.0713	1.76	257.85	1.75	0.038	2.48	0.0012	4.41	0.71
5.1	0.63	0.04	1.3	0.64	234	67	34455	3030	11.4	0.0616	2.33	264.49	0.81	0.032	2.47	0.0012	1.99	0.33
5.2	0.58	0.05	1.4	0.64	243	72	34632	3149	11.0	0.0914	2.05	260.33	0.90	0.048	2.24	0.0013	1.83	0.40
6	0.62	0.04	1.9	0.82	189	93	44147	2454	18.0	0.0652	2.32	260.55	0.88	0.035	2.48	0.0013	1.95	0.36
7	0.50	0.03	1.7	0.84	232	85	45398	3011	15.1	0.0733	2.53	288.19	0.81	0.035	2.66	0.0012	1.97	0.31

continued...

Table 6.3 continued

Sample	Uncorrected ages (Ma)								Corrected isotopic ratio ‡			Corrected age (Ma)	
	$^{207}Pb/^{206}Pb$	2s abs	$^{206}Pb/^{238}U$	2s abs	$^{207}Pb/^{235}U$	2s abs	$^{208}Pb/^{232}Th$	2s abs	$^{208}Pb/^{232}Th$	1σ (%)	$^{208}Pb/^{232}Th$	2s abs
Chekha*												
1.1	1232	53	22	1.0	38	2.0	32	4.5	0.0015	7.1	30	4.3
1.2	4582	37	75	7.9	712	106	66	3.8	0.0013	2.9	25	1.5
2	2176	178	24	1.1	69	8.0	24	0.6	0.0010	1.2	21	0.5
4.1	2162	48	25	0.8	70	3.1	27	2.4	0.0012	4.4	24	2.1
4.2	2251	73	25	0.8	74	4.1	23	0.9	0.0010	1.8	21	0.8
5	1796	69	24	0.8	56	2.9	24	0.6	0.0011	1.2	23	0.6
6.1	1637	128	23	0.8	48	3.9	23	0.6	0.0011	1.3	22	0.6
6.2	1554	136	23	0.9	48	4.0	23	0.7	0.0011	1.5	22	0.7
GHS **												
1.1	757	104	24	0.9	33	2.0	23	2.0	0.0011	4.4	23	2.0
1.2	922	98	24	0.9	36	2.2	25	2.2	0.0012	4.5	24	2.1
2.1	908	73	25	0.9	37	1.9	26	2.4	0.0013	4.6	25	2.3
2.2	677	91	24	0.9	33	1.8	25	2.2	0.0012	4.5	24	2.2
3.1	697	113	25	1.0	33	2.2	25	2.1	0.0012	4.3	23	2.0
3.2	744	126	24	0.5	33	2.1	25	0.9	0.0012	1.8	25	0.9
4	965	72	25	0.9	38	1.9	25	2.2	0.0012	4.4	24	2.1
5.1	659	100	24	0.4	32	1.6	25	1.0	0.0012	2.0	24	0.9
5.2	1454	78	25	0.4	48	2.2	26	1.0	0.0012	1.8	25	0.9
6	782	97	25	0.4	34	1.7	26	1.0	0.0013	2.0	26	1.0
7	1022	103	22	0.4	35	1.9	24	0.9	0.0012	2.0	24	1.0

*B06/64ii, see Figure 6.11, ** B06/67, see Figure 6.9, † c. 20 % uncertainty on concentration, ‡ corrected using ^{206}Pb

The interpretation of both the U–Pb and Th–Pb monazite data may be compromised by the presence of excess ^{206}Pb, which is ubiquitous in Th-rich minerals such as monazite (e.g. Parrish, 1990). Excess ^{206}Pb cannot be unambiguously resolved without an accurate measurement of the ^{204}Pb content, which, as mentioned previously, is not possible with the LA–ICP–MC–MS method

for small sample sizes. Nevertheless, an assessment of excess ^{206}Pb contents from young metamorphic and igneous monazites strongly suggests that the amount of excess ^{206}Pb is unlikely to account for more than ~1 Ma difference in age. Therefore, the ^{206}Pb correction to the ^{206}Pb–^{238}U age is within the uncertainty of the intercept age on the Tera–Wasserburg diagram. Theoretically the ^{208}Pb–^{232}Th age should be free of the problematic effect of excess ^{206}Pb. However, in this case we assumed concordancy of both samples, at 20.4 Ma (GHS) and 23.4 Ma (Chekha Formation), in order to calculate the amount of common ^{208}Pb. The effect though, of ~1 Ma excess ^{206}Pb, in proportion to the common-Pb correction already applied is considered minimal. For the most reasonable monazite age estimate (i.e. taking the effect of excess ^{206}Pb into consideration), all ages quoted above (U–Pb and Th–Pb) should be considered maximum values.

Table 6.4 Summary of U-Pb and Th-Pb monazite ages (Ma)

	Chekha Fm. (B06/64)	GHS (B06/67)
U-Pb	20.4 ± 1.6	23.4 ± 1.2
Th-Pb (using ^{206}Pb)	21.9 ± 1.0	24.47 ± 0.49
Th-Pb (using ^{207}Pb)	22.49 ± 0.94	24.41 ± 0.66

In conclusion, given the uncertainties on the data, monazite crystallization in both units could be broadly coeval around 22–23 Ma. However, the data imply that monazite grains in the Chekha Formation are *younger* than those in the GHS sample, from which I infer that monazite formation in the basal Radi klippe (Chekha Formation) post-dated monazite formation in the underlying GHS by at least 2 Myr, at ~ 22 and ~24 Ma respectively.

6.2.5 Discussion

Formation of monazite

Owing to the mapping of elements to discriminate between accessory phases (see above), it is proposed with some confidence that the principal formation of monazite in both samples (Chekha Formation and GHS) was post-garnet growth. In support of this is the evidence that monazite does not appear to have crystallised on pre-existing (detrital) monazite grains, as a) the age data do not suggest any older component, and b) high-contrast BSE images do not reveal textures indicative of detrital cores (e.g. Rasmussen and Muhling, 2007). This is in contrast to the range of monazite ages recorded in the metamorphic core (GHS) in central Nepal, which span the

Phanerozoic (Martin et al., 2007), but is consistent with monazite ages from a correlative unit, the Haimanta Group in the Sutlej valley (Chapter 3) (i.e. one monazite generation in the Oligocene/Early Miocene).

Therefore, the monazite ages obtained must represent late prograde metamorphism, peak metamorphic conditions, or even retrograde metamorphism, as a result of a number of possible monazite-forming reactions (Corrie and Kohn, 2008 and references therein). Fortunately, accompanying textural and chemical data for the analysed grains can elucidate the mode (or modes) of formation. All monazites analysed here hint at being the product of prograde metamorphism, as opposed to retrograde (i.e. decreasing pressure and temperature) metamorphism, for the following reasons:

- There is no association with (e.g. intergrowth with) any retrograde phase e.g. allanite or chlorite (e.g. Bollinger and Janots, 2006).
- Euhedral grain morphology suggests primary crystallisation, and not retrograde formation. This is more common to the monazite grains analysed from the Chekha Formation than from the underlying GHS. However, considering the high strain experienced by the GHS sample (in the immediate footwall to the lower STD), subhedral and/or pitted monazite in the GHS may indicate post-crystallisation deformation and modification of originally euhedral monazite crystals (cf. euhedral monazite grains in samples from the Chekha Formation, located above the high-strain shear zone). 'Unprotected' regions of the GHS sample (e.g. in the matrix and away from any pressure shadows around porphyroblasts) feature 'deformed' grains (e.g. monazite 5 in Fig. 6.9), whereas euhedral 'undeformed' monazites are located in 'protected' sites (e.g. monazite 1 in Fig. 6.10, shielded by garnet).
- The (late-stage) Fe-rich alteration product associated with garnet porphyroblasts (around the edges and along cracks), which is also phosphorus-rich (i.e. a major element in monazite), is not associated with any monazite, which, had there been any retrograde monazite formation, would have surely been localized here where there was evidently available phosphorus.

- Thorium zonation preserved in monazite grains (from Th-rich cores to Th-low rims) is consistent with prograde metamorphism (Kohn and Malloy, 2004).

Prograde monazite formation has been attributed to reactions involving major silicate minerals (e.g. Ferry, 2000; Kingsbury et al., 1993; Kohn and Malloy, 2004; Smith and Barreiro, 1990; Wing et al., 2003) but recent studies involving the mass balance of necessary reactions strongly suggest that the breakdown of accessory (REE) phases (e.g. allanite) is a more important control (Corrie and Kohn, 2008; Janots et al., 2008; Tomkins and Pattison, 2007; Yang and Pattison, 2006). Considering the samples from the Chekha Formation, and the accessory phases included in garnet as well those restricted to the matrix assemblage (see element maps, Fig. 6.8), it is inferred that allanite and apatite (and possibly Fe-oxides e.g. ilmenite) broke down post garnet-growth, leading to the formation of monazite (according to reactions presented in Tomkins and Pattison, 2007, and Janots et al., 2008). The Chekha Formation samples also exhibit phosphorus-rich garnet 'alteration' (B06/62, Fig. 6.8) *or* large apatite grains (relative to apatite inclusions in garnet, B06/64, Fig. 6.8). These may be by-products of the *allanite* + *apatite* → *monazite* prograde reaction, wherein excess phosphorus either forms phosphorus-rich garnet 'alteration', or new apatite, depending on the CaO whole rock composition (B06/62 has a relatively lower CaO content than B06/64; Appendix C1.2). This theory could be tested by modelling the mass balance of the reaction.

The zonation and contents of Y in garnet and monazite are consistent with the inferred timing of allanite breakdown to form monazite (that is, post-garnet growth), with monazite grains depleted in Y owing to the earlier sequestration of Y in garnet (Figs. 6.14 and 6.15). Further evidence of monazite growth post-garnet growth is the lack of Y annuli in garnet, which has been attributed to allanite breakdown *during* garnet growth, (Tomkins and Pattison, 2007; Yang and Pattison, 2006).

As the temperature for allanite dissolution in metasediments is influenced by the whole-rock composition (Janots et al., 2008 and references therein), temperature estimates for this reaction range between 500 and 600 °C (Catlos et al., 2002 and references therein), however Janots et al. (2008) recently presented a minimum temperature constraint of 560 °C. Taking the peak

metamorphic temperature estimated here for the Chekha Formation (using garnet rim analyses) and the fact that allanite breakdown and monazite formation occurred post-garnet growth, data in the present study are not only consistent with previous estimates, but suggest that for this sample, allanite breakdown was restricted to temperatures above 580 °C. The timing of monazite formation (allanite dissolution) with respect to the growth of staurolite (also post-garnet growth, Fig. 6.5a–c) has not been ascertained in this study. Other studies on garnet-bearing pelites suggest that the reaction occurs prior to the growth of staurolite (Tomkins and Pattison, 2007; Yang and Pattison, 2006).

The chemically distinct zones in monazite grains from the Chekha Formation are interpreted to reflect discontinuous reactions during the same metamorphic event (e.g. Foster et al., 2000). The transition from zone 1 to 2 (high Th to low Th, and low Y in both) is consistent with sub-solidus crystallisation during prograde metamorphism (i.e. increasing temperature) (Kohn and Malloy, 2004). The outer zone (zone number 3), where the trends in Y and Th are reversed (relatively higher Th and high Y), suggests a change in the mode of formation. Obviously at this point in the crystallisation history of monazite, the dissolution of a phase (or phases) released Y and Th into the system. The accessory phases zircon and apatite can contain significant amounts of Y (Yang and Pattison, 2006 and references therein), as can the major silicate mineral garnet (e.g. Pyle and Spear, 1999). The dissolution of zircon is excluded, given that the peak metamorphic grade of the Chekha Formation was not high enough to dissolve zircon, as is apatite, for the reason that relatively large apatite grains in the matrix (sample B06/64, Fig. 6.8) indicates that apatite was stable. Garnet dissolution may occur during decompression (e.g. Foster et al., 2004), although garnet porphyroblasts in the same sample as the one from which monazites were analysed (B06/64) do not look particularly resorbed (euhedral and no apparent alteration, Fig. 6.8). Alternatively (having discredited mineral dissolution as the Y source), high-Y overgrowths may suggest the presence of melt or melt crystallisation (Tomkins and Pattison, 2007 and references therein). In light of the leucogranite intrusion at the locality sampled (B06/64, Fig. 6.5d–e) it is inferred that fluids (and localised high temperatures, i.e. a contact metamorphic aureole) associated with this intrusion led to Y-rich overgrowths on pre-existing monazite grains. Evidence of 'seeping' REE fluids along

grain boundaries (e.g. 'monazite? 3' and 'monazite 4', Fig. 6.11) supports this hypothesis, as does the inference that brittle intrusive features in psammites (Fig. 6.5e) indicate elevated pore fluid pressures related to melt intrusion. Fluid flux from local intrusions may also provide a reasonable explanation for the phosphorus-rich garnet 'alteration' of uncertain origin.

The monazite overgrowths are considered too thin to have been analysed with certainty using the laser ablation technique, although they may have been partially sampled in monazite analyses which targeted rimward regions. However, this is not detectable in any of the data. The age of monazite in the Chekha Formation (~22 Ma) may then also represent the timing of leucogranite intrusion presumed responsible for monazite overgrowths. An analytical instrument with higher spatial precision could better resolve the age of the Y-rich rims, and thus the inferred timing of leucogranite intrusion. Following on from this, it would be valuable to then know the source and mechanism for the intrusions, but this cannot be unequivocally determined without petrographic and/or chemical analysis of the leucogranite.

The reaction responsible for prograde monazite formation in the GHS is much harder to ascertain, as accessory phases are generally rare in the sample analysed (Fig. 6.7). However, it is reasonable to suggest that the same allanite breakdown reaction was involved, as allanite is identified in one garnet, and apatite is preserved as an inclusion in monazite (e.g. monazite 3, Fig. 6.9). The prograde temperature for the reaction in this sample cannot be estimated (as was for the Chekha Formation sample) owing to the fact that the estimated temperatures (Table 6.2) are not considered representative of peak metamorphic conditions (see above). The relatively low abundance of monazite (product) is consistent with formation from similarly low amounts of allanite and apatite (reactants). As in one of the Chekha Formation samples (B06/62), phosphorus-rich garnet 'alteration' suggests an excess of phosphorus following the saturation of monazite. The GHS sample (B06/67) has a similar CaO whole rock content to B06/62 (Appendix C1.2), and is thus consistent with the proposed theory that this feature is characteristic of relatively low-CaO rocks wherein the formation of new apatite is limited. The patchy chemical zonation in the GHS monazite grains may reflect crystal modification during deformation and/or multiple crystallisation/reprecipitation under high temperature (sillimanite stability field) conditions.

In summary, monazite ages date the timing of peak metamorphism, after garnet-growth following the breakdown of allanite and apatite. In the Chekha Formation this reaction took place above 580 °C. High-Y overgrowths in monazites in the Radi klippe above the lower STD (Chekha Formation) formed in response to localised leucogranite intrusions (i.e. contact metamorphism). The crystallisation history of monazite in the samples studied from the Chekha Formation took place under relatively low-strain conditions (euhedral crystals), in contrast to monazite in the underlying GHS, where high temperature deformation was probably responsible for anhedral, 'altered'-looking monazite morphologies.

Tectonic implications of monazite age data

Motion on the lower STD (coupled with movement on the MCT below) facilitated extrusion of the GHS after peak metamorphism, i.e. after ~24 Ma, as constrained by the age of metamorphic (prograde) monazite in sample B06/67 deformed by top-to-the-NE sense of shear. Unfortunately, no minimum age constraint can be determined from the data presented here, but could be determined from muscovite (Ar–Ar) cooling ages. Theoretically, samples from both sides of the shear zone (footwall and hanging wall rocks) would present the same age, as muscovite Ar closure temperatures (typically 300–350 °C) are broadly equivalent to the brittle–ductile transition in the continental crust (e.g. Passchier and Trouw, 1998, and references therein), and the lack of a brittle overprint on the lower STD shear zone suggests this fault operated wholly within the ductile regime. Muscovite cooling ages from structurally lower down the GHS (SW of Tashigang, Fig. 6.4), between 11 and 14 Ma, could be used to infer a minimum age of shearing on the lower STD. This assumes however, that the lower GHS (i.e. south of the KT) behaved as a coherent block during extrusion, and given the penetrative S-directed ductile shear in the GHS (associated with movement on the MCT) it is unlikely to be entirely valid. Nevertheless, the cooling ages present a reasonable approximation for the purpose of this discussion. Thus, ductile motion on the upper STD (12–10 Ma) initiated much later and outlasts ductile motion on the lower STD at the base of the Radi klippe (constrained between 24 and ~ 11 Ma). Preliminary data from the base of the Lingshi and Ura klippen in western Bhutan (Fig. 6.1), from leucogranites in the Chekha Formation deformed by N-directed shear (associated with motion the lower STD), are consistent with an

earlier (lower) STD having operated in the Early Miocene: U–Pb zircon ages representing pre- to syn-tectonic (ductile) motion on the lower STD, are 22–16 Ma; muscovite (Ar–Ar) cooling ages from the same samples are 13–11 Ma, and signify the end of ductile motion (i.e. the transition into the brittle, upper crustal regime) (D. Kellet, unpublished data, pers. comm.). These data constrain ductile motion on the lower STD in western Bhutan to between 22 and ~ 11 Ma.

These results support the inference that motion on the MCT and lower STD in Bhutan were coeval in the early Miocene, as first proposed by Grujic et al. (2002), and is consistent with the concept of an early pulse of (lower) GHS extrusion (Hollister and Grujic, 2006). However, this does not unequivocally prove the process of channel flow, and other extrusion mechanisms are likely to be equally valid based on these data alone. Evidently a more comprehensive view of the thermal evolution of the GHS (via *P–T–t* path analysis) is required to investigate this, and the discussion below may contribute to this. Also, despite the fact that relatively older ages of motion on shear zones, metamorphism and melting are found in the lower GHS (KT footwall) compared to the upper GHS (KT hanging wall), there remains a lack of geochronological data (compiled in Table 6.5 and presented in Figures 6.1 and 6.18) to firmly substantiate this.

Although Grujic et al. (2002) infer that the KT was an out–of–sequence thrust from its structural position above the klippen and the fact that it post-dated N-directed movement on the lower STD (not proven, see above), the lack of a direct cross-cutting relationship between the KT and the lower STD casts some doubt upon this interpretation, and motion on the KT could have been coeval with, or older than, motion on the lower STD (Yin, 2006). However, brittle structures observed at the trace of the KT suggest that motion at least outlasted (or post-dated) motion on the purely ductile lower STD, as the KT continued to remain active into the brittle regime (i.e. at higher crustal levels).

_P–T_ comparisons

Pressure–temperature (*P–T*) data from the GHS immediately underlying the lower STD at the base of the Radi klippe, represent a partially re-equilibrated assemblage, thus a direct comparison to published *P–T* data from neighbouring areas in the GHS (Daniel et al., 2003; Davidson et al., 1997) cannot be made. However, petrographic observations allow some discussion.

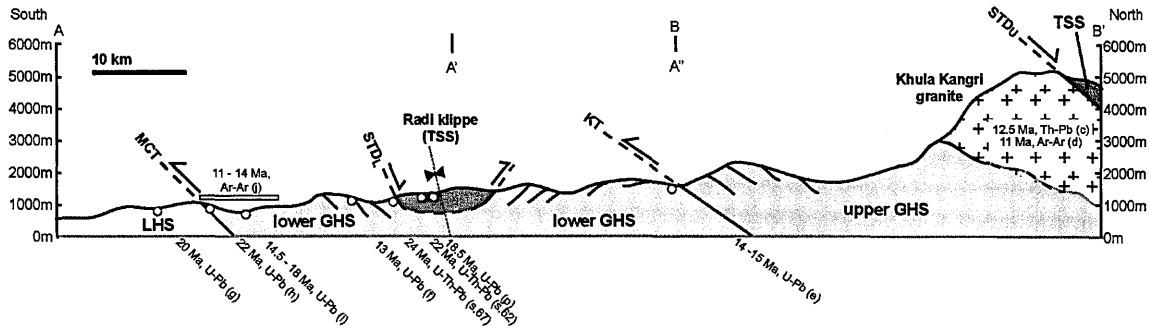

Fig. 6.18 Cross-section through eastern Bhutan (lines A–A'–A'' and B–B' in Figure 6.1) annotated with all available Cenozoic age data (Table 6.5). From these data it is inferred that south-directed thrusting on the MCT initiated at ~22 Ma, followed by melting in the lower GHS between ~ 18 and 14 Ma and cooling of the same rocks to ~350°C by 11 Ma. Ductile motion on the upper STD spanned 12 to 10 Ma. Earlier motion, between 15 and 14 Ma would have been simultaneous with thrusting on the KT. Abbreviations as in Fig. 6.1. Note that a comparison with this cross-section with one through the Sutlej valley is provided in Appendix A.

Table 6.5 Key Cenozoic age data from Bhutan

key*	Age (Ma)	Isotopic system	Mineral	Lithology	Reference
(a)	20.5 - 17.0	U-Pb	zircon (rims), monazite	granite	Carosi et al., 2006
(b)	14.0 - 15.1	Rb-Sr	micas	granite (Gophu La)	Ferrara et al., 1991
(c)	12.5 ± 0.4	Th-Pb	monazite	granite (Khula Kangri)	Edwards & Harrison, 1997
(d)	10.7 - 11.4	Ar-Ar	micas	granite (Khula Kangri)	Maluski et al., 1988
(e)	14.2 - 15.0	U-Pb	monazite, xenotime	pegmatite	Daniel et al., 2003
(f)	13.4 ± 0.2	U-Pb	xenotime	leucogranite	Daniel et al., 2003
(g)	20.0 ± 0.2	U-Pb	monazite (metamorphic)	quartz-feldspar gneiss	Daniel et al., 2004
(h)	22 ± 1	U-Pb	monazite	biotite-schist	Daniel et al., 2005
(i)	14.5 - 18	U-Pb	monazite, xenotime	leucosome/migmatite	Daniel et al., 2003
(j)	11.0 - 14.1	Ar-Ar	muscovite	paragneiss	Stuwe & Foster, 2001
(k)	13.2 ± 0.2	Ar-Ar	muscovite	leucogranite	D. Kellet (unpublished, DBH 003)
(l)	11.5 ± 0.2	Ar-Ar	muscovite	leucogranite	D. Kellet (unpublished, DBH 027)
(m)	11.7 ± 0.2	Ar-Ar	muscovite	leucogranite	D. Kellet (unpublished, DBH 067)
(n)	11.1 ± 0.2	Ar-Ar	muscovite	leucogranite	D. Kellet (unpublished, DBH 080)
(o)	14 - 15	U-Pb	zircon	eclogite	Warren et al. (2008)/D. Grujic (unpublished)
(p)	18.5 ± 1	U-Pb	monazite	pegmatite	R. Parrish (unpublished, RP 87)
(q)	< 23	U-Pb	monazite	granite	R. Parrish (unpublished, RP 106)

* refer to Figures 6.1 and 6.18

Estimated peak *P–T* conditions experienced by kyanite-bearing migmatites in the GHS, between the Radi klippe and the MCT to the SW are presented in Davidson et al. (1997) and Daniel et al. (2003) (samples 93Bp96 and D62b respectively, the approximate locations of which are shown in Fig. 6.4). In the immediate hanging wall to the MCT, peak metamorphic conditions reached 800 °C and 12–13 kbars (D62b, Daniel et al., 2003), while further upsection (approximately equidistant between the MCT and lower STD at the base of the Radi klippe) peak metamorphic conditions reached were ~700 °C and ~9 kbars (93Bp96, Davidson et al., 1997). As no kyanite was observed *in situ* SE of Tashigang on the road towards the Radi klippe (i.e. at higher structural levels in the lower GHS), only sillimanite, this suggests a trend towards lower *P* at peak

T of metamorphism: from a maximum of 13 kbars at its base, to at most 7 kbars (based roughly on the position in *P–T* space of the Al-silicate stability fields, and a maximum temperature of 700 °C) in the upper levels. This presents an apparent barometric difference of 6 kbars, which is *greater* than that implied by the estimated lithostatic gradient across the structural height of the section (for a horizontal distance of 15 km between the MCT and the base of the Radi klippe based on Figure 6.4, and an average dip of 40–60 °C), of approximately 2.5–3.5 kbars. Steeper than lithostatic pressure gradients may result from structural extension following peak metamorphism, or from synmetamorphic ductile shear (Jamieson et al., 1996). This calculation assumes that 1) the samples analysed equilibrated at the same time, and 2) there is no structural discontinuity through the section.

In fact, the approximate age of peak metamorphism in the lower GHS, 22 ± 1 Ma (Daniel et al., 2003) (Fig. 6.18), is younger than expected for a more deeply buried part of the section (considering the age of monazite crystallisation determined here, equivalent to the top of the section in consideration, of ~24 Ma), and requires further investigation. The possible effect of shear heating on these samples, both used to obtain *P–T* estimates and located next to or within shear zones (either the MCT or lower STD) perhaps calls for an assessment, to include, for example, the *P–T* analysis of samples located at further distances from the shear zones. A comparative thermobarometric method (e.g. as in Fraser et al., 2000) is a recommended technique in determining *P* and *T gradients* across a given transect.

Fraser et al. (2000) also highlight a possible flaw in the second assumption made above (that is, that the section is one structurally coherent unit) in identifying two cryptic thrusts within the GHS in the Langtang transect of Nepal. High-resolution geochronologic is also valuable to this investigation, as diachronous peak metamorphic ages can also help identify cryptic thrusts (e.g. Nanga Parbat, Foster et al., 2002).

The *P–T* data presented here for the Chekha Formation are the first of such, and so there are no independent results with which to compare to, at least not in Bhutan. However, the observations and data presented in this chapter have implications for potential correlations of the Chekha

Formation in particular along the length of the Himalayan orogen. These implications are discussed in the following chapter.

Estimated rates of exhumation

Rates of exhumation either side of the lower STD (basal Radi klippe) can be estimated for the samples analysed here using 1) the age of monazite as representative of the age of peak pressure (maximum depth of burial), and 2) muscovite cooling ages (e.g. Stüwe and Foster, 2001) to approximate the time both the GHS and Chekha Formation units passed through the brittle–ductile transition (with the assumptions that i) exhumation across the GHS was synchronous (which is unlikely, see above), and ii) motion of the lower STD was restricted to the ductile regime, consistent with field observations, and therefore the cooling age of the GHS is approximately equivalent to the cooling age of the Chekha Formation).

Given that pressures recorded in the lower structural levels of the lower GHS (i.e. south of the KT) exceed 9 kbars (Daniel et al., 2003; Davidson et al., 1997), peak *P* (maximum burial, not to be confused with *P* at T_{max}) in the GHS immediately below the lower STD is estimated at ~8 kbars. The age of monazite (~24 Ma) at this locality is presumed a reasonable estimate of the age of this peak *P*, although without detailed analysis of the *P–T* path, e.g. with pseudosections (cf. Figs. 3.6 and 3.7) it is impossible to say whether the age is an overestimate or underestimate. Using the maximum cooling age data available from the lower GHS, of 14 Ma (Stüwe and Foster, 2001), and assuming that this corresponds to a cooling pressure of ~2 kbars, ~22 km of the lower GHS was exhumed over a period of 10 Ma (assuming a lithostatic gradient of 3.7 km/kb). This suggests an exhumation rate of 2.2 mm yr^{-1} and is within the range of estimated rates of extrusion for the GHS (2–4 mm yr^{-1}, Searle et al., 2003). However, with the minimum cooling age of 11 Ma the exhumation rate is reduced to 1.7 mm yr^{-1}. Furthermore, if monazite formation was in fact before or after maximum burial, the rate of exhumation calculated will be minimum or maximum, respectively (overestimating and underestimating the duration of time elapsed between maximum burial and muscovite closure, respectively), and therefore the application of the monazite-forming reaction needs to be considered more carefully.

Applying the same calculation to the Chekha Formation (hanging wall to the lower STD), with a peak pressure of 7.3 kbars (Table 6.2) at ~22 Ma (age of monazite), yields more rapid rates of exhumation relative to the underlying GHS, of ~2.5 mm yr^{-1} and 1.8 mm yr^{-1} (for cooling ages of 14 and 11 Ma respectively). However, the rate calculated *must* be a maximum seeing as monazite formed *after* garnet and the peak *P–T* estimate uses garnet rim analyses, thus peak *P* (at least the one calculated for here) must have pre-dated 22 Ma, and as a result the true exhumation rate must be slower (i.e. more time for exhumation across the same vertical distance).

Neither of these exhumation rates can account for lateral extrusion (i.e. at constant depth) that may be an important process in the channel flow model (cf. Figure 3 in Jamieson et al., 2004).

6.2.6 Conclusions

The following conclusions are made from the analysis of pelitic samples from the hanging wall (Chekha Formation) and footwall (lower GHS) to the lower STD in eastern Bhutan (basal Radi klippe):

- Monazite formed during prograde metamorphism from the breakdown of allanite and apatite; in the Chekha Formation (garnet–staurolite schist) this reaction occurred >580 °C;
- Monazite crystallised at ~ 22 Ma in the Chekha Formation and ~24 Ma in the underlying GHS, and provide a maximum constraint on the timing of N-directed movement on the lower STD, and is consistent with coeval movement in the Early Miocene with the MCT, facilitating exhumation of the mid-crust (GHS)*;
- A steeper than lithostatic baric gradient recorded in the lower GHS could be the result of syn-metamorphic ductile shearing during extrusion*, but evidence is scant and assumes a structurally coherent unit
- Estimated exhumation rates for the GHS are comparable to or lower than other estimates of GHS exhumation in other Himalayan regions (2.2–1.7 mm yr^{-1}, cf. 2–4 mm yr^{-1}), while calculated exhumation rates for the Chekha Formation are faster (2.5–1.8 mm yr^{-1}), although these do represent maximum rates. Analysis of where monazite lies on the *P–T* path however,

as well as cooling ages for the Chekha Formation and underlying GHS are required before further conclusions can be made;

- *These data are consistent with the pulsed channel flow model (Hollister and Grujic, 2006), but do not prove its existence, and more data are required to test mechanisms of mid-crustal exhumation in Bhutan (as for other Himalayan regions, see next chapter).

6.3 Further work in Bhutan

There is plenty of further work to be done in Bhutan, including (but certainly not limited to) the following, which highlight possible avenues for investigation relating specifically to the above study, as well as to some regions of Bhutan where geological data are sorely lacking.

- Muscovite (Ar–Ar) cooling ages from samples across the lower STD (including the samples analysed here; Fig. 6.4a) would provide a minimum constraint on the age of ductile motion on the lower STD at the base of the Radi klippe. In conjunction with published muscovite cooling ages from lower down the same GHS section (Stüwe and Foster, 2001) an analysis of the rates of extrusion across this part of the lower GHS would be possible (c.f. Vance et al., 1998).

- More sophisticated pressure-temperature-time analysis (e.g. using pseudosections) from samples of the Chekha Formation (staurolite–garnet–chlorite phyllitic–schist, B06/97) and underlying GHS (kyanite–garnet–biotite ± sillimanite gneiss, B06/101) around the Ura klippe (Fig. 6.1) would test the results from this study, for a structurally equivalent section.

- Discrepancies between the three main maps utilised in this study of Bhutanese geology (Bhargava, 1995; Hollister and Grujic, 2006; Richards, 2004 based on Gansser, 1983) reveal areas of ambiguity that could not be addressed due to either lack of suitable samples or the time constraint on the PhD project. Some of these are listed here for future reference.

1. The area south of Paro and Thimpu features a unit known as the Paro metasediments (Fig. 6.1). These amphibolite-facies rocks have been variously assigned to the LHS (specifically the Jaishidanda Formation, between 'upper' and 'lower' MCTs (Hollister and Grujic, 2006) or upper GHS (Bhargava, 1995). Not enough work has been done on this area to discount the possibility that these rocks are part of the Chekha Formation, and form another klippe. Kinematic analysis around

this unit would help determine its tectonic position, whether as a TSS klippe, a window ('Paro window') into the LHS, or neither.

I have only three samples from one locality (B06/102) in this region. One of these samples (B06/102iii), a garnet–mica schist, features syn-tectonic garnet porphyroblasts with characteristic spiral inclusion trails (Fig. 6.19). Note that garnet porphyroblasts in this sample bear an uncanny likeness, in terms of their apparent degree of rotation (of ~ 540°, determined from the number of spirals preserved by inclusions), and size (4–5 mm), to garnets from sample I05/78i in the Shimla klippe, Sutlej valley (Fig. 5.2). Major element analysis across a garnet porphyroblast in B06/102iii also reveals bell-shaped Mn zonation, indicative of prograde garnet growth (as does garnet in the Shimla klippe sample). An age for garnet growth in this sample would test the relationship between the two samples further, as garnet from I05/78ii from the Shimla klippe is unique with a pre-Tertiary age (Chapter 4).

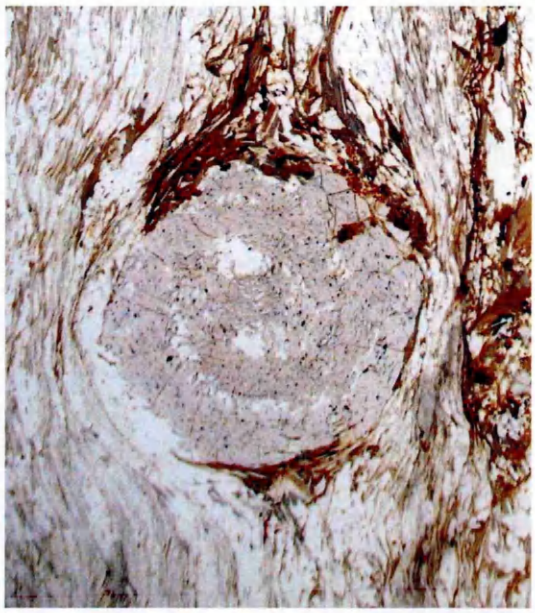

Fig. 6.19 Plane polarised light image of garnet porphyroblast (in sample B06/102iii) from the 'Paro window' with a spiral inclusion trail indicative of syn-tectonic growth. Garnet diameter 5 mm.

Only allanite (located in the matrix), and no monazite, was identified in this sample, which may point to a lower-grade of metamorphism than the samples analysed above, but as for all accessory phase analysis, an thorough assessment of the textural context of the accessory phase is required. NB. R. Parrish collected samples of 'Paro metasediments' (mica schist, quartzite, calc-silicate and marble) during the same field trip.

2. The tectonic role, timing and location (especially in western to central Bhutan) of the Kakhtang thrust are fairly poorly constrained. Samples collected on the road from Dungkhar to Lhuentse (N–S transect, Fig. 6.1) straddle the supposed trace of the Kakhtang thrust. *P–T* analysis of these samples may help clarify the position of the thrust, and confirm observations made by Daniel et al. (2003) further east.

3. The Black Mountain klippe lacks structural and metamorphic data. How does it compare to the other klippen? Does it form part of a larger outcrop as presented by Bhargava (1995), incorporating the Tang Chu and Ura klippen? There is much more geological work to be done in the south central region of Bhutan.

- The only Tertiary geochronologic data from the LHS in Bhutan is the age of metamorphic monazite in the east of Bhutan, dated at 20 ± 2 Ma, and is within error of the age of metamorphic monazite in the GHS above (Daniel et al., 2003, Fig. 6.18). Although it has been demonstrated that monazite may form across a wide range of *P–T* conditions, assuming these data do broadly represent prograde/peak metamorphism, then the age contrast between the LHS and GHS across the MCT is far less (almost negligible) in Bhutan when compared to the Sutlej valley, where metamorphism in the MCT footwall (Jutogh Group, LHCS) occurred about 10 to 15 Myr after peak metamorphism in the overthrust GHS. More data is required to investigate the nature and timing of metamorphism in the LHS, and its relationship to movement on the MCT and metamorphism in the overthust GHS.

Chapter 7

Discussion

7.1 The upper boundary to the crystalline core of the Himalaya

7.1.1 A comparison of the tectono-thermal histories of two basal formations from the Tethyan Sedimentary Series from the western and eastern Himalaya

The Haimanta Group in the western Himalaya (Sutlej valley, Chapter 3) and the Chekha Formation in the eastern Himalaya (Bhutan, Chapter 6) both represent Neoproterozoic–Cambrian units at the base of the Tethyan Sedimentary Series (TSS). Both units occupy equivalent structural positions within the Himalayan orogen, in the hanging wall to the South Tibetan Detachment (STD). The STD studied in the two regions is characterised by N-directed ductile deformation across a narrow shear zone (<2 km wide), below which lie sillimanite-bearing gneisses and/or migmatites of the Greater Himalayan Sequence (GHS). From the base of both the Haimanta Group and Chekha Formation (STD hanging wall immediately above the detachment) a rapid decrease in metamorphic grade upsection is recorded: from amphibolite grade garnet–staurolite (and kyanite in the Sutlej valley) mica schists, to greenschist grade biotite schists, up into unmetamorphosed TSS sediments *sensu stricto*. Over the same section, the strain intensity also decreases, from a regular crenulation foliation, into less pervasive fabrics (e.g. spaced cleavage), until only sedimentary bedding in the unmetamorphosed uppermost sediments is recognisable. This contrasts with the structural style in the STD footwall, where pervasive planar ductile fabrics in GHS gneisses (and in the Sutlej valley, mylonite at the GHS–Akpa granite contact) reflect even higher strain. Thus, the STD represents a major (ductile) shear zone, and forms a continuous and gradational contact between the high-grade GHS (footwall) and the unmetamorphosed TSS (hanging wall), and is recognisable as such between regions in the western and eastern Himalaya, separated by over 1000 km.

Furthermore, the *P–T–t* conditions experienced by the Haimanta Group and the Chekha Formation are comparable, with prograde metamorphism apparently coeval with the underlying GHS (Table 7.1). In metapelites from both the Haimanta Group and Chekha Formation, garnet

porphyroblasts overgrew a pre-existing tectonic fabric, and were followed by the growth of staurolite which grew syn-tectonically. Following peak *T* the Haimanta Group experienced ductile flattening, and although there are insufficient data from the Radi klippe (Chekha Formation) to demonstrate that this is also true for the Bhutan section, its resemblance to the Haimanta Group implies it is reasonable to suggest so.

Table 7.1 *P-T-t* comparison between the Haimanta Group (Sutlej valley, NW India) and the Chekha Formation (Radi klippe, Bhutan)

	Haimanta Group	Chekha Formation	G2 [3]	G3 [3]
age of peak metamorphism	30 - 23 Ma[1]	~22 Ma	29 -15 Ma [1]	32 -17 Ma [1]
age of peak metamorphism in underlying GHS	40 - 22 Ma[2]	~24 Ma	-	-
peak *P*	7 - 8 kbars	7 kbars	8.0 kbars	6.0 kbars
peak *T*	660 °C	550 - 620 °C	723 °C	605 °C
average Oligocene/Early Miocene rate of exhumation	1.3 mm/yr	< 1.8 - 2.5 mm/yr	-	-
muscovite (cooling) Ar-Ar age	~13 Ma	14- 11 Ma (?)	~ 3 Ma [4]	~ 3 Ma [4]

Data from Chapters 3 (Haimanta Group) and 6 (Chekha Formation). [1] Peak P to Peak T. [2] unpublished monazite ages (E. Catlos pers. comm. in Vannay et al., 2004; Caddick (2004), where the monazite age 23.4 ± 2.9 Ma corresponds to the time between peak P and peak T). [3] From Figure 4 in Jamieson et al. (2004), [4] assuming ~400°C closure temperature.

In the geochronologic analysis of the Haimanta Group/Chekha Formation, monazite has been used to constrain the age of peak metamorphism, supported by a thorough textural and chemical analysis of both monazite and garnet, where garnet growth preceded monazite or overlapped with early monazite formation. Detrital and/or retrograde monazites were not identified. Only for the Haimanta Group has this age been more tightly constrained to the *P–T* path, where a detailed *P–T*–deformation path has been established via the application of petrographic observations to pseudosections (Figs. 3.7–3.9). 'Peak metamorphism' in the Haimanta Group lasted from 30 Ma (peak *P*) to 23 Ma (peak *T*), a duration of 7 Myr. In the case of the Chekha Formation monazite formation occurred within 5 Myr (Table 6.4) at about ~22 Ma, which could reflect a different rate of metamorphism, or a difference in whole rock chemistry and the availability of essential components for monazite formation. Without a detailed *P–T* path it is unclear whether this age corresponds to peak *P*, peak *T*, or both. The tectonic implication of this is that cooling and exhumation rates may be significantly under- or over-estimated, and thus monazite ages should be assigned to *P–T* conditions with care.

Although the study of the Chekha Formation lacks the detail provided for the Haimanta Group, the strong similarity between the two units suggests that they underwent a similar tectono-thermal history: 1) prograde metamorphism coeval with the underlying GHS during the Eocene/Early Oligocene (and in Bhutan possibly into the Late Oligocene); 2) exhumation during the Early Miocene (~23–16 Ma); 3) re-coupling of the GHS and Haimanta Group/Chekha Formation on passing through the brittle–ductile transition during the mid-Miocene (~16–11 Ma), after which average exhumation rates were halved (where the same calculation as applied in Section 3.5.2 to the Haimanta Group is used here to estimate exhumation rates between 0.5 and 0.7 mm yr^{-1} for the Chekha Formation, based on cooling ages of 14–11 Ma, at 2 kbars). Thus, the GHS and Haimanta Group/Chekha Formation were apparently exhumed through the upper crust as a coherent tectonic block (juxtaposed in their present disposition).

In summary, these observations suggest that a common tectonic process was active in the early evolution of the Himalayan mid-crust, an inference which is strengthened by the recognition of laterally equivalent units (Section 7.1.3). The deformation and metamorphism proximal to the STD shear zones recorded here contribute to our understanding of the role of the STD in the construction of the Himalaya, including its relationship to the exhumation of the mid-crust.

7.1.2 Implications for models of mid-crustal extrusion

The empirical data used here to determine the tectono-metamorphic evolution of the STD hanging wall (Haimanta Group/Chekha Formation), and its relationship with that of the underlying GHS, are important both for the assessment of models addressing mid-crustal extrusion in the Himalaya, such as the channel flow model (Jamieson et al., 2004, see Chapter 1), and for constraining future tectono-thermal models. Predictions of the *P–T–t* evolution across the putative channel are given (Fig. 7.1a, b), and although the (continuum mechanics) model does not predict discrete faults, the ductile STD at the base of the Haimanta Group/Chekha Formation, with negligible brittle displacement within it, is considered a reasonable representation of the true ductile upper boundary to the underlying extruded GHS material (channel or otherwise), from which *P–T–t* data can be tested against model predictions (e.g. Figure 4, Jamieson et al., 2004). Regions affected by significant upper crustal (i.e. brittle) deformation, that undoubtedly disrupts

the idealised channel structure (Harris, 2007 and references therein), are intrinsically more difficult places in which to test the model. I interpret the Haimanta Group/Chekha Formation to represent the region between the upper boundary of the extruded channel, and the top of the exhumed crust, within the upper "GHS" of the model (Fig. 7.1c), consistent with i) the suggestion that the Chekha Formation (and by inference the Haimanta Group also) lies at the top of the rheologically-defined channel (Hollister and Grujic, 2006), ii) specific features of the Haimanta Group, such as the widespread presence of a regular crenulation cleavage and the absence of *in situ* melt (Section 3.5.3), are "incompatible with extreme ductile flow", and so the unit must lie structurally above the extruded low-viscosity channel, and iii) *P–T* conditions that are similar to model results from this region (Table 7.1). Thus, I consider the G2 and G3 particle paths (Fig. 7.1c, Jamieson et al., 2004) to be representative of the possible particle paths undergone by the Haimanta Group/Chekha Formation.

Compared to thermometry results from the Haimanta Group/Chekha Formation (Table 7.2), model temperatures in the "STD" hanging wall are comparable close to the fault, but increasingly overestimated with increasing distance from the fault (by ~150 °C, 8.5 km up section) (Fig. 7.1a). Model pressures are underestimated for rocks in the immediate hanging wall (by 1.5–2 kbars), but closely matched 8.5 km above the "STD" (Fig. 7.1b, Table 7.2). The resultant *P–T* gradients across the "STD" appear steeper than the model predicts (Fig. 7.1a, b). However, since the model presented in Jamieson et al. (2004) does not incorporate the ductile flattening proposed for the Haimanta Group (and perhaps also applicable to the Chekha Formation), then the relatively steep *P–T* gradients do not necessarily invalidate the channel flow model, but may require its modification. Suffice to say, more *P–T* data are required across the metamorphic core in both the Sutlej valley and Bhutan, to determine accurate *P–T* gradients across the putative channel before further conclusions can be drawn. Further studies in these areas are particularly important since the numerous studies from central Nepal, if not balanced by other areas, will invite the fallacy that the Nepalese sector is representative of the whole orogen.

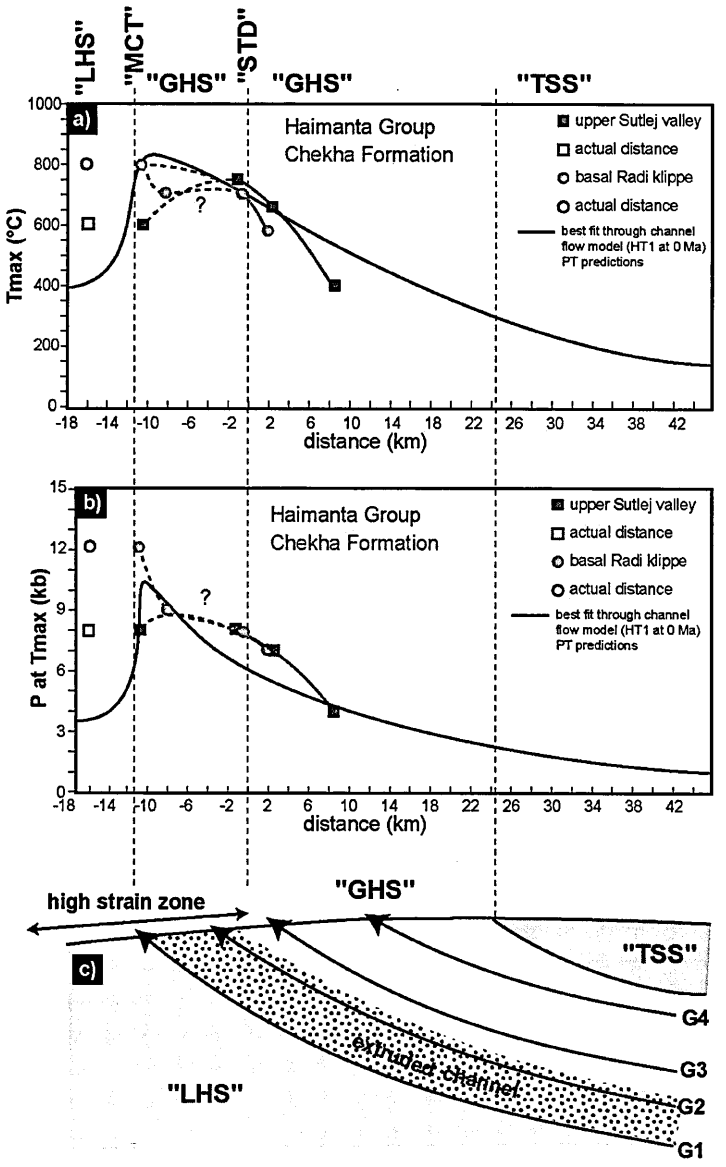

Fig. 7.1 Peak metamorphic grade profiles across the upper boundary of the channel in the channel flow model, compared with data from the upper Sutlej valley and basal Radi klippe in Bhutan (Table 7.2), adapted from Figure 8 in Jamieson et al. (2004). "MCT", model Main Central thrust which represents the model protolith boundary; "STD", model "South Tibetan detachment" which represents the upper boundary of the extruded channel; "LHS", model Lesser Himalayan Sequence; "GHS", model Greater Himalayan Sequence; "TSS", model Tethyan Sedimentary Sequence. Distance is from "STD"; 'actual distance' data are not used in the profiles drawn, and instead the data are plotted at the base of the "GHS" to which they correspond, in order to present approximate profiles between the "STD" and "MCT".

Table 7.2 STD hanging wall and footwall *P-T* data

structural distance above STD	upper Sutlej valley, NW India		basal Radi klippe, Bhutan	
	peak T	P at T_{max}	peak T	P at T_{max}
8.5 km	400 °C	4 kbars	-	-
2.5 km	660 °C	7 kbars	-	-
2 km	-	-	580 °C	7 kbars
-0.5 km	-	-	700 °C (?)	8 kbars (?)
-1 km	750 °C [1]	8 kbars [1]	-	-
-8 km	-	-	700 °C [2]	9 kbars [2]
-16 km	600 °C [1]	8 kbars [1]	800 °C [3]	12-13 kbars [3]

Data from Chapters 3 (Sutlej valley) and 6 (Radi klippe). [1] Vannay et al. (2004), [2] Davidson et al. (1997), [3] Daniel et al. (2003)

Although the relative timings of metamorphism (both prograde and retrograde) in the Haimanta Group/Chekha Formation, suggesting coeval burial and exhumation, are consistent with the channel flow model (Figure 4c, Jamieson et al., 2004), the absolute timings (apart from the age of peak *P*) are not (Table 7.1). There are two striking dissimilarities: i) the time between peak *P* and peak *T* for both G2 and G3 particle paths (~14 Ma) is *twice* that estimated for the Haimanta Group; ii) muscovite cooling ages are ~10 Ma younger in the channel flow model. With regards to this latter point, Jamieson et al. (2004) highlight that the published model 'HT1' represents a denudational end-member (and therefore overestimates exhumation and cooling rates), and suggests that strain localisation, not considered in the model, would efficiently extrude the GHS channel at lower rates of denudation. Kohn (2008, p.269), however, argues that such modifications to the model, wherein migmatitic channel rocks do not remain at high *T* for as long, are cooled earlier, and at further distances from the locus of focused surface denudation (towards which the channel flows) "may allow *T–t* histories to be matched, but is tantamount to shutting down channel flow altogether"! The discrepancy in the duration of peak metamorphism (i.e. between peak *P* and peak *T*) between model and empirical data will be reduced by decreasing the denudation rate in the model, but again, would the required restriction on channel flow essentially undermine it as a viable mechanism?

Co-existing models of Himalayan orogenesis e.g. critical taper (Kohn, 2008) and tectonic-wedging (Webb et al., 2007; Yin, 2006) do not predict the *P–T–t* evolution across the upper boundary of the exhumed mid-crustal wedge (see Section 1.2.3). In Kohn's (2008) schematic thermo-mechanical critical taper model there is the potential for normal faulting in the hinterland, yet this is placed at a lateral distance of ~250 km from the active thrust at the base of the wedge (Figure 3c, Kohn, 2008) and surely is not analogous to the STD observed in the field, at a lateral distance from the MCT between ~50 km (Sutlej valley) and ~150 km (Bhutan, between the MCT and *upper* STD)? This implies that the STD does not play a major role in the tectonic evolution of the Himalaya, in contrast with the concept of channel flow.

Mechanisms of STD formation, and by implication also of mid-crustal extrusion, may require further consideration of the STD's possible role in pre-Tertiary deformation. Clearly, pre-

Himalayan tectonics (e.g. Gehrels et al., 2006a; Gehrels et al., 2006b) should be dissociated (if at all possible!) from Himalayan events before testing model predictions. The kinematic evidence suggesting that the STD initiated as a S-directed thrust, and later evolved into an N-directed detachment (e.g. Burchfiel et al., 1992; Vannay and Hodges, 1996; Wyss et al., 1999), not only has implications for slip estimates along the fault, but also for the thermal evolution of the orogenic core in its hanging wall.

7.1.3 Correlatives of the Haimanta Group and Chekha Formation, and characterisation of the STD system

Correlative units of the Haimanta Group/Chekha Formation can be recognised in the central Himalaya (Table 7.3), herein called the South Tibetan Formations. In all bar one of these sections, a ductile shear zone (lower STD) marks the lower boundary, and a ductile–brittle fault (upper STD), the upper boundary. The one exception to this is in western Garhwal, where the Jhala Normal Fault is associated with only minor brittle–ductile faulting. However, it is suggested that the contact(s) with the augengneiss (that is "taken as the boundary between the GHS and the Harsil Formation" (p. 40, Prince, 1999)) may represent the lower ductile STD, much like the lower contact of the Akpa granite in the Sutlej valley does. The lower, ductile STD is associated with a major break in structural styles, whereas the predominantly brittle upper STD represents the main metamorphic break between the GHS (including the South Tibetan Formations; metamorphosed) and the TSS (unmetamorphosed), and can be recognised as so in the field (see source references in Table 7.3). The upper and lower STDs are comparable to the different types of channel boundary e.g. rheological and thermal (Grujic, 2006). Both Cambrian and Miocene granite plutons intrude the metasediments of the South Tibetan Formations. The Leo Pargil dome may be analogous to the Chako dome (Chapter 5). All age data from the lower STD shear zone to date indicate that normal motion on this structure was coeval with Early Miocene decompression of the GHS (following peak metamorphism, known as the 'M2' or 'Neohimalayan' high–*T* phase, Table 7.1; Gleeson and Godin, 2006), including the intrusion of Miocene granites such as the Manaslu leucogranite (Table 7.3). All available ages of motion on the upper STD fault are consistent with initiation immediately following cessation of movement on the ductile STD below, which continued from the ductile

Table 7.3 STD hanging wall stratigraphy in regions studied and correlative units and structures (from right to left, western to eastern Himalaya)

	Sutlej valley, NW India E78° 30'	Garhwal (Gangotri), NW India E78° 45'	Nar valley, central Nepal E84° 15'	Everest, Nepal E87° 00'	E Bhutan E91° 40'
TSS					
Upper STD (ductile-brittle)	N and W flanks of Leo Pargil dome?	Malari Fault	Phu detachment (<19 Ma)	Qomolangma detachment (16 Ma)	Upper STD*/Gonto La detachment (12-8 Ma)
metasediments	Haimanta Group	Harsil Formation	Upper GHS	Everest Series (or North Col Formation)	Chekha Formation
domal structure	Leo Pargil dome	-	Chako dome	-	-
granite	Akpa gr. (488 Ma)	Bhairongathi gr. (assumed Cambrian)	Manaslu leucogranite (24-19 Ma)	-	-
Lower STD (ductile)	Sangla detachment (~23-16 Ma)	(Jhala Normal Fault)	Chame detachment (24-18 Ma)	Lhotse detachment (18-17 Ma)	Lower STD (~11<24 Ma)
GHS	Vaikrita Group	GHS	Lower GHS	GHS	Lower GHS
source	this study, Chapters 3 and 5	Foster et al. (2000), Prince (1999)	Gleeson and Godin (2006)	Searle et al. (2003, 2006)	this study, Chapter 6

TSS, Tethyan Sedimentary Series; GHS, Greater Himalayan Sequence; STD, South Tibetan detachment

* the upper STD has been mapped in the Lingshi Basin and Tang Chu klippe, as a ductile fault between the Chekha Formationa and TSS, although no details are presented in the text (Figure 1 in Hollister and Grujic, 2006).

(~mid-crustal) into the brittle (upper crustal) regime. Although age data are limited, motion on the upper (and possibly also lower) STD appears to young towards the east. Nevertheless, this could reflect the exhumation of deeper sections of the GHS in the east, e.g. Cottle et al. (2007b) document the younging of metamorphism, magmatism and deformation down the tectonic-transport direction (i.e. northwards), by 5 to 7 Myr. Further evidence supporting the inference that deeper crustal material is exposed in the eastern Himalaya, is the juxtaposition of the Indus–Tsangpo Suture east of the eastern syntaxis (Namche Barwa) against the MCT (Yin, 2006).

Both north- and south-vergent structures have been recorded across the lower ductile STD in the western Himalaya (e.g. Vannay and Hodges, 1996; Wyss et al., 1999), central (Nepalese) Himalaya (Figure 5 in Gleeson and Godin, 2006), and eastern Himalaya (Bhutan, Chapter 6), and less commonly from the upper ductile–brittle STD (SE Tibet, Burchfiel et al., 1992). The significance and timing of early (ductile) south-directed thrusting on the STD requires further investigation. Does it represent early Palaeozoic tectonism (see above) or does it form an integral part of the early evolution of Himalayan orogenesis? Is there unequivocal evidence for early and persistent normal movement, or is there more evidence for alternating north–south motion, lending weight to the tectonic-wedging model (e.g. Webb et al., 2007)?

The upper–lower STD relationship described above represents one of several styles of the STD system (representing the system observed across one transect, rather than the system of all STD-related faults across the length of the orogen). Cottle et al. (2007a) document another style in the Dzakaa Chu valley, Tibet (45 km NE of the Everest region), where the STD equates to a ~1 km thick zone of distributed ductile shear, with similarly distributed late-stage, steeply dipping brittle features. The lack of a discrete detachment fault considered capable of accommodating large amounts of brittle displacement is a distinguishing feature of this STD system. Without positive identification of an upper, predominantly brittle STD in the Sutlej valley (rather, only the presence of steeply-dipping minor normal brittle faults distributed north of Morang, Fig. 3.1) this transect is perhaps more reminiscent of the Dzakaa Chu valley transect, where in the Sutlej valley the rheological contrast between the Akpa granite and the metasediments preferentially partitioned

strain (generating a discrete ductile shear zone), for which there is apparently no comparable rheological (lithological) contrast in the Dzakaa Chu valley.

The more commonly recognised contact between the GHS (gneiss/migmatite) and TSS (typically unmetamorphosed sediments, at most, greenschist-grade) is predominantly brittle, and with no intermediary unit (i.e South Tibetan Formations), e.g. the Malari Fault (Saraswati and Dhauli valleys, Garhwal Himalaya; Prince, 1999), and the Bhote Kosi and Nyalam detachments in the Nepalese Himalaya (Burchfiel et al., 1992). Thus, the South Tibetan Formations may be truly discontinuous along-strike, or simply excised by discrete brittle (STD) faulting in some places. Alternatively, South Tibetan Formations have been overlooked. For example, Gleeson and Godin (2006, p.730) state that "detailed mapping indicates that similar ['intermediate' i.e. South Tibetan Formations] units do not outcrop in the Langtang region...or in the Shisha Pangma area...(Inger and Harris, 1992; Reddy et al., 1993; Searle et al., 1997).", yet:

i) the trace of the STD in Inger and Harris (Langtang Normal Fault in Figures 1 and 2, 1992) is disputed by Searle et al. (1997, p. 300);

ii) Reddy et al. (1993) a) only *infer* the location of the STD (in their Figure 1); b) suggest decoupling of units in the mid–upper GHS in the Langtang valley and interpret the contact as tectonic and associated with S-directed thrusting (their p. 386). However, "a detailed structural investigation" was specifically *precluded* in this area, and thus this tectonic contact *could* be comparable to the (N-directed) lower ductile STD;

iii) Searle et al. (1997, p.300) map a thin (~200 m) *layer of pelites* and calc-silicate marbles *bounded by two discrete detachments*, above the 'classic' sillimanite-grade gneisses and leucogranite in the STD footwall (their Figures 4 and 5).

Still, three styles or modes of the STD system's evolution are recognised: i) two discrete STDs, including a lower ductile STD and an upper ductile–brittle STD which bound the South Tibetan Formations and includes Cambrian and/or Miocene granites and possible GHS-domes (Table 7.3); ii) one diffuse (< 1 km thick) ductile STD shear zone (e.g. Dzakaa Chu, Cottle et al., 2007a); iii) one predominantly brittle STD fault (e.g. Bhote Kosi and Nyalam detachments,

Burchfiel et al., 1992). Variations in the type of STD system along strike of the orogen are likely to have been caused by regional heterogeneities localising strain, both lithological e.g. granite intrusions, and structural, e.g. the Cambro–Ordovician unconformity in the TSS (e.g. Wiesmayr and Grasemann, 2002 and references therein). This unconformity may represent the upper ductile–brittle STD in some transects, but be unrecognisable as such owing to tectonism. The variable partitioning of strain between different lithologies (e.g. pelitic versus psammitic) is also inevitable, and the foreseeable result is different STD system styles, despite the same underlying tectonic cause(s).

7.1.4 Tectonic significance of the STD

As aforementioned, the STD was potentially an active structure in pre-Himalayan tectonics, and may not be the major Himalayan fault we commonly hold it to be. We need a better understanding of the evolution of the STD, ductile and brittle, and to reconcile the timing of south- and north-directed shearing upon it to address this issue. These data will also inform models in which the STD is considered to be a passive roof fault, in which hanging wall rocks (TSS) are 'fixed' relative to the extruding footwall rocks (GHS) (Cottle et al., 2007a and references therein; Vanderhaeghe and Teyssier, 2001). In the Nar valley, the lower ductile Chame detachment represents this passive roof fault, but the upper, younger brittle Phu detachment may be linked to 'true' extension, associated with far-field critical taper adjustments (Godin et al., 2006a). Note that some late-stage brittle STD deformation may be attributable to late-stage large-amplitude buckling of the GHS (e.g. Godin et al., 2006a; see Chapter 5).

7.2 Comparison of mid-crustal extrusion in the Sutlej valley and Bhutan

Although tectonic processes are comparable in the young Himalayan orogen (i.e. Late Eocene–Oligocene prograde metamorphism of the basal TSS and GHS, and Early Miocene exhumation/extrusion coupled to motion on the MCT and STD), the mid-Miocene marks an apparent change in tectonics. In the Sutlej valley the locus of mid-crustal exhumation jumped towards the foreland (to exhume the Jutogh Group/LHCS, Chapter 2), whereas in Bhutan exhumation propogated towards the hinterland (to exhume the KT hanging wall, upper GHS,

Chapter 6). With current two-dimensional tectonic models of Himalayan orogenesis (e.g. channel flow) this is an intriguing observation to incorporate. The following large-scale processes are certainly temporally associated with this mid-Miocene tectonic transition, but as yet it is unclear if and how they may have influenced Himalayan tectonics to produce the east–west lateral variation now observed in the exhumed mid-crust:

- lateral sub-surface heterogeneity, including i) steep versus shallow subduction of the Indian plate, and 'slab-tear' (e.g. Xiao et al., 2007) and ii) rapid large-scale removal of the lithosphere between 8 and 12 Ma (Jimenez-Munt et al., 2008);
- movement on the Karakoram fault (a large-scale right-lateral strike-slip fault that extends at least 750 km from the Pamirs in the NW to the Kailas region of SW Tibet in the SE) with ductile shearing between 15.68 ± 0.52 Ma and 13.73 ± 0.28 Ma (Searle and Phillips, 2007).

7.3 Future modelling of the thermal evolution of the mid-crust of the Himalayan orogen

The following points are essential for future modelling of Himalayan tectonics. The list complements those in Hodges (2006), Harrison (2006) and Yin (2006), and is by no means exhaustive:

- The determination of precise *P–T–t–d* paths and not just 'peak metamorphic' conditions, as the timing between peak *P* and peak *T* may prove to be diagnostic (*in situ* age data must have a textural, and preferably chemical, context); *P–T–t* path topology also remains an invaluable record of the tectono-thermal history of the rock, and may be used to infer tectonic discontinuities between rock packages with different *P–T–t* paths, especially where structures in the field (e.g. late-stage brittle deformation) are complex and obscure tectonic relationships.
- Consideration and testing of models other than channel flow (e.g. critical taper, Kohn, 2008; tectonic-wedge, Webb et al., 2007). The channel flow model has been widely considered by a broad earth science community (e.g. from petrologists to geophysicists), thus presenting challenges to a variety of disciplines. Harrison (2006) summarised the main disagreements with the channel flow model, e.g. the lack of Asian material found in the exhumed GHS, and the

stratigraphic continuity of the GHS along strike of the orogen. In response these are dispelled by Jamieson et al. (2006), and the model continues to be developed and honed. Future models can only benefit from an integrated approach which critically assesses model predictions.

- When did India and Asia collide (Aitchison et al., 2007; Garzanti, 2008)? The answer has obvious implications for estimates of how much material has been underthrust, and for the thermal evolution of the orogen ('how long have the rocks been 'cooking' for?').

- The tectonic-wedging model (Webb et al., 2007; Yin, 2006) contrasts with current models for the evolution of the Himalaya, in that the STD and MCT merge upwards towards the south, in contrast with the commonly held belief that they merge at depth towards the north. With such a unique requirement surely higher-resolution imaging of the sub-surface structure, in addition to further (at-surface) structural evidence will propel or dispel this model efficiently.

7.4 Conclusions

- The Haimanta Group and Chekha Formation, separated by ~1000 km, are correlative units (with comparable structural styles, positions within the tectonic architecture of the orogen and *P–T–t* paths) as a result of a common Eocene–Early Miocene tectono-thermal process in the early evolution of the Himalayan orogen. Both units are juxtaposed against sillimanite-gneisses and migmatites of the GHS beneath, across the STD, a ductile N-directed shear zone (< 2 km), which is considered analogous to the model "STD" in the channel flow model (Jamieson et al., 2004).

- *P–T* gradients across the STD in the Sutlej valley (inc. Haimanta Group) and Bhutan (inc. Chekha Formation) are steeper than those predicted by the channel flow model (Jamieson et al., 2004), although ductile flattening, which is shown to have affected the Haimanta Group but is not incorporated into the model, would create an artificially steeper *P–T* gradient.

- The coeval burial and exhumation of the Haimanta Group/Chekha Formation and the GHS is consistent with channel flow model results, but the time elapsed between peak *P* and peak *T* is significantly overestimated by the model, and muscovite cooling ages are ~ 10 Myr too late

compared to the empirical data. Lower denudation rates in the channel flow model yield more accurate results but potentially undermine the validity of the channel flow mechanism.

- *P–T–t* model results are required from contesting tectonic models, including critical taper (e.g. Kohn, 2008) and tectonic-wedging (e.g. Webb et al., 2007).
- Effects of pre-Himalayan metamorphism and deformation (e.g. Gehrels et al., 2006a) need to be dissociated from *P–T*–deformation data used to assess the mechanism and role of the STD in the Cenozoic evolution of the orogen.
- In Himalayan regions between the Sutlej valley and Bhutan, correlative metasedimentary units to the Haimanta Group/Chekha Formation can be found, and are collectively termed the South Tibetan Formations. They, along with Cambrian and/or Miocene granites, are bounded by a discrete ductile shear zone (lower STD) below, and a discrete ductile–brittle fault (upper STD) above. Ductile STD motion is constrained to the Miocene and youngs towards the eastern Himalaya, which may just reflect the exhumation of deeper mid-crustal rocks.
- Other STD system styles include a ~ 1 km thick zone of distributed ductile shear (i.e. no discrete faults, or major brittle deformation), and a discrete brittle fault which juxtaposes sillimanite gneisses of the GHS directly against unmetamorphosed Tethyan sediments.
- The mid-Miocene saw a transition in the locus of mid-crustal extrusion, which propagated towards the foreland (southwards) in the Sutlej valley and towards the hinterland (northwards) in Bhutan. This difference in tectonic evolution is yet to be incorporated into a three-dimensional tectonic model of the Himalaya. Processes initiated or active in the mid-Miocene (e.g. slab tear, large-scale removal of the lithosphere, movement on the Karakoram Fault) may have been influential.

Chapter 8

Summary of conclusions

This chapter summarises the principal results of this thesis, as described in detail in Chapters 2 to 7.

8.1 Sutlej valley (Chapters 2, 3 and 5)

- Uraninite grains from deformed leucogranites in the Jutogh Group yielded Proterozoic U–Pb crystallization ages, attesting to a crustal melting event in these rocks at c. 1810 Ma. This date also confirms the LHS affinity of the Jutogh Group, despite superficial similarities to the GHS metasediments of the Vaikrita Group.

- U–Pb systematics of the same uraninite grains record a Tertiary overprint at 10.5 ± 1.1 Ma during the Himalayan orogeny, constraining late Miocene metamorphism of this LHS section.

- The Haimanta Group, at the base of the Tethyan sediments and structurally above the GHS, record a history of burial and heating to 610–620 °C and c. 7–8 kbars, at c. 30 Ma. Subsequent decompression was accompanied by further heating to a peak T of <660 °C, the development of a pervasive crenulation cleavage, and the growth of staurolite and kyanite porphyroblasts. Cooling was accompanied by further decompression, and by c. 13 Ma the Haimanta Group had reached a temperature between 300 and 350 °C at c. 2 kbars.

- The Jutogh Group, the Vaikrita Group (GHS) and the Haimanta Group each have a distinct P–T–t path; taken together these indicate a complex tectono-thermal evolution of the mid-crust of the Himalaya in NW India, summarised as follows:

  - Prograde metamorphism of the GHS and Haimanta Group during the Eocene–Early Oligocene;

  - In the Late Oligocene, whilst the Haimanta Group underwent decompression (at c. 1.3 mm yr^{-1}) during continued heating, the underlying GHS saw either further burial and heating (under the STD 'thrust') or isobaric heating prior to its exhumation;

- Coeval thrust movement on the MCT and extension on the STD in the Early Miocene facilitated rapid exhumation (and isothermal decompression) of the GHS (at 2–4 mm yr^{-1}), compared to the Haimanta Group; and the Jutogh Group, overthrust by the GHS along the MCT, was buried and metamorphosed.
- During the mid-Miocene the Haimanta Group and GHS were re-coupled at the brittle–ductile transition and exhumed together, in line with cessation of movement on the MCT and STD. Rates of exhumation for the GHS and Haimanta Group slowed to c. 0.6 mm yr^{-1}. The Jutogh Group, meanwhile, experienced isobaric heating indicative of thermal relaxation post- (MCT) thrusting.
- From the Late Miocene, thrusting propagated towards the foreland of the orogen, and the Jutogh Group was rapidly exhumed (at ~2.3 mm yr^{-1}). Decoupled exhumation of the GHS and Jutogh Group at this time is not consistent with current channel flow models (Jamieson et al., 2004), but may be reconciled with a southward (foreland-directed) migration of the locus of focused surface denudation in the mid-Miocene.

8.2 Sm–Nd garnet geochronology (Chapter 4)

- The treatment of garnet separates with H_2SO_4 preferentially leaches the phosphate monazite, confirming earlier work of Anczkiewicz and Thirlwall (2003).
- Duplicate analyses will always yield the most robust age determinations.
- Low Sm/Nd values indicate the presence of Nd-rich inclusions, and multiple analyses provide information on the nature of them (e.g. age, Nd concentration).
- If Nd-rich inclusions are not completely removed from the garnet separate, but are the same age as the garnet, then the isochron will still yield an accurate age; but if they are *not* the same age as the garnet, then the age will be erroneous.
- In both the above cases the age will also be rendered imprecise, because the Sm/Nd ratio of the contaminated garnet separate will be much lower than that of the pure garnet.

- If an *in-situ* garnet analysis is contaminated by LREE-rich inclusions such as monazite, allanite or apatite, then they will dominate the LREE budget; in contrast, ilmenite and zircon inclusions have negligible effect on the concentrations of the LREE Sm and Nd.
- There are inherent problems in dating Ca-rich rocks (i.e. those with Ca-accessory phases such as apatite and allanite) using Sm–Nd garnet geochronology.

8.3 Bhutan (Chapter 6)

- Monazite in the Chekha Formation formed during prograde metamorphism from the breakdown of allanite and apatite at >580 °C.
- Peak metamorphism occurred at ~ 22 Ma in the Chekha Formation and ~24 Ma in the underlying GHS.
- Estimated exhumation rates for the GHS are comparable to or lower than other estimates of GHS exhumation in other Himalayan regions (2.2–1.7 mm yr^{-1}, cf. 2–4 mm yr^{-1}), while calculated exhumation rates for the Chekha Formation are faster (2.5–1.8 mm yr^{-1}), although further analysis of the *P–T–t* paths for both units is required to corroborate this.
- Data are consistent with but do not prove that pulsed channel flow (Hollister and Grujic, 2006) was active in Bhutan during the Miocene.

8.4 Comparison of data from the Sutlej valley and Bhutan, with model results for the tectono-thermal evolution of the Himalaya (Chapter 7)

- The Haimanta Group (Sutlej valley), Chekha Formation (Bhutan) and correlative metasedimentary units in Garhwal and Nepal, bounded by discrete faults (a lower shear zone and an upper ductile–brittle fault) associated with the STD system, are collectively termed the South Tibetan formations. Comparable metamorphism and deformation in these rocks is the result of a common Eocene–Early Miocene tectono-thermal process.
- Other transects across the STD are either characterised by distributed ductile shear only, or a discrete major brittle fault.

- *P–T* gradients across the STD in the Sutlej valley and Bhutan are steeper than those predicted by the channel flow model (Jamieson et al., 2004), but may be an artefact of ductile flattening across the section.
- A channel flow model with lower denudation rates than HT1 (Jamieson et al., 2004) is required to yield results comparable to empirical data collected in the Himalaya. This may undermine the validity of the channel flow mechanism.
- To accurately quantify Himalayan processes, pre-Himalayan (e.g. early Palaeozoic) metamorphism and deformation must be isolated from that resulting from the Himalayan orogeny.
- In the mid-Miocene the locus of mid-crustal extrusion shifted towards the foreland in the Sutlej valley and towards the hinterland in Bhutan. These different tectonic responses, yet to be incorporated into models of Himalayan orogenesis, may have been the result of large-scale, laterally heterogeneous sub-surface processes.

References

Ahmad, T., Harris, N., Bickle, M., Chapman, H., Bunbury, J. and Prince, C., 2000. Isotopic constraints on the structural relationships between the Lesser Himalayan Series and the High Himalayan Crystalline Series, Garhwal Himalaya. Geological Society of America Bulletin 112, 467-477.

Aitchison, J.C., Ali, J.R. and Davis, A.M., 2007. When and where did India and Asia collide? Journal of Geophysical Research-Solid Earth 112.

Alsdorf, D., Brown, L., Nelson, K.D., Makovsky, Y., Klemperer, S. and Zhao, W.J., 1998. Crustal deformation of the Lhasa terrane, Tibet plateau from Project INDEPTH deep seismic reflection profiles. Tectonics 17, 501-519.

Amato, J.M., Johnson, C.M., Baumgartner, L.P. and Beard, B.L., 1999. Rapid exhumation of the Zermatt-Saas ophiolite deduced from high-precision Sm-Nd and Rb-Sr geochronology. Earth and Planetary Science Letters 171, 425-438.

Amelin, Y., 2004. Sm-Nd systematics of zircon. Chemical Geology 211, 375-387.

Anczkiewicz, R., Platt, J.P. and Thirlwall, M.F., 2007. Behaviour of the Sm-Nd and Lu-Hf geochronometers in garnet during HT and UHT metamorphism. Geochimica et Cosmochimica Acta 71, A25-A25.

Anczkiewicz, R. and Thirlwall, M., 2003. Improving precision of Sm-Nd garnet dating by H_2SO_4 leaching - a simple solution to the phosphate inclusion problem. In: D. Vance, W. Mueller and I.M. Villa (Editors), Geochronology: Linking the Isotopic Record with Petrology and Textures. Special Publication Geological Society of London, London, pp. 83-91.

Anczkiewicz, R., Platt, J.P., Thirlwall, M.F. and Wakabayashi, J., 2004. Franciscan subduction off to a slow start: evidence from high-precision Lu-Hf garnet ages on high grade-blocks. Earth and Planetary Science Letters 225, 147-161.

Argles, T.W., Platt, J.P. and Waters, D.J., 1999. Attenuation and Excision of a Crustal Section During Extensional Exhumation: The Carratraca Massif, Betic Cordillera, Southern Spain. Journal of the Geological Society, London 156, 149-162.

Argles, T.W., Prince, C.I., Foster, G.L. and Vance, D., 1999. New garnets for old? Cautionary tales from young mountain belts. Earth and Planetary Science Letters 172, 301-309.

Arita, K., 1983. Origin of inverted metamorphism in the lower Himalaya, Central Himalaya. Tectonophysics 95, 43-60.

Ayres, M. and Harris, N., 1997. REE fractionation and Nd-isotope disequilibrium during crustal anatexis: Constraints from Himalayan leucogranites. Chemical Geology 139, 249-269.

Ayres, M., Harris, N. and Vance, D., 1997. Possible constraints on anatectic melt residence times from accessory mineral dissolution rates: An example from Himalayan leucogranites. Mineralogical Magazine 61, 29-36.

Baxter, E.F., Ague, J.J. and DePaolo, D.J., 2002. Prograde temperature-time evolution in the Barrovian type-locality constrained by Sm/Nd garnet ages from Glen Clova, Scotland. Journal of the Geological Society 159, 71-82.

Bea, F., 1996. Residence of REE, Y, Th and U in granites and crustal protoliths; Implications for the chemistry of crustal melts. Journal of Petrology 37, 521-552.

Beaumont, C., Jamieson, R.A., Nguyen, M.H. and Lee, B., 2001. Himalayan tectonics explained by extrusion of a low-viscosity crustal channel coupled to focused surface denudation. Nature 414, 738-742.

Beaumont, C., Jamieson, R.A., Nguyen, M.H. and Medvedev, S., 2004. Crustal channel flows: 1. Numerical models with applications to the tectonics of the Himalayan-Tibetan orogen. Journal of Geophysical Research-Solid Earth 109, doi:10.1029/2003JB002809.

Bettinelli, P., Avouac, J.P., Flouzat, M., Jouanne, F., Bollinger, L., Willis, P. and Chitrakar, G.R., 2006. Plate motion of India and interseismic strain in the Nepal Himalaya from GPS and DORIS measurements. Journal of Geodesy 80, 567-589.

Bhargava, O.N. (Editor), 1995. The Bhutan Himalaya: a geological account. Geological Survey of India Special Publication, 39. Geological Survey of India, Calcutta, 245 pp.

Bhattacharya, A., Mohanty, L., Maji, A., Sen, S.K. and Raith, M., 1992. Non-ideal mixing in the phlogopite-annite boundary: constraints from experimental data on Fe-Mg partitioning and a reformulation of the biotite-garnet geothermometer. Contributions to Mineralogy and Petrology 111, 87-93.

Blichert-Toft, J. and Frei, R., 2001. Complex Sm-Nd and Lu-Hf isotope systematics in metamorphic garnets from the Isua supracrustal belt, West Greenland. Geochimica et Cosmochimica Acta 65, 3177-3189.

Bollinger, L. and Janots, E., 2006. Evidence for Mio-Pliocene retrograde monazite in the Lesser Himalaya, far western Nepal. European Journal of Mineralogy 18, 289–297.

Bollinger, L., Henry, P. and Avouac, J.P., 2006. Mountain building in the Nepal Himalaya: Thermal and kinematic model. Earth and Planetary Science Letters, 244(1-2): 58-71.

Bowtell, S.A., Cliff, R.A. and Barnicoat, A.C., 1994. Sm-Nd Isotopic Evidence on the Age of Eclogitization in the Zermatt-Saas Ophiolite. Journal of Metamorphic Geology 12, 187-196.

Brown, R.L. and Gibson, H.D., 2006. An argument for channel flow in the southern Canadian Cordillera and comparison with Himalayan tectonics. In: R.D. Law, M.P. Searle and L. Godin (Editors), Channel Flow, Ductile Extrusion and Exhumation in Continental Collision Zones. Geological Society, London, Special Publications, pp. 543-559.

Burchfiel, B.C., Chen, B., Hodges, K.V., Yuping, L., Royden, L.H., Changrong, D. and Jiene, X., 1992. The South Tibetan detachment system, Himalayan orogen: Extension contemporaneous with and parallel to shortening in a collisional mountain belt. Geological Society of America Special Paper 269, 1-41.

Burg, J.P., Brunel, M., Gapais, D., Chen, G.M. and Liu, G.H., 1984. Deformation of Leucogranites of the Crystalline Main Central Sheet in Southern Tibet (China). Journal of Structural Geology 6, 535-542.

Caddick, M., 2004. The Tectonometamorphic Evolution of the Central and Western Himalaya. PhD Thesis, Cambridge University.

Caddick, M.J., Bickle, M.J., Harris, N.B.W., Holland, T.J.B., Horstwood, M.S.A., Parrish, R.R. and Ahmad, T., 2007. Burial and exhumation history of a Lesser Himalayan schist: Recording the formation of an inverted metamorphic sequence in NW India. Earth and Planetary Science Letters 264, 375-390.

Caddick, M., Bickle, M., Harris, N. and Parrish, R., 2006. Contrasting depth-temperature-time histories of the High and Lesser Himalaya of NW India. Journal of Asian Earth Sciences 26, 129.

Caddick, M.J. and Thompson, A.B., 2008. Quantifying the tectono-metamorphic evolution of pelitic rocks from a wide range of tectonic settings: Mineral compositions in equilibrium. Contributions to Mineralogy and Petrology DOI 10.1007/s00410-008-0280-6.

Caro, G., Bourdon, B., Birck, J.-L. and Moorbath, S., 2006. High-precision 142Nd/144Nd measurements in terrestrial rocks: Constraints on the early differentiation of the Earth's mantle. Geochimica et Cosmochimica Acta 70, 164-191.

Carosi, R., Montomoli, C., Rubatto, D. and Visona, D., 2006. Normal-sense shear zones in the core of the Higher Himalayan Crystallines (Bhutan Himalaya). In: R.D. Law, M.P. Searle and L. Godin (Editors), Channel Flow, Ductile Extrusion and Exhumation in Continental Collision Zones. Geological Society, London, Special Publications, pp. 425-444.

Catlos, E.J., Gilley, L.D. and Harrison, T.M., 2002. Interpretation of monazite ages obtained via in situ analysis. Chemical Geology 188, 193-215.

Catlos, E.J., Harrison, T.M., Kohn, M.J., Grove, M., Ryerson, F.J., Manning, C.E. and Upreti, B.N., 2001. Geochronologic and thermobarometric constraints on the evolution of the Main Central Thrust, central Nepal Himalaya. Journal of Geophysical Research-Solid Earth 106, 16177-16204.

Chambers, J.A., Argles, T., Horstwood, M., Harris, N., Parrish, R. and Ahmad, T., 2008. Tectonic implications of Palaeoproterozoic anatexis and Late Miocene metamorphism in the Lesser Himalayan Sequence, Sutlej Valley, NW India. Journal of the Geological Society, London 165, 725-737.

Chambers, J.A., Caddick, M., Argles, T., Horstwood, M., Sherlock, S., Harris, N., Parrish, R. and Ahmad, T., *in review*. Empirical constraints on extrusion mechanisms from the upper margin of an exhumed high-grade orogenic core, Sutlej Valley, NW India. Tectonophysics.

Christensen, J.N., Rosenfeld, J.L. and Depaolo, D.J., 1989. Rates of Tectonometamorphic Processes from Rubidium and Strontium Isotopes in Garnet. Science 244, 1465-1469.

Clark, M.K. and Royden, L.H., 2000. Topographic ooze: Building the eastern margin of Tibet by lower crustal flow. Geology 28, 703-706.

Coggon, R. and Holland, T.J.B., 2002. Mixing properties of phengitic micas and revised garnet-phengite thermobarometers. Journal of Metamorphic Geology 20, 683-696.

Cohen, A.S., O'Nions, R.K., Siegenthaler, R. and Griffin, W.L., 1988. Chronology of the Pressure-Temperature History Recorded by a Granulite Terrain. Contributions to Mineralogy and Petrology 98, 303-311.

Coleman, M.E. and Hodges, K.V., 1998. Contrasting Oligocene and Miocene thermal histories from the hanging wall and footwall of the South Tibetan detachment in the central Himalaya from Ar-40/Ar-39 thermochronology, Marsyandi Valley, central Nepal. Tectonics 17, 726-740.

Connolly, J.A.D., 1990. Multivariable phase diagrams: an algorithm based on generalized thermodynamics. American Journal of Science 290, 666-718.

Connolly, J.A.D., 2005. Computation of phase equilibria by linear programming: A tool for geodynamic modeling and its application to subduction zone decarbonation. Earth and Planetary Science Letters 236, 524-541.

Connelly, J.N., 2006. Improved dissolution and chemical separation methods for Lu-Hf garnet chronometry. Geochemistry Geophysics Geosystems 7.

Corrie, S.L. and Kohn, M.J., 2008. Trace-element distributions in silicates during prograde metamorphic reactions: implications for monazite formation. Journal of Metamorphic Geology 26, 451-464.

Cottle, J.M., Jessup, M.J., Newell, D.L., Searle, M.P., Law, R.D. and Horstwood, M.S.A., 2007a. Structural insights into the early stages of exhumation along an orogen-scale detachment: The South Tibetan Detachment System, Dzakaa Chu section, Eastern Himalaya. Journal of Structural Geology 29, 1781-1797.

Cottle, J.M., Searle, M.P., Horstwood, M., Waters, D.J., Noble, S.R. and Parrish, R., 2007b. U(-Th)-Pb age constraints on the timing and duration of channel flow in the Mt. Everest region, eastern Himalaya, Eos Transactions, AGU 88(52), Fall Meeting Supplement, Abstract T34C-06.

Dahlen, F.A., 1990. Critical Taper Model of Fold-and-Thrust Belts and Accretionary Wedges. Annual Review of Earth and Planetary Sciences 18, 55-99.

Daniel, C.G., Hollister, L.S., Parrish, R.R. and Grujic, D., 2003. Exhumation of the Main Central Thrust from lower crustal depths, Eastern Bhutan Himalaya. Journal of Metamorphic Geology 21, 317-334.

Dasgupta, S., 1995. Jaishidanda Formation. In: O.N. Bhargava (Editor), The Bhutan Himalaya: a geological account. Geological Survey of India Special Publication. Geological Survey of India Special Publication, pp. 79-88.

Davidson, C., Grujic, D.E., Hollister, L.S. and Schmid, S.M., 1997. Metamorphic reactions related to decompression and synkinematic intrusion of leucogranite, High Himalayan Crystallines, Bhutan. Journal of Metamorphic Geology 15, 593-612.

Debon, F., Le Fort, P., Sheppard, S.M.F. and Sonet, J., 1986. The Four Plutonic Belts of the Transhimalaya-Himalaya: a chemical, mineralogical, isotopic, and chronologic synthesis along a Tibet-Nepal section. Journal of Petrology 27, 219-250.

DeCelles, P.G., Gehrels, G.E., Quade, J., LaReau, B. and Spurlin, M., 2000. Tectonic implications of U-Pb zircon ages of the Himalayan orogenic belt in Nepal. Science 288, 497-499.

DeCelles, P.G., Robinson, D.M., Quade, J., Ojha, T.P., Garzione, C.N., Copeland, P. and Upreti, B.N., 2001. Stratigraphy, structure, and tectonic evolution of the Himalayan fold-thrust belt in western Nepal. Tectonics 20, 487-509.

DeWolf, C.P., Zeissler, C.J., Halliday, A.N., Mezger, K. and Essene, E.J., 1996. The role of inclusions in U-Pb and Sm-Nd garnet geochronology: Stepwise dissolution experiments and trace uranium mapping by fission track analysis. Geochimica et Cosmochimica Acta 60, 121-134.

Dickin, A.P., 2005. Radiogenic Isotope Geology. Cambridge University Press, Cambridge.

Dietrich, V. and Gansser, A., 1981. The leucogranites of Bhutan Himalaya. Schweizerische Mineralogische Und Petrographische Mitteilungen 61., 177-202.

Dodson, M.H., 1973. Closure temperature in cooling geochronological and petrological systems. Contributions to Mineralogy and Petrology 40, 259-274.

Edwards, M.A. and Harrison, T.M., 1997. When did the roof collapse? Late Miocene north-south extension in the high Himalaya revealed by Th-Pb monazite dating of the Khula Kangri granite. Geology 25, 543-546.

Edwards, M.A., Kidd, W.S.F., Li, J.X., Yu, Y.J. and Clark, M., 1996. Multi-stage development of the southern Tibet detachment system near Khula Kangri. New data from Gonto La. Tectonophysics 260, 1-19.

England, P.C. and Holland, T.J.B., 1979. Archimedes and the Tauern eclogites: The role of bouyancy in the preservation of exotic eclogite blocks. Earth and Planetary Science Letters 44, 287-294.

Ferry, J.M., 1984. A Biotite Isograd in South-Central Maine, U.S.A.: Mineral Reactions, Fluid Transfer, and Heat Transfer. Journal of Petrology 25, 871-893.

Ferry, J.M., 2000. Patterns of mineral occurrence in metamorphic rocks. American Mineralogist 85, 1573-1588.

Fitzsimons, I.C.W. and Harley, S.L., 1994. The Influence of Retrograde Cation Exchange on Granulite P-T Estimates and a Convergence Technique for the Recovery of Peak Metamorphic Conditions. Journal of Petrology 35, 543-576.

Foster, G., Gibson, H.D., Parrish, R., Horstwood, M., Fraser, J. and Tindle, A., 2002a. Textural, chemical and isotopic insights into the nature and behaviour of metamorphic monazite. Chemical Geology 191, 183-207.

Foster, G., Kinny, P., Vance, D., Prince, C. and Harris, N., 2000. The significance of monazite U-Th-Pb age data in metamorphic assemblages; a combined study of monazite and garnet chronometry. Earth and Planetary Science Letters 181, 327-340.

Foster, G., Parrish, R.R., Horstwood, M.S.A., Chenery, S., Pyle, J. and Gibson, H.D., 2004. The generation of prograde P-T-t points and paths; a textural, compositional, and chronological study of metamorphic monazite. Earth and Planetary Science Letters 228, 125-142.

Foster, G., Vance, D., Argles, T. and Harris, N., 2002b. The tertiary collision-related thermal history of the NW Himalaya. Journal of Metamorphic Geology 20, 827-843.

Fraser, G., Worley, B. and Sandiford, M., 2000. High-precision geothermobarometry across the High Himalayan metamorphic sequence, Langtang Valley, Nepal. Journal of Metamorphic Geology 18, 665-681.

Fraser, J.E., Searle, M.P., Parrish, R.R. and Noble, S.R., 2001. Chronology of deformation, metamorphism, and magmatism in the southern Karakoram Mountains. Geological Society of America Bulletin 113, 1443-1455.

Fuhrman, M.L. and Lindsley, D.H., 1988. Ternary feldspar modeling and thermometry. American Journal of Science 73, 201-215.

Gaetani, M. and Garzanti, E., 1991. Multicyclic History of the Northern India Continental-Margin (Northwestern Himalaya). Aapg Bulletin-American Association of Petroleum Geologists 75, 1427-1446.

Ganguly, J., Tirone, M. and Hervig, R.L., 1998. Diffusion kinetics of samarium and neodymium in garnet, and a method for determining cooling rates of rocks. Science 281, 805-807.

Gansser, A., 1964. Geology of the Himalayas. Regional Geology. Wiley Interscience, London-New York-Sydney, 289 pp.

Gansser, A., 1983. Geology of the Bhutan Himalaya. Birkhauser Boston, 180 pp.

Garzanti, E., 2008. Comment on "When and where did India and Asia collide?" by Jonathan C. Aitchison, Jason R. Ali, and Aileen M. Davis. Journal of Geophysical Research-Solid Earth 113.

Gehrels, G.E., DeCelles, P., Martin, A.J., Ojha, T. and Pinhassi, G., 2003. Initiation of the Himalayan Orogen as an Early Palaeozoic Thin-skinned Thrust belt. Geological Society of America Today 13, 4-9.

Gehrels, G.E., DeCelles, P.G., Ojha, T.P. and Upreti, B.N., 2006a. Geologic and U-Pb geochronologic evidence for early Paleozoic tectonism in the Dadeldhura thrust sheet, far-west Nepal Himalaya. Journal of Asian Earth Sciences 28, 385-408.

Gehrels, G.E., DeCelles, P.G., Ojha, T.P. and Upreti, B.N., 2006b. Geologic and U-Th-Pb geochronologic evidence for early Paleozoic tectonism in the Kathmandu thrust sheet, central Nepal Himalaya. Geological Society of America Bulletin 118, 185-198.

Gehrels, G. E., Valencia, V. A., and Ruiz, J., 2008, Enhanced precision, accuracy, efficiency, and spatial resolution of U-Pb ages by laser ablation-multicollector-inductively coupled plasma-mass spectrometry: Geochemistry Geophysics Geosystems, v. 9.

Gleeson, T.P. and Godin, L., 2006. The Chako antiform: A folded segment of the Greater Himalayan sequence, Nar Valley, Central Nepal Himalaya. Journal of Asian Earth Sciences 27, 717-734.

Godin, L., 2003. Structural evolution of the Tethyan sedimentary sequence in the Annapurna area, central Nepal Himalaya. Journal of Asian Earth Sciences 22, 307-328.

Godin, L., Brown, R.L., Hanmer, S. and Parrish, R., 1999. Back folds in the core of the Himalayan orogen: An alternative interpretation. Geology 27, 151-154.

Godin, L., Gleeson, T.P., Searle, M.P., Ullrich, T.D. and Parrish, R.R., 2006a. Locking of southward extrusion in favour of rapid crustal-scale buckling of the Greater Himalayan sequence, Nar valley, central Nepal. In: R.D. Law, M.P. Searle and L. Godin (Editors), Channel Flow, Ductile Extrusion and Exhumation in Continental Collision Zones. Geological Society, London, Special Publications, pp. 269-292.

Godin, L., Grujic, D., Law, R.D. and Searle, M.P., 2006b. Channel flow, extrusion, and exhumation in continental collision zones: an introduction. In: R.D. Law, M.P. Searle and L. Godin (Editors), Channel Flow, Ductile Extrusion and Exhumation in Continental Collision Zones. Geological Society, London, Special Publications, pp. 1-23.

Godin, L., Kellet, D. and Larson, K.P., 2007. Orogenic superstructure behaviour and mid-crustal plastic flow in the central Nepal Himalaya. Eos Transactions, AGU 88(52), Fall Meeting Supplement, Abstract T31D-0672.

Godin, L., Parrish, R.R., Brown, R.L. and Hodges, K.V., 2001. Crustal thickening leading to exhumation of the Himalayan Metamorphic core of central Nepal: Insight from U-Pb Geochronology and Ar-40/Ar-39 Thermochronology. Tectonics 20, 729-747.

Goscombe, B., Gray, D. and Hand, M., 2006. Crustal architecture of the Himalayan metamorphic front in eastern Nepal. Gondwana Research 10, 232-255.

Grasemann, B., Fritz, H. and Vannay, J.C., 1999. Quantitative kinematic flow analysis from the Main Central Thrust Zone (NW-Himalaya, India): implications for a decelerating strain path and the extrusion of orogenic wedges. Journal of Structural Geology 21, 837-853.

Grauch, R.I., 1989. Rare Earth Elements in Metamorphic Rocks. In: B.R. Lipin and G.A. McKay (Editors), Geochemistry and Mineralogy of Rare Earth Elements. Reviews in Mineralogy. Mineralogical Society of America, Washington D. C., pp. 147-167.

Gregory, C.J., Rubatto, D., Allen, C.M., Williams, I.S., Hermann, J. and Ireland, T., 2007. Allanite micro-geochronology: A LA-ICP-MS and SHRIMP U–Th–Pb study. Chemical Geology 245, 162-182.

Grujic, D., 2006. Channel flow and continental collision tectonics: an overview. In: R.D. Law, M.P. Searle and L. Godin (Editors), Channel Flow, Ductile Extrusion and Exhumation in Continental Collision Zones. Geological Society, London, Special Publications, pp. 25-37.

Grujic, D., Casey, M., Davidson, C., Hollister, L.S., Kundig, R., Pavlis, T. and Schmid, S., 1996. Ductile extrusion of the Higher Himalayan Crystalline in Bhutan: Evidence from quartz microfabrics. Tectonophysics 260, 21-43.

Grujic, D., Hollister, L.S. and Parrish, R.R., 2002. Himalayan metamorphic sequence as an orogenic channel: insight from Bhutan. Earth and Planetary Science Letters 198, 177-191.

Guilbert, J.M. and Park, C.F., 1986. The Geology of Ore Deposits. W. H. Freeman and Company, New York, 985 pp.

Guillot, S., Maheo, G., de Sigoyer, J., Hattori, K.H. and Pecher, A., 2008. Tethyan and Indian subduction viewed from the Himalayan high- to ultrahigh-pressure metamorphic rocks. Tectonophysics 451, 225-241.

Guo, L., Zhang, J.J. and Zhang, B., 2008. Structures, kinematics, thermochronology and tectonic evolution of the Ramba gneiss dome in the northern Himalaya. Progress in Natural Science 18, 851-860.

Hames, W.E. and Bowring, S.A., 1994. An empirical evaluation of the argon diffusion geometry in muscovite. Earth and Planetary Science Letters 124, 161-167.

Harlavan, Y. and Erel, Y., 2002. The release of Pb and REE from granitoids by the dissolution of accessory phases. Geochimica et Cosmochimica Acta 66, 837-848.

Harper, C.L. and Jacobsen, S.B., 1992. Evidence from coupled 147Sm-143Nd and 146Sm-142Nd systematics for very early (4.5-Gyr) differentiation of the Earth's mantle. Nature 360, 728-732.

Harris, N., 2007. Channel flow and the Himalayan-Tibetan orogen - a critical review. Journal of the Geological Society 164, 511-523.

Harris, N., Caddick, M., Kosler, J., Goswami, S., Vance, D. and Tindle, A.G., 2004. The pressure-temperature-time path of migmatites from the Sikkim Himalaya. Journal of Metamorphic Geology 22, 249-264.

Harris, N. and Inger, S., 1992. Trace-Element Modelling of Pelite-Derived Granites. Contributions to Mineralogy and Petrology 110, 46-56.

Harris, N. and Massey, J., 1994. Decompression and Anatexis of Himalayan Metapelites. Tectonics 13, 1537-1546.

Harris, N., McMillan, A., Holness, M., Uken, R., Watkeys, M., Rogers, N. and Fallick, A., 2003. Melt generation and fluid flow in the thermal aureole of the Bushveld Complex. Journal of Petrology 44, 1031-1054.

Harrison, T. M., Catlos, E. J., and Montel, J.-M., 2002, U-Th-Pb dating of Phosphate Minerals, in Kohn, M. J., Rakovan, J., and Hughes, J. M., eds., Phosphates: Geochemical, geobioloical and materials importance: Reviews in Mineralogy and Geochemistry, p. 523-552.

Hassett, W. and Leech, M.L., 2007. Early Miocene granitoids from the Leo Pargil gneiss dome, northwest Himalaya, Eos Transactions, AGU 88(52), Fall Meeting Supplement, Abstract T31D-0668.

Hatcher, R.D.J. and Merschat, A.J., 2006. The Appalachian Inner Piedmont: an exhumed strike parallel, tectonically forced orogenic channel. In: R.D. Law, M.P. Searle and L. Godin (Editors), Channel Flow, Ductile Extrusion and Exhumation in Continental Collision Zones. Geological Society, London, Special Publications, pp. 517-541.

Hauck, M.L., Nelson, K.D., Brown, L.D., Zhao, W.J. and Ross, A.R., 1998. Crustal structure of the Himalayan orogen at similar to 90 degrees east longitude from Project INDEPTH deep reflection profiles. Tectonics 17, 481-500.

Hayden, H.H., 1904. The Geology of the Spiti with parts of the Bashur and Rupshu. Geological Survey of India 36, 121.

Heim, A. and Gansser, A., 1939. Central Himalaya. Geological Observations of the Swiss Expedition 1936. Hindustan Publishing Corporation (India), Delhi, 245 pp.

Henry, P., LePichon, X. and Goffe, B., 1997. Kinematic, thermal and petrological model of the Himalayas: Constraints related to metamorphism within the underthrust Indian crust and topographic elevation. Tectonophysics, 273(1-2): 31-56.

Hodges, K.V., 2006. A synthesis of the Channel Flow - Extrusion hypothesis as developed for the Himalayan-Tibetan orogenic system. In: R.D. Law, M.P. Searle and L. Godin (Editors), Channel Flow, Ductile Extrusion and Exhumation in Continental Collision Zones. Geological Society, London, Special Publications, pp. 71-90.

Hodges, K.V., Burchfiel, B.C., Royden, L.H., Chen, Z. and Liu, Y., 1993. The Metamorphic Signature of Contemporaneous Extension and Shortening in the Central Himalayan Orogen - Data from the Nyalam Transect, Southern Tibet. Journal of Metamorphic Geology 11, 721-737.

Hoisch, T.D., 1990. Empirical calibration of six geobarometers for the mineral assemblage quartz+muscovite+biotite+plagioclase+garnet. Contributions to Mineralogy and Petrology 104, 225-234.

Holland, T.J.B., 2007. http://rock.esc.cam.ac.uk/astaff/holland/ax.html.

Holland, T.J.B., Baker, J.M. and Powell, R., 1998. Mixing properties and activity-composition relationships of chlorites in the system MgO-FeO-Al_2O_3-SiO_2-H_2O. European Journal of Mineralogy 10, 395-406.

Holland, T.J.B. and Powell, R., 1998. An internally consistent thermodynamic data set for phases of petrological interest. Journal of Metamorphic Geology 16, 309-343.

Hollister, L.S. and Grujic, D., 2006. Pulsed channel flow in Bhutan. In: R.D. Law, M.P. Searle and L. Godin (Editors), Channel Flow, Ductile Extrusion and Exhumation in Continental Collision Zones. Geological Society, London, Special Publications, pp. 415-423.

Horstwood, M.S.A., Foster, G.L., Parrish, R.R., Noble, S.R. and Nowell, G.M., 2003. Common-Pb corrected in situ U-Pb accessory mineral geochronology by LA-MC-ICP-MS. Journal of Analytical Atomic Spectrometry 18, 837-846.

Hubbard, M.S., 1996. Ductile shear as a cause of inverted metamorphism: Example from the Nepal Himalaya. Journal of Geology 104, 493-499.

Imayama, T. and Arita, K., 2008. Nd isotopic data reveal the material and tectonic nature of the Main Central Thrust zone in Nepal Himalaya. Tectonophysics 451, 265-281.

Inger, S. and Harris, N., 1992. Tectonothermal Evolution of the High Himalayan Crystalline Sequence, Langtang Valley, Northern Nepal. Journal of Metamorphic Geology 10, 439-452.

Inger, S. and Harris, N., 1993. Geochemical constraints on leucogranite magmatism in the Langtang Valley, Nepal Himalaya. Journal of Petrology 34, 345-368.

Jain, A.K., Kumar, D., Singh, S., Kumar, A. and Lal, N., 2000. Timing, quantification and tectonic modelling of Pliocene-Quaternary movements in the NW Himalaya: evidence from fission track dating. Earth and Planetary Science Letters 179, 437-451.

Jain, A.K. and Manickavasagam, R.M., 1993. Inverted Metamorphism in the Intracontinental Ductile Shear Zone During Himalayan Collision Tectonics. Geology 21, 407-410.

Jamieson, R.A., Beaumont, C., Hamilton, J. and Fullsack, P., 1996. Tectonic assembly of inverted metamorphic sequences. Geology 24, 839-842.

Jamieson, R.A., Beaumont, C., Nguyen, M.H. and Grujic, D., 2006. Provenance of the Greater Himalayan Sequence and associated rocks: predictions of channel flow models. In: R.D. Law, M.P. Searle and L. Godin (Editors), Channel Flow, Ductile Extrusion and Exhumation in Continental Collision Zones. Geological Society, London, Special Publications, 165-182.

Jamieson, R.A., Beaumont, C., Medvedev, S. and Nguyen, M.H., 2004. Crustal channel flows: 2. Numerical models with implications for metamorphism in the Himalayan-Tibetan orogen. Journal of Geophysical Research-Solid Earth 109, doi:10.1029/2003JB002811.

Janda, C., Hager, C., Grasemann, B., Draganits, E., Vannay, J.C., Bookhagen, B. and Thiede, R.C., 2001. Fault-slip analysis of the active extruding Lesser Himalayan Crystalline Wedge in the Sutlej Valley (NW-Himalayas). Journal of Asian Earth Sciences 19, 30-31.

Janots, E., Engi, M., Berger, A., Allaz, J., Schwarz, J.-O. and Spandler, C., 2008. Prograde metamorphic sequence of REE minerals in pelitic rocks of the Central Alps: implications for allanite-monazite-xenotime phase relations from 250 to 610 °C. Journal of Metamorphic Geology 26, 509–526.

Jessup, M.J., Tracy, R.J., Searle, M.P. and Law, R.D., 2004. Staurolite schist marks right-way-up metamorphic isograds at the top of the High Himalayan slab; Mount Everest, Tibet/Nepal. In: M.P. Searle, R.D. Law and L. Godin (Editors), Channel Flow, Ductile Extrusion and Exhumation of Lower-mid Crust in Continental Collision Zones, Geological Society, London.

Jimenez-Munt, I., Fernandez, M., Verges, J. and Platt, J.P., 2008. Lithosphere structure underneath the Tibetan Plateau inferred from elevation, gravity and geoid anomalies. Earth and Planetary Science Letters 267, 276-289.

Jung, S., Kroner, A. and Kroner, S., 2007. A similar to 700 Ma Sm-Nd gamet-whole rock age from the granulite facies Central Kaoko Zone (Namibia): Evidence for a cryptic high-grade polymetamorphic history? Lithos 97, 247-270.

Kingsbury, J.A., Miller, C.F., Wooden, J.L. and Harrison, T.M., 1993. Monazite Paragenesis and U-Pb Systematics in Rocks of the Eastern Mojave Desert, California, USA - Implications for Thermochronometry. Chemical Geology 110, 147-167.

Koch-Müller, M., 1997. Experimentally determined Fe-Mg exchange between synthetic staurolite and garnet in the system MgO-FeO-Al2O3-SiO2-H20. Lithos 41, 185-212.

Kohn, M.J., 2003. Geochemical zoning in metamorphic minerals. In: R.L. Rudnick, H.D. Holland and K.K. Turekian (Editors), Treatise on Geochemistry. Elsevier, Oxford, pp. 229–261.

Kohn, M.J. and Malloy, M.A., 2004. Formation of monazite via prograde metamorphic reactions among common silicates: implications for age determinations. Geochimica et Cosmochimica Acta 68, 101-113.

Kohn, M.J., Wieland, M.S., Parkinson, C.D. and Upreti, B.N., 2004. Miocene faulting at plate tectonic velocity in the Himalaya of central Nepal. Earth and Planetary Science Letters 228, 299-310.

Kohn, M.J., Wieland, M.S., Parkinson, C.D. and Upreti, B.N., 2005. Five generations of monazite in Langtang gneisses: implications for chronology of the Himalayan metamorphic core. Journal of Metamorphic Geology 23, 399-406.

Kosler, J., and Sylvester, P. J., 2003, Present trends and the future of zircon in geochronology: laser ablation ICPMS, in Hanchar, J. M., and Hoskin, P. W. O., eds., Zircon: Reviews in Mineralogy and Geochemistry, p. 243-271.

Le Fort, P., 1975. Himalayas - Collided Range - Present Knowledge of Continental Arc. American Journal of Science A275, 1-44.

Le Fort, P., Cuney, M., Deniel, C., France-Lanord, C., Sheppard, S.M.F., Upreti, B.N. and Vidal, P., 1987. Crustal generation of the Himalayan leucogranites. Tectonophysics 134, 39-57.

Leech, M.L., 2007. Did the Karakoram fault interupt mid-crustal channel flow in the western Himalaya?, Eos Transactions, AGU 88(52), Fall Meeting Supplement, Abstract T34C-08.

Leech, M.L., Singh, S., Jain, A.K., Klemperer, S.L. and Manickavasagam, R.M., 2005. The onset of India-Asia continental collision: Early, steep subduction required by the timing of UHP metamorphism in the western Himalaya. Earth and Planetary Science Letters 234, 83-97.

Li, X.H., 1994. A Comprehensive U-Pb, Sm-Nd, Rb-Sr and Ar-40-Ar-39 Geochronological Study on Guidong Granodiorite, Southeast China - Records of Multiple Tectonothermal Events in a Single Pluton. Chemical Geology 115, 283-295.

Lombardo, B., Pertusati, P. and Borghi, S., 1993. Geology and tectonomagmatic evolution of the eastern Himalaya along the Chomolungo-Makalu transect. In: P.J. Treloar and M.P. Searle (Editors), Himalayan Tectonics. Geological Society, London, Special Publications, pp. 341-355.

Ludwig, K.R., 2003. Users manual for Isoplot/Ex version 3.0: a geochronological toolkit for Microsoft Excel. Berkeley Geochronology Center Spec. Pub. No. 4, Berkeley, California, 70 pp.

Mahar, E.M., Baker, J.M., Powell, R., Holland, T.J.B. and Howell, N., 1997. The effect of Mn on mineral stability in metapelites. Journal of Metamorphic Geology 15, 223-238.

Makovsky, Y., Klemperer, S.L., Ratschbacher, L. and Alsdorf, D., 1999. Midcrustal reflector on INDEPTH wide-angle profiles: An ophiolitic slab beneath the India-Asia suture in southern Tibet? Tectonics 18, 793-808.

Maluski, H., Matte, P., Brunel, M. and Xiao, X., 1988. Argon 39- Argon 40 dating of metamorphic and plutonic events in the North and High Himalayas belts (southern Tibet-China). Tectonics 7, 299-326.

Mancktelow, N.S., 1995. Nonlithostatic Pressure During Sediment Subduction and the Development and Exhumation of High-Pressure Metamorphic Rocks. Journal of Geophysical Research-Solid Earth 100, 571-583.

Marquer, D., Chawla, H.S. and Challandes, N., 2000. Pre-alpine high-grade metamorphism in High Himalaya crystalline sequences: Evidence from Lower Palaeozoic Kinnaur Kailas granite and surrounding rocks in the Sutlej Valley (Himachal Pradesh, India). Eclogae Geologicae Helvetiae 93, 207-220.

Martin, A.J., DeCelles, P.G., Gehrels, G.E., Patchett, P.J. and Isachsen, C., 2005. Isotopic and structural constraints on the location of the Main Central thrust in the Annapurna Range, central Nepal Himalaya. Geological Society of America Bulletin 117, 926-944.

Martin, A.J., Gehrels, G.E. and DeCelles, P., 2007. The tectonic significance of (U, Th)/Pb ages of monazite inclusions in garnet from the Himalaya of central Nepal. Chemical Geology 244, 1-24.

Metcalfe, R.P., 1990. A thermotectonic evolution for the Main Central Thrust and Higher Himalaya, Western Garhwal, India, University of Leicester.

Miller, C., Kloetzli, U., Frank, W., Thöni, M. and Grasemann, B., 2000. Proterozoic crustal evolution in the NW Himalaya (India) as recorded by circa 1.80 Ga mafic and 1.84 Ga granitic magmatism. Precambrian Research 103, 191-206.

Miller, C., Thöni, M., Frank, W., Grasemann, B., Klötzli, U., Guntli, P. and Draganits, E., 2001. The early Palaeozoic magmatic event in the Northwest Himalaya, India: source, tectonic setting and age of emplacement. Geological Magazine 138, 237-251.

Miyashiro, A., 1994. Metamorphic Petrology. UCL Press Limited, London, 404 pp.

Molnar, P. and England, P., 1990. Temperatures, heat flux and frictional stress near major thrust faults. Journal of Geophysical Research 95, 4833-4856.

Mukhopadhyay, D.K., Ghosh, T.K., Bhadra, B.K. and Srivastava, D.C., 1997. Structural and metamorphic evolution of the rocks of the Jutogh Group, Chur half-klippe, Himachal Himalayas: A summary and comparison with the Simla area. Proceedings of the Indian Academy of Sciences-Earth and Planetary Sciences 106, 197-207.

Murphy, M.A., 2007. Isotopic characteristics of the Gurla Mandhata metamorphic core complex: Implications for the architecture of the Himalayan orogen. Geology 35, 983-986.

Nabelek, P.I. and Labotka, T.C., 1993. Implications of Geochemical Fronts in the Notch Peak Contact-Metamorphic Aureole, Utah, USA. Earth and Planetary Science Letters 119, 539-559.

Naha, K. and Ray, S.K., 1970. Metamorphic History of Jutogh Series in Simla Klippe, Lower Himalayas. Contributions to Mineralogy and Petrology 28, 147-164.

Nelson, K.D., Zhao, W.J., Brown, L.D., Kuo, J., Che, J.K., Liu, X.W., Klemperer, S.L., Makovsky, Y., Meissner, R., Mechie, J., Kind, R., Wenzel, F., Ni, J., Nabelek, J., Chen, L.S., Tan, H.D., Wei, W.B., Jones, A.G., Booker, J., Unsworth, M., Kidd, W.S.F., Hauck, M., Alsdorf, D., Ross, A., Cogan, M., Wu, C.D., Sandvol, E. and Edwards, M., 1996. Partially molten middle crust beneath southern Tibet: Synthesis of project INDEPTH results. Science 274, 1684-1688.

Pant, N.C., Kundu, A., Kumar, R., Dorka, B.S. and Prasher, S., 2006. Palaeoproterozoic metamorphism in the Jeori-Wangtu Gneissic Complex (JWGC), western Himalayas. Journal of Asian Earth Sciences 26, 585-604.

Parrish, R.R., 1990. U-Pb dating of monazite and its application to geological problems. Canadian Journal of Earth Sciences 27, 1431-1450.

Parrish, R.R., Carr, S.C. and Parkinson, D., 1988. Eocene extensional tectonics and geochronology of the southern Omineca belt, British Columbia and Washington. Tectonics 7, 181-212.

Parrish, R.R., Gough, S.J., Searle, M.P. and Waters, D.J., 2006. Plate velocity exhumation of ultrahigh-pressure eclogites in the Pakistan Himalaya. Geology 34, 989-992.

Parrish, R.R. and Hodges, K.V., 1996. Isotopic constraints on the age and provenance of the Lesser and Greater Himalayan sequences, Nepalese Himalaya. Geological Society of America Bulletin 108, 904-911.

Passchier, C.W. and Trouw, R.A.J., 1998. Microtectonics. Springer, Berlin-Heidelberg-New York, 289 pp.

Paudel, L.P. and Arita, K., 2000. Tectonic and polymetamorphic history of the Lesser Himalaya is central Nepal. Journal of Asian Earth Sciences 18, 561-584.

Pearce, N.J.G., Perkins, W.T., Westgate, J.A., Gorton, M.P., Jackson, S.E., Neal, C.R. and Chenery, S.P., 1997. A compilation of new and published major and trace element data for NIST SRM 610 and NIST SRM 612 glass reference materials. Geostandards Newsletter-the Journal of Geostandards and Geoanalysis 21, 115-144.

Pilgrim, G.E. and West, W.D., 1928. The structure and correlation of the Simla rocks. Memoirs of the Geological Survey of India 53, 1-140.

Platt, J.P., 1986. Dynamics of orogenic wedges and the uplift of high-pressure metamorphic rocks. Geological Society of America Bulletin 97, 1037-1053.

Pollington, A.D. and Baxter, E.F., 2007. Developing New Methods for Microsampling and Sm/Nd Dating of Zoned Garnet. Eos Transactions, AGU 88(52), Fall Meeting Supplement, Abstract V33E-03.

Powell, R. and Holland, T.J.B., 2001. Course Notes for "THERMOCALC Workshop 2001: Calculating Metamorphic Phase Equilibria" (on CD-ROM).

Powell, R., Holland, T.J.B. and Worley, B., 1998. Calculating phase diagrams involving solid solutions via non- linear equations, with examples using THERMOCALC. Journal of Metamorphic Geology 16, 577-588.

Prince, C.I., 1999. The timing of prograde metamorphism in the Garhwal Himalaya, India, The Open University, Milton Keynes.

Prince, C., Harris, N. and Vance, D., 2001. Fluid-enhanced melting during prograde metamorphism. Journal of the Geological Society, London 158, 233-241.

Prince, C.I., Kosler, J., Vance, D. and Gunther, D., 2000. Comparison of laser ablation ICP-MS and isotope dilution REE analyses - implications for Sm-Nd garnet geochronology. Chemical Geology 168, 255-274.

Pyle, J.M. and Spear, F.S., 1999. Yttrium zoning in garnet: Coupling of major and accessory phases during metamorphic reactions. Geological Materials Research 1, 2-49.

Quigley, M., Liangjun, Y., Gregory, C., Corvino, A., Sandiford, M., Wilson, C.J.L. and Xiaohan, L., 2008. U–Pb SHRIMP zircon geochronology and *T–t–d* history of the Kampa Dome, southern Tibet. Tectonophysics 446, 97-113.

Rasmussen, B. and Muhling, J.R., 2007. Monazite begets monazite: evidence for dissolution of detrital monazite and reprecipitation of syntectonic monazite during low-grade regional metamorphism. Contributions to Mineralogy and Petrology 154, 675-689.

Ratschbacher, L., Frisch, W., Liu, G. and Chen, C., 1994. Distributed deformation in southern and western Tibet during and after the Indian-Asia collision. Journal of Geophysical Research 99(B10), 19917-19945.

Reddy, S.M., Searle, M.P. and Massey, J.A., 1993. Structural evolution of the high Himalayan gneiss sequence, Lantang valley, Nepal. In: P.J. Treloar and M.P. Searle (Editors), Himalayan Tectonics. Geological Society Special Publication, pp. 375-389.

Renne, P.R., Swisher, C.C., Deino, A.L., Karner, D.B., Owens, T.O. and DePaolo, D.J., 1998. Intercalibration of standards, absolute ages and uncertainties in $^{40}Ar/^{39}Ar$ dating. Chemical Geology 145, 117-152.

Richards, A., 2004. Isotopic Mapping of Major Himalayan Structures, The Open University, Milton Keynes.

Richards, A., Argles, T., Harris, N., Parrish, R., Ahmad, T., Darbyshire, F. and Draganits, E., 2005. Himalayan architecture constrained by isotopic tracers from clastic sediments. Earth and Planetary Science Letters 236, 773-796.

Richards, A., Parrish, R., Harris, N., Argles, T. and Zhang, L., 2006. Correlation of lithotectonic units across the eastern Himalaya, Bhutan. Geology 34, 341-344.

Robinson, D.M., DeCelles, P.G., Patchett, P.J. and Garzione, C.N., 2001. The kinematic evolution of the Nepalese Himalaya interpreted from Nd isotopes. Earth and Planetary Science Letters 192, 507-521.

Santosh, M., Yokoyama, K., Biju-Sekhar, S. and Rogers, J.J.W., 2003. Multiple tectonothermal events in the granulite blocks of southern India revealed from EPMA dating: Implications on the history of supercontinents. Gondwana Research 6, 29-63.

Scaillet, B., France-Lanord, C. and Le Fort, P., 1990. Badrinath-Gangotri Plutons (Garhwal, India) - Petrological and Geochemical Evidence for Fractionation Processes in a High Himalayan Leukogranite. Journal of Volcanology and Geothermal Research 44, 163-188.

Scherer, E.E., Cameron, K.L. and Blichert-Toft, J., 2000. Lu-Hf garnet geochronology: Closure temperature relative to the Sm-Nd system and the effects of trace mineral inclusions. Geochimica et Cosmochimica Acta 64, 3413-3432.

Searle, M.P., Law, R.D., Godin, L., Larson, K.P., Streule, M.J., Cottle, J.M. and Jessup, M.J., 2008. Defining the Himalayan Main Central Thrust in Nepal. Journal of the Geological Society, London 165, 523-534.

Searle, M.P., Law, R.D. and Jessup, M.J., 2006. Crustal structure, restoration and evolution of the Greater Himalaya in Nepal - South Tibet: implications for channel flow and the ductile extrusion of the middle crust. In: R.D. Law, M.P. Searle and L. Godin (Editors), Channel Flow, Ductile Extrusion and Exhumation in Continental Collision Zones. Geological Society, London, Special Publications, pp. 355-378.

Searle, M.P., Parrish, R.R., Hodges, K.V., Hurford, A., Ayres, M.W. and Whitehouse, M.J., 1997. Shisha Pangma leucogranite, south Tibetan Himalaya: Field relations, geochemistry, age, origin, and emplacement. Journal of Geology 105, 295-317.

Searle, M.P. and Phillips, R.J., 2007. Relationships between right-lateral shear along the Karakoram fault and metamorphism, magmatism, exhumation and uplift: evidence from the K2-Gasherbrum-Pangong ranges, north Pakistan and Ladakh. Journal of the Geological Society 164, 439-450.

Searle, M.P. and Rex, A.J., 1989. Thermal-Model for the Zanskar Himalaya. Journal of Metamorphic Geology 7, 127-134.

Searle, M.P., Simpson, R.L., Law, R.D., Parrish, R.R. and Waters, D.J., 2003. The structural geometry, metamorphic and magmatic evolution of the Everest massif, High Himalaya of Nepal-South Tibet. Journal of the Geological Society 160, 345-366.

Sharma, V.P., 1977. Geology of the Kulu-Rampur belt, Himachal Pradesh. Geological Survey of India Memoir 106, 235– 407.

Sherlock, S.C. and Kelley, S.P., 2002. Excess argon in HP-LT rocks: a UV laserprobe study of phengite and K-free minerals. Chemical Geology 182, 619-636.

Shreve, R.L. and Cloos, M., 1986. Dynamics of sediment subduction, melange formation, and prism accretion. Journal of Geophysical Research 91, 10229 - 10245.

Simonetti, A., Heaman, L.M., Hartlaub, R.P., Creaser, R.A., MacHattie, T.G. and Bohm, C., 2005. U-Pb zircon dating by laser ablation-MC-ICP-MS using a new multiple ion counting Faraday collector array. Journal of Analytical Atomic Spectrometry 20, 677-686.

Simpson, R.L., Parrish, R.R., Searle, M.P. and Waters, D.J., 2000. Two episodes of monazite crystallization during metamorphism and crustal melting in the Everest region of the Nepalese Himalaya. Geology 28, 403-406.

Singh, S., Claesson, S., Jain, A.K., Gee, D.G., Andreasson, P.G. and Manickavasagam, R.M., 2006. 2.0 Ga granite of the lower package of the Higher Himalayan Crystallines, Maglad Khad, Sutlej valley, Himachal Pradesh. Journal of the Geological Society of India 67, 295-300.

Singh, S. and Jain, A.K., 1993. Deformational and strain patterns of the Jutogh Nappe along the Sutlej Valley in Jeori-Wangtu region, Himachel Pradesh, India. Journal of Himalayan Geology 4, 41-55.

Singh, S. and Jain, A.K., 2003. Himalayan Granitoids. In: S. Singh (Editor), Explorer Granitoids of the Himalayan Collisional Belt. Journal of the Virtual Explorer, Electronic Edition, pp. 1-20.

Smith, H.A. and Barreiro, B., 1990. Monazite U-Pb Dating of Staurolite Grade Metamorphism in Pelitic Schists. Contributions to Mineralogy and Petrology 105, 602-615.

Spear, F.S., 1991. On the interpretation of peak metamorphic temperatures in light of garnet diffusion during cooling. Journal of Metamorphic Geology 9, 379-388.

Spear, F.S., 1993. Metamorphic Phase Equilibria and Pressure-Temperature-Time Paths. Mineralogical Society of America, Washington, D. C., 799 pp.

Spear, F.S. and Parrish, R.R., 1996. Petrology and Cooling Rates of the Valhalla Complex, British Columbia, Canada. Journal of Petrology 37, 733-765.

Stacey, J.S. and Kramers, J.D., 1975. Approximation of Terrestrial Lead Isotope Evolution by a 2-Stage Model. Earth and Planetary Science Letters 26, 207-221.

Storey, C. D., Smith, M. P., and Jeffries, T. E., 2007, In situ LA-ICP-MS U–Pb dating of metavolcanics of Norrbotten, Sweden: Records of extended geological histories in complex titanite grains: Chemical Geology, v. 240, p. 163-181

Stowell, H.H. and Goldberg, S.A., 1997. Sm-Nd garnet dating of polyphase metamorphism; northern Coast Mountains, South-eastern Alaska, USA. Journal of Metamorphic Geology 15, 439-450.

Stüwe, K. and Foster, D., 2001. Ar-40/Ar-39, pressure, temperature and fission track constraints on the age and nature of metamorphism around the main central thrust in the eastern Bhutan Himalaya. Journal of Asian Earth Sciences 19, 85-95.

Swapp, S.M. and Hollister, L.S., 1991. Inverted Metamorphism within the Tibetan Slab of Bhutan - Evidence for a Tectonically Transported Heat-Source. Canadian Mineralogist 29, 1019-1041.

Tangri, S.K. and Pande, A.C., 1995. Tethyan Sequence. In: O.N. Bhargava (Editor), The Bhutan Himalaya: a geological account. Geological Survey of India Special Publication, Calcutta, pp. 109-141.

Thakur, V.C., 1992. Geology of Western Himalaya. Physics and Chemistry of the Earth, 19. Pergamon Press, Oxford-New York, 366 pp.

Thiede, R.C., Arrowsmith, J.R., Bookhagen, B., McWilliams, M.O., Sobel, E.R. and Strecker, M.R., 2005. From tectonically to erosionally controlled development of the Himalayan orogen. Geology 33, 689-692.

Thiede, R.C., Arrowsmith, J.R., Bookhagen, B., McWilliams, M.O, Sobel, E.R. and Strecker, M.R., 2006. Dome formation and extension in the Tethyan Himalaya, Leo Pargil, northwest India. Geological Society of America Bulletin 118, 635-650.

Thiede, R.C., Bookhagen, B., Arrowsmith, J.R., Sobel, E.R. and Strecker, M.R., 2004. Climatic control on rapid exhumation along the Southern Himalayan Front. Earth and Planetary Science Letters 222, 791-806.

Thompson, A.B., 1976. Mineral reactions in Pelitic Rocks. 2. Calculation of Some P-T-X(Fe-Mg) Phase Relations. American Journal of Science 276, 425-454.

Tomkins, H.S. and Pattison, D.R.M., 2007. Accessory phase petrogenesis in relation to major phase assemblages in pelites from the Nelson contact aureole, southern British Columbia. Journal of Metamorphic Geology 25, 401-421.

Thoni, M., 2002. Sm-Nd isotope systematics in garnet from different lithologies (Eastern Alps): age results, and an evaluation of potential problems for garnet Sm-Nd chronometry. Chemical Geology 185, 255-281.

Thorpe, R.S., Tindle, A.G. and Williamsthorpe, O., 1995. Radioelement Distribution in the Tertiary Lundy Granite (Bristol Channel, Uk). Geological Magazine 132, 413-425.

Trivedi, J.R., Gopalan, K. and Valdiya, K.S., 1984. Rb-Sr Ages of Granitic-Rocks within the Lesser Himalayan Nappes, Kumaun, India. Journal of the Geological Society of India 25, 641-654.

Valdiya, K.S., 1988. Tectonics and evolution of the central sector of the Himalaya. Philosophical Transactions of the Royal society of London A 326, 151-175.

Vance, D., Ayres, M., Kelley, S. and Harris, N., 1998a. The thermal response of a metamorphic belt to extension: constraints from laser Ar data on metamorphic micas. Earth and Planetary Science Letters 162, 153-164.

Vance, D., Bickle, M., Ivy-Ochs, S. and Kubik, P.W., 2003. Erosion and exhumation in the Himalaya from cosmogenic isotope inventories of river sediments. Earth and Planetary Science Letters 206, 273-288.

Vance, D. and Harris, N., 1999. Timing of prograde metamorphism in the Zanskar Himalaya. Geology 27, 395-398.

Vance, D. and Holland, T., 1993. A Detailed Isotopic and Petrological Study of a Single Garnet from the Gassetts Schist, Vermont. Contributions to Mineralogy and Petrology 114, 101-118.

Vance, D. and O'Nions, R.K., 1990. Isotopic Chronometry of Zoned Garnets - Growth-Kinetics and Metamorphic Histories. Earth and Planetary Science Letters 97, 227-240.

Vance, D. and O'Nions, R.K., 1992. Prograde and retrograde thermal histories from the central Swiss Alps. Earth and Planetary Science Letters 114, 113-129.

Vance, D., Strachan, R.A. and Jones, K.A., 1998b. Extensional versus compressional settings for metamorphism: Garnet chronometry and pressure-temperature-time histories in the Moine Supergroup, northwest Scotland. Geology 26, 927-930.

Vanderhaeghe, O. and Teyssier, C., 2001. Partial melting and flow of orogens. Tectonophysics 342, 451-472.

Vannay, J.-C. and Grasemann, B., 2001. Himalayan inverted metamorphism and syn-convergence extension as a consequence of a general shear extrusion. Geological Magazine 138, 253-276.

Vannay, J.-C., Grasemann, B., Rahn, M., Frank, W., Carter, A., Baudraz, V. and Cosca, M., 2004. Miocene to Holocene exhumation of metamorphic crustal wedges in the NW Himalaya: Evidence for tectonic extrusion coupled to fluvial erosion. Tectonics 23, TC1014.

Vannay, J.-C. and Hodges, K.V., 1996. Tectonomorphic evolution of the Himalayan metamorphic core between the Annapurna and Dhaulagiri, central Nepal. Journal of Metamorphic Geology 14, 635–656.

Vannay, J.-C., Sharp, Z.D. and Grasemann, B., 1999. Himalayan inverted metamorphism constrained by oxygen isotope thermometry. Contributions to Mineralogy and Petrology 137, 90-101.

Warren, C., Chakungal, J., Grujic, D., Jamieson, R.A., Moynihan, D., Ghalley, K.S. and Wangda, D., 2008. Pelitic and mafic granulite-eclogites from NW Bhutan: PTt history and tectonic implications. Journal of Metamorphic Geology *in prep.*

Waters, D.J. and Lovegrove, D.P., 2002. Assessing the extent of disequilibrium and overstepping of prograde metamorphic reactions in metapelites from the Bushveld aureole. Journal of Metamorphic Geology 20, 135-149.

Watson, E.B. and Harrison, T.M., 1983. Zircon Saturation Revisited - Temperature and Composition Effects in a Variety of Crustal Magma Types. Earth and Planetary Science Letters 64, 295-304.

Watts, D.R. and Harris, N.B.W., 2005. Mapping granite and gneiss in domes along the North Himalayan antiform with ASTER SWIR band ratios. Geological Society of America Bulletin 117, 879-886.

Webb, A.G., Yin, A., Harrison, T.M., Celerier, J. and Burgess, P.W., 2007. The leading edge of the Greater Himalayan Crystalline complex revealed in the NW Indian Himalaya: Implications for the evolution of the Himalayan orogen. Geology 35, 955-958.

Webb, P.C. and Brown, G.C., 1984. The Eastern Highlands granites: heat production and related geochemistry, BGS - Imperial College - Open University.

Wheeler, J., Treloar, P.J. and Potts, G.J., 1995. Structural and metamorphic evolution of the Nanga Parbat syntaxis, Pakistan Himalayas, on the Indus gorge transect: the importance of early events. Geological Journal 30, 349-371.

White, N.M., Pringle, M., Garzanti, E., Bickle, M., Najman, Y., Chapman, H. and Friend, P., 2002. Constraints on the exhumation and erosion of the High Himalayan Slab, NW India, from foreland basin deposits. Earth and Planetary Science Letters 195, 29-44.

White, R.W., Powell, R., Holland, T.J.B. and Worley, B.A., 2000. The effect of TiO_2 and Fe_2O_3 on metapelitic assemblages at greenschist and amphibolite facies conditions: mineral equilibria

calculations in the system K_2O-FeO-MgO-Al_2O_3-SiO_2-H2O-TiO_2-Fe_2O_3. Journal of Metamorphic Geology 18, 497-511.

Wiesmayr, G. and Grasemann, B., 2002. Eohimalayan fold and thrust belt: Implications for the geodynamic evolution of the NW-Himalaya (India). Tectonics 21.

Williams, M. L., Jercinovic, M. J., Goncalves, P., and Mahan, K., 2006, Format and philosophy for Collecting, compiling, and reporting microprobe monazite ages: Chemical Geology, v. 225, p. 1-15.

Wing, B.A., Ferry, J.M. and Harrison, T.M., 2003. Prograde destruction and formation of monazite and allanite during contact and regional metamorphism of pelites: petrology and geochronology. Contributions to Mineralogy and Petrology 145, 228-250.

Wu, C., Nelson, K.D., Wortman, G., Samson, S., Yue, Y., Li, J., Kidd, W. and Edwards, M., 1998. Yadong cross structure and South Tibetan Detachment in the east central Himalaya (89°–90°E). Tectonics 17, 28-45.

Wyss, M., Hermann, J. and Steck, A., 1999. Structural and metamorphic evolution of the northern Himachal Himalaya, NW India - (Spiti-eastern Lahul-Parvati valley traverse). Eclogae Geologicae Helvetiae 92, 3-44.

Xiao, L., Wang, C.Z. and Pirajno, F., 2007. Is the underthrust Indian lithosphere split beneath the Tibetan Plateau? International Geology Review 49, 90-98.

Yang, P.S. and Pattison, D., 2006. Genesis of monazite and Y zoning in garnet from the Black Hills, South Dakota. Lithos 88, 233-253.

Yin, A., 2006. Cenozoic tectonic evolution of the Himalayan orogen as constrained by along-strike variation of structural geometry, exhumation history, and foreland sedimentation. Earth-Science Reviews 76, 1-131.

Zeitler, P.K., Koons, P.O., Bishop, M.P., Chamberlain, C.P., Craw, D., Edwards, M.A., Hamidullah, S., Jan, M.Q., Khan, M.A., Khattak, M.U.K., Kidd, W.S.F., Mackie, R.L., Meltzer, A.S., Park, S.K., Pecher, A., Poage, M.A., Sarker, G., Schneider, D.A., Seeber, L. and Shroder, J.F., 2001. Crustal reworking at Nanga Parbat, Pakistan: Metamorphic consequences of thermal-mechanical coupling facilitated by erosion. Tectonics 20, 712-728.

Zeitler, P.K., Sutter, J.F., Williams, I.S., Zartman, R.E. and Tahirkheli, R.A.K., 1989. Geochronology and temperature history of the Nanga Parbat-Haramosh Massif, Pakistan. In: L.L. Malinconico and R.J. Lillie (Editors), Tectonics of the Western Himalayas. Geological Society of America, Special Publications, pp. 1-22.

Zhang, H.F., Harris, N., Parrish, R., Kelley, S., Zhang, L., Rogers, N., Argles, T. and King, J., 2004. Causes and consequences of protracted melting of the mid-crust exposed in the North Himalayan antiform. Earth and Planetary Science Letters 228, 195-212.

Zhou, B. and Hensen, B.J., 1995. Inherited Sm/Nd Isotope Components Preserved in Monazite Inclusions within Garnets in Leucogneiss from East Antarctica and Implications for Closure Temperature Studies. Chemical Geology 121, 317-326.

Appendix A: Locality and sample catalogue

- Localities are mapped on Figures A1.1 (lower Sutlej valley, also see Fig. 2.1), A1.2 (upper Sutlej valley, also see Fig. 3.1), and 6.1 (Bhutan)
- Hand samples are held at the OU, thin sections are in the possession of J. Chambers.
- See Appendix C1 for whole rock major and trace element (XRF) data

Abbreviation/symbol	In column...	Means...
x	Sample (suffix to number)	not *in-situ* (i.e. float material)
Ss	Structural measurements	Plane of schistosity (dominant foliation)
Ls	Structural measurements	Lineation on Ss
Sf	Structural measurements	Plane of fault
Lf	Structural measurements	Lineation on Lf
So	Structural measurements	Plane of bedding
Lc	Structural measurements	Major fold hinge
MFH	Structural measurements	Minor fold hinge
italicised text	Structural measurements	Determined from thin section
a	Sections	perpendicular to lineation
b	Sections	parallel to lineation

Structural measurements:

- Reported as dip and dip direction for planar surfaces (right hand rule employed, i.e. dip down thumb if right hand placed on surface) and plunge and plunge direction for lineations.

- Averages reported for multiple structural measurements.

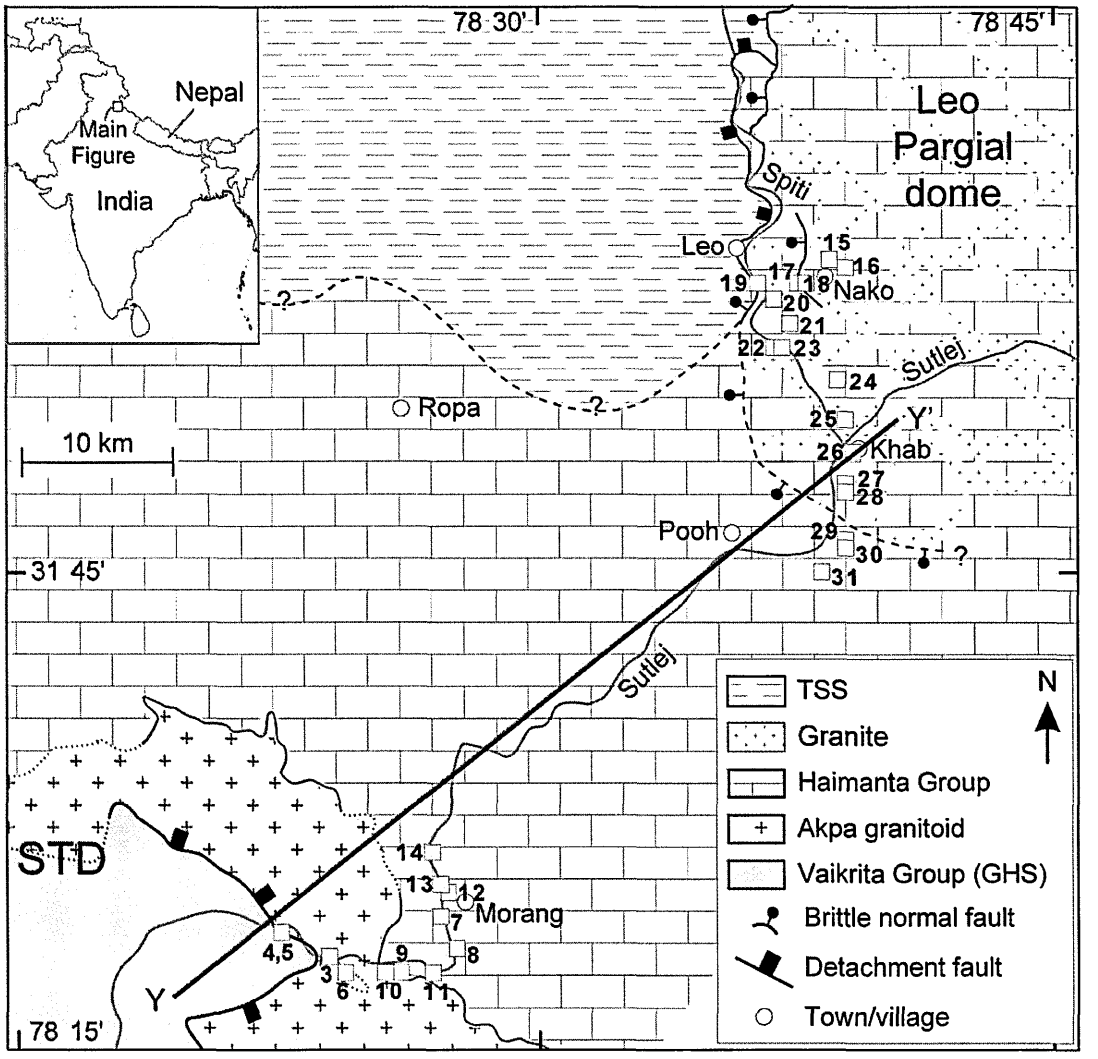

Fig. A1.1 Map of upper Sutlej valley localities

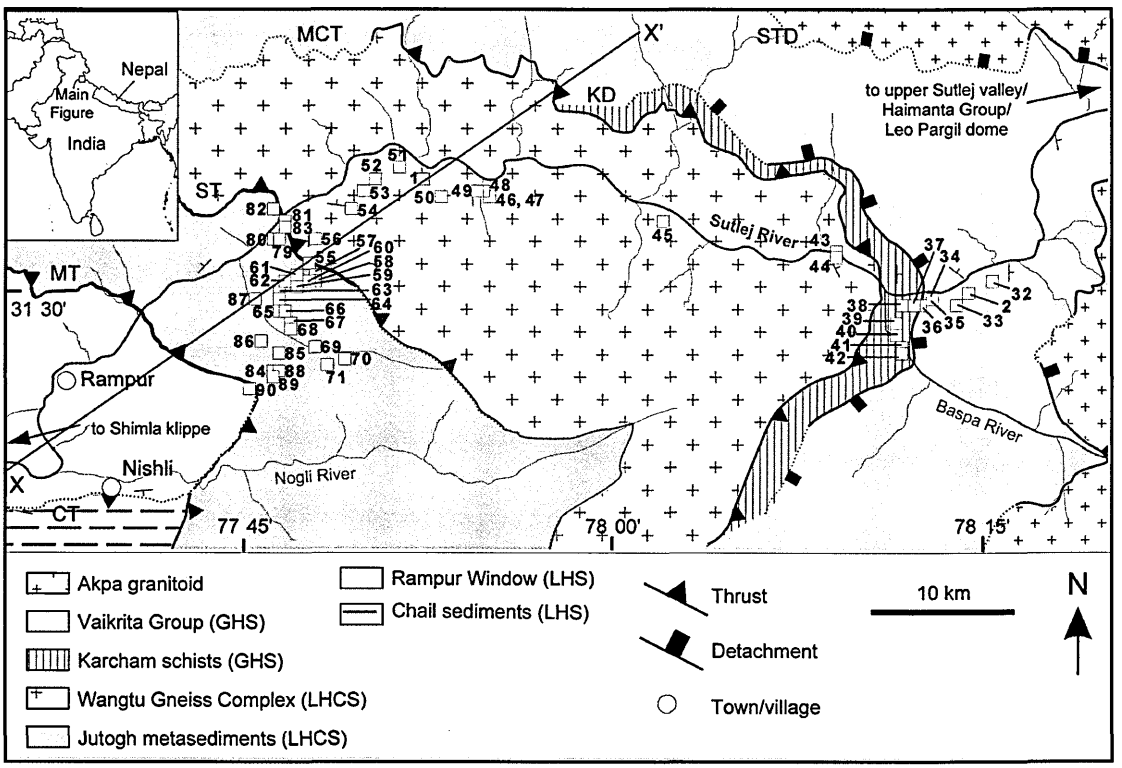

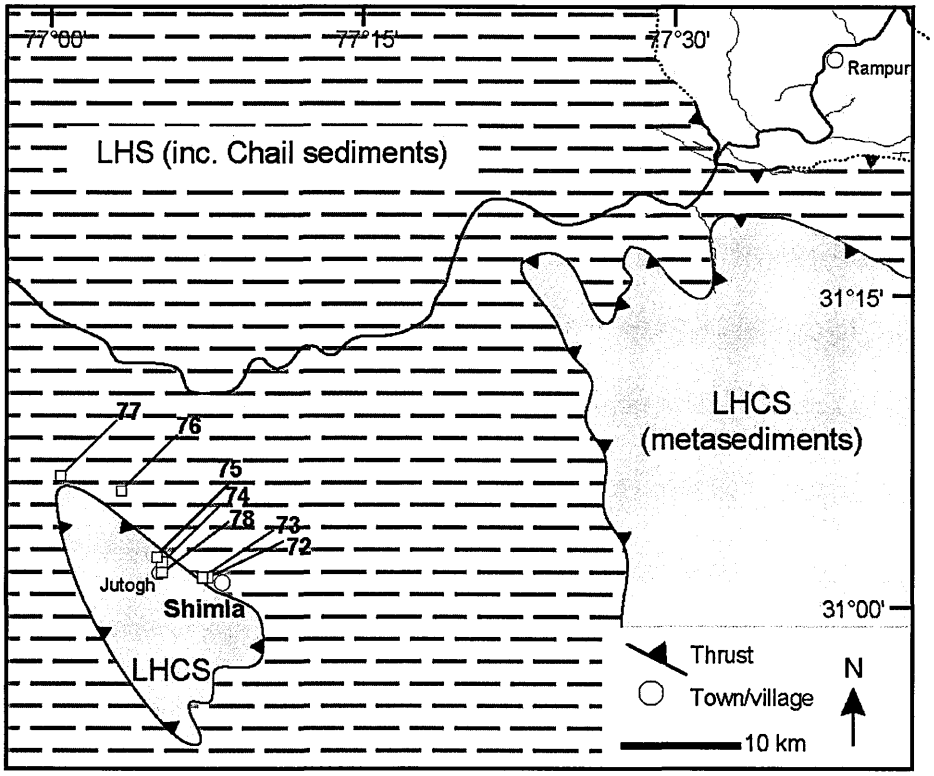

Fig. A1.2 Maps of lower Sutlej valley localities

Locality N°	Locality	GPS			Unit	Lithology	Additional features	Sample	Structural measurements			Sections cut		XRF data
		Longitude	Latitude	Elevation (m)					Ss / other Ss	Ls / other Ls	sense of shear (top to/criteria)	std	probe	
I05/1	Sarahan- Wangtu	31.5656	77.8666	1692	Wangtu Complex	augengneiss	migmatitic/ pegmatitic; fsp augen (av. 2cm, <6cm)							
I05/2	E of Karcham	31.5020	78.2297	1874	Vaikrita	mylonite								
I05/3	N of Akpa	31.5886	78.3796	2444	Akpa	granite	weakly foliated to undeformed; qz veins 5cm; tu-gt lgr veins 10cm							
I05/4	Rarang	31.5991	78.3569	2553	Akpa	granite	sheared		23/063	21/051	NE / augen			
I05/5	Rarang	31.5979	78.3551	2418	Vaikrita	gneiss	banded; minor augen	gt gneiss	16/094	11/048	NE / shear zones			
I05/6	Akpa Bridge	31.5808	78.3865	2217	Vaikrita	pelitic schist	sheared		12/101 / Sf 55/276	10/039 / Lf 41/314	S / s-c fabric			
I05/7	Morang Bridge	31.6053	78.4358	2284	Haimanta	pelitic schist	fine-gr, graphite	i) gt-ky?-mica schist	06/025	03/087	*i) slight top to SE / asym tails on gt pbl*	x	x	x
							fine-gr, graphite	ii) gt-st?-mica schist			*ii) 070 (ENE)*	x	x	x
							med-gr	iii) x2 gt-ky?-mica schist				x	x	x
I05/8	Morang	31.5904	78.4425	2320	Haimanta	psammite/ pelite schist, calcareous layers, minor lgr	folded alternating layers	i) gt-st-ky-mica schist	12/081	MFH: 04/142, 06/149	i) *225 (SW) ? / micro-shear zone*	x	x	x
								ii) gt-st-ky-mica schist				x	x	x
								iii) amph-gt calcareous layer						
								iv) tu lgr						
I05/9*	Morang-Akpa	31.5826	78.4140	2356	Haimanta	psammitic schist	hyalophane	hyalophane-mica schist*				x	x	x
I05/10*	Morang-Akpa	31.5819	78.4064	2261	Haimanta	psammitic/ pelitic schist	faulted/sheared/mineralised; hyalophane	i) mafic/ hornfelsic gneiss						
								ii) hyalophane-paragneiss*				x	x	x
I05/11	Morang	31.5822	78.4290	2251	Haimanta	psammitic> pelitic schist	weakly faulted/sheared/mineralised; late kinking in pelite x-cuts crenulation		14/051	10/002				
I05/12	N of Morang Bridge	31.6140	78.4379	2298	Haimanta	psammitic> pelitic schist	tightly folded, faulted; amph-calc layer	i) gt? -mica schist						
								ii) x4 amph-gt?-calcareous layer						
I05/13	Road N of Morang Bridge	31.6199	78.4344	2290	Haimanta	psammitic> pelitic schist > calcareous layers	qz veins	gt-st/ky?- mica schist	11/017	07/062		x	x	x

Locality N°	Locality	GPS			Unit	Lithology	Additional features	Sample	Structural measurements			Sections cut		XRF data
		Longitude	Latitude	Elevation (m)					Ss / other Ss	Ls / other Ls	sense of shear (top to/criteria)	std	probe	
I05/14	S of Spillo	31.6335	78.4302	2297	Haimanta	psammitic> pelitic schist		i) x4 gt-st-mica schist				x	x	x
							black p'blasts	ii) calcareous						
I05/15	Nako	31.8862	78.6307	3665	Haimanta/ Leo Pargil	granite > psammite >> pelite > calc layer		i) amph-diop?-calcareous layer						
							pale cream granite	i) wm-gt granite						
							dark, fine-gr psammite (<40%feldspathic); coarser-gr pelite, foxy red bi; clots of sill?; lots of tu = metasom	iii) mica (inc wm clots) schist				x	x	x
I05/16	Nako	31.8834	78.6352	3768	Haimanta	psammite/ pelite>granite	very elongate mafic boudins (act, alm-gt) - limited to outer edge/layer	ix) gt-mica schist (bi p'blasts: best on exterior surface)				x	x	
							boudin	ii) granite						
I05/17	S of Nako	31.8770	78.6123	3305	Haimanta? TSS?	carbonate, psammite> pelite interbeds	sheared/folded/banded; deformed tu-lgr x-cuts	carbonate	35/303 Sf 40/283	28/266 Lf 33/288	W or NW / stepped qtz fibres			
I05/18	S of Nako	31.8755	78.6181	3370	Haimanta? TSS?	dolomitic marble	weathers pale brown, contact meta with lg	x) marble (and bi-gneiss) w/ green ep, orange gross-gt, green act. white trem	15/263	14/269				
I05/19	S of Leo	31.8768	78.5943	2907	Haimanta? TSS?	dolomite, wm-tu-gt lgr, bi gneiss	sheared		22/331	16/287				
I05/20	S of Leo	31.8687	78.6013	3052	Haimanta	granite	brown-black ultramylonite; ~20cm gt-rich (2-4mm) pelitic layer	grey 2-mica granite; cm-scale fsp augen						
I05/21	Nako-Khab	31.8566	78.6078	3067	Haimanta	psammitic/ pelitic schist	crenulated schist, wm-tu-bi (books) lgr and early grey 2-mica granite x-cuts (=stoped blocks)							
I05/22	Nako-Khab	31.8493	78.6013	3017	Haimanta	granite, gneiss		ky-sill paragneiss				x	x	x
I05/23	Nako-Khab (Spiti River)	31.8487	78.6047	3051	Haimanta	bi-schist, granite, calcareous layer	med to coarse-gr; grey	ix) amph-gt calcareous layer						
								iix) gt bi schist						
I05/24	Nako-Khab (Spiti River)	31.8332	78.6311	2980	Haimanta + granite	psammitic/ pelitic schist	med to coarse-gr pelite; grey, fine-gr psammite; x-cutting lgr (50% of outcrop)							

Locality N°	Locality	GPS			Unit	Lithology	Additional features	Sample	Structural measurements			Sections cut		XRF data
		Longitude	Latitude	Elevation (m)					Ss / other Ss	Ls / other Ls	sense of shear (top to/criteria)	std	probe	
I05/25	N of Khab	31.8177	78.6355	2687	Haimanta	psammitic> pelitic schist	crenulated; x-cutting granite (50% of outcrop)	i) sill gneiss ii) calcareous layer, red gt ± green diop						
I05/26	Spitit-Sutlej confluence	31.8032	78.6423	2556	Haimanta + granite	psammitic>> pelitic schist > granite	fine-gr, grey, bi-psammite; some gt ± diop calc layers		16/346	02/262				
I05/27	S of Khab	31.7909	78.6358	2434	Haimanta + granite	psammitic> pelitic schist; granite	more grey granite and less x-cutting than stoped country rock areas seen, i.e. less 'spidery'; calc layers (gt amph)		17/316	12/274	NNW / shear fractures, asymm boudinage of tu-lgr			
I05/28	S of Khab	31.7852	78.6380	2426	Haimanta	psammite/ pelite (60/70%) > granite (<30% max)	non-systematic micro-folding	i) ky-st-gt? schistose altered granite				x	x	x
								ii) cord-st-ky schist				x	x	x
I05/29	Khab-Poo (Titan Khub Bridge)	31.7671	78.6376	2582	Haimanta	psammite> pelite>calcareous	<5% tu-wm lgr x-cutting veins/splurges; planar-monoclinal folds on outcrop scale; fractures w/ calc rxn haloes?		24/348	15/298				
I05/30	S of Titan Khub Bridge	31.7623	78.6363	2594	Haimanta	psammitic/ pelitic schist	minor pegmatitic veins x-cutting (tu line their edges)	gt-ky-st mica schist	37/269 So 55/229	36/273				
I05/31	Khab-Poo (S side of Dabling Bridge)	31.7528	78.6260	2629	Haimanta	psammitic/ pelitic schist	psammite (60-70%), pelite (30-40%); one <0.5m pegmatitic vein pinching out here	i) st-gt-mica schist ii) mica schist	28/264	23/274	*W? / p shadows on p'blasts*	x	x	x
I05/32	Peo-Karcham (E of Karcham)	31.5084	78.2427	1873	Vaikrita	psammitic/ pelitic gneiss	med-gr; boudinaged-disaggregated qz veins	i) ky-gt paragneiss, graphite	19/073	10/008	S	x	x	x
							looks like Haimanta sample I05/8	ii) x2 gt-ky-st paragneiss				x	x	x
								iii) x2 gt paragneiss						
I05/33	Peo-Karcham (E of Karcham)	31.4963	78.2190	1850	Vaikrita	mylonite	psammite>pelite, minor gt in psammite (possibly present in coarse-gr pelite); migmatitic textures (bi selvedges to qz blobs); boudinaged foliation (strong planar fabric)		43/036	33/001				
I05/34	Bridge E of Karcham	31.4987	78.2057	1890	Vaikrita	mylonite	psammite (inc isolated pink gt) > pelite > mafic layer (boudinaged, two-tone gt - black cores, red/pink rims)		37/084	25/036				

Locality N°	Locality	GPS			Unit	Lithology	Additional features	Sample	Structural measurements			Sections cut		XRF data
		Longitude	Latitude	Elevation (m)					Ss / other Ss	Ls / other Ls	sense of shear (top to/criteria)	std	probe	
I05/35	E of Karcham (just E of hydroelectric st)	31.4966	78.1983	1814	Vaikrita	mylonite	psammitic; less strain than IO5/34		39/088	36/074				
I05/36	E of Karcham (just E of hydroelectric st)	31.4963	78.1973	1812	Karcham	mica schist	interlayered w/ qz veins; s-c fabric; more scaley(coarser-gr) to the W	gt-mica schist	39/083	37/062	WSW / s-c fabric, qz lenses	x	x	
I05/37	E of Karcham (just E of hydroelectric st)	31.4960	78.1917	1817	Karcham	psammitic/ pelitic gneiss	gt		41/090	24/044				
I05/38	Karcham	31.4963	78.1851	1816	Karcham	mica schist	steep fractures	gt-st? -mica schist				x	x	x
I05/39	N end of Sangla Valley	31.4863	78.1827	1861	Karcham	psammitic> pelitic schist	folded, boudinaged qz veins	gt-mica schist (psammitic), graphite [plus addendum to I01/49]				x	x	
I05/40	N end of Sangla Valley	31.4780	78.1829	1916	Karcham	mylonitic'/ banded schist/gneiss			40/087	29/034				
I05/41	N end of Sangla Valley	31.4707	78.1846	1939	Karcham	mica schist	fine-gr; numerous folded + boudinaged qz veins; interbedded mm-scale pelite	gt-mica schist (psammitic)	42/079			x	x	
I05/42	N end of Sangla Valley	31.4695	78.1867	2083	Karcham? Vaikrita?	mica schist	fine-gr; 50% interbedded w/ mm-scale gt-pelite; numerous folded + boudinaged qz veins	x2 gt-mica schist (psammitic)	45/078	24/021		x	x	
I05/43	Choling	31.5249	78.1398	1918	Wangtu C/ Karcham basalts?	pelitic schist/ paragneiss	mafic interlayers; x-cutting gt-tu-wm-lgr	i) x2 gt-tu lgr ii) gt-tu lgr iii) mafic gneiss			S / augen, qz 'blebs'			
I05/44	Choling	31.5230	78.1401	1951	Wangtu Complex/ Karcham?	paragneiss		gt? paragneiss						
I05/45	E of Wangtu	31.5422	78.0252	1579	Wangtu Complex	bi augen gneiss with pelitic and mafic layers/ boudins	layers (<1m) split/pinch out into bi/chl-rich zones; boudinaged lgr	i) gt-pelite (lens in augengneiss) ii) gt-mica schist iii) mafic body						

Locality N°	Locality	GPS			Unit	Lithology	Additional features	Sample	Structural measurements			Sections cut		XRF data
		Longitude	Latitude	Elevation (m)					Ss / other Ss	Ls / other Ls	sense of shear (top to/criteria)	std	probe	
I05/46	W of Wangtu	31.5550	77.9133	1529	Wangtu Complex	paragneiss, mafic layers, augengneiss	crenulated; mafic layers (fine-gr, lineated amph, plag, qz pods rimmed by amph) bounded by coarse bi layers <5cm; monoclinal folds on outcrop scale; p. melting		45/327	29/275 MFH 09/267				
I05/47	W of Wangtu	31.5561	77.9110	1555	Wangtu Complex	paragneiss > mafic layers	undeformed p. melt leucosomes		36/293	23/268				
I05/48	W of Wangtu	31.5593	77.9062	1540	Wangtu Complex	paragneiss > mafic layers	minor folds with tu-lgr in hinge/core		38/296	32/258				
I05/49	W of Wangtu	31.5600	77.9037	1584	Wangtu Complex	calc-silicate; mylonite		i) x2 minor calc-sil layer: gt (orange), diop (bottle green), amph (black, elongate) ii) 'matrix' to calc-sil layer (gt, diop, qtz/CO3)	47/267	37/297				
I05/50	W of Wangtu	31.5557	77.8809	1657	Wangtu Complex	mafic layers > pelite > augengneiss	fine-gr foliated mafic layers inc. Fe-rich areas (weathered red-brown); oarse-gr bi-pelite layers; augen (2-3cm) gneiss		41/243	36/272				
I05/51	Wangtu-Sarahan	31.5717	77.8523	1708	Wangtu Complex	augen gneiss, minor mafic layers	sheared black bands		48/349	37/301				
I05/52	Wangtu-Sarahan	31.5662	77.8373	1610	Wangtu Complex	augen gneiss, mafic layers, minor pelite	p.melt, x-cutting lgr; mafic layers w deformed qz veins; coarse-gr pelite layers w 0.5-1cm qz veins		76/017	57/307				
I05/53	Wangtu-Sarahan	31.5591	77.8263	1624	Wangtu Complex	paragneiss	micro-folded; p. melt; deformed qz veins		78/312 (SW), 61/005 (NE)	67/340 (SW),57/339 (NE)				
I05/54	Wangtu-Sarahan	31.5474	77.8204	1661	Jutogh?	mica schist	cren/micro-folded; p.melts; boudinaged qz veins		61/014	56/350				
I05/55	Jeori-Sarahan	31.5171	77.7913	1844	Shear zone (Wangtu Complex - Jutogh)	melange of amphibolite gneiss	lgr, qz veins; friable matrix inc bi, chl, cu mineralisation; sigmoidal fabric; >50m thick		36/318	29/351	SSE / s-c fabric, qts 'blebs', rotated + fractured clasts			
I05/56	Sarahan	31.5305	77.7968	2065	Wangtu Complex/ Jutogh	augen gneiss	pelite (inc smoky qz blebs) and mafic layers		34/004	31/013 MFH: 04/293	SSW / asymmetric folds, fsp augen, qz 'blebs'			

Locality N°	Locality	GPS			Unit	Lithology	Additional features	Sample	Structural measurements			Sections cut		XRF data
		Longitude	Latitude	Elevation (m)					Ss / other Ss	Ls / other Ls	sense of shear (top to/criteria)	std	probe	
I05/57= I01/59	Sarahan	31.5110	77.7953	2168	Wangtu Complex/ Jutogh	pelitic schist	tightly folded; coarse wm	st-gt-mica schist				x	x	x
I05/58	Sarahan	31.5081	77.7953	2193	Wangtu Complex/ Jutogh	pelitic schist-gneiss	fine-gr; kink bands/tight folds		48/007	46/026	S / kink folds			
I05/59	Sarahan	31.5036	77.7839	2257	Wangtu Complex/ Jutogh	chl-gt schist	fine-gr; higher gt concentration around qz vein		42/320	28/349 MFH 33/292				
I05/60	Sarahan	31.5070	77.7915	2203	Wangtu Complex/ Jutogh	wm-chl-mica schist	minor gt		55/358	47/035				
I05/61	Sarahan	31.5100	77.7840	2023	Jutogh	wm-chl-mica schist >> augengneiss	kinked; schist gt-rich in float; mafic gneiss layers/ boudins		34/213	30/017	SSW / kfs augen			
I05/62	SW of Sarahan	31.5069	77.7766	1970	Jutogh	psammitic gneiss	pervasively kinked; bands of qz/fsp and bi/chl		14/330	10/016 MFH 10/287	S / s-c fabric			
I05/63	Head of valley, SW of Sarahan	31.4996	77.7732	2084	Jutogh	psammitic gneiss	deformed tu-lgr	i) x2 lgr	28/325	25/353 MFH 15/300	S / s-c fabric, qtz boudins, tu clots	x	x	x
							pervasively kinked	ii) gt paragneiss (country rock)				x	x	x
I05/64	Head of valley, SW of Sarahan	31.4976	77.7736	2019	Jutogh	grey mylonite	sigmoidal fsp + qz augen; p.melts (bi selvedges) 1-10cm	mylonite	36/002	35/005	S / qtz/fsp 'clasts			
I05/65	SW of Sarahan	31.4917	77.7740	2048	Jutogh	psammitic/ pelitic schist	fewer kinks, i.e. a more planar fabric; gt pbl in isolated area of outcrop	ky-mica schist w/ smoky qz blebs, bronze bi	28/318	20/001	S / qtz 'bleb's/lenses	x	x	x
I05/66	SW of Sarahan	31.4906	77.7784	1999	Jutogh	mica schist	weakly folded; boudinaged qz veins <40cm - richer mineralogy assoc w/ these	i) gt-mica schist w/ smoky qz blebs	22/321	13/017		x	x	x
								ii) x2 st gt mica schist w/ smoky qz						
I05/67	SW of Sarahan	31.4826	77.7796	2022	Jutogh	chl-wm schist	infrequent kinks, more like pervasive cm-scale folds w flat-lying hinge lines; no smoky qz blebs; bi pbl interbedded w/ more psammitic schist		08/229	04/356 MFH 08/328				
I05/68	SW of Sarahan	31.4807	77.7826	2010	Jutogh	psammitic/ pelitic schist	microfolded; steeply dipping brittle faults spaced ~5m throughout most of the outcrop	i) gt(av 1cm)-mica schist	25/297	16/348		x	x	
								ii) gt mica schist: gt-pbl (singles) + WR				x	x	x
								ii) gt mica schist: gt-pbl (singles) + WR, graphite				x	x	x

Locality N°	Locality	GPS			Unit	Lithology	Additional features	Sample	Structural measurements			Sections cut		XRF data
		Longitude	Latitude	Elevation (m)					Ss / other Ss	Ls / other Ls	sense of shear (top to/criteria)	std	probe	
I05/68 cont.	SW of Sarahan	31.4807	77.7826	2010	Jutogh	psammitic/ pelitic schist		ii) gt mica schist: gt-pbl (singles) + WR v) gt pbl (~2cm)				x	x	x
I05/69	SW of Sarahan	31.4702	77.7952	1976	Jutogh	chl-wm schist	fine-gr; minor fleks of bi		17/334	13/002				
I05/70	SW of Sarahan	31.4644	77.8172	1913	Jutogh	paragneiss, lgr	boudinaged qz veins; lgr boudin: m-scale, large tu (<2cm), wm books	i) tu-lgr	35/049	22/352	S / qtz/fsp 'blebs'	x	x	x
								ii) tu-lgr				x	x	x
								iii) x2 paragneiss (country rock)				x	x	x
I05/71	SW of Sarahan	31.4599	77.8042	1957	Jutogh	psammitic/ orthogneiss > paragneiss > boudinaged mafic layers	pervasively kinked/ crenulated; mm-scale banding; fine-gr, cream-grey ortho-gneiss w qz-fsp augen <1cm; fine-gr, grey paragneiss; fine-gr, dark grey-green boudinaged mafic layers (chl, act?); folded + boudinaged qz veins + tu lgr veins	i) tu lgr vein in paragneiss	23/111	09/040 Lc 04/025		x	x	x
								ii) gt paragneiss				x	x	x
I05/72	Shimla	31.0997	77.1413	2060	Shimla klippe 'Jutogh'	psammitic/ pelitic schists		gt-mica schist, graphite (grey-blue sheen)	21/193	06/270	W / s-c fabric			
I05/73	Shimla-Jutogh	31.0993	77.1373	2079	Shimla klippe 'Jutogh'	psammitic schist	fine-gr; 10-20 cm planar beds; mm-scale gneissose banding; minor mica; graphite?		23/289	21/266				
I05/74	Shimla-Jutogh	31.1085	77.1066	1884	Shimla klippe 'Jutogh'	carbonate, sandstone interbeds	carbonate: med-gr (0.5-1mm), grey, cm-spaced brown-red Fe-rich laminae (mm); sandstone: fine-gr, black-grey; minor folded qz veins; steep brittle fractures, qz filled plus fault breccia		21/152	08/080				
I05/75 (~I01/72)	Shimla-Jutogh (just below Juotgh Cantonment)	31.1132	77.1044	1836	Shimla klippe 'Jutogh'	psammitic/ pelitic schist	boudinaged qz veins; brittle fractures	gt(<1cm)-mica schist (singles and WR)	21/266	19/273	E / s-c fabric, gt pbl	x	x	x
I05/76	Jutogh-Halog	31.1554	77.0742	1655	Shimla Slates	graphitic slate	dark grey-black slate; brittle fractures inc fault gouge; large qz veins weathered red (fluids)		43/302	40/289				
I05/77	Halog	31.1659	77.0260	1463	Shimla Slates	slate	finely laminated; chl/graphitic sheen; bi/oxide fleks, <1mm + acicular (visible on foliation plane)		24/075	22/073				

Locality N°	Locality	GPS			Unit	Lithology	Additional features	Sample	Structural measurements			Sections cut		XRF data
		Longitude	Latitude	Elevation (m)					Ss / other Ss	Ls / other Ls	sense of shear (top to/criteria)	std	probe	
I05/78	Jutogh	31.1021	77.1054	1873	Shimla klippe 'Jutogh'	various: psammite, pelite, mafic (amph-chl), grey-white carbonate	friable schist; folded	i) gt psammitic schist (singles and WR)				x	x	x
								ii) gt-st psammitic schist						x
I05/79	W of Jeori (+ of Sutlej)	31.5321	77.7714	1253	Wangtu Complex/ Jutogh	paragneiss	pervasively kinked (cm-scale); folded + boudinaged qz veins; minor mafic layers		54/241	25/170 MFH 37/295				
I05/80	W of Jeori (+ of Sutlej)	31.5303	77.7682	1343	Wangtu Complex/ Jutogh	bi augen gneiss	augen <1cm, pervasively kinked; boudinaged qz veins		43/230	23/164 MFH 43/291				
I05/81	W of Jeori (+ of Sutlej)	31.5417	77.7749	1462	Wangtu Complex/ Jutogh	gt paragneiss	pervasively kinked (cm-scale); folded + boudinaged qz veins; minor mafic layers	gt-mica schist (singles and WR)	48/008	48/005		x	x	x
I05/82	W of Jeori (+ of Sutlej)	31.5468	77.7674	1531	Wangtu Complex/ Jutogh	psammitic/ pelitic schist	fine-gr; broadly folded; psammite: qz/fsp, wm, chl; pelite: bi, st/tu, ky relic; dark red gt	gt-mica schist						
I05/83	W of Jeori (E of Sutlej)	31.5392	77.7785	1196	Wangtu Complex/ Jutogh Shear zone?	gt amphibolite	sheared; microfine laminae	gt amphibolite						
I05/84	Nr Kinu, SW of Sarahan	31.4564	77.7705	2058	Jutogh	mica schist	fine to med-gr	x) x3 gt-chl (ctd pseudomorphs) schist	28/006	28/007	S / s-c fabric	x	x	x
I05/85	Kinu-Jeori	31.4677	77.7722	2128	Jutogh	chl-wm schist	fine-gr; minor bi poss in chl layers		32/011					
I05/86	Kinu-Jeori	31.4728	77.7602	1912	Jutogh	gt-chl-wm schist	chl pseudomorph of ctd/st?		27/347	26/338	S / s-c fabric			
I05/87	Kinu-Jeori	31.4957	77.7566	1610	Jutogh	paragneiss/ mica schist	boudinaged qz veins	gt-st? -mica schist (singles and WR)	45/002	41/321		x	x	x
I05/88	Kinu-Tiklik/ Taklesh	31.4565	77.7728	2254	Jutogh	chl-wm schist	fine-gr; boudinaged qz veins (3-10cm long); bi or ky p'blasts? see I05/90		21/332	10/036	NE / s-c fabric			
I05/89	Kinu-Tiklik/ Taklesh	31.4522	77.7684	2297	Jutogh	chl-wm schist	boudinaged qz veins; mafics in float; bi or ky p'blasts? see I05/90		19/080	04/012				
I05/90	Top of pass bt Kinu+Tiklik/ Taklesh	31.4443	77.7526	2895	Jutogh/ Rampur quartzite	chl-wm schist	crenulated, kinked; ~1m quartzite beds interlayered w/ dark-green chl schist	ky(not chrome-mica) - chl-wm schist	32/321 (NE), 16/302 (SW)	30/181 (NE), 6/010 (SW)		x	x	x

*Samples I05/9 and I05/10ii

Adjacent to the Akpa Granite, and less than 5 km from the STD, abundant (c. 20% model volume) hyalophane ((K,Ba)Al(Si,Al)$3O_8$; see Tindle, 2008 for more information) poikiloblasts are found in the Haimanta Group, in a biotite–graphite schist and a paragneiss (localities I05/9 and I05/10 respectively, Fig. A1.1). The BaO content of hyalophane is ~2 wt % in sample I05/9, and between 4 and 7 wt % (increasing from rim to core) in sample I05/10ii (Table A1, Fig. A1.3). The poikiloblasts are weakly perthitic (typically at the edges of the p'blasts, but also present in less common sub-grain domains, Fig. A1.5c–f), rarely twinned, and some feature chemical alteration associated with fractures (Figs. A1.4, I05/10ii). Inclusion trails are aligned oblique (45–80°) to the main foliation, and consist of bands of graphite (Fig. A1.5a–b), quartz, plagioclase (anorthite-rich, as in the matrix), biotite and muscovite, with accessory zircon and apatite. Monazite, a datable accessory phase (Chapters 3 and 6), can also be found in hyalophane but is unlikely to be a true inclusion as it is typically interstitial and spatially-related to cracks in the 'host' crystal. In the matrix, monazite forms anhedral clusters. Mica inclusions are smaller than matrix mica which suggests an increase in the metamorphic grade since the growth of hyalophane. Locally (I01/26; Caddick, 2004) large (~2–5 mm) tourmaline porphyroblasts are found, some of which are intergrown with a feldspar phase which strongly resemables hyalophane. Tourmaline inclusion trails are micro-folded, and distinct from the external fabric.

Table A1.1 Hyalophane electron microprobe analyses (weight % oxide), Haimanta Group, Sutlej valley (Fig. A1.1)

sample	comment	SiO_2	TiO_2	Al_2O_3	FeO	SrO	**BaO**	CaO	Na_2O	K_2O	Rb_2O	Total
I05/9	spot analysis	63.05	0.02	19.08	0.02	0.04	**2.33**	0.03	1.11	14.07	0.01	99.75
	spot analysis	62.70	0.00	19.10	0.02	0.05	**2.49**	0.09	1.08	14.19	0.03	99.81
I05/10ii	spot analysis	61.14	0.01	19.46	0.01	0.05	**4.75**	0.01	1.47	12.63	0.08	99.63
	spot analysis	60.08	0.00	19.76	0.01	0.06	**6.08**	0.05	1.59	11.92	0.00	99.60
Distance (mm)	profile											
0.00	1 (rim)	61.00	0.02	19.53	0.07	0.06	**4.95**	0.00	1.42	12.48	0.00	99.60
0.31	2	61.10	0.00	19.41	0.02	0.09	**4.62**	0.02	1.45	12.61	0.04	99.39
0.92	4	60.09	0.04	19.76	0.02	0.10	**5.89**	0.04	1.57	12.00	0.04	99.57
1.53	6	59.88	0.04	19.70	0.04	0.09	**6.07**	0.04	1.48	11.94	0.12	99.47
1.84	7	59.29	0.05	19.83	0.00	0.07	**6.68**	0.04	1.53	11.59	0.03	99.13
2.15	8	58.99	0.03	19.91	0.02	0.13	**6.88**	0.04	1.53	11.67	0.06	99.31
2.45	9 (core)	59.57	0.04	19.64	0.00	0.06	**6.74**	0.03	1.47	11.70	0.05	99.31
2.76	10	59.48	0.04	19.84	0.01	0.09	**6.59**	0.03	1.57	11.77	0.01	99.44

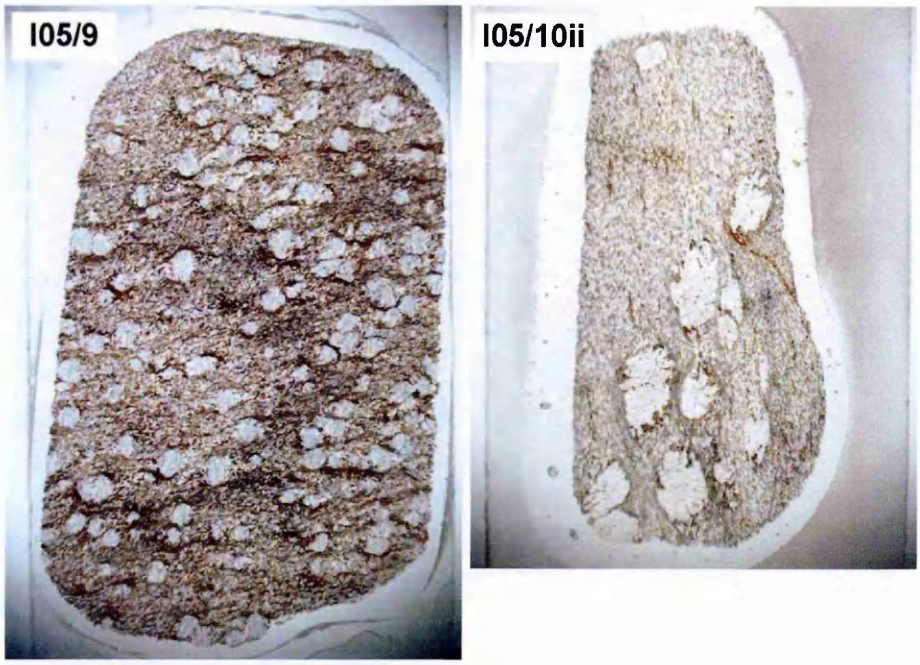

Fig. A1.3 Photographs of hyalophane poikiloblasts in thin sections of Haimanta Group metasediments. Width of sections, 2.5 cm.

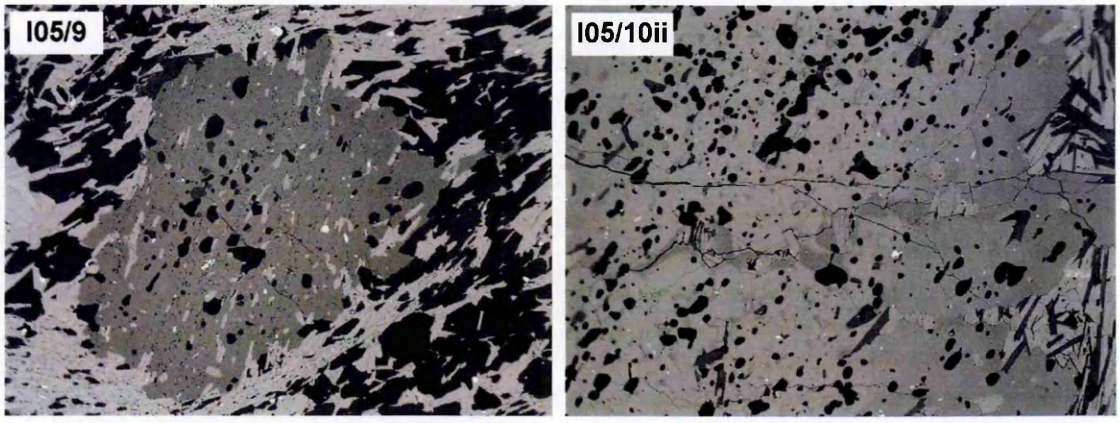

Fig. A1.4 Back scatter electron images of hyalophane poikiloblasts, with inclusion trails (graphite, mica and quartz) aligned oblique (~ 45°) to the external fabric (I05/9), and chemical alteration associate with fractures (I05/10ii). Width of view (both images), 2.5 mm.

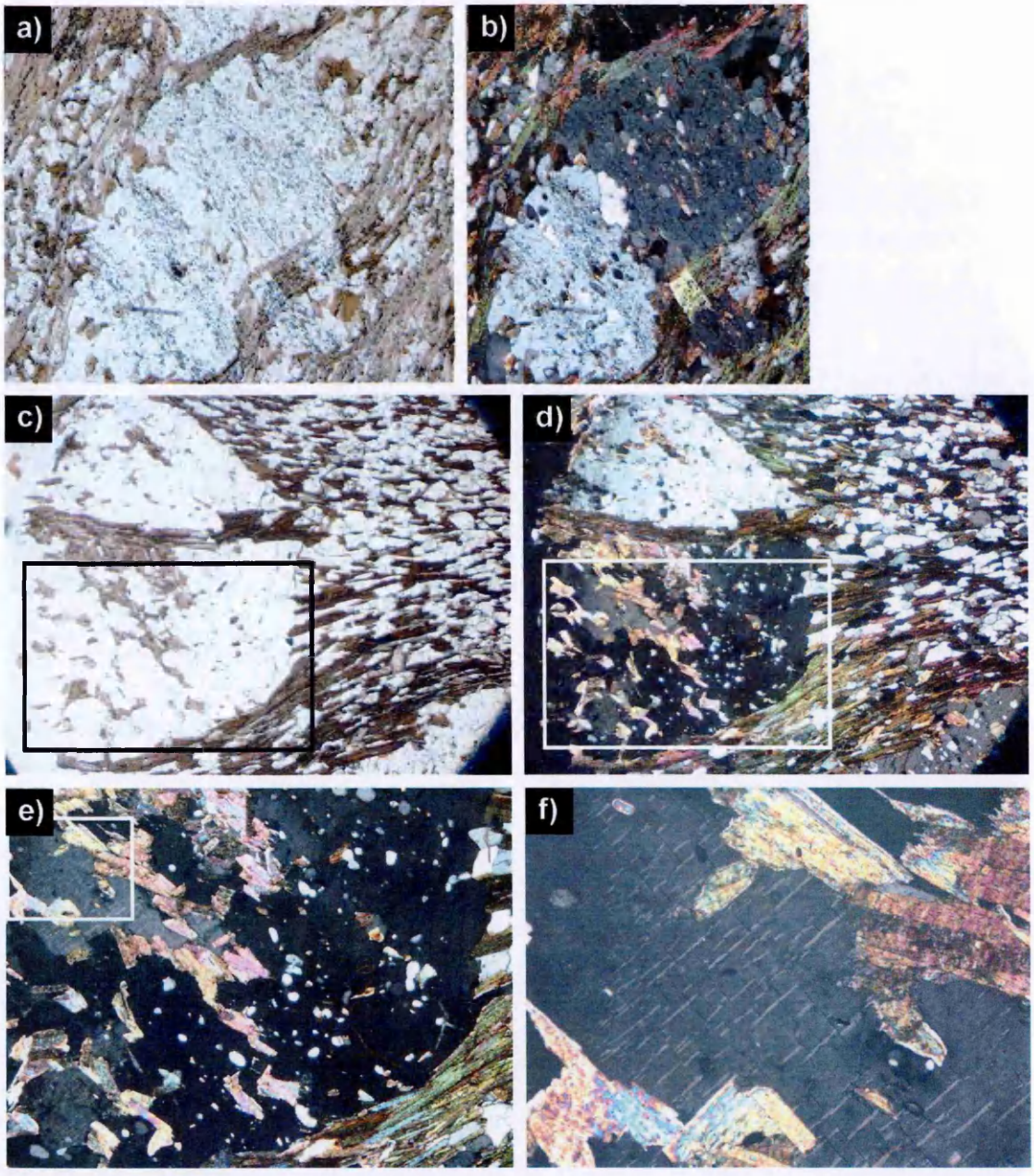

Fig. A1.5 Microphotographs of hyalophane poikiloblasts (approx 2 mm diameter in a)–b), and 4 mm diameter in c)–d)): (**a**) bands of graphite inclusion tails are aligned across the p'blasts at ~80° angle to the external fabric; late white mica laths overgrow fabric (including graphite), bottom right of p'blast, clearer in b) (I05/9); (**b**) same as a) but through cross polarised light; (**c**) fractured p'blast and associated biotite replacement (I05/10ii); (**d**) same as c) but through cross polarised light; (**e**) boxed area in c) and d) showing sub-grain detail; (**f**) boxed area in e) showing perthitic texture.

The spatial coincidence of hyalophane to the contact with the Akpa granite, plus the unusual whole-rock chemistry (Appendix C1.1) may suggest fluid-assisted growth during, or immediately following, the intrusion of the Akpa Granite in the early Palaeozoic, assuming the source of Ba was

from fluids flushed from the granite into the proximal metasediments. Similarly, Ba may have been introduced along fault-related pathways associated with the South Tibetan Detachment. As hyalophane grew early with respect to the main foliation, late (i.e. post-tectonic) growth associated with contact metamorphism related to any Miocene leucogranite intrusions can be ruled out. However, hyalophane mineralisation documented in Scotland, in a stratabound zone of barium and lead–zinc–iron–sulphide mineralization in Middle Dalradian metasedimentary rocks, e.g. graphitic schists of the Ben Eagach Schist formation north of Aberfeldy, and the Argyll Group at Corrie Loch Kander, near Braemar (Tindle, 2008 and references therein) is considered *authigenic* in origin (via seafloor exhalative activity). Furthermore, some hyalophane textures in the Dalradian rocks suggest growth during regional metamorphism, in response to the Grampian orogeny (Fortey and Beddoe-Stephens, 1982). Thus, these rocks are analogous (not only texturally, but also chemically) to the hyalophane-bearing schists in the Haimanta Group, and it is inferred that hyalophane in the Haimanta Group grew during the Himalayan orogeny. This is consistent with the size of the poikiloblasts (1 to 5 mm) and the lack of deformation (e.g. recrystallisation) and/or alteration that one would expect had the hyalophane poikiloblasts grown earlier. Also, the Haimanta Group and Dalradian rocks are similar in age (Neoproterozoic–Cambrian), and so hyalophane mineralisation may reflect similar seafloor conditions at that time.

Elsewhere in the Himalaya, Ba-rich (0.4–0.5 %) poikiloblastic K-feldspar megacrysts are found in the North Col Formation (Nepal) (Weinberg and Searle, 1999), a unit which correlates to the Haimanta Group (Table 7.3). However, textural and chemical evidence suggests that these poikiloblasts are the product of late-stage autometasomatism, and in this respect contrast with the poikiloblasts found at the Haimanta Group–Akpa granite contact in the Sutlej valley.

Although the occurrence of hyalophane is not common (Tindle, 2008) it could be easily overlooked. The hyalophane porphyroblasts here were originally misidentified in the field as garnet (a common porphyroblast in the region, also wrapped by the matrix and of a similar size). In thin section hyalophane is similar in appearance to cordierite, but can also be easily mistaken for more familiar feldspar phases such as K-feldspar or plagioclase unless subject to major element analysis.

See Hetherington et al. (2008) for more details regarding Ba mineralisation.

References

Fortey, N.J. and Beddoe-Stephens, B., 1982. Barium Silicates in Stratabound Ba-Zn Mineralization in the Scottish Dalradian. Mineralogical Magazine 46, 63-72.

Hetherington, C.J., Lundmark, M., Graeser, S. and Giere, R., 2008. The chemistry of barium anomalies in the Berisal complex, Simplon Region, Switzerland. International Journal of Earth Sciences 97, 51-69.

Tindle, A.G., 2008. Minerals of Britain and Ireland. Terra Publishing, Harpenden, Herts, 624 pp.

Weinberg, R.F. and Searle, M.P., 1999. Volatile-assisted intrusion and autometasomatism of leucogranites in the Khumbu Himalaya, Nepal. Journal of Geology 107, 27-48.

Locality N°	Locality	GPS			Unit	Lithology	Additional features	Sample	Structural measurements			Sections cut		XRF data
		Longitude	Latitude	Elevation (m)					Ss / other Ss	Ls / other Ls	sense of shear (top to/criteria)	std	probe	
B06/1	en route to Punakha	89.8633	27.5246	2130	HHCS, nr KT	mica-schist	med-coarse gr; sheared; small tu-lgr veins			shallow NW-dipping	SE / ksp 'blasts			
B06/2	SE of Punakha Dzong	89.8642	27.5785	1233	HHCS, nr KT, Takhsang Gneiss	gneiss	coarse-gr; qz pods	ia)+ib) bi-gt gneiss ii) sill gneiss	34/007			x	x	
B06/3	inbt old+new Punakha	89.8706	27.5708	1238	HHCS, nr KT, Takhsang Gneiss	sill gneiss	intra-bed meso-scale folds; gt-lgr 'sills'							
B06/4	S of new Punakha	89.8679	27.5436	1274	HHCS, nr KT	schist	garnetiferous bands <10cm in width (gt <2cm)	gt (av 1cm) schist, heavily weathered				x	x	
B06/5	N of Dungkhar	91.1143	27.8546	1614	HHCS, above KT	gneiss, migmatite, leucogranite, slate, ex-eglogite, marble	mixed river float:	i)x gt-tu lgr with sill-atoll gt ii)x gt (2-3mm)-bi-sill gneiss iii)x gt(<1cm)-bi-sill gneiss iv)x " gt(<1cm)-bi-sill gneiss (sill-bi intergrowths) v)x dark, fine-gr laminated rock (~TSS/Checkha) TA) ex-eclogite						
B06/6	Dungkhar village	91.1136	27.8189	1931	HHCS, above KT	gneiss; calc-sil layers; leucogranite	fine grey banded (variable bi+qz) gneiss; calc-sil layers:amph/diop ± pale pink fsp/calcite; gt-lgr (tonalite?), gt<6mm, av.2-3mm		15/254	04/333				
B06/7	Dungkhar-Lhuentse Road	91.1106	27.8154	2013	HHCS, above KT, Takhsang Gneiss	migmatite; gneiss; pegmatite	80% migmatite; fine grey banded gneiss; coarse bi>tu pegmatite		27/005	23/344				
B06/8	Dungkhar-Lhuentse Road	91.0997	27.7924	2374	HHCS, above KT	gneiss	med-coarse bi-sill±gt gneiss, gts av 2mm; wm-gt(<5mm)-tu lgr w/ interleaves of gneiss		25/021	20/347				
B06/9	Dungkhar-Lhuentse Road	91.1334	27.7495	2299	HHCS, above KT, Takhsang Gneiss	migmatite	migmatite (<70% l'some/lgr: gt<4mm, tu, wm); minor gneissose bands 30-40cm wide		25/301	24/297	ESE / asymmetric leucocratic 'blebs'			
B06/10	Dungkhar-Lhuentse Road	91.1407	27.7297	1499	HHCS below KT (DG map-above KT)	gneiss	few% tu-wm lgr stringers	fine grey gt(<3mm, av 1.5mm) schistose gneiss	17/046 / c surface: 12/169	16/038 / c surface: Ls 07/221	SW / qz-fsp blebs	x	x	

Locality N°	Locality	GPS			Unit	Lithology	Additional features	Sample	Structural measurements			Sections cut		XRF data
		Longitude	Latitude	Elevation (m)					Ss / other Ss	Ls / other Ls	sense of shear (top to/criteria)	std	probe	
B06/11	Dungkhar-Lhuentse Road, along valley	91.1337	27.7301	1320	HHCS below KT (DG map-above KT)	calc-silicate ~gneiss	fine, grey, gt+amph/diop elongate lenses define foliation; negligible lgr + sill		36/013 / Sf 57/161	24/322				
B06/12	Dungkhar-Lhuentse Road, along valley	91.1385	27.7258	1326	HHCS below KT (DG map-above KT)	gneiss	grey banded; variably richer calc-sil+mica layers; minor tu-lgr in foliation boudinage (symmetric) necks		16/323	12/289				
B06/13	Dungkhar-Lhuentse Road, along valley	91.1452	27.7209	1342	HHCS below KT (DG map-above KT)	calc-sil ~gneiss	includes granular marble		33/041	32/032	SW / some *isolated* asymm folds			
B06/14	Dungkhar-Lhuentse Road, along valley	91.1461	27.7196	1341	HHCS below KT (DG map-above KT)	fractured gneisses	numerous subvertical faults, heavily mineralised (Fe oxides, Cu oxides-blue in places); calc flowstone; few weak striae in dark grey mineralised gouge				S / *if* subsidiary reidal fractures to the fault (dipping gently N)			
B06/15	Dungkhar-Lhuentse Road, nr Lhuentse	91.1559	27.7137	1271	HHCS below KT (DG map-above KT)	mica-schist	wm-bi±gt(uncommon, 1-2mm); little sign of lsome development; more low-angle faults, a few high-angle faults w/ cruch breccia and grey gouge		16/335	16/313	S / chevron-style folds			
B06/16*	Dungkhar-Lhuentse Road, nr Lhuentse	91.1586	27.7118	1278	HHCS below KT (DG map-above KT)	psammitic/pelitic schist	kink folds; ±gt (av 1mm); wm pervasive enough not to be secondary (=no sill)	cumm-bi schist	25/008	19/318		x	x	
B06/17	Dungkhar-Lhuentse Road, nr Lhuentse	91.1671	27.7014	1299	HHCS below KT (DG map-above KT)	psammitic/pelitic schist	psammite:fine-gr, competent; pelite:coarse-gr, wm pervasive enough not to be secondary (=no sill), gt-lsome (bi inclusions nr gt rims); ky w/ lsomes, or just qz?; *meso-scale isoclinal folds*	coarse-gr ky schist, rare anhedral gt (cm-scale)	42/011			x	x	
B06/18	Dungkhar-Lhuentse Road, nr Lhuentse	91.1654	27.6987	1283	HHCS below KT (DG map-above KT)	quartzite/psammite; pelitic-schist interlayers	in pelitic layers: gt 1-2cm, no ky in hand specimen; minor lsome		12/046	07/007				
B06/19	Dungkhar-Lhuentse Road, nr Lhuentse	91.1721	27.6889	1306	HHCS below KT (DG map-above KT)	psammite	minor pelitic layers		50/104	22/034 / MFH 26/036	SE / asymm folds			

Locality N°	Locality	GPS			Unit	Lithology	Additional features	Sample	Structural measurements			Sections cut		XRF data
		Longitude	Latitude	Elevation (m)					Ss / other Ss	Ls / other Ls	sense of shear (top to/criteria)	std	probe	
B06/20	Dungkhar-Lhuentse Road, nr Lhuentse+camp at hydroelectric station	91.1799	27.6745	1319	HHCS below KT	gneiss	lsome pods/lenses, no sill/ky evident		58/052	56/034				
B06/21	Dungkhar-Lhuentse Road, nr Lhuentse Hospital	91.1829	27.6731	1331	HHCS below KT, Paro metaseds or Chekha (see Grujic map)	gneiss; migmatite	abundant red gts 4-10mm; ky 1-2mm -->mu reaction includes ky); partial bi pseudomorphs of ky/gt; lsome	gt-ky graphitic schist	47/060	42/036		x	x	
B06/22	S of Lhuentse	91.1875	27.6708	1214	HHCS below KT, Paro metaseds	gneissose schist	± gt	gt schist	70/077	20/036				
B06/23	S of Lhuentse	91.1906	27.6660	1221	HHCS below KT, Paro metaseds	orthogneiss	gt: few mm<1cm, larger xls non-euhedral, quite red, bi rim; tu		82/290	32/018				
B06/24	S of Lhuentse	91.2014	27.6645	1213	HHCS below KT, Paro metaseds	orthogneiss; (further S:) schist	gt-tu orthogneiss; gt-schist: inc thin layer w/ cm-gt		58/067					
B06/25	S of Lhuentse	91.2136	27.6534	1229	HHCS below KT, Paro metaseds	schist	gt 1-5mm; locally variable lsome as cm-scale pods/lenses	(TA) Bh06/25i gt schist (TA) Bh06/25ii gt(4-5mm) schist	63/015	61/015				
B06/26	S of Lhuentse	91.2095	27.6245	1238	HHCS below KT, Paro metaseds	augengneiss	gt		45/298	18/008				
B06/27	S of Lhuentse, N of Japanese (Tangmachu) bridge	91.2095	27.6153	1202	HHCS below KT, Paro metaseds	schist	scaley	gt (0.5-1mm)-wm schist, plus individual gts	42/306	39/345	SE / qtz 'blebs'	x	x	
B06/28	S of Lhuentse, S of Tangmachu Bridge	91.2146	27.6018	1151	HHCS below KT, Paro metaseds	psammitic/pelitic schist	mesoscale-folded psammite; gt (~3mm, dark red) in pelitic layers; boudinaged qz veins		49/034	42/355	S / some qtz 'blebs'			
B06/29	S of Lhuentse, S of Tangmachu Bridge	91.2140	27.5969	1130	HHCS below KT, Paro metaseds	quartzite	banded: 2-50cm bands; thin interlayers of mica	(TA)Bh06/29x gt-st?phyllite-schist - for poss s.o.s. work	39/037	28/083	S / one long mica aggregate 'fish'			

Locality N°	Locality	GPS			Unit	Lithology	Additional features	Sample	Structural measurements			Sections cut		XRF data
		Longitude	Latitude	Elevation (m)					Ss / other Ss	Ls / other Ls	sense of shear (top to/criteria)	std	probe	
B06/30	S of Lhuentse, S of Tangmachu Bridge	91.2163	27.5903	1179	HHCS MCT zone, Paro metaseds	augenmylonite, asymmetrically folded qtzite, flinty psdeudotachlyte, mafic mylonite	syndef qz veins	TA sampled mafic mylonite for geochem purposes	30/065	18/009	S / ksp augen			
B06/31	S of Lhuentse, S of Tangmachu Bridge	91.2150	27.5862	1174	LHS MCT zone	gneiss // 50m S: phyllite-schist	fine-gr; meso-scale asym folds inc qz veins; minor mafic layers [TA sampled] // 'fish-scale' phyllite-schist w/ transposing foliation (=s-c fabric)	i) coarse gt(1-2mm, euhe-anhedral)-st?-chl phyllite-schist ii) " (this one for WR)	55/053		S / augen, qtz blebs, asymm folds in mylonitic fabric	x	x	
B06/32	S of Lhuentse, S of Tangmachu Bridge	91.2054	27.5671	1115	LHS	phyllite-schist	coarse chl ±gt (2-3mm); psammitic gneiss layers		47/301	24/006	S / numerous qtz/qtz-fsp 'blebs'			
B06/33	S of Lhuentse, Rangmandu Bridge	91.2063	27.5588	1102	LHS	phyllite, quartzite			qtzite dips steeply W					
B06/34	S of Lhuentse	91.2034	27.5425	1137	LHS	chl-phyllites	folded('mushed') phyllites ±small gt; competent psammitic gneiss/quartzite		12/052	10/013				
B06/35	Nr Tangmachu Bridge	91.2155	27.6080	1218	HHCS MCT zone, Jaishidanda Fm?	schist	gt: 3-4mm av<1cm, abundant, dark red, euhedra; ky: av 0.2 x 0.5-1cm long; 5-10% deformed lsome/pegmatite w/ larger ky	i) gt-ky schist [TA sampled whole gts av 3-4mm, one 1cm]	46/021	46/021	SSW / some gts, qtz-fsp 'blebs', assymetric qz tails on augen	x	x	
	"...100m down track					100m S: gneiss, migmatite	gt: less abundant; ky: more abundant, larger, aligned; tu lgr	x) ky-gt migmatite				x	x	
B06/36	Nr Tangmachu Bridge	91.2153	27.6013	1177	LHS	interleaved quartzites, phyllites	craggy		55/018	51/355	S?(incomplete trans of earlier steep Ss) / sigmoidal qtz blebs			
B06/37	Nr Tangmachu Bridge	91.2164	27.5984	1231	LHS	interleaved quartzites, phyllites, grading into quartzite	craggy; only thin chl-wm layers at bottom 15m of outcrop		58/358	57/003				
B06/38	S of Tangmachu Bridge	91.1924	27.5358	1184	LHS	quartzites	<1m beds; x-beds; white talc-chl phyllite interlayers [Gansser also notes this] cm-10cm thick; mafic layer	mafic layer	30/050	28/025				
B06/39	S of Tangmachu Bridge	91.1807	27.5281	1167	LHS	quartzites	~ B06/38; strong lineation		53/081	15/003				

Locality N°	Locality	GPS			Unit	Lithology	Additional features	Sample	Structural measurements			Sections cut		XRF data
		Longitude	Latitude	Elevation (m)					Ss / other Ss	Ls / other Ls	sense of shear (top to/criteria)	std	probe	
B06/40	N of archery camp, Lhuentse valley	91.1812	27.5014	1035	LHS	phyllites	gt: <4mm, ass w/ edge of mafic layer+not throughout; chl retrogression; folded mafic layer; qz stringers def with foliation	coarse-gr bi-gt phyllite	steepest 52/026 / c surface: 25/194			x	x	
B06/41	Shongar Dzong	91.1425	27.2713	912	LHS	quartzite	<1m beds; bi fleks in phyllite interbeds		42/285	14/358				
B06/42	track leading NW from Shongar Dzong	91.1357	27.2736	834	HHCS	gneiss	rocks in the wall inc. (HHCS) coarse(r) wm schists ±gt		30/328					
B06/43	furthest point on track leading NW from Shongar Dzong	91.1297	27.2762	817	HHCS	leucocratic gneiss boulders	(consistently since last locality)							
B06/44	pretzel road', W of Mongar	91.1468	27.2836	832	LHS	quartzite	5-20cm beds; boulder of leucogneiss; strong lineation		53/343	49/006				
B06/45	pretzel road', W of Mongar	91.1490	27.2898	939	LHS	phyllite	folded; chl-wm							
B06/46	pretzel road', W of Mongar	91.1540	27.2945	1047	LHS	quartzite/phyllite	interleaved; wm-chl phyllite		42/272	04/359				
B06/47	pretzel road', W of Mongar	91.1529	27.2999	1122	LHS	phyllite; mafic layers	gt(2-3mm)-rich phyllite layer in float but not even bi *in situ*]; fine-gr mafics inc qz stringers							
B06/48	NW from Barshing Camp	91.5807	27.2183	2223	LHS	phyllite	chl-wm; qz stringers along foliation; minerlisation ass.w/ fault e.g. red hematite weathering with qz veins		60/013	53/356	S / s-c fabric, gouge fabrics/drag on layers in minor fault zone			
B06/49	NW from Barshing Camp	91.5785	27.2150	2225	LHS	quartzite	thin beds (5-10cm); heavily jointed; tight folding in places, also kink folds; green-grey layers=more pelitic, or higher strain?		41/017	29/329	S / tight asymmetric folds in quartzite			
B06/50	NW from Barshing Camp	91.5640	27.2200	2196	LHS	quartzite	elongate bi fleks							
B06/51	NW from Barshing Camp	91.5529	27.2277	2250	Jaishidanda Fm?LHS?	carbonaceous phyllite; psammites	grey; deformed qz veins/lenses	gt(2-3mm) phyllite	41/336	35/004	S / qtz blebs/'blasts	x	x	
								x) st? phyllite				x	x	

Locality N°	Locality	GPS			Unit	Lithology	Additional features	Sample	Structural measurements			Sections cut		XRF data
		Longitude	Latitude	Elevation (m)					Ss / other Ss	Ls / other Ls	sense of shear (top to/criteria)	std	probe	
B06/52	NW from Barshing Camp	91.5520	27.2367	2364	MCT zone: (1) Basong FM?Jaishidanda Fm-HHCS	1) phyllite/psammite; 2) psammite; 3) leucogneiss; 4)augenmylonite	1) phyllite: rusty:fault-related mineralisation?irridescent:contact meta?) /psammite: inc sparse mm gts?; 2) psammite w/ boudinaged+sheaths of tu (contact meta from granite?, pre-Him def?); 4)augenmylonite: hints of migmatite; 5) float: coarse gt (3-6mm)-rich schists ±ky	1) psammite, interleaves of gt-phyllite? (possibly discarded); 2) psammite sampled by TA	40/008 phyllite, 41/001 qtzite, 45/010 gneiss	39/003 phyllite, 37/015 qtzite, 42/359 gneiss	S / fsp 'blasts			
B06/53	NW from Barshing Camp	91.5486	27.2382	2394	MCT zone: Basong Fm?Jaishidanda Fm-HHCS	orthogneiss // 100m NW: quartzite, augenmylonite	90% orthogneiss w strung-out tu pods, <10% coarse schistose paragneiss ±gt,ky // 100m NW: highly-strained qzites, augenmylonite; black fault gouge layer 10-20cm thick, small-scale brittle faulting		35/012	32/341	S / s-c fabric			
B06/54	NW from Barshing Camp	91.5453	27.2376	2423	MCT zone: Jaishidanda Fm-HHCS	mylonite; ultramylonite // 100-200m NW(down section): phyllite/quartzite	(dark grey-green*) augen+ (white) tu-lgr mylonite, *chl-grade=MCT at lower grade than often seen; thin (50cm) v dark ultramylonite; weathers/fractures like qzite (blocky) // 100-200mNW(down section): phyllite/qzite; bi-gt(<1mm) schist, qz veins/lenses deformed w fol; inbt black fault gouge, cataclastic layer	bi-gt(av 1mm) schist; abundant green bi, calcite, epidote/clinozoisite	48/010	45/340	S / augen/s-c fabric	x	x	
B06/55	NW from Barshing Camp	91.5281	27.2414	2587	HHCS	mica schist; orthogneiss	coarse gt, <0.5cm		25/035	23/003				
B06/56	NW from Barshing Camp	91.5268	27.2415	2581	HHCS?Jaishidanda Fm?	phyllitic schist; psammite	coarse gt(<0.5cm) in schist; tightly folded psammite	gt(3-6mm)-phyllite schist	31/338	26/009		x	x	
B06/57	NW from Barshing Camp	91.5214	27.2441	2586	HHCS	leucogneiss;phyllites/psammites // further N: mica schist; gneiss	gt-mica schist; pale orange gt (high Ca) gneiss, fsp-qz-rich = granodiorite-type protolith		40-50/019	48/009				
B06/58	NW from Barshing Camp	91.5218	27.2470	2564	HHCS	gneiss	pale orange (high Ca) gt (~3mm)							
B06/59	Yongphula helipad/runway	91.5201	27.2529	2564	HHCS	para/leucogneiss	cruddy rock							

Locality N°	Locality	GPS			Unit	Lithology	Additional features	Sample	Structural measurements			Sections cut		XRF data
		Longitude	Latitude	Elevation (m)					Ss / other Ss	Ls / other Ls	sense of shear (top to/criteria)	std	probe	
B06/60	Yongphula	91.5219	27.2503	2553	HHCS	paragneiss	coarse paragneiss; fine-med gr tu-wm lgr (weakly boudinaged in places); interfingering of lgr along folation planes of gneiss // 50-100m downsection:gt-ky paragneiss	x) coarse gt(<2cm!)-ky(<1cm long!) paragneiss, plus 3 huge gts-NOT from this bit of float. NB. In situ too weathered - only intended for petrography	47/330			x	x	
B06/61	river channel down from Yongphula, Kaglung	91.5313	27.2722	1708	HHCS	leuco/paragneiss // float: schistose gneiss, marble, quartizte/marble?	early-late stage tu-lgr (undef-def tu-clusters/pods), high strain, boudinaged layers // float: bright green chl-tu lgr ±red gt; marble (some chloritised); pink qtzite/marble - peppered w tiny gt?!piemonte?	x) coarse gt(3mm av)-ky(1-2cm long av)-rich schistose gneiss						
B06/62	Rangjung	91.6728	27.3614	1210	TSS (Chekha Fm)	schist	also fine-gr gt psammites	gt(1-3mm)-st schist w/ bi fleks	12/064	10/050	SW / asymm pressure shadows on gt p'blasts	x	x	x
B06/63	Rangjung	91.6718	27.3601	1184	TSS (Chekha Fm) ~Sutlej Haimanta Fm calc-sil	psammites>calc-silicate>pelites	boudinaged/folded psammites, gt locally distributed	med-coarse gr calc-silicate	16/067	63/347				
B06/64	Rangjung	91.6736	27.3588	1175	TSS, Chekha/ Jaishidanda Fm?	lgr; pelites/psammites	coarse-gr tu-wm lgr (minor gt), undef-part def (folded boudinaged) = syn-late(after) def (STD movement) intrusion	i) coarse gr gt-st(<3mm) schist ii) " plus <1cm psammitic bands x) gt-st? schist	28/294 (--> N at lower, SE end of exposure)	18/242 (--> NE at lower, SE end of exposure)	NE/ shear bands and asymm pressure shadows on gt p'blasts	x x	x x	x x
B06/65	W of Rangjung, Vocational Training village	91.6512	27.3573	943	TSS (Chekha Fm)	schists; x-cutting lgr	dark grey schists					x	x	
B06/66	bt Rangjung + Lungtenzampa	91.6363	27.3511	1000	TSS (Chekha Fm)	schist	med-coarse gr bi schist, <0.5mm tu needles (poss aligned)		45/024	38/050				
B06/67	Lungtenzampa valley, Thundi Bridge	91.6236	27.3486	964	HHCS	gneissose schist	float: gt-gneiss ±ky/sill; migmatites; megacrystic augengeniss	coarse gneissose schist w abundant gt(1-2mm av) + sill +ky?	67/345	60/024	rare, N / asymm foliation boudinage/minor shears	x	x	x
B06/68	Riju Bridge, nr Tashigang	91.5755	27.3460	790	HHCS	gneiss; lgr	gt gneiss; locally large gts <4cm, sub-anhedral oft in lsome, prob pre-Him; large strike-slip fault		76/326 / fault: 65/088	33/050 / fault: 10/170	ambiguous			

Locality N°	Locality	GPS			Unit	Lithology	Additional features	Sample	Structural measurements			Sections cut		XRF data
		Longitude	Latitude	Elevation (m)					Ss / other Ss	Ls / other Ls	sense of shear (top to/criteria)	std	probe	
B06/69	Tashiyangtse, E of Dzong	91.4969	27.5849	1775	HHCS v close the KT (just above?)	augengneiss; lgr veins/sills	coarse bi-leuco/augen(1cm av) gneiss (thick banding av 0.5cm); concordant tu-lgr veins/sills 10-20cm wide; rel high strain: strong lineation, elongate tu pods in lgr; sparse gts (or Fe weathering?)		09/339	08/350	S / s-c fabric/augen			
B06/70	S of Tashiyangtse	91.5153	27.5323	1564	HHCS	augengneiss	coarse-gr		40/314					
B06/71	S of Tashiyangtse	91.5135	27.5234	1430	HHCS	leucogneiss; paragneiss; psammite; lgr	leucogneiss inc ky-lsome (boudinaged); bi-gneiss; folded psammite; bi-lgr ±gt (later, less def)	coarse ky-gt gneiss: ky(bright green-blue), gt(<few cm, poililoblastic), st? (yellow, not poikiltic)	22/341	19/001		x	x	
B06/72	S of Tashiyangtse	91.5224	27.5081	1424	HHCS	faulted psammites	(Fe)red-brown + (S)yellow fault mineralisation; fine-gr psammite							
B06/73	S of Tashiyangtse	91.5389	27.4943	1362	HHCS	leucogneiss; mafic layers	deformed bi-leucogneiss; mafic layers 0.5-1m	fine-gr gt(2-5mm, poikiloblastic, skeletal)-bearing mafic layer	02/296, 16/336	01/261, 11/354 / MFH 30/295		x	x	
B06/74	S of Tashiyangtse	91.5518	27.4663	1340	HHCS	augengneiss	banded augengneiss + bi-tu-lsome/lgr; minor boudinaged mafic layers inc ~5mm gts		47/163	34/104				
B06/75	Tashigang-Mongar, nr Chazam Bridge	91.5428	27.3358	701	HHCS	paragneiss	gneiss: coarse sill ±gt(anhedral, poikiloblastic, <2cm); regular lsome stringers (1-3cm thick, every 2-20cm, av 5-10cm)		81/070	67/019 (sill fibres)	S>N / tu/fsp 'blasts			
B06/76	Tashigang-Mongar	91.5378	27.3309	709	HHCS	paragneiss	gneiss: coarse sill ±gt; 5-10%lgr; meso-scale folds		77/262	28/350				
B06/77	Tashigang-Mongar	91.5319	27.3255	697	HHCS	paragneiss	sill-lsome ±large anhedral poikilitic gt; meso-scale folds	i) coarse-gr gt(2mm av)-ky gneiss ii) gt (2mm av)-ky gneiss (least weathered of the 2 samples)	56/010	47/328		x x	x x	
B06/78	Tashigang-Mongar	91.5257	27.3222	725	HHCS	paragneiss	possible migmatite-lsome; float: ky-gt gneiss		61/046	43/348				
B06/79	Tashigang-Mongar	91.5222	27.3183	704	HHCS	schistose gneiss	coarse-gr, garnetiferous layers 1-10mm, ky-gt lsome	gt-ky schistose gneiss	63/042	31/336		x	x	
B06/80	Tashigang-Mongar, S of Roling Bridge	91.4972	27.3087	653	HHCS	leucogneiss	coarse-gr; outcrop-scale gentle folds		46/047	15/323				
B06/81	Tashigang-Mongar, S of Roling village	91.4875	27.3044	687	HHCS	leucogneiss	2 concordant tu-lgr layers (20-40cm wide, consistent width i.e. no boudinage)	TAx) chl-gt-chromite? lgr	63/019	44/320				

Locality N°	Locality	GPS			Unit	Lithology	Additional features	Sample	Structural measurements			Sections cut		XRF data
		Longitude	Latitude	Elevation (m)					Ss / other Ss	Ls / other Ls	sense of shear (top to/criteria)	std	probe	
B06/82	Tashigang-Mongar, S of Roling village	91.4772	27.2994	726	MCT: HHCS-Jaishidanda Fm?	gneiss/phyllite-schist	alternating 1-2m layers of (strained) fine-gr gneiss (inc augengneiss, bi-ps) + lgr, with phyllite-schist	coarse-gr st-gt-ky phyllite schist	50/040	30/341	S / ksp augen, qtz/fsp blebs, s-c fabric	x	x	
B06/83	Tashigang-Mongar, S of Roling village	91.4758	27.2985	756	LHS	quartzites-mylonite	highly jointed, strongly lineated, red-orange-stained; (strange?) gt in green layer - too small to sample, see photo		65/002	41/297				
B06/84	Tashigang-Mongar, S of Roling village	91.4727	27.2978	755	LHS	psammite/quartzite; pelite-phyllite	chl-wm (minor bi) pelite-phyllite; lots of qz (fault[MCT?]-related fluids?) pods/lenses (poss originally fold hinges now boudinaged), attenuated+boudinaged fold limbs, recumbent folds (deci-m scale)		43/024	37/333				
B06/85	Tashigang-Mongar, S of Roling village	91.4693	27.2965	759	LHS	quartzite	regular thinly bedded (or compressed?); fine chl+wm on surfaces, some flekked with (aligned) bi; stained red - 'seeped' from adjacent (Fe)phyllites poss		44/054	35/357				
B06/86	Mongar-Ura (top of 'pretzel road')	91.1659	27.2991	1538	LHS	quartzites interlayed with phyllite	10-50cm thick beds white qzites; white flowstone (related to brittle faulting)		27/300	01/031				
B06/87	Mongar-Ura (top of 'pretzel road')	91.1591	27.3098	1613	LHS	phyllite	coarse bi(2-3mm long)-flekked chl-wm phyllite; psammite layers; abundant qz veins, lgr veins (60%qz, 40%fsp)		52/261	31/193				
B06/88	Mongar-Ura	91.1520	27.3095	1668	Jaishidanda Fm?	[NE end of outcrop] phyllite-schist // [SW end of outcrop] psammite	[NE end of outcrop] boudinaged/folded qz veins/lenses // [SW end of outcrop] beds 0.5-2m	i) med-coarse gr, gt(1-2mm)-bi phyllite-schist, tu <5mm	40/277	05/003	S / s-c fabric	x	x	
								ii) med-coarse gr, gt(<1mm, abundant)-bi-phyllite-schist, tu <5mm				x	x	
B06/89	Mongar-Ura	91.1464	27.3093	1698	HHCS	paragneiss	± gt(<1mm); strung out qz veins; strong fabric		49/299	08/020				
B06/90	Mongar-Ura	91.1313	27.3146	1793	HHCS	lgr/gneiss	coarse-gr; weak fabric							

Locality N°	Locality	GPS			Unit	Lithology	Additional features	Sample	Structural measurements			Sections cut		XRF data
		Longitude	Latitude	Elevation (m)					Ss / other Ss	Ls / other Ls	sense of shear (top to/criteria)	std	probe	
B06/91	Mongar-Ura, Namlingchu Bridge	91.1090	27.3503	2211	HHCS	schistose-gneiss	huge ky (<5cm long) on E side of bridge	coarse gt(euhedral, violet-pink,2-5mm) ± ky (poss sill in places?) schistose-gneiss	45/254	05/343		x	x	
B06/92	SW Ura klippe	90.9458	27.4173	3665	TSS (Chekha Fm) HHCS (lgr)	lgr	coarse, granular (2-3mm) bi-wm lgr // NE: fine-gr, foliated white lgr (looks like qzite!)..evidence of granite intrusion into qzite ~200m N on road		27/278, 35/305	05/200, 04/026	equal parts sinistral, dextral, symmetric			
B06/93	SW Ura klippe	90.9410	27.4189	3647	TSS (Chekha Fm)	gneissose-schist	coarse-gr	i) gt (<0.5cm) gneissose schist ii) gt (pink, 1-2mm) gneissose schist w/ qz veins	33/307	15/324	N (consistent) / shear bands	x	x	
B06/94	SW Ura klippe	90.9390	27.4161	3605	TSS (Chekha Fm)	pelitic schists	orange+green(Cu) staining; granite intrusions	[gravel] gt (<1cm)-st (stubby) schist			N / shear bands	x	x	
B06/95	NE Ura klippe, N of Sheylangla	90.8760	27.4786	3570	TSS (Chekha Fm)	phyllite	grey phyllite, bi (aligned fleks, ~1-2mm long); qz veins/lenses aligned along foliation		15/069	08/011				
B06/96	NE Ura klippe, N of Sheylangla	90.8640	27.4894	3466	TSS (Chekha Fm)	psammite; pelitic interlayers; calcareous lavers	5-50cm psammitic 'beds'; thin pelitic interlayers; bi (=grey colour), common 1-2mm red euhedral gts							
B06/97	NE Ura klippe, N of Sheylangla	90.8696	27.4969	3432	TSS (Chekha Fm)	psammites/pelites // NW: quartzites	med-gr, st(0.5cm)+gt(1-2mm) p'blasts (chl in boudinaged pblasts in float piece, thin pe laye on ps) // NW: qzites, increasingly sheared	i) gt (1-2cm, resorb-chl, anatase) psammite, heterogeneous ii) gt (abundant, 1-3mm) pelite, retrograde chl x) st-gt(1-2mm)-chl phyllite-schist, st: non-poik + fractured in discrete pieces, st growing into gt? (marked on section), coarse chl matrix inc fringes/p shadows	22/023	20/002		x x x	x x x	

Locality N°	Locality	GPS			Unit	Lithology	Additional features	Sample	Structural measurements			Sections cut		XRF data
		Longitude	Latitude	Elevation (m)					Ss / other Ss	Ls / other Ls	sense of shear (top to/criteria)	std	probe	
B06/98	NE Ura klippe, quarry	90.8315	27.4906	3004	TSS (Chekha Fm) HHCS (granite)	sheeted granite	gt-tu granite; ~concordant crenulated mica schist schlieren (pelite layers inc wrapped gt, poss chl rims); no tectonised boundaries (ie not sheared)							
B06/99	NE Ura klippe	90.8208	27.4929	2935	TSS (Chekha Fm) HHCS (granite)	psammitic/pelitic schist (~80%); leucogranite (10-20%)	scaley psammites; deformed leucogranite		25/138	24/146	SE (not ubiqutous) / s-c fabric			
B06/100	NE Ura klippe, quarry	90.8181	27.5031	2916	HHCS	gneiss = stromatic migamtite	grey, med-gr, mm-scal (ie thin) banding; 5% lgr/lsome (2-20cm thick, stringers/lenses)		21/160	20/186				
B06/101 =02RP15	NE Ura klippe	90.8115	27.5152	2821	HHCS	migmatite	restite?, coarse-gr; ky-lsome	i) ky(embayed, fractured xls, 1-5mm)-gt(pink, 1-2mm, abundant)-bi gneiss/migmatite (section i2): amph?or sill; ky growth into gt) ii) ky-gt migmatite, fibrolite?				x x	x x	
B06/102 =06/RP1	Thimpu-Paro	89.5381	27.3180	2166	HHCS (Paro metaseds)	psammite, pelite	highly folded/faulted, flowstone	i) whole ~1cm gts, distinctive 's'-shaped inclusion trails in gt cores ii) gt-mica schist - WR for i) iii) gt-mica schist - sample more competent, smaller gts (av. 0.5cm)	Fold plane: 220/20	MFH: 15/160		x	x	
B06/103	N of camp at Sharma Zampa/ Gunitsawa army base, Yaksa path	89.2862	27.6078	2954	HHCS	calc-silicate gneiss	strongly foliated; concordant qz veins/stringers, discordant pegamtitic veins; float: sill-gneiss		gently dipping N		~N (crude measurement) / discordant, boudinaged qtz vein			
B06/104	N of camp at Sharma Zampa/ Gunitsawa army base, W end of helipad	89.2833	27.6076	2871	HHCS	migmatitic-gneiss	sill, minor ~2mm gt							

Locality N°	Locality	GPS			Unit	Lithology	Additional features	Sample	Structural measurements			Sections cut		XRF data
		Longitude	Latitude	Elevation (m)					Ss / other Ss	Ls / other Ls	sense of shear (top to/criteria)	std	probe	
B06/105	N of camp at Sharma Zampa/ Gunitsawa army base, E side of river	89.2810	27.6088	2849	HHCS	granite (<50%) in gneiss	bi-sill-(minor gt) gneiss							
B06/106	N of camp at Sharma Zampa/ Gunitsawa army base	89.2849	27.6027	2888	HHCS	gneiss (above qzite)	sill-bi gneiss (above qzite)	RP: gneiss	dipping W	~SE-NW	SE / asymmetric qz/lgr boudins			
B06/107	Chele La	89.3489	27.3685	3784	HHCS (Paro metaseds... see Gansser)	phyllite; quartzite; calc-sil; paragneiss	isoclinal recumbent folds dipping gently N	RP06 15: graphitic phyllite; RP06 16: quartzite; NH2: gt(0.5-1cm) calc-sil						
B06/108	Chele La	89.3539	27.3827	3491	HHCS (Paro metaseds)	calc-silicate	gt-rich	RP06 17: calc-silicate						
B06/109	Chele La	89.3503	27.3881	3409	HHCS (Paro metaseds)	marble	banded, inc radiating masess of tremolite	RP06 18: marble						
B06/110	Chele La	89.3624	27.3761	3442	HHCS (Paro metaseds)	mica schist	coarse-gr	RP06 19:mica schist						
B06/111	Chele La	89.4204	27.3865	2400	HHCS (Paro metaseds)	mica schist; marble	coarse-gr schist; tremolite-bearing banded marble	RP06 20: mica schist	14/010 (marble)					

*This sample was mistaken as a sillimanite-biotite schist in the field, but following analysis on the electron microporbe was correctly identified as a schistose cummingtonite-biotite ultramafic rock. The complete assemblage is cummingtonite-biotite-quartz-rutile-apatite, plus accessory zircon. Fibrous masses of cummingtonite are dominant. The rutile crystals are large, and potentially datable (Zack et al., 2007). The fact that the only Ca-phase in the assemblage is apatite suggests that this is a hydrothermally altered mafic rock (Mg-rich, Ca-poor). Considering the sample's location with respect to a major fault (close to but probably above the Kakhtang Thrust) it is plausible that this rather unusual rock is the result of fluid alteration/retrograde metamorphism of a pre-existing mafic intrusion during fault movement. It is unlikely to be an uplifted segment of hydrothermally altered seafloor as this rock type is not widespread (no other occurrences reported from Bhutan at least), unless it has since been faulted out.

Zack, T., Luvizotto, G.L., Barth, M. and Stockli, D.F., 2007. U/Pb Rutile Dating in Granulite-Facies Rocks by LA-ICP-MS. Eos Transactions, AGU 88(52), Fall Meeting Supplement, Abstract V34C-05.

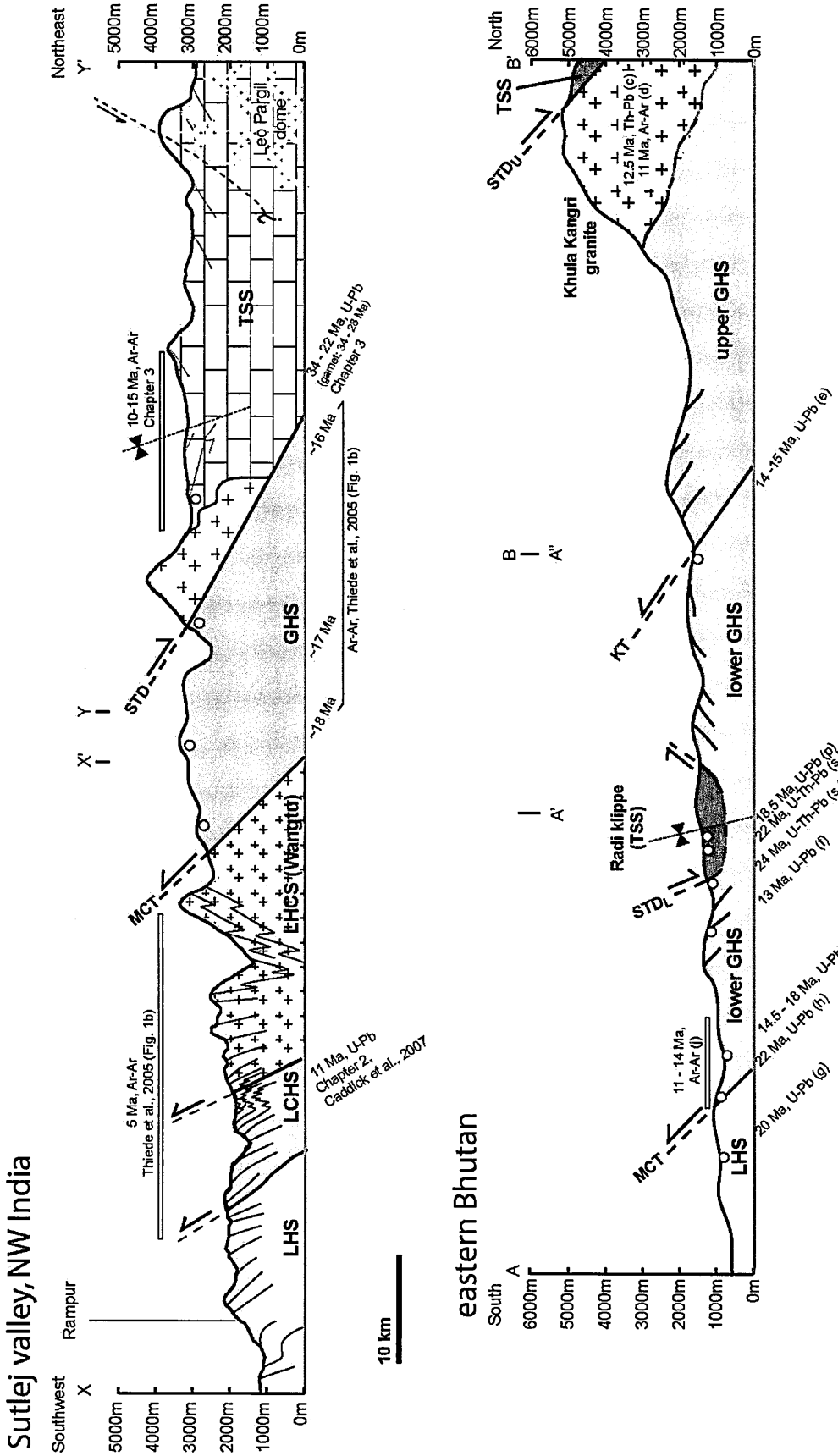

Fig. A2.1 Cross-sections through the Sutlej valley and eastern Bhutan. See Figures A1.1 and A1.2 (Sutlej), and 6.1 (Bhutan) for lines of sections. Both drawn to scale, and at same scale. Annotated with all available Cenozoic age data (for Bhutan data, see Table 6.5 for references).

Appendix B: Analytical techniques

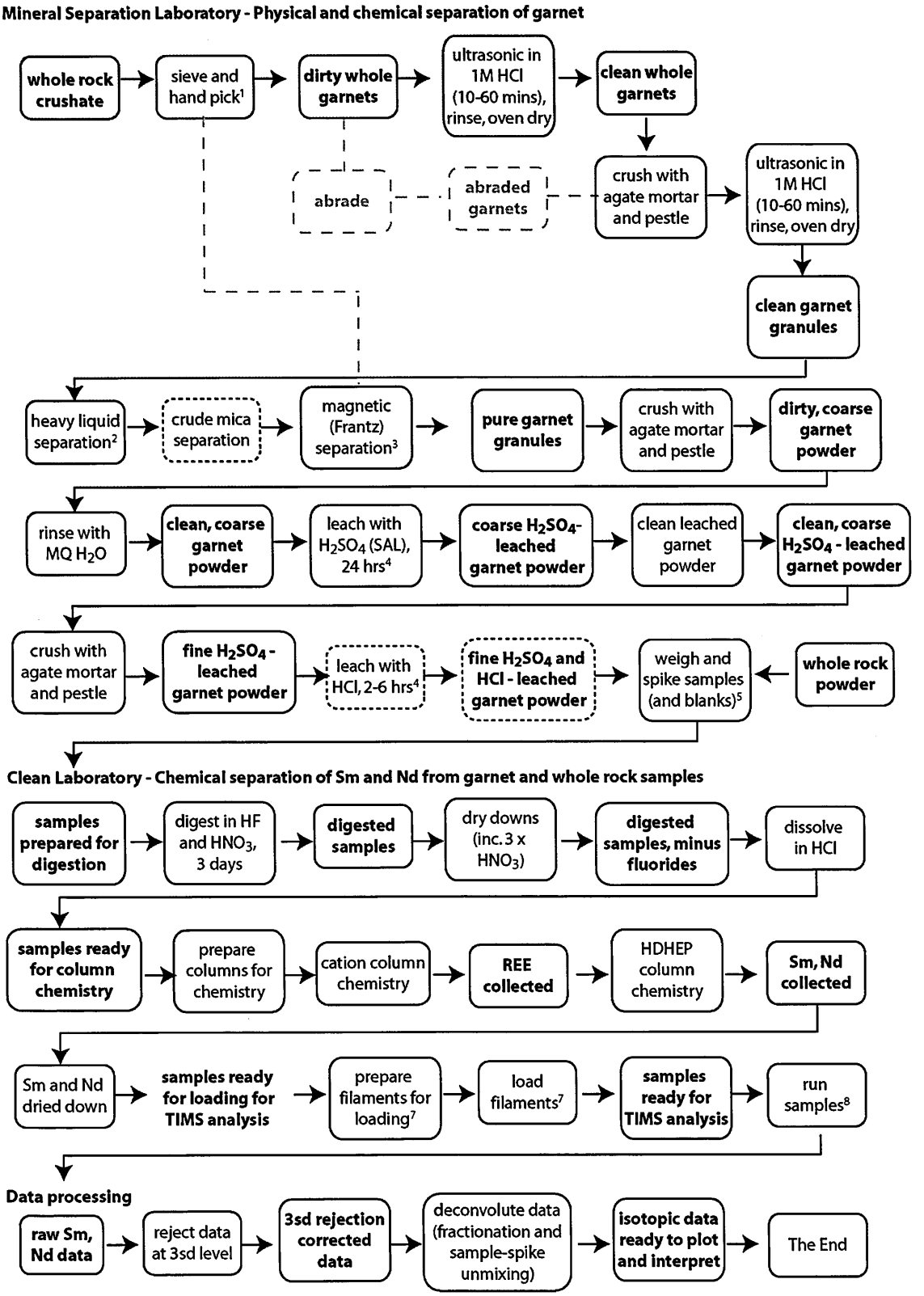

Flowchart detailing the method for whole-rock and garnet geochronology. Steps 1 to 8 refer to the following protocols. Stages in boxes that are short-dashed were optional. Stages/routes greyed out and in boxes that are long-dashed represent methods not taken here but were considered.

STEPS 1–3 (garnet separation)

1. Crushing, Sieving, Hand-picking

Trimming	Trim weathered surfaces off 50-100g whole rock samples.	
Cleaning	Clean samples in distilled water.	Ultrasonic cleaning seems a bit over the top...
Crushing	Crush using jaw crusher (John Watson's lab) for coarse crushate.	Individual grt grains may be picked from a coarse crushate, but *do not* retain remainder for WR analysis if you do so!
Sieving	Use a stack of small sieves for a range of size fractions; Prince (1999) favoured 200μm; Chambers took fractions of >1mm, 0.3-1μm, 150-300 μm and 90-150 μm.	clean sieves in large ultrasonic bath in Min Sep Lab: wire mesh basket to put items in, cover with water, need to plug in, controls on side facing wall; and dry gently in oven in there, or on side
Hand picking	Pick separates for optically-pure garnet under stereomicroscopes in Min Sep Lab (number 2 for minerals, number 1 for forams only).	Use tweezers or fine brushes. Picking under propanol reduces reflections and light scatter. Cover grains well, or surface tension hinders picking. Can tape paper (scrap in draw on opposite side of room) to the platform for diffuse light. No paper can be used to pick out pure garnets. Submerging in ethanol greatly improves identification of small, transparent inclusions like monazite or zircon (Anczkiewicz & Thirlwall, 2003)

2. Heavy Liquid Separation, using Sodium Polytungstate (to separate dense mineral phases, e.g. garnet)

Some general points:

- Always use Milli-Q water for all procedures (washing, dilution, filtering etc): Start → let it settle to 18.2 → 'production'. Na-PT may react with the Ca in tap water, rendering it useless.
- Na-PT is non-toxic. However, eye protection and gloves should be worn while handling the liquid. In event of spillage on skin/eye, rinse with copious amounts of (tap!) water at the sink.
- Na-PT should be stored in Nalgene (FEP) bottles, not glass.
- Do not leave Na-PT exposed to air for long, as it solidifies on evaporation.
- Separation is slow, but effective, due to the high viscosity of Na-PT. Allow several hours for full procedure (including cleaning).

Apparatus required:

- ~250 ml sodium polytungstate (2.85g/mL at 20°C) or **LST Fastfloat*** (sodium heteropolytungstate), which is less viscous (2.8±0.02g/mL at 20°C) and easier to recover, although so fast that heavy material can simply block up the bottom
- teardrop-shaped separating funnel, with basal tap
- plastic filter paper holder, preferably with detachable base funnel with outlet for evacuation pump
- filter paper
- conical beaker for decanting heavy fraction, preferably with outlet for evacuation pump
- rubber bungs (for seals if pumping)
- MQ water supply (for washing and re-diluting heavy liquid)
- Clamp stand for separating funnel
- Funnels for pouring liquid and mineral separates into separating funnel

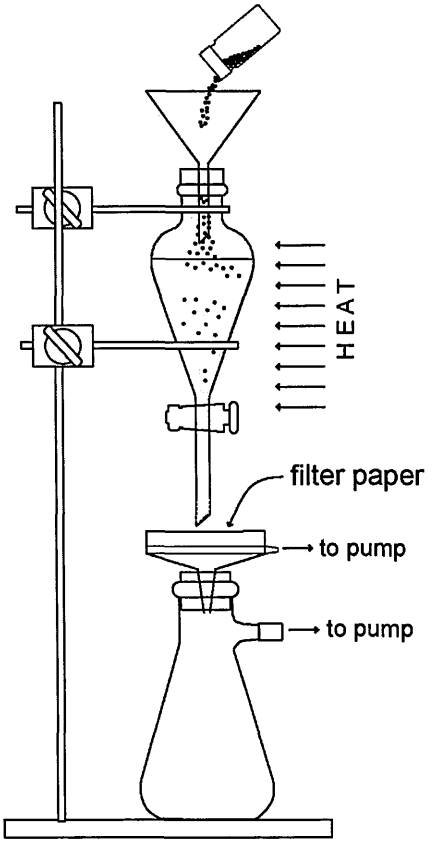

*http://www.polytungstate.co.uk/heavyliquids

Method:

1. Wipe all glassware, and clean funnel with acetone and then MQ water.
2. Grease tap either side of the small hole in the middle, remember to put the end back on the tap!
3. Dampen large, heavy-duty filter paper in filter holder with MQ water to seal it down.
4. Optional: Turn pump on (small black tap at end of tube); compressor will operate automatically in a few seconds.
5. Clean flask in MQ water.
6. Pour heavy liquid into funnel from Nalgene bottle, up to near the top, rinse funnel with MQ into flask/beaker A
7. Tip in all of sieved mineral separate using a piece of paper made into a funnel (secure with sellotape) – of same sized grains – and stir/shake (with bung on top).
8. Leave for 1-2 hours for different phases to separate (note that an increase in temperature will increase the density, therefore a fan heater directed onto the apparatus will improve bi-gt fractionation); leave parafilm on top as temporary cover.

9. Decant off heavy fraction into filter by opening the basal tap (gently, might want to rock tap back and forth, want to avoid sudden rush of material); close again once desired fraction is obtained.
   (Liquid will take time to pass filter.)
10. Retain heavy liquid in flask/beaker A for addition of other Na-PT washings.
11. Remove filter paper with heavy fraction (using tweezers or the end of a pair of scissors) and rinse into evaporation dish/beaker with MQ water from bottle. Agitate vigorously to mix/wash separate with MG from squeezy bottle.
12. Decant off liquid into flask A (see above), fines will be removed from the heavy fraction – repeat as necessary (e.g. 3 or 4 times)
13. Dry heavy fraction in oven, 60°C (ready for repeating the separation procedure if required).
14. Filter off heavy liquid containing light fraction in same way as above (remember to rinse funnel at this point with MQ), retaining light fraction of mineral separate in same way (if required).
15. Re-filter heavy liquid filtrates to clean them before returning to storage bottle.
16. You will need to evaporate water from washing procedure to regain previous density:

With Fastfloat ~250mL evaporated off in 1 hour on hot plate setting 10 (stirring, especially at the beginning, to avoid separation and prevent chaotic bubbling). Alternatively put open beakers in the oven in the picking lab, 50-60°C.

Using the density meter:

1. Turn on meter (top)
2. Pipette water into right hand side little opening so that liquid goes directly in.
3. Fill meter with liquid – no air bubbles!
4. Take density measurement
   for water, should be 1.00g/mL…calibrate now if not (NB. accurate to 3dp, so 0.998 ok)
5. Expel liquid from meter (squirt out if water, but if liquid you want to recover then suck back out with the pipette)
6. Rinse very thoroughly if not water that has just been through (<5 times through with MQ)
7. Turn meter off

3. Magnetic (Frantz) separation (NIGL, Keyworth)

With settings of 20 (slope)/10° (tilt), garnet can be successfully separated from non- or weakly magnetic minerals such as quartz and feldspar, which are likely to be in the same heavy fraction as garnet following heavy liquid separation.

STEP 4 (leaching)

Sample:

Pre-Leaching Preparation Empty vial weight:	_____ g
Vial + mineral weight:	_____ g
Weight of mineral separate:	_____ g
Fine crushing *Equipment: long Teflon beaker, funnel and* ***small*** *agate mortar*	
Rinse agate mortar with MQ water, then acetone; dry with kimwipe	
Place cling film on the desk and then clean plain paper	
Take garnet separate to the mortar, wet with MQ water, crush to <50um carefully (silty grainsize). Transfer to evaporating dish so as not to overfill teflon vial	Crush a little garnet each time, avoid splashing & loss of material
Transfer the finely crushed garnet into the long teflon beaker through funnel with MQ water from squeezy bottle carefully.	Be careful! Try not to lose material.
Pre-leaching cleaning	
Screw top on beaker, ultrasonic 15 minutes, discard top water	
Add MQ water, ultrasonic 15 minutes, discard top water	
Add acetone, ultrasonic 15 minutes, discard top acetone	
Rinse with MQ water in beaker, then discard water	*Repeat 3 times*
Add 1% HNO_3 and place on hotplate (**Z134**) 130°C for 15-30 mins	Use baffle e.g. another pot
Cool, discard HNO_3	
Add MQ water, ultrasonic 10 minutes, discard water using pipette	*Repeat 2 times*
Place in oven – **min. sep. lab** (or on hotplate), at 50°C to dry (overnight)	Re-weigh now

H_2SO_4 garnet leaching **removes phosphate inclusions** from garnet (especially monazite and apatite):

98% H_2SO_4 at 180°C on a hotplate

H_2SO_4 leaching	
Add 4 ml 98% H_2SO_4 (Aristar) to the long beaker, replace top, and place on the hotplate 180°C for ~**24** hrs.	In **Z134** again
Allow to cool. Leaching time:	_____ **hrs**
Post-leaching cleaning	
Ultrasonic the 98% H_2SO_4 10 minutes, discard leachate	In **Z134** still

Add MQ water to the residue, ultrasonic 10 minutes, discard water.	*Repeat at least 4x* ***min. sep. lab** now
Add acetone (instead of ethanol) and ultrasonic 15 minutes, discard acetone	*Repeat both steps, then final step twice more*
Add MQ water, ultrasonic 10 minutes, discard water	
Transfer to agate pestle/mortar and re-crush under MQ water to as fine a powder as possible prior to digestion step. Rinse out into evaporating dish, then savillex vial using funnel, as before.	
Place in the oven at 50°C; evaporate to dryness slowly, with care	May lose sample

HCl garnet leaching **removes silicate inclusions** from garnet (especially allanite):

6M HCl in a heated ultrasonic bath

Pre-leaching weighing	
Weigh beaker + powder twice prior to HCl leaching.	_____ g
HCl Leaching	
Add 6M QD HCl to the long beaker (e.g. half full), replace top, and place in ultrasonic bath at 69°C for 2/4/6 hrs *(Anczkiewicz 30 mins at 60°C)*	
Leaching time:	_____ **hrs**
Post-leaching cleaning	
Carefully decant leachate from beaker into clean 15ml savillex vial; pipette out dregs but take care not to remove any solid residue	(Pasteur pipette)
Add MQ water to the residue to rinse, ultrasonic 15 minutes	
Carefully decant MQ H_2O rinse from beaker into same 15ml savillex vial with HCl leachate; pipette out dregs as before but leave solid residue.	Label 15ml vials for spiking
Place residue in the oven at 50°C; evaporate to dryness slowly	(Best overnight)
Post-leaching weighing	
Weigh beaker + powder twice to estimate weight of material lost to leaching (take this as the weight of leachate).	Record weight

STEP 5 (sample spiking)

You will need:

n samples (powders)
Spike bottle (FEP + white cap)
15M TD HNO_3 in FEP bottle
15ml Teflon vial of 15M TD HNO_3
Small Teflon pot MQ H_2O
15ml teflon vial marked "Sm-Nd"
n clean digestion vials (for *n* samples)
n clean digestion vials (for *n* blanks)
Nd spike pipette tip in plastic capsule
Squeezy bottle MQ (to clean spatula)
Large pipette tips
Small pipette tips (for blanks)
Blue-topped pipette (200µl-1ml)
Black pipette + yellow top (40-200µl)
Orange-topped pipette (0.2-5µl) for blanks
Small metal spatula
Gloves
Parafilm, kimwipes (in balance room)
Derek's Spike Book (spike cupboard in Z134)

Which spike and how much?

Spikes are kept in Z134 cupboard, in FEP bottles with white screw tops. The spike names are scratched on the bottle sides (not labelled for accurate weighing). Use the appropriate spike for each digestion:

	Sm/Nd ratio	**[Nd]**	**Spike**	**amount**
Garnet	High	Low	SmNd High	*See table below*
Whole rock (including accessory phases e.g. monazite, allanite)	Low	High	SmNd Low	~200µl for 100mg sample for typical concentrations
Blanks, forams	Low	low	SmNd Low Dil	5µl (5mg) for each TPB (total procedural blank)

Amount of spike required for garnet samples:

Grt picked (mg)	**Spike req'd** (µl)	**(droplets)**	**Grt picked** (mg)	**Spike req'd** (µl)	**(droplets)**
10	33	13	110	357	143
20	65	26	120	390	156
30	97	39	130	422	169
40	130	52	140	455	182
50	162	65	150	487	195
60	195	78	160	520	208
70	227	91	170	552	221
80	260	104	180	585	234
90	292	117	190	617	247
100	325	130	200	650	260

Balance Room Procedures

Balance room is at end of clean suite of labs.

Move carefully and slowly during weighing procedures to avoid mistakes and disturbance.

Weigh twice and record each weight; allow balance to settle (1-2mins) before recording weight.

Weigh consistently: allow similar amount of time for settling; use anti-static gun sparingly.

Weigh solutions in sealed vials, with balance closed, to avoid evaporation losses.

Wear gloves, coat and hat for weighing.

Tare (empty) sample beaker	Tare beaker ready for HNO_3	For **WR, Grts** (not **blanks**)
Add 15M HNO_3	Add 250 µl 15M TD HNO_3 to beaker with spike for all samples and blanks	Use 200-1000 µl pipette (blue) plus large tips.
Tare sample beaker	Tare beaker ready for sample powder	
Add powder	Transfer <100mg sample powder (for WR) to the new, weighed teflon beaker.	Swirl so all powder is wetted, replace lid
Weighing	Weigh beaker again, record weight, calculate how much spike required.	For **WR, Grts** (not **blanks**)
Weigh spike bottle	Remove parafilm from spike bottle and weigh carefully (weigh twice, record both weights, take average)	Use balance in balance room in clean suite; wear gloves for all weighing; record to nearest 0.1 mg; let readings settle before recording
Tare beaker	Record beaker number and tare on balance.	De-static beaker first with anti-static gun (use consistently, not excessively) This may not be needed if the anti-static ion bar is working well.
Prepare spike	Squeeze total amount of spike required for batch of samples *in stages* from spike bottle into clean 'Sm-Nd' beaker. Record weight used in Derek's red spike book (in lab cupboard).	Weigh spike bottle first Squirt initial guessed amount Reweigh spike bottle Repeat until enough spike in beaker Recap bottle and parafilm carefully
Spiking	Add appropriate amount of correct spike* to each beaker, using Nd spike tip on 40-200µl pipette (yellow/black). [Usually ~200µl for 100mg **WR** sample, 5µl for **Blank**]	*See list amounts of spike required for **WR, Blanks**; Table for **Grts**. Nd spike tip kept in its own plastic container in Z134. Wash Nd spike tip before use with MQ H_2O, and dry before use.
Weighing	Weigh spike in beaker and record weight.	For **WR, Grts, Blanks**

Progress sheet for steps 1–4 (garnet separation and leaching)

SAMPLE	
	Completed
picking	
crushate	
sieve into fractions: >1mm, 300um-1mm, 150-300um, 90-150um	
pick gts (start with largest possible fraction)	
ultrasonic in 1M HCl, 10-60mins	
oven to dry	
crush (use large agate pestle/mortar) to 150<300um	
ultrasonic in 1M HCl, 10-60mins	
oven to dry	
heavy liquid separation - always use **MQ** water!	
clean all glassware (acetone) and rinse all apparatus (MQ)	
grease tap a little either side of hole	
screw tap end on	
dampen large, heavy duty filter paper in filter holder with MQ	
pour heavy liquid into funnel, up to near top	
rinse funnel into waste beaker (wb)	
pour in sieved/crushed mineral separate using paper funnel	
shake/stir	
leave for 1-2 hours (parafilm on top as temp cover, fan heater on-to keep density high)	
decant off **heavy fraction**, heavy liquid into wb	
remove filter paper e.g. using tweezers/scissors, rinse into evap dish with MQ	
decant off water (+fines) into wb	
repeat rinsing (x3 or x4), agitate to mix/wash, decant into wb	
dry heavy fraction in oven (60℃)	
decant off **light fraction** + rest of heavy liquid, rinse funnel (MQ), all into wb	
*decant off water (+fines) into wb	
*repeat rinsing (x3 or x4), agitate to mix/wash, decant into wb	
*dry light fraction in oven (60℃)	
**optional procedure - depends on if you want to keep light fraction*	
refilter heavy liquid from wb	
into oven to increase density to original value	
frantz (magnetic separation) *- NIGL*	
leaching (see additional protocol sheet) - H2SO4 and/or HCl?	
clean gt granules	
colour.....	
inclusions.....	
fine crushing	
pre-leaching cleaning	
leaching	
post-leaching cleaning	

Progress sheet for step 5 (weighing and spiking)

SAMPLE				
	Completed			
weighing + spiking				
gt powder (as fine as talcum powder)				
tare (empty) sample beaker				
add 250uml 15M TD HNO3 to sample beaker				
tare sample beaker				
add gt powder <100g, swirl				
weigh **sample** beaker (with lid on), calculate total amount of spike required		weight #1		
		weight #2		
		sample weight average		
		amount of spike required		
remove parafilm from spike bottle, weigh and record in Derek's spike book		weight #1		
		weight #2		
		average	BEFORE	
tare Sm-Nd beaker (with lid on)				
squeeze total amount of spike required for batch of samples *in stages* from spike bottle into Sm-Nd beaker				
reweigh spike bottle and record in Derek's spike book		weight #1		
		weight #2		
		average	AFTER	
add correct amount of **spike** to beaker using Nd spike tip		weight #1		
		weight #2		
		spike weight average		

Progress sheets for step 6 (Sm–Nd separation, for garnet separates)

SAMPLES			
		Completed	
digestion	day 1		
label teflon vials			
add HF [0.75ml 20mg gt]			
add NHO3 if needed for 12:1 HF:HNO3			
brown socket hex caps on (use green cranks)			
leave for 3 days on hotplate @ 180℃			
after a few hours check for leaks (bubbling)			
HF-HNO3 dry-downs			
swirl beakers to collect condensate around lids/rims, then remove lids			
dry down ~ 12hrs, 140℃ (note not in digestion bloc k)	day 4		
label hood			
add 250 µl 15M TD HNO3 (1) to each beaker	day 5		
ultrasonic for 10 mins			
reflux 15-30 mins			
dry down ~1hr, 140℃			
add 250 µl 15M TD HNO3 (2) to each beaker			
ultrasonic for 10 mins			
reflux 15-30 mins			
dry down ~1hr, 140℃			
add 250 µl 15M TD HNO3 (3) to each beaker			
ultrasonic for 10 mins			
reflux 15-30 mins			
dry down *completely* ~2 hours, 140℃			
add 4ml **6M** QD HCl			
ultrasonic for 10 mins			
reflux @180℃ for at least 24 hrs	end day 5		
	can leave samples in this form if needed		

HCl dry-downs	day 6	FOR GT SAMPLES ONLY:	**Completed**
		pre-cleaning cation columns	
dry-down HCl-sample beakers overnight [~14hrs, 145°C, in digestion block]		drain	15mins
add 0.5ml **6M** QD HCl	day 7	8ml **6M** QD HCl (1ml then 7ml)	45mins
ultrasonic for ~10 mins		1ml MQ H2O	10mins
reflux ~ 5 mins		5ml **2.5M** HCl (1ml then 4ml)	35mins
dry down (<1hr15, 145℃, not in digestion block)		8ml **6M** QD HCl (1ml then 7ml)	45mins
add 0.5ml **6M** QD HCl		1ml MQ H2O	10mins
ultrasonic for ~10 mins		1ml MQ H2O	
reflux ~ 5 mins		store	
dry down (<1hr15, 145℃, not in digestion block)		rinse + drain waste beakers	
add 1ml **1M** HCl			
reflux for a few hours; leave to cool (timed overnight program)		reflux X conical beakers	
		rinse small pipette tips	
solution clear and homogeneous?	day 8	rinse centrifuge tips	
clean cation columns	day 8	label X conical beakers	
drain	15mins	label small pipette tips	
8ml **6M** QD HCl (1ml then 7ml)	45mins	label centrifuge tips	
1ml MQ H2O *(can add more if need to stall here)*	10mins	**centrifuge** (use rack)	
equilibrate - 0.6ml **1M** HCl		pipette	
keep wet - 0.6ml **1M** HCl		centrifuge (5 mins)	
cation column separation		rinse 1 small + 1 large pipette tips	
pipette samples into columns (leave any residue)			
wash #1 100µl **2.5M** HCl to each column			
wash #2 100µl **2.5M** HCl to each column			
wash #3 100µl **2.5M** HCl to each column			
elute 5ml **2.5M** HCl to each column (1ml then 4ml)	35mins		
replace waste beakers with conical beakers			
add 2.5ml **6M** HCl to each column (1ml then 1.5ml)	25mins		
dry down conical beakers @140℃, 7hrs (overnight ti med program)			
empty waste beakers			
clean cation columns	end day 8		
8ml **6M** QD HCl (1ml then 7ml)	45mins		
1ml MQ H2O	10mins		
add 1ml MQ H2O and store away columns			
rinse and drain holders, waste beakers, tweezers			

FOR GT SAMPLES ONLY:	day 9	reflux 2X conical beakers
pre-cleaning DEP columns		rinse small pipette tips
drain	20mins	
4ml **6M** QD HCl (1ml then 3ml)	1hr40mins	label 2X conical beakers (Sm, Nd)
4ml **0.33M** QD HCl (1ml then 3ml)	1hr40mins	label small pipette tips
3ml **0.66M** QD HCl (1ml then 2ml)	1hr15mins	
4ml **6M** QD HCl (1ml then 3ml)	1hr40mins	rinse 1 small + 1 large pipette tips
1ml **0.33M** QD HCl	30mins	
add 1ml **0.33M** QD HCl, store away columns		
rinse and drain holders, waste beakers, tweezers		
DEP column separation	day 10	
drain	20 mins	
add 2ml (or 4ml if not pre-cleaned the day before) **6M** QD HCl (1ml then 1 or 3ml)	55 mins	add 50µl 0.33M HCl to dried REE beakers
equilibrate - 0.5ml **0.33M** HCl	15 mins	
equilibrate - 0.5ml **0.33M** HCl	15 mins	
pipette 50µl of samples into columns		
wash #1 100µl **0.33M** HCl to each column		
wash #2 100µl **0.33M** HCl to each column		
wash #3 100µl **0.33M** HCl to each column		
elute - 3.5ml **0.33M** HCl to each column (1ml then 2.5ml)	1h30	
replace waste beakers with conical beakers		
add 4ml **0.33M** HCl to each column (1ml then 3ml)	Nd - 1h40	
dry down conical beakers @140℃, 7hrs (overnight ti med program)?	Nd	
elute - 1.5ml **0.66M** HCl to each column (1ml then 0.5ml)	40 mins	
replace waste beakers with conical beakers		
add 2ml **0.66M** HCl to each column (1ml then 1ml)	Sm - 1h	
dry down conical beakers @140℃, 7hrs (overnight ti med program)?	Sm	
empty waste beakers		
clean DEP columns	end day 10	
4ml **6M** QD HCl (1ml then 3ml)	1h40	
1ml **0.33M** QD HCl	30mins	
add 1ml **0.33M** QD HCl, store away columns		
rinse and drain holders, waste beakers, tweezers		
Ready to dissolve and load onto filaments		

Progress sheets for step 6 (Sm–Nd separation, for whole rocks)

SAMPLES				
		Completed		
digestion	day 1			
label teflon vials				
add HF [3ml per 100mg WR]				
add NHO3 if needed for 12:1 HF:HNO3				
brown socket hex caps on (use green cranks)				
leave for 3 days on hotplate @ 180℃				
after a few hours check for leaks (bubbling)				
HF-HNO3 dry-downs				
swirl beakers to collect condensate around lids/rims, then remove lids				
dry down ~ 12hrs, 140℃ (note: not in digestion blo ck)	day 4			
label hood				**Completed**
add 250 µl 15M TD HNO3 (1) to each beaker	day 5	reflux X 15ml flat-based beakers		
ultrasonic for 10 mins		label 15ml flat-based beakers		
reflux 15-30 mins				
dry down ~1hr, 140℃		reflux X small flat-based beakers		
add 250 µl 15M TD HNO3 (2) to each beaker		label small flat-based beakers		
ultrasonic for 10 mins				
reflux 15-30 mins		rinse X small pipette tips		
dry down ~1hr, 140℃		label small pipette tips		
add 250 µl 15M TD HNO3 (3) to each beaker				
ultrasonic for 10 mins				
reflux 15-30 mins				
dry down *completely* ~2 hours, 140℃				
add 8ml **6M** QD HCl - add 4ml then decant into 15ml beaker, then add last 4ml				
ultrasonic for 10 mins				
reflux @180℃ for at least 24 hrs	end day 5			
can leave samples in this form if needed				

HCl dry-downs	day 6		**Completed**
transfer 650µl sample into small flat-based beaker		save small pipette tips for columns	
dry-down HCl-sample beakers overnight [130℃, 3hrs?]			
add 0.5ml **6M** QD HCl	day 7		
ultrasonic for ~10 mins			
reflux ~ 5 mins			
dry down (<1hr15, 145℃)			
add 0.5ml **6M** QD HCl			
ultrasonic for ~10 mins			
reflux ~ 5 mins		reflux X conical beakers	
dry down (<1hr15, 145℃)		rinse centrifuge tips	
add 0.5ml **1M** HCl		label X conical beakers	
reflux for a few hours; leave to cool (timed overnight program)		label centrifuge tips	
solution clear and homogeneous? If not try another 0.5ml 1M HCl and a quick reflux	day 8		
clean cation columns	day 8		
drain	15mins		
8ml **6M** QD HCl (1ml then 7ml)	45mins		
1ml MQ H2O *(can add more if need to stall here)*	10mins	**centrifuge** (use rack)	
equilibrate - 0.6ml **1M** HCl		pipette	
keep wet - 0.6ml **1M** HCl		centrifuge (5 mins)	
cation column separation		rinse 1 small + 1 large pipette tips	
pipette samples into columns (leave any residue)			
wash #1 100µl **2.5M** HCl to each column			
wash #2 100µl **2.5M** HCl to each column			
wash #3 100µl **2.5M** HCl to each column			
elute 5ml **2.5M** HCl to each column (1ml then 4ml)	35mins		
replace waste beakers with conical beakers			
add 2.5ml **6M** HCl to each column (1ml then 1.5ml)	25mins		
dry down conical beakers @140℃, 7hrs (overnight ti med program)			
empty waste beakers			
		reflux 2X conical beakers	
clean cation columns	end day 8	rinse small pipette tips	
8ml **6M** QD HCl (1ml then 7ml)	45mins		
1ml MQ H2O	10mins	label 2X conical beakers (Sm, Nd)	
add 1ml MQ H2O and store away columns		label small pipette tips	
rinse and drain holders, waste beakers, tweezers			
		rinse 1 small + 1 large pipette tips	

DEP column separation	day 9		**Completed**
drain	20 mins		
add 2ml (or 4ml if not pre-cleaned the day before) **6M** QD HCl (1ml then 1 or 3ml)	55 mins	add 50µl 0.33M HCl to dried REE beakers	
equilibrate - 0.5ml **0.33M** HCl	15 mins		
equilibrate - 0.5ml **0.33M** HCl	15 mins		
pipette 50µl of samples into columns			
wash #1 100µl **0.33M** HCl to each column			
wash #2 100µl **0.33M** HCl to each column			
wash #3 100µl **0.33M** HCl to each column			
elute - 3.5ml **0.33M** HCl to each column (1ml then 2.5ml)	1h30		
replace waste beakers with conical beakers			
add 4ml **0.33M** HCl to each column (1ml then 3ml)	Nd - 1h40		
dry down conical beakers @140℃, 7hrs (overnight ti med program)?	Nd		
elute - 1.5ml **0.66M** HCl to each column (1ml then 0.5ml)	40 mins		
replace waste beakers with conical beakers			
add 2ml **0.66M** HCl to each column (1ml then 1ml)	Sm - 1h		
dry down conical beakers @140℃, 7hrs (overnight ti med program)?	Sm		
empty waste beakers			
clean DEP columns	end day 9		
4ml **6M** QD HCl (1ml then 3ml)	1h40		
1ml **0.33M** QD HCl	30mins		
add 1ml **0.33M** QD HCl, store away columns			
rinse and drain holders, waste beakers, tweezers			
Ready to dissolve and load onto filaments			

STEP 7 (making and loading filaments)

The geometry of the filament is crucial to the success of TIMS analysis.

Use new or clean filament holders (i.e. not abraded or deformed) and the Finnigan welding kit (in the Triton lab).

1. Making

Stage	Description	Comments
Choose Jig	Ta singles: L-shaped piece which holds filament holder in place should be screwed onto the main jig (chunky bit with large hole in centre) so that the assembly looks (a bit) like a dog. Re doubles: Remove the L-shaped piece from the main jig. The holder is screwed directly onto the side of the main jig.	Use small screwdriver in plastic box containing 'Filament-making gubbins'. Wear GLOVES throughout!
Position holder	Place filament holder onto the jig by sliding two flat legs down astride the large screw until the feet sit securely on the small pegs. Secure by screwing in screw, not overtight.	When making many filaments, there's no need to unscrew the large screw much when removing and replacing holders.
Select wire	Re: long strips on foam in long cardboard box. Ta: Roll in plastic box. Springy ribbon.	Re for Nd, Ta for Sm, Sr etc.
Cut wire	Use scissors in plastic box to cut 1 inch piece of ribbon. Ideal length when place in jig clamp just reaches sides of clamp.	
Position wire	Using tweezers, place ribbon on clamp opposite filament posts. Make sure ribbon is central and in correct orientation. Then smoothly screw in clamp so that the ends of the ribbon are bent round towards the filament posts.	You may need to wind out the clamp a little way to allow ribbon to slot into space, using grey plastic knob.
Weld	Wear goggles here. Turn on the power supply for the welder. Carefully pinch welder prongs over end of ribbon and post, taking care not to touch any other metal part with welder. To weld, squeeze the handle fully once. Repeat for other post.	Light sparking may occur on welding, but excessive sparking suggests filament holder is not clean, or too irregular. A quiet, neat weld is best. Gently test the ribbon is secure with the tweezers.
Remove filament	Gently loosen the grey knob to allow the filament free. Then carefully unscrew the metal screw a few turns, making sure you don't catch the filament prongs with your finger. Gently lift the finished filament straight up, clear of the clamp.	Store in a filament box, and label. The filament is now ready for outgassing, but make them in batches to fill the outgasser (24 filaments is full).

2. Loading

You will need:

- Teflon block with filemant-sized holes, attaches to a powered ammeter
- Clean very small microlitre pipette tips
- 0.1-200µl pipettor
- 0.01M H_3PO_4 (loading solution)
- Parafilm

Additionally for Nd:

- 2 Re doubles for each sample – cleaned and outgassed
- 2.5M HCl for dissolving up sample Nd (what's left after DEP columns)

Additionally for Sm:

- 1 Ta single for each sample – cleaned and outgassed

Procedure for Nd (from Sharma et al., 1996):

1. Add 1 µl HCl to each sample to allow time for them to dissolve
2. position filament in Teflon block
3. Melt small amounts of parafilm onto the filament ribbon (take care not to use too much force and bend the ribbon) to create a small (~1 to 1.5mm) gap in the centre of the filament. This will prevent the load spreading as it is heated and then evaporated.
   [fluctuates with Re ribbon, but melts sufficiently well at approx. 0.6-0.85A]
4. Load sample/standard in 2 x 0.55 µl as to ensure the whole 1 µl is loaded.
5. Dry down carefully/slowly by turning the current up
6. Change pipette tip
7. Load 1 µl H_3PO_4
8. Dry down carefully/ slowly by turning the current up
9. Burn off parafilm [approx. 1.1-1.3A]
10. 'Smoke' off H_3PO_4 (white whispy smoke), and let ribbon glow a dull red momentarily [approx. 1.5-1.7A] before turning it off.

Procedure for Sm:

1. Add 1 µl H_3PO_4 to each sample to allow time for them to dissolve
2. position filament in Teflon block
3. Load sample/standard in 2 x 0.55 µl as to ensure the whole 1 µl is loaded.
4. Dry down carefully/ slowly by turning the current up

For stds only:

5. *Change pipette tip*
6. *Load 1 µl H_3PO_4*
7. *Dry down carefully/ slowly by turning the current up*

8. Burn off H_3PO_4 (but don't wait for white whispy smoke! don't seem to get it from Ta ribbon, unlike Re ribbon). When >1.5A be efficient in turning up the A till the red glow - Ta ribbon deforms readily, but take care as to not get too high as the filament may burn through if you're being too vigorous/ambitious (definitely a good idea to practice Sm with loading the stds first!) – the be sharpish in turning it off [approx. 1.5-1.7A]

NB. Parafilm is not used on Ta ribbon for 2 reasons: a) the load does not seem to spread as readily as on Re; b) melting parafilm off the Ta ribbon causes even more problematic deformation of the ribbon when heated up to burn off the H_3PO_4

Sharma, M., Papanastassiou, D.A., Wasserburg, G.J. and Dymek, R.F., 1996. The issue of the terrestrial record of Sm-146. Geochimica Et Cosmochimica Acta, 60(11): 2037-2047.

STEP 8 (TIMS analysis on the OU Triton)

STUDENT'S GUIDE to TIMS ANALYSIS on the OU TRITON: PROTOCOL 8

UNLOADING MAGAZINE

Allow at least 1 hour between turning the last filament off and venting/opening the chamber, to prevent thermal shock damage to delicate ceramic components in the source.

TUNE software > ACCESSORIES window
- Click **HV OFF** Green light turns red
- Click **Analyser Gate CLOSED** Green light turns red
- **Close Analyser Gate/Line of Sight manually**

Metal projection RHS of source, clockwise screw **in** with ratchet wrench, finger-tight

DIAGNOSTIC > Instrument Menu
- **Connect MS** before removing magazine Can monitor vacuum in sample wheel window
- **Turn KEY** by green+ red buttons on front right of Triton body **¼ turn anticlockwise**

Pumps wind down, and then a hiss as the chamber comes up to air

Wear gloves for unloading magazine
- **Undo catch** on front of magazine chamber; the door will pop open when the chamber is at atmosphere (a few mins)
- **Place clean sheet of A4 paper inside** chamber on base (to catch swarf etc)
- **Unscrew hexagonal bolt on retaining arm** (just right of centre, top) and **flip** carefully **aside** (to right)
- **Remove magazine/sample wheel** carefully from chamber:
    - Locate green/black magazine handle in central magazine spindle
    - Screw in barrel (clockwise) to engage magazine
    - Unscrew handle (anticlockwise) and gently pull magazine out (it may be slightly warm)
    - Support weight (use 2 hands) and point screw thread end slightly upwards to ensure it doesn't drop off the handle…
- **Transfer magazine** onto **black stand** in **clean hood by window:**
    - Locate central spindle, and turn until stubby metal pin fits into groove on holder wheel
    - Screw in green/black handle to holder
    - Unscrew black barrel anticlockwise to disengage magazine, but you don't have to unscrew completely/remove handle…unless the magazine is hot, in which case do remove the handle seeing as the screw thread can seize up on cooling!

Close and latch the chamber door if it will be open for more than a few minutes (i.e. you have not already loaded your filaments). In which case you should also evacuate the chamber again by turning the KEY by green+ red buttons ¼ turn clockwise (to vertical).

- **Remove filaments** from the magazine assembly

(flip catch at the top of the metal notched wheel to stop the wheel spinning).
You may either keep/store these if they have not been run, or remove them for recycling/disposal.
If they are not your filaments make sure you retain them all intact in a filament box in case they are needed.

Exchange extraction plate now (clean one for each magazine load)

LOADING MAGAZINE

Wear gloves for loading magazine
- **Load filaments** onto the magazine:

EVAP to left (if magazine handle to your right), ION or blank plate to your right

- **Test all the filament holders for short circuits**

Green circuit tester - one pin to the top of the slit plate, other pin to one of the back posts. Noise = a short circuit, most likely because a filament post is too close to the slit plate (there is very little clearance) - the errant post may need gentle bending to realign it

- **Inspect the contact posts** of the filaments by rotating the wheel and checking that they are not bent or misaligned, and gently realign any that are misshapen

- **Check slit plates are on properly** (might need a good push on if they are new and stiff)

[- Vent the chamber if it is not already open to air: Turn KEY by green + red buttons ¼ turn anticlockwise Pumps wind down, and then a hiss as the chamber comes up to air]

- **Remove magazine** carefully **from black stand** in clean hood by window
If the handle screw thread was sticking, wipe the thread of the handle and the magazine thread with a kimwipe wetted with IPA (Iso-Propyl Alcohol) to remove dirt.
DO NOT lubricate with any other substance!
    - Screw in black barrel clockwise
    - Unscrew green/black handle and remove magazine from holder

- **Place clean sheet of A4 paper inside** chamber on base (to catch swarf etc)

- **Transfer magazine to sample chamber**:
    - Screw in green/black handle to holder, jiggling a little as you go to make sure it goes on properly and the threads don't stick
    - Unscrew black barrel anticlockwise to disengage magazine
    - One you've removed the handle, the bolt in the centre at the back should be flush with the back of the magazine – if not the z-focus might stray when running!

- **Flip back retaining arm** and **screw in hexagonal bolt** – do not overtighten

- DIAGNOSTIC > Sample Wheel window >
Click on one of the symbols with a circular arrow just below the 'Set' button (this rotates the magazine through 360 degrees).

- **Watch the magazine as it turns** in the chamber to ensure there are no snags (nasty grinding noises) – if so, hit 'Stop' button on Sample Wheel screen below rotate symbols.

- If all clear, **remove A4 sheet, wipe o-ring seal** on door (with IPA if you want, never acetone though), **close chamber door** and lock with catch.

- **Turn KEY** by green+ red buttons on ¼ turn clockwise (horizontal to vertical)
Should hear pumps kick in, and in sequence the red vacuum lights should start turning green:

$FV10^{-1}$	(Fore Vacuum)	after about 2 minutes
TP>50%(Turbo Pump)		after another minute or so
Ampl Valve	(Amplifier valve)	(same time)
HV 10^{-4} (High Voltage)		after about another 2 minutes
HV Electronic		(same time)
Green button		(same time)

Only the Analyser Gate light should be still red at this stage.

- After about 5-10 minutes pump-down (red lights in RH column of Instrument Status, inc HV, turn green), the vacuum will be good enough for the software to allow you to **Initialize the magazine**:
DIAGNOSTIC > Sample Wheel – Click 'Initialize Sample Wheel' button (takes 6 mins)
Finds the best contact point on each filament
Should 'find' all your filaments – if not, could be a short circuit, or if * appears next to the position, posts could be bent (duff contact) OR could be playing up and neither (though rarely happens). Initialise again before resorting to unloading the wheel to investigate.

- **Leave to pump down** for good vacuum e.g. overnight

- Can **set cup configuration** now for minimal noise when ready to run (see below), **manually open the analyser gate** (ratchet anticlockwise, piston out) and **prepare a run sheet** (C:\Triton\User\triton\Results Sheets).

RUNNING STANDARDS/SAMPLES

Status at the start of a typical day: Magazine loaded
HV OFF
Analyser Gate shut (check whether shut manually)

CHECK pressures: FV Press 2×10^{-2} mbar
HV Source Press 2×10^{-7} mbar or lower
Ion Getter Press 5×10^{-9} mbar or lower

The Amplifier Temperature should be within about 0.2 of 36.4°C; if not, this could indicate a vacuum problem in the amplifier housing.

1) Check cups for background noise

- TUNE > Chart Recorder window (graph along lower half of screen with traces running along). - Click 'Set Offsets' button on toolbar ('Normalization' icon)
- Set offsets to 0.001 apart (and rescale from -0.001 to 0.009) to check that no one trace is particularly noisy (overlapping others)

Centre cup is always slightly noisier – trace more squiggly – but not overlapping
In certain circumstances (e.g. after a run terminated automatically with a .pex file), the magnet stops scanning and no traces will be visible (except old ones).
To restore the traces, go to the Scan Control tab (TUNE), and click the SET button. Check you have the correct axial mass in the drop-down menu box (145 for Nd, 147 for Sm).

2) Cup configuration (you may have already done this)

TUNE > Cup configuration tab
Check that you have the Faraday cups in the correct positions for your analysis; if not **open** the **correct file** and click **'Set Collection'** to change the cups to their pre-defined positions (all lights green once done)

Nd

Standards: Nd145-Sm-Ce_dt.ccf

Cup	L4	L3	L2	L1	C	H1	H2	H3	H4
Isotope	140Ce	142Nd	143Nd	144Nd	145Nd	146Nd	147Nd	148Nd	150Nd

Samples: Nd145-Sm-noCe_dt.ccf

Cup	L4	L3	L2	L1	C	H1	H2	H3	H4
Isotope	½ mass	½ mass	143Nd	144Nd	145Nd	146Nd	147Nd	148Nd	150Nd

Note that for running samples, there is a different configuration for Nd, which deflects 140Ce and 142Nd ½ mass unit out. This deflects the Ce beam from the L4 and L3 Faraday cups, reducing interference on Nd, and reducing cup wear.

Sm

Standards and samples: Sm147C_id_dt.ccf

Cup	L4	L3	L2	L1	C	H1	H2	H3	H4
Isotope	142Nd	144Sm	145N	146Nd	147Sm	148Sm	149Sm	150Sm	152Sm

For dynamic analysis (i.e. using the SEM) e.g. for blanks:
Nd: Nd145-Sm-Ce_dt-SEM.ccf
Sm: Smdynamic.ccf

3) Initial Setup

- DIAGNOSTIC > Instrument Menu > **'Disconnect MS'** (lights on window grey out) or close Diagnostic altogether before running any filaments
- ACCESSORIES > Click **HV ON** (Red light turns green)
- **Check Analyser Gate is manually open.** If closed, ratchet anticlockwise, piston out. (closed in the software though)

For dynamic analysis (i.e. using the SEM) e.g. for blanks:
Need to turn on the SEM. TUNE > Centre Cup> 'deselect Faraday'

4) Choose filament to run

TUNE > Sample Wheel tab
Check current position, and use drop-down menu to change
Light will turn yellow, and say 'Running' next to it, then green once filament(s) in correct position

It is always best to **run standards before samples** (avoids contaminating standards with spike from samples, potentially left on extraction plate, which could lead to poor std reproducibility), **at least 3** if not more.

5) Heat up filament(s)
- TUNE > Filament Control tab (IONI and EVAP lights on LHS are green if in position)
- **Set 'Max values'** by typing in desired current value for each filament to be initially (automatically) heated up to:

Nd on Re ribbon: IONI 4500 (speed 210 mA/min); EVAP 800 (speed 70 mA/min)
Sm on Ta ribbon: EVAP 2000 (speed 150 mA/min)
Test on standards before running samples!
- Click 'Start' buttons on left hand side to **start filaments heating**

(they change to 'Stop' buttons, so you can pause the filaments at any time)
DO NOT hit 'RESET' buttons by mistake – turns off the filaments immediately, which is annoying because a) means you have to heat them up again (takes time), and b) may damage/alter the sample load.

[GO AND DO A GAIN NOW IF THE FIRST RUN OF THE DAY – SEE BELOW]

Keep an eye on the **HV Source Pressure rising above 4x10-7** during heating. If it does slow down/stop turning up the evaporation filament until the pressure has dropped again.

Keep the **Analyser Gate closed** during heating to protect the vacuum in the flight tube (Ion Getter). If the pressure is rising rapidly, it suggests a lot of volatiles on the filament, which must be evaporated and removed from the chamber before running.

6) Do GAIN Calibration (one at start of every day) *(not required for dynamic analysis)*
TUNE > Detector calibration tab > Click GAIN button
Gain calibration runs for about 10 minutes, so do it immediately after starting to heat the filaments (you can't heat up the filaments after starting a GAIN but they will go on heating during it)
Note you don't see the traces, rather specks of colour tracking across.

7) Find beam
Once the filaments have heated up (~25mins for Nd, ~15mins for Sm) **open the analyser gate**
You made need to adjust the scale in the Chart recorder window bearing in mind that Nd signals can leap up to 10V! whereas Sm can be a bugger to find and you will to look at near-baseline values
Remember you can adjust the x-axis scale too (in seconds).
TUNE > Source Lenses tab
To find a beam initially, you can **load up** the most **recent focus settings file** ('Open folder' button, top left). This may find a beam if the loads are behaving consistently. However, beams often shift along the filament during heating and tuning, so the last focus position saved may not be appropriate for the new filament. This is partly why it is important to be as consistent as possible in making and loading filaments.
The most sensitive lenses are the extractions lenses so try moving them around (but not too wildly); also bear in mind that your load might not be perfectly in the centre of the filament (50 on the 'wheel fine tuning')

For dynamic analysis (i.e. using the SEM) e.g. for blanks:
Have the centre cup set to 150Nd or 149Sm – these are the spikes and will be the largest signal to find/focus on.

8) Focus and tune beam
TUNE > Source Lenses tab
Now you want to focus the beam and grow it by increasing the EVAP (and IONI if Nd), which is a bit of a 'black art'...

If you have a big enough beam you can do an **'auto' tune** for all lenses (large tab to left, uncheck the box to the left of Wheel Fine Tuning to exclude it).
If the beam is too small, the software may not be able to do this. You will have to turn up the EVAP filament first to increase the beam.

The traces may 'jump' up off the scale if the focussing finds a more intense beam; quickly adjust the scale on the Chart recorder. **Try not to let the beam in any cup rise above 10V**. If it does, turn the Evaporation filament down quickly (by replacing the Max value with a lower one, and clicking Start).
You can monitor individual values in the 'Intensities' chart in the Accessories window (RHS).

For dynamic analysis (i.e. using the SEM) e.g. for blanks:
Scale is count per second (cps, at right hand side of chart recorder). SEM will trip out if cps >800,000 cps. Aim for between 100,000 and 700.000 cps.

You can manually tune the wheel or do an auto, although if you loaded in the middle and it finds a very off-centred beam then trust your own judgement.
It may be a case of using the position it finds as strongest to grow the beam, and then finding the true position of the load before running.

Re-tune several times before running, each time remembering to **save your positions** in a file with the date, element, your initials ('save' icon at top)

9) Peak centre/Peak scan
Once you have a stable beam of a reasonable size (>0.25V, say), check the peak shape and centring:
TUNE > Scan Control tab >
First click 'Peak Centre'
The machine performs two scans across the peak (forwards and backwards), as a check on the mass calibration. The software plots two red lines, which should be coincident, marking the peak mass. If they are too far out, the Peak centre automatically runs again.
Next, **click 'Peak Scan'**
This compares the peak shapes of all the specified peaks, which should all be coincident. If any are offset significantly, some correction may be needed. [Ask IJP, BC, or TWA about adjusting the cups]. The peak shapes should be nearly identical, and symmetrical, with broad plateaux and narrow shoulders.

For dynamic analysis (i.e. using the SEM) e.g. for blanks:
Try to do a peak centre at the start of each run, especially if opt out of running the peak centres in the method file (to save time and collect more blocks of data). Important because the magnet is peak hopping and you want to avoid this drifting.

10) Grow beam
Now you can **turn up the filaments** to increase and stabilize the beam ready for running
TUNE > Filament Control tab
Nd runs well with the IONI filament adjusted to give a Pyrometer temperature of **1750**°C, so aim for this.
Sm seems to run well around **1450**°C, but is much more erratic.
This filament can be turned up to this point now, or gradually while incrementing the EVAP, as you'll find that the turning up the EVAP filament does effect the pyrometer temperature too. Occasionally, the pyrometer may get misaligned (you'll tell because the temp won't have risen with the increase in IONI). It's on the side of the chamber. Align it on the bright filament by using the black circle in the view finder pointing into the chamber, and gently tweaking the pyrometer.
Increment the 'Max Value' for the EVAP filament, and click 'Start'.
You should see the beam rise. Don't rush this heating stage. You get a feel for the optimum speed, and it varies with the Re ribbon thickness (among other things).

TUNE > Source Lenses tab
After each current increase, check the focus on the beam.
As the filament heats up, the location of the most intense beam, or the most stable beam, may shift. Every filament behaves slightly differently
Look for a higher beam just above or below the current WFT position, and then Z-focus, followed by the others (individually or as a block on AUTO).
Alternate between turning up the filament(s), and tuning the beam, until you have achieved a stable beam at the intensity you require.

Nd
Ideally should be run on **4-7V** beams, though any stable beam above 1V will be OK for a difficult sample.
4400-4800mA (IONI) and **1300-1800mA (EVAP)** are typical range of values for the final run – however, Re ribbon changes from batch to batch, so there is an element of trial and error to these.
If you take **an hour tuning** a Nd beam, this generally results in a **reasonable beam** which has not fractionated too much. Nd generally can be persuaded to form a long-lasting, stable beam (commonly falling gradually at the start of the run, but levelling off later on).
If you start collecting data on a rising beam, monitor the intensity to make sure it does not rise above 10 V. If it does, abort and turn the beam down slightly.

For blanks:
4250-4575mA (IONI)** and **700-1500mA (EVAP)
A good run typically has a 25,000 to 90,000 cps range for max. 150Nd (the spike)

Sm
Trickier to run than Nd. Ta filaments seem variable, so **some samples need turning up to 2100mA, while others won't produce a beam until 2800Ma.**
- **SmE standard** tends to develop a **rising beam from ~2700mA** – but may need turning down as pyrometer T (and beam) climbs too rapidly.
- **Samples** with less material on filament (e.g. some whole rocks) will **rise, and then fall fairly quickly**. You need to be prompt in running these, preferably while the beam is still rising.
- **Garnets** seem to **run similarly to SmE**, on a rising beam easily sustainable for 90 ratios, but reluctant to develop a beam initially. Once the beam starts, it may need turning down to curb the rise of intensity and filament temperature.

For blanks:
2225-2750mA (IONI)
Really tricky to run – until the filament reaches a threshold temperature the beam does not rise above ~500cps, but as soon as it does (~1300°C on the pyrometer) T excels and the beam starts hiking up rapidly. Best practice is to turn down the evap now to curb the increase but to also start the run – this beam will die soon after reaching its peak. More than half of the blanks I/Tom ran did not see through all 100 blocks set in the method file.

11) RUN!
Check you have a good stable beam, do a final focus, and save the focus positions.
METHOD EDITOR (Taskbar)
Check you have the correct cup configuration and method file

METHOD FILES:
Nd standards **145Nd_ax_Sm_Ce_corrected_stat**
Nd samples **145Nd_ax_Sm_noCe_corrected_stat**
Sm standards **147SmCidstd** (baseline every block, 9 blocks of 10 ratios in total)
Sm samples **147SmCidsample** (baseline every other block, so 4 ½ in total)
(double check cup configuration in the method file is the same as the one you have open)

For dynamic analysis (i.e. using the SEM) e.g. for blanks:
Nd: Nd-dynamic-SEM-IJP
Sm: Sm-dynamic-IJP

If you want **to leave the analysis running** (e.g. end of day), **check the 'After run' box** (RHS), and then choose 'fildown_vclose.pex' from the drop-down list.
Note you can't change this once the run has begun so make your mind up before
This will turn the filaments down (to 10mA, not completely off), and close the Gate Valve, after the run finishes, to maintain the vacuum.

Click the Green triangle in the toolbar (top left of screen). A dialogue box will prompt you for a filename. It may be easiest to find the folder with your previous runs in, select one of these, and then alter it (rather than type a new one out).
Once you hit 'Save', the analysis starts.

For Nd and Sm, the method performs a Peak Centre, and then does a baseline measurement, before the first ratios are collected, so it's a few minutes before you can monitor the data in Data Evaluation.

12) Monitoring a run
TUNE > Chart recorder
Keep an eye on the beam: if it rises or falls severely, you should **terminate** (red square) and re-tune. Only terminate when collecting and NOT during a baseline or peak centre – the magnet is moving.

DATA EVALUATION
You can monitor the data here.
Select the black lightening strike icon (turns yellow) for 'online evaluation' that updates as you run.

146/144 Nd	Fractionation*. Natural value is **0.7219** Ideally a run should start slightly below this, and rise through it monotonically, as with continuing fractionation the reservoir of lighter isotopes is depleted and the isotopic composition becomes increasingly heavier (the 'reservoir effect').
143/144 Nd	Desired ratio. You can check this value against the expected value (range for stds in the literature is 0.511850-0.511860 although here at the OU they do tend to run slightly on the low side e.g, 0.511849 is fine), or you may have an idea what it should be for a sample Keep an eye out for fliers. One or two very extreme fliers can be rejected offline at 3 s.d.– see IJP's std compilation spreadsheet ('rejection corrector')
147 Sm	If there is much of this in a Nd run, the chemistry isn't working properly. Compare against 140Ce which equates to background signal for samples.
144 Nd	For tracking beam intensity through the run

NB. Nd **runs take ~1hr 20mins** at present

152/147 Sm	Fractionation*. Natural value is **1.78316**
146 Nd	Monitor for Nd contamination/interference. The beam intensity should be essentially zero for a minimal interference correction
149/147 Sm	**SmE standard value** is 0.**9216**. **Spiked samples** should give values around **1 to 3**

NB. Sm **runs take 10 mins** at present

* If a run doesn't reach natural fractionation value it means there is a lot on the filament (reservoir not depleted)

13) Finishing analysis

After the analysis has finished, make sure you click RB and then RN in DATA EVALUATION to ensure the software has recorded/refreshed all the data.

If you are running another sample immediately:

- RESET both filaments
- Close Analyser Gate (in software, not manually)
- Move Sample Wheel to next filament position to run
- Set Max Values for heat-up
- Start heating filaments

Then you can look at the data, and update the standard compilation (if you ran a standard), or offline correct if necessary.

To export you data:

- DATA EVALUATION > right click and select *all* columns (in measured data, ratios, filament)
- 'Export to ASCII' (Ex icon, 3rd from right, top toolbar)
- Check 'not marked' and 'time in seconds' (recommended) > ok > save in your personal folder C\Triton\User\Triton\Data\Personal folders
- Check 'marked' and 'full export' (optional) > ok > save in your personal folder C\Triton\User\Triton\Data\Personal folders … as a complete record for yourself

14) End of the day

If you're not doing a run:

- HV off
- Close Gate Valve (in software, not manually)

If you're leaving a sample running:

- Make sure you have tagged the 'fildown_vclose.pex' file on to the Method Editor for the run. Note that if you use this tag and then abort a run, the filaments are automatically turned down to zero – this can be irksome…! But also note that once you have started the run you cannot check the 'after run' box – also irksome!

TROUBLESHOOTING

- Save file when starting run with incorrect filename

Wait for run to finish. Go to C\Triton\User\Triton\Data…find you magazine folder and rename all 3 corresponding files (text doc, DAT doc, Finnigan Measured Data File)

- Green triangle in method editor not 'activatable'

Might still think it's taking a measurement (did you terminate during a baseline? Try not to…)
Quit method file – reopen. If this doesn't work, try quitting method editor – reopen. If this doesn't work quit tune (don't worry, your filament will remain heated) - reopen. And if this doesn't work restart computer
On restart activate 2nd screen by going to display in the control panel

- Computer and machine not 'talking' to each other

Red button under cups reboots machine – press once (audible beep 1 second later) whilst restarting computer

FAQs

Does it matter whether the amplifier rotates left or right?

Depends on the relative abundance of isotopes of the element you're analysing
E.g. the relative abundance of Nd isotopes are broadly similar so that the effect of a decayed signal on one amplifier is not significant when it starts from the next cup, so right or left won't make a difference (left is the default so that might be more common than most)…
…but with Sr for e.g. the decay of the signal from the cup collecting Sr88 may affect the Sr87 data, because its relative abundance is much smaller in comparison, esp if high precision work
Look at the A4 table of the 'Relative abundances of naturally occurring isotopes on the desk

Why do an offline 3 s.d. correction when the data evaluation does a 2 s.d. calculation?

The sd calculated by the program/data evaluation includes flyers so the 2 sd ends up unrepresentatively large. By taking it offline we can omit the odd flyer and calculate the true sd (essentially a narrower range about the mean).

Why bother 'disconnecting ms' in DIAGNOSTIC before runs?

Apparently in the hierarchy of the software DIAGNOSTIC takes precedent and this might screw with TUNE…but it might not either (so don't worry if you forgot to disconnect).

***OFFLINE CORRECTIONS ***

For Nd:
Make a note of how many online ratios were taken
Copy 143Nd/14Nd ratios into 3s.d. correction worksheet
Note how many ratios have been taken, and calculate how many ratios have been rejected
For a std: Copy and paste *special* the ratio values, 1se, 2se into the std compilation sheet

(currently the sample data is calculated using the raw intensities – copied over and separated into blocks – from which ratios are calc. prob could copy direct offline corrected ratios*…but still a bit manual – best to set up a macro…or a new simply spreadsheet??
*measured ratios used: 143/144, 150/144, 146/144, 148/144, 145/144)

B2 Methods for the U–Th–Pb LA–ICPMS analysis of accessory minerals

B2.1 Initial identification using element maps

Element maps (5 x 4 mm^2) taken on an electron microprobe is an efficient and thorough means of identifying different accessory phases in and around garnet-porphyroblasts, while also revealing their relative abundance and textural occurrence. The elements Ca, P, La, and Fe act as discriminants from which monazite, allanite, apatite and ilmenite (all common accessory phases in pelitic samples) can be indentified. Although some of these minerals are not suitable for U–Th–Pb analysis e.g. ilmenite, it is useful to be able to distinguish them from the other phase (e.g. ilmenite and allanite can share a similar grain morphology and size, and have similar levels of brightness in back scatter electron images, relative to monazite). This element mapping method is important in the confirmation (or not) of early phases (e.g. inclusions in garnet) and later phases (e.g. present in the matrix).

B2.2 Locating small grains (accessory phases) in the laser ablation cell

As the laser ablation cell only provides transmitted or reflected light as a visual aid, phases that have been identified and located on the electron microprobe (i.e. back scatter electron images) are difficult and therefore time-consuming to re-locate just 'by eye' when the sections are loaded ready for LA–ICPMS analysis. This is especially true of allanite occluded by garnet, where it can be extremely difficult if not impossible to discern where the included phase is at all (Fig. B2.1).

A process wherein the coordinates of the grains to be analysed are recorded in the electron microprobe system, and then converted to coordinates for the laser system greatly improves both the efficiency of, and confidence in, the relocation process. All that is required are three distinctive marks (e.g. red marker pen spots) on the sample slide/mount (preferably at the corners and/or edges on the slide), for which the coordinates on the electron microprobe system are already known. These three marks are directly located on loading the slide/mount into the laser ablation cell, and 'new' coordinates for the marks are recorded. These coordinates form the new spatial reference, and entered into an excel spreadsheet (at NIGL in the LA–ICPMS laboratory) from which it is possible to convert all 'old' coordinates for the grains to be analysed, into 'new' coordinates for the laser system. In detail: 1) the red marker spots were ablated; 2) the section was removed from the

cell and the carbon coating (required for electron microprobe analysis) was removed with a diamond paste; 3) the slide was cleaned and re-loaded into the laser ablation cell, where the centre of the ablation pits became the reference points.

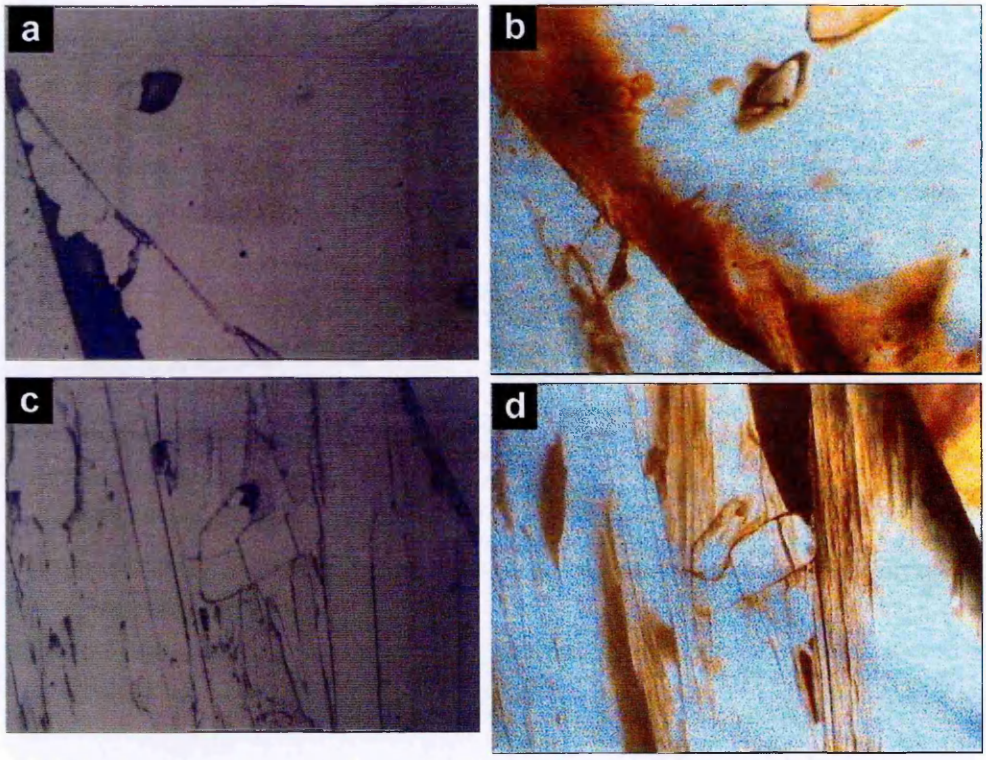

Fig. B2.1 a) and **b**) are transmitted and reflected light images, respectively, of 'allanite 5' (p. 141, Fig. 6.12). Allanite is impossible to distinguish from the host garnet, but the grain does lie in the centre of each image. In comparison, 'monazite 1' in the matrix (p. 140, Fig. 6.11), shown in **c**) and **d**), can be located relatively easily.

B3 U(–Th)–Pb geochronology via LA–ICPMS

U(–Th)–Pb geochronology relies on the following isotope systems. Note that the basic principle of radioactive decay is covered in Chapter 4 (Section 4.2).

System	*Decay constant (Ma^{-1})*	*Solution*
$^{238}U \rightarrow {}^{206}Pb$	1.55125×10^{-4}	$^{206}Pb = {}^{238}U\ (e^{\lambda_{238}t}-1)$
$^{235}U \rightarrow {}^{207}Pb$	9.8585×10^{-4}	$^{207}Pb = {}^{235}U\ (e^{\lambda_{235}t}-1)$
$(^{207}Pb/^{206}Pb)^*$		$(^{207}Pb/^{206}Pb)^* = 1/137.88 \times [(e^{\lambda_{235}t}-1)/(e^{\lambda_{238}t}-1)]$
$^{232}Th \rightarrow {}^{208}Pb$	4.9475×10^{-5}	$^{208}Pb = {}^{232}Th\ (e^{\lambda_{232}t}-1)$

From Harrison et al., 2002

In an ideal closed system age estimates from the U and Th isotopic systems would agree within the errors of measurement; however this cannot be taken for granted. Furthermore, the accuracy of U(–Th)–Pb dating is compromised by the necessity for a correction to account for inherited (or 'common') Pb. The non-radiogenic Pb isotope, ^{204}Pb, is measured to correct the radiogenic Pb isotopes (denoted Pb*) for their common-Pb component (Horstwood et al., 2003). If the ^{204}Pb content is so small that it is impossible to measure accurately, then a graphical correction is possible on a Tera-Wasserburg plot (see Sections 3.4.2 and 6.2.4 iii). With Th-rich minerals e.g. monazite and allanite, excess ^{206}Pb derived from ^{230}Th must also be taken into account.

Laser ablation inductively coupled plasma mass spectrometry (**LA-ICPMS**) has been used routinely in this thesis. As an *in situ* technique, it offers better precision and detection limits than the electron microprobe (e.g. Williams et al., 2006), which is vital for a) the successful analysis of young minerals in which there has been limited time for the radiogenic daughter isotope(s) to accumulate, and b) for an accurate common-Pb correction. In comparison to high-resolution secondary ion mass spectrometry (SIMS or SHRIMP [Sensitive High Mass Resolution Ion MicroProbe]), LA-ICPMS remains the more viable option for many, as ion-probes are expensive and limited to a relatively small number of laboratories worldwide. A SIMS analysis also currently up to 5 times as long as it does for a LA-ICPMS analysis (< 5 mins), hence the latter presents a

more efficient technique in terms of both time and money. Furthermore, U(–Th)–Pb dating via LA-ICPMS continues to be a rapidly developing technique with improvements in analytical and spatial precision that approach that of SIMS (e.g. Gehrels et al., 2008). It is now possible to accurately correct for fractionation related to both the physical ablation process as well as elemental/isotopic fractionation during time-of-flight in the mass spectrometer. A time-resolved analysis can identify distinct age domains within one sample grain. The future applicability of LA–ICPMS for U(–Th)–Pb dating relies on the availability of suitable mineral standards to the geologic community, for matrix matching between the standard and sample remains necessary for an accurate measurement. This is increasingly important as minerals other than the conventional zircon and monazite are explored with regards to U(–Th)–Pb geochronology e.g. allanite (Gregory et al., 2007) and titanite (Storey et al., 2007).

Appendix C: Data tables

C1.1 Sutlej valley samples

sample	IO5/7i	IO5/7ii	IO5/7iii	IO5/7iii rpt	IO5/8i	IO5/8ii	IO5/8ii rpt	IO5/9	IO5/10ii
unit	Haimanta	Haimanta	Haimanta	Haimanta	Haimanta	Haimanta	Haimanta	Haimanta	Haimanta
lithology	schist	schist	schist	schist	schist	schist	schist	schist	gneiss
notes									
batch no.	X1592M	X1592M	X1592M	X1592M	X1592M	X1592M	X1592M	X1592M	X1592M
wt. %									
SiO_2	69.79	68.34	44.18	43.49	56.79	58.32	58.07	49.82	55.33
TiO_2	0.534	0.469	1.071	1.088	0.888	0.838	0.860	0.898	0.942
Al_2O_3	12.84	11.76	21.13	20.88	21.07	19.85	20.51	19.27	19.94
Fe_2O_3	3.71	4.83	14.35	14.57	8.40	7.91	7.98	9.09	6.74
MnO	0.097	0.101	0.673	0.661	0.100	0.083	0.082	0.107	0.082
MgO	1.76	4.48	7.14	7.30	3.82	3.74	3.87	4.45	3.75
CaO	3.02	2.04	2.17	2.05	0.42	0.37	0.37	2.27	1.68
Na_2O	3.34	1.87	3.13	3.40	1.28	1.28	1.19	4.67	2.77
K_2O	2.15	2.89	4.43	4.34	5.43	5.39	5.47	7.33	5.60
P_2O_5	0.140	0.117	0.130	0.123	0.207	0.151	0.158	0.180	0.116
LOI	2.68	3.12	1.77	2.17	1.60	1.46	1.67	0.73	1.44
Total	100.06	100.02	100.17	100.07	100.01	99.40	100.23	98.82	98.40
total alkalis	8.51	6.81	9.73	9.79	7.13	7.04	7.03	14.27	10.05
Al_2O_3/alkalis	1.51	1.73	2.17	2.13	2.95	2.82	2.92	1.35	1.98
batch no.	X1595T	X1595T	X1595T	X1595T	X1595T	X1595T	X1595T	X1595T	X1595T
ppm									
Rb	92	143	205	207	228	226	231	230	246
Sr	147	74	139	131	70	69	72	167	181
Y	19.7	15.2	98.6	102.2	36.6	29.8	31.0	27.7	28.0
Zr	130	113	205	212	168	149	153	134	146
Nb	10.4	9.0	25.0	24.6	18.0	17.3	17.2	18.6	18.0
Ba	1341	1198	1885	1905	1810	1811	1858	2917	7153
Pb	26	bd	12	12	22	20	21	53	34
Th	11	10	24	27	18	16	18	27	19
U	bd	bd	5	bd	4	3	4	5	4
Sc	10	9	32	37	21	21	23	25	24
V	80	64	160	171	149	141	143	162	169
Cr	61	60	202	204	136	127	132	147	132
Co	9	11	30	34	19	21	21	32	12
Ni	30	20	99	99	43	41	40	67	24
Cu	bd	15	67	66	21	17	16	31	26
Zn	55	45	92	92	126	97	86	136	174
Ga	15	13	27	28	28	26	25	28	26
Mo	bd	bd	bd	bd	bd	bd	bd	bd	bd
As	9	bd	bd	7	bd	bd	bd	bd	bd
S	bd	1138	344	385	264	55	51	211	2955

na, not analysed

bd, below detection

Continued...

C1.1 Sutlej valley samples *continued*

sample	IO5/13	IO5/14i	IO5/15iii	IO5/22	IO5/22 rpt	IO5/28i	IO5/28i rpt	IO5/28ii	IO5/31i
unit	Haimanta	Haimanta	Haimanta/LP	Haimanta	Haimanta	Haimanta/LP	Haimanta/LP	Haimanta/LP	Haimanta
lithology	schist	schist	schist	gneiss	gneiss	schist	schist	schist	schist
notes									
batch no.	X1592M	X1592M	X1592M	X1592M	X1592M	X1592M	X1592M	X1592M	X1592M
wt. %									
SiO_2	57.34	53.25	58.15	68.00	67.85	44.12	45.16	64.98	64.12
TiO_2	0.840	0.831	0.799	0.762	0.739	1.453	1.425	0.820	0.777
Al_2O_3	19.78	19.10	19.00	14.95	14.61	20.27	19.82	19.41	17.22
Fe_2O_3	8.17	9.54	7.04	6.19	6.02	9.87	9.17	5.37	5.96
MnO	0.098	0.108	0.075	0.063	0.062	0.063	0.058	0.033	0.095
MgO	3.29	6.13	4.32	4.88	4.64	12.25	11.19	4.78	2.91
CaO	0.94	1.59	0.73	0.37	0.37	0.63	0.59	0.39	0.82
Na_2O	2.19	4.44	3.24	0.74	1.52	2.38	3.12	1.14	2.23
K_2O	5.65	3.67	5.14	3.30	3.36	2.31	2.85	1.46	4.32
P_2O_5	0.158	0.184	0.109	0.205	0.186	0.408	0.363	0.214	0.112
LOI	1.57	0.44	1.09	0.19	0.19	6.01	5.79	1.69	1.78
Total	100.02	99.29	99.70	99.66	99.53	99.76	99.53	100.28	100.35
total alkalis	8.78	9.71	9.10	4.42	5.25	5.32	6.56	2.99	7.37
Al_2O_3/alkalis	2.25	1.97	2.09	3.39	2.78	3.81	3.02	6.49	2.34
batch no.	X1595T	X1595T	X1595T	X1595T	X1595T	X1595T	X1595T	X1595T	X1595T
ppm									
Rb	219	169	353	151	146	174	153	66	150
Sr	109	167	64	28	28	33	33	21	88
Y	30.6	27.4	30.5	28.3	29.4	48.3	48.1	31.3	22.4
Zr	145	138	157	183	181	544	564	176	143
Nb	16.3	16.2	13.7	13.6	13.4	21.1	21.0	14.3	13.3
Ba	1596	499	754	507	479	215	203	380	807
Pb	32	16	15	bd	bd	bd	bd	bd	27
Th	18	21	17	12	11	22	23	15	16
U	5	6	4	3	4	5	5	4	bd
Sc	19	22	20	16	18	23	24	19	20
V	143	150	138	112	104	125	135	140	139
Cr	130	138	122	122	109	154	170	118	127
Co	23	29	24	10	9	14	15	19	17
Ni	53	84	60	47	45	54	58	40	39
Cu	53	7	4	9	8	4	5	3	16
Zn	114	62	82	64	62	90	96	97	81
Ga	27	28	26	19	18	20	22	28	22
Mo	bd	bd	bd	bd	bd	bd	bd	bd	bd
As	bd	bd	bd	bd	bd	bd	bd	bd	bd
S	383	bd	bd	bd	bd	bd	bd	bd	179

na, not analysed
bd, below detection

Continued...

C1.1 Sutlej valley samples *continued*

sample	IO5/32i	IO5/32ii	I05/38	IO5/81	IO5/57	IO5/63ii	IO5/65	IO5/66i	IO5/68i	IO5/68ii	IO5/68iii
unit	Vaikrita	Vaikrita	Karcham	Jutogh	Jutogh	Jutogh	Jutogh	Jutogh	Jutogh	Jutogh	Jutogh
lithology	gneiss	gneiss	schist	schist	schist	gneiss	schist	schist	schist	schist	schist
notes											
batch no.	X1592M	X1592M	X1747M	X1593M	X1592M	X1592M	X1592M	X1593M	X1593M	X1593M	X1593M
wt. %											
SiO_2	46.61	68.76	50.27	70.70	66.35	68.98	61.17	64.81	67.30	70.94	58.42
TiO_2	0.834	0.548	0.814	0.494	0.574	0.611	0.734	0.768	0.835	0.757	1.065
Al_2O_3	19.49	13.45	25.36	14.47	17.41	15.91	16.63	18.20	15.58	13.41	20.35
Fe_2O_3	11.09	4.94	10.37	4.74	6.15	4.86	6.72	5.19	6.69	6.23	8.06
MnO	0.083	0.077	0.171	0.254	0.052	0.042	0.044	0.055	0.099	0.036	0.054
MgO	8.97	2.41	2.16	1.32	2.51	1.51	6.41	1.99	2.07	1.73	2.52
CaO	0.80	2.63	0.66	2.92	0.24	1.95	0.29	1.89	1.58	0.39	0.61
Na_2O	4.72	4.20	0.58	2.74	0.69	1.85	0.31	0.64	0.57	0.35	0.45
K_2O	5.03	2.50	6.48	2.24	4.50	3.73	4.02	4.75	3.98	3.99	5.73
P_2O_5	0.150	0.145	0.259	0.106	0.192	0.153	0.196	0.222	0.182	0.162	0.187
LOI	2.22	0.72	2.73	0.82	1.89	1.41	3.05	1.90	2.03	2.23	2.77
Total	100.00	100.37	99.87	100.81	100.55	101.00	99.58	100.42	100.92	100.22	100.22
total alkalis	10.55	9.33	7.72	7.90	5.43	7.53	4.63	7.29	6.13	4.73	6.78
Al_2O_3/alkalis	1.85	1.44	3.28	1.83	3.21	2.11	3.59	2.50	2.54	2.83	3.00
batch no.	X1595T	X1595T	X1746T	X1594T	X1595T	X1594T	X1594T	X1594T	X1594T	X1594T	X1594T
ppm											
Rb	200	91	376	152	258	163	190	252	240	193	281
Sr	84	150	50	78	35	158	20	66	35	33	41
Y	33.7	20.4	50.2	31.6	30.2	30.6	26.0	30.8	44.1	32.1	47.8
Zr	160	124	187	149	166	176	209	213	239	217	303
Nb	18.8	11.1	16.8	10.8	14.7	12.9	16.0	16.4	14.8	14.3	19.8
Ba	1128	750	827	322	613	727	367	844	746	676	1004
Pb	17	21	35	85	7	18	7	23	13	22	25
Th	18	10	31	19	19	18	25	27	25	22	33
U	5	bd	7	4	5	7	6	5	7	4	9
Sc	23	12	25	10	16	13	12	14	17	13	21
V	198	77	176	52	66	60	62	59	75	63	97
Cr	139	75	137	58	71	65	65	64	61	58	80
Co	26	10	22	11	14	11	11	18	18	8	17
Ni	69	29	55	22	28	24	34	36	34	11	26
Cu	6	16	49	6	4	13	3	16	21	31	31
Zn	112	76	200	161	77	26	58	109	69	73	83
Ga	30	17	36	17	23	19	22	23	20	18	27
Mo	bd	bd	bd	bd	bd	bd	bd	bd	bd	3	4
As	bd	bd	bd	bd	bd	bd	bd	9	bd	bd	bd
S	bd	408	247	bd	bd	bd	bd	bd	788	1259	263

na, not analysed

bd, below detection

Continued...

C1.1 Sutlej valley samples *continued*

sample	IO5/68iv	IO5/70iiix	IO5/70iiiy	IO5/71i	IO5/71ii	IO5/84x	IO5/87	IO5/90i	IO5/90i rpt
unit	Jutogh	Jutogh	Jutogh	Jutogh	Jutogh	Jutogh	Jutogh	Jutogh/Rampur	Jutogh/Rampur
lithology	schist	gneiss	gneiss	gneiss	gneiss	schist	schist	schist	schist
notes									
batch no.	X1593M	X1593M	X1593M	X1593M	X1593M	X1593M	X1593M	X1593M	na
wt. %									
SiO_2	66.20	65.17	67.29	64.91	67.84	66.29	59.13	73.65	
TiO_2	0.877	0.772	0.705	0.859	0.718	0.640	0.993	0.895	
Al_2O_3	16.39	15.88	15.10	15.24	15.39	16.93	19.19	15.98	
Fe_2O_3	6.81	6.10	5.66	6.68	5.47	6.23	7.51	3.30	
MnO	0.101	0.087	0.081	0.068	0.077	0.071	0.053	0.005	
MgO	1.81	3.00	1.29	2.42	1.52	1.69	2.93	0.25	
CaO	1.12	0.31	2.21	1.55	2.62	0.79	0.40	0.33	
Na_2O	0.43	0.45	2.70	1.74	3.12	1.10	1.38	0.70	
K_2O	4.29	5.76	3.41	4.29	2.54	4.34	6.37	3.51	
P_2O_5	0.179	0.179	0.171	0.154	0.167	0.197	0.199	0.243	
LOI	1.93	2.24	1.31	1.46	0.96	2.62	2.26	2.09	
Total	100.13	99.96	99.92	99.37	100.42	100.89	100.41	100.96	
total alkalis	5.84	6.53	8.32	7.59	8.28	6.23	8.15	4.55	
Al_2O_3/alkalis	2.81	2.43	1.82	2.01	1.86	2.72	2.36	3.51	
batch no.	X1594T	X1594T	X1594T	X1594T	X1594T	X1594T	X1595T	X1594T	X1594T
ppm									
Rb	223	324	248	223	131	250	265	203	208
Sr	32	13	146	111	185	55	31	196	199
Y	43.6	30.7	39.7	37.0	36.1	36.4	39.3	41.4	41.3
Zr	250	232	217	227	213	214	291	260	246
Nb	16.2	23.1	16.4	17.2	14.9	16.3	18.4	15.0	15.4
Ba	866	462	534	783	748	611	813	678	702
Pb	12	7	25	18	30	12	14	39	39
Th	25	24	23	23	24	26	32	24	25
U	5	8	7	4	4	6	7	5	6
Sc	16	15	13	16	15	12	19	16	16
V	74	57	52	71	63	66	81	62	62
Cr	65	53	58	57	62	70	71	47	48
Co	17	34	14	15	13	17	16	bd	2
Ni	30	48	22	25	22	28	24	15	16
Cu	17	24	20	12	12	18	16	14	13
Zn	66	92	87	82	75	101	57	8	8
Ga	22	24	20	21	18	24	27	21	22
Mo	bd	bd	bd	bd	bd	bd	bd	bd	bd
As	bd	bd	9	14	6	bd	17	bd	bd
S	323	2182	1259	bd	bd	bd	bd	bd	bd

na, not analysed

bd, below detection

Continued...

C1.1 Sutlej valley samples *continued*

sample	IO5/75	IO5/78i	IO5/78ii	IO5/63i	IO5/63i2 rpt	IO5/70i	IO5/70i rpt	IO5/70ii
unit	Shimla-Jutogh	Shimla-Jutogh	Shimla-Jutogh	Jutogh	Jutogh	Jutogh	Jutogh	Jutogh
lithology	schist	schist	schist	l'granite	l'granite	l'granite	l'granite	l'granite
notes								
batch no.	X1593M	X1593M	X1593M	X1593M	X1593M	X1593M	na	X1593M
wt. %								
SiO_2	64.46	63.21	65.31	75.93	76.33	74.47		76.40
TiO_2	0.803	0.770	0.744	0.048	0.050	0.058		0.045
Al_2O_3	17.69	16.82	16.59	14.93	14.94	15.54		14.29
Fe_2O_3	6.21	7.69	6.52	0.93	0.91	0.99		1.06
MnO	0.055	0.117	0.105	0.023	0.021	0.013		0.014
MgO	2.15	2.45	2.17	0.26	0.27	0.47		0.43
CaO	0.57	0.81	0.98	1.02	1.02	0.92		0.68
Na_2O	0.73	2.65	3.21	2.76	2.73	4.54		3.80
K_2O	5.01	2.90	2.30	2.98	2.92	1.75		1.98
P_2O_5	0.156	0.092	0.156	0.161	0.152	0.189		0.199
LOI	2.87	2.75	1.91	1.43	1.43	1.16		1.26
Total	100.71	100.25	100.00	100.48	100.77	100.09		100.14
total alkalis	6.31	6.36	6.49	6.76	6.67	7.21		6.45
Al_2O_3/alkalis	2.80	2.65	2.56	2.21	2.24	2.15		2.21
batch no.	X1594T	X1594T	X1594T	X1594T	X1594T	X1594T	X1594T	X1594T
ppm								
Rb	271	138	102	110	111	84	77	77
Sr	45	107	108	96	97	121	121	71
Y	46.4	28.6	26.0	16.5	15.3	26.1	23.5	25.3
Zr	188	182	178	27	25	34	33	25
Nb	17.8	12.5	11.5	12.1	12.7	10.0	9.1	5.4
Ba	695	456	386	172	177	130	125	144
Pb	bd	bd	6	36	35	29	31	22
Th	30	10	10	bd	bd	5	6	bd
U	bd	bd	bd	4	4	9	9	12
Sc	20	16	15	bd	bd	bd	bd	bd
V	116	114	110	bd	bd	5	5	5
Cr	89	86	81	8	6	5	13	4
Co	14	15	13	bd	bd	5	5	4
Ni	28	38	36	bd	bd	11	13	6
Cu	8	4	14	17	16	8	8	7
Zn	22	34	37	9	11	20	21	19
Ga	24	21	22	18	17	18	17	14
Mo	bd	bd	bd	bd	bd	bd	bd	bd
As	36	bd	bd	bd	bd	bd	bd	bd
S	bd	bd	bd	266	257	53	51	280

na, not analysed

bd, below detection

C1.2 Bhutan samples

sample	B06/62	B06/62 rpt	B06/64i	B06/64ii	B06/67*	B06/67
unit	Chekha	Chekha	Chekha	Chekha	GHS	GHS
lithology	schist	schist	schist	schist	gneiss	gneiss
batch no.	X1747M	X1747M	X1747M	X1747M	X1747M	X1747M
wt. %						
SiO_2	58.57		54.96	58.81	73.41	73.42
TiO_2	0.923		0.921	0.819	0.737	0.734
Al_2O_3	20.92		23.59	20.45	12.89	13.13
Fe_2O_3	8.66		7.75	6.68	5.16	5.27
MnO	0.106		0.130	0.083	0.117	0.127
MgO	2.11		2.08	1.96	1.35	1.38
CaO	0.26		0.62	1.00	0.20	0.23
Na_2O	0.71		1.23	1.67	0.56	0.59
K_2O	5.06		6.17	5.08	2.75	2.84
P_2O_5	0.100		0.140	0.162	0.092	0.115
LOI	2.7		2.48	1.98	1.74	1.77
Total	100.14		100.06	98.68	99.01	99.60
total alkalis	6.04		8.01	7.74	3.51	3.66
Al_2O_3/alkalis	3.47		2.94	2.64	3.67	3.59
batch no.	X1746T	X1746T	X1746T	X1746T	X1746T	X1746T
ppm						
Rb	251	251	289	258	146	149
Sr	42	41	71	91	46	49
Y	45.5	46.7	39.1	32.3	33.9	34.6
Zr	189	193	135	145	231	226
Nb	20.3	20.1	21.0	19.6	13.9	13.7
Ba	863	860	1025	867	379	391
Pb	24	26	71	77	19	19
Th	27	28	25	24	18	18
U	bd	6	5	4	bd	3
Sc	23	22	20	16	12	10
V	132	137	149	136	89	95
Cr	122	120	135	120	69	69
Co	21	19	19	17	7	11
Ni	35	32	39	41	28	28
Cu	24	23	12	13	14	14
Zn	153	151	108	107	63	65
Ga	30	29	35	32	17	16
Mo	bd	bd	bd	bd	bd	bd
As	bd	bd	bd	bd	15	16
S	bd	bd	56	bd	bd	bd

na, not analysed; bd, below detection

* sample (ultrasonic) washed in 1M HCl (followed by a thorough wash with MQ H_2O) to assess the degree of internal weathering

C2.1 Garnet and plagioclase feldspar analyses, samples I05/8i and I05/14i (Haimanta Group pelites) (Fig. 3.5)

	Weight % oxide									Cations per formula unit							% End-members	
Garnet	SiO_2	TiO_2	Al_2O_3	FeO	MnO	MgO	CaO	Y_2O_3	Total	Si	Al	Fe^{3+}	Fe^{2+}	Mn	Mg	Ca	Fe/(Fe+Mg)	Spess.	Gross.
8i																			
core	37.13	0.01	21.10	32.14	4.40	2.77	2.57	0.40	100.53	2.99	2.00	0.03	2.13	0.30	0.33	0.22	0.87	10.03	7.32
inner rim	37.74	0.00	21.65	34.17	1.71	3.46	2.67	0.00	101.40	2.98	2.02	0.02	2.23	0.11	0.41	0.23	0.85	3.83	7.49
inner rim	37.88	0.00	21.55	34.31	2.15	3.55	2.28	0.03	101.75	2.99	2.00	0.03	2.23	0.14	0.42	0.19	0.84	4.81	6.34
14i																			
core	37.52	0.04	21.31	32.51	5.11	3.82	1.02	0.06	101.37	2.97	1.99	0.06	2.10	0.34	0.45	0.09	0.82	11.52	2.82
rim	38.16	0.03	21.63	33.80	2.20	4.82	1.19	0.03	101.84	2.99	1.99	0.03	2.18	0.15	0.56	0.10	0.80	4.87	3.27
rim	38.18	0.01	21.52	33.83	2.14	4.83	1.16	0.05	101.73	2.99	1.99	0.03	2.19	0.14	0.56	0.10	0.79	4.74	3.21
Plagioclase	SiO_2		Al_2O_3	FeO	Na_2O	K_2O	CaO		Total	Si	Al			K	Na	Ca	% Anorthite		
8i - profile 1 (parallel)																			
inner core	62.13		23.04	0.09	8.51	0.06	4.47		98.31	2.79	1.22			0.00	0.74	0.22	22.43		
outer core	62.35		23.59	0.08	8.44	0.07	4.92		99.44	2.77	1.24			0.00	0.73	0.23	24.25		
outer core	60.17		22.84	0.04	8.07	0.05	4.55		95.72	2.77	1.24			0.00	0.72	0.22	23.69		
inner rim	64.62		22.49	0.12	9.40	0.08	3.25		99.95	2.84	1.17			0.00	0.80	0.15	15.97		
rim	64.47		22.63	0.06	9.29	0.12	3.29		99.86	2.84	1.18			0.01	0.79	0.16	16.24		
rim	63.89		22.63	0.20	9.15	0.08	3.62		99.56	2.83	1.18			0.00	0.79	0.17	17.87		
8i - profile 1 (parallel)																			
inner core	62.41		23.84	0.03	8.47	0.05	4.98		99.78	2.77	1.24			0.00	0.73	0.24	24.46		
outer core	62.76		23.58	0.02	8.63	0.09	4.61		99.69	2.78	1.23			0.01	0.74	0.22	22.64		
outer core	62.42		23.47	0.06	8.62	0.07	4.78		99.42	2.78	1.23			0.00	0.74	0.23	23.38		
inner rim	64.41		22.39	0.03	9.42	0.08	3.25		99.58	2.85	1.17			0.00	0.81	0.15	15.96		
inner rim	64.42		22.32	0.03	9.38	0.07	3.28		99.51	2.85	1.16			0.00	0.80	0.16	16.14		
rim	63.57		23.08	0.07	9.09	0.07	4.01		99.89	2.81	1.20			0.00	0.78	0.19	19.52		
rim	63.77		22.56	0.08	9.24	0.07	3.56		99.29	2.83	1.18			0.00	0.79	0.17	17.49		
8i - profile 1 (perp.)																			
core	61.93		22.58	0.03	8.51	0.08	4.30		97.43	2.80	1.20			0.00	0.75	0.21	21.70		
inner rim	64.60		22.27	0.05	9.29	0.08	3.42		99.71	2.85	1.16			0.00	0.79	0.16	16.83		
rim	64.23		22.38	0.02	9.24	0.10	3.34		99.30	2.84	1.17			0.01	0.79	0.16	16.53		
rim	64.45		22.77	0.09	9.35	0.07	3.74		100.46	2.83	1.18			0.00	0.80	0.18	18.01		
14i																			
core	65.23		21.84	0.06	9.68	0.06	2.86		99.73	2.87	1.13			0.00	0.83	0.13	13.97		
core	65.19		21.94	0.05	9.73	0.07	2.83		99.80	2.87	1.14			0.00	0.83	0.13	13.78		
rim	64.57		22.54	0.09	9.35	0.07	3.39		100.01	2.84	1.17			0.00	0.80	0.16	16.63		
rim	64.61		22.38	0.10	9.43	0.08	3.38		99.98	2.84	1.16			0.00	0.81	0.16	16.46		

C2.2 Garnet analyses from Sutlej Valley samples selected for Sm–Nd TIMS and LA–ICPMS analysis (Chapter 4, Fig 4.7)

Sample	Distance	Weight % oxide									% End-members			
Group (Unit)	(μm)	SiO_2	TiO_2	Al_2O_3	FeO	MnO	MgO	CaO	Y_2O_3	Total	Alm.	Spess.	Pyrope	Gross.
I05/14i	0	37.99	0.00	21.09	35.27	1.74	4.56	0.93	0.05	101.62	75.63	3.87	17.87	2.48
Haimanta	102	37.58	0.04	20.98	33.75	2.42	4.58	0.98	0.02	100.34	73.60	5.44	18.16	2.66
Group	203	37.81	0.04	21.29	33.93	3.26	4.40	0.95	0.05	101.73	72.68	7.29	17.34	2.54
(TSS)	305	37.91	0.03	21.11	33.82	3.97	4.03	0.96	0.08	101.91	72.58	8.87	15.85	2.56
	407	37.73	0.05	20.99	33.54	4.41	3.88	0.97	0.05	101.61	72.04	9.89	15.31	2.60
	508	37.75	0.04	21.23	33.36	4.76	3.81	1.00	0.03	101.97	71.48	10.66	15.02	2.67
	610	37.50	0.04	21.03	33.09	5.08	3.67	1.02	0.07	101.50	71.06	11.45	14.58	2.72
	711	37.76	0.05	21.10	32.80	5.16	3.60	1.04	0.10	101.60	71.32	11.55	14.18	2.81
	813	37.66	0.06	21.18	32.84	5.34	3.59	1.02	0.06	101.74	70.93	12.01	14.18	2.73
	915	37.58	0.04	21.19	32.78	5.49	3.58	1.08	0.09	101.82	70.36	12.37	14.19	2.88
	1016	37.56	0.01	21.14	32.58	5.52	3.50	1.12	0.06	101.50	70.45	12.45	13.90	3.02
	1118	37.70	0.02	21.19	32.82	5.56	3.56	1.04	0.06	101.95	70.46	12.49	14.08	2.79
	1220	37.46	0.03	21.13	32.78	5.49	3.58	1.01	0.14	101.62	70.46	12.41	14.23	2.71
	1321	37.60	0.04	21.12	32.87	5.28	3.53	1.01	0.08	101.53	71.27	11.88	13.97	2.73
	1423	37.59	0.06	21.03	33.12	5.08	3.71	1.02	0.04	101.64	70.99	11.44	14.69	2.71
	1525	37.69	0.04	21.24	33.33	4.88	3.85	0.93	0.10	102.06	71.17	10.97	15.23	2.46
	1626	37.73	0.01	21.17	33.43	4.54	3.90	0.89	0.03	101.72	71.87	10.19	15.42	2.37
	1728	37.92	0.04	21.21	33.34	4.27	3.78	1.02	0.06	101.64	72.74	9.54	14.85	2.76
	1829	37.70	0.05	21.25	33.59	3.84	4.14	1.05	0.01	101.64	72.02	8.62	16.36	2.81
	1931	37.87	0.05	21.19	33.89	3.33	4.32	0.93	0.05	101.63	72.96	7.43	16.97	2.50
	2033	37.80	0.03	21.27	34.15	2.87	4.58	0.95	0.04	101.69	72.83	6.43	18.04	2.52
	2134	38.10	0.02	21.31	34.53	2.22	4.76	0.99	0.05	101.97	73.66	4.93	18.62	2.63
	2236	37.94	0.06	21.18	35.01	1.77	4.47	1.04	0.02	101.49	75.59	3.95	17.53	2.79
I05/32ii	0	38.40	0.00	21.52	31.76	1.31	4.47	4.69	0.00	102.14	66.69	2.88	17.34	12.30
Karcham	101	38.45	0.00	21.65	30.81	1.06	4.81	5.34	0.01	102.13	64.13	2.34	18.64	13.91
schists	201	36.92	0.03	21.15	30.91	1.10	4.82	5.15	0.01	100.08	63.10	2.52	19.44	13.23
(GHS)	302	38.43	0.00	21.41	30.82	1.21	4.22	5.89	0.05	102.02	64.55	2.66	16.37	15.41
	503	38.35	0.13	21.32	30.72	1.47	3.66	6.33	0.00	101.98	64.93	3.23	14.20	16.69
	604	38.42	0.02	21.38	30.51	1.69	3.51	6.75	0.00	102.27	63.87	3.71	13.61	17.64
	704	38.14	0.03	21.33	30.29	2.07	3.17	7.08	0.00	102.11	63.16	4.59	12.37	18.45
	805	38.06	0.04	21.24	29.75	2.56	2.61	7.42	0.00	101.68	63.20	5.69	10.22	19.68
	905	38.16	0.06	21.14	29.69	3.06	2.34	7.68	0.01	102.15	62.55	6.79	9.12	20.20
	1006	38.09	0.15	21.23	29.58	3.46	2.09	7.63	0.00	102.23	62.77	7.68	8.14	20.20
	1107	37.91	0.05	21.23	29.32	3.88	1.92	7.62	0.03	101.96	62.26	8.66	7.56	20.20
	1207	37.86	0.05	21.12	29.24	4.08	1.86	7.51	0.00	101.72	62.31	9.12	7.32	19.97
	1308	37.96	0.03	21.13	29.14	4.39	1.84	7.43	0.02	101.94	62.01	9.78	7.24	19.73
	1509	37.93	0.04	21.02	28.89	4.67	1.87	7.25	0.00	101.67	61.76	10.43	7.34	19.33
	1610	37.91	0.04	21.05	28.88	4.89	1.79	7.25	0.05	101.87	61.55	10.92	7.05	19.28
	1710	37.92	0.05	21.08	28.60	5.14	1.74	7.19	0.03	101.75	61.42	11.46	6.82	19.25
	1811	37.89	0.04	21.07	28.47	5.16	1.80	7.30	0.05	101.78	60.77	11.53	7.08	19.44
	1912	37.99	0.03	21.07	28.46	5.22	1.78	7.39	0.13	102.06	60.57	11.63	6.96	19.63
	2012	37.99	0.03	21.01	28.33	5.10	1.78	7.38	0.05	101.66	60.88	11.37	6.96	19.76
	2213	37.92	0.03	22.28	27.96	4.84	1.92	7.43	0.01	102.37	60.68	10.80	7.53	20.14
	2314	37.82	0.04	21.10	28.21	4.79	1.91	7.73	0.05	101.66	59.85	10.73	7.53	20.51
	2415	37.82	0.03	20.97	28.70	4.70	2.02	7.36	0.03	101.62	60.70	10.52	7.96	19.43
	2515	37.89	0.08	21.02	28.91	4.30	2.20	7.10	0.10	101.59	61.74	9.59	8.64	18.91
	2616	37.83	0.00	20.96	29.57	4.01	2.31	6.84	0.04	101.56	62.57	8.97	9.10	18.05
	2716	37.97	0.01	21.10	29.97	3.74	2.41	6.63	0.02	101.85	63.48	8.35	9.46	17.52
	2817	38.32	0.04	21.24	29.88	3.57	2.49	6.53	0.04	102.11	64.19	7.89	9.68	17.47
	3219	37.94	0.02	21.18	30.36	3.29	2.58	6.61	0.02	102.00	63.84	7.35	10.15	17.36
	3320	38.03	0.04	21.15	30.11	3.16	2.55	6.81	0.03	101.88	63.81	7.03	9.99	18.00
	3421	37.94	0.03	21.17	30.34	3.05	2.54	6.86	0.01	101.92	63.87	6.80	9.97	18.02
	3622	38.16	0.04	21.09	30.23	2.70	2.60	7.11	0.03	101.96	63.92	5.99	10.13	18.76
	3722	38.23	0.03	21.11	30.36	2.44	2.52	7.32	0.00	102.01	64.27	5.40	9.84	19.30
	3924	38.08	0.07	21.28	31.04	1.86	2.55	7.01	0.00	101.89	66.21	4.12	9.96	18.64
	4024	38.14	0.02	21.23	31.21	1.71	2.61	7.00	0.00	101.93	66.34	3.80	10.19	18.54
	4125	38.22	0.01	21.26	31.13	1.63	2.73	6.83	0.02	101.82	66.61	3.60	10.64	18.21
	4225	37.56	0.03	21.17	30.63	1.56	2.80	6.87	0.04	100.65	65.81	3.50	11.09	18.40
	4326	38.12	0.01	21.44	30.58	1.60	3.17	7.09	0.00	102.00	64.16	3.54	12.39	18.57
	4427	38.50	0.02	21.35	30.74	1.37	3.66	6.19	0.02	101.83	65.61	3.01	14.15	16.48
	4527	38.45	0.00	21.73	30.99	1.15	4.18	5.52	0.08	102.11	65.86	2.54	16.22	14.64
	4628	38.58	0.02	21.44	31.19	1.02	4.69	4.99	0.03	101.95	65.80	2.24	18.10	13.14
	4770	38.12	0.02	21.23	30.21	2.77	2.56	6.87	0.02	101.57	64.52	6.15	10.02	18.30

Continued...

Continued...

Sample	Distance	Weight % oxide									% End-members			
Group (Unit)	(μm)	SiO_2	TiO_2	Al_2O_3	FeO	MnO	MgO	CaO	Y_2O_3	Total	Alm.	Spess.	Pyrope	Gross.
57ii	0	37.93	0.00	21.24	34.67	2.98	2.99	1.92	0.20	101.92	76.18	6.65	11.75	5.40
Jutogh	98	37.90	0.00	21.32	35.13	3.03	3.18	1.51	0.24	102.30	76.46	6.77	12.49	4.21
Group	197	37.86	0.00	21.01	34.76	3.09	3.13	1.55	0.23	101.64	76.37	6.91	12.32	4.37
(LHS)	394	37.81	0.01	21.03	34.51	3.37	3.10	1.73	0.28	101.85	75.33	7.55	12.22	4.83
	590	37.80	0.03	21.06	34.47	3.77	2.95	1.61	0.25	101.93	75.39	8.45	11.61	4.50
	689	37.90	0.01	20.97	34.54	3.86	3.00	1.60	0.27	102.15	75.08	8.62	11.78	4.45
	886	37.85	0.02	20.89	34.26	4.14	2.92	1.51	0.22	101.80	74.98	9.26	11.50	4.21
	1083	37.78	0.02	21.05	34.08	4.07	2.93	1.51	0.22	101.66	75.04	9.12	11.54	4.27
	1673	37.79	0.06	20.70	34.18	3.84	2.84	1.51	0.30	101.22	75.95	8.60	11.18	4.30
	1771	37.71	0.01	21.08	34.25	3.78	2.99	1.53	0.32	101.66	75.35	8.49	11.82	4.29
	1870	37.70	0.02	21.04	34.24	3.68	2.92	1.60	0.30	101.49	75.66	8.26	11.55	4.51
	2067	37.52	0.01	21.13	34.38	3.45	3.13	1.73	0.31	101.66	74.86	7.78	12.43	4.80
	2165	37.97	0.00	21.05	34.57	3.28	3.15	1.68	0.28	101.98	75.59	7.32	12.37	4.69
	2263	38.30	0.00	21.12	34.74	3.17	3.17	1.64	0.22	102.36	76.08	7.01	12.33	4.60
	2362	37.81	0.02	21.08	35.13	3.11	3.11	1.53	0.22	102.01	76.45	6.96	12.27	4.24
	2460	37.89	0.01	21.21	34.80	3.18	2.79	1.87	0.09	101.84	76.61	7.11	10.99	5.28
66i a	0	37.63	0.06	21.10	33.72	1.55	1.96	5.11	0.13	101.26	74.22	3.49	7.77	14.39
Jutogh	100	37.69	0.04	21.06	32.80	1.87	2.12	5.88	0.04	101.49	70.73	4.20	8.37	16.21
Group	199	38.84	0.00	20.55	32.67	1.77	1.99	4.75	0.06	100.63	75.42	3.85	7.64	14.25
(LHS)	299	37.77	0.04	21.21	31.23	1.95	1.90	7.45	0.05	101.60	67.03	4.38	7.47	20.48
	1395	37.63	0.13	21.06	30.01	3.87	1.79	7.01	0.03	101.52	64.34	8.68	7.09	19.25
	1495	37.64	0.14	21.05	30.37	3.68	1.81	6.88	0.01	101.58	65.06	8.26	7.16	18.89
	1595	37.76	0.12	21.00	29.62	3.67	1.72	7.52	0.04	101.45	63.73	8.20	6.78	20.75
	1694	37.65	0.12	21.01	30.25	3.76	1.69	6.95	0.00	101.43	65.15	8.43	6.69	19.18
	1794	37.58	0.19	20.96	30.73	3.78	1.72	6.48	0.00	101.44	66.30	8.49	6.81	17.89
	1894	37.54	0.23	20.90	30.10	3.78	1.68	6.94	0.00	101.16	65.16	8.49	6.65	19.24
	1994	37.68	0.17	21.08	30.14	3.63	1.67	7.10	0.01	101.48	65.17	8.13	6.60	19.66
	2093	37.59	0.20	21.09	30.47	3.61	1.61	7.18	0.06	101.82	65.15	8.10	6.37	19.67
	2193	37.41	0.21	21.11	30.89	3.53	1.55	6.89	0.02	101.61	66.23	7.95	6.16	18.93
	2293	37.70	0.16	20.91	30.03	3.52	1.53	7.77	0.02	101.64	64.07	7.88	6.04	21.25
	2592	37.89	0.24	20.98	28.91	3.55	1.56	8.42	0.02	101.56	62.29	7.89	6.13	23.26
	2791	37.64	0.25	20.93	30.68	3.66	1.77	6.13	0.00	101.06	67.47	8.20	6.96	17.27
	2990	37.58	0.16	21.08	30.31	3.59	1.80	6.55	0.00	101.06	66.22	8.05	7.11	18.33
	3090	37.69	0.18	20.94	30.14	3.92	1.72	6.88	0.04	101.51	64.95	8.79	6.79	18.98
	3289	37.47	0.10	21.18	29.88	3.95	1.79	6.95	0.00	101.33	64.14	8.90	7.12	19.15
	3389	37.69	0.10	20.97	30.33	3.80	1.74	6.81	0.01	101.44	65.33	8.51	6.85	18.78
	3588	37.79	0.10	21.07	31.25	2.50	1.95	6.88	0.00	101.54	67.24	5.58	7.69	18.97
	3688	37.73	0.08	21.32	31.06	2.21	1.91	7.00	0.04	101.35	67.66	4.95	7.54	19.53
	4087	37.63	0.00	21.14	33.92	1.71	2.06	4.57	0.12	101.14	74.98	3.85	8.16	12.93
66i b	0	37.74	0.02	21.26	33.39	1.62	2.22	5.37	0.10	101.72	72.39	3.64	8.74	14.88
	98	37.74	0.03	21.21	33.26	2.13	2.11	5.32	0.06	101.85	71.80	4.78	8.33	14.68
	294	37.72	0.09	21.04	30.66	3.44	1.88	6.49	0.00	101.32	66.48	7.70	7.41	18.04
	490	38.93	0.08	20.96	29.97	3.70	1.67	6.67	0.02	101.99	67.23	8.04	6.40	19.22
	588	37.64	0.15	21.16	30.18	3.81	1.65	7.02	0.00	101.60	65.00	8.54	6.53	19.39
	785	37.46	0.13	20.97	30.60	4.11	1.60	6.60	0.02	101.48	65.54	9.27	6.35	18.13
	981	37.45	0.17	20.96	30.30	3.91	1.54	7.05	0.05	101.44	64.97	8.81	6.11	19.38
	1079	37.66	0.22	21.00	30.95	3.62	1.64	6.65	0.03	101.77	66.61	8.10	6.45	18.33
	1177	37.82	0.20	21.02	30.32	3.75	1.63	6.81	0.00	101.54	66.02	8.36	6.40	19.00
	1275	37.79	0.32	20.93	30.31	3.66	1.62	7.15	0.00	101.78	65.34	8.16	6.34	19.75
	1373	37.64	0.26	20.99	30.08	3.56	1.69	7.40	0.00	101.62	64.42	7.96	6.66	20.32
	1471	37.49	0.17	21.01	31.13	3.63	1.94	6.01	0.00	101.36	67.03	8.18	7.67	16.57
	1569	37.68	0.20	21.09	29.94	3.63	1.69	7.27	0.02	101.52	64.62	8.12	6.68	20.10
	1667	37.69	0.19	21.01	29.97	3.69	1.77	7.10	0.00	101.41	64.67	8.25	6.97	19.64
	1765	37.73	0.15	21.05	29.83	3.58	1.73	7.58	0.00	101.63	63.71	8.01	6.83	20.75
	2157	37.65	0.04	21.37	33.42	1.70	2.09	5.49	0.11	101.87	72.30	3.83	8.26	15.20
	2256	37.74	0.05	21.09	32.94	1.94	2.02	5.82	0.07	101.67	71.18	4.34	7.96	16.09
	2354	37.67	0.06	21.03	33.00	1.63	2.05	5.50	0.21	101.14	72.62	3.66	8.09	15.50

Continued...

Continued...

Sample	Distance	Weight % oxide									% End-members			
Group (Unit)	(μm)	SiO_2	TiO_2	Al_2O_3	FeO	MnO	MgO	CaO	Y_2O_3	Total	Alm.	Spess.	Pyrope	Gross.
78ii	0	37.27	0.02	20.95	38.18	1.35	2.89	0.78	0.04	101.47	83.17	3.06	11.53	2.16
Jutogh	101	37.24	0.00	21.11	37.80	0.86	3.39	0.91	0.00	101.31	81.84	1.96	13.58	2.50
Group'	203	37.34	0.02	21.05	37.72	0.59	3.45	1.01	0.00	101.18	82.02	1.34	13.76	2.78
(LHS?)	304	37.38	0.02	21.24	37.79	0.68	3.25	1.08	0.02	101.46	82.43	1.54	12.95	2.99
	405	37.34	0.03	21.13	37.91	0.87	3.20	1.17	0.02	101.66	81.92	1.97	12.75	3.22
	506	37.44	0.00	21.09	37.72	1.28	3.05	1.07	0.00	101.64	81.90	2.90	12.15	2.95
	608	37.29	0.00	21.10	37.72	1.62	2.69	1.04	0.04	101.49	82.60	3.67	10.74	2.90
	709	37.11	0.00	21.01	36.75	2.12	2.96	1.06	0.08	101.09	80.21	4.84	11.90	2.94
	810	37.23	0.00	21.08	36.36	2.51	2.82	1.07	0.06	101.13	79.90	5.72	11.31	2.99
	1013	37.33	0.00	21.11	35.80	3.24	2.74	1.32	0.06	101.61	77.89	7.35	10.96	3.67
	1215	37.28	0.02	20.99	35.44	3.86	2.66	1.21	0.04	101.50	77.13	8.76	10.63	3.36
	1316	37.44	0.03	21.02	35.41	3.89	2.61	1.20	0.05	101.65	77.38	8.80	10.39	3.34
	1519	37.18	0.02	20.97	34.45	4.66	2.82	1.20	0.05	101.35	74.66	10.61	11.28	3.32
	1722	37.54	0.00	21.03	34.08	5.34	2.67	1.22	0.01	101.90	73.85	12.06	10.60	3.38
	1823	37.22	0.03	21.09	33.84	5.76	2.56	1.22	0.14	101.85	73.15	13.11	10.23	3.37
	1924	37.33	0.00	20.85	33.45	5.91	2.50	1.20	0.15	101.39	73.16	13.41	9.99	3.36
	2025	37.23	0.01	21.04	33.47	6.08	2.50	1.06	0.21	101.61	73.11	13.84	9.99	2.97
	2127	37.20	0.01	21.03	33.41	6.11	2.48	1.09	0.15	101.47	73.00	13.92	9.94	3.04
	2228	37.06	0.03	21.08	33.29	6.23	2.41	1.10	0.19	101.40	72.88	14.24	9.70	3.08
	2228	37.23	0.00	20.87	33.30	6.21	2.45	1.12	0.20	101.39	72.85	14.13	9.81	3.13
	2328	37.01	0.00	20.88	33.47	6.21	2.40	1.01	0.20	101.18	73.20	14.21	9.67	2.81
	2429	36.98	0.02	21.05	33.29	6.28	2.49	1.09	0.16	101.35	72.44	14.38	10.03	3.02
	2529	37.11	0.02	20.93	33.44	6.44	2.31	1.06	0.05	101.35	72.97	14.70	9.28	2.94
	2932	37.39	0.02	20.98	33.34	6.27	2.47	1.27	0.05	101.79	72.31	14.20	9.86	3.52
	3133	37.27	0.03	20.98	33.25	6.06	2.40	1.16	0.09	101.24	73.33	13.76	9.57	3.27
	3233	37.04	0.05	20.88	33.27	6.13	2.42	1.31	0.17	101.28	72.48	14.00	9.74	3.64
	3334	37.42	0.02	21.10	33.59	6.00	2.55	1.18	0.05	101.92	72.87	13.58	10.17	3.28
	3434	37.40	0.03	21.02	33.97	5.65	2.48	1.25	0.05	101.85	73.74	12.80	9.88	3.47
	3535	37.35	0.00	20.93	34.12	5.37	2.55	1.21	0.00	101.53	74.16	12.19	10.19	3.35
	3635	37.36	0.07	21.09	34.35	4.87	2.43	1.25	0.14	101.56	75.71	11.04	9.68	3.51
	3736	37.13	0.01	21.14	35.09	4.45	2.54	1.31	0.08	101.75	75.87	10.14	10.20	3.61
	3836	37.33	0.03	21.17	35.49	3.84	2.54	1.34	0.02	101.75	77.32	8.71	10.12	3.72
	4138	37.43	0.00	21.13	36.61	2.37	2.95	1.15	0.04	101.67	79.61	5.37	11.73	3.18
	4238	37.17	0.00	21.16	36.77	2.08	3.11	1.16	0.10	101.54	79.46	4.74	12.46	3.18
	4439	37.49	0.00	21.15	37.18	1.48	3.37	0.99	0.04	101.70	80.41	3.35	13.40	2.74
	4540	37.58	0.02	21.13	37.39	1.14	3.47	1.05	0.02	101.80	80.69	2.56	13.76	2.88
	4641	37.50	0.02	21.17	37.54	0.99	3.36	1.03	0.00	101.61	81.48	2.24	13.35	2.83
	4741	37.16	0.02	21.42	38.18	1.17	3.12	0.90	0.00	101.97	82.21	2.66	12.53	2.46
	4842	37.30	0.04	21.18	38.24	1.43	2.91	0.77	0.00	101.86	82.93	3.24	11.64	2.11

Almandine (Alm.), Spessartine (Spess.), Grossular (Gross.)

C2.3 Major mineral analyses from the Chekha Group and GHS, Bhutan, used for *P–T* analysis (Chapter 6)

Phase	Analysis	SiO_2	TiO_2	Al_2O_3	FeO	MnO	MgO	CaO	Na_2O	K_2O	ZnO	Total
B06/62 - Chekha Fm												
garnet	core	37.51	0.07	20.98	32.71	4.80	1.84	2.78	0.00	0.00		100.77
garnet	inner rim	37.55	0.05	20.98	36.50	0.40	2.73	2.64	0.00	0.00		100.88
staurolite	average	27.65	0.59	53.61	13.35	0.05	1.43	0.00	0.03	0.00	1.01	97.72
biotite	average of 9	35.78	1.74	19.36	19.38	0.02	9.19	0.05	0.21	8.72		
muscovite	average of 9	46.20	0.50	35.57	1.32	0.00	0.60	0.01	1.27	8.98		94.51
plagioclase	average of 10	62.76	0.00	23.63	0.05	0.00	0.00	4.70	8.91	0.07		100.19
B06/67 - GHS												
garnet	core	37.03	0.01	20.83	33.31	4.66	3.08	1.65	0.00	0.00		100.70
garnet	rim	37.31	0.00	20.88	35.80	2.39	2.55	1.88	0.00	0.00		100.97
biotite	average of 9	36.46	1.74	19.97	18.85	0.04	9.46	0.04	0.24	8.00		94.99
muscovite	average of 12	46.87	0.80	35.49	1.04	0.00	0.67	0.01	1.09	9.00		95.00
plagioclase	average of 11	62.93	0.00	23.18	0.03	0.01	0.01	4.34	8.95	0.09		99.56

C3. ID–TIMS (Triton, Open University) Nd standard (La Jolla, 150ng) data

date	06/07/06	06/07/06	06/07/06	06/07/06	06/07/06	10/07/06	10/07/06	12/07/06	05/08/06	27/10/06	29/10/06	08/11/06	08/11/06	08/11/06			
magazine #	79	79	79	79	79	80	80	80	84	102	102	103	103	103	average	2 s.d.	ppm
$^{140}Ce/^{144}Nd$	0.000003	0.000001	0.000005	0.000010	0.000025	0.000121	0.000008	0.000022	0.000038	0.000025	0.000096	0.000027	0.000077	0.000033			
1se	0.000000	0.000000	0.000000	0.000000	0.000001	0.000002	0.000000	0.000001	0.000001	0.000001	0.000003	0.000001	0.000002	0.000001			
2se	0.000001	0.000001	0.000001	0.000001	0.000001	0.000005	0.000001	0.000001	0.000003	0.000002	0.000005	0.000001	0.000004	0.000002			
$^{142}Nd/^{144}Nd$	1.141845	1.141824	1.141842	1.141827	1.141831	1.141854	1.141830	1.141842	1.141856	1.141844	1.141850	1.141858	1.141856	1.141848			
1se	0.000006	0.000006	0.000003	0.000003	0.000003	0.000003	0.000003	0.000003	0.000003	0.000004	0.000003	0.000004	0.000003	0.000003			
2se	0.000011	0.000011	0.000007	0.000006	0.000006	0.000006	0.000007	0.000006	0.000007	0.000007	0.000007	0.000009	0.000007	0.000006			
$^{143}Nd/^{144}Nd$	0.511851	0.511847	0.511849	0.511848	0.511849	0.511851	0.511846	0.511848	0.511851	0.511849	0.511847	0.511848	0.511849	0.511850			
1se	0.000002	0.000002	0.000001	0.000001	0.000001	0.000001	0.000001	0.000001	0.000001	0.000001	0.000001	0.000002	0.000001	0.000001			
2se	0.000004	0.000004	0.000003	0.000002	0.000002	0.000002	0.000002	0.000002	0.000003	0.000003	0.000002	0.000003	0.000003	0.000002			
$^{145}Nd/^{144}Nd$	0.348402	0.348403	0.348404	0.348403	0.348407	0.348405	0.348406	0.348404	0.348404	0.348403	0.348403	0.348402	0.348401	0.348404	0.348404	0.000003	8.633033
1se	0.000001	0.000001	0.000001	0.000001	0.000001	0.000001	0.000001	0.000001	0.000001	0.000001	0.000001	0.000001	0.000001	0.000001			
2se	0.000002	0.000002	0.000002	0.000001	0.000002	0.000001	0.000001	0.000001	0.000002	0.000083	0.000066	0.000049	0.000086	0.000156			
$^{146}Nd/^{144}Nd$	0.723525	0.723128	0.722165	0.722315	0.720965	0.721982	0.722472	0.722123	0.722912	0.721268	0.720849	0.723499	0.722836	0.723420			
1se	0.000007	0.000040	0.000018	0.000050	0.000016	0.000020	0.000037	0.000033	0.000058	0.000042	0.000033	0.000025	0.000043	0.000078			
2se	0.000013	0.000081	0.000037	0.000100	0.000033	0.000039	0.000075	0.000067	0.000116	0.000083	0.000066	0.000049	0.000086	0.000156			
$^{147}Sm/^{144}Nd$	0.000006	0.000004	0.000002	0.000003	0.000004	0.000003	0.000004	0.000002	0.000002	0.000000	0.000001	0.000001	0.000001	0.000002			
1se	0.000000	0.000000	0.000000	0.000000	0.000000	0.000000	0.000000	0.000000	0.000000	0.000000	0.000000	0.000000	0.000000	0.000000			
2se	0.000001	0.000001	0.000000	0.000000	0.000000	0.000000	0.000000	0.000000	0.000000	0.000000	0.000000	0.000000	0.000000	0.000000			
$^{148}Nd/^{144}Nd$	0.241581	0.241586	0.241584	0.241584	0.241587	0.241584	0.241587	0.241583	0.241581	0.241581	0.241579	0.241584	0.241583	0.241583	0.241583	0.000004	18.111854
1se	0.000002	0.000002	0.000001	0.000001	0.000001	0.000001	0.000001	0.000001	0.000001	0.000001	0.000001	0.000001	0.000001	0.000001			
2se	0.000003	0.000003	0.000002	0.000002	0.000002	0.000001	0.000002	0.000002	0.000002	0.000002	0.000002	0.000002	0.000002	0.000002			
$^{150}Nd/^{144}Nd$	0.236462	0.236459	0.236459	0.236458	0.236460	0.236486	0.236463	0.236487	0.236482	0.236478	0.236477	0.236484	0.236486	0.236481	0.236473	0.000024	100.040936
1se	0.000002	0.000002	0.000001	0.000001	0.000001	0.000001	0.000001	0.000001	0.000001	0.000001	0.000001	0.000001	0.000001	0.000001			
2se	0.000004	0.000004	0.000002	0.000002	0.000002	0.000002	0.000002	0.000002	0.000003	0.000003	0.000002	0.000003	0.000002	0.000002			
$^{142}Nd/^{144}Nd$	1.141844	1.141824	1.141842	1.141826	1.141829	1.141839	1.141830	1.141839	1.141850	1.141841	1.141836	1.141855	1.141844	1.141844	1.141839	0.000018	15.672506
corrected																	
1se	0.000006	0.000005	0.000003	0.000003	0.000003	0.000003	0.000003	0.000003	0.000003	0.000004	0.000003	0.000004	0.000003	0.000003			
2se	0.000011	0.000010	0.000007	0.000006	0.000006	0.000006	0.000007	0.000006	0.000007	0.000007	0.000007	0.000009	0.000006	0.000006			
$^{143}Nd/^{144}Nd$	0.511852	0.511848	0.511850	0.511848	0.511850	0.511852	0.511846	0.511848	0.511851	0.511849	0.511847	0.511848	0.511849	0.511850	0.511849	0.000004	6.854057
corrected																	
1se	0.000002	0.000002	0.000001	0.000001	0.000001	0.000001	0.000001	0.000001	0.000001	0.000001	0.000001	0.000002	0.000001	0.000001			
2se	0.000004	0.000004	0.000003	0.000002	0.000002	0.000002	0.000002	0.000002	0.000003	0.000003	0.000002	0.000003	0.000003	0.000002			

se, standard error

s.d., standard deviation

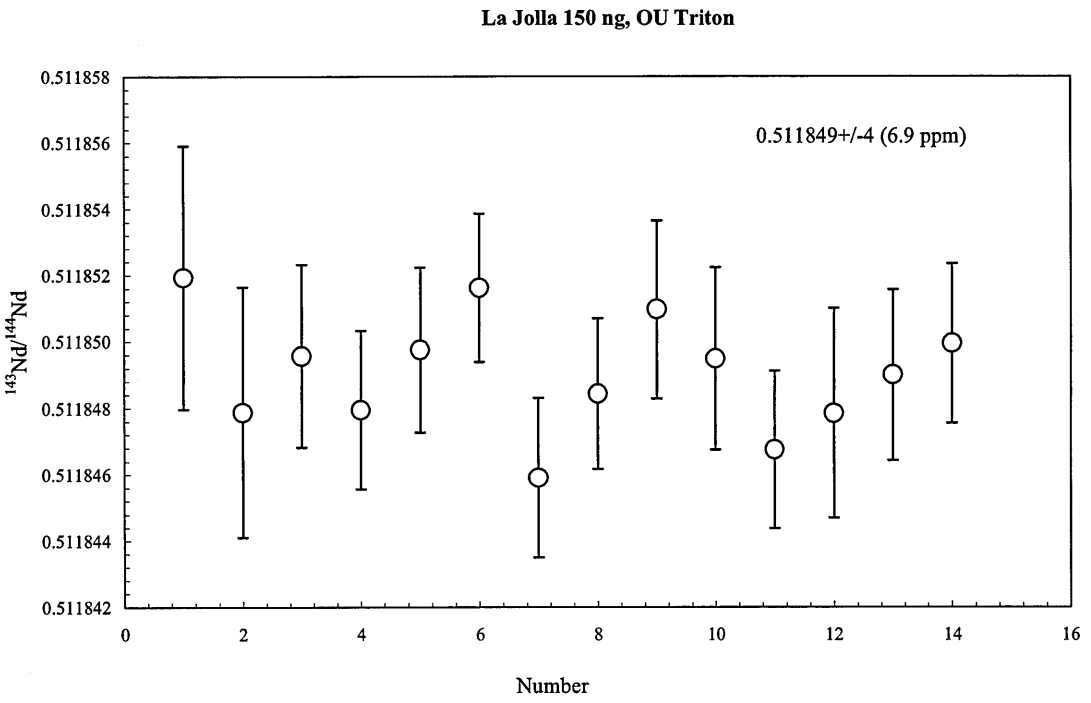
La Jolla 150 ng, OU Triton
0.511849+/-4 (6.9 ppm)
$^{143}Nd/^{144}Nd$
0.511858
0.511856
0.511854
0.511852
0.511850
0.511848
0.511846
0.511844
0.511842
0
2
4
6
8
10
12
14
16
Number

C4 LA–ICPMS trace element data

C4.1.1 Garnet I05/14i (ppm)

	garnet I05/14i						inclusion(s) I05/14i					
	1	2	3	4	5	6	1	2	3	4	5	6
Si*	176458	176458	176458	176458	176458	176458	176458	176458	176458	176458	176458	176458
^{43}Ca	6898	6985	5973	7240	7577	7248	8951	6763	15954	14530	10844	18825
^{44}Ca	6846	6954	5766	7158	7575	7096	8867	6482	15566	14333	10982	18842
Sc	290	255	213	311	312	312	306	223	289	303	335	320
Ti	238	301	1222	312	151	261	238	260	2868	302	211	292
V	74	84	48	88	62	75	72	69	88	81	75	79
Cr	89	121	43	121	60	92	82	89	142	104	81	87
Mn	20501	27061	27479	35093	36982	35287	20163	24226	32818	34290	39298	36968
Fe	247431	236178	202089	237168	233412	229940	240931	204292	242897	232088	244610	242207
Co	13.01	12.69	10.92	12.40	11.80	12.33	12.96	10.78	13.01	12.25	12.35	12.82
Ni	0.24	0.20	0.36	0.38	0.19	0.22	0.17	bd	0.46	0.25	0.29	0.26
Ga	6.13	9.42	7.26	9.33	8.94	9.31	6.15	8.87	8.58	9.32	8.83	8.99
Rb	0.08	0.06	0.05	0.13	0.20	0.13	0.10	0.07	0.12	0.12	0.29	0.13
Sr	0.07	0.03	0.06	0.09	0.16	0.06	1.54	0.21	5.12	4.29	1.65	6.32
Y	416.36	372.81	318.01	574.16	678.18	590.74	461.39	305.89	555.88	586.48	797.99	616.61
Zr	25.83	9.86	72.91	6.51	186.23	4.83	175.48	215.15	30.19	23.06	5.12	108.64
Nb	0.04	0.04	3.11	0.07	0.03	0.03	0.04	0.05	7.46	0.06	0.03	0.05
Ba	0.02	bd	bd	bd	bd	bd	0.03	bd	0.03	bd	bd	bd
La	0.02	bd	0.01	0.00	0.01	bd	0.61	0.08	1.91	1.56	0.51	2.26
Ce	0.05	0.01	0.03	0.00	0.02	0.01	2.07	0.26	7.36	6.00	1.95	8.86
Pr	0.01	0.00	0.00	0.00	0.00	0.00	0.34	0.05	1.26	1.04	0.33	1.46
Nd	0.06	0.11	0.07	0.09	0.06	0.07	1.87	0.36	6.53	5.46	1.84	7.96
Sm	0.50	0.74	0.53	0.77	0.56	0.68	1.35	0.72	3.54	3.31	1.54	4.43
Eu	0.37	0.44	0.32	0.44	0.36	0.43	0.54	0.39	0.98	0.95	0.56	1.17
Gd	6.49	8.92	6.69	9.07	8.60	9.58	7.63	7.16	12.56	13.47	10.51	15.13
Tb	3.56	4.38	3.63	5.31	5.40	5.69	4.00	3.60	5.62	6.00	6.26	6.57
Dy	49.13	53.02	46.23	76.06	87.44	82.13	54.24	41.31	73.81	80.18	101.59	85.27
Ho	15.20	14.15	11.93	23.17	31.38	24.44	16.98	10.96	22.21	24.21	38.23	24.74
Er	59.03	47.93	39.55	89.42	142.40	88.76	65.37	36.08	82.29	91.42	179.44	88.29
Tm	10.93	7.98	6.34	16.73	31.64	15.52	12.08	5.94	14.79	16.74	40.06	15.64
Yb	87.07	56.30	45.33	135.32	297.07	119.62	94.63	43.84	114.26	133.22	390.82	121.28
Lu	13.63	8.10	6.30	20.84	52.69	17.26	15.13	6.14	17.09	20.34	70.28	16.99
Hf	0.56	0.22	2.07	0.14	6.10	0.11	5.55	5.53	0.78	0.76	0.12	3.05
Ta	0.02	0.04	0.30	0.04	0.02	0.03	0.03	0.02	0.89	0.04	0.01	0.04
Pb	0.06	0.00	0.02	0.01	0.02	bd	0.15	0.02	0.18	0.16	0.05	0.26
Th	0.02	0.01	0.18	0.01	0.32	bd	0.10	0.33	0.12	0.17	0.04	0.54
U	0.27	0.15	0.78	0.15	1.80	0.06	1.98	2.15	1.73	1.45	0.40	3.13

bd, below detection

* normalising value

C4.1.2 Garnet I05/32ii (ppm)

	garnet I05/32ii											
	1	2	3	4	5	6	7	8	9	10	11	12
Si	146860	175172	176140	183420	181505	178562	167873	181247	186009	189379	185143	186119
^{43}Ca	38545	50989	56061	55765	52989	53548	52849	52826	56531	53958	52609	52547
^{44}Ca*	37879	50029	54889	53674	51816	52173	52602	51816	54460	53031	51816	52531
Sc	77	183	243	250	308	330	269	306	277	207	315	346
Ti	355	488	501	538	706	736	527	866	509	609	1031	755
V	54	61	78	63	79	75	66	68	77	67	76	69
Cr	76	44	108	80	114	96	82	95	101	70	112	75
Mn	6722	12786	19705	25289	29675	33884	31094	28726	24584	15506	32289	33848
Fe	184448	218640	220075	222753	222914	217542	210326	223907	234213	245036	229977	226587
Co	11.47	11.15	9.95	9.33	9.01	8.03	7.42	8.45	9.55	10.83	8.32	7.07
Ni	bd	bd	bd	0.38	bd	bd	bd	bd	0.58	0.28	0.74	bd
Ga	5.54	7.39	7.43	7.36	7.51	6.51	6.14	7.27	7.44	7.30	7.23	7.24
Rb	bd	0.02	bd	0.02	0.05	0.07	0.21	0.03	0.04	0.04	0.05	0.12
Sr	0.01	0.01	0.15	0.04	0.02	0.11	0.40	0.03	bd	bd	0.04	0.11
Y	102.15	83.22	109.26	137.31	333.28	499.37	352.21	219.93	133.52	100.75	390.31	537.65
Zr	3.19	3.85	3.72	218.02	3.86	3.23	279.89	3.99	3.41	3.96	3.91	2.66
Nb	2.77	1.43	0.57	0.54	0.57	0.31	0.41	0.56	0.46	0.71	0.40	0.41
Ba	bd	bd	bd	bd	bd	bd	bd	bd	bd	bd	bd	bd
La	0.01	0.00	1.65	0.01	0.03	0.01	0.17	0.02	0.03	bd	0.01	0.01
Ce	0.02	0.02	4.14	0.11	0.09	0.02	0.34	0.07	0.13	0.04	0.05	0.04
Pr	0.01	0.01	0.52	0.02	bd	0.01	0.05	0.02	0.02	0.01	0.01	0.01
Nd	0.21	0.21	1.93	0.21	0.12	0.16	0.38	0.33	0.24	0.22	0.09	0.19
Sm	0.90	0.79	0.98	0.60	0.43	0.41	0.34	0.21	0.43	0.85	0.19	0.33
Eu	0.26	0.29	0.37	0.29	0.19	0.17	0.19	0.18	0.23	0.27	0.20	0.17
Gd	3.74	2.99	2.49	2.56	2.81	2.48	1.84	1.97	1.81	2.90	3.10	2.44
Tb	1.38	1.12	1.06	1.08	1.60	1.71	0.85	1.08	0.85	1.06	1.79	1.57
Dy	14.51	10.82	12.57	13.61	25.01	33.00	15.93	17.55	12.50	12.97	31.81	34.10
Ho	3.36	2.52	3.49	3.88	9.74	14.67	10.45	6.47	4.17	3.37	12.17	16.60
Er	9.51	7.33	11.89	14.10	39.83	76.30	101.53	28.38	15.55	9.68	52.31	92.55
Tm	1.19	0.98	1.86	2.27	7.49	18.33	46.74	5.05	2.60	1.45	9.92	23.24
Yb	6.74	4.95	12.46	17.21	61.18	187.08	845.23	42.75	21.15	8.26	92.44	239.10
Lu	0.81	0.77	2.10	2.82	11.47	36.67	257.53	8.09	3.98	1.09	16.84	49.66
Hf	0.07	0.05	0.04	4.55	0.10	0.06	7.61	0.05	0.06	0.06	0.05	0.06
Ta	0.13	0.11	0.11	0.15	0.18	0.13	0.23	0.17	0.17	0.12	0.17	0.19
Pb	0.02	0.02	0.07	bd	0.03	0.02	0.07	bd	0.03	bd	bd	0.05
Th	bd	bd	1.88	0.10	0.04	0.02	0.39	0.05	0.05	0.02	0.03	0.03
U	0.05	0.03	0.63	0.92	0.10	0.11	1.39	0.13	0.10	0.08	0.14	0.15

bd, below detection

* normalising value

Continued...

C4.1.2 Garnet I05/32ii (ppm) *continued*

	inclusion(s) I05/32ii											
	1	2	3	4	5	6	7	8	9	10	11	12
Si	157571	175133	178380	178629	168401	152454	166981	174938	176571	180357	166479	174246
^{43}Ca	39718	51065	55089	56513	54180	52708	52750	52921	55593	53528	53108	54799
^{44}Ca*	37879	50029	54889	53674	51816	52173	52602	51816	54460	53031	51816	52531
Sc	81	192	240	259	313	274	270	314	266	204	305	346
Ti	459	296	546	573	690	388	900	656	498	601	819	583
V	60	56	92	71	69	71	66	69	73	67	69	69
Cr	78	42	122	99	112	93	85	91	101	69	92	76
Mn	6807	12675	21744	25680	29544	29583	31150	29033	24188	15312	31885	34254
Fe	185216	206313	232129	227263	219491	191882	208090	222476	232131	243312	226638	227206
Co	11.07	9.83	9.96	9.40	9.14	7.01	7.55	7.96	8.69	10.41	7.68	7.45
Ni	bd	0.78	bd	bd	0.51	bd	bd	0.29	0.23	0.33	0.28	0.21
Ga	6.03	9.64	9.86	7.69	7.07	6.18	6.09	6.80	6.72	7.05	6.09	6.04
Rb	0.07	0.04	0.03	0.05	0.02	0.09	0.20	0.05	bd	0.02	0.09	0.08
Sr	0.40	20.51	48.78	1.78	2.08	5.01	5.32	0.87	1.21	bd	0.13	0.12
Y	115.70	107.40	243.04	145.31	318.12	422.58	350.37	226.68	129.05	102.68	392.14	525.31
Zr	762.42	5.31	36.30	8.80	3.81	2.25	582.90	3.99	3.32	8.13	3.53	3.29
Nb	3.64	0.42	0.48	0.54	0.40	0.23	0.55	0.50	0.32	0.69	0.47	0.35
Ba	bd	0.08	0.11	bd	0.12	bd	bd	bd	bd	bd	bd	bd
La	2.66	349.62	450.75	18.96	13.36	1.42	40.04	6.97	2.38	0.03	0.25	0.02
Ce	5.54	703.32	906.21	40.50	27.62	4.50	80.98	13.56	4.88	0.05	0.54	0.06
Pr	0.49	77.86	92.61	4.36	2.79	0.72	8.31	1.46	0.61	0.02	0.06	0.02
Nd	2.73	275.44	356.93	15.79	10.45	3.86	29.96	5.55	2.10	0.29	0.29	0.23
Sm	1.48	46.75	67.65	3.77	2.59	1.07	5.23	1.22	0.89	0.55	0.20	0.23
Eu	0.43	7.91	10.89	0.70	0.47	0.28	0.93	0.37	0.29	0.22	0.18	0.19
Gd	5.18	34.85	49.17	5.48	4.10	3.33	4.93	1.84	2.16	2.34	2.42	2.37
Tb	1.61	3.94	7.29	1.22	1.56	1.47	1.10	1.18	1.03	1.08	1.66	1.69
Dy	18.11	21.13	45.21	14.84	26.12	28.89	17.62	20.11	13.33	12.23	27.63	35.53
Ho	4.12	3.62	8.71	4.62	9.08	12.05	10.88	6.78	4.00	3.38	11.26	17.10
Er	10.99	8.07	20.49	15.40	36.73	62.52	106.25	27.45	15.43	10.18	54.82	91.90
Tm	1.64	1.28	2.46	2.38	6.71	14.05	48.05	5.08	2.52	1.42	12.08	23.38
Yb	9.77	7.30	14.09	17.80	56.00	144.05	858.31	42.96	20.28	9.12	117.02	234.08
Lu	1.19	0.97	2.00	3.11	9.97	29.33	253.07	8.13	3.82	1.31	22.08	47.16
Hf	19.83	0.04	0.82	0.19	0.07	bd	18.15	0.03	0.09	0.14	0.07	0.08
Ta	0.21	0.04	0.13	0.18	0.16	0.12	0.23	0.19	0.14	0.10	0.18	0.15
Pb	0.12	2.45	3.94	0.23	0.17	0.20	0.47	0.05	0.18	0.02	0.02	0.03
Th	1.17	169.21	169.57	11.20	7.57	0.16	17.88	3.98	1.89	bd	0.09	0.03
U	1.58	37.23	39.97	1.89	0.88	0.42	3.69	0.61	0.15	0.12	0.08	0.08

bd, below detection

* normalising value

C4.1.3 Garnet I05/57 (ppm)

	garnet I05/57								inclusion(s) I05/57							
	1	2	3	4	5	6	7	8	1	2	3	4	5	6	7	8
Si*	176739	176739	176739	176739	176739	176739	176739	176739	176739	176739	176739	176739	176739	176739	176739	176739
^{43}Ca	9311	10715	9254	11743	10968	9718	10218	9968	7859	10586	12474	12287	9493	8069	10206	10540
^{44}Ca	9397	10730	8930	11680	10879	9990	10291	10085	7856	10355	12893	12209	9000	8225	10342	10560
Sc	18	20	17	30	24	30	20	22	15	19	22	30	24	26	21	22
Ti	24	69	11785	231	166	97	46	35	17	81	9370	214	88	108	45	40
V	7	10	17	21	19	22	9	7	6	10	21	21	16	18	9	7
Cr	49	67	60	72	82	62	70	58	35	61	95	71	67	54	65	63
Mn	18344	20055	17700	23495	28044	26383	20304	18637	15334	18708	24475	24180	26750	22563	20324	19335
Fe	275565	332567	265619	350359	387812	404991	438793	433416	230425	309269	367766	359909	360170	344091	436802	447823
Co	11.21	13.02	10.50	12.61	13.08	13.01	12.76	12.08	9.44	12.65	13.94	12.82	12.50	11.24	12.80	12.42
Ni	bd	0.57	0.70	bd	bd	bd	bd	bd	bd	2.02	0.66	bd	bd	bd	bd	bd
Ga	3.15	3.94	3.23	4.85	4.93	4.43	3.97	3.36	2.72	4.79	4.82	4.67	6.31	3.97	3.77	3.41
Rb	0.40	0.26	0.21	0.12	0.37	0.20	0.30	0.32	0.71	12.95	0.33	0.07	0.27	0.17	2.02	0.32
Sr	0.20	0.15	0.23	bd	0.32	0.19	0.24	0.26	0.17	0.39	0.29	0.05	0.69	0.17	0.26	0.27
Y	1455.87	1912.59	1530.62	870.64	2160.63	1348.43	1681.59	1320.14	1183.41	1806.60	2288.15	989.72	1781.32	1157.09	1661.27	1441.59
Zr	26.74	2.76	1.91	2.88	4.26	25.17	2.72	1.81	13.72	2.67	3.37	2.89	2.86	11.50	2.61	410.11
Nb	0.01	bd	37.48	bd	0.59	0.28	bd	bd	bd	0.01	30.86	0.01	0.09	0.40	bd	0.01
Ba	bd	bd	bd	bd	bd	bd	bd	bd	bd	1.83	bd	bd	bd	bd	bd	bd
La	bd	bd	0.03	0.01	bd	0.01	bd	bd	bd	0.07	bd	bd	146.02	0.03	bd	bd
Ce	bd	bd	0.02	bd	0.03	0.03	bd	0.01	0.01	0.17	0.03	bd	292.28	0.06	bd	0.01
Pr	bd	0.01	bd	bd	bd	0.01	bd	bd	bd	0.02	bd	bd	40.59	0.01	bd	bd
Nd	0.06	0.13	0.07	0.37	0.12	0.16	0.13	bd	bd	0.25	0.20	0.24	119.14	0.11	0.09	bd
Sm	0.69	1.13	1.26	2.95	1.46	1.16	0.83	0.53	0.51	1.22	1.89	2.88	21.97	0.97	0.75	0.63
Eu	0.58	1.02	0.95	2.07	1.30	0.97	0.72	0.48	0.43	1.06	1.56	2.22	4.74	0.81	0.74	0.53
Gd	14.38	20.85	20.99	32.43	24.72	18.49	17.01	12.31	11.31	19.14	31.10	35.38	34.40	15.54	17.27	13.87
Tb	10.08	14.82	13.64	15.93	16.44	11.75	12.02	9.33	8.02	13.78	19.98	17.75	15.28	9.94	12.21	9.97
Dy	170.32	230.94	200.06	146.93	251.42	162.16	199.92	153.43	137.02	217.79	280.79	170.04	195.58	138.88	199.13	165.74
Ho	57.07	71.68	58.03	26.12	78.92	48.72	66.58	56.06	45.75	67.10	83.05	30.11	60.13	42.03	65.13	60.86
Er	220.71	264.97	196.40	54.47	296.18	186.90	240.44	228.17	175.13	245.24	271.38	63.71	236.14	157.45	237.76	247.64
Tm	35.06	43.07	28.82	5.80	48.24	29.76	38.62	38.92	27.95	39.36	40.57	6.74	38.65	25.56	37.23	41.81
Yb	240.97	299.36	176.97	28.53	318.97	209.56	260.38	283.81	191.16	274.59	259.26	32.62	290.58	175.81	249.81	307.77
Lu	35.88	43.90	23.67	3.08	43.10	28.62	35.93	45.35	28.15	38.93	33.31	3.27	39.48	24.10	34.91	48.95
Hf	0.84	0.03	0.08	0.16	0.10	0.78	0.04	0.06	0.42	bd	0.08	0.14	0.12	0.32	0.04	12.24
Ta	0.02	0.02	6.40	bd	0.09	0.05	0.02	0.02	0.02	0.03	5.83	bd	0.05	0.06	bd	0.02
Pb	bd	bd	bd	0.05	0.10	0.03	bd	bd	0.06	0.51	0.03	0.06	0.18	0.04	0.06	bd
Th	0.10	0.06	0.12	0.03	0.14	0.20	bd	bd	115.66	0.49	0.21	bd	77.53	0.32	0.02	0.16
U	0.25	0.04	0.08	0.08	0.21	0.33	bd	bd	0.19	0.65	0.08	0.03	1.50	0.25	0.24	2.03

bd, below detection

* normalising value

C4.1.4 Garnet I05/66i (ppm)

	garnet I05/66i							inclusion(s) I05/66i						
	1	2	3	4	5	6	7	1	2	3	4	5	6	7
Si	157986	161884	173343	179508	135363	114940	201560	143725	166750	157586	173771	155033	114940	177383
P	41	38	49	48	25	19	48	34	458	40	43	34	19	35
^{43}Ca	40104	47561	47852	50977	40475	36398	52342	39708	47582	47973	51175	41052	36398	51342
^{44}Ca*	39309	46456	46813	50029	39309	35735	50029	39309	46456	46813	50029	39309	35735	50029
Sc	45	51	20	23	20	18	22	35	52	19	25	22	18	20
Ti	179	368	772	772	349	136	612	146	329	733	785	387	136	645
V	11	25	43	41	25	17	37	15	21	42	40	27	17	40
Cr	2	106	168	153	94	89	222	17	85	154	145	112	89	203
Mn	10955	11747	24540	27126	12964	10024	24876	10753	11772	23902	26779	13040	10024	23869
Fe	218054	214787	220912	237075	187192	159488	250474	204556	217393	216458	235090	190919	159488	234246
Co	9.16	10.74	10.79	12.14	9.57	6.81	13.38	8.38	10.58	10.02	11.73	9.64	6.81	12.49
Ni	0.14	0.32	0.40	0.31	0.18	0.18	0.73	0.12	0.34	0.34	0.26	0.19	0.18	0.44
Ga	4.20	4.11	4.79	4.66	3.49	3.19	5.33	3.62	4.26	3.70	4.07	3.79	3.19	5.45
Rb	0.04	0.02	0.02	0.01	0.01	0.12	1.26	0.07	0.02	bd	0.01	0.01	0.12	2.19
Sr	0.02	0.02	0.42	0.52	0.00	0.15	0.25	0.10	0.45	0.09	0.10	bd	0.15	1.53
Y	244.77	150.92	1.58	3.41	19.06	444.32	19.59	370.72	146.32	3.42	3.74	28.61	444.32	17.06
Zr	2.81	2.71	5.90	5.96	2.94	155.13	5.32	1.75	171.38	52.55	76.83	58.15	155.13	4.73
Nb	0.07	0.01	0.88	0.50	0.05	0.01	0.26	0.06	0.12	0.98	0.55	0.05	0.01	0.50
Ba	bd	bd	0.16	0.13	bd	bd	6.74	0.02	bd	bd	0.09	bd	bd	11.64
La	0.00	0.00	0.01	0.01	0.00	0.00	0.00	0.00	0.12	0.04	0.01	0.01	0.00	9.09
Ce	bd	0.00	0.01	0.01	0.00	0.00	0.01	0.01	0.33	0.14	0.03	0.03	0.00	22.00
Pr	0.00	0.00	0.00	0.00	bd	0.00	bd	0.01	0.04	0.02	0.01	0.01	0.00	2.87
Nd	0.03	0.01	0.01	0.00	0.01	0.00	0.01	0.03	0.22	0.12	0.01	0.03	0.00	8.98
Sm	0.34	0.08	bd	bd	0.05	0.06	0.11	0.22	0.16	0.08	0.01	0.07	0.06	1.97
Eu	0.26	0.04	0.00	0.00	0.03	0.05	0.03	0.16	0.06	0.01	0.01	0.02	0.05	0.13
Gd	3.73	1.10	0.03	0.06	0.54	1.13	0.83	2.75	1.07	0.20	0.06	0.77	1.13	2.17
Tb	1.65	0.69	0.02	0.01	0.25	0.93	0.26	1.52	0.67	0.05	0.02	0.33	0.93	0.38
Dy	20.81	11.17	0.17	0.27	2.27	21.86	2.55	24.53	10.79	0.50	0.30	3.20	21.86	2.51
Ho	6.22	4.08	0.05	0.12	0.52	13.12	0.56	10.45	3.99	0.13	0.13	0.79	13.12	0.51
Er	26.45	18.72	0.17	0.51	1.74	95.65	1.78	59.15	19.27	0.58	0.55	2.62	95.65	1.60
Tm	5.63	4.17	0.06	0.15	0.30	30.17	0.28	15.87	4.57	0.10	0.13	0.42	30.17	0.26
Yb	49.79	41.34	0.61	1.50	2.73	373.46	2.46	178.10	46.62	0.94	1.36	3.66	373.46	2.43
Lu	7.79	7.74	0.19	0.30	0.41	78.66	0.40	35.89	8.95	0.27	0.36	0.61	78.66	0.29
Hf	0.04	0.05	0.13	0.11	0.05	4.79	0.08	0.03	5.51	1.85	2.76	1.90	4.79	0.10
Ta	0.02	0.02	0.33	0.28	0.04	0.01	0.13	0.02	0.04	0.35	0.30	0.06	0.01	0.18
Pb	0.01	0.01	0.06	0.05	0.01	0.01	0.24	0.02	0.05	0.12	0.04	0.02	0.01	0.49
Th	bd	bd	0.03	0.00	bd	0.04	0.08	0.00	0.11	25.77	0.04	0.01	0.04	13.42
U	0.00	0.00	0.02	bd	0.00	0.42	0.03	0.01	0.89	2.92	0.32	0.15	0.42	1.49

bd, below detection
* normalising value

C4.1.5 Garnet I05/78ii (ppm)

	garnet I05/78ii														
	1	2	3	4	5	6	7	8	9	10	11	12	13	14	15
Si*	174448	174448	174448	174448	174448	174448	174448	174448	174448	174448	174448	174448	174448	174448	174448
P	252	157	326	225	195	204	230	205	227	164	207	97	199	321	298
^{43}Ca	7315	8050	6592	9305	10253	8592	9226	8123	9033	8053	10255	4869	8908	5934	6518
^{44}Ca	7450	8154	6727	9531	10359	8614	9015	8160	9309	8151	10397	4968	9082	6147	6603
Sc	109	131	116	108	103	172	151	107	133	125	205	68	99	126	127
Ti	126	64	138	181	133	8276	575	123	397	368	284	17	170	70	262
V	46	44	48	31	42	82	83	35	77	37	69	17	47	35	36
Cr	136	113	132	6	71	137	131	13	87	41	59	16	133	74	83
Mn	4089	8511	8092	21902	14451	37703	40361	39732	42434	18729	35773	12613	16533	9494	8808
Fe	270243	272896	286202	249486	272858	268994	252616	228962	261551	213811	263382	153945	261684	281993	280646
Co	14.69	14.47	14.14	12.67	13.64	13.59	11.71	10.06	12.01	11.05	12.65	7.78	13.34	14.31	14.52
Ni	0.16	0.14	0.11	0.42	1.92	0.76	0.44	0.24	0.47	0.33	0.17	0.08	0.26	0.13	0.25
Ga	5.47	5.70	6.47	8.67	7.17	8.67	8.62	7.21	8.06	6.87	9.28	2.94	7.57	5.82	5.76
Rb	0.01	0.05	0.45	0.37	0.57	0.19	0.17	0.27	0.18	0.84	0.19	0.01	0.10	0.01	bd
Sr	0.00	0.02	0.03	0.05	0.27	0.07	0.11	0.16	0.11	0.03	0.07	0.00	0.03	bd	0.01
Y	102.25	545.96	75.97	257.84	300.36	1070.26	1341.05	1280.90	1346.34	259.08	979.07	138.01	574.09	80.64	81.40
Zr	18.26	21.33	7.34	4.65	16.51	17.59	104.57	50.21	226.74	10.32	5.15	0.94	6.69	27.31	4.73
Nb	0.00	bd	0.06	1.11	0.20	12.33	1.96	0.70	2.83	2.13	0.19	0.00	0.23	0.00	0.40
Ba	bd	bd	0.31	0.20	1.28	0.02	bd	0.06	bd	0.56	0.05	bd	bd	bd	bd
La	bd	bd	0.00	0.00	0.03	0.02	0.00	0.03	0.01	0.01	0.00	0.00	0.00	bd	0.00
Ce	0.00	bd	0.01	0.02	0.07	0.06	0.02	0.10	0.02	0.03	0.01	0.01	0.01	bd	0.00
Pr	0.00	0.00	0.00	0.01	0.02	0.01	0.01	0.04	0.00	0.01	0.01	0.00	0.00	bd	0.00
Nd	0.11	0.06	0.10	0.32	0.30	0.23	0.25	0.39	0.20	0.21	0.26	0.06	0.17	0.05	0.08
Sm	1.17	0.84	0.82	3.25	2.46	2.25	2.59	2.05	2.30	1.97	2.46	0.61	1.87	0.59	0.71
Eu	0.60	0.49	0.47	1.16	0.95	1.10	1.29	0.98	1.17	0.78	1.04	0.28	0.71	0.42	0.43
Gd	12.48	13.24	9.71	21.94	20.26	29.04	34.76	25.05	34.21	15.82	27.69	7.67	20.03	8.10	9.26
Tb	4.56	6.95	3.30	6.13	6.71	13.09	16.20	13.16	15.75	5.08	12.27	3.05	8.06	2.98	3.31
Dy	28.08	78.36	20.55	45.02	52.16	153.51	193.31	182.28	192.78	40.43	136.02	25.32	83.12	20.47	21.55
Ho	3.57	19.43	2.62	8.09	10.20	41.37	53.48	58.03	54.13	8.20	34.99	4.44	20.59	3.13	3.00
Er	5.99	53.59	4.63	21.81	28.85	141.39	183.12	235.05	191.74	23.54	113.15	10.30	68.00	6.08	5.50
Tm	0.58	6.57	0.46	3.17	4.33	23.95	31.43	45.46	33.57	3.62	18.19	1.28	10.36	0.66	0.57
Yb	3.08	35.48	2.31	20.33	28.77	171.41	232.20	374.99	257.33	23.97	125.36	7.12	70.73	4.06	3.15
Lu	0.43	4.29	0.32	2.47	3.99	23.25	32.37	56.29	36.34	2.99	16.84	0.77	9.88	0.54	0.43
Hf	0.46	0.55	0.11	0.10	0.48	0.45	3.29	1.05	6.63	0.25	0.08	0.02	0.14	0.73	0.09
Ta	0.00	0.00	0.01	0.12	0.03	1.49	0.22	0.10	0.20	0.10	0.06	bd	0.03	0.00	0.04
Pb	0.00	0.00	0.03	0.03	0.09	0.02	0.01	0.03	0.01	0.03	0.01	0.02	0.01	0.01	0.01
Th	0.00	0.00	0.00	0.01	0.02	0.04	0.07	0.14	0.10	0.01	bd	0.00	bd	0.00	bd
U	0.10	0.11	0.02	0.06	0.11	0.18	0.95	0.29	1.47	0.07	0.08	0.00	0.05	0.13	0.02

bd, below detection
* normalising value

Continued...

C4.1.5 Garnet I05/78ii (ppm) *continued*

	inclusion(s) I05/78ii														
	1	2	3	4	5	6	7	8	9	10	11	12	13	14	15
Si*	174448	174448	174448	174448	174448	174448	174448	174448	174448	174448	174448	174448	174448	174448	174448
P	244	153	310	338	162	197	196	2366	237	282	223	133	201	267	246
^{43}Ca	7481	8606	6887	9796	10086	8426	9434	5560	8923	7708	11290	8342	8613	6162	6829
^{44}Ca	7591	8486	6861	9712	10206	8599	9518	5765	9131	8020	11176	8547	8800	6283	7062
Sc	110	133	117	121	110	174	151	81	133	109	212	116	95	125	123
Ti	127	72	164	217	147	7554	4053	5394	397	580	470	39	3268	75	993
V	48	48	50	30	40	83	86	30	77	46	79	30	51	35	43
Cr	140	115	136	5	113	127	128	12	88	72	60	35	154	97	135
Mn	4166	9190	8507	22168	15860	38239	42709	29692	41991	17496	38231	22253	16125	9628	9167
Fe	275723	286959	289043	265522	285735	272327	269216	170124	259414	195658	291669	268177	250737	290493	296035
Co	14.95	15.09	14.04	14.42	13.93	13.29	12.46	7.98	12.06	9.94	14.01	13.50	13.10	14.91	15.41
Ni	0.15	0.22	0.16	8.86	2.54	0.80	0.71	0.44	0.44	0.43	1.17	bd	0.39	0.22	0.31
Ga	5.53	5.67	6.41	8.54	6.55	8.56	8.23	4.89	8.14	6.04	8.69	4.77	6.20	5.43	5.74
Rb	0.01	0.06	1.05	16.12	2.38	0.19	0.22	0.75	0.18	1.52	1.32	0.04	0.09	0.01	0.01
Sr	0.00	0.02	0.02	1.50	0.41	0.10	0.12	0.37	0.12	0.02	0.33	0.00	0.04	0.01	0.01
Y	104.43	589.18	73.32	469.58	255.14	1078.34	1430.39	5027.24	1358.00	595.99	1064.98	265.44	458.55	91.02	100.99
Zr	13.37	2.62	295.86	89.09	5.75	12.17	77.87	409.43	174.59	5.74	6.00	2.17	55.94	1484.29	5.00
Nb	0.00	bd	0.07	1.35	0.61	16.81	6.17	5.03	3.24	3.28	0.39	0.01	5.35	0.03	1.84
Ba	bd	bd	1.25	9.26	2.09	0.03	0.07	0.19	bd	0.76	1.37	bd	0.06	bd	0.03
La	0.00	bd	0.01	0.09	0.04	0.03	0.02	0.43	0.01	0.02	0.02	0.00	0.01	0.00	0.00
Ce	0.00	0.00	0.02	0.33	0.08	0.06	0.04	4.11	0.02	0.20	0.05	0.00	0.08	0.03	0.00
Pr	0.00	0.00	0.01	0.14	0.02	0.01	0.01	1.81	0.01	0.09	0.02	0.00	0.03	0.00	bd
Nd	0.11	0.08	0.10	1.58	0.26	0.22	0.19	18.89	0.18	1.29	0.43	0.09	0.40	0.10	0.09
Sm	1.19	0.88	0.78	5.93	2.03	2.02	2.43	30.38	2.25	5.15	3.60	0.94	2.15	0.74	0.88
Eu	0.63	0.56	0.46	1.78	0.85	1.01	1.18	11.01	1.14	1.51	1.30	0.47	0.80	0.44	0.55
Gd	12.82	14.07	8.87	35.49	17.64	27.70	32.41	142.32	33.74	36.50	36.31	12.42	19.86	8.64	10.77
Tb	4.64	7.43	3.20	31.11	5.89	12.63	15.81	66.09	15.72	11.95	14.97	5.28	7.74	3.23	3.89
Dy	28.65	85.72	19.95	78.13	45.28	150.34	198.83	693.45	193.55	95.29	155.97	46.96	71.62	21.94	26.26
Ho	3.64	20.89	2.64	13.68	8.90	41.75	57.85	165.79	55.27	18.13	37.52	9.24	15.66	3.63	3.78
Er	6.05	58.48	4.71	31.32	25.55	145.35	207.76	540.70	196.30	48.63	115.51	22.39	49.85	7.68	7.33
Tm	0.58	7.07	0.49	4.02	3.92	24.82	35.91	101.54	34.47	6.65	18.35	2.68	7.04	0.96	0.80
Yb	3.17	38.53	2.82	23.77	27.02	180.08	268.92	737.59	264.25	40.96	123.83	14.59	47.35	6.82	4.49
Lu	0.45	4.71	0.43	2.58	3.79	24.65	37.53	94.26	37.88	5.28	16.06	1.74	6.44	1.09	0.62
Hf	0.32	0.05	8.12	2.30	0.11	0.30	2.25	10.85	5.13	0.12	0.11	0.04	1.62	43.52	0.08
Ta	0.00	0.00	0.01	0.12	0.06	1.94	0.74	0.47	0.24	0.11	0.07	0.00	0.58	0.02	0.21
Pb	0.01	0.00	0.03	0.12	0.12	0.02	0.02	0.29	0.01	0.03	0.05	0.02	0.01	0.10	0.02
Th	bd	bd	0.02	0.31	0.01	0.04	0.06	6.99	0.09	0.38	0.13	bd	0.07	0.86	0.00
U	0.07	0.01	1.50	1.85	0.06	0.15	0.55	8.69	1.20	1.61	0.84	0.00	0.54	6.99	0.02

bd, below detection
* normalising value

C4.2 Staurolite, I05/14i (ppm)

	staurolite I05/14i						inclusion(s) I05/14i					
	1	2	3	4	5	6	1	2	3	4	5	6
Si*	131210	131210	131210	131210	131210	131210	131210	131210	131210	131210	131210	131210
^{43}Ca	964	2159	1784	109	258	195	2172	8374	7897	80	70	265
^{44}Ca	623	2111	1519	72	11	bd	1967	8031	7853	84	28	41
Sc	3	2	2	25	4	3	3	4	4	29	10	15
Ti	2961	2809	2370	25748	3277	3604	2460	2867	3107	31481	29909	2808
V	218	186	184	237	223	230	173	199	226	230	134	205
Cr	202	175	109	145	228	191	167	176	146	110	119	195
Mn	766	614	542	450	641	947	602	691	717	414	718	523
Fe	87542	70836	73184	86249	82180	97153	71989	87856	89097	84296	76387	142637
Co	41.00	34.00	36.27	30.49	38.22	45.90	37.00	41.48	41.71	26.19	24.29	71.07
Ni	35.88	27.04	33.61	84.52	33.64	32.61	43.65	51.91	37.72	88.04	28.83	211.63
Ga	193.00	183.69	168.52	71.19	180.53	225.99	158.73	166.98	205.06	40.12	94.47	97.72
Rb	0.03	0.29	0.14	113.69	0.53	0.77	0.11	0.15	0.02	131.67	5.90	39.17
Sr	11.28	33.78	27.93	0.30	0.03	0.02	31.93	36.71	12.50	0.36	0.23	0.51
Y	0.33	0.11	0.15	0.39	0.08	0.83	0.66	18.97	22.61	0.39	0.37	1.15
Zr	6.29	14.09	1.50	1.26	0.18	98.28	14.10	0.02	389.79	0.22	1.04	0.43
Nb	4.59	3.95	3.30	81.21	4.41	4.73	3.10	4.14	4.16	100.14	63.36	8.32
Ba	1.33	5.36	3.57	290.01	0.69	2.11	4.22	5.63	1.07	336.28	13.45	129.52
La	0.04	0.04	0.05	0.06	0.01	0.00	0.14	1.28	1.40	0.07	0.07	0.09
Ce	0.08	0.10	0.10	0.13	0.03	0.01	0.29	5.13	5.95	0.14	0.15	0.23
Pr	0.01	0.01	0.01	0.01	0.00	0.00	0.03	0.87	0.94	0.02	0.02	0.03
Nd	0.05	0.02	0.02	0.06	0.01	0.02	0.13	4.12	5.11	0.06	0.08	0.12
Sm	bd	0.02	0.02	0.01	bd	0.01	0.05	2.20	2.18	0.02	0.03	0.03
Eu	0.04	0.07	0.08	0.02	0.00	bd	0.11	0.49	0.44	0.02	0.02	0.04
Gd	0.02	bd	bd	0.05	bd	bd	0.13	3.14	3.83	0.05	0.03	0.12
Tb	0.01	bd	0.00	0.01	0.00	0.01	0.01	0.62	0.76	0.01	0.01	0.03
Dy	0.05	0.02	0.02	0.05	bd	0.06	0.16	4.18	4.69	0.06	0.09	0.16
Ho	0.00	bd	bd	0.01	bd	0.02	0.02	0.81	0.91	0.01	0.01	0.03
Er	0.04	0.01	0.01	0.03	bd	0.14	0.06	1.89	2.76	0.03	0.03	0.09
Tm	0.00	0.01	0.02	0.00	bd	0.03	0.00	0.21	0.39	0.00	0.01	0.01
Yb	bd	0.09	bd	0.01	0.03	0.34	0.07	1.30	2.60	0.01	0.04	0.03
Lu	0.02	0.01	0.00	0.00	bd	0.10	0.01	0.15	0.52	bd	0.01	0.01
Hf	0.29	0.42	0.07	0.04	bd	2.75	0.39	bd	12.58	0.01	0.04	0.01
Ta	0.87	0.92	0.63	7.68	0.79	0.89	0.59	0.92	0.95	9.44	7.19	0.84
Pb	1.30	3.98	2.98	2.03	0.08	0.06	4.69	4.05	1.55	2.33	0.85	2.50
Th	0.02	0.02	0.02	27.73	bd	0.21	0.03	0.06	0.87	0.45	0.02	0.02
U	0.29	0.20	0.09	0.56	0.07	0.93	0.52	1.75	5.62	0.60	0.62	1.02

bd, below detection
* normalising value

C4.3 NIST glass 612 (ppm)

DATE	23.04.07	23.04.07	23.04.07	23.04.07	23.04.07	23.04.07	Daily: 23 April			24.04.07	24.04.07	24.04.07	24.04.07	24.04.07	24.04.07
run/no.	A1	A2	A9	A10	A17	A18	mean	std dev	1x rsd %	A1	A2	A9	A10	A17	A18
Si	339861.72	330197.88	335167.84	339957.16	326206	344110.31	335916.82	6731.82	2.0	335916.75	335916.78	335916.78	335916.78	335916.78	335916.78
P															
^{43}Ca	85157.07	83957.95	86244.81	85922.3	85670.24	85131.7	85347.35	806.65	0.9	82943.61	82974.44	87811.82	87317.79	85930.63	88493.6
^{44}Ca	85262.51	85262.51	85262.51	85262.51	85262.51	85262.51	85262.51	0.00	0.0	82742.13	83607.61	87591.07	86817.17	85850.01	88414.99
Sc	41.3	41.18	41.16	41.25	40.58	40.2	40.95	0.45	1.1	39.38	39.81	42.77	41.96	41.53	43.33
Ti	39.77	40.05	42.32	42.64	40.57	41.04	41.07	1.18	2.9	39.93	40.27	42.45	40.37	41.32	41.97
V	37.09	35.91	38.25	38.49	37.26	38.4	37.57	1.01	2.7	36.14	36.71	38.43	37.38	38.25	37.69
Cr	33.56	33.71	36.28	36.68	34.52	36.45	35.20	1.43	4.1	34.26	34	35.6	34.24	35.45	35.86
Mn	34.92	35.01	35.82	36.37	35.03	37.44	35.77	1.00	2.8	34.13	35	36.38	36.33	35.94	35.93
Fe	53.69	58.24	53.82	58.63	56.61	56.84	56.31	2.12	3.8	58.08	55.7	58.07	56.08	56.37	53.51
Co	32.86	32.34	33.83	33.2	31.98	34.52	33.12	0.94	2.8	32.29	32.37	33.3	33.03	33.03	33.29
Ni	36.93	35.08	36.96	35.19	36.32	37.51	36.33	1.00	2.8	35.92	35.35	37.09	36.67	36.23	36.18
Ga	32.55	31.83	32.29	33.48	31.61	34.24	32.67	1.01	3.1	31.82	31.54	33.42	32.97	32.03	33.12
Rb	31.57	31.06	31.72	32.5	31.5	33.23	31.93	0.79	2.5	30.77	30.66	32.74	32.24	32.45	32.49
Sr	74.32	73.69	73.89	73.68	74.24	75.56	74.23	0.71	1.0	71.8	71.62	77.2	76.37	73.97	77.36
Y	40.69	40.51	40.43	40.05	41.03	39.02	40.29	0.70	1.7	39.27	38.82	42.32	41.77	40.4	43.5
Zr	39.39	39.29	39.02	38.77	39.55	37.74	38.96	0.66	1.7	37.73	37.69	40.84	40.5	39.33	41.84
Nb	42.25	41.81	42.69	42.53	42.21	43.04	42.42	0.43	1.0	40.95	41.03	43.94	43.61	42.59	43.76
Ba	38.98	38.42	39.89	39.33	39.91	40.34	39.48	0.71	1.8	37.49	38.26	41.81	40.75	38.76	41.09
La	35.63	35.73	35.88	35.81	35.93	35.12	35.68	0.30	0.8	34.31	34.51	37.67	37.21	35.9	37.64
Ce	37.97	37.51	38.52	39.33	38.76	39.72	38.64	0.82	2.1	37.02	37.11	40.24	39.7	38.78	39.6
Pr	37.97	37.75	38.36	38.71	38.47	38.62	38.31	0.38	1.0	36.76	36.81	40.2	40.04	38.45	39.81
Nd	35.57	34.79	35.2	35.49	35.32	35.13	35.25	0.28	0.8	33.93	33.64	37.36	36.99	35.55	36.94
Sm	38.01	38.11	38.3	38.25	38.66	37.94	38.21	0.26	0.7	36.58	36.44	40.13	40.53	38.74	40.64
Eu	35.7	35.5	35.7	36.14	36.28	36.08	35.90	0.31	0.9	34.5	34.25	37.63	37.37	36.59	37.69
Gd	39.31	39.29	39.9	39.18	40.54	38.62	39.47	0.66	1.7	38.12	37.39	41.83	41.76	40.23	42.36
Tb	38.07	38.19	38.36	38.08	39.29	37.88	38.31	0.50	1.3	36.8	36.29	40.41	40.67	38.95	41.22
Dy	37.5	37.33	37.25	36.5	37.5	36.41	37.08	0.50	1.3	35.98	34.94	39.57	39.19	37.79	39.95
Ho	39.64	39.58	39.86	39.49	40.33	38.64	39.59	0.55	1.4	38.37	37.27	42.37	41.94	40.26	42.79
Er	39.99	39.51	39.49	39.73	40.04	39.51	39.71	0.25	0.6	38.52	37.41	41.93	41.78	40.33	42.53
Tm	40.01	39.68	39.79	39.26	40.66	39.94	39.89	0.46	1.2	38.3	37.8	41.99	42.19	40.56	42.58
Yb	41.31	41.38	41.25	40.7	42.58	40.79	41.34	0.67	1.6	39.38	39.27	43.91	44.28	42.45	43.99
Lu	39.83	39.46	39.44	39.39	40.22	38.26	39.43	0.66	1.7	37.85	37.45	41.89	41.79	40.49	42.62
Hf	37.64	38.5	38.08	37.59	38.7	36.59	37.85	0.76	2.0	36.2	36.1	40.21	40.13	38.84	41.21
Ta	41.31	41.22	41.52	41.16	42.01	40.82	41.34	0.40	1.0	39.82	39.17	43.81	43.56	42.25	44.29
Pb	34.86	34.05	36.38	36.14	36.23	35.77	35.57	0.92	2.6	34.13	34.27	36.97	35.22	36.31	37.46
Th	38.78	38.94	39.32	39.03	40.3	38.43	39.13	0.64	1.6	37.43	37.21	41.14	41.27	40.09	42.48
U	34.77	34.33	36.67	36.51	36.33	37.92	36.09	1.32	3.7	33.97	34.33	37.15	36.81	36.99	37.04

Continued...

C4.3 NIST glass 612 (ppm) *continued*

DATE	24.04.07	24.04.07	24.04.07	24.04.07	24.04.07	24.04.07	Daily: 24 April			25.04.07	25.04.07	25.04.07	25.04.07	25.04.07
run/no.	C1	C2	C9	C10	C17	C18	mean	std dev	1x rsd (%)	A1	A2	A11	A12	C1
Si	332088.09	337301.63	346245.88	330426.16	330028.69	339410.44	335916.80	4267.10	1.3	335916.88	335916.84	335916.84	335916.84	338324.69
P														
^{43}Ca	86142.46	84592.08	84378.48	86203.36	84249.1	85979.39	85584.73	1794.12	2.1	85207.09	85417.86	84992.48	85720.91	84695.86
^{44}Ca	85262.52	85262.52	85262.51	85262.51	85262.51	85262.49	85549.84	1543.98	1.8	84677	86446.23	85417.74	84878.55	85262.5
Sc	41.67	41.02	40.03	41.03	42.19	41.93	41.39	1.19	2.9	40.71	41.68	41.38	40.45	40.88
Ti	40.93	41.24	40.53	40.14	39.73	42.51	40.95	0.96	2.3	39.79	43.06	42	38.92	42.62
V	36.88	37	38.22	37.67	35.31	36.65	37.19	0.93	2.5	37.24	37.23	37.35	37.05	37
Cr	34.36	34.37	36.06	35.22	32.92	33.53	34.66	0.98	2.8	35.03	34.11	34.87	34.59	37.38
Mn	34.92	35.65	35.11	36.54	33.86	35.07	35.41	0.87	2.5	35.43	35.45	34.3	36.72	35.36
Fe	44	64.93	59.26	60.23	44.71	49.92	55.07	6.19	11.2	59.5	51.98	<26.36	109.27	62.12
Co	32.95	32.44	34.02	31.67	32.2	32.9	32.79	0.63	1.9	32.3	33.84	32.58	33.04	32.98
Ni	35.6	36.09	36.36	37.21	35.08	35.1	36.07	0.71	2.0	35.96	36.2	37.2	34.46	37.87
Ga	31.92	32.11	33.62	32.13	31.82	31.3	32.32	0.76	2.4	32.05	32.84	32.16	32.5	32.38
Rb	31.9	31.04	32.25	31.79	30.93	31.17	31.70	0.75	2.4	31.32	32.33	31.36	32.04	31.63
Sr	75.64	73.25	73.08	73.32	75.97	75.28	74.57	2.00	2.7	73.77	74.54	73.86	74.25	73.78
Y	41.74	40.05	39.87	39.67	42.92	41.42	40.98	1.51	3.7	40.2	41.19	40.38	40.69	40.16
Zr	40.3	39.05	37.76	38.95	40.76	40.81	39.63	1.41	3.6	39.14	39.27	39.27	39.05	40.87
Nb	42.92	41.8	42.08	42.17	43.29	42.27	42.53	1.00	2.4	42.18	42.47	42.08	42.58	42.87
Ba	40.12	38.84	39	38.66	39.9	40.09	39.56	1.27	3.2	39.83	38.22	39.5	39	41.43
La	37.03	35.28	35.22	34.81	37.75	36.91	36.19	1.32	3.6	35.43	36.45	35.97	35.37	36.92
Ce	39.05	37.65	38.67	38.09	38.49	38.3	38.56	1.00	2.6	38.12	38.82	38.29	38.4	39.05
Pr	39.31	37.59	37.74	37.84	39.37	38.88	38.57	1.21	3.1	37.87	38.88	38.38	37.86	38.39
Nd	36.65	34.5	34.62	34.72	36.4	36.31	35.63	1.30	3.7	35.25	35.21	35.29	35.15	35.9
Sm	38.84	38.29	37.98	36.94	40.16	39.32	38.72	1.51	3.9	37.75	39.24	38.61	37.57	39.75
Eu	36.8	35.54	35.24	35.13	37.24	36.98	36.25	1.24	3.4	35.38	36.8	36.18	35.22	36.38
Gd	41.06	39.19	38.74	38.42	40.94	41.74	40.15	1.70	4.2	38.95	41	39.91	38.98	40.53
Tb	40.12	37.61	37.94	36.98	40.52	39.92	38.95	1.74	4.5	37.62	40.01	38.79	37.58	39.61
Dy	38.04	37.39	36.44	35.86	39.88	38.82	37.82	1.72	4.5	36.6	38.65	36.9	37.67	39.3
Ho	41.35	39.19	38.76	38.78	41.72	41.52	40.36	1.82	4.5	39.11	41.12	39.8	39.53	41.04
Er	41.1	39.64	38.88	37.94	42.75	41.99	40.40	1.88	4.6	39.43	40.35	40.14	39.05	40.24
Tm	41.57	39.55	38.84	38.38	42.53	42.27	40.55	1.86	4.6	39.3	41.15	40.32	39.11	40.88
Yb	42.6	41.27	40.48	40.48	44.21	42.83	42.10	1.87	4.4	40.68	43.23	41.24	41.67	41.59
Lu	41.26	39.21	38.69	38.2	42.49	41.61	40.30	1.90	4.7	38.86	41.26	40.29	38.46	41.04
Hf	39.82	37.76	37	36.4	41.7	40.41	38.82	2.04	5.3	37.38	39.6	38.36	37.5	38.91
Ta	43.23	40.96	40.49	39.74	44.23	43.89	42.12	1.96	4.6	41.01	42.29	41.5	41.23	42.65
Pb	38.46	33.54	34.99	34.53	37.06	36.65	35.80	1.56	4.3	34.95	36.22	35.7	34.77	36.91
Th	41.21	38.63	38.16	37.77	42.97	41.32	39.97	2.04	5.1	38.36	41.19	39.58	38.5	40.47
U	36.51	35.04	35.5	34.94	36.09	36.41	35.90	1.11	3.1	35.27	36.3	35.58	35.57	36.41

Continued...

C4.3 NIST glass 612 (ppm) *continued*

DATE	25.04.07	25.04.07	25.04.07	Daily: 25 April			30.04.07	30.04.07	30.04.07	30.04.07	30.04.07	30.04.07	30.04.07	30.04.07
run/no.	C2	C11	C12	mean	std dev	1x rsd (%)	A2	A10	A11	A20	A21	B1	B2	B10
Si	334911.38	329929.03	340502.28	335916.85	3016.36	0.9	335916.78	335916.78	335916.75	335916.78	335916.78	348368.94	338882.38	328310.84
P							63.24	35.06	71.02	62.24	80.3	56.03	65.31	38.03
^{43}Ca	85562.13	85219.89	85458.79	85284.38	328.99	0.4	82858.75	92730.12	89832.96	87817.91	84910.05	84791.02	85892.29	85125.62
^{44}Ca	85262.5	85262.49	85262.5	85308.69	520.78	0.6	83166.33	92676.34	88462.53	91277.4	85639.59	85262.52	85262.52	85262.52
Sc	41.08	40.83	41.66	41.08	0.45	1.1	40.31	45.37	42.75	43.35	38.81	40.85	41.35	41.13
Ti	41.74	39.52	40.63	41.04	1.54	3.7	40.8	43.9	42.07	43.01	39.21	40.67	41.49	40.99
V	37.28	37.4	37.1	37.21	0.14	0.4	36.64	37.22	38.02	39.96	39.47	37.27	36.21	38.72
Cr	36	33.74	31.85	34.70	1.62	4.7	34.88	35.9	37.2	38.11	39.67	35.16	34.93	33.89
Mn	36.49	34.52	35.18	35.43	0.84	2.4	36.41	41.14	38.8	40.03	38.52	35.31	35.27	35.96
Fe	60.73	52.71	41.12	62.49	21.85	35.0	54.55	51.9	56.95	62.78	55.24	55.48	56.4	59.65
Co	33.26	32.46	32.47	32.87	0.52	1.6	31.81	33.32	34.76	32.81	32.14	33	32.49	32.34
Ni	35.43	35.95	35.65	36.09	1.05	2.9	34.63	36.06	36.36	35.86	36.56	36.45	35.38	36.53
Ga	32.11	31.82	33.67	32.44	0.59	1.8	31.32	33.65	32.6	32.68	32.2	32.7	31.78	32.11
Rb	31.69	31.77	31.25	31.67	0.37	1.2	30.36	33.26	33.34	34.38	34.23	31.65	30.84	32.38
Sr	74.36	74.94	71.95	73.93	0.90	1.2	71.83	81.92	78.07	79.44	73.1	73.56	74.19	73.55
Y	40.54	40.9	40.12	40.52	0.38	0.9	39.3	46.84	42.52	43.42	38.36	40.49	40.36	39.9
Zr	38.96	38.69	39.04	39.29	0.67	1.7	37.84	44.72	41.41	40.93	37.12	39.14	39.03	38.78
Nb	42.31	42.48	41.22	42.27	0.49	1.2	40.82	46.12	44.01	44.79	41.93	42.12	42.12	42.38
Ba	39.67	39.13	37.08	39.23	1.26	3.2	38.48	43.66	41.14	42.47	40.6	39.87	37.99	39.45
La	35.74	36.16	34.1	35.77	0.85	2.4	34.43	40.67	37.95	38.12	35.04	35.88	35.35	35.59
Ce	38.87	38.39	36.88	38.35	0.68	1.8	36.65	42.17	41.26	41.06	40.03	38.49	37.7	38.58
Pr	38.46	38.47	37.15	38.18	0.53	1.4	36.53	42.76	40.8	41.01	38.7	38.29	37.75	38.12
Nd	35.5	35.41	33.9	35.20	0.58	1.6	33.65	39.83	37.19	38.02	34.98	35.36	34.95	35.02
Sm	38.1	38.08	37.43	38.32	0.82	2.2	36.34	44.05	40.83	41.21	37.45	38.6	37.41	38.22
Eu	35.78	36.01	35.13	35.86	0.59	1.7	33.73	40.83	38.47	39.18	35.93	35.89	35.44	36.07
Gd	39.21	39.18	40.3	39.76	0.79	2.0	38.09	45.77	41.86	42.87	38.24	39.79	38.71	40.09
Tb	38.4	38.47	37.12	38.45	1.01	2.6	36.23	44.78	40.85	42.16	37.5	38.3	37.82	38.95
Dy	36.75	36.67	37.27	37.48	1.00	2.7	35.06	43.54	39.85	40.53	36.4	37.29	36.82	37.53
Ho	40.24	39.26	38.8	39.86	0.87	2.2	37.44	46.25	42.35	42.97	38.68	39.77	39.26	39.88
Er	40.1	39.98	38.31	39.70	0.71	1.8	37.59	46.77	42.33	43.32	38.5	39.59	39.51	39.69
Tm	39.87	39.71	39.46	39.98	0.74	1.9	37.44	46.8	42.62	43.94	38.35	40.12	39.56	39.63
Yb	42.45	40.84	41.06	41.60	0.86	2.1	38.91	48.84	43.66	44.75	39.64	41.52	40.92	41.56
Lu	40.29	39.07	38.53	39.73	1.13	2.8	37.43	45.91	42.05	43.92	38.04	39.78	39.04	39.86
Hf	38.32	38.82	35.74	38.08	1.19	3.1	35.76	44.86	40.89	41.94	37.09	38.25	37.54	38.37
Ta	41.99	41.29	39.78	41.47	0.89	2.1	38.83	48.1	43.78	44.79	40.71	41.68	41.03	41.55
Pb	34.74	34.81	36.3	35.55	0.85	2.4	32.35	39.19	37.57	37.71	36.64	36	35.12	34.51
Th	39.75	39.49	37	39.29	1.31	3.3	35.98	45.72	41.13	41.61	37.69	39.66	38.75	39.02
U	36.53	35.46	33.82	35.62	0.87	2.4	32.19	38.32	37.25	38.22	38.89	35.91	34.62	36.35

Continued...

C4.3 NIST glass 612 (ppm) *continued*

DATE	30.04.07	30.04.07	30.04.07	30.04.07	30.04.07	Daily: 30 April			Over total period of analysis		
run/no.	B11	C1	C2	C10	C11	mean	std dev	1x rsd (%)	mean	std dev	1x rsd (%)
Si	328105.28	345694.09	324986.59	342689.44	330297.25	335916.82	6923.59	2.1	335917	5295.97	1.6
P	55.1	54.36	61.39	49.51	49.35	57.00	12.46	21.9	57	12.46	21.9
^{43}Ca	85889.96	85255.34	85292.57	86354.93	84488.09	86249.20	2569.95	3.0	85708	1812.82	2.1
^{44}Ca	85262.52	85262.53	85262.53	85262.52	85262.52	86409.41	2720.60	3.1	85743	1821.34	2.1
Sc	41.14	41.25	41.33	39.9	39.43	41.31	1.73	4.2	41	1.20	2.9
Ti	40.5	40.8	41.24	40.75	39.36	41.14	1.29	3.1	41	1.19	2.9
V	37.19	37.08	36.85	40.53	38.6	37.98	1.36	3.6	38	1.05	2.8
Cr	34.35	33.82	34.83	38.23	36.09	35.93	1.84	5.1	35	1.56	4.4
Mn	35.26	35.44	34.94	36.84	36.51	36.96	2.02	5.5	36	1.51	4.2
Fe	55.57	54.74	57.42	59.67	55.79	56.63	2.77	4.9	57	9.94	17.4
Co	32.99	32.46	32.99	32.84	33.3	32.87	0.72	2.2	33	0.68	2.1
Ni	35.68	36.6	35.47	37.82	36.11	36.12	0.77	2.1	36	0.82	2.3
Ga	32.09	32.48	32.26	32.19	31.68	32.29	0.57	1.8	32	0.70	2.2
Rb	31.93	31.56	31.3	33.58	32.85	32.44	1.28	4.0	32	0.95	3.0
Sr	75.51	74.68	73.95	71.69	72.73	74.94	3.07	4.1	75	2.12	2.8
Y	41.43	41.06	40.71	38.93	38.21	40.89	2.35	5.7	41	1.60	3.9
Zr	39.92	39.92	39.26	37.24	36.92	39.40	2.13	5.4	39	1.48	3.8
Nb	42.75	42.45	42.35	41.36	41.58	42.68	1.47	3.4	43	1.03	2.4
Ba	39.22	38.88	39.9	38.28	38.58	39.89	1.70	4.3	40	1.34	3.4
La	36.18	36.21	35.98	34.22	33.84	36.11	1.87	5.2	36	1.34	3.7
Ce	38.59	38.73	38.14	38.57	37.55	39.04	1.62	4.1	39	1.17	3.0
Pr	38.65	38.5	38.39	36.86	36.86	38.71	1.81	4.7	38	1.25	3.3
Nd	35.49	35.62	35.56	33.49	33.16	35.56	1.86	5.2	35	1.30	3.7
Sm	38.45	38.82	38.56	35.79	35.91	38.59	2.32	6.0	39	1.59	4.1
Eu	36.06	36.25	36.08	34.75	33.7	36.34	2.05	5.6	36	1.38	3.8
Gd	39.85	40.06	40.06	37.54	36.87	39.98	2.40	6.0	40	1.70	4.3
Tb	38.82	39.01	38.73	36.47	35.41	38.85	2.54	6.6	39	1.79	4.6
Dy	37.3	37.63	37.88	35.02	34.04	37.61	2.53	6.7	38	1.78	4.7
Ho	40.19	40.39	40.24	37.27	36.44	40.09	2.62	6.5	40	1.84	4.6
Er	40.55	40.67	39.91	37.29	36.7	40.19	2.73	6.8	40	1.89	4.7
Tm	40.07	40.63	40.28	37.34	36.81	40.28	2.81	7.0	40	1.92	4.8
Yb	41.89	42.57	41.53	38.45	38.4	41.74	2.87	6.9	42	1.97	4.7
Lu	39.82	40.41	39.92	37.05	36.72	40.00	2.67	6.7	40	1.92	4.8
Hf	38.09	38.9	38.31	35.89	35.14	38.54	2.69	7.0	38	1.99	5.2
Ta	41.16	42.15	41.62	39.41	38.8	41.82	2.56	6.1	42	1.85	4.4
Pb	35.02	35.74	35.29	35.6	34.1	35.76	1.75	4.9	36	1.39	3.9
Th	38.99	40.15	39.54	36.61	36.04	39.30	2.63	6.7	39	1.97	5.0
U	35.41	35.78	35.36	36.27	35.61	36.17	1.77	4.9	36	1.32	3.7

C4.4 K23 garnet (ppm)

K23	GT1 #1	GT1 #2	GT1 #3	GT1 #4	GT1 #5	GT1 #6	GT2 #1	GT2 #2	GT2 #3	GT2 #4	GT4 #1	GT4 #2	Daily: 23 April		
DATE	23.04.07	23.04.07	23.04.07	23.04.07	23.04.07	23.04.07	23.04.07	23.04.07	23.04.07	23.04.07	23.04.07	23.04.07	mean	std dev	1x rsd (%)
Si	196387.69	195621.06	193105.45	194751.92	194361.03	192476.77	187534.89	184174.52	190387.17	192282.42	189525.08	195332.41	192162	3665	1.9
P															
^{43}Ca	38190.67	38042.23	38229.13	38173.06	38339.74	38207.82	38184.25	38320.68	38359.70	38253.60	38109.12	38390.30	38233	105	0.3
^{44}Ca	37879.15	37879.15	37879.15	37879.15	37879.15	37879.15	37879.15	37879.15	37879.15	37879.15	37879.15	37879.15	37879	0	0.0
Sc	137.65	140.96	142.63	142.89	143.34	144.28	136.93	138.84	136.78	145.80	144.67	151.77	142	4	3.1
Ti	2875.66	2885.25	2904.70	2884.38	2916.86	2833.85	2877.15	2885.89	2897.18	2930.35	2753.47	2766.12	2868	56	1.9
V	163.23	165.12	165.97	164.82	166.39	162.19	161.08	162.08	162.01	170.94	156.85	155.84	163	4	2.5
Cr	400.64	406.59	407.67	405.86	411.99	400.89	406.20	401.54	402.34	401.98	387.09	399.34	403	6	1.5
Mn	2222.16	2219.78	2220.46	2223.51	2228.09	2214.01	2170.64	2163.09	2196.92	2230.85	2210.19	2239.70	2212	24	1.1
Fe	81787.95	82105.60	81883.66	82467.62	82089.74	81239.41	79854.71	79430.23	80813.64	81834.03	80416.06	82429.29	81363	1015	1.2
Co	55.59	56.42	55.83	56.34	55.96	55.78	55.26	54.12	55.26	56.37	55.25	56.74	56	1	1.3
Ni	52.36	52.45	51.72	52.13	51.29	51.35	54.54	50.34	50.52	51.22	50.86	51.87	52	1	2.2
Ga	6.22	6.38	6.27	6.15	6.28	6.26	6.17	5.84	6.14	6.43	5.92	6.09	6	0	2.8
Rb	bd	0.02	0.01	bd	0.01	0.09	0.04	0.03	0.02	0.02	0.02	0.01	0	0	88.7
Sr	0.25	0.27	0.27	0.26	0.26	0.27	0.32	0.53	0.27	0.28	0.68	0.25	0	0	41.7
Y	62.48	62.36	62.29	62.44	62.51	63.38	62.90	63.13	62.97	62.53	62.00	62.33	63	0	0.6
Zr	63.03	62.84	62.90	63.05	63.03	63.15	63.63	64.11	63.96	62.98	58.75	57.49	62	2	3.3
Nb	0.09	0.08	0.08	0.07	0.08	0.09	0.10	0.11	0.08	0.09	0.11	0.07	0	0	13.8
Ba	bd	bd	bd	bd	bd	bd	bd	0.18	bd	bd	0.17	bd	0	0	3.2
La	0.02	0.02	0.02	0.02	0.02	0.02	0.03	0.03	0.02	0.03	0.05	0.02	0	0	38.9
Ce	0.22	0.23	0.23	0.22	0.23	0.21	0.25	0.24	0.24	0.22	0.28	0.21	0	0	8.0
Pr	0.09	0.10	0.10	0.09	0.09	0.10	0.09	0.11	0.10	0.10	0.09	0.09	0	0	6.3
Nd	1.20	1.20	1.18	1.18	1.17	1.14	1.18	1.24	1.25	1.14	1.18	1.08	1	0	3.7
Sm	1.45	1.36	1.33	1.39	1.35	1.35	1.37	1.33	1.38	1.37	1.25	1.33	1	0	3.5
Eu	0.80	0.84	0.80	0.81	0.79	0.81	0.81	0.81	0.80	0.80	0.77	0.76	1	0	2.6
Gd	4.22	4.30	4.11	4.14	4.26	3.91	4.22	4.08	4.14	4.09	4.41	3.85	4	0	3.8
Tb	1.03	1.07	1.00	1.00	1.05	1.00	1.08	1.00	1.07	1.01	1.02	1.03	1	0	2.9
Dy	9.54	9.27	9.35	9.13	9.42	9.32	9.39	9.58	9.43	9.38	9.23	9.38	9	0	1.3
Ho	2.49	2.48	2.41	2.39	2.43	2.52	2.50	2.48	2.49	2.43	2.50	2.39	2	0	1.9
Er	8.42	8.53	8.37	8.54	8.36	8.46	8.44	8.57	8.60	8.52	8.48	8.39	8	0	0.9
Tm	1.37	1.38	1.36	1.31	1.36	1.37	1.35	1.44	1.37	1.39	1.36	1.36	1	0	2.2
Yb	9.62	9.96	9.96	9.84	9.96	9.69	9.85	10.02	9.95	10.14	10.03	9.71	10	0	1.6
Lu	1.55	1.54	1.56	1.53	1.57	1.55	1.51	1.58	1.51	1.59	1.61	1.65	2	0	2.7
Hf	1.40	1.45	1.39	1.42	1.41	1.42	1.40	1.43	1.39	1.43	1.35	1.31	1	0	2.7
Ta	0.01	0.00	0.01	0.01	0.00	0.01	0.01	0.01	0.01	bd	0.01	bd	0	0	30.8
Pb	bd	bd	0.03	0.02	bd	bd	0.02	0.02	bd	0.01	0.02	bd	0	0	25.8
Th	bd	bd	bd	0.01	bd	0.01	bd	bd	bd	0.01	0.01	bd	0	0	19.5
U	0.01	0.01	0.01	0.01	bd	bd	bd	bd	0.01	0.01	0.01	0.01	0	0	22.8

bd, below detection

Continued...

C4.4 K23 garnet (ppm) *continued*

K23	GT1 #1	GT1 #2	GT1 #3	GT1 #4	GT1 #5	GT5 #1	GT5 #2	GT5 #3	Daily: 30 April			Over total period of analysis			
DATE	30.04.07	30.04.07	30.04.07	30.04.07	30.04.07	30.04.07	30.04.07	30.04.07	mean	std dev	1x rsd (%)	mean	std dev	1x rsd (%)	
Si	186192.56	188093.22	186220.78	191236.78	184814.88	185041.33	183776.36	189727.45	186888	2584	1.4	190052	4155	2.2	Si
P	107.01	105.32	100.71	104.57	101.21	98.82	98.37	106.65	103	3	3.4	103	3	3.4	P
^{43}Ca	37761.88	38089.18	37688.38	38169.64	37938.20	37850.57	37685.68	38107.19	37911	194	0.5	38105	215	0.6	^{43}Ca
^{44}Ca	37879.16	37879.16	37879.16	37879.16	37879.16	37879.16	37879.16	37879.16	37879	0	0.0	37879	0	0.0	^{44}Ca
Sc	131.04	134.16	139.35	140.24	137.16	135.06	136.23	134.93	136	3	2.2	140	5	3.5	Sc
Ti	2850.05	2881.84	2862.33	2844.91	2852.34	2859.38	2783.81	2862.04	2850	29	1.0	2860	47	1.6	Ti
V	153.11	156.58	155.81	156.86	156.96	155.68	152.77	157.24	156	2	1.1	160	5	3.1	V
Cr	390.23	395.64	390.87	390.46	395.19	388.82	381.79	387.10	390	4	1.1	398	8	2.1	Cr
Mn	2159.95	2197.42	2182.18	2185.18	2186.01	2160.37	2164.19	2185.22	2178	14	0.6	2198	26	1.2	Mn
Fe	88276.34	89567.62	88684.51	90531.73	89352.25	88901.24	88554.41	90543.91	89302	869	1.0	84538	4098	4.8	Fe
Co	53.15	53.86	53.90	55.86	54.32	53.77	53.97	55.51	54	1	1.7	55	1	1.9	Co
Ni	49.48	50.19	49.29	52.18	50.85	49.95	50.74	51.13	50	1	1.9	51	1	2.3	Ni
Ga	6.05	6.03	6.17	6.30	6.11	6.14	6.02	6.34	6	0	2.0	6	0	2.4	Ga
Rb	0.01	0.01	0.01	0.01	0.02	0.00	0.01	0.01	0	0	34.3	0	0	99.1	Rb ~bd
Sr	0.26	0.27	0.27	0.26	0.26	0.25	0.24	0.27	0	0	3.9	0	0	36.2	Sr
Y	57.89	57.72	58.70	58.67	57.99	58.99	58.63	58.83	58	0	0.8	61	2	3.5	Y
Zr	59.21	59.71	59.40	59.76	58.34	59.46	59.05	58.57	59	1	0.9	61	2	3.7	Zr
Nb	0.09	0.09	0.08	0.08	0.08	0.08	0.07	0.08	0	0	5.2	0	0	11.8	Nb ~bd
Ba	bd	bd	bd	0.02	bd	bd	bd	bd	0	-		0	0	73.3	Ba ~bd
La	0.02	0.02	0.02	0.02	0.02	0.02	0.02	0.02	0	0	9.2	0	0	36.3	La ~bd
Ce	0.21	0.22	0.21	0.21	0.21	0.21	0.22	0.22	0	0	2.4	0	0	7.4	Ce ~bd
Pr	0.10	0.10	0.10	0.09	0.09	0.09	0.09	0.09	0	0	2.2	0	0	5.3	Pr ~bd
Nd	1.12	1.18	1.09	1.10	1.09	1.10	1.07	1.14	1	0	3.1	1	0	4.4	Nd
Sm	1.29	1.27	1.32	1.27	1.28	1.27	1.31	1.31	1	0	1.6	1	0	3.8	Sm
Eu	0.77	0.77	0.80	0.75	0.77	0.77	0.78	0.79	1	0	1.9	1	0	2.7	Eu
Gd	3.78	3.93	4.09	3.87	3.85	3.84	3.89	4.04	4	0	2.7	4	0	4.4	Gd
Tb	0.93	0.98	0.97	0.97	0.93	0.97	0.93	0.95	1	0	2.1	1	0	4.7	Tb
Dy	8.64	8.60	8.54	8.62	8.50	8.86	8.41	8.56	9	0	1.5	9	0	4.5	Dy
Ho	2.23	2.22	2.28	2.23	2.25	2.25	2.22	2.24	2	0	0.9	2	0	4.9	Ho
Er	7.64	7.76	7.95	7.93	7.68	7.68	7.68	7.69	8	0	1.6	8	0	4.6	Er
Tm	1.22	1.24	1.30	1.24	1.21	1.24	1.22	1.25	1	0	2.3	1	0	5.4	Tm ~bd
Yb	8.85	9.09	9.63	9.26	8.81	9.18	8.99	9.02	9	0	2.9	10	0	4.6	Yb
Lu	1.37	1.43	1.50	1.45	1.41	1.40	1.40	1.37	1	0	2.9	2	0	5.7	Lu ~bd
Hf	1.25	1.27	1.29	1.30	1.24	1.25	1.28	1.20	1	0	2.6	1	0	5.8	Hf ~bd
Ta	0.00	0.01	0.01	0.01	0.01	0.01	0.01	0.01	0	0	24.1	0	0	27.8	Ta ~bd
Pb	bd	0.01	0.01	0.01	0.05	bd	0.01	bd	0	0	117.6	0	0	69.0	Pb ~bd
Th	0.00	0.00	0.00	bd	bd	0.00	0.00	0.00	0	0	33.7	0	0	52.8	Th ~bd
U	0.00	0.01	bd	bd	0.00	0.01	0.00	0.00	0	0	40.3	0	0	39.5	U ~bd

C5. LA–ICPMS U(–Th)–Pb allanite data

15/02/2008	^{204}Pb (cps)	^{206}Pb (mV)	^{207}Pb (mV)	^{208}Pb (mV)	^{232}Th (mV)	^{238}U (mV)	Pb (ppm) †	Th (ppm) †	U (ppm) †
Standards									
manmon 9	-8	3.4	0.18	87.5	2.32	63	1965	121041	894
manmon 10	-19	3.4	0.18	89.0	2.39	62	1934	124678	884
manmon 11	-255	3.9	0.20	101.2	2.53	65	2017	132152	921
FC-1 9	-48	2.7	0.11	3.6	0.94	550	1619	48799	7821
FC-1 10	-96	3.1	0.13	3.8	0.99	517	1523	51474	7350
FC-1 11	-336	4.2	0.17	3.8	1.00	670	1972	51905	9522
LU1 allanite 1	764	1.7	0.29	26.8	0.19	9	952	9888	125
LU1 allanite 2	43	0.9	0.10	15.7	0.13	5	506	6778	65
LU1 allanite 3	437	1.8	0.23	28.9	0.21	9	982	10994	124
LU1 monazite 1	43	20.1	1.54	163.5	1.78	130	9281	92692	1852
LU1 monazite 2	446	25.8	2.08	211.4	1.97	146	12308	102824	2074
LU1 monazite 3	27	25.1	1.90	201.5	1.94	139	10905	101149	1979
manmon 12	6	3.4	0.18	88.4	2.35	63	2415	110676	1059
manmon 13	126	3.4	0.18	88.7	2.46	65	2414	115957	1090
manmon 14	89	3.7	0.19	97.1	2.52	64	2395	118814	1073
FC-1 12	-191	2.5	0.10	3.5	0.90	492	1747	42674	8260
FC-1 13	-100	2.3	0.10	3.1	0.82	400	1422	38732	6709
FC-1 14	-244	2.3	0.09	3.0	0.79	447	1581	37216	7501
Sample (see Fig. 6.12)									
B06/64 allanite 1	2139	1.2	0.89	3.0	0.13	6	409	5932	99
B06/64 allanite 2	2083	1.2	0.87	2.7	0.07	9	395	3287	145
B06/64 allanite 3.1	2630	1.6	1.11	3.6	0.09	5	501	4407	81
B06/64 allanite 3.2	2456	1.4	1.02	3.4	0.14	7	459	6370	111
B06/64 allanite 4	2504	1.6	1.16	3.7	0.07	4	466	3531	67
B06/64 allanite 6	754	0.7	0.47	1.7	0.07	2	184	3318	35
B06/64 allanite 7.1*	1812	1.6	1.12	3.7	0.09	5	389	4309	91
B06/64 allanite 7.2*	2867	1.6	1.11	3.7	0.07	5	554	3400	83
B06/64 allanite 5*	1022	0.9	0.61	2.0	0.06	4	238	2661	67
Standards									
LU1 allanite 4	198	2.1	0.29	33.6	0.28	4	517	13073	71
LU1 allanite 5	-86	1.1	0.14	20.6	0.19	2	226	8820	34
LU1 allanite 6	-121	1.3	0.17	23.2	0.25	3	270	11594	43
LU1 monazite 4	-246	29.5	2.16	234.9	2.48	116	11144	117115	1952
LU1 monazite 5	-154	26.0	1.99	212.3	2.15	119	10967	101209	1991
LU1 monazite 6	-146	24.5	1.87	206.3	2.18	96	8750	102926	1613
manmon 15	-288	4.5	0.24	119.2	3.21	44	2125	130129	916
manmon 16	-234	4.4	0.23	115.1	3.14	42	1872	127480	874
manmon 17	-287	4.6	0.23	119.9	3.24	45	1965	131474	925
FC-1 15	30	3.0	0.13	4.2	1.15	295	1300	46754	6093
FC-1 16	-45	3.0	0.13	3.8	1.05	310	1315	42471	6408
FC-1 17	-47	3.9	0.16	4.7	1.29	382	1632	52423	7889
Other									
B06/64 garnet	33	0.0	0.00	0.0	0.00	0	0	0	0
LU1 allanite raster	472	3.6	0.44	40.9	0.34	17	1700	13697	341
LU1 monazite raster	475	33.4	2.75	266.9	2.44	132	17870	99048	2732

*Data may require some reprocessing (slight shift after gains were run), † c. 20 % uncertainty on concentration

continued	Uncorrected isotopic ratios								
	$^{207}Pb/^{206}Pb$	1σ (%)	$^{238}U/^{206}Pb$	1σ (%)	$^{207}Pb/^{235}U$	1σ (%)	$^{208}Pb/^{232}Th$	1σ (%)	Rho
Standards									
manmon 9	0.0591	0.58	11.01	1.07	0.740	1.22	0.0267	1.21	0.88
manmon 10	0.0592	0.59	11.07	1.05	0.738	1.21	0.0265	1.13	0.87
manmon 11	0.0586	0.51	11.10	1.03	0.728	1.15	0.0283	1.08	0.90
FC-1 9	0.0470	0.85	116.53	1.02	0.056	1.33	0.0027	1.14	0.77
FC-1 10	0.0469	0.81	117.43	1.02	0.055	1.31	0.0027	1.09	0.78
FC-1 11	0.0468	0.59	117.68	1.05	0.055	1.21	0.0027	1.11	0.87
LU1 allanite 1	0.1681	0.75	3.20	1.26	7.248	1.47	0.0985	1.24	0.86
LU1 allanite 2	0.1369	0.99	3.04	1.92	6.207	2.16	0.0857	1.42	0.89
LU1 allanite 3	0.1461	0.52	3.00	1.02	6.719	1.15	0.0969	1.08	0.89
LU1 monazite 1	0.0851	0.23	4.84	1.11	2.422	1.13	0.0659	1.14	0.98
LU1 monazite 2	0.0915	0.26	4.09	1.03	3.083	1.06	0.0762	1.10	0.97
LU1 monazite 3	0.0857	0.12	4.38	1.02	2.701	1.03	0.0737	1.25	0.99
manmon 12	0.0602	0.57	10.83	3.49	0.767	3.53	0.0272	2.76	0.99
manmon 13	0.0588	0.58	10.96	3.46	0.739	3.50	0.0263	2.54	0.99
manmon 14	0.0585	0.54	10.94	3.45	0.737	3.49	0.0279	2.54	0.99
FC-1 12	0.0472	0.89	114.40	3.44	0.057	3.55	0.0028	2.60	0.97
FC-1 13	0.0480	1.00	114.46	3.43	0.058	3.58	0.0027	2.50	0.96
FC-1 14	0.0476	1.00	114.62	3.43	0.057	3.58	0.0028	2.50	0.96
Sample (see Fig. 6.12)									
B06/64 allanite 1	0.8029	0.19	5.70	4.15	19.414	4.15	0.0178	3.78	1.00
B06/64 allanite 2	0.7838	0.30	8.76	3.93	12.330	3.95	0.0286	2.58	1.00
B06/64 allanite 3.1	0.8098	0.16	3.92	3.62	28.501	3.63	0.0272	2.92	1.00
B06/64 allanite 3.2	0.8063	0.17	5.78	3.62	19.218	3.62	0.0184	2.50	1.00
B06/64 allanite 4	0.8131	0.14	3.48	3.47	32.257	3.48	0.0361	2.68	1.00
B06/64 allanite 6	0.8066	0.28	4.41	3.53	25.239	3.54	0.0171	2.67	1.00
B06/64 allanite 7.1*	0.8002	0.14	5.68	3.91	19.409	3.91	0.0303	5.82	1.00
B06/64 allanite 7.2*	0.8109	0.14	3.59	3.44	31.111	3.45	0.0369	2.57	1.00
B06/64 allanite 5*	0.7878	0.28	6.77	3.56	16.039	3.57	0.0256	2.71	1.00
Standards									
LU1 allanite 4	0.1532	0.70	3.33	3.50	6.337	3.57	0.0880	2.49	0.98
LU1 allanite 5	0.1445	0.89	3.62	3.55	5.502	3.66	0.0786	3.45	0.97
LU1 allanite 6	0.1304	1.09	3.83	3.68	4.693	3.84	0.0675	3.31	0.96
LU1 monazite 4	0.0876	0.21	4.18	3.47	2.891	3.47	0.0684	2.56	1.00
LU1 monazite 5	0.0875	0.14	4.37	3.56	2.764	3.56	0.0719	2.47	1.00
LU1 monazite 6	0.0870	0.10	4.45	3.44	2.697	3.44	0.0688	2.48	1.00
manmon 15	0.0586	0.46	10.60	4.37	0.763	4.40	0.0275	1.08	0.99
manmon 16	0.0586	0.47	11.30	4.37	0.715	4.39	0.0272	1.05	0.99
manmon 17	0.0587	0.46	11.49	4.35	0.704	4.37	0.0274	1.05	0.99
FC-1 15	0.0479	0.83	114.56	4.35	0.058	4.43	0.0027	1.04	0.98
FC-1 16	0.0476	0.75	118.17	4.35	0.056	4.42	0.0027	1.06	0.99
FC-1 17	0.0468	0.64	117.66	4.35	0.055	4.40	0.0027	1.08	0.99
Other									
B06/64 garnet									
LU1 allanite raster	0.1268	0.63	4.93	4.35	3.544	4.40	0.0871	2.29	0.99
LU1 monazite raster	0.0931	0.35	3.73	4.38	3.444	4.39	0.0821	1.25	1.00

*Data may require some reprocessing (slight shift after gains were run)

continued	Uncorrected ages (Ma)							
	$^{207}Pb/^{206}Pb$	2σ abs	$^{206}Pb/^{238}U$	2σ abs	$^{207}Pb/^{235}U$	2σ abs	$^{208}Pb/^{232}Th$	2σ abs
Standards								
manmon 9	572.0	25.2	560.3	9.8	562.7	15.2	532.2	13.0
manmon 10	576.1	25.7	557.3	9.5	561.0	15.0	527.9	12.1
manmon 11	553.4	22.1	556.2	9.2	555.6	13.8	564.4	12.4
FC-1 9	48.4	40.8	55.1	0.9	54.9	1.3	54.6	1.2
FC-1 10	46.4	38.9	54.7	0.9	54.5	1.3	55.1	1.2
FC-1 11	36.9	28.2	54.5	0.9	54.2	1.1	54.6	1.2
LU1 allanite 1	2538.4	25.0	1754.4	43.1	2142.4	176.2	1899.0	49.2
LU1 allanite 2	2188.3	34.4	1832.9	76.1	2005.5	231.1	1661.4	49.3
LU1 allanite 3	2301.3	17.8	1854.9	33.5	2075.1	120.4	1869.1	42.1
LU1 monazite 1	1317.0	8.8	1210.0	23.7	1249.1	44.3	1290.4	30.3
LU1 monazite 2	1457.4	9.8	1409.2	24.6	1428.5	50.4	1484.9	34.0
LU1 monazite 3	1331.9	4.6	1326.8	22.9	1328.8	42.3	1437.3	37.1
manmon 12	611.0	24.8	569.6	41.4	578.0	53.6	541.7	30.3
manmon 13	558.0	25.3	563.0	40.5	562.0	51.3	525.5	27.0
manmon 14	546.8	23.6	563.9	40.5	560.5	50.9	556.7	28.7
FC-1 12	58.5	42.5	56.1	3.9	56.2	4.1	56.4	2.9
FC-1 13	96.9	47.5	56.1	3.9	57.0	4.2	54.9	2.8
FC-1 14	79.7	47.7	56.0	3.9	56.5	4.2	55.6	2.8
Sample (see Fig. 6.12)								
B06/64 allanite 1	4926.9	5.4	1041.6	93.2	3062.6	975.3	356.2	27.1
B06/64 allanite 2	4892.5	8.6	696.5	57.6	2629.9	690.0	569.8	29.7
B06/64 allanite 3.1	4939.1	4.5	1465.5	118.2	3436.5	1138.3	543.2	32.1
B06/64 allanite 3.2	4932.9	4.9	1027.9	80.2	3052.8	885.7	367.9	18.5
B06/64 allanite 4	4944.9	3.9	1630.1	127.6	3558.2	1194.5	716.8	39.1
B06/64 allanite 6	4933.5	7.9	1318.4	102.4	3317.5	1040.8	341.7	18.4
B06/64 allanite 7.1*	4922.1	4.0	1044.6	88.0	3062.4	937.7	603.5	71.2
B06/64 allanite 7.2*	4941.0	4.0	1582.6	122.4	3522.6	1163.4	732.2	38.3
B06/64 allanite 5*	4899.9	7.9	887.8	67.4	2879.1	774.7	511.6	28.0
Standards								
LU1 allanite 4	2381.7	23.7	1691.6	134.0	2023.6	378.9	1704.1	88.4
LU1 allanite 5	2281.6	30.6	1572.1	125.1	1900.9	343.3	1530.0	109.3
LU1 allanite 6	2103.1	38.2	1495.3	122.7	1766.0	312.5	1320.8	90.2
LU1 monazite 4	1374.1	8.2	1383.0	106.0	1379.5	185.7	1337.8	70.8
LU1 monazite 5	1371.6	5.4	1329.5	104.3	1345.7	182.6	1402.6	71.5
LU1 monazite 6	1361.2	3.8	1307.0	98.9	1327.7	172.8	1345.7	68.9
manmon 15	553.0	19.9	581.4	53.0	575.6	65.9	548.1	9.6
manmon 16	554.0	20.4	546.5	49.6	548.0	61.9	542.3	9.1
manmon 17	555.3	20.1	538.0	48.6	541.3	60.7	547.0	9.1
FC-1 15	94.9	39.4	56.0	4.9	56.9	5.2	54.2	0.9
FC-1 16	79.1	35.7	54.3	4.7	54.9	5.0	54.3	0.9
FC-1 17	40.2	30.5	54.6	4.8	54.2	4.9	55.0	1.0
Other								
B06/64 garnet								
LU1 allanite raster	2053.4	22.4	1190.4	112.7	1537.2	275.4	1688.8	77.4
LU1 monazite raster	1489.0	13.2	1532.6	149.8	1514.4	268.4	1594.8	35.6

*Data may require some reprocessing (slight shift after gains were run)

NB. Standard/sample data are presented in order of analysis.

Appendix D: Mineral standards

D1 The K23 garnet 'standard' for garnet LA–ICPMS analysis

D1.1 Background

Fragments (mm-sized) of a garnet megacryst, K23 (collected in Kakanui, New Zealand, and sent to J. Chambers courtesy of Thomas Zack, University of Heidelberg) were mounted in a 4 mm thick resin block (Fig. D1.1). Despite the presence of late alteration veins/cracks that are chemically distinct from the bulk of the garnet crystal (easy to spot and can be avoided during analysis), and the lack of 'accepted' trace element concentration values (due to some inter-lab inconsistency and insufficient data), the homogeneity of the K23 garnet means that it is a good sample to monitor the long-term reproducibility (the variability of a measurement made by *different* operators on the *same* instrument) of garnet analyses; not to be confused with either repeatability (the variability of a measurement made by the *same* operator on the *same* instrument), precision from counting statistics or accuracy (the uncertainty of the 'true value'). No data from the K23 garnet have been published, although it is hoped that one day the 'critical mass' of data will be reached permitting a publishable garnet 'standard' dataset (T. Zack, *pers. comm.*, 2007). A value of 5.3 CaO wt % was used for normalisation purposes, the average of a subtle, but real CaO variation within the K23 garnet between 5.1 and 5.4 wt %.

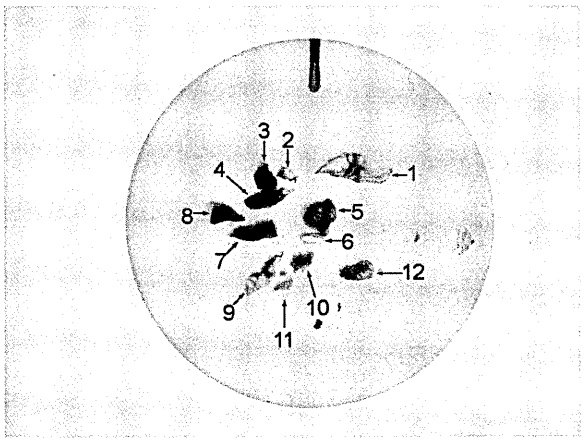

Fig. D1.1 Fragments of garnet K23 in resin block (diameter 2.5 cm).

D1.2 Results

The K23 garnet 'standard' yielded an equivalent or better external repeatability than the NIST glass standard (analysed over the same analytical period), for all trace elements >2 ppm concentration and including several at the 1 ppm level (highlighted cells, Table D1.1). Notable

improvement is seen in the repeatability of the analysis of Fe (4.8% rsd cf. 17.4% rsd, K23 and NIST respectively) and P (3.4% rsd cf. 21.9% rsd, K23 and NIST respectively).

Table D1.1 Comparison of LA-ICPMS standard data

	NIST glass std (Appendix C4.3)			K23 garnet 'std' (Appendix C4.4)				Comparison		
	mean	std dev	1x rsd (%)	mean		std dev	1x rsd (%)	mean NIST/ mean K23	NIST rsd - K23 rsd	
Si	335917	5295.97	1.6	190052		4155	2.2	2	-0.6	Si
P	57	12.46	21.9	103		3	3.4	1	18.5	P
^{43}Ca	85708	1812.82	2.1	38105		215	0.6	2	1.5	^{43}Ca
^{44}Ca	85743	1821.34	2.1	37879		0	0.0	2	2.1	^{44}Ca
Sc	41	1.20	2.9	140		5	3.5	0	-0.6	Sc
Ti	41	1.19	2.9	2860		47	1.6	0	1.3	Ti
V	38	1.05	2.8	160		5	3.1	0	-0.3	V
Cr	35	1.56	4.4	398		8	2.1	0	2.3	Cr
Mn	36	1.51	4.2	2198		26	1.2	0	3.0	Mn
Fe	57	9.94	17.4	84538		4098	4.8	0	12.5	Fe
Co	33	0.68	2.1	55		1	1.9	1	0.1	Co
Ni	36	0.82	2.3	51		1	2.3	1	-0.1	Ni
Ga	32	0.70	2.2	6		0	2.4	5	-0.3	Ga
Rb	32	0.95	3.0	0	~bd	0	99.1	1713	-96.1	Rb
Sr	75	2.12	2.8	0		0	36.2	249	-33.4	Sr
Y	41	1.60	3.9	61		2	3.5	1	0.4	Y
Zr	39	1.48	3.8	61		2	3.7	1	0.0	Zr
Nb	43	1.03	2.4	0	~bd	0	11.8	502	-9.4	Nb
Ba	40	1.34	3.4	0	~bd	0	73.3	322	-69.9	Ba
La	36	1.34	3.7	0	~bd	0	36.3	1612	-32.6	La
Ce	39	1.17	3.0	0	~bd	0	7.4	172	-4.3	Ce
Pr	38	1.25	3.3	0	~bd	0	5.3	401	-2.1	Pr
Nd	35	1.30	3.7	1		0	4.4	31	-0.8	Nd
Sm	39	1.59	4.1	1		0	3.8	29	0.3	Sm
Eu	36	1.38	3.8	1		0	2.7	46	1.1	Eu
Gd	40	1.70	4.3	4		0	4.4	10	-0.2	Gd
Tb	39	1.79	4.6	1		0	4.7	39	0.0	Tb
Dy	38	1.78	4.7	9		0	4.5	4	0.2	Dy
Ho	40	1.84	4.6	2		0	4.9	17	-0.3	Ho
Er	40	1.89	4.7	8		0	4.6	5	0.1	Er
Tm	40	1.92	4.8	1	~bd	0	5.4	31	-0.6	Tm
Yb	42	1.97	4.7	10		0	4.6	4	0.1	Yb
Lu	40	1.92	4.8	2	~bd	0	5.7	27	-0.8	Lu
Hf	38	1.99	5.2	1	~bd	0	5.8	29	-0.6	Hf
Ta	42	1.85	4.4	0	~bd	0	27.8	6265	-23.3	Ta
Pb	36	1.39	3.9	0	~bd	0	69.0	2088	-65.1	Pb
Th	39	1.97	5.0	0	~bd	0	52.8	8465	-47.9	Th
U	36	1.32	3.7	0	~bd	0	39.5	5865	-35.8	U

bd, below detection

An inter-laboratory comparison shows a good fit to data from four laboratories (Fig. D1.2 and Table D1.2). Two laboratories (numbers 5 and 6) deviate from the other five labs (which includes my OU data, 'lab 7').

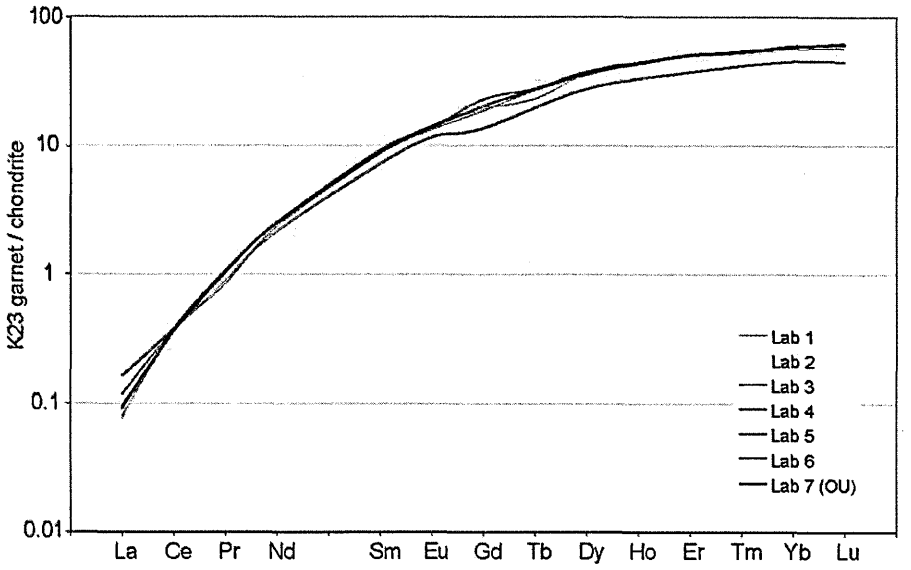

Fig. D1.2 Inter-laboratory comparison of LA–ICPMS K23 garnet data (Table D1.2).

Table D1.2 K23 garnet inter-lab. LA-ICPMS data (normalised to chondrite, McDonough & Sun, 1995)

	Lab 1	Lab 2	Lab 3	Lab 4	Lab 5	Lab 6	Lab 7 (OU)*	*Mean*	*1s.d.*
La	0.08	0.09	0.08	0.09	0.16	0.12	0.09	*0.10*	*0.03*
Ce	0.36	0.36	0.37	0.38	0.38	0.37	0.37	*0.37*	*0.01*
Pr	1.03	1.06	1.07	1.06	0.92	0.85	1.03	*1.00*	*0.08*
Nd	2.50	2.48	2.50	2.51	2.17	2.36	2.52	*2.43*	*0.13*
Sm	8.74	9.31	8.76	9.22	7.23	8.67	8.98	*8.70*	*0.69*
Eu	13.44	13.78	14.21	13.71	11.62	13.39	14.02	*13.45*	*0.86*
Gd	19.39	19.80	19.25	22.79	13.65	18.79	20.36	*19.15*	*2.76*
Tb	25.82	26.68	23.17	27.74	na	27.29	27.66	*26.40*	*1.73*
Dy	35.70	35.97	36.21	37.41	27.67	35.27	36.82	*35.01*	*3.31*
Ho	43.38	42.23	42.78	44.49	na	43.92	43.43	*43.37*	*0.80*
Er	49.43	48.99	50.49	49.85	37.32	50.17	51.15	*48.20*	*4.85*
Tm	51.26	51.58	54.56	53.30	na	53.53	53.29	*52.92*	*1.26*
Yb	55.96	59.09	56.67	58.57	45.33	58.27	59.49	*56.20*	*4.96*
Lu	59.13	60.21	57.28	62.67	45.14	61.48	61.11	*58.15*	*5.99*

na, not analysed

Data from laboratories 1 to 6 courtesy of T. Zack, apart from * (in Appendix C4.4)

D2 The Δ33 Uraninite U-Pb internal standard

Small grains of euhedral uraninite from a sample of leucogranite from southern Tibet were used as a U–Pb LA–ICPMS internal standard for dating uraninite from this study. The sample was collected by BC Burchfiel, KV Hodges, and L Royden from the east side of the Rongbuk Valley, northeast of Mt Everest (86°50'E, 28°10'N, approximately) and other geological and age information for this sample is contained in Copeland et al. (1988). In that study, monazite analyses are inherited with a maximum age of ~21 Ma and there is reported a single somewhat imprecise concordant U–Pb age of zircon of 19.5 ± 0.4 Ma. Subsequent to that study, uraninite and further monazite analyses were obtained from this same sample, as shown in the following table. The five uraninite analyses have a weighed mean $^{206}Pb/^{238}U$ age of 19.93 ± 0.17 Ma and a weighted mean $^{207}Pb/^{206}Pb$ age of 41 ± 1 Ma, indicating slight normal discordance. This discordance is attributed to excess ^{207}Pb arising from preferential incorporation of ^{231}Pa during crystallisation (see Parrish and Noble, 2003). In this study, a reference age of 20.0 Ma is used for the Δ33 uraninite used to calculate the ages of uraninite unknowns in the samples for this study using LA–ICPMS analysis with similar laser settings. Thus the uraninite data in this study are matrix matched to a uraninite standard.

The U–Pb data in the accompanying table used the ID–TIMS method and were made at the Geological Survey of Canada in 1995 by R Parrish using methods summarised in Parrish et al. (1987). The LA–ICPMS data for the Δ33 uraninites are also shown in an accompanying table to illustrate the quality of the analyses and reproducibility of the data.

References

Copeland, P., Parrish, R.R., and Harrison, T.M., 1988, Identification of inherited radiogenic Pb in monazite and its implications for U-Pb systematics; Nature, 333, 760-763.

Parrish, R. R., Roddick, J. C., Loveridge, W. D., and Sullivan, R. W., 1987, Uranium-Lead analytical techniques at the geochronology laboratory; Geological Survey of Canada Paper 87-2, p. 3-7.

Parrish, R.R., and Noble S.R., 2003, Zircon U–Pb geochronology by isotope dilution – thermal ionisation mass spectrometry (ID–TIMS), in John M. Hanchar and Paul W.O. Hoskin, eds., Zircon, Reviews in Mineralogy and Geochemistry, v. 53 p. 183-213, Mineralogical Society of America and Geochemical Society.

Laser Ablation U-Pb analyses

Sample	206/238norm	error %	207/235norm	error %	206/238 age age(Ma)	2s err (Ma)	207/206 age (Ma)	2s err (Ma)
Uraninite crystals from sample Δ33								
Analysis 1	0.00315	1.0	0.0199	2.4	20.3	0.4	-11	103
Analysis 2	0.00297	1.6	0.0193	2.6	19.1	0.6	60	95
Analysis 3	0.00264	0.9	0.0172	2.7	17.0	0.3	59	122
Analysis 4	0.00293	0.8	0.0208	2.3	18.9	0.3	263	97
Analysis 5	0.00331	0.9	0.0220	2.2	21.3	0.4	106	95
Analysis 6	0.00349	0.9	0.0224	2.0	22.4	0.4	31	87
Analysis 7	0.00329	1.8	0.0210	2.8	21.2	0.7	13	103
Analysis 8	0.00347	0.9	0.0227	2.2	22.3	0.4	69	95
Analysis 9	0.00310	1.0	0.0197	2.0	20.0	0.4	-3	85
Analysis 10	0.00281	1.3	0.0171	2.3	18.1	0.5	-105	93
Analysis 11	0.00296	0.7	0.0187	2.3	19.0	0.3	-13	105
Mean	0.00310	8.7	0.0201	9.6	20.0	1.7	43	92

Notes:
Uncertainties are based upon the signal intensity measurement errors; the reproducibility of these standards is quadratically included in all uncertainties of unknowns
Common Pb correction in these analyses was negligible
norm, refers to normalised values of measured ratios, using a mean age of 20.0 Ma as determined from ID-TIMS measurements

Isotope dilution U-Pb analyses

Analysis	Weight (mg, microns)	U (ppm)	Pb** (ppm)	206Pb^ 204Pb	Pbc^^ (pg)	Th*** U	206Pb*^ 238U	1 std err (%)	207Pb*^ 235U	1 std err (%)	207Pb*^ 206Pb	1 std err (%)	206Pb*^ 238U	2 std err (Ma)	207Pb*^ 235U	2 std err (Ma)	207Pb*^ 206Pb	2 std err (Ma)	Corr. coeff
Uraninite crystals from sample Δ33																			
U-5	1.7	951450	2673	60490	5.2	0.044	0.003110	0.3	0.02008	0.3	0.04681	0.03	20.0	0.1	20.2	0.1	39.5	1.4	0.99
U-4	6.2	700800	1971	221800	3.8	0.050	0.003111	0.42	0.02009	0.42	0.04684	0.03	20.0	0.2	20.2	0.2	40.9	1.3	0.99
U-3	1.0	581010	1638	9061	12.4	0.063	0.003114	0.16	0.02011	0.16	0.04684	0.07	20.0	0.1	20.2	0.1	40.9	3.2	0.91
U-6	24.3	850980	2378	39230	101	0.044	0.003094	0.08	0.01998	0.12	0.04684	0.05	19.9	0.1	20.1	0.1	40.9	2.5	0.94
U-8	6.8	926650	2582	98610	12.2	0.050	0.003083	0.17	0.01991	0.19	0.04685	0.05	19.8	0.1	20.0	0.1	41.3	2.4	0.97
Weighted Mean													20.0	0.2			41	1	

** radiogenic Pb
*** atomic ratio of Th to U, calculated from radiogenic 208Pb/206Pb
^ Measured ratio, corrected for spike and Pb fractionation (0.09%/amu)
^^ Total common Pb in analysis, corrected for fractionation and spike
*^ Corrected for blank Pb and U, and common Pb (Stacey-Kramers model Pb equivalent to interpreted age of mineral)